

AD-A244 162



ARO 28904.1-MACF

(2)

# Developments in Mechanics

DTIC  
S D  
JAN 07 1992

Volume 16

Proceedings  
of the  
Twenty-Second Midwestern Mechanics Conference

This document has been approved  
for public release and sale; its  
distribution is unlimited.

*Edited by*  
**R. C. Batra and B. F. Armaly**

University of Missouri - Rolla  
Rolla, Missouri  
October 6-9, 1991

## REPORT DOCUMENTATION PAGE

Form Approved

OMB No. 0704-0188

Public reporting burden for this collection of information is estimated to average 1 hour per response, including the time for reviewing instructions, searching existing data sources, gathering and maintaining the data needed, and completing and reviewing the collection of information. Send comments regarding this burden estimate or any other aspect of this collection of information, including suggestions for reducing this burden, to Washington Headquarters Services, Directorate for Information Operations and Reports, 1215 Jefferson Davis Highway, Suite 1204, Arlington, VA 22202-4302, and to the Office of Management and Budget, Paperwork Reduction Project (0704-0188), Washington, DC 20503.

1. AGENCY USE ONLY (Leave blank)	2. REPORT DATE Oct 1991	3. REPORT TYPE AND DATES COVERED Final 1 Jun 91 - 31 May 92	
4. TITLE AND SUBTITLE Twenty-Second Midwestern Mechanics Conference		5. FUNDING NUMBERS DAAL03-91-G-0197	
6. AUTHOR(S) R.C. Batra and B.F. Armaly (editors)		8. PERFORMING ORGANIZATION REPORT NUMBER	
7. PERFORMING ORGANIZATION NAME(S) AND ADDRESS(ES) University of Missouri-Rolla Rolla, MO 65401-0249		10. SPONSORING/MONITORING AGENCY REPORT NUMBER ARO 28904.1-MA-CF	
9. SPONSORING/MONITORING AGENCY NAME(S) AND ADDRESS(ES) U. S. Army Research Office P. O. Box 12211 Research Triangle Park, NC 27709-2211		11. SUPPLEMENTARY NOTES The view, opinions and/or findings contained in this report are those of the author(s) and should not be construed as an official Department of the Army position, policy, or decision, unless so designated by other documentation.	
12a. DISTRIBUTION/AVAILABILITY STATEMENT Approved for public release; distribution unlimited.		12b. DISTRIBUTION CODE	
13. ABSTRACT (Maximum 200 words)  Developments in Mechanics, Volume 16, is the Proceedings of the 22nd Midwestern Mechanics Conference hosted by the University of Missouri - Rolla, October 6-9, 1991. The conference was sponsored by the Department of Mechanical and Aerospace Engineering and Engineering Mechanics, and the School of Engineering, with financial support also provided by the U. S. National Science Foundation and the U. S. Army Research Office.			
14. SUBJECT TERMS Mechanics, Conference		15. NUMBER OF PAGES 635	
		16. PRICE CODE	
17. SECURITY CLASSIFICATION OF REPORT UNCLASSIFIED	18. SECURITY CLASSIFICATION OF THIS PAGE UNCLASSIFIED	19. SECURITY CLASSIFICATION OF ABSTRACT UNCLASSIFIED	20. LIMITATION OF ABSTRACT UL

# Twenty-Second Midwestern Mechanics Conference...

October 6-9, 1991  
University of Missouri - Rolla  
Rolla, Missouri



Accession For	
NTIS CRA&I	<input checked="" type="checkbox"/>
DTIC TAB	<input type="checkbox"/>
Unannounced	<input type="checkbox"/>
Justification	
By	
Distribution/	
Availability Codes	
Dist	Avail and/or Special
A-1	

Edited by R. C. Batra and B. F. Armaly

Hosted by  
The Department of Mechanical & Aerospace Engineering  
& Engineering Mechanics, and  
The School of Engineering, University of Missouri - Rolla

92-00320



92 1 6 108

### **Board of Directors of the Midwestern Mechanics Conference**

B. F. Armaly	University of Missouri - Rolla
R. C. Batra	University of Missouri - Rolla
L. E. Ehlers	University of Nebraska - Lincoln
R. E. Ekstrom	University of Nebraska - Lincoln
J. F. Hamilton	Purdue University
J. B. Ligon	Michigan Technological University
W. Soedel	Purdue University

### **Conference Organizing Committee**

B. F. Armaly	Conference Co-Chairman
R. C. Batra	Conference Chairman
R. L. Davis	
W. Eversman	
M. C. Jischke	Conference Honorary Chairman
L. R. Koval	
W. Ries	Conference Coordinator

### **Scientific Committee**

B. S. AbdulNour	University of Wyoming
S. Abrate	University of Missouri - Rolla
R. C. Batra	University of Missouri - Rolla
T. Dewhurst	University of Maine - Orono
L. R. Dharani	University of Missouri - Rolla
M. S. Qatu	Dresser Industries, Inc.
D. N. Riahi	University of Illinois - Urbana
T. G. Shawki	University of Illinois - Urbana
G. L. Viegelaan	Michigan Technological University
H. M. Zbib	Washington State University



## Foreword

Developments in Mechanics, Volume 16, is the Proceedings of the 22nd Midwestern Mechanics Conference hosted by the University of Missouri - Rolla, October 6-9, 1991. The conference was sponsored by the Department of Mechanical and Aerospace Engineering and Engineering Mechanics, and the School of Engineering, with financial support also provided by the U. S. National Science Foundation and the U. S. Army Research Office. The generous support of the sponsors is deeply appreciated.

The Midwestern Mechanics Conference has been held every other year since 1950. The conference serves as an excellent forum for the exchange of ideas, and is a catalyst for future research. Over the years, it has developed an outstanding reputation for attracting renowned speakers and participants with diverse areas of interest in mechanics. The 1991 conference is the twenty-second in this series.

A large number of papers in these proceedings were invited, but editorially no distinction has been made between invited and contributed papers. Persons who helped organize one or more technical session are listed as members of the scientific committee. All authors were allowed two pages. The authors are free to publish their work in a suitable journal. Even though paper summaries were reviewed, the authors of accepted papers were not requested to incorporate reviewers' suggestions and/or correct typographical errors noticed. The summaries included in the proceedings were photographically reproduced; the authors are therefore responsible for their content.

A special session was organized on Current and Future Research Funding Trends from governmental agencies. Appreciation is expressed to the representatives of the National Science Foundation, Army Research Office, and the Department of Energy for their contributions to the conference.

The sessions and papers are identified by a series of letters and numerals. The first letter indicates the day of the session (M = Monday, T = Tuesday, W = Wednesday). The next letter indicates whether the session is in the morning (M) or afternoon (A), and the Roman numeral following this stands for the set of sessions in the morning or afternoon. The number following the dash distinguishes parallel sessions. Thus, TAI-4 signifies a session in the first set of sessions (right after lunch) on Tuesday afternoon. To find a paper by an author, first find the session number, and then the page number for that session.

The local organizing committee sincerely appreciates the time and effort authors have spent in preparing and submitting numerous interesting papers. We are grateful to the authors, participants, session chairs, and session organizers for making the conference a successful one. The financial support provided by the U. S. National Science Foundation and the Army Research Office is gratefully acknowledged. R. C. Batra is also indebted to Mrs. Sandy Seid for taking care of the work associated with the conference cheerfully.

The Editors

## **Monday Morning, October 7, 1991**

### **General Session**

Representatives from the NSF, ARO, and DOE: "Current and Future Research Funding Trends in Mechanics"

### **Parallel Sessions 10:00 - 12:00**

<b>Session MM-1</b>	<b>Composites</b> .....	<b>1</b>
<b>Session MM-2</b>	<b>Impact/Penetration</b> .....	<b>7</b>
<b>Session MM-3</b>	<b>Nonlinear Elasticity</b> .....	<b>14</b>
<b>Session MM-4</b>	<b>Fluid Mechanics</b> .....	<b>20</b>
<b>Session MM-5</b>	<b>Experimental Solid Mechanics</b> .....	<b>28</b>
<b>Session MM-6</b>	<b>Beams/Plates/Shells</b> .....	<b>35</b>

## **Monday Afternoon, October 7, 1991**

### **Parallel Sessions 1:00 - 3:00**

<b>Session MAI-1</b>	<b>Composites II</b> .....	<b>45</b>
<b>Session MAI-2</b>	<b>Material Characterization for Dynamic Problems</b> .....	<b>52</b>
<b>Session MAI-3</b>	<b>Elasticity</b> .....	<b>60</b>
<b>Session MAI-4</b>	<b>Fluids</b> .....	<b>66</b>
<b>Session MAI-5</b>	<b>Experimental Solid Mechanics</b> .....	<b>71</b>
<b>Session MAI-6</b>	<b>Finite Element Solution of Problems</b> .....	<b>80</b>
<b>Session MAI-7</b>	<b>Vibrations</b> .....	<b>90</b>

**Parallel Sessions 3:30 - 5:30**

<b>Session MAII-1</b>	<b>Composites III</b> .....	<b>97</b>
<b>Session MAII-2</b>	<b>Material Instability I</b> .....	<b>113</b>
<b>Session MAII-3</b>	<b>Elasticity</b> .....	<b>118</b>
<b>Session MAII-4</b>	<b>Numerical Methods</b> .....	<b>131</b>
<b>Session MAII-5</b>	<b>Fracture</b> .....	<b>140</b>
<b>Session MAII-6</b>	<b>Mathematical Methods</b> .....	<b>156</b>

**Tuesday Morning, October 8, 1991**

**Parallel Sessions 8:00 - 10:00**

<b>Session TMI-1</b>	<b>High Temperature Composites I</b> .....	<b>169</b>
<b>Session TMI-2</b>	<b>Viscoplasticity</b> .....	<b>175</b>
<b>Session TMI-3</b>	<b>Elasticity</b> .....	<b>181</b>
<b>Session TMI-4</b>	<b>Turbulent Flows</b> .....	<b>185</b>
<b>Session TMI-5</b>	<b>Granular Materials/Fluids</b> .....	<b>197</b>
<b>Session TMI-6</b>	<b>Mathematical Methods</b> .....	<b>203</b>

**Parallel Sessions 10:30 - 12:30**

<b>Session TMII-1</b>	<b>High Temperature Composites II</b> .....	<b>212</b>
<b>Session TMII-2</b>	<b>Material Instability II</b> .....	<b>219</b>
<b>Session TMII-3</b>	<b>Continuum Mechanics</b> .....	<b>227</b>
<b>Session TMII-4</b>	<b>Crack/Creep</b> .....	<b>234</b>
<b>Session TMII-5</b>	<b>Numerical Methods in Metal Forming I</b> .....	<b>241</b>

<b>Session TMII-6</b>	<b>Plates/Shells</b> .....	<b>249</b>
-----------------------	----------------------------	------------

## **Tuesday Afternoon, October 8, 1991**

### **Parallel Sessions 1:30 - 3:30**

<b>Session TAI-1</b>	<b>Composites IV</b> .....	<b>260</b>
<b>Session TAI-2</b>	<b>Material Instability III</b> .....	<b>267</b>
<b>Session TAI-3</b>	<b>Continuum Mechanics</b> .....	<b>273</b>
<b>Session TAI-4</b>	<b>Flow Separation</b> .....	<b>279</b>
<b>Session TAI-5</b>	<b>Numerical Methods in Metal Forming II</b> .....	<b>289</b>
<b>Session TAI-6</b>	<b>Constitutive Modelling</b> .....	<b>296</b>
<b>Session TAI-7</b>	<b>Beams/Plates/Shells</b> .....	<b>304</b>

### **Parallel Sessions 4:00 - 6:00**

<b>Session TAI-1</b>	<b>Composites V</b> .....	<b>314</b>
<b>Session TAI-2</b>	<b>Expert Systems for Manufacturing/Modelling</b> .....	<b>329</b>
<b>Session TAI-3</b>	<b>Mechanics of Concrete and Structures</b> .....	<b>345</b>
<b>Session TAI-4</b>	<b>Newtonian and Non-Newtonian Fluids</b> .....	<b>354</b>
<b>Session TAI-5</b>	<b>Granular Materials/Fluids</b> .....	<b>365</b>
<b>Session TAI-6</b>	<b>Experimental Fluid Mechanics</b> .....	<b>376</b>

## **Wednesday Morning, October 9, 1991**

### **Parallel Sessions 8:00 - 10:00**

<b>Session WMI-1</b>	<b>Composites VI</b> .....	<b>389</b>
<b>Session WMI-2</b>	<b>Material Instability IV</b> .....	<b>401</b>
<b>Session WMI-3</b>	<b>Continuum Mechanics</b> .....	<b>408</b>
<b>Session WMI-4</b>	<b>Fluids (Convection)</b> .....	<b>415</b>
<b>Session WMI-5</b>	<b>Magneto-Elasticity</b> .....	<b>424</b>
<b>Session WMI-6</b>	<b>Plates/Shells</b> .....	<b>434</b>
<b>Session WMI-7</b>	<b>Vibrations</b> .....	<b>446</b>

### **Parallel Sessions 10:30 - 12:30**

<b>Session WMII-1</b>	<b>Fiberglass Resin Composites</b> .....	<b>464</b>
<b>Session WMII-2</b>	<b>Material Instability V</b> .....	<b>472</b>
<b>Session WMII-3</b>	<b>Mechanical Systems</b> .....	<b>477</b>
<b>Session WMII-4</b>	<b>Fluids</b> .....	<b>489</b>
<b>Session WMII-5</b>	<b>Stress Analysis</b> .....	<b>505</b>
<b>Session WMII-6</b>	<b>Plates/Shells</b> .....	<b>518</b>
<b>Session WMII-7</b>	<b>Belts</b> .....	<b>533</b>

## **Wednesday Afternoon, October 9, 1991**

### **Parallel Sessions 1:30 - 3:30**

<b>Session WA-1</b>	<b>Thermal and Mechanical Problems</b> .....	<b>543</b>
---------------------	--	------------

<b>Session WA-2</b>	<b>Damage Mechanics/Crack/Plasticity . . . . .</b>	<b>560</b>
<b>Session WA-3</b>	<b>Mechanical Systems/Mechanics . . . . .</b>	<b>570</b>
<b>Session WA-4</b>	<b>Modelling Related Problems . . . . .</b>	<b>582</b>
<b>Session WA-5</b>	<b>Stress Analysis of Structural Components . . . . .</b>	<b>596</b>
<b>Session WA-6</b>	<b>Plates/Shells . . . . .</b>	<b>614</b>

## ONR's MECHANICS OF COMPOSITES RESEARCH PROGRAM

YAPA D. S. RAJAPAKSE  
Office of Naval Research  
Mechanics Division  
Arlington, VA. 22217

An overview will be provided of the research thrust in Mechanics of Composites within the Mechanics Division at the Office of Naval Research. Recent accomplishments will be summarized and future research directions will be discussed.

Naval structures operate in a variety of hostile environments and are subjected to complex loading conditions. Composite materials have been used extensively in high performance naval aircraft and missile structures. Composites have the potential of providing many advantages, including greater depth capabilities and enhanced stealth characteristics for submersibles. There is increased activity in thick composites research, especially in the area of the response of thick composites to compressive stress fields.

Research issues being addressed include three-dimensional constitutive equations and lamination theories, micromechanics, damage evolution, failure modes and mode coupling, failure theories, environmental effects, dynamic response and quantitative nondestructive evaluation.

Recent accomplishments which will be presented include: three-dimensional lamination theories based on micromechanics considerations; mixed mode delamination crack growth; compression failure in unidirectional composites; moisture induced damage and effects of stress; impact damage models and concepts for controlling impact damage; coupling between local material failure and structural failure; leaky Lamb wave technique for characterization of composite mechanical properties and defects; scanning acoustic microscopy for assessment of near surface microstructure.

# ASSESSMENT OF OVERALL PLASTIC STRAIN PREDICTIONS USING MICROMECHANICAL MODELS OF FIBROUS MEDIA

George J. Dvorak and Yehia A. Bahei-El-Din

Institute Center for Composite Materials and Structures  
and Department of Civil Engineering  
Rensselaer Polytechnic Institute  
Troy, New York 12180

Numerous analytical models have been proposed for prediction of the inelastic response of fibrous composites. In one class of models, micromechanical aspects of the composite are accounted for, and the overall strains are computed from constitutive behavior of the phases and their mutual constraints. Representation of the fiber/matrix interaction vary considerably among available material models. The self-consistent (Hill 1965) and Mori-Tanaka (1973) methods rely on Eshelby's solution of an inclusion problem in which a single elastic inclusion is embedded in an infinite elastic matrix, while the whole assembly is subjected to remote uniform stress or strain fields. In their application to elastic-plastic composites, these methods are modified so that successive problems are solved under incremental loading while the matrix assumes the instantaneous moduli computed with a plasticity model of the matrix material (Dvorak and Bahei-El-Din 1979, Lagoudas and Gavazzi 1990). The phase stresses and strains are known only in average sense, and the overall yield surface is found as the locus of overall stresses which correspond to initial yielding in the matrix. In this case, the assumed normality of the matrix plastic strain increment in the matrix stress space is carried into the overall stress space.

A semi-phenomenological bimodal theory (Dvorak and Bahei-El-Din 1987) was developed based on experimental observations from tests conducted on a boron/aluminum composite (Dvorak et al. 1988). The theory postulates two plastic deformation modes in fibrous composites, matrix-dominated mode (MDM), and fiber-dominated mode (FDM). In the MDM, plastic straining of the fibrous composite is caused by plastic slip on matrix planes which are parallel to the fiber longitudinal direction. Apart from specifying the direction of the slip planes, the fiber does not participate in this mode. In the FDM, both the fiber and the matrix deform together, and the overall response is found from an averaging model such as the self-consistent or Mori-Tanaka models. The overall yield surface consists of two branches, each corresponds to the onset of yielding in the composite derived from one of the postulated deformation modes. In this model too, the overall plastic strain increment is normal to the relevant branch of the yield surface.

More accurate micromechanical representation of fibrous media is found in periodic array models in which the microgeometry in the transverse plane is idealized by periodic dispersion of the fibers into the matrix. Under overall uniform fields, the response of the composite aggregate can be found from analysis of a unit cell. While numerous microgeometrical idealizations appear in the literature, only the Periodic Hexagonal Array



(PHA) model (Dvorak and Teply 1985, Teply and Dvorak 1988) provided upper and lower bounds on the overall instantaneous stiffness and compliance. In a typical PHA analysis under overall uniform fields, the local fields are assumed to be piecewise uniform and solution of the unit cell is found using the finite element method. Transformation of the local yield condition in each subelement to the overall stress space provides a cluster of overall yield branches, each corresponds to initial yielding in a matrix subelement. In this case, the overall plastic strain vector must lie within the cone of normals found from the overall yield branches which contain the loading point (Dvorak et al. 1990).

Reliability of the predictions offered by the above models can be evaluated only in comparison with experiments. This has been hindered by the lack of general experiments which can provide critical evaluation of theoretical models. The present paper is concerned with both experimental evaluation and theoretical predictions of the overall plastic strains and yield surfaces in fibrous composites. The paper presents results of an experimental/theoretical program aimed at development and evaluation of the micromechanical models described above. Specifically, overall yield surfaces and plastic strains found from multiaxial tests on a boron/aluminum composite are presented. Numerical simulations using three different models, the PHA model, the bimodal theory, and a modified Mori-Tanaka scheme, are also presented and compared to the experimental results. The paper addresses questions related to the notion of a yield surface and normality of plastic strains in fibrous media.

The results indicate that reliability of the predictions varied significantly, particularly where plastic strains are concerned. Only the PHA model appear to be of value in this regard, but the shape and position of the overall yield surfaces were well predicted even by the matrix-dominated mode of the bimodal theory.

#### References

- Dvorak, G.J. and Bahei-El-Din, Y.A., 1979, *Journal of the Mechanics and Physics of Solids*, Vol. 27, pp. 51-72.
- Dvorak, G.J. and Bahei-El-Din, Y.A., 1987, *Acta Mechanica*, Vol. 69, pp. 219-241.
- Dvorak, G.J., Bahei-El-Din, Y.A., Macheret, Y. and Liu, C.H., 1988, *Journal of the Mechanics and Physics of Solids*, Vol. 36, pp. 665-687.
- Dvorak, G.J., Bahei-El-Din, Y.A., Shah, R.S. and Nigam, H., 1990, *Inelastic Deformation of Composite Materials*, G.J. Dvorak, ed., Springer-Verlag, pp. 283-306.
- Dvorak, G.J. and Teply, J.L., 1985, *Plasticity Today: Modeling, Methods and Applications*, A. Siczuk and V. Bianchi, eds., Elsevier, Amsterdam, pp. 623-642.
- Hill, R., 1965, *Journal of the Mechanics and Physics of Solids*, Vol. 13, pp. 189-198.
- Lagoudas, D.C. and Gavazzi, A.C., 1990, *Inelastic Deformation of Composite Materials*, G.J. Dvorak, ed., Springer-Verlag, pp. 465-485.
- Mori, T. and Tanaka, K., 1973, *Acta Metallurgica*, Vol. 21, pp. 571-574.
- Teply, J.L. and Dvorak, G.J., 1988, *Journal of the Mechanics and Physics of Solids*, Vol. 36, pp. 29-58.

# THERMOVISCOPLASTICITY THEORY BASED ON OVERSTRESS APPLIED TO METAL MATRIX COMPOSITE ANALYSIS

Erhard Krempl  
Mechanics of Materials Laboratory  
Rensselaer Polytechnic Institute  
Troy, N.Y. 12180-3590

The thermoviscoplasticity theory based on overstress (TVBO) considers all inelastic deformation rate dependent and consequently does not use separate constitutive assumptions for time(rate)-independent plasticity and creep. Also, the concept of a yield surface and associated loading and unloading conditions are not employed. The small strain rate is the sum of the elastic, inelastic, and thermal strain rates (for the isothermal, case a finite deformation version is also available). The latter is the product of the temperature dependent coefficient of thermal expansion and the temperature rate. The inelastic strain rate is only a function of the overstress, the difference between the stress and the equilibrium stress, a state variable of TVBO. It represents the stress which can be sustained in equilibrium after inelastic deformation has occurred. Two other state variables, the kinematic stress and the rate-independent (isotropic) stress, are also part of the theory. The former sets the slope of the stress-strain diagram at the maximum strain of interest which can be positive, zero, or negative. For the modeling of cyclic neutral behavior, the rate-independent stress is constant but has a growth law for the modeling of cyclic hardening (softening). The rate form of Hooke's law constitutes the elastic strain rate. All constants can be a function of temperature and it is assumed that identification of the material properties under several isothermal conditions is sufficient to model the behavior under varying temperature. In the quasi elastic regions, the contribution of the inelastic strain rate is negligibly small and stress-strain diagrams appear to be linear. As the stress increases the inelastic contributions increase also and yielding is modeled before significant inelastic flow sets in. TVBO was shown to model rate sensitivity, creep, relaxation, and cyclic hardening (softening) in uniaxial and biaxial loading. For high temperature, a recovery of state formulation is also available.

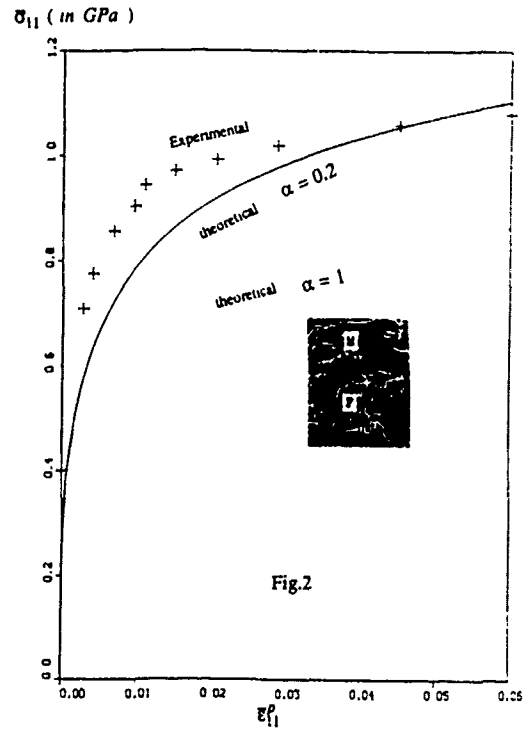
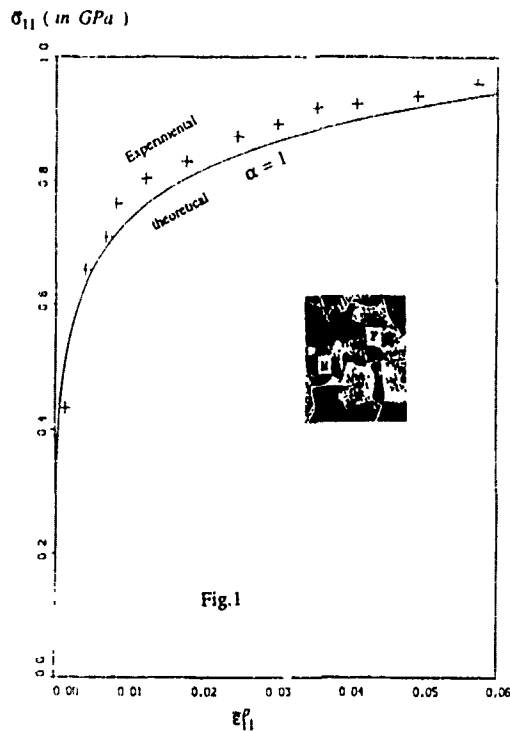
The isotropic TVBO is combined with the Vanishing Fiber Diameter composite model (VFD) proposed by Dvorak and Bahai-El-Din to obtain a representation of metal matrix fibrous composite behavior. Fiber volume fraction characterizes the composite. Three model systems (Gr/Al, B/Al, and SiC/Ti) are investigated using available material data and assumed but realistic properties. Investigations include the effect of residual stresses due to fabrication on the thermal cycling behavior (Gr/Al) and the subsequent isothermal stress-strain behavior (B/Al). Residual stresses can redistribute during rest periods at no load and cause a marked asymmetry in the stress-strain behavior in the fiber direction. For SiC/Ti, numerical experiments were performed to elucidate the behavior under in-phase and out-of-phase thermomechanical cycling. Significant ratchetting is observed in the transverse direction.

## A THEORETICAL MODEL FOR THE PLASTIC BEHAVIOR OF STABLE DUAL-PHASE STEELS

A. Bhattacharyya and G.J. Weng  
Department of Mechanics and Materials Science  
Rutgers University  
New Brunswick, New Jersey 08903

The morphological influence of the martensitic phase with prior phase transformation on the deformation behavior of isotropic dual-phase steels is studied by a simple, although approximate, theory using Eshelby's(1957) classical solution of a misfitting inclusion in an infinite medium. The finite concentration effect is incorporated using Mori-Tanaka's(1973) concept of average stress. The theory is intended for randomly oriented spheroidal inclusions though extension to the ellipsoidal case is conceptually straight forward. The analysis unfolds after that of Qiu and Weng(1991). A parametric study is done to uncover the effect of phase transformation strain on the overall volume change of the two-phase composite. It is analytically shown that the dual-phase system is rendered plastically incompressible when the constituent phases share the same bulk moduli. For the isotropic system, the effective stress of the ductile matrix is insensitive to the prior phase transformation strain but the subsequent total strain of the two-phase system in general depends on it. When both phases share the same bulk moduli, the latter dependence becomes constant and thus the subsequent plastic behavior of the composite according to this model remains independent of the prior phase transformation strain. Such will not be the case when the bulk moduli of the phases are not the same. Moreover, we assume, as is reasonable for most steels, that the phases share the same elastic moduli. Thus the yield stress of the composite also turns out to be the same as the yield stress of the matrix. The overall implication is that the composite, like the ductile matrix, can be represented by five parameters, two of them elastic -  $\kappa$  and  $\mu$  - and three of them plastic -  $\sigma_y$ ,  $h$  and  $n$  - when the modified Ludwik equation is chosen as the plastic constitutive equation for the ductile phase. The Prandtl-Reuss flow rule can also be used.

In order to conduct a theoretical study of the morphological influence of the inclusions on the overall behavior of the composite, the phenomenological Considere Criterion is used to find the anticipated uniaxial stress and strain at necking. Consistent with experimental observations of Sugimoto et al.(1985) as also that of Koo and Thomas(1977), it is found that any kind of reinforcement is beneficial to the composite, with the disc type providing the best ductility and strength. A quantitative assessment is provided. Subsequently, the elastoplastic behavior of the composite is



compared with the experimental data of Sugimoto et al(1985) for dual phase steels, at aspect ratios  $\alpha=1$  and 0.2. Reasonably good results are obtained as evident from Figures 1 and 2 above.

## References

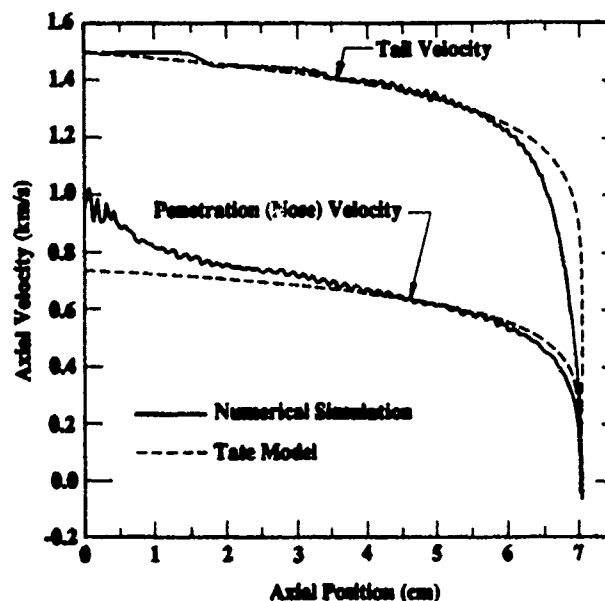
- [1] J.D. Eshelby, 1957, The determination of the Elastic field of an Ellipsoidal Inclusion and related problems, *Proceedings of the Royal Society of London*, Vol. A241, pp. 376-396.
- [2] T. Mori and K. Tanaka, 1973, Average Stress in the Matrix and Average Elastic Energy of Materials with Misfitting Inclusions, *Acta Metallurgica*, Vol.31, pp. 571-574.
- [3] Y.P. Qiu and G.J. Weng, 1991, The influence of inclusion shape on the overall elasto-plastic behavior of a two-phase Isotropic Composite, *Int. J. Solids Structures*, Vol.27, No.12, pp. 1537-1550.
- [4] K. Sugimoto, T. Sakaki, T. Fukusato and O. Miyagama, 1985, Influence of Martensitic Morphology on Initial Yielding and Strain Hardening in 0.11C-1.36Mn Dual Phase Steel, *Journal of Iron and Steel Institute of Japan*, Vol.71, No.8, pp. 994-1001.
- [5] J.Y. Koo and G. Thomas, 1977, Design of Duplex Fe/X/0.1C Steels for Improved Mechanical Properties, *Metallurgical Trans. A*, Vol.8A, pp. 525-528.

## NUMERICAL EXAMINATION OF LONG-ROD PENETRATION

Charles E. Anderson, Jr.  
Southwest Research Institute  
P. O. Drawer 28510  
San Antonio, TX 78228-0510

The theory of Tate<sup>1</sup> has been applied very successfully to the penetration of long-rod projectiles into semi-infinite targets. The theory is based on a one-dimensional modified steady-state Bernoulli theory where the strength of the projectile  $Y_p$  and the resistance of the target  $R_t$  to penetration are explicitly accounted for in the model. A comparison of numerical simulations of the time-dependent penetration of a tungsten-alloy long-rod projectile into a hardened-steel target with the Tate model demonstrates that the Tate model presents a reasonably accurate picture of the time history of long-rod penetration, Fig. 1.<sup>2</sup>

Fig. 1. Projectile Nose and Tail Velocities versus Interface Position for Penetration into 4340 Steel Target.



There are two relatively minor discrepancies between the predictions of the Tate model and the numerical simulations. The analytical model predicts that the rear of the projectile decelerates too late and too rapidly at the very end of penetration, and it predicts that the projectile is fully eroded, i.e., the final length of the projectile is zero. The first discrepancy is a consequence of the model not explicitly accounting for a plastic zone within the projectile near the projectile/target interface. It is seen from the numerical simulations that projectile material begins to decelerate when it enters the plastic zone. Numerical simulations also show a residual portion of the penetrator remaining in the bottom of the impact crater which is in agreement with experiment.<sup>2</sup> Full erosion of the rod is predicted from the Tate equation as a consequence of the assumption of a constant  $R_t$  with  $R_t > Y_p$ .

1. A. Tate, "A Theory for the Deceleration of Long Rods after Impact," *J. Mech. Phys. Solids*, 15, 387-399 (1967).
2. C. E. Anderson, Jr. and J. D. Walker, "An Examination of Long-Rod Penetration," submitted for publication, 1991.

Wright<sup>3</sup> has highlighted the theoretical difficulties with the Tate model, but in practical applications of the model, these criticisms appear to manifest themselves largely in the difficulty to determine an accurate value for the target resistance  $R_t$  from first principles.  $R_t$  embodies both the compressive strength of the target as well as the need to account for target confinement in a one-dimensional context. Hence,  $R_t$  incorporates the effect of the extent and rate of plastic deformation within the target; thus,  $R_t$  changes with impact velocity.<sup>4</sup> Although the target resistance  $R_t$  can be used to rank target materials, care must be exercised since  $R_t$  is not an intrinsic material parameter.

Time-resolved depth-of-penetration experiments and numerical simulations are used to examine  $R_t$  as a function of penetration depth for long-rod penetration into semi-infinite targets, Fig. 2.<sup>4</sup> It is found that  $R_t$  changes considerably during penetration, Fig. 3, and that the values which are used in predicting penetration performance must be considered to be an average over the entire penetration profile.<sup>4</sup>

Fig. 2. Projectile Nose and Tail Positions versus Time for Penetration into S-7 Steel Target.

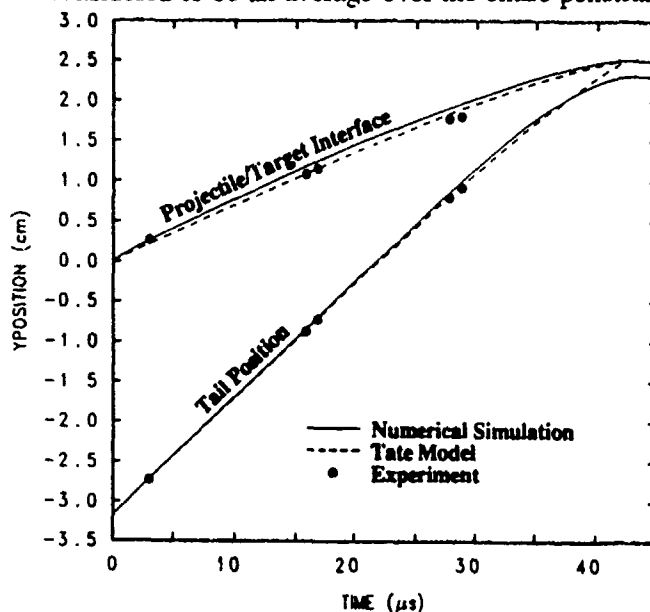
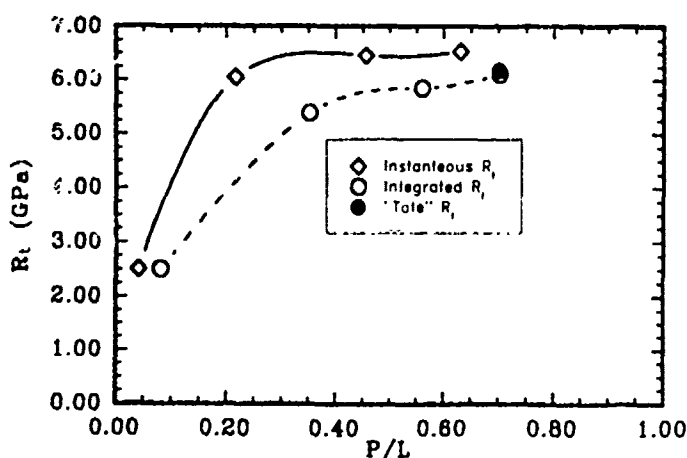


Fig. 3. Calculated Target Resistance versus Normalized Depth of Penetration into S-7 Steel Target.



3. T. W. Wright, "A Survey of Penetration Mechanics for Long Rods," in *Computational Aspects of Penetration Mechanics*, J. Chandra and J. E. Flaherty, (Eds.), pp. 85-106, Springer-Verlag, Berlin-Heidelberg (1983).

4. C. E. Anderson, Jr., J. D. Walker, and G. E. Hauver, "Target Resistance for Long-Rod Penetration," *Computational Impact Mechanics*, W. K. Liu, T. Belytschko, and T. Aizawa (Eds.), Elsevier Press International, 1991.

# **PENETRATION INTO SOIL TARGETS CHARACTERIZED BY A POWER-LAW SHEAR FAILURE ENVELOPE**

Vincent K. Luk  
Senior Member, Technical Staff  
Division 9123  
Advanced Projects III

Sandia National Laboratories  
Albuquerque, New Mexico 87185

## **SUMMARY**

An analytical penetration model was developed for ogival-nose projectiles that penetrated semi-infinite soil targets at normal incidence. Post-test target observations and triaxial, material-test data on samples cored from the soil targets guided the model development. Constitutive models of soil targets use a locked hydrostat to approximate the pressure-volumetric relationship and idealize the shear strength-pressure behavior with a power-law shear failure envelope. Previous constitutive models of geological targets adapt the constant shear strength for reinforced-concrete targets (Luk and Forrestal, 1987) and the Mohr-Coulomb and the Mohr-Coulomb with a Tresca-limit yield criteria for soil targets (Forrestal and Luk, 1991).

The target analysis was simplified by using the spherical cavity-expansion approximation to describe the dynamic expansion of spherical cavities from zero initial radii for elastic-plastic materials with a locked hydrostat and a power-law shear failure envelope. The target resistance to penetration is measured in terms of the normal stresses on the projectile nose. These stresses are approximated by the radial stresses at the cavity surface that are related to the cavity-expansion velocity from the results of the spherically symmetric cavity-expansion analysis. Penetration equations were derived to calculate the depth of penetration from the resistance force on the projectile nose. The predicted penetration depths are in reasonable agreement with penetration data from field tests.

## **REFERENCES**

- Forrestal, M. J. and Luk, V. K., 1991, "Penetration into Soil Targets," submitted to International Journal of Impact Engineering.
- Luk, V. K. and Forrestal, M. J., 1987, "Penetration into Semi-Infinite Reinforced-Concrete Targets with Spherical and Ogival Nose Projectiles," International Journal of Impact Engineering, Vol. 6, No. 4, pp. 291-301.

## FAILURE OF DUCTILE BEAMS SUBJECTED TO LARGE DYNAMIC LOADS

Norman Jones and Wei Qin Shen  
Impact Research Centre  
Department of Mechanical Engineering  
The University of Liverpool  
P.O. Box 147, Liverpool L69 3BX, U.K.

### ABSTRACT

The behaviour of structures when subjected to large dynamic loads has been examined by many authors with the aid of the plastic methods of analysis [1]. In some practical applications, failure or damage, is associated with excessive displacements of a structure. However, in other situations, a designer must estimate the maximum possible impact load or maximum energy absorption in order to assess the safety of a structure or component. These quantities are limited by the ductility of the material, which, however, is assumed infinite in most theoretical and numerical studies on structural crashworthiness [2] and impact energy absorption. In practice, a structure or component may tear and fail due to excessive local plastic strains.

The dynamic inelastic failure of beams has been examined for the two extreme cases of impulsive loading [3] and impact loading [4,5]. Various failure modes have been identified and some success has been achieved in predicting the failure of impulsively loaded beams. It is observed that a tensile tearing failure may occur at sufficiently large impulsive loads which produce large transverse displacements and geometry changes. Thus, the bending moment and the membrane force combine to control plastic flow of the beam. On the other hand, it is observed that a transverse shear failure, which is manifested by transverse shear sliding at the supports, may develop at higher impulsive velocities. In this case, the transverse displacements of a beam remain small and plastic flow is governed by a transverse shear force and a bending moment.

The impact loading case is much more difficult to characterise and further research is required [6,7]. It is observed that either a tensile tearing failure or a transverse shear failure may occur depending on the impact location of the striker. However, other failure modes may also develop which are not observed in the impulsive loading case. For example, a local failure may develop from the indentation site on the beam surface produced immediately underneath the impact point of the striker. Impacts near a support may also involve complex plastic interactions between the bending moment, membrane force and the transverse shear force.



Some recent studies have explored the use of a criterion based on a critical density of plastic work in order to predict the dynamic failure of beams [8]. This approach has been used to examine some experimental results on aluminium alloy beams subjected to large impulsive velocities which cause either a tensile tearing failure within the span due to rupture of the material or a transverse shear failure at the supports. Theoretical predictions are made for this particular problem using an interaction yield surface which combines the influences of bending moment, transverse shear force and axial tensile force [9]. These results are used to identify the conditions associated with the two major failure modes identified in the experimental tests on the strain rate insensitive beams.

Currently, the validity of this critical density of plastic work criterion is being explored for the impact failure of beams struck at any point on the span by blunt masses. It is anticipated that the failure mode will change from a tensile tearing failure mode to a transverse shear failure mode as the impact point moves from the mid-span to a support. An initial exploration of this energy density failure criterion for the impact failure of a clamped circular plate struck by a blunt projectile reveals some interesting insight into the penetration problem, particularly on the shape and size of projectiles on penetrator capability. It is possible that this failure criterion, or a modified version, could also be used for the dynamic failure of other plates and shells.

#### REFERENCES

1. Jones, N., Structural Impact, Cambridge University Press (1989).
2. Jones, N. and Wierzbicki, T., Structural Crashworthiness, Butterworths, London (1983).
3. Jones, N., Trans. ASME, 98(B1), 131-136 (1976).
4. Liu, J. H. and Jones, N., Int. J. Impact Engineering, 6(4), 303-335 (1987).
5. Jones, N., Structural Failure, Ed. T. Wierzbicki and N. Jones, John Wiley and Sons, New York, 133-159 (1989).
6. Yu, J. and Jones, N. Computers and Structures, 32(2), 281-293 (1989).
7. Yu, J. and Jones, N., Int. J. Solids and Structures, 27(9), 1113-1137 (1991).
8. Shen, W. Q. and Jones, N., 'Failure criterion and three failure modes of a clamped beam under impulsive loading', Impact Research Centre Report No. ES/59/90, Department of Mechanical Engineering, University of Liverpool, 1990.
9. Shen, W.Q. and Jones, N., 'Interaction yield surfaces for the plastic behaviour of beams due to combined bending, tension and shear', Impact Research Centre Report No. ES/57/90, Department of Mechanical Engineering, University of Liverpool, 1990.

## IMPACT STUDIES ON S-2 GLASS/PHENOLIC

S. J. Bless  
B.M. Azzi  
N.S.Brar

University of Dayton Research Institute  
Dayton, OH 45469-0180

Impact failure of S-2 Glass® composites was studied. Target resistance to penetration was determined by shooting projectiles with various nose shapes through .5-inch panels. Projectile deceleration was measured; Fig. 1 shows results for penetrating impacts.

There appear to be five penetration modes of glass composites - shock, double shear, single shear, cavity expansion, and tensile stretching. Two of these lend themselves to careful study: shock, which can be enhanced by use of blunt projectiles, and cavity expansion, which dominates with sharp projectiles. For both of these penetration modes, we have developed models to relate the target resistance to basic material properties - the shock impedance and the lateral compressive strength, respectively.

Tensile strength was measured by means of a split Hopkinson bar. Two specimen designs were employed in testing bundles of fibers. Tests were performed at strain rates that are characteristic of impact. The tensile strength of glass fibers was found to be strain rate dependent; Figure 2 shows a stress strain curve from a split Hopkinson bar test at a moderate strain rate. Due to compliance in the fixture, the measured strain overestimates the actual strain in the glass itself. The modulus derived from this curve is much higher than the elastic modulus and therefore can not be real. The strength, however, should be correct. The coefficient of variation of strength of the S-2 Glass® fibers used in this study is about 1 %, which implies that the strength of the filament is very near that measured for the bundle<sup>[2]</sup> (Figure 2).

Compressive strength and shock impedance were determined by five plate impact. Target diagnostics were with manganin piezoresistive gauges. No clear HEC was observed, but the shock impedance was well defined and was only slightly more than epoxy.

Penetration models of the shock penetration phase are in good agreement with the experimental shock impedance. However, analysis of the cavity expansion penetration phase (based on reference 1), assuming lateral cavity expansion, indicates that the effective target strength is less than that which is measured statically. The reason is probably loss of shear strength due to tensile hoop failure. Better results might be obtained with a tensile failure/shear failure model, such as has been used with some success for brittle materials.

## References

1. Z. Rosenberg and M. Forrestal, Perforation of Aluminum Plates With Conical-Nosed Rods - Additional Data and Discussion, J. Mech. Phys., 236-238, 1988.
2. S. Tsai and S. Schulman, A Statistical Analysis of Bundle Tests, Technical Report AFML-TR-67-351, Air Force Material Laboratory, Wright Patterson Air Force Base, Dayton, Ohio, April 1968.

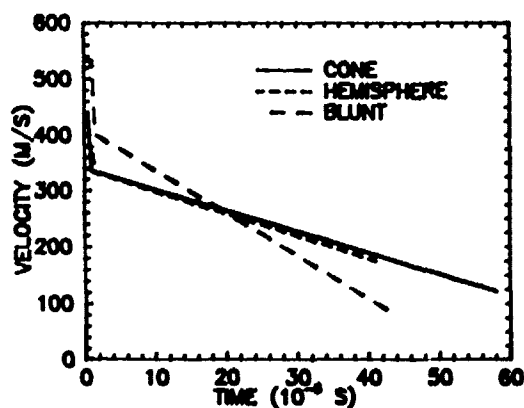


Figure 1. Projectile deceleration during penetration of 0.5-in S-2 Glass® phenolic composite panel as function of projectile nose shape (Projectile mass 4.8 g).

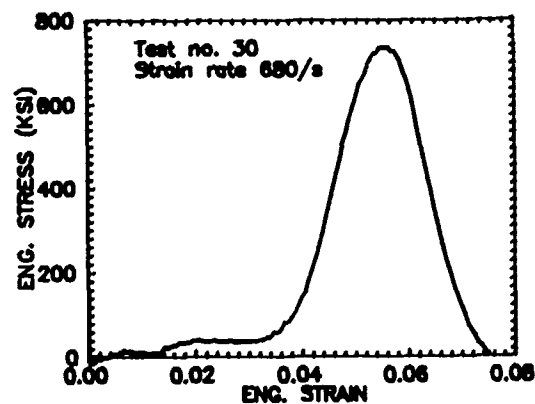


Figure 2. Stress-strain behavior of S-2 Glass® fiber at moderate strain rate from test with the split Hopkinson bar.

# LARGE DAMPED MOTIONS OF ELASTIC STRUCTURES

STUART S. ANTMAN  
Department of Mathematics and  
Institute for Physical Science and Technology  
University of Maryland  
College Park, Maryland 20742

This lecture describes large motions of nonlinearly elastic rods subject to nonlinear viscous dissipation. The nature of suitable dissipative mechanisms is first discussed in a very simple setting of discrete mechanics and then in a more general setting for continua. It is shown that in physically and mathematically natural dissipations the dependence of stress on strain rate must be intimately related to its dependence on strain.

Next the specific problem of the longitudinal motion of a nonlinearly viscoelastic bar carrying a heavy tip mass is studied in the asymptotic limit as the ratio of the mass of the bar to that of the tip mass goes to zero. A rigorous mathematical analysis shows that the governing equations can have a very surprising structure. Finally the analogous asymptotical problem for flexural motion is treated. Here the asymptotics offers an attractive description of snapping motions.

# ACCELERATION WAVES IN ELASTIC PLANAR RODS

H. Cohen  
Department of Applied Mathematics  
University of Manitoba, Winnipeg, Manitoba, Canada

We model a rod as a directed curve  $C_d$ , whose motion in physical space  $\mathcal{E}$  we specify by the vector valued functions

$$\mathbf{r} = \mathbf{r}(s, t) \quad , \quad \mathbf{d}_a = \mathbf{d}_a(s, t) \quad , \quad a = 1, 2, 3, \quad (1)$$

where  $t$  denotes time and  $s$  is a material (convected) coordinate. The vector  $\mathbf{r}$  is the position vector to a moving curve  $C$ , the axis of the rod, which is parameterized by the convected coordinate  $s$ . The vectors  $\mathbf{d}_a$ , the directors, define a vector triad distribution on  $C$  which models the motion of the cross sections  $\mathcal{D}$  of the rod. We assume that the  $\mathbf{d}_a$  are an orthonormal triad, with two of its vectors in the plane of  $\mathcal{D}$  and the third orthogonal to  $\mathcal{D}$ . This assumption restricts the motion of the cross sections to be rigid. A dynamical theory of rods founded on these assumptions is usually called *Cosserat rod theory*.

We assume that  $C$  moves in a fixed plane  $\mathcal{P}$  in  $\mathcal{E}$ , with the cross sections  $\mathcal{D}$  always perpendicular to  $\mathcal{P}$ . We refer to rods and rod motions restricted in this way as *planar*. We choose  $\mathbf{d}_1$  along the unit normal to  $\mathcal{D}$  and  $\mathbf{d}_3$  along the unit normal to  $\mathcal{P}$ . While  $\mathbf{d}_a$  constitute a basis which is fitted to the cross sections  $\mathcal{D}$ , there is another basis of importance, the Frenet basis  $(\mathbf{t}, \mathbf{p}, \mathbf{d}_3)$ , which is fitted to the axis  $C$ , where  $\mathbf{t}$  and  $\mathbf{p}$  are its unit tangent and unit principal normal, respectively. We introduce a fixed orthonormal basis  $\mathbf{e}_i$  ( $i = 1, 2, 3$ ) of  $\mathcal{E}$ , with  $\mathbf{e}_3 = \mathbf{d}_3$ . Then, we can write

$$\mathbf{t} = \cos \theta \mathbf{e}_1 + \sin \theta \mathbf{e}_2 \quad , \quad \mathbf{p} = -\sin \theta \mathbf{e}_1 + \cos \theta \mathbf{e}_2, \quad (2)$$

$$\mathbf{d}_1 = \cos \psi \mathbf{e}_1 + \sin \psi \mathbf{e}_2 \quad , \quad \mathbf{d}_2 = -\sin \psi \mathbf{e}_1 + \cos \psi \mathbf{e}_2, \quad (3)$$

in which the angles  $\theta, \psi$  have an obvious geometric interpretation. We also introduce the angle  $\gamma$  between  $\mathbf{t}$  and  $\mathbf{d}_1$ , which is clearly related to  $\theta$  and  $\psi$  by

$$\gamma = \theta - \psi. \quad (4)$$

We choose an arbitrary (planar) configuration  $C_{dR}$  as the reference configuration, relative to which we may assess the motion of  $C_d$ . We assume  $s$  to be arc length in  $C_R$ . Then, we see that

$$\mathbf{r}' = \lambda \mathbf{t}, (\lambda \equiv \partial/\partial s), \quad (5)$$

where  $\lambda$  measures the ratio of arc lengths in the configuration  $C$  to that in  $C_R$ . We call  $\lambda$  the stretch,  $\gamma$  the shear and define  $f$ , the flexure, by

$$f = \psi'. \quad (6)$$

The set  $(\lambda, \gamma, f)$  are deformation variables. Together with their values in  $C_{dR}$  they fully characterize the strain of  $C_d$  relative to  $C_{dR}$ . We note the restrictions  $\lambda > 0$ ,  $|\gamma| < \pi/2$ , which are imposed by considerations of impenetrability of matter. When the reference configuration  $C_{dR}$  has a straight axis, with cross sections orthogonal to the it, we easily compute that  $\lambda_R = 1, \gamma_R = f_R = 0$ . We note further, from (4), that

$$f = \lambda \kappa - \gamma' \quad , \quad \kappa = \theta', \quad (7)$$

where  $\kappa$  is the curvature of  $C$ .

The kinematics of the rod is characterized by the time derivatives of the motion. Sufficient for our purpose are the velocities and accelerations, defined respectively for planar motions by

$$\mathbf{v} = \dot{\mathbf{r}}, \mathbf{v} = \dot{\psi}, \text{ and } \mathbf{a} = \ddot{\mathbf{r}}, \alpha = \ddot{\psi}, (\dot{\phantom{x}} \equiv \partial/\partial t). \quad (8)$$

We characterize a wave on a rod by a moving singular point  $w = s_w(t)$  on  $\mathcal{C}$ , whose location in space is defined by its position vector  $\mathbf{r}_w = \mathbf{r}_w(t) = \mathbf{r}(s_w(t), t)$ . A singular point is one at which some field variables or their derivatives, generically denoted by  $\Phi$ , have jump discontinuities  $[\Phi]$ , where  $[\Phi] = \Phi^- - \Phi^+$ ,  $\Phi^\pm = \lim_{\epsilon \rightarrow 0} \Phi(w \pm \epsilon)$ . An acceleration wave is defined by the conditions  $[\mathbf{a}] \neq 0$ ,  $[\alpha] \neq 0$ ,  $[\mathbf{v}] = 0$ ,  $[\dot{\mathbf{v}}] = 0$ . The speed of propagation,  $U_R = \dot{s}_w$ , is clearly the speed of the wave as seen relative to an observer fixed in the reference configuration  $\mathcal{C}_R$ . For the treatment of acceleration waves certain relations between the jumps in the time and spatial derivatives are important. These are the compatibility relations

$$[\dot{\Phi}] = -U_R[\Phi'], \quad [\ddot{\Phi}] = U_R^2[\Phi''], \quad (9)$$

the first of which is valid when  $[\Phi] = 0$ , while the latter is valid when  $[\Phi] = [\Phi'] = 0$ .

The field equations arise as local forms of the global laws of balance of linear and angular momentum for the rod. When the velocities of the rod are continuous, as they are for acceleration waves, these local forms are the differential equations

$$\mathbf{n}' = \rho_R \mathbf{a}, \quad \mathbf{m}' + \mathbf{r}' \times \mathbf{n} = K_R \alpha \mathbf{e}_3, \quad (10)$$

where  $\mathbf{n}$  and  $\mathbf{m}$  are the stress force and bending moment, respectively, with  $\mathbf{n} \perp \mathbf{m}$ ,  $\mathbf{m} = m \mathbf{e}_3$ ;  $\rho_R$  and  $K_R$  are the mass and inertia densities of the rod per unit length of  $\mathcal{C}_R$ , respectively. Equations (10) hold at all points of  $\mathcal{C}$  which are not singular; at singular points the jumps of these equations prevail. We have excluded the inclusion of body force and moment from (10) as a matter of convenience.

We write  $\mathbf{n} = n_t \mathbf{t} + n_p \mathbf{p}$  and assume nonlinear constitutive relations of the form

$$n_t = n_t(\lambda, \gamma; s), \quad n_p = n_p(\lambda, \gamma; s), \quad m = (f; s), \quad (11)$$

subject to the further condition that either one or both  $n_{p,\lambda} = 0$ ,  $n_{t,\gamma} - n_p = 0$  will hold. The forms in (11) and the additional conditions are those which will be seen to give rise to waves that are uncoupled with respect to the deformation set  $(\lambda, \gamma, f)$ .

To investigate the wave propagation problem we form the jump of the field equations (10), insert the definitions (7) and accelerations (8), the constitutive relations (11), utilize the compatibility relations (9), and take components with respect to the  $(\mathbf{t}, \mathbf{p}, \mathbf{e}_3)$  basis, to arrive at a set of linear equations in the strain gradient jumps  $([\lambda'], [\gamma'], [f'])$ . The set of all such jumps may be taken as the column vectors  $\mathbf{w} = ([\lambda'], [\gamma'], [f'])^T$  of a three-dimensional vector space  $\mathcal{W}$ , the elements of which we refer to as the wave mode vectors; we use the superscript T to denote the transpose of a matrix. The aforementioned linear set takes the form

$$(\mathbf{Q} - U_R^2 \mathbf{K}_R) \mathbf{w} = \mathbf{0}, \quad (12)$$

where  $\mathbf{Q}, \mathbf{K}_R$  are the  $3 \times 3$  matrices

$$\mathbf{Q} = \begin{pmatrix} n_{t,\lambda} & n_{t,\gamma} - n_p & 0 \\ n_{p,\lambda} & n_{p,\gamma} + n_t & 0 \\ 0 & 0 & m_{,f} \end{pmatrix}, \quad \mathbf{K}_R = \text{diag}(\rho_R, \rho_R, K_R). \quad (13)$$

Equation (12) defines an eigenvalue problem on  $\mathcal{W}$ , whose eigenvalues  $U_R^2$  define the three possible wave speeds, and whose eigenvectors  $\mathbf{w}$  are the associated wave modes. The wave speeds, which we assume to be real and distinct, are given by the solution of the characteristic equation  $\det(\mathbf{Q} - U_R^2 \mathbf{K}_R) = 0$ . We note that  $\mathbf{Q}$  is generally non-symmetric, while  $\mathbf{K}_R$  is positive-definite. We conclude that, with respect to  $\mathbf{K}_R$  as metric on  $\mathcal{W}$ , the wave modes will be generally non-orthogonal.

Three possible situations arise dependent upon whether one or both of  $n_{p,\lambda} = 0$ ,  $n_{t,\gamma} - n_p = 0$ , hold. When both of these hold the wave speeds and modes are given by

$$U_{R\lambda}^2 = n_{t,\lambda} / \rho_R, \quad [\lambda'] \neq 0, \quad [\gamma'] = 0, \quad [f'] = 0; \quad (14)$$

$$U_{R\gamma}^2 = (n_{p,\gamma} + n_t) / \lambda \rho_R, \quad [\gamma'] \neq 0, \quad [\lambda'] = 0, \quad [f'] = 0; \quad (15)$$

$$U_{Rf}^2 = m_{,f} / K_R, \quad [f'] \neq 0, \quad [\lambda'] = 0, \quad [\gamma'] = 0. \quad (16)$$

We call these principal plane waves. These waves have pure wave modes, for the effects of stretch, shear and flexure are completely uncoupled within them. For the two remaining situations in which one, but not both, of the constitutive restrictions hold, we find wave speeds that are the same as in (14)-(16). However, now the associated modes (14), (15) couple the effects of stretch and shear, while (16) remains unchanged.

For a list of works which expand on this topic, we refer the reader to: H. Cohen *On Wave Propagation and Evolution in Rods*, *Rend. Sem. Mat. Univ. Politecn. Torino*, Vol.47 (1991).

## NON-AXISYMMETRIC NECKING

Yi-chao Chen  
Department of Mechanical Engineering  
University of Houston  
Houston, Texas 77204

Necking is a well-known instability phenomenon that has stimulated many theoretical studies. Among others, Antman [1] studies the phenomenon by using an elastic rod theory that allows both radial and axial deformations, and finds solutions that appear to represent necking deformation. Owen [2] shows that Antman's solution is stable in the sense that it minimizes the total strain energy in a certain function space.

In the above works, only axisymmetric deformations are considered. However, experimental observations have revealed certain non-axisymmetric deformations at the initial stage of the development of necks. For example, Buisson and Ravi-Chandar [3] observe, in a uniaxial tension experiment with polycarbonate, the formation of a "shear band" preceding the necking deformations. It forms a certain angle with the axis, which increases as the tension progresses with the shear band eventually evolving into an axisymmetric neck.

In this paper, we study the onset of this non-axisymmetric deformation by using an energy stability criterion.

Consider axisymmetric deformations of an elastic rod that is stretched by a loading device which specifies the axial displacements of the ends of the rod. The material of the rod has the property that the axial force required for a homogeneous stretch  $\lambda$  of the rod is a strictly increasing function of  $\lambda$  in the ranges of small and large deformations, and strictly decreasing in the intermediate deformation range. Two stretches  $\lambda_1$  and  $\lambda_2$ , one in the small deformation range and the other in the large deformation range, can be determined by the Maxwell equal area rule, that characterizes the necking behavior. Specifically, when the specified displacement is such that the corresponding homogeneous stretch  $\lambda$  is between  $\lambda_1$  and  $\lambda_2$ , an inhomogeneous half-necking solution is possible, that consists of two approximately homogeneous sections characterized by  $\lambda_1$  and  $\lambda_2$ , and a smooth transition section connecting the two approximately homogeneous sections.

For a given  $\lambda$  between  $\lambda_1$  and  $\lambda_2$ , the half-necking solution has a lower total strain energy than the homogeneous solution does, provided that the length of the rod is

sufficiently large. Here, the last condition is critical. It is shown in the paper that for a short rod the half-necking solution has a higher strain energy. Equivalently, for a rod of given length, the half-necking solution will have a higher strain energy than the homogeneous solution does if  $\lambda$  is sufficiently close to  $\lambda_1$ .

Such a behavior can be explained as follows: As the value of  $\lambda$  exceeds  $\lambda_1$ , a part of the rod tends to shift to a deformation state  $\lambda_2$  that provides a large stretch so that the remaining rod can stay at the deformation state  $\lambda_1$  of small stretch. The increase in strain energy due to shifting the part to  $\lambda_2$  is less than that required by deforming the entire rod to the homogeneous stretch  $\lambda$ . The energy reduction depends on the value of  $\lambda - \lambda_1$ . When this value is small, the energy reduction due to the shifting is also small. On the other hand, the shifting is accompanied by a rapid change in radial deformation occurring in the transition section, which incurs an increase in the total strain energy. This increase is virtually independent of the value of  $\lambda - \lambda_1$ , and might well offset the reduction in the strain energy due to the shifting when  $\lambda - \lambda_1$  is small. In fact, it is shown in the paper that when  $\lambda$  is sufficiently close to  $\lambda_1$ , the homogeneous deformation has the lowest energy among all smooth axisymmetric deformations.

It then follows naturally that a deformation with two homogeneous stretches  $\lambda_1$  and  $\lambda_2$  but without transition may have a lower total strain energy. In this paper, one such deformation is constructed, which consists of two parts: One is a homogeneous axisymmetric deformation with axial stretch  $\lambda_1$ , and the other a homogeneous non-axisymmetric deformation with a principal stretch  $\lambda_2$ , the principal direction forming a non-zero angle with the axis of the rod. These two parts are connected together continuously without a transition. Such a deformation pattern has a similar form to that observed by Buisson and Ravi-Chandar, with the non-axisymmetric deformation corresponding to the shear band. A direct calculation shows that, for certain values of  $\lambda$ , this non-axisymmetric deformation pattern has a lower total strain energy than that of the homogeneous deformation, and consequently lower than that of the half-necking deformation. As the value of  $\lambda$  increases, the energy difference between the axisymmetric half-necking deformation and the non-axisymmetric deformation decreases, and becomes negative at a certain point, giving rise to a stable axisymmetric half-necking deformation.

## References

1. Antman, S. S., Nonuniqueness of equilibrium states for bars in tension, *J Math Anal Appl* 44 (1973), 333-349.
2. Owen, N. C., Existence and stability of necking deformations for nonlinearly elastic rods, *Arch. Rational Mech. Anal.* 98 (1987) 357-383.
3. Buisson, G. and Ravi-Chandar, K., On the constitutive behaviour of polycarbonate under large deformation, *Polymer* 31 (1990), 2071-2076.



## SCALINGS AND CONSTRAINTS IN STRUCTURAL MECHANICS

Paolo Podio-Guidugli  
Dipartimento di Ingegneria Civile  
Università di Roma "Tor Vergata"  
00173 ROMA – ITALY

An interesting conceptual problem in continuum mechanics is to derive from three-dimensional elasticity the equations of structural mechanics, in particular, the equations of rods, plates, and shells. In the problem's long history two main lines of thought emerge, both aiming to capture the peculiar character of structures as continuous bodies, their "thinness". One line, which can be traced back to Cauchy and Poisson (1827–1828), points to a judicious use of asymptotic expansion techniques in a thinness parameter, and has led to the development of the *scaling method* by Ciarlet, Destuynder and coworkers [1]. The other line, whose roots are in a famous paper by Kirchhoff (1850), sees structures as continuous bodies that are constitutively capable only of deformations belonging to a certain specific class; its more recent implementation is the *constraint method* employed in [2] and later papers.

The purpose of this presentation is twofold: (i) to discuss the formal structure of the scaling method, and possible generalizations of it; (ii) to indicate how the scaling and the constraint method supplement and lend significance to one another.

- [1] P.G. Ciarlet, *Plates and Junctions in Elastic Multi-Structures: an Asymptotic Analysis*. Masson, 1990.
- [2] P. Podio-Guidugli, An exact derivation of the thin plate equation. *J. Elasticity*, 22, 121–133, 1989.

# NUMERICAL SIMULATION OF A VORTEX/SHOCK INTERACTION \*

M. Shu †

R. K. Agarwal ‡

McDonnell Douglas Research Laboratories

P. O. Box 516, St. Louis, Missouri 63166

Washington University

Campus Box 1185, One Brookings Dr., St. Louis, Missouri 63130

Recently, there has been much interest in acoustic design issues such as the reduction of structural fatigue and interior noise related to the use of both high- and low-bypass jet propulsion in commercial aircraft. As always, there is public interest in reducing the noise levels around airports. With the use of high-performance nozzles in commercial and military aircraft, noise levels generated by jet engines become an increasingly important design constraint and there is growing awareness of noise related to shocks in the jet exhaust. Although the usefulness of computational fluid dynamics has been proven for many applications, the use of these techniques has been quite limited in some areas. Currently, a numerical algorithm is being developed that is capable of simulating gas-dynamic physics for the fundamental study of supersonic/acoustic phenomena. The algorithm employs an alternating-direction-implicit scheme to integrate the finite-volume formulation of the unsteady Euler equations in time. Flux-differences are upwind and total-variation-diminishing flux-limiters are incorporated to establish second-order spatial accuracy. The solution methodology and a multitude of code-validation test problems have been published by Shu and Agarwal. <sup>1</sup> We intend to use this shock-capturing code to study a simple two-dimensional vortex/shock interaction and evaluate the code's utility for more complex interactions.

Our preliminary study resulted in a numerical time-evolution solution of the convection of a strong vortex through a normal shock. These results are shown as a series of pressure contour plots in Fig. 1. The solution was obtained on a 220-cell-by-100-cell grid. Pressure contour plots are shown every 0.1 nondimensional time units starting at 0.15. The deflection of the shock due to the presence of the vortex is evident by time 0.25. At this time, the vortex center has coalesced with the shock. The deflection of the shock is due to the clockwise circulation. Upstream of the shock, the vortex velocity contributes to higher Mach number flow above the vortex core and lower Mach number flow below the vortex core. In turn, downstream of the shock, pressures are higher above the vortex core and lower below the vortex core. At time 0.35, the vortex center has been convected through the shock and branching of the shock is noticeable near the high-pressure region above the vortex. As time progresses, the branching of the shock becomes more pronounced, as shown for time 0.45 and time 0.55.

The computed solution is qualitatively compared with the experimental findings of Naumann and Hermanns. <sup>2</sup> The shock branching shown in the computed solution is also compared to the numerical results of Meadows, Kumar and Hussaini. <sup>3</sup> The computed results are in qualitative agreement with experimental and numerical data of other investigators. The high resolution of the flow features in the computed solution gives an indication of the potential of the method for further analysis of more complex interactions.

The solutions presented in the abstract resulted from a preliminary study. A more thorough analysis of the approach and resulting solutions will be performed. In the complete paper, the governing equations and specifics of the time-integration scheme will be presented. A complete description of the hybrid vortex model will be given. Grid generation and boundary conditions will be described in full detail. A more comprehensive treatment of background, results, discussion, and conclusions will be included.

\* This research was conducted under the McDonnell Douglas Independent Research and Development Program

† Research Associate, McDonnell Douglas Research Laboratories, Doctoral Candidate, Washington University

‡ Program Director, McDonnell Douglas Research Laboratories, Affiliate Professor, Washington University.

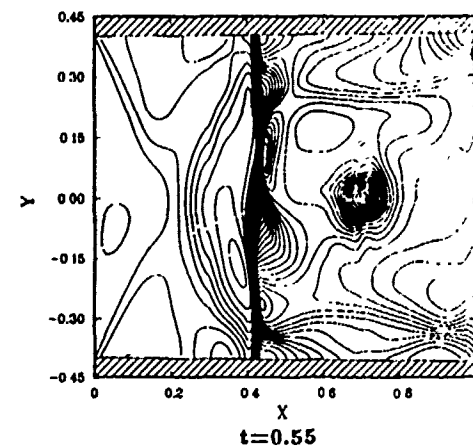
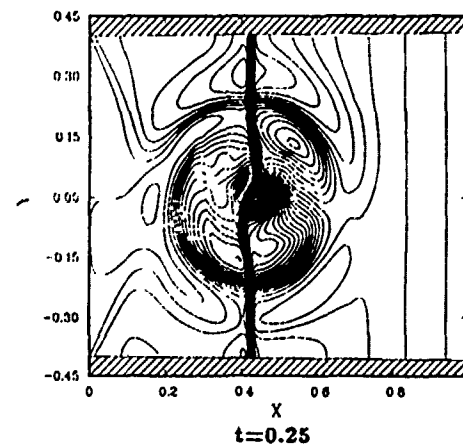
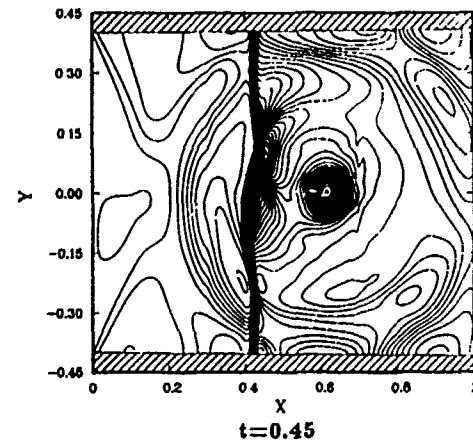
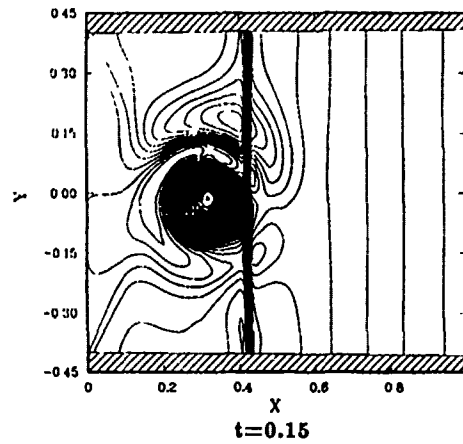
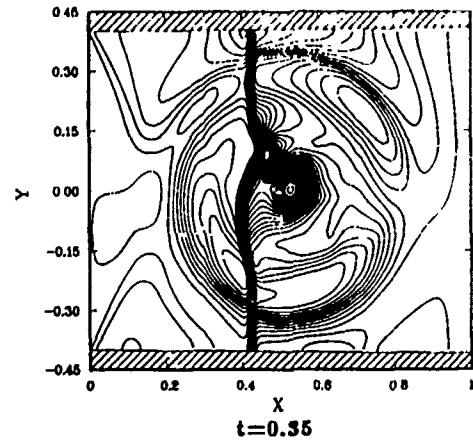
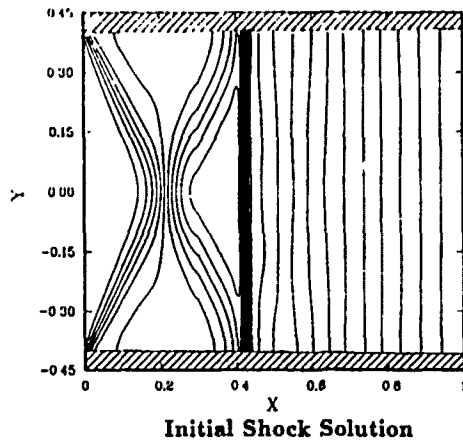
<sup>1</sup> Shu, M. and Agarwal, R. K., "Numerical Simulation of Supersonic Unsteady Flow Using Euler Equations," AIAA Paper 90-0415, 1990

<sup>2</sup> Naumann, A. and Hermanns, E., "On the Interaction Between a Shock Wave and a Vortex Field," AGARD CP 131, 1973

<sup>3</sup> Meadows, K. R., Kumar, A. and Hussaini, M. Y., "A Computational Study on the Interaction between a Vortex and a Shock Wave," AIAA Paper 89-1043, 1989.

Fig. 1 Time Evolution of Shock/Vortex Interaction

$M_i = 1.1$  220x100 grid MDUNS2D Solution  $k = 3.07$



# IMPLEMENTATION OF A TVD SHOCK VISCOSITY FOR IMPACT CALCULATIONS

David J. Benson  
Dept. of AMES R-011  
University of California, San Diego  
La Jolla, CA 92092

It is well known that the numerical solution of problems involving impact by explicit finite difference or finite element methods requires the addition of a term, usually referred to as the "shock viscosity," to eliminate spurious oscillations behind the shock wave [1]. Several different forms for the shock viscosity have been proposed in the literature [2-5], but the most common form is the isotropic bulk viscosity, which is treated like a pressure term in the momentum and energy equations. For a 1-D flow without shear stresses, the equations of motion are given by Eq. 1, where the density, velocity, pressure, shock viscosity and total energy per unit volume are  $\rho$ ,  $u$ ,  $P$ ,  $Q$ , and  $\mathcal{E}$  respectively.

$$\begin{aligned}\rho_{,t} + (\rho u)_{,x} &= 0 \\ \rho u_{,t} + (\rho u^2 + (P + Q))_{,x} &= 0 \\ \mathcal{E}_{,t} + (\mathcal{E}u + (P + q)u)_{,x} &= 0\end{aligned}\tag{1}$$

The most prevalent form of the shock viscosity contains both linear and quadratic terms in the velocity jump across the element. The coefficient  $a$  is the sound speed, and  $c_Q$  and  $c_L$  are chosen to be large enough to damp the oscillations after the shock. Typical values are 1.5 and 0.06 for  $c_Q$  and  $c_L$ , respectively. A consequence of using the viscosity is the shock is spread over three to six elements. For the quadratic form (no linear term), von Neumann and Richtmyer [1] were able to show that the numerical shock width is independent of the shock strength. When the linear term is added, the viscosity has the tendency to spread weak shocks more than strong shocks.

$$Q = \max(c_Q \rho |\Delta u| \Delta u + c_L a \rho \Delta u, 0)\tag{2}$$

For problems where shocks are significant features of the solution, such as problems involving impact and penetration, the mesh must be fine enough so that the numerical shock width is small in comparison to the other dimensions in the problem. The cost of

a calculation is therefore dependent on how well a shock wave is resolved. For theoretical reasons, a shock must be at least two elements wide in a monotonic solution.

This paper presents a shock viscosity with near optimal shock resolution in two dimensions. It is based on the one-dimensional formulations developed by Christensen [2]. In a previous paper [3], a flux-limited shock viscosity was implemented. The form of the viscosity is identical to Eq. (2), but the velocity jump across the element is approximated using Eq. (3), where the derivative of the velocity with respect to  $x$  is a second order approximation subject to the monotonicity constraints of van Leer [4].

$$\Delta u = u_{i+1} - u_i + \frac{\Delta x}{2} \left( \frac{\partial u_{i+1}}{\partial x} + \frac{\partial u_i}{\partial x} \right) \quad (3)$$

While this higher order accurate approximation results in a nearly optimal shock width, there is single oscillation occurring after the shock. Christensen has recently reformulated his work in terms of a Godunov scheme [5] on a staggered mesh. A total variation diminishing (TVD) scheme is used to limit the velocity jump across the element, where  $r$ , is the ratio of the velocity gradients in adjacent elements.

$$\Delta u = (1 - \phi(r_i, r_{i+1})) [u_{i+1} - u_i] \quad (4)$$

This new formulation is tested with a variety of TVD limiters and compared to the previous formulation. At the expense of a small amount of shock resolution, the single oscillation in the previous formulation can be removed.

## REFERENCES

1. Von Neumann, J., and Richtmyer, R. D., "A Method for the Numerical Calculation of Hydrodynamic Shocks," *Journal of Applied Physics*, Vol. 21, 1950.
2. Christensen, R., personal communication, Lawrence Livermore National Laboratory, 1990.
3. Benson, D. J., "A New Two-Dimensional Flux-Limited Shock Viscosity," submitted to *Computer Methods in Applied Mechanics and Engineering*, in press, 1991.
4. Van Leer, B., "Towards the Ultimate Conservative Difference Scheme. IV. A New Approach to Numerical Convection," *Journal of Computational Physics*, Vol. 23, pp. 276-299, 1977.
5. Godunov, S. K., "Finite Difference Method for Numerical Computation of Discontinuous Solutions of the Equations of Fluid Dynamics," *Matematicheskii Sbornik*, Vol. 47, No. 3, pp. 271-306, 1959.

## CHARACTERISTICS OF JET FLAMES ISSUED FROM ELLIPTIC NOZZLES

S.R.Gollahalli

School of Aerospace and Mechanical Engineering  
University of Oklahoma, Norman, OK 73019

The application of noncircular nozzles as a means of controlling mixing characteristics of gas jets with ambient fluids has received considerable attention. Since combustion characteristics of gas jet flames are controlled by the mixing characteristics of jet fluid and surrounding air, modifications of the initial geometry of the jet offer a convenient way of improving its combustion and pollutant emission characteristics. Elliptic jets with a small aspect ratio (major axis/minor axis) have been found to produce 8 to 10 times the entrainment of surrounding air by circular jets. Although the flow structure and mixing characteristics of elliptic jets have been studied extensively, the available information on the characteristics of elliptic nozzle flames is limited. This study was performed to compare the combustion and pollutant emission characteristics of a turbulent propane jet issued from an elliptic nozzle and a circular nozzle of equal exit area. In most of the studies the aspect ratio of the elliptic nozzle was 3:1 and the flames issued from both circular and elliptic nozzles were kept in the burner-attached configuration. The liftoff and reattachment behavior, temperature profiles, concentration profiles of fuel, oxygen, carbon dioxide, carbon monoxide, nitric oxide, and soot, flame radiation, opacity of the flame samples, the profiles of the streamwise component of the mean velocity and r.m.s. value of the velocity fluctuation in the streamwise direction were measured. A limited series of experiments was also performed with the elliptic nozzles of aspect ratios 2:1 and 4:1 to determine the influence of aspect ratio. Some measurements in the nonburning jets issued from elliptic and circular nozzles are also included.

The experimental facility comprised of a vertical combustion chamber of square cross section (76 cm x 76 cm) and 117 cm high. The chamber was provided with an air-cooled pyrex glass window (20 cm x 20 cm x 92 cm) on all the side walls. During gas sampling and probing temperature field, one of the glass windows was replaced with a slotted metal sheet through which the probes were introduced. The burner assembly mounted to the floor of the chamber consisted of a contoured nozzle section located concentrically inside a 162 mm i.d. steel pipe. For this study, a circular nozzle tip of exit diameter 9.5 mm i.d. was used. The elliptic nozzle tips were made to have the same exit area as that of the circular nozzle. The elliptic nozzle tips were made by milling the semi-ellipse profiles in two separate pieces and bonding them together. The junction between the elliptic and circular sections was flared to produce a smooth transition. The jet-fluid was supplied from gas cylinders through pressure regulators and filters. Combustion air was supplied from an oil-less rotary-vane compressor to the annulus between the outer pipe and the nozzle. Fuel jets were ignited with a pilot Bunsen flame which was withdrawn during tests. Direct color photography with 35 mm Kodacolor 100 ASA film was used to determine the shape and dimensions of the visible flame. A two-mirror (200 mm diameter) schlieren system with a xenon stroboscopic light source of flash duration 1.5  $\mu$ s was used to visualize the flow structure in the near-nozzle region of the flames. The temperature field was probed with a silica-coated platinum-platinum/13% rhodium thermocouple (type R) with a bead diameter 0.25 mm. Gas samples were withdrawn from the flames through a cooled stainless steel probe of tip diameter 1 mm and were treated to remove

particulates and moisture with a series of filters and ice-chilled moisture traps. They were analyzed for the concentrations of  $\text{CO}_2$  and  $\text{CO}$  with nondispersive infrared analyzers, of  $\text{O}_2$  with a polarographic analyzer, of  $\text{NO}$  with a chemiluminescent analyzer, and of  $\text{C}_3\text{H}_8$  with a gas chromatograph. The flow field in the vicinity of the flame base was probed with a laser Doppler velocimeter. Both nozzle and air-flow streams were seeded with magnesium oxide particles whose average size was about  $5\text{ }\mu\text{m}$ . In all runs 8000 validated samples with a sampling time less than 2s. were acquired. Some experiments were repeated 3 to 5 times to establish repeatability.

In this study the technique of diluting jet fluid to study the flame liftoff and reattachment characteristics was employed. In this procedure, the jet fluid (propane) was diluted (with nitrogen) while keeping the nozzle exit velocity constant until the flame transitions occurred. The critical values of the mole fraction of the fuel in the jet fluid  $x_p$  at liftoff and blowout transitions were taken as measures of the flame stability. Higher the dilution the jet flame could withstand before the transitions, better the flame stability was considered to be in the absence of dilution. This method has an advantage for the present study, because the nozzle exit velocity was maintained constant and its influence on the factors associated with flow field was suppressed, the changes in flame stability can be attributed to only the burner geometry which is the variable of primary interest. With elliptic nozzle, the first transition termed laminar liftoff occurs at  $x_p = 0.38$ , the second transition termed turbulent liftoff occurs at  $x_p = 0.33$ , as compared to the corresponding values of  $x_p$  equal to 0.32 and 0.27 in circular nozzle flames. This implies that elliptic nozzle flames require more reactive component in the jet fluid to avoid the transitions of burner-attached flame to liftoff and blowout conditions.

From the concentration profiles it is noticed that fuel persists longer in the circular nozzle flame than in the elliptic nozzle flame. For instance, the value of  $x_p$  decreases to 0.2 at  $x/D=40$  in the circular nozzle flame, whereas the same value is reached at  $x/D=30$  in the elliptic nozzle flame. The rapid depletion of propane is caused by the greater dilution due to the higher entrainment in elliptic nozzle flame. A comparison of temperature profiles reveals that in the near-nozzle region circular nozzle flame has a higher peak temperature (1030 K) compared to elliptic nozzle flame (980 K). But, in the midflame and far-nozzle regions, elliptic nozzle flame has higher peak values. Also, the profiles in elliptic nozzle flame are much flatter. As diffusion controlled homogeneous reactions are dominant in the near-nozzle region, the more rapid development of shear layer and higher degree of mixing with air in elliptic nozzle flame lead to a lower peak temperature. The following are the highlights of the combustion product concentration profiles: (i) in the near-nozzle region, oxygen concentration is zero on the axis and increases sharply outside the reaction zone in both the flames; (ii) in the midflame region the rate of increase of oxygen concentration in the radial directions is higher in the elliptic nozzle flame; (iii) in the far-nozzle region, there is no significant difference in oxygen concentration profiles in circular and elliptic nozzle flames; (iv) carbon monoxide concentration reaches highest peak values in the midflame region in both flames; (v) in the near nozzle region, both  $\text{CO}$  and  $\text{CO}_2$  profiles have wider peaks in the elliptic nozzle flames; (vi) in the far-nozzle region  $\text{CO}$  and  $\text{CO}_2$  peak concentrations are higher in the elliptic nozzle flame; (vii) in the near-nozzle region, the peak concentration of  $\text{NO}$  is lower in the elliptic nozzle flame. In the midflame region the peak value of  $\text{NO}$  concentration is higher in the elliptic nozzle flame, and in the far-nozzle region, it is about same in both flames. The velocity profiles show, for the same volume flow rate, a higher peak value of the streamwise velocity in the elliptic nozzle flame compared to that in the circular nozzle flame, which indicates that the flow is squeezed in the elliptical nozzle. The potential core in the circular nozzle flame extends to  $x/D = 10$ , whereas in the elliptic nozzle flame it disappears before  $x/D=6$ . The turbulence measurements substantiate these observations. Hence, elliptic nozzle configuration offers a convenient method of tailoring the combustion characteristics of diffusion flames.

# THREE-DIMENSIONAL EFFECTS IN A CURVED DUCT

Tony W.H. Sheu, Jaimey J.M. Hao  
Institute of Naval Architecture, National Taiwan University,  
73 Chou-Shan Rd., Taipei, Taiwan, R. O. C.

## ABSTRACT

A NOSIMPLE-IN3 computer code is developed to study the wall effect in third dimension of a 90° bend square duct. The contravariant velocities are used as dependent variables rather than primitive velocities. The convection terms are discretized by QUICK scheme for internal points and power-law scheme for boundary points. The resulting algebraic equations are solved by semi-implicit SIMPLER solution algorithm. The computed differences between two- and three- dimensional results are displayed on the symmetry plane.

## INTRODUCTION

Most of dependent variables for momentum equations in a transformed set of Navier-Stokes equations use Cartesian velocities. The solution quality is known to be degraded as the angles between transformed coordinates and velocity vectors increase. The present study, on the other hand, uses contravariant velocities to solve incompressible viscous flow that SIMPLE-like [1] solution algorithm can be safely employed.

## BASIC FORMULATION

The governing equations after being transformed to a non-orthogonal coordinate system  $(\xi, \eta, \zeta)$  can be represented as follows:

$$\frac{\partial(\rho J \phi)}{\partial t} + \frac{\partial}{\partial \xi}(\rho J U \phi) + \frac{\partial}{\partial \eta}(\rho J V \phi) + \frac{\partial}{\partial \zeta}(\rho J W \phi) = \frac{\partial}{\partial \xi}(\Gamma J g^{11} \frac{\partial \phi}{\partial \xi}) + \frac{\partial}{\partial \eta}(\Gamma J g^{22} \frac{\partial \phi}{\partial \eta}) + \frac{\partial}{\partial \zeta}(\Gamma J g^{33} \frac{\partial \phi}{\partial \zeta}) + S_1^{\phi} + S_2^{\phi}$$

The definitions of above variables can be found in [2]. The dependent variables used here for velocities are contravariant velocities  $U, V, W$ . The convective terms are discretized by QUICK upwind scheme [3]. The resulting algebraic equations are solved by a SIMPLER solution algorithm [1].

## NUMERICAL RESULTS

The developed NOSIMPLE-IN3 (Non-Orthogonal SIMPLE-INcompressible 3D) code was used to predict the flowfield in 90° bend square duct. The investigated flow condition and configuration were the same as those described in [4]. The computed three dimensional velocities at symmetric plane are compared with the corresponding two dimensional results by NOSIMPLE code [5]. The resulting difference is illustrated in Fig.1 for demonstrating wall effect in third dimension.



## CONCLUSIONS

A contravariant-velocity-based finite volume code was developed. The present study shows the effect of wall on computed solution.

## REFERENCES

- [1] Patankar, S.V., Numerical Heat Transfer and Fluid Flow, McGraw-Hill Book Company, 1980.
- [2] Jaimey J.M. Hao, On a contravariant-velocity-based finite volume discretization method, to appear in Master Thesis, Institute of Naval Architecture, National Taiwan University, R.O.C., June 1991.
- [3] Leonard, B.P., A stable and accurate convective modeling procedure based on quadratic upstream interpolation, J. Comput. Meths. Appl. Mech. Engrg., 19, 59-98, 1979.
- [4] Humphrey, J.A.C., Taylor, A.M.K., and Whitelaw, J.H., Laminar flow in a square duct of strong curvature, J. Fluid Mech., Vol.83, Part3, 509-527, 1977.
- [5] Tony W.H. Sheu, J.C. Liao, Numerical prediction of free convection in an arbitrary cavity using SIMPLE family algorithm, Proceeding of the Sixth International Conference held at Swansea, Numerical Methods in Laminar and Turbulent Flow Vol.6, Part 2, 1145-1155, 1989.

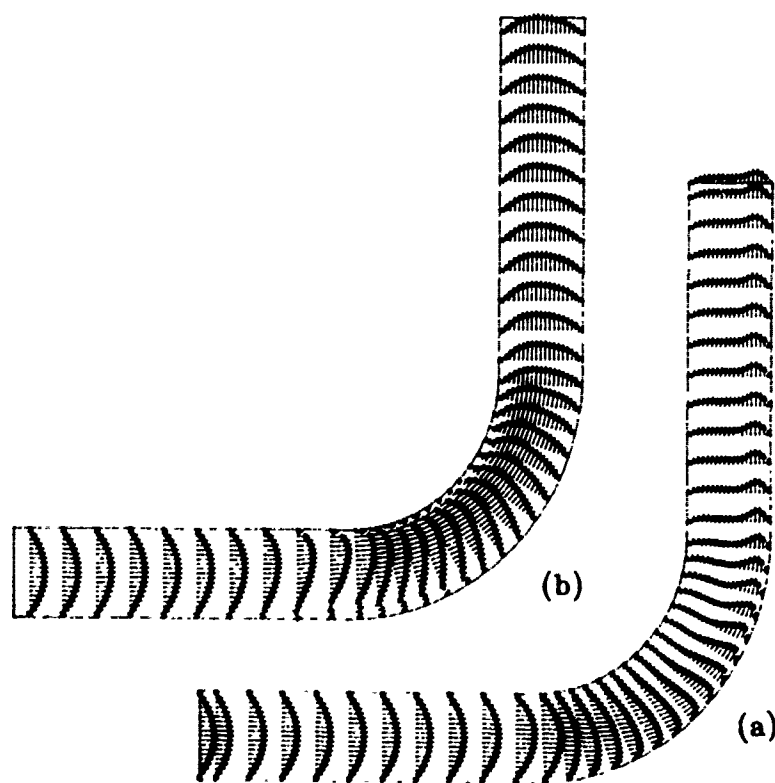


Fig.1 Computed longitudinal velocity vector plots  
(a) three dimensional (b) two dimensional

## TORSION TEST OF METALS IN THE FINITE DEFORMATION RANGE

H.C. Wu and Z.Y. Xu  
Department of Civil and Environmental Engineering  
The University of Iowa, Iowa City, IA 52242

and

P.T. Wang  
Fabricating Technology Division  
Alcoa Laboratories, Alcoa Center, PA 15069

Metal tubes and solid specimens have been tested in torsion up to a shear strain of 1.3. Long cylindrical specimens have been used to mitigate the end effect due to gripping. A specially designed axial-torsional extensometer has been used for this experiment. The effect of wall-thickness on the stress-strain curve has been studied. The results are compared with the experimental results of the solid cylindrical specimens of the same material.

Pure torsion and simple torsion tests have also been conducted to investigate the axial effect. Special attention has been given to the measurement of axial elongation or contraction during the pure torsion test and the measurement of axial stress during simple torsion test.

# RECENT EXPERIMENTS WITH THE TORSIONAL SPLIT HOPKINSON BAR TECHNIQUE

Amos Gilat  
The Ohio State University  
Department of Engineering Mechanics  
Columbus, Ohio 43210

The split Hopkinson bar technique is widely used for testing materials under dynamic loading. The technique was introduced by Kolsky in 1949 for testing in compression but has since been modified for tensile and torsional loadings. The presentation describes two recent research projects conducted using the technique.

In the first project the torsional split Hopkinson bar technique is used for testing ceramics. The technique is commonly used for testing ductile materials and its application to very brittle materials is examined carefully. Tests have been conducted with specimens made of aluminum oxide and titanium diboride. Most of the tests were done with spool-shaped specimens which is the standard geometry used for testing ductile materials. In addition, a method was developed for testing small prism-shaped specimens. This was done in an effort to develop a screening test for newly developed materials in which specimens are machined from thin plates. The experiments have been modeled with three dimensional elastic finite element analysis. Since the materials are very brittle, correlation can be made between the initial elastic response measured in the tests and the calculated response. The results provide a strong indication of strain rate sensitivity. The stresses in the specimens when initial fracture occurs appear to be higher than the stresses reported from tests at quasi-static rates.

In the second project the torsional split Hopkinson bar is modified for testing at elevated temperatures by heating the specimen to the testing temperature and keeping the rest of the system at room temperature. This was done by developing a rapid heating technique and a new connection between the specimen and the bars that allows transmission of the torsional waves and minimizes heat conduction to the bars. Results will be presented from tests with Haynes-188 at a temperature of 1000°C and a strain rate of 1150 sec<sup>-1</sup>

## MEASUREMENT OF TACTILE STRESS DISTRIBUTION BY IMAGE PROCESSING

Sushii Niitsu

Dept. of Mechanical Engineering, Tokyo Denki University,  
Kanda-nishikicyo 2-2, Chiyodaku, 101 Tokyo JAPAN

Kensuke Ichinose

Dept. of Mechanical Engineering, Tokyo Denki University,  
Kanda-nishikicyo 2-2, Chiyodaku, 101 Tokyo JAPAN

### ABSTRACT

The image processing system which can measure and analyze the contacting pressure distribution is developed. The pressure distribution loaded on the special elastic sheet is measured by using a pressure-optical conversion technique. A new image processing procedure [1,2] is applied to an optical image. The measuring scope is  $320 \times 300 \text{ mm}^2$  square, and  $64 \times 60$  points of force in this area are obtained. The Spatial resolution is  $5 \times 5 \text{ mm}^2$  square. The measuring range of force is from 5gf to 1,200gf on each unit ( $5 \times 5 \text{ mm}^2$ ), and the resolution power of force is 5gf/unit. Total processing procedure of each one frame takes within 0.2 second by personal computer.

### MEASURING METHOD

The developed measuring system is constructed with a transparent glass plate, a special elastic sheet (FUJI Film Co.), two light sources made by 180 ultra bright LED devices, CCD camera, video frame memory, and computer as shown in Fig.1. An elastic sheet has many small conical shapes ( $5 \times 5 \text{ mm}^2$ ) arranged at regular interval on one side. This sheet is put on the glass plate and force is applied on the elastic sheet. Two light sources are located at the side of the glass plate. A ray of light is incident into the glass plate from two facing each other side. The ultra bright LED devices are used as a light source, because its red ray having a long wavelength can pass through a glass with high transmissivity and is not reflected at small particles in or on a glass plate which dimension are less than the wavelength. An ultra bright LED device emits steady and non-flicking light and the intensity of light can be controlled easily by applying voltage. The CCD camera is placed under the glass plate and gets the image of the contacting surface between the glass plate and the elastic sheet. The analog image signal through the low pass filter is digitized by the high speed A/D converter and the digital image data of 8 bits are stored into 256Kbytes (512x482bytes) frame memory. The image data is calculated and the pressure distribution is obtained.

This measurement uses a pressure-optical conversion technique. Figure 2 shows the principle of this technique. A ray from the side is completely reflected in the glass plate. If the elastic sheet does not attach the glass plate, its ray does not reach the CCD camera. But if the elastic sheet attaches the glass plate, a condition of the complete reflection is broken in

the contacting area and this area emits a light.

Each elastic cone occupies  $5 \times 5 \text{ mm}^2$  and corresponds  $8 \times 8$  pixels of image data. The total scope of measurement is  $320 \times 300 \text{ mm}^2$ . Measuring processes by the computer are as follows; (1): Digitizing image signal; (2): Calculation of light intensity of each cone (Summation of partial image data of  $8 \times 8$  pixels) (3): Multiple location weight function on the distribution of light intensity. (4): Conversion of light intensity into pressure with the calibration curve. Figures 3 show the samples of measurements. It takes less than 0.2 second (180286-16MHz) to get one pressure distribution.

#### REFERENCES

- [1] Y. Niitsu, Y. Noda: Trans. of Japan Society of Mech. Engrs., 52-476 C, (in Japanese) (1986) pp.1141-1146
- [2] Y. Niitsu, K. Ikegami: Proc. of Int. Conf. on ADVANCED MECHATRONICS in Tokyo, (1989) pp.432-437

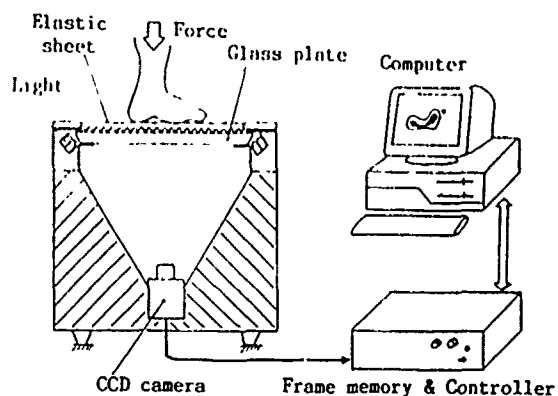


Fig.1 Construction of the measuring system: The force applied on the elastic sheet is obtained.

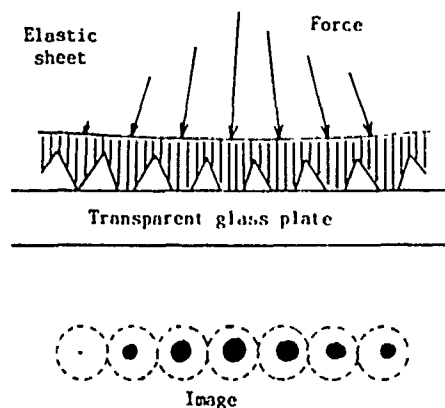
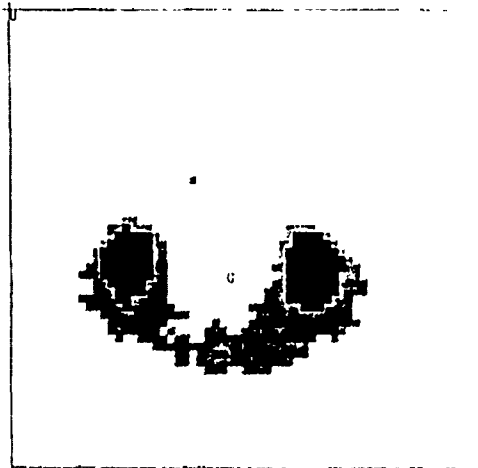
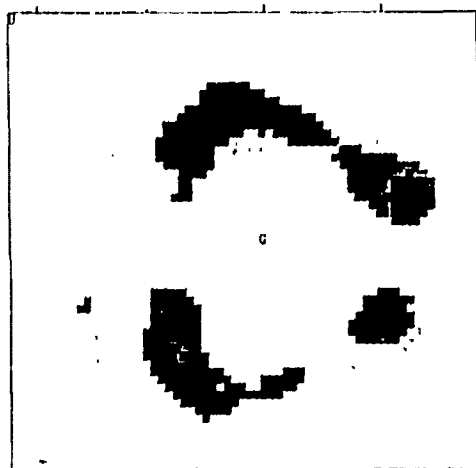


Fig.2 The principle of measurement: Pressure-optical conversion technique is used for the measurement. A number,  $64 \times 60$ , of elastic cones are arranged with separation distance 5mm.



Figs.3 Samples of measurement (Pressure distributions of foot and hip patterns). The lightest gray level points represent the pressure from  $20 \text{ gf/cm}^2$  to  $200 \text{ gf/cm}^2$  (from  $5 \text{ gf/unit}$  to  $50 \text{ gf/unit}$ ), and darkest gray level points represent more than  $960 \text{ gf/cm}^2$ . The mark of 'G' indicates the center of total force.

# YIELD AND FLOW BEHAVIOR OF INITIALLY ANISOTROPIC ALUMINUM TUBE UNDER MULTIAXIAL STRESSES

Takenobu Takeda

(Faculty of Engineering, Yamagata University,  
4-3-16 Jonan, Yonezawa 992, Japan)

## INTRODUCTION

Yield functions allowing for initial anisotropy have been proposed by several investigators<sup>1)</sup>. However, the present author<sup>2)</sup> proposed an anisotropic yield function expressed by means of combining Drucker's yield function with Hill's quadratic yield function. This yield function is able to include the effects of the third stress invariant and initial anisotropy, i.e.,

$$f = J_2^{-1/2} (J_2 + \Lambda_{ijkl} \sigma_{ij}' \sigma_{kl}') - C J_3^{-1/2}, \quad (1)$$

where  $J_2$  and  $J_3$  are the second and third stress invariants,  $\Lambda_{ijkl}$  is the anisotropy parameter and  $C$  is a parameter allowing for the effect of  $J_3$ .

In this investigation, experiments are carried out on 1050 aluminum tubes with initial anisotropy under combined loadings. Yield and flow behavior are determined, and the applicability of Eq.(1) is examined.

## EXPERIMENTAL PROCEDURE

Specimens were 1050 aluminum tubes of 40 mm outer dia., 2 mm wall thickness and 110 mm length. The tubes in the as-received condition had been subjected to progressive reductions by hot extruding and cold drawing processes. They were fully annealed by heating at 550°C for 1 hr in our laboratory.

Specimens were deformed along three different loading paths, maintaining the stress ratios  $\sigma_x : \sigma_y : \tau_{xy} = \text{const.}$ ,  $\sigma_y / \sigma_x = \text{const.}$  and  $\sqrt{3} \tau_{xy} / \sigma_x = \text{const.}$ , where  $\sigma_x$ ,  $\sigma_y$  and  $\tau_{xy}$  are axial, hoop and shear stresses respectively.

## RESULTS AND DISCUSSION

When subjecting a specimen to loading with a constant stress ratio  $\sigma_x : \sigma_y : \tau_{xy} = 1 : \tan^2 \theta : \tan \theta$ , only the major principal stress  $\sigma_1$  acts on the plane inclined at angle  $\theta$  to the specimen axis. Figure 1 shows the relation between the flow stress ratio and angle  $\theta$ . Here,  $\sigma_f$  is the flow stress in uniaxial tension, expressed by Ludwik's equation  $\sigma_f = \sigma_s + k \epsilon^n$ , where  $\sigma_s = 9.26$  MPa,  $k = 501.3$  MPa and  $n = 0.68$ . As angle  $\theta$  increases, the ratio  $\sigma_1 / \sigma_f$  rises to a maximum value and then decreases gradually. Figure 2 shows the variation of the principal strain increment direction  $\theta'$  with the principal stress direction  $\theta$ . The value of  $\theta'$  was obtained by the least squares method, assuming the plastic strain path to be straight. The angle  $\theta' - \theta$  increases in a negative direction with angle  $\theta$  and changes sinusoid-

ally. Figures 3 and 4 show the yield surfaces in the  $\sigma_x - \sigma_y$  and  $\sigma_x - \sqrt{3}\tau_{xy}$  planes. As the equi-strain surfaces described by the proof stresses at various offset strains have similar forms, dimensionless coordinate systems were adopted. The arrows indicate the directions of the plastic strain increment vectors. In Fig. 3, the broken curve was described in order to separate the effect of  $J_3$  from the presence of initial anisotropy. The  $C$  value was obtained by substituting the dimensionless stress value on the loading path  $\sigma_y / \sigma_x = 1/2$  into Drucker's yield function. In Fig. 4, the yield surface becomes inflated in the direction of the torsion axis. The curves described by heavy lines in Figs. 1, 3 and 4 are the results calculated from Eq.(1). The solid curve in Fig. 2 was calculated using the associated normality flow rule. The parameter values are given in Table 1.

## CONCLUSIONS

Multiaxial stress tests were carried out on fully annealed 1050 aluminum tubes with initial anisotropy. The yield surfaces could be expressed precisely by the proposed yield function. In addition, it was verified that this yield function played the role of plastic potential in defining the direction of the plastic increment vector.

## REFERENCES

- 1) For example, Hill, R., Math. Proc. Camb. Phil. Soc., 85 (1979), p.179.
- 2) Takeda, T. and Nasu, Y., J. Strain Analysis, 26 (1991), p. 47.

Table 1 Parameter Values in Eq.(1).

C	A <sub>xyxy</sub>	A <sub>yyzz</sub>	A <sub>zzxx</sub>	A <sub>xyxy</sub>
1.265	-0.5472	-0.3889	-1.0343	0.3475

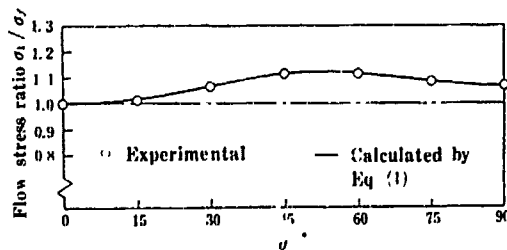


Fig. 1 Relation between flow stress ratio and principal stress direction  $\theta$ .

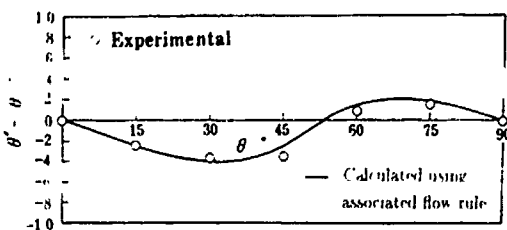


Fig. 2 Variation of principal strain increment direction  $\theta'$  with principal stress direction  $\theta$ .

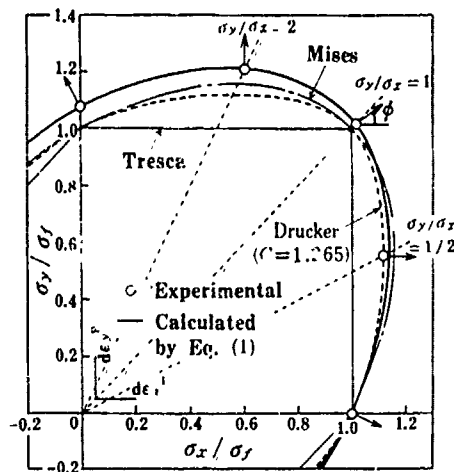


Fig. 3 Yield surface in  $\sigma_x - \sigma_y$  plane.

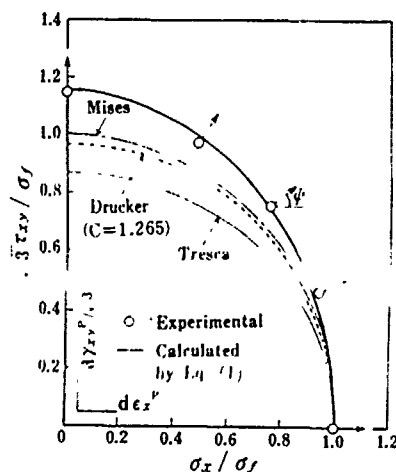


Fig. 4 Yield surface in  $\sigma_x - \sqrt{3}\tau_{xy}$  plane.

## EXPERIMENTAL STUDY OF RHA PLATE PERFORATION BY A SHAPED-CHARGE JET; HOLE SIZE AND MASS LOSS

Martin N. Raftenberg  
U. S. Army Ballistic Research Laboratory  
Aberdeen Proving Ground, MD 21005

A shaped-charge warhead with a conical, OFHC copper liner was fired into a plate of rolled homogeneous armor (RHA), a quenched and tempered, medium carbon, martensitic steel. The charge produced a stretching jet with a tip speed of 7.7 mm/ $\mu$ s. Two parameters were varied, namely the standoff, or separation between cone base and plate, and the target plate thickness. Standoffs of 264 and 1059 mm and plate thicknesses of 12.7, 25.4, and 50.8 mm were considered.

Flash radiographs reveal that at the short standoff, the jet was still intact prior to impact and throughout the perforation process. At long standoff, the jet had broken up into particles prior to impact. Radiographs were also used to observe the time course of fragmentation and hole formation in the plate.

The final hole radius, which ranged from 10.7 to 17.4 mm, was found to decrease with increasing plate thickness and to increase with increasing standoff. A "spall ring" and "ejecta ring" were identified as the regions on the exit side and entrance side, respectively, from which material had been removed from the plate. The spall ring radius ranged from 22.0 to 42.5 mm. It was found to increase with increasing plate thickness, but no systematic dependence on standoff was observed. The ejecta ring radius ranged from 19.3 to 23.3 mm. Here no systematic dependence on plate thickness or standoff was detected.

The total mass lost by the plate was found to increase with increasing plate thickness and exhibited little dependence on standoff. The data were fitted by empirical expressions in the form of hole radius as a function of plate thickness and standoff, and spall ring radius and mass lost as functions of plate thickness only.



## ON THE THEORIES OF LAMINATED COMPOSITE CURVED BEAMS

Mohamad S. Qatu  
Dresser Industries  
274 East First Avenue  
Columbus Ohio 43201

Laminated composite materials are used as structural components in various applications (aerospace, automotive, marine, ...). While these structural components can be beams, plates or shells, often encountered among these applications are beams. Beams can be straight or curved. Curved beams or often described as arches when they are open and as rings when they are closed. Open curved beams can have deep or shallow curvature. Two survey studies [1,2] exist on the vibration analysis of curved beams which list more than 200 references on the subject. Almost all the references dealt with isotropic beams. Only eight of these references dealt with composite sandwich beams of three-layers. The analysis of generally laminated curved beams is virtually non-existent.

This paper is concerned with the development of the fundamental equations for laminated composite beams of shallow and deep curvature and present some results for simple support boundaries. Only thin beams will be addressed and the effects of shear deformation and rotary inertia are neglected.

### 1. BEAMS OF SHALLOW CURVATURE

The strain displacement relations for such beams are [Ref. 3]

$$\epsilon^0 = \frac{\partial u_0}{\partial x} + \frac{w_0}{R}, \quad \kappa = -\frac{\partial^2 w_0}{\partial x^2} \quad (1)$$

The equations of motion are:

$$\begin{bmatrix} L_{11} & L_{12} \\ L_{21} & L_{22} \end{bmatrix} \begin{bmatrix} u_0 \\ w_0 \end{bmatrix} + \begin{bmatrix} -\bar{\rho} & 0 \\ 0 & \bar{\rho} \end{bmatrix} \frac{\partial^2}{\partial t^2} \begin{bmatrix} u_0 \\ w_0 \end{bmatrix} = \begin{bmatrix} -p_x \\ +p_n \end{bmatrix} \quad (2)$$

where  $L_{11} = A_{11} \frac{\partial^2}{\partial x^2}$ ,  $L_{22} = D_{11} \frac{\partial^4}{\partial x^4} - 2 \frac{B_{11}}{R} \frac{\partial^2}{\partial x^2} + \frac{A_{11}}{R^2}$

$$\text{and } L_{12} = L_{21} = -B_{11} \frac{\partial^3}{\partial x^3} + \frac{A_{11}}{R} \frac{\partial}{\partial x}, \quad (3)$$

where  $R$  is the radius of curvature and  $A_{11}$ ,  $B_{11}$  and  $D_{11}$  are defined in [3].

## 2. DEEP BEAMS

The strain displacement relations for deep beams (Ref. 4)

$$\epsilon^0 = \frac{\partial u_0}{\partial x} + \frac{w_0}{R}, \quad \kappa = -\frac{\partial^2 w_0}{\partial x^2} + \frac{1}{R} \frac{\partial u_0}{\partial x} \quad (4)$$

The operators in the equations of motion (2) for deep beams become:

$$L_{11} = A_{11} \frac{\partial^2}{\partial x^2} + \frac{2B_{11}}{R} \frac{\partial^2}{\partial x^2} + \frac{D_{11}}{R^2} \frac{\partial^2}{\partial x^2}, \quad L_{22} = D_{11} \frac{\partial^4}{\partial x^4} - 2 \frac{B_{11}}{R} \frac{\partial^2}{\partial x^2} + \frac{A_{11}}{R^2}$$

$$\text{and } L_{12} = L_{21} = -B_{11} \frac{\partial^3}{\partial x^3} + \frac{A_{11}}{R} \frac{\partial}{\partial x} + \frac{B_{11}}{R^2} \frac{\partial}{\partial x} + \frac{D_{11}}{R} \frac{\partial^3}{\partial x^3} \quad (5)$$

## 3. EXACT SOLUTIONS

For simple support boundary conditions (i.e.  $w = N = M = 0$  on  $x = 0, a$ ), there exist an exact solution for the free vibration problem ( $P_x = P_z = 0$ ).

which is  $u = A_m \sin(\alpha x) \sin(\omega t)$ , and  $w = C_m \cos(\alpha x) \sin(\omega t)$ ;  $\alpha = m\pi/a$  (6)

Substituting this into the equations (2), (3) and (5) yields a  $2 \times 2$  matrix. The matrix determinant should be set to zero for the free vibration

problem to obtain the frequency parameter  $\Omega_1 = \omega a \sqrt{12\rho/E h^2}$ . The

following table compares the results obtained using the above theories. It shows that for a curvature ratio of 1, the difference may exceed 10%.

Frequency parameters for simply supported  $[0,90]$  laminated beams,  $a/h=100$ .

$\frac{a}{R}$	Deep beam results				Shallow beam results			
	$m=1$	2	3	4	1	2	3	4
0	9.870	39.48	88.83	157.9	9.870	39.48	88.83	157.9
0.2	9.810	39.43	88.83	157.9	9.849	39.46	88.81	157.9
0.5	9.499	39.12	88.52	157.8	9.749	39.35	88.70	157.8
0.8	8.947	38.54	87.94	157.4	9.568	39.16	88.51	157.6
1.0	8.451	38.01	87.40	156.6	9.402	38.99	88.33	157.4

## References

1. S. Markus and T. Nanasi, "Vibrations of Curved Beams," Shock and Vibration Digest, Vol 7, No. 4, pp. 3-14, 1981.
2. P.A.A. Laura and M.J. Maurizi, "Recent Research on Vibrations of Arch-Type Structures," Shock Vibration Digest, Vol 19, No. 1, pp. 6-9, 1987.
3. M.S. Qatu, "Inplane Vibration of Slightly Curved Laminated Composite beams," submitted for publication.
4. M.S. Qatu, "Equations for Vibration Analysis of Thin and Moderately Thick Laminated Deep Beams," submitted for publication.

# BENDING ANALYSIS OF CANTILEVERED COMPOSITE SHALLOW SHELLS USING FINITE ELEMENT AND RITZ METHODS

Mohamad S. Qatu  
Dresser Industries  
274 East First Avenue  
Columbus Ohio 43201

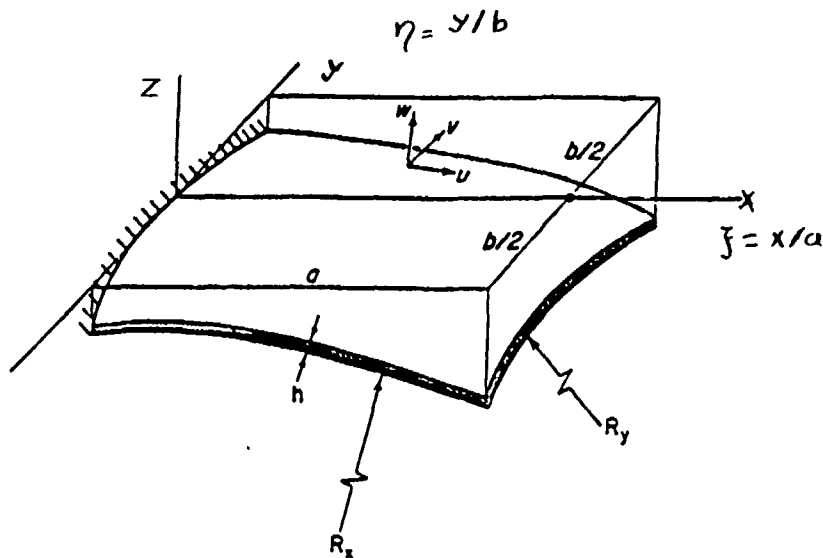
Ali Al-Gothani  
Ventura Engineering  
7610 Olentangy River RD  
Columbus Ohio 43235

Shallow shell problems have exact solutions for only a very restricted set of boundary conditions and lamination sequences. Numerical methods such as the Ritz and Finite Element Methods (FEM) are particularly useful for the remaining types of problems.

The present work uses strain and kinetic energy functionals as well as load potentials developed earlier (1) for laminated shallow shells having arbitrary radii of curvature. These are used with the Ritz method and FEM to solve for deflections and stresses within statically loaded shallow shells. A cantilevered shallow shell of rectangular planform, as shown in the figure below, will be considered in the analysis. The Ritz method require the satisfaction of only the geometric boundary conditions (zero displacements and slopes at  $x=0$  for cantilever boundary conditions). This is achieved by choosing the displacement components as

$$u(\xi, \eta) = \sum_{i=1}^I \sum_{j=0}^J \alpha_{ij} \xi^i \eta^j; \quad v(\xi, \eta) = \sum_{k=1}^K \sum_{l=0}^L \beta_{kl} \xi^k \eta^l \quad \text{and} \quad w(\xi, \eta) = \sum_{m=2}^M \sum_{n=0}^M \gamma_{mn} \xi^m \eta^n$$

where the  $\alpha_{ij}$ ,  $\beta_{kl}$  and  $\gamma_{mn}$  are coefficients to be determined.



Utilizing the assumed displacement functions in the energy functionals, and carrying out the necessary minimization, yields simultaneous linear algebraic equations to be solved for the static loading problems (2).

Shallow shell elements have also been used to find the displacements and stresses at particular points of the shell under gravity loading. Four- and eight-noded lagrangian rectangular elements were used in the analysis (3). The following table shows nondimensional deflections at two points of the outer free edge of the shell as well as nondimensional stress resultants at the middle of the clamped edge. The Nondimensional parameters are the same as that used in Ref. (2).

As can be seen from the table, convergence of the displacements is sufficiently good in both the Ritz method and FEM. Convergence for stress resultants is not as good as that for the displacement. This is because stress resultant calculations involve derivatives of the displacement. It seems that force and moment resultants predicted by FEM are less than those predicted by the Ritz method except for  $N_y$  when eight-noded elements are used. The table also shows that considerably less Degrees Of Freedom (DOF) are needed for the Ritz method than those needed for FEM to get comparable accuracy. Further results will be given in later publications.

Comparison of Deflection and Stress Resultants Obtained by Different Methods For a [0,90,0] Cylindrical Shallow Shell Under Gravity Load  
 $E_1/E_2 = 15.40$ ,  $G_{12}/E_2 = 0.79$ ,  $\nu_{12} = 0.3$ ,  $a/b = 1$ ,  $a/h = 100$ ,  $a/Ry = 0.5$

FEM Models: I 100 Four-Noded Elements, II 400 Four-Noded Elements  
 III 36 Eight-Noded Elements, VI 100 Eight-Noded Elements

Model	DOF	$\xi = 1, \eta = 0$			$\xi = 1, \eta = 0.5$			$\xi = 0, \eta = 0$					
		$\bar{u}$	$\bar{v}$	$-\bar{w}$	$\bar{u}$	$\bar{v}$	$-\bar{w}$	$\bar{N}_x$	$\bar{N}_y$	$\bar{N}_{xy}$	$\bar{M}_x$	$\bar{M}_y$	$\bar{M}_{xy}$

#### The Ritz Method (Ref. 2)

108	0.001	0	0.050	-0.004	0.039	0.327	9.9	0.3	0	7.4	0.2	0
147	0.001	0	0.047	-0.004	0.039	0.328	15.8	0.4	0	7.5	0.2	0
192	0.001	0	0.045	-0.004	0.039	0.328	15.7	0.4	0	7.4	0.2	0

#### The Finite Element Method

I	605	0.001	0	0.036	-0.004	0.044	0.321	11.4	0.3	0	4.2	0.1	0
II	2205	0.001	0	0.038	-0.004	0.044	0.321	12.0	0.4	0	5.3	0.1	0
III	665	0.001	0	0.035	-0.004	0.048	0.343	12.4	1.1	0	5.7	0.1	0
IV	1705	0.001	0	0.038	-0.004	0.045	0.328	12.4	1.2	0	6.3	0.1	0

#### REFERENCES

1. Leissa, A.W. and Qatu, M.S., "Equations of Elastic Deformation for Laminated Composite Shallow Shells," J. Applied Mechanics, to appear, 1991
2. Leissa, A.W. and Qatu, M.S., "Stress and Deflection Analysis of Composite Cantilevered Shallow Shells," J. Engineering Mechanics, to appear, 1991
3. Hughes, T.J., "The Finite Element Method", Printice-Hall, Inc., 1987.

## A SYMBOLIC-NUMERICAL STUDY OF THE NONLINEAR VIBRATION OF LAMINATED SHELL PANELS

**Raouf A. Raouf**

Mechanical Engineering Department  
United States Naval Academy  
Annapolis, MD 21402

**Anthony N. Palazotto**

Department of Aeronautics and Astronautics  
Air Force Institute of Technology  
Wright-Patterson Air Force Base, OH 45433

In [1], the authors develop a nonlinear theory for the dynamic response of arbitrarily laminated anisotropic shell panels. The theory allows for slight compression across the thickness of the panel and accounts for tangential and rotary inertia. The equations of motion are asymptotically consistent with the stated kinematic assumptions. To eliminate algebraic errors, the theory is developed completely within the symbolic manipulators MACSYMA [2] and Mathematica [3]. Moreover, these manipulators produce error free computer codes to be used in the numerical verification of the results. Qualitative analysis shows that such a panel can experience a variety of complicated dynamical phenomena when subjected to a near-resonant harmonic excitation. These phenomena include jumps and various bifurcations.

In this paper, the above theory is used to perform a single-mode, multi-harmonic analysis of a laminated panel. The Rayleigh-Ritz technique is used to reduce the nonlinear dynamic partial differential equations of the panel to an ordinary differential equation of the form

$$m \frac{d^2 u_n}{dt^2} + \omega_n^2 u_n + \alpha_1 u_n^2 + \alpha_2 u_n^3 = 0 \quad (1)$$

where  $t$  is time and  $u_n$  is the amplitude of the  $n^{th}$  spatial mode. Next, the method of harmonic balance is used for the temporal analysis. Thus,  $u_n$  is expanded as

$$u_n = \sum_{k=0}^{nh} a_k \cos k\omega t + b_k \sin k\omega t \quad (2)$$

The above expansion is substituted into equation (1) and the coefficients of various harmonics are equated. This results in a set of nonlinear algebraic equations to be solved for the amplitudes of the harmonics and the nonlinear natural frequency  $\omega$ .

An apparent disadvantage of the above procedure is the algebraic complexity that increases as the number of harmonics increases, thus limiting the ability to produce more accurate results. A pure symbolic analysis is too slow and a pure numerical analysis must be preceded by cumbersome algebra. A combination of the two, however, provides the best approach. The symbolic manipulator is used to perform the algebraic analysis symbolically and eventually produce a computer code that numerically assembles and solves the resulting nonlinear equations for the amplitudes of the harmonics and the nonlinear natural frequency. Unlike previous approaches, this numerical code is generic, it takes the number of harmonics ( $nh$ ) as an input. The symbolic manipulator is run only once to produce the code, the rest of the analysis is numerical. This approach proved to be very efficient in investigating the nonlinear dynamic characteristics of a laminated shell panel.

### ACKNOWLEDGEMENTS

This research was initiated under grant no. AFOSR-89-0010 by the Air Force Office of Scientific Research. It is also supported by a grant from the United States Naval Academy Research Council.

### REFERENCES

1. Raouf, R. A., and Palazotto, A. N., "Nonlinear Dynamic Response of Anisotropic, Arbitrarily Laminated Shell Panels: An Asymptotic Analysis", *Composite Structures*, in press, 1991.
2. *MACSYMA Reference manual*, Document No. SM1050030.013, November, 1988.
3. Wolfram, S. *Mathematica: A System for Doing Mathematics by Computer*, Addison-Wesley Publishing Company, Inc., 1988.

# LARGE STRAIN PREDICTIONS FOR CYLINDRICAL MEMBRANES USING A STRESS FUNCTION

Saeed Foroudastan<sup>1</sup> and John Peddieson, Jr.<sup>2</sup>

<sup>1</sup>Textron Aerostructures, Nashville, Tennessee 37202

<sup>2</sup>Department of Mechanical Engineering, Tennessee Technological  
University, Cookeville, Tennessee 38505

Large deformation membrane problems exhibit many features (boundary layers and nonunique load/deflection characteristics, for example) of nonlinear structural response and are pertinent to applications involving inflatable structures, cable nets, and superplastic forming. Of the exact governing equations for membranes, those associated with axisymmetric static deformations of a circular cylinder are among the least complicated. As such, they deserve detailed study. One way to write these equations is as follows.

$$T_z = (\psi^2 + (av)^2)^{1/2}/a, \quad T_\theta = \psi' + ap, \quad V = V(-L) - \int_{-L}^z q(\hat{z}) d\hat{z} \quad (1)$$

$$e_z = e_z(T_z, T_\theta), \quad e_\theta = e_\theta(T_z, T_\theta), \quad e_\theta^z = \partial e_\theta / \partial T_z, \quad e_\theta^\theta = \partial e_\theta / \partial T_\theta \quad (2)$$

$$u = ae_\theta, \quad w = w(-L) - (L+z) + \int_{-L}^z ((1+e_z(\hat{z}))^2 + (ae_\theta(\hat{z}))^2)^{1/2} d\hat{z} \quad (3)$$

$$\psi'' + (e_\theta^z(\psi\psi' + a^2VV') - (1+e_z)\psi) / (ae_\theta^\theta(\psi^2 + (av)^2)^{1/2}) = -ap' \quad (4)$$

In (1-4)  $z$  is the axial coordinate (with origin at the membrane's center),  $\psi$  is a stress function,  $T_z$  and  $T_\theta$  are axial and circumferential Lagrangian stress resultants respectively,  $V$  is the axial component of  $T_z$ ,  $p$  and  $q$  are radial and axial loads per unit of undeformed area respectively,  $u$  and  $w$  are radial and axial displacements respectively,  $e_z$  and  $e_\theta$  are axial and circumferential linear extensions respectively,  $\hat{z}$  is a dummy variable, a prime denotes differentiation,  $a$  is the membrane's radius, and  $L$  is its half length.

In the present work (1-4) are used as follows. The pressures  $p(z)$  and  $q(z)$ , the stress resultant  $V(-L)$ , and the displacement

$w(-L)$  are regarded as known. Equation (1c) then determines  $V(z)$ . The quantities appearing in (2) can be put in terms of  $\psi$  with the aid of (1a,b). Then  $u$  and  $w$  can be expressed in terms of  $\psi$  using (3) and (4) becomes a second order ordinary differential equation to solve for  $\psi(z)$ . Boundary conditions on one of each of the pairs  $T_z(-L)$ ,  $u(-L)$ , and  $T_z(L)$ ,  $u(L)$  are specified and converted to boundary conditions on  $\psi(-L)$  and  $\psi(L)$  using (1a) and (3a). Once the boundary value problem is solved for  $\psi(z)$ , the stress resultants, strains, and displacements can be found from (1a,b), (2a,b), and (3) respectively. The advantage of this formulation is that only one nonlinear differential equation must be solved iteratively.

The governing equation (4) holds for any constitutive equations of the form (2a,b). When the plane stress form of Hooke's law  $e_z = (T_z - \nu T_\theta)/(Eh)$ ,  $e_\theta = (T_\theta - \nu T_z)/(Eh)$  is used ( $E$  being Young's modulus,  $\nu$  Poisson's ratio, and  $h$  the membrane's thickness) it reduces to

$$\psi'' - \psi/a^2 + ((\nu ap - Eh)\psi - \nu a^2 VV')/(a(\psi^2 + (aV)^2)^{1/2}) = -ap' \quad (5)$$

Equation (5) was solved for a variety of loadings by an iterative finite difference method. Some typical computed results are shown in Figures 1 and 2 for  $p=\text{constant}$ ,  $q=0$ ,  $u(\pm L)=0$ ,  $w(\pm L)=0$ . (In this case the value of  $V(-L)$  required to make  $w(L)=0$  must be determined by trial and error.) It can be seen that the numerical approach is capable of yielding solutions for values of the loading parameter  $pa/(Eh)$  much larger than those which would produce failure in most real materials.

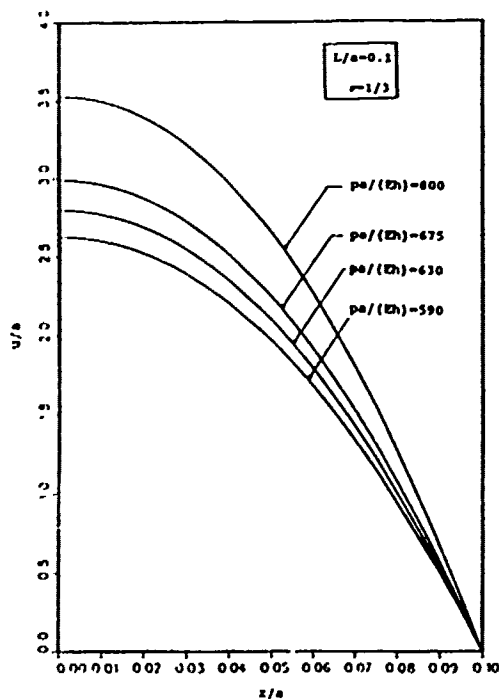


Figure 1. Radial Displacement for Fixed Ends

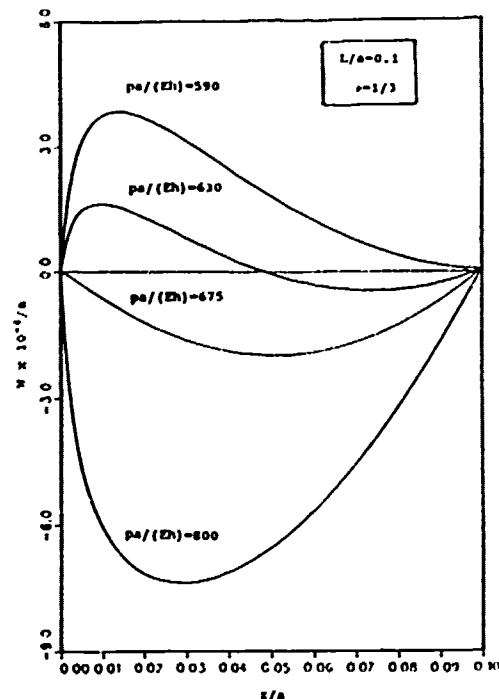


Figure 2. Axial Displacement for Fixed Ends



# An Analysis on Dynamic Elastic and Plastic Stability of Shallow Spherical Shells With Ends Clamped Under Step Loading

## Abstract

Liu Pu (Dept. of Naval Architecture & Ocean Engineering, Shanghai Jiao Tong University, 200030, P.R. China)

### 1. Introduction

Dynamic instability of structures bearing dynamic load is a less well understood phenomenon than the static one. The influence of plastic yielding furtherly complicates the problem. Many previous researchers treated the problem by rigid-plasticity method in which only plastic deformation is considered. In this paper, by an approximate model for the dynamic plastic yielding process of shallow spherical shells, a simplified method is proposed to analyse the dynamic elastic and plastic instability problem.

### 2. Basic equations

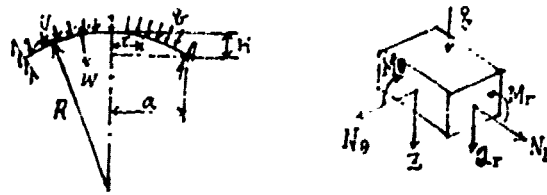


Fig. 1

For shallow spherical shells under step load shown in Fig. 1 motion equations could be derived as follows:

$$\begin{aligned} u'' + u'/x - u/x^2 + g(w) &= (1-\nu^2) a^3 q_1^p / (Eh^3) \\ \nabla^4 w - 12(\epsilon_r + \nu \epsilon_\theta)(w'' + \eta^2) &- 12(\epsilon_\theta + \nu \epsilon_r)(w'/x + \eta^2) \\ &= 4m^2 \eta^4 p - m^4 a^4 (q_2^p + q_3^p) / (Eh^4) - \eta^2 m^4 \ddot{w} \end{aligned}$$

where  $u, w$ , etc. possess meanings generally appointed.  $q_1^p, q_2^p$  and  $q_3^p$  are effective plastic loads caused by plastic deformation.

### 3. the plastic yielding model of the shell

under well-distributed external load, the plastic yielding of the shell first occur at point A or B in Fig. 2. Then plastic deformation develop along both meridional and normal direction. The influence of plastic deformation may be expressed through effective plastic loads, as shown in Fig. 2.

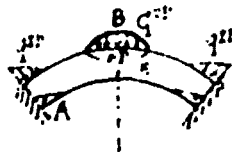


Fig. 2

Through Mises yielding criterion, the boundary of plastic area could be obtained.

$$P_2 z^2 + 2P_1 z + P_0 = 3\epsilon_y^2/4$$

where  $P_0, P_1, P_2$  are quantities concerned with strains in middle surface. The two plastic area could be expanded as,

$$0 \leq x \leq x^{op}:$$

$$z^{op} = z^0 + \frac{1}{2} z'' x^2 + \dots$$

$$x^{ip} \leq x \leq 1:$$

$$z^{ip} = z^1 - z^1'(1-x) + \frac{1}{2} z^{1''}(1-x)^2 + \dots$$

Through integral in the plastic area, effective plastic load could be obtained. If taking deflection as  $w = a_0 f(x)$ , where  $a_0$  is motion amplitude,  $f(x)$  is deflection function satisfying boundary conditions, then by Galerkin technique, motion equations may be derived as follows.

1). Elastic deformation

$$\Psi(a_0) = \ddot{a}_0 + b_1 \dot{a}_0 + b_2 a_0^2 + b_3 \dot{a}_0^3 + b_4 p = 0$$

2). Plastic yielding has occurred at  $x=0$

$$\Psi(a_0) + \phi^{op}(a_0) = 0$$

Pl. Plastic yielding has also occurred at  $x=1$

$$\Psi(a_0) + \phi^{op}(a_0) + \phi^{ip}(a_0) = 0$$

$\phi^{op}, \phi^{ip}$  are quantities concerned with plastic deformation. Calculations have been made for shells made of bi-linear materials. The results are in accordance with those in ref. (2).

#### 4. Conclusions

Two-area plastic yielding model is proposed to analyse the dynamic elastic-plastic instability of shallow spherical shells. The results show that it is feasible to use approximate model to describe the complicated development of plastic area. This is of great significance in researching the dynamic elastic plastic instability of more complicated structures.

#### Reference.

1. Jones N., and Ahn c.s., Dynamic buckling of complete rigid-plastic spherical shells, J. Applied Mech., Vol. 41, 1974
2. Kao R., Nonlinear dynamic buckling of spherical caps with initial imperfections, Computers & Structures, Vol. 12, 1980
3. Jones N., Dosreis H.L.M., On the dynamic buckling of a simple elastic-plastic model, Int. J. Solids & Structures, Vol. 16, 1980
4. Song B. Q., and Jones N., Dynamic buckling of elastic-plastic complete spherical shells under step loading, Int. J. Impact Engineering, Vol. 1, 1983

## Damage Mechanisms under Impact by Interlaminar Sensors

David Hui<sup>\*</sup> and Piyush K. Dutta<sup>\*\*</sup>

The work deals with the formulation of the damage mechanisms of graphite-epoxy composite and aluminum plates under impact via Hopkinson Bar impact tests. The various modes of failure such as matrix cracking, delamination and fiber breakage under perforation impact are examined. Further, an examination of energy absorption and the wave mechanics behavior of composite plates are presented. The research involves an innovative sensing system utilizing thin films of pressure sensitive (piezopolymer) material in lamina boundaries of a composite panel. The study constitutes a fundamental understanding of the energy absorption and failure modes.

In particular, the sensors in interlaminar locations are employed to study the wave propagation through the thickness and in the planar directions of the interior of the panels. The leading edge of these waves are sensed by the sensor film at every laminate layer. The compressive wave reflects back from the free surface as a tensile wave. During the propagation of the reflected tensile wave, the sensor signals indicate whether the interlaminar debonding (delamination) occurs. A high speed data acquisition system is used to monitor the wave propagation and the signals are recorded in the first few micro-seconds after impact. The stress versus time signals are recorded and are used to determine the energy absorption in each layer. The theoretical model of wave propagation agrees with the experimental results.

\* University of New Orleans, Dept. of Mechanical Engineering,  
New Orleans, LA 70148

\*\* US Army Cold Regions Research and Engineering Laboratory,  
Hanover, New Hampshire 03755

presented at Society of Engineering Science , SES 1991 meeting

# SPLINE-BASED METHODS OF PARAMETER ESTIMATION FOR ELASTIC BEAMS WITH VARIABLE FLEXURAL RIGIDITY

Shive K. Chaturvedi  
Wei Ho  
Department of Civil Engineering  
The Ohio State University  
Columbus, Ohio 43210

## ABSTRACT

During the past two decades several types of parameter estimation or also known as inverse problems in solid and structural mechanics area have been tackled by a number of researchers [1-7]. The kind of problems looked at include structural integrity of offshore oil and gas platforms, damage assessment of large space structures and vibrating plates and beams. The inverse problems have become even more important with the advent of fiber reinforced composite materials and structures in various material utilization sectors. Presence of various flaws and damage modes and their subsequent growth in a composite structural element cannot be ruled out, and the gross effects of these damage modes can be a spatially varying reduction in stiffness and strength properties.

The present paper is aimed at addressing the estimation of stiffness variation along the length of a simply supported Euler-Bernoulli beam. Practically such a problem may include a damaged short-fiber reinforced composite beam. Banks and Crowley method [7] will be extended to address a number of unanswered questions related to implementation, limitations, numerical accuracies, convergence rates and other aspects of spline-based techniques.

For an undamaged simply supported beam with a constant mass density and constant moment of inertia but variable stiffness  $E(x)$ , the normalized equation of motion can be given as [8]

$$u_{tt} + D^2(\alpha(x)D^2u) = f(t,x), \quad 0 \leq x \leq 1, \quad t > 0$$

where  $\alpha(x) = IE(x) / \rho$

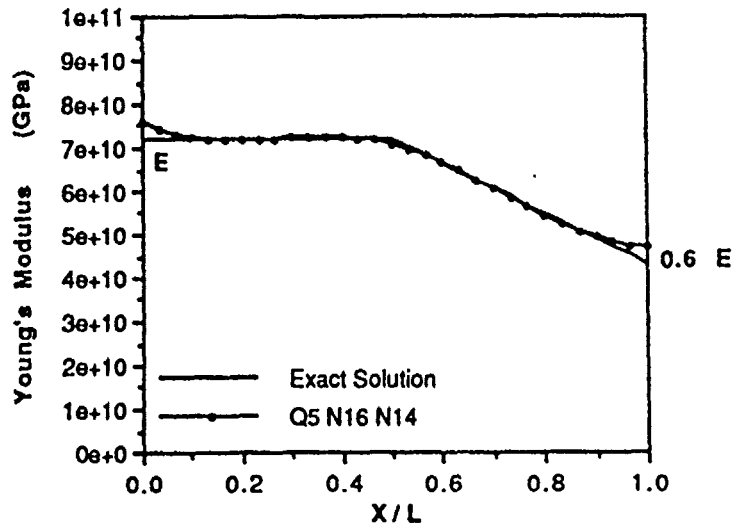
The boundary conditions and initial conditions can be given as

$$u(t,0) = u(t,1) = u_{xx}(t,0) = u_{xx}(t,1) = 0$$

$$u(0,x) = \phi(x)$$

$$u_t(0,x) = \psi(x)$$

The problem is to find the variation of  $\alpha(x)$  for the known solution  $u(x,t)$ . One of the results for variation of stiffness  $E$  along the beam is compared with the estimated one (through inverse solution approach) as shown below.



Comparison of Exact and Estimated (NSEG=14, Q=5) Parameters, QINTSOL's Output Used as Observation Values.

#### REFERENCES

1. Coppolino, R. N. and Rubin, S., "Detectability of Structural Failures in Offshore Platforms by Ambient Vibration Monitoring", *Proceeding of the Offshore Technology Conference*, Vol. 1, Paper OTC 3865, pp. 101-110, May 1980.
2. Chen, Tay-Chung and Garba, J. A., "On Orbit Damage Assessment for Large Space Structures", *Proceeding of ADM Conference*, 1987.
3. Juang, J. N. and Pappa, R. S., "An Eigensystem Realization Algorithm for Modal Parameter Identification and Model Reduction", *AIAA Journal of Guidance, Control and Dynamics*, Vol. 8, No. 5, pp. 620-627, 1985.
4. Qiu, C. H. and Chen, Y. M., "Inverse Problems for Elastic Plates with Variable Flexural Rigidity", *Int. J. Solids Structures*, Vol. 22, No. 8, pp. 901-908, 1986.
5. Barcilon, V., "Inverse Problem for a Vibrating Beam", *J. Appl. Math. Phys.*, 27, pp. 346-358, 1976.
6. Gladwell, G. M. L., England, A. H. and Wang, D., "Examples of Reconstruction of an Euler-Bernoulli Beam from Spectral Data", *Journal of Sound and Vibration*, 119, pp. 81-94, 1987.
7. Banks, H. T. and Crowley, J. M., "Parameter Identification in Continuum Models", *Journal of Astronautical Sciences*, Vol. 33, No. 1, January-March, pp. 85-94, 1985.
8. Ho, Wei, "Parameter Estimation for Elastic Beams with Variable Flexural Rigidity", M. S. Thesis, The Ohio State University, 1990.

# ON APPROXIMATE CLOSED-FORM SOLUTIONS FOR BUCKLING OF ANISOTROPIC RECTANGULAR PLATES

Robert Reiss and Oscar Barton  
Department of Mechanical Engineering  
Howard University  
Washington, D.C. 20059

The classical biaxial buckling eigenvalue equation for anisotropic rectangular plates is

$$\begin{aligned} D_{11} W_{,xxxx} + D_{16} W_{,xxxy} + 2(D_{12} + 2D_{66}) W_{,xxyy} + D_{26} W_{,xyyy} + \\ D_{22} W_{,yyyy} = -\lambda(W_{,xx} + \beta W_{,yy}) \end{aligned} \quad (1)$$

where  $\lambda$  is the applied axial load  $P_x$ ,  $\beta$  is the given ratio of applied axial loads  $P_y/P_x$ ,  $W$  is the buckled mode shape, and subscripts following the comma denote differentiation with respect to the argument indicated. Further, the constants  $D_{ij}$  are the usual flexural stiffness properties of the plate. Equation (1) is valid for arbitrary homogeneous anisotropic plates as well as laminated plates whose orthotropic plies are materially and geometrically symmetric about the laminate's middle plane. The mathematical description of this problem is completed by appending appropriate boundary conditions to Eq. (1).

With the exception of orthotropic laminates ( $D_{16}=D_{26}=0$ ) with pinned boundary conditions, closed form solutions are not available. In this study, approximate closed form solutions will be sought.

Equation (1) may be discretized, using finite-elements, finite differences or the Raleigh-Ritz approach, to obtain

$$[K] \{\alpha_i\} = \lambda_i [M] \{\alpha_i\} \quad (2)$$

where  $\lambda_i$  is the eigenvalue corresponding to the eigenvector  $\{\alpha_i\}$ , and  $[K]$  and  $[M]$  are, respectively, the symmetric positive definite stiffness and mass matrices. Recently, an approximate solution to Eq. (2) has been developed [1]

$$\lambda_i = \frac{K_{11}}{M_{11}} - M_{11}^{-2} \sum_{n \neq 1} \frac{(M_{11} K_{ni} - K_{11} M_{ni})^2}{M_{11} K_{nn} - M_{nn} K_{11}} \quad (3)$$

Equation (3) is exact to within cubic terms involving the off-diagonal elements  $M_{ij}$ ,  $K_{ij}$  ( $i \neq j$ ).

If the Ritz method of discretization is employed, the right hand side of Eq. (3) is explicitly known in terms of the flexural stiffnesses  $D_{ij}$ . As long as the coupling terms  $D_{16}$  and  $D_{26}$  are not too large when compared to the largest of the other stiffness coefficients, Eq. (3) will determine the buckling eigenvalues quite accurately. Such is the case for symmetric angle-ply laminates even when the orthotropic stiffness ratios  $E_1/E_2$  is very large.

Another approximate approach for solving Eq. (2) can be developed if each stiffness  $D_{ij}$  are known functions of a single parameter. An orthotropic plate whose material axes are oriented at an angle  $\theta$  to the plate axes is such an example. In this case each  $D_{ij}$  is a specified function of  $\theta$ . For pinned plates, Eq. (3) is exact to within terms of order  $\theta^3$  and  $(\frac{\pi}{2}-\theta)^3$ . Therefore, Eq. (3) may be used to compute  $\lambda_i$ ,  $d\lambda_i/d\theta$  and  $d^2\lambda_i/d\theta^2$  at  $\theta=0$  and  $\pi/2$ . Since  $\lambda_i(\theta)$  must be an even function of  $\theta$  and has periodicity  $\pi$ , it may be approximately represented by

$$\lambda_i(\theta) \approx \frac{1}{2} a_0 + a_2 \cos 2\theta + a_4 \cos 4\theta + a_6 \cos 6\theta \quad (4)$$

where the coefficients of the Fourier series are uniquely determined by  $\lambda_i$  and  $d^2\lambda_i/d\theta^2$  evaluated at 0 and  $\pi/2$ . Equation (4) provides a useful approximation even when  $D_{16}$  and/or  $D_{26}$  is large compared to the other stiffnesses.

Numerical examples will illustrate both methods.

#### References

- [1] R. Reiss and B. Qian, "Eigenvalues of Self-Adjoint Systems Determined by Eigensensitivity Analysis", Proc. PACAM II, Valparaiso, Chile, Jan. 1991, pp. 563-566.

# Optical Measurement of Deformation Fields Near Propagating Bimaterial Interface Cracks<sup>1</sup>

Hareesh V. Tippur<sup>2</sup> and Ares J. Rosakis<sup>3</sup>

## Abstract

A recently developed real time, full field, grating shearing interferometry - *Coherent Gradient Sensing* (CGS) [1,2] is used to map deformation fields near quasi-statically and dynamically growing interfacial cracks in bimaterial composite specimens. The bimaterial specimens are made by bonding equal thickness PMMA and Aluminum sheets. The specimens are subject to three point bending. An initial starter notch, cut along the interface, facilitates crack initiation and subsequent growth along the interface. A displacement controlled loading device is used to achieve quasi-static crack growth while dynamic crack growth is accomplished by impact loading the bimaterial specimen in a drop weight tower. In both the situations, the interference fringes representing crack tip deformation  $[\partial(\sigma_{11} + \sigma_{22})/\partial x_1]$  is recorded in the PMMA half of the specimen using transmission CGS. High speed photography with framing rates of approximately 150,000 frames/sec is used to record interference patterns during dynamic crack growth. Typical fringe patterns seen near a dynamically propagating crack are shown in Figure 1. Very high crack speeds, nearly 80% of the Rayleigh wave speed for PMMA, are observed during dynamic crack growth.

The quasi-static results are analyzed using the crack tip deformation fields proposed by Rice *et.al.*, [3] and are compared with the finite element computations performed by Shih and O'Dowd [4]. An over deterministic least square curve fitting of the experimental data is used to measure crack tip complex stress intensity factor  $K$  and crack tip mode mixity. Good agreement between experimental measurements and computations are observed regarding energy release rate.

In the dynamic experiments, different wave speeds in the two halves of the specimen clearly seem to affect the crack tip deformation fields both prior to and after crack initiation. Estimates of complex  $K$  and mode mixity are also obtained from the dynamic fringe patterns.

## References

- [1]. H.V. Tippur, S. Krishnaswamy and A.J. Rosakis, 'Optical Mapping of Crack Tip Deformations Using the Methods of Transmission and Reflection Coherent Gradient Sensing: A Study of Crack Tip  $K$ -dominance', Caltech Report SM 89-11, 1989, (To appear

---

<sup>1</sup>for presentation at 22nd Midwestern Mechanics Conference, University of Missouri-Rolla, MO, October 1991

<sup>2</sup>Assistant Professor, Department of Mechanical Engineering, Auburn University, AL

<sup>3</sup>Associate Professor, Department of Aeronautics and Applied Mechanics, California Institute of Technology, CA



in Int. J. Fracture).

[2]. S. Krishnaswamy, H.V. Tippur and A.J. Rosakis, 'Measurement of Transient Crack Tip Deformation Fields Using the Method of Coherent Gradient Sensing', Caltech Report SM 90-1, 1990, (To appear in J. Mech. and Phy. Solids).

[3]. J.R. Rice, Z. Suo, and J.S. Wang, 'Mechanics and Thermodynamics of Brittle Interfacial Failure in Bimaterial Systems', Metal-Ceramic Interfaces, Acta-Scripta Metallurgica Proceedings Series, 4, pp 269-294, 1990.

[4]. C.F. Shih and N.P. O'Dowd, Private Communications, 1990.

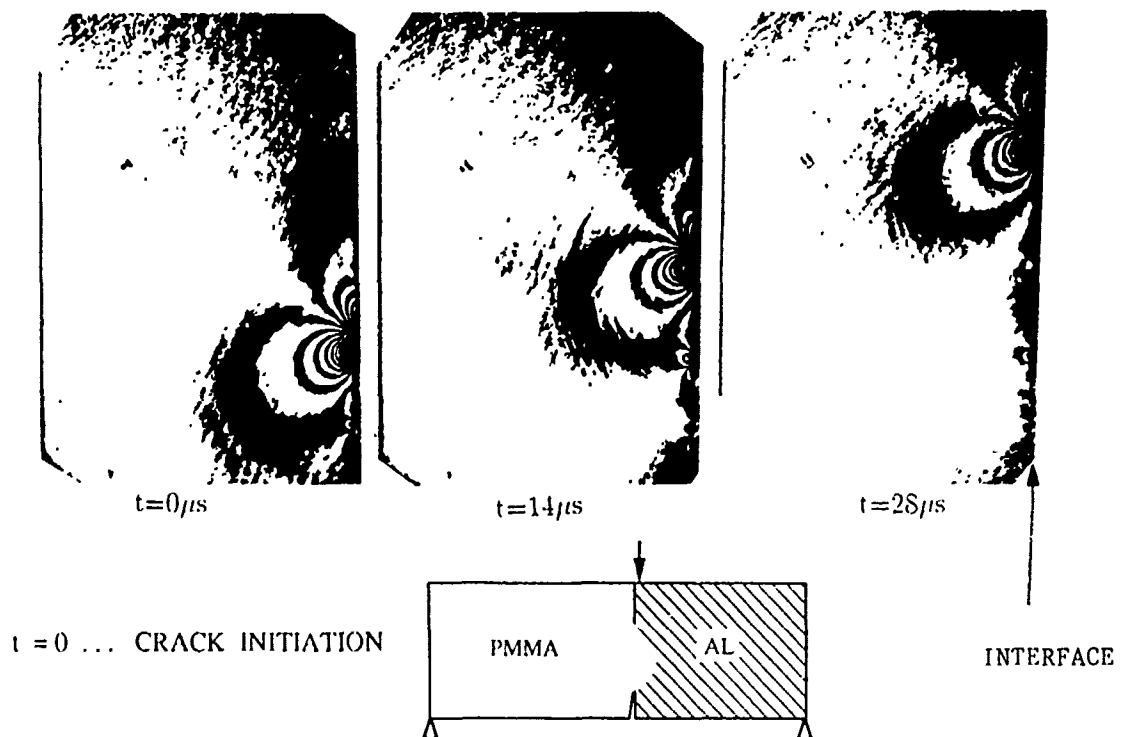


FIGURE 1.

CHARACTERIZATION OF MATERIAL PROPERTIES  
AT HIGH STRAIN-RATES USING THE TAYLOR IMPACT TEST

by  
S.E. Jones  
The University of Alabama  
Peter P. Gillis  
University of Kentucky  
and  
J.C. Foster, Jr., J.W. House, and L. L. Wilson  
AFATL, Eglin AFB, FL

The Taylor impact test has been used for a number of years to provide estimates for the dynamic yield stress of ductile, isotropic materials. Initially, these estimates were accomplished from post-test measurements by means of one-dimensional mathematical theory [1]. Through the years this theory has been improved and revised to include a number of material properties. There are too many contributions to specifically mention here.

The direction that most contemporary thinking has taken is to employ a large scale computer analysis to include as many effects as possible [2]. There are obvious advantages to this. However, the one-dimensional models still offer researchers the ability to study the dominant features of the impact event. It is this direction that the authors have chosen.

In 1987, the authors [3] offered an alternative to the classical Taylor equation of motion for the undeformed section of the specimen.

The new equation included a relative velocity term which accounted for the mass loss across the rigid-plastic interface. Later, this equation was used as the basis for a theory which separated the analysis into two fairly distinct regimes [4]. The two regimes represent early time deformation close to the anvil face that is dominated by extremely high strain rate behavior of the specimen material. The second regime accounts for most of the event and is characterized by constant plastic wave speed relative to the anvil face. This phase of the deformation is carried out at a much lower average strain rate than the primary phase.

Based on some simplifying assumptions regarding the geometry of the mushrooming region, an elementary theory which estimates stress as a function of strain rate is devised. This theory is used to characterize the high strain rate behavior of several useful materials. To a large extent, uncertainties about the simplified mushroom geometry have been shown to have little influence on the results [5].

1. G. I. Taylor, Proc. R. Soc. London Ser. A, 194, 289 (1948).
2. G. R. Johnson and T. J. Holmquist, J. Appl. Phys., 64, 3901 (1988).
3. S. E. Jones, P. P. Gillis, and J. C. Foster, Jr., J. Appl. Phys., 61, 499 (1987).
4. S. E. Jones, P. P. Gillis, J. C. Foster, Jr., and L. L. Wilson, J. Engr. Matls. Tech. (Trans. ASME) (to appear).
5. J. D. Cinnamon, S. E. Jones, J. C. Foster, Jr., and P. P. Gillis, Proc. 6th Intl. Conf. Mech Behavior Matls (1991) (to appear).

# **Material Constitutive Characterization and Continuum Fracture Toughness In Fracture and Failure Evaluations**

**V. Gensheimer DeGiorgi, P. Matic and G. C. Kirby III**  
**Mechanics of Materials Branch**  
**Naval Research Laboratory**  
**Washington, DC 20375-5000**

## **Introduction**

Structural performance and integrity analyses require high levels of confidence in constitutive characterizations, failure criteria and numerical techniques. Key issues in accurate numerical simulations of structural performance include an accurate material constitutive characterization and an appropriate failure criteria. Given an accurate constitutive response and appropriate failure criteria, derivable failure parameters can be calculated from the analysis results. The constitutive response should be valid for the range of deformation prior to fracture. Modern ductile alloys will often experience large amounts of deformations prior to failure. In the presence of a crack, large local strains and deformations will occur in the near crack tip region even if global strains are at moderate levels. The material characterization should therefore be capable of accurately representing large strains.

NRL has demonstrated the ability to accurately predict continuum alloy response through the combined use of analytical, computational and experimental methods to determine the monotonic material response from initial deformation to final fracture. Fracture is defined by a local failure criteria which uses the strain energy density required for material fracture at a point in the continuum as the failure criteria. The critical strain energy density is determined from uncracked round bar tensile specimens. There are no a priori assumptions as to location or mode of failure. Global and local response of the component modeled will determine the failure location.

## **Material Constitutive Representation**

The uniaxial tensile test specimen is often used to obtain global load-displacement data. In principle, the results from this test can be readily normalized to uniaxial material stress-strain data. However, the necking phenomenon has been a formidable obstacle to accurate constitutive characterization of ductile materials. When constitutive parameters are determined from data obtained prior to necking when uniaxial and homogeneous deformations are assumed to exist, the resulting constitutive characterization is strictly valid only when the effective stress and strain measures do not exceed the bounds of the uniaxial data. For ductile engineering materials, such as

HY and HSLA steels, the uniaxial data obtained prior to necking describes only a small portion of the full strain range experienced prior to fracture of a tensile specimen.

### **Local Failure Criteria**

The ideal failure parameter is independent of load level and mode of failure. Typically fracture parameters are dependent on the crack tip stress and strain field. Fracture due to separation of material at points in the continuum away from a crack cannot be detected using conventional fracture criteria. Large strain deformation which occurs prior to fracture in modern high toughness alloys invalidate analyses using LEFM techniques. The dependence of J and J-type parameters on the presence of an HRR field limits the applicability of these parameters. The use of strain energy density required for material fracture on the continuum level as a failure criteria does not require any additional verification of the form of the stress, strain or energy fields. The strain energy density is determined from the generalized stress and strain tensors. The critical strain energy density is determined from a series of round bar uncracked tensile tests. The point of material fracture is determined from experimental data. The stress and strain components at fracture are determined from computational simulations using the geometry independent Cauchy stress-logarithmic strain constitutive response.

The critical strain energy density has been found to be dependent on the constraint state. Thick short tensile specimens which approximate plane strain conditions have a lower critical strain energy density value for HY-100 than long thin specimens which approximate plane stress conditions. Inclusion of the known variation of the local fracture parameter in the criticality evaluation is required for an accurate representation of local fracture initiation.

### **Verification and Application Problems**

The capability to accurately predict the global and local behavior of cracked and uncracked components using critical strain energy density as a local failure criteria has been demonstrated by comparisons of numerical simulation and experimental results. Current work has concentrated on HY and HSLA steels. Two and three dimensional numerical simulations of standard compact tension specimen have been completed. Two dimensional simulations of three-point bend specimens have also been completed. In addition, qualitative comparisons have been made between observed behavior and numerical simulation results for surface cracks and complex structural components.

### **Selected References**

- P. Matic, "Numerically Predicting Ductile Material Behavior from Tensile Specimen Response," J. Theor. Appl. Fracture Mech., Vol. 4, 1985, p. 13.
- P. Matic, G. C. Kirby III and M. I. Jolles, "The Relationship of Tensile Specimen Size and Geometry Effects to Unique Constitutive Parameters for Ductile Materials," Proceedings of the Royal Society, Vol. 417A, 1988, p. 309.
- V. G. DeGiorgi, G. C. Kirby III and M. I. Jolles, "Prediction of Classical Fracture Initiation Toughness," Eng. Fracture Mechanics, Vol. 33, No. 5, 1989, p. 773.

## A DYNAMIC FAILURE MODEL FOR DUCTILE MATERIALS

A. M. Rajendran and D. J. Grove  
University of Dayton Research Institute  
Dayton, Ohio 45469-0120

This paper presents a recently developed continuum mechanics based dynamic failure model for ductile metals. Ductile failure often initiates due to void nucleation and growth. The nucleation process is controlled by either the stress (tensile pressure) or strain states of the loading conditions. For instance, in the bi-axial stretching of a thin sheet, the process is controlled by plastic deformation. The nucleation threshold strain under uniaxial/bi-axial stress states is orders of magnitude higher than under uniaxial strain. However, in a plane plate impact (uniaxial strain) condition, the void nucleation is controlled by the high tensile stresses generated due to shock wave interactions. In general, the high triaxial stress state enhances the ductile void growth process. The modeling of the ductile failure process requires careful consideration of the influence and sensitivity of stress/strain states as well as strain rates on the nucleation and growth processes of microvoids. The void generation degrades the strength and stiffness of the initially void-free material.

Realistic modeling of this failure process requires an accurate description of the strain rate and temperature dependent plastic flow in the intact material surrounding the microvoids. This is all the more important when the evolution law for ductile void growth is based on the plastic deformation in the intact material. For this reason, we incorporated a state variable based viscoplastic theory into the model formulation.

The RDG model considered a viscoplastic constitutive description for the matrix and the porous aggregate materials. The stress and strain based void nucleation process was modeled through a Gaussian function with a mean stress and/or strain threshold. The material becomes plastically compressible upon void nucleation and growth; therefore, the RDG model includes a pressure dependent yield function for describing plastic flow in the porous aggregate. There are four phases in the model. In the first phase, the intact material is described by the Bodner-Partom viscoplastic model. The void nucleation is introduced in the second phase. The void-contained aggregate is described in the third phase using an associated plastic flow rule derived from a pressure dependent yield function. The last phase of modeling is the coalescence of voids leading to complete failure. In the RDG model, separate modeling of the coalescence process is not needed. The void growth law is such that the growth rate is rapidly increased as the damage approaches its critical value.

Model constants were determined for OFHC copper, Armco Iron, tantalum, 1020, HY100, C1008, Mar200, Mar250, and AF1410 steels, and 6061-T6 and 7039-T64 aluminums. The quasi-static and split Hopkinson bar tensile stress-strain data, and stress gauge data from a plate impact experiment were employed in the model constant determination scheme. We applied the new model to describe the failure process in different geometrical configurations. Ductile failure of a tensile specimen due to necking, spallation in a target due to a single flyer plate impact, pore collapsing due to double flyer (multiple shocking) impact, complex spall patterns in a solid cone target, and spallation in a target due to projectile penetration have been simulated using the RDG model. The results are shown in Figures 1-4.

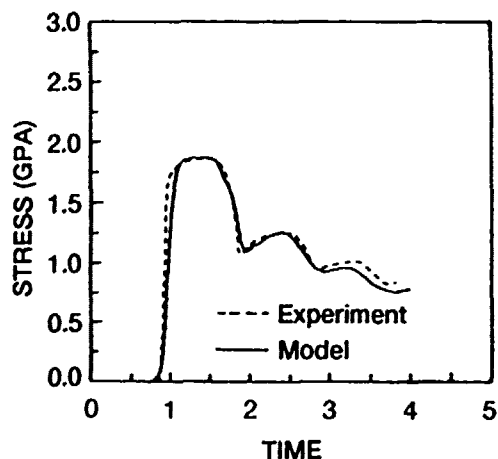


Figure 1. Model Comparison of Stress History in a Plane Plate Impact Test.

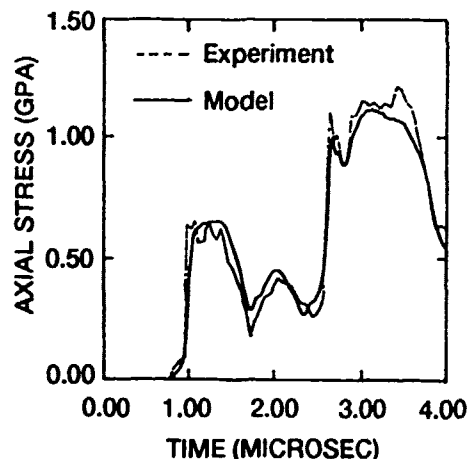


Figure 2. Model Comparison of Stress History in a Double Flyer Impact Test.

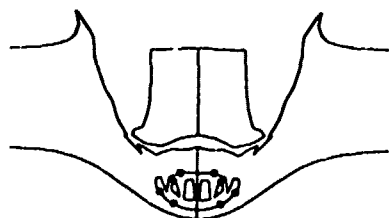


Figure 3. Model Simulation of Spall in a Target Plate Due to Projectile Penetration.

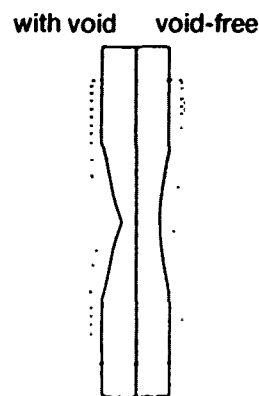
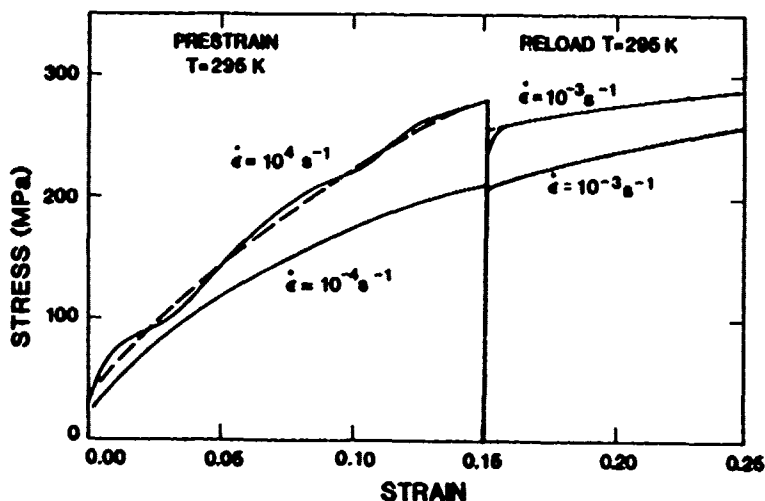


Figure 4. Model Simulation of Necking Evolution in a Dynamic Tensile Specimen.

# CONSTITUTIVE MODEL DEVELOPMENT FOR DYNAMIC DEFORMATION IN METALS

P. S. Follansbee, Los Alamos National Laboratory  
MS G756, Los Alamos, NM, 87545

The prediction of material performance during an impact event requires an understanding of the dynamic stress ( $\sigma$ ) - strain ( $\epsilon$ ) behavior. In computer calculations strain rate effects are often introduced by adding a rate term to a constitutive relation, giving an equation of the form  $\sigma = \sigma(\epsilon, \dot{\epsilon})$ . We have shown that an equation of this form does not properly account for the rate dependent deformation mechanisms that are responsible for the strain rate sensitivity as well as the temperature ( $T$ ) dependence of the flow stress. The figure below illustrates this with the stress-strain curves for two, initially annealed oxygen-free-electronic copper compression samples tested at room temperature. One curve shows the measured response of a specimen tested (prestrained) to a strain of 15% at an applied strain rate of  $10^{-4} \text{ s}^{-1}$  followed by continued straining at a strain rate of  $10^{-3} \text{ s}^{-1}$ , while the second curve shows the response of another specimen at a prestrain strain rate of  $10^4 \text{ s}^{-1}$  followed by continued straining at a strain rate of  $10^{-3} \text{ s}^{-1}$ .



Because the strain (15%), strain rate ( $10^{-3} \text{ s}^{-1}$ ), and temperature (295K) are the same for both specimens for the second part of the loading sequence (following the rate change), the simple equation given above specifies that the yield stress at this point should be identical for both specimens, which is clearly not the case.

The failure in the simple equation to capture this behavior is due to the inability of this formalism to separate the kinetics of



strain hardening from the kinetics that determine the variation of the yield stress at a given state. In the data shown the 8 orders of magnitude difference in the initially imposed strain rate has yielded, through strain-rate dependent hardening, states (determined by the hardness, or more precisely, the dislocation density) which are dissimilar for the two specimens. Thus, the reload yield stresses differ for these two specimens, even when they are reloaded at identical strain rates and temperatures.

Experiments such as the one described here illustrate that the constitutive equations used to model deformation of copper must separate the kinetics of hardening from the kinetics operative at a given state.

One model that does incorporate this feature has been developed by Follansbee and coworkers at Los Alamos National Laboratory following the previous work of Kocks and Mecking. The governing equation for the general case is written as

$$\frac{\sigma}{\mu(T)} = \frac{\sigma_0}{\mu_0} + s_1(\dot{\epsilon}, T) \frac{\hat{\sigma}_1}{\mu_0} + s_2(\dot{\epsilon}, T) \frac{\hat{\sigma}_2}{\mu_0}$$

where  $\mu$  is the shear modulus. This equation relates the stress to the current strain rate, temperature, and two state parameters,  $\hat{\sigma}_1$  and  $\hat{\sigma}_2$ . One of these could represent the resistance to dislocation motion provided by intrinsic obstacles (e.g., solute atoms, dispersoids, the Peierls barrier, etc.) whereas the second could represent the resistance provided by the evolving dislocation density. In this equation the  $s_i$ -terms specify the contribution that temperature and strain rate make to assist dislocations past these obstacles. The value of the second, evolving state parameter is described by an differential equation of the form

$$\frac{d\hat{\sigma}_2}{d\epsilon} = \theta_0 \left[ 1 - F \left( \frac{\hat{\sigma}_2}{\hat{\sigma}_{2s}(\dot{\epsilon}, T)} \right) \right]$$

where  $\hat{\sigma}_{2s}$  is the maximum, or saturation value of  $\hat{\sigma}_2$ , which varies with temperature and strain rate according to separate kinetics from those specified by the  $s_i$  values.

This model has been applied to copper [1], nickel and nickel-carbon alloys [2], titanium and titanium alloys [3], iron, low and high carbon steel, several stainless steels, and tantalum. Application and continued development of this model is discussed.

- [1] P.S. Follansbee and U.F. Kocks, Acta Metall. 36, 81, 1988.
  - [2] P.S. Follansbee, J.C. Huang, and G.T. Gray, Acta Metall. 38, 1241, 1990.
  - [3] P.S. Follansbee and G.T. Gray, Metall. Trans 20A, 863, 1989.
- Work performed under the auspices of the U.S. Dept of Energy.

## CONCEPTS OF SURFACE FORCE FOR EVOLVING PHASE INTERFACES

Morton E. Gurtin  
Department of Mathematics  
Carnegie Mellon University  
Pittsburgh, PA 15213

The concept of stress within a phase interface is nonstandard, chiefly because of accretion (the creation and deletion of material points as the interface evolves). Here I will focus attention on the basic differences between interfacial stress and the more standard notions of stress encountered in continuum mechanics. A chief difference between theories involving phase transitions and the more classical theories of continuum mechanics is the presence of *accretion*, the creation and deletion of material points as the phase interface moves relative to the underlying material, and the interplay between accretion and deformation leads to conceptual difficulties. Three force systems are needed: *deformational forces* that act in response to the motion of material points; *accretive forces* that act within the crystal lattice to drive the crystallization process; *attachment forces* associated with the exchange of atoms between phases. Because of the nonclassical nature of these force systems, it is not at all clear whether there should be additional balance laws, let alone what they should be and how they should relate to the classical momentum balance laws. For that reason, *I base most considerations of this nature on invariance*. A new idea, that of *lattice observers*, is introduced: lattice observers study the crystal lattice and measure the velocity of the accreting crystal surface; they act in addition to the standard *spatial observers*, who measure the gross velocities of the continuum.

The balance laws with appropriate constitutive equations lead to a new interface condition: when surface effects are neglected, this condition reduces to one proposed by Abeyaratne and Knowles for shock-induced phase transformations; for statical situations the condition reduces to one deduced by Leo and Sekerka as an Euler-Lagrange equation for the statical stability of the interface.

The work I will discuss was done in collaboration with Allan Struthers.

# THE PROPERTIES OF SHAPE MEMORY ALLOYS - IN PARTICULAR PSEUDOELASTICITY

by

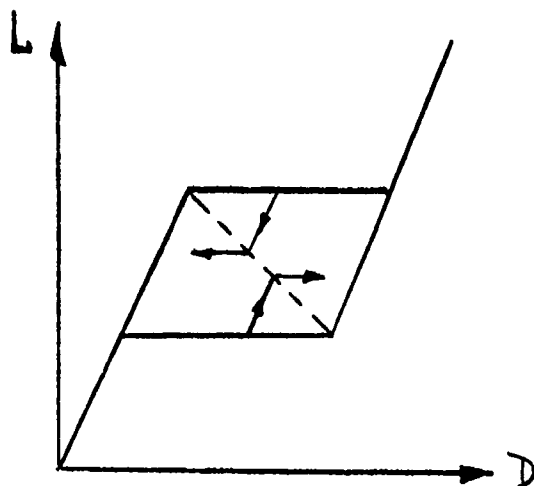
Ingo Müller

, Physikalische Ingenieurwissenschaft

TU Berlin

Shape memory alloys exhibit a strong dependence of the load-deformation characteristic upon temperature which is due to an austenitic-martensitic phase transition and to martensitic twinning. At low temperatures the behaviour is quasiplastic with an elastic range, yield, and residual deformation. At high temperature the behaviour is pseudoelastic: The specimen returns to the initial state in an isothermal loading-unloading cycle but in such a cycle its state performs a hysteresis loop.

The quasiplastic hysteresis can be explained by assuming frozen equilibria and mechanically unstable or metastable internal structural elements. Contrary to this the pseudoelastic hysteresis requires thermodynamic arguments. Phase equilibrium between the martensite and austenite is unstable due to coherency energies between regions of different phases. As a consequence there is yield and recovery inside the hysteresis loop as soon as phase equilibrium is reached. The nature of the metastable states inside the hysteresis loop is as yet unclear and, in particular, it is unclear why they should loose their (meta)stability as observed, see Figure.



The talk aims at a full description of the observed phenomena and it provides partial answers to the questions posed by the phenomenon of pseudoelasticity.

#### References:

- Müller, I. Pseudoelasticity in Shape Memory Alloys - An Extreme Case of Thermoelasticity. IMA preprint No. 168 Minneapolis (1985). Also: Proc. of Symp. "Termoelasticità Finita" Acc. Naz. Linc. N. 76 (1986).
- Müller, I. On the Size of the Hysteresis in Pseudoelasticity. Cont. Mech. Thermodyn. 1.(1989)
- Müller, I., Xu, H. On the Pseudoelastic Hysteresis. Acta Metall. Mater. (in press) (1991)

## DISTORTION ENERGY IN ELASTIC-PLASTIC MATERIALS — A MACROSCOPIC ASSESSMENT —

A. PAGLIETTI

Istituto di Meccanica Teorica ed Applicata  
Università di Udine, 33100 Udine, Italy

No matter how perfect it looks, every solid harbours a myriad of microscopic defects in its atomic structure. The number of defects, however, is still negligible with respect to the number of atomic positions that are free from defects. As a consequence, they do not essentially affect the elastic response of the material, which is mainly the result of elastic interatomic forces. The defects strongly affect, however, the post-elastic behaviour of the material, as each of them acts as a singularity that triggers the production of other defects, thus leading to permanent deformation and rupture. The evaluation of the defect content of the material is, therefore, an issue of great practical interest. Is there any macroscopic means of doing this?

Thermodynamics enables us to find a positive answer to this question, and quite a practical one for that. In doing so it also sets a new bridge between the microscopic properties of the material and its macroscopic behaviour. The analysis hinges on the fact that there is a thermodynamic limit to the elastic deformation that a material can suffer (see [1] and [2]). According to this limit the elastic region in strain space is defined by

$$u \leq T s \quad (1)$$

where  $u = u(\epsilon^e, T, \xi)$  is the specific internal energy of the material,  $s$  its specific entropy and  $T$  absolute temperature. The quantities  $\epsilon^e$  and  $\xi$  stand respectively for elastic strain and a set of variables defining the inelastic behaviour of the material. If the elastic range is known, relation (1) can be exploited to obtain further information on the material. In the present work, relation (1) is exploited to obtain the value of the internal energy that remains entrapped in the material surrounding the defects, once the macroscopic stress is removed. This energy is due to the

microscopic distortions produced by the defects and is maintained by a self-equilibrium system of forces, finely distributed in the microscopic structure of the material and not resulting in any macroscopic stress. As such these forces cannot be removed simply by removing all macroscopic stress from the material. This means, in particular, that the free energy of the material surrounding the defects (as distinguished from that of the whole material) cannot reach its minimum value at the macroscopic stress-free state. From this observation and from relation (1), the values of the elastic limit of the material and the energy entrapped in it due to microscopic defects can be related to each other.

Explicit formulae are provided for the special, but practically important case of elastic-plastic materials in uniaxial states of stress. The material behaviour in the elastic range is supposed to be that of a linear thermo-elastic material. The free energy entrapped in the material surrounding the defects turns out to be given by

$$\overline{\Delta\psi} = E [(\epsilon_t + \epsilon_c)^2 - (\epsilon_{t0} + \epsilon_{c0})^2] / 4\rho \quad (2)$$

where  $\epsilon_t$ ,  $\epsilon_c$ ,  $\epsilon_{t0}$  and  $\epsilon_{c0}$  are respectively the elastic limits in tension and compression in the initial state and after a defect affecting process.  $E$  denotes elastic modulus and  $\rho$  is mass density. Moreover, the part of the above free energy of distortion resulting in macroscopic strain at vanishing macroscopic stress (permanent elastic deformation) is calculated to be given by

$$\Delta\psi = E (\epsilon_t + \epsilon_c)^2 / 8\rho, \quad (3)$$

while the relevant permanent elastic strain is

$$\Delta\epsilon = -(\epsilon_t + \epsilon_c) / 2. \quad (4)$$

## REFERENCES

1. A. Paglietti: Thermodynamic Nature and Control of the Elastic Limit in Solids. *Int.J.Non-Linear Mech.* **24**, 571-583 (1989).
2. A. Paglietti: Thermodynamic Limit to Elasticity: A Simpler Proof and Some Direct Consequences. In: *New Developments in Structural Mechanics*, Int. Meeting in Memory of M.Romano, Catania, July 4-6, 1990 (in press).

## MECHANICS OF PHASE NUCLEATION IN SOLIDS

L. Truskinovsky  
Department of Aerospace Engineering and Mechanics  
107 Akerman Hall  
110 Union Street SE  
University of Minnesota  
Minneapolis, MN 55455

Elastic solids undergoing phase transformations comprise an important class of "smart materials". Among the most well known are shape memory alloys, magnetostrictive alloys, ferroelectrics, and transformation toughened ceramics. Since the enhanced mechanical properties are a consequence of the strains associated with the transformation, the mechanism of the transformation is currently a subject of intense interest. Important variables that are associated with these transformations include: the elastic parameters, type of loading, presence of defects (stress concentrators), etc.

Considerable progress has been made in our understanding of the absolute stability of elastic phases under applied loads. However, the presence of metastable phases in these transformations, which is apparently a generic phenomenon, remains a major puzzle. Since the metastable phase is only infinitesimally stable, the nucleation of a second, absolutely stable phase, indicates that the metastable phase is unstable with respect to the special finite perturbations. One of the crucial problems which must be addressed in the design of the new materials is to establish the corresponding energetical limits of the metastability.

We discuss several model problems related to some basic features of the nucleation phenomenon in solids vis-a-vis that in liquids. Among the topics are the following: nucleation in the infinite matrix and inside inclusions, heterogeneous nucleation, nonlocal (gradient) effects, and the generation of elastic waves.

BEHAVIOR OF NON-AFFINE VISCOELASTIC  
MODELS UNDER STEP SHEAR STRAIN

by

Millard W. Johnson

Department of Engineering Mechanics  
and the Engine Research Center  
The University of Wisconsin, Madison

and

David S. Malkus

Department of Engineering Mechanics  
and the Center for the Mathematical Sciences  
The University of Wisconsin, Madison

Abstract

One of the basic motions to consider in investigating the suitability of a model for viscoelastic fluids is the stress relaxation after an impulsive step in shear strain. The model considered here is based on non-affine kinematics and can exhibit an S-shaped stress-velocity gradient curve for steady simple shear. For step simple shear strain, which is spatially homogeneous in the velocity gradient by assumption, three versions of the model, which are supposedly equivalent formulations, are found to yield different results for the damping function and the Lodge-Meissner function. Two integral versions of the model yield results which have previously been thought to be unacceptable on physical grounds while a differential equation version yields results acceptable on the same basis. A numerical solution of the initial value problem for the differential equation yields results which we believe should be acceptable on a physical basis. The solution is found to exhibit spatial inhomogeneity at large strains and long times so that the shear strain is not well defined. The numerical results agree qualitatively with the results from one of the integral models for step simple shear strain.



# PATTERN SELECTION IN THE BÉNARD PROBLEM FOR A VISCOELASTIC FLUID

Michael and Yuriko Renardy  
Department of Mathematics and ICAM  
Virginia Tech  
Blacksburg, VA 24061-0123

We discuss pattern selection in the Bénard problem for a viscoelastic fluid. Double periodicity of the solutions with respect to a hexagonal lattice is assumed. Both steady and oscillatory onsets of instability are considered. For steady onset, we find that the rolls are the only bifurcating solution which can be stable. For oscillatory onset, a variety of patterns can be stable, depending on the parameters of the problem.

**FLOW BETWEEN ECCENTRIC ROTATING CYLINDERS:  
BIFURCATION AND STABILITY**

A.Z. Szeri

Department of Mechanical Engineering  
University of Pittsburgh  
Pittsburgh, PA 15261

**ABSTRACT**

The effect of cylinder eccentricity on Couette-Taylor transition is investigated here for flow between infinite rotating cylinders. The method of analysis is Fourier expansion of the conservation equations in the axial direction, followed by projection onto a polynomial subspace. Critical points of the solution, which are characterized by singularity of the Jacobian matrix, are located via parametric continuation. This computational scheme permits an extension of the DiPrima & Stuart results to higher values of the eccentricity ratio; it also makes it possible to move far from the critical point into the supercritical Reynolds number regime. The first bifurcation from Couette flow is found to be supercritical, while supercritical flow is shown to consist of regions of plain motion with recirculation, separating toroidal vortex regions. The domain of recirculating flow is asymmetric with respect to the line of centers, and on increasing the supercritical Reynolds number its axial dimension decreases while its radial dimension, in the plain separating the vortex cells, increases.

The results established here for critical Reynolds number agree well with those of DiPrima & Stuart at eccentricities where their small perturbation solution is applicable, and there is good agreement with the experimental data of Vohr. The torque calculations compare favorably with the experimental data of Donnelly & Simon for the concentric case and with the data of Castle & Mobbs for non-zero eccentricity.

## A FLOW VISUALIZATION METHOD WITH EMBEDDED TIME CODE STREAKS

Tzong-Shyan Wung and Fun-Gang Tseng  
Institute of Applied Mechanics  
National Taiwan University  
Taipei 10764, Taiwan, Republic of China

Flow visualization which utilizes optical methods to observe flow fields is applied throughout in the study of fluid mechanics and transport processes. Traditional visualization methods provide intuitive observation of flow motion and qualitative interpretation of physical phenomena. Quantitative flow visualization, on the other hand, has capabilities of providing instantaneous maps of magnitudes, such as velocity or vorticity, over extended areas. Recently developed methods including particle streak velocimetry, particle image velocimetry and laser speckle velocimetry incorporate modern computer, optics technologies and image processes to determine instantaneous velocity fields. Conventional particle streak velocimetry relies on the integration of trajectories of particles which scatter light as exposing in the illuminating light-sheet. To quantify each image streak, temporal information of a trajectory is required not only to provide an exposure duration time to calculate velocity, but also to remove the ambiguity of the direction of velocity vectors. Chopping the illuminating light to a certain code is one of the solutions. The recorded streaks, however, consist of several line segments of the same gray level which may be time-consuming to link them into correct particle trajectories.

The image grabbing technique presented in this paper has the capability of real time capturing particle trajectories in a light-illuminating sheet with embedded time code to facilitate further analysis of velocity and vorticity fields. It can be used to both qualitative and quantitative visualization of a two-dimensional flow field with less efforts on the late image analysis. Figure 1 dictates the arrangement of the image system. The camera video signal carries image information in a standard NTSC RS-170 format at 30 frames per second. This analog signal is then digitized through an analog-to-digital (A/D) converter to produce 8-bit output, with which each pixel may have one out of 256 possible gray levels. Pixels flow from A/D converter into an input-look up table (ILUT). Pixel values below a lowcut value is set to 0, and that above the lowcut to a finite non-zero value. To encode the time marks to the particle streaks, one can vary the constant output value of the ILUT after an arbitrary time range. In principle, we can encode particle streaks into 255 different time marks in an 8-bit data. The streaks with embedded time code allow one to analyze flow velocity field with less labor because the streaks will be displayed in a continuous mode if the particles remain in the sheet of light, in contradiction to the line segments with chopped light source.

The second novel process used in the present setup is the real-time arithmetic-logical unit (ALU). The main function of the ALU in the system is to compare and to select the larger value from input pixel values of the A/D converter and feedback channel from the image frame buffer. The larger pixel value is then written into the frame buffer which can be used to extract velocity vectors by usual image processing techniques. The benefit of this process is obvious. If the output values of the ILUT are set to monotonically increasing with time, then the ALU selects larger values, rather than summation of two values, from the newly coming image (i.e., A/D converter)

and the old stored image in the frame buffer, resulting in a superposition of images while keeping the updated largest values. This procedure has several advantages over the conventional long exposure of image by a film or a shutter-controlled CCD camera on that: (1) the background noise of an image will not grow with time, because the binarization of image by the ILUT already reduces most of noises; (2) since only the maximum pixel values are recorded in the frame buffer, the image will not overexpose as appeared in a film or not cause image blooming as with a CCD camera; (3) in the case of visualization of unsteady flow the trajectories of particles may appear crossover. In this technique, the latest streak will always show in a continuous path while the previous streak looks underlaid. This pattern facilitates the analysis of velocity vectors. An output look-up table (OLUT) can further transform pixel values and display the image on a monitor through a digital-to-analog (D/A) converter. Pseudo-color OLUts and color monitor may be used to enhance human visual perception of image as shown in the sketch. The image system is operated at a real-time base, that is at a rate of 30 frames per second.

Figures 2-4 demonstrate the flow visualization by the present technique of natural convection of a heat-generating module placed in an enclosure heated from below. Figure 2 presents two rotating cells in the enclosure as a result of 30 second exposure for qualitative observation of flow structure. The time-code embedded streaks of the flow field is shown in Fig. 3. Each streak consists of four gray levels. The streak starts with green color and ends with blue, dictating the flow direction clearly. The tails on both ends have shorter durations because they are used to indicate the starting and the ending of a series of time marks. The intermediate segments of yellow and red can be used to derive the magnitude of velocity. It can be seen that even several streaks are clustered together, one may distinguish between them more easily than the image acquired by the traditional technique. Figure 4 depicts the flow pattern of unsteady motion in the enclosure. The streaks are recorded in eight gray levels, namely, ultramarine, green, yellow, red, magenta, purple, cobalt blue and blue. Several streaks are crossed over the others, but the analysis does not suffer much from the linkage of line segments and distinction of trajectories with different time code.

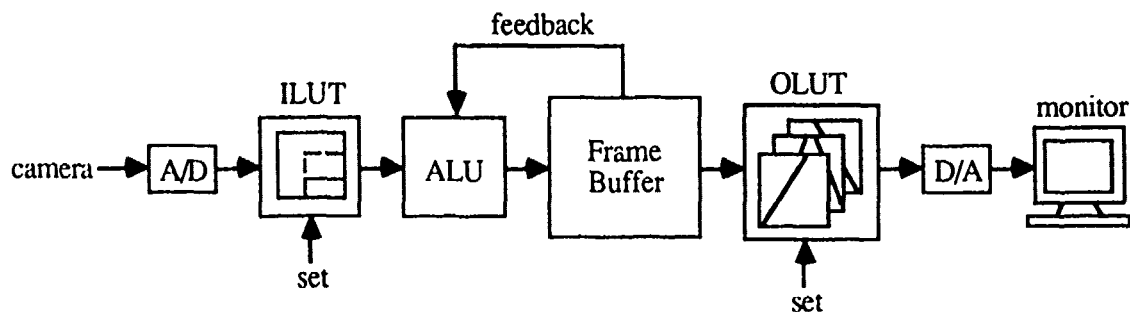


Fig. 1 Schematic of the image system



Fig. 2 Streak image with long exposure



Fig. 3 Streaks with embedded time code

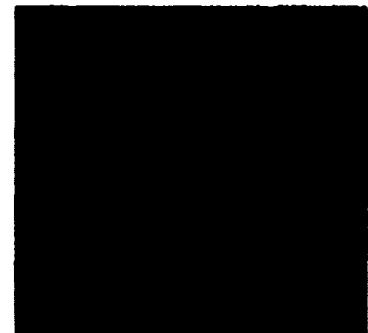


Fig. 4 Streaks in unsteady flow

# ON BEHAVIOR OF METALS AT HIGH STRAIN RATES

Akhtar S. Khan

School of Aerospace and Mechanical Engineering

The University of Oklahoma

Norman, OK 73019, USA

## ABSTRACT

Different experimental techniques which are used to study behavior of metals at high strain rates will be critically examined. Results of a new experiment to study large finite plastic behavior at high strain rates will be presented. Comparisons with predictions using a leading constitutive model will be shown, and a new viscoplastic constitutive model, valid for a very large strain rate range ( $10^{-5}$  to  $10^4 \text{ sec}^{-1}$ ), will be presented.

# **Constant Structure Experiments for the Evaluation of Flow Equations for Rate - Dependent Metal Flow**

by

Vivek R. Dave and Stuart B. Brown  
Massachusetts Institute of Technology  
Materials Science and Engineering Department  
Cambridge, MA

## **Abstract**

Current constitutive models for metals track flow behavior as well as deformation-induced structural changes, and they require experiments which can decouple these two effects. Constant structure experiments attempt to do this by abruptly changing boundary conditions and measuring material response. If the structure doesn't evolve during the transient, then the material response characterizes the inherent flow behavior of the material. In this work, strain rate change and relaxation experiments are critically examined. Previous methods of conducting the tests and interpreting their results are shown to be problematic. A new method is suggested, one which overcomes previous problems, but raises new questions about flow characteristics, material structural evolution and appropriate assumptions for models.

Experimental work is presented for 1145 polycrystalline aluminum at .61  $T_m$ . All tests were done on a servohydraulic testing system with extensometer-implemented strain control. The test information was digitally recorded at a rate of 2500 Hz. The test temperature was maintained at 300 degrees Celsius to within less than 2 degrees deviation in the gage length. Rate increments and decrements were conducted starting from an initial strain rate of .007/s. Relaxation tests were also conducted from the same initial strain rate. Issues associated with machine dynamical performance were examined, but they have little impact on the results presented here. The reason for this is that irrespective of machine performance, the data sampling rate is sufficiently high to capture material response. *Also, there is no dependence on any kind of fixed control*

signal history (strain, in this case), and no assumptions are made concerning the point at which the material has reached a new strain rate. Strain rate information is computed directly from the strain-time history, and this together with the stress-time history is sufficient to characterize the material response at any point after the change in conditions.

*The tests indicate that a power law representation of the stress-strain rate behavior is not appropriate at these strain rates and temperature. Also, much care must be taken in applying the constant strain criterion for the evaluation of constant structure behavior. This criterion assumes that for small strains after the change in conditions, the change in structure is due to geometric hardening only, and that recovery and rate-dependent processes have a lesser impact on structure evolution. This would imply that although the dislocation structure has changed after the change in conditions, the amount of that change is a function of plastic strain increment only. This is a simplification, and its validity may be examined by looking at the evolution of material response with increasing strain offset from the point of the jump. In this work, strain offsets ranging from .00005 to .03 are examined. Material hardening behavior is also calculated in order to evaluate the effect of material structural evolution with strain offset. A significant difference in hardening is found between rate increment and rate decrement experiments. This means that examining material response at constant strain offset doesn't guarantee that tests at different strain rates will have undergone the same amount of structural change.*

The evolution of material behavior as indicated by the hardening data is asymmetric for rate increments and rate decrements. *This means that the effect of rate-dependent structural evolution on the material response determined at a given offset will be different for different strain rates.* In order to determine the true constant structure response at any point after a change in conditions, rate-dependent contributions must be taken into account. This requires a model of these rate-dependent structural evolution processes. This model may include dynamic recovery and thermally-activated dislocation rearrangements, and possibly static recovery. In the rate increments, static recovery is not expected to have a great impact, but for relaxation tests at high temperatures, it may. Climb-assisted dislocation rearrangements could also be considered for the higher temperatures. Regardless of the specific form of the model chosen, the current work does indicate the need for a more precise representation of material evolution processes in order to better determine the constant structure material response as measured by change experiments.

## VISUAL X-Y DISPLACEMENT MEASUREMENT BY IMAGE PROCESSING

Yasushi Niitsu

Dept. of Mechanical Engineering, Tokyo Denki University,  
Kanda-nishikicyo 2-2, Chiyodaku, 101 Tokyo JAPAN

Kensuke Ichinose

Dept. of Mechanical Engineering, Tokyo Denki University,  
Kanda-nishikicyo 2-2, Chiyodaku, 101 Tokyo JAPAN

Kozo Ikegami

Res. Lab. of Precision and Intelligence, Tokyo Institute of Technology,  
4259 Nagatsuta, Midoriku, Yokohama, 227 JAPAN

### INTRODUCTION

The non-contact type two directional (X-Y) displacement measuring system is developed. This system is composed by a mesh (grid) pattern as a traced object, optical lens system, optical fiber scope, CCD camera, frame memory and a micro-computer. The lines of the grid pattern are measured and pursued by using the high speed image processing of the projection technique.

The sampling rate is less than 0.2 second by using 180286-16MHz CPU and the spatial resolution is about 2.5 micro meter. This technique can be applied in various fields such as high temperature strain measurement and positioning and control of X-Y table. [1,2]

### MEASURING METHOD AND SYSTEM

Figure 1 shows the measuring system. The optical fiber scope is used to transfer the image of the grid pattern, from the object lens to the CCD camera. The analog image signal taken by the CCD camera is digitized to 512x480 points binary image data. A personal computer (16MHz-180286) calculates displacement and controls the X-Y table. The mesh pitch of the grid pattern is 0.5mm, the width of the lines is 0.002mm, and the accuracy is 1/100.

The measurement of displacement is to pursue the mesh lines in each direction. If the line goes outside the processing region, the next line comes from another side and it is pursued again. The total movement of the grid is calculated with the number of passing lines and the difference between initial and current line positions. The distance of grid pattern (0.5mm) corresponds to about 200 pixels length on the image data. High quality part of 288x288 pixels region is chosen as a window and the projection technique is applied to this region. The pixels which have black level are counted in horizontal and vertical direction at each line as ray integrals. Those ray integrals construct the projections as shown in Fig.2. The projections have one or two peaks caused by lines of the grid. Subsequently to smoothing, the Laplacian operation (Second difference) such as following equation is applied to the



projections in order to emphasize the peaks.

$$F_j = 2 F_j - F_{j+m} - F_{j-m}, \quad m = 16 \quad (1)$$

where  $F_j$  is  $j$ -th ray integral. Sixteen is adopted as the value of  $m$  by the experiment. The results of this calculation are shown in Fig.3. Threshold levels are calculated as 2 times of mean values of emphasized projections, and peak position are obtained as the mean positions of upper than threshold. It takes about 0.18 second to measure X-Y displacement. If movement of the grid during one measuring cycle is larger than half of a grid width, the direction of movement is recognized by mistake.

### CONCLUSIONS

The non-contact type two directional (X-Y) displacement measuring system is developed. A new high-speed projection technique, which can measure the position of the grid pattern, is used. Sampling time of X-Y displacement is less than 0.2 second and the spatial resolution is 2.5 micro meter (1/200 of grid distance).

### REFERENCES

- [1] A. Horiguchi, Y. Niitsu and K. Ikegami; Proc. of Int. Conf. on ADVANCED MECHATRONICS in Tokyo, (1989) pp.
- [2] Y. Niitsu, A. Horiguchi and K. Ikegami; Proc. of Int. Conf. on Experimental Mechanics in Denmark, (1990) pp.

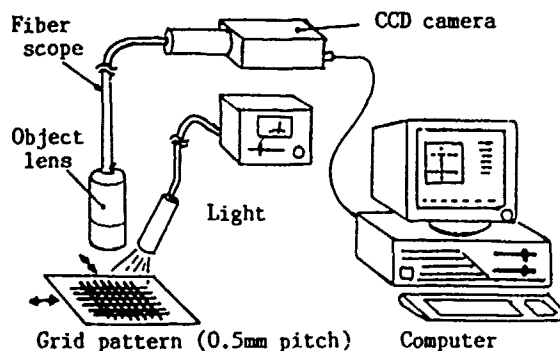


Fig. 1. Schematic figure of the measuring system. This system composed of CCD camera, optical fiber scope, frame memory and computer.

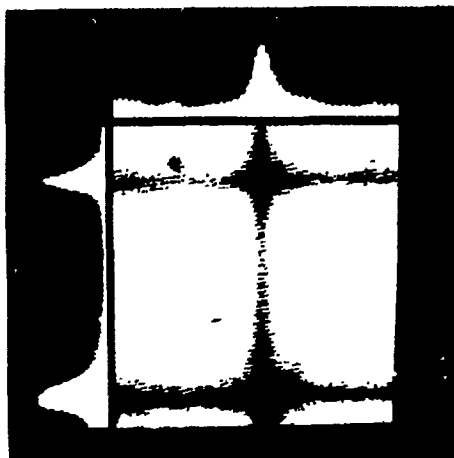


Fig.2. Projections of binary image. Points of dark level are counted up along horizontal and vertical lines.

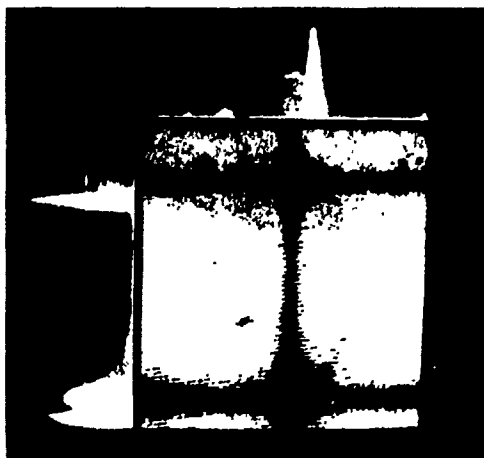


Fig.3. Smoothing and emphasizing operations for the projections of binary image in Fig.2. Lines show the threshold levels.

# EXPERIMENTAL EVALUATION OF THE TAYLOR-TYPE POLYCRYSTAL MODEL FOR THE FINITE DEFORMATION OF AN FCC METAL (OFHC COPPER)

Tusit Weerasooriya  
Army Materials Technology Laboratory  
Watertown, MA 02172

## ABSTRACT

Large deformation uniaxial compression and fixed-end and free-end torsion (simple shear) experiments were conducted for annealed OFHC Copper to obtain stress-strain behavior of the material. The stress-strain behavior for these experiments were also predicted using a Taylor type rate dependent polycrystal model by Asaro and Needleman<sup>1</sup>. Simulation of these experiments was conducted using a recently developed, highly efficient, fully implicit time integration scheme by Kalidindi et al.<sup>2</sup> In the initial phase of the simulation, the evolution of the constituent single crystal slip system deformation resistance was estimated using the experimentally determined compressive stress-strain behavior of the polycrystal. With this crystal constitutive behavior, the stress-strain behavior of the polycrystal for simple shear was computed. In addition, evolution of the crystallographic texture was computed for both compression and simple shear tests.

Experimental shear stress was insensitive to changing from fixed-end to free-end condition of testing. The predicted shear stress-strain behavior for simple shear test compared reasonably well with the experimental results. The simulated axial stress response agrees qualitatively (compressive) with the experimental observations, but over estimates the experimentally observed axial compressive stress.

- 
1. ASARO, R. J. AND NEEDLEMAN, A. *Texture Development and Strain Hardening in Rate Dependent Polycrystals*. Acta Metall., v. 33, 1985, p. 923.
  2. KALIDINDI, S. R., BRONKHORST, C. A. AND ANAND, L. *Crystallographic Texture Evolution in Bulk Deformation Processing of FCC Metals*. to appear in Journal of the Mechanics and Physics of Solids.

In uniaxial compression tests, the simulated stress-strain behavior decreases with an increase of strain rate sensitivity or decrease of the latent hardening for the same strain. In simple shear, shear stress response is not sensitive to changes in either strain rate sensitivity or latent hardening. The axial and hoop stresses decrease with the increase in strain rate sensitivity. With the decrease of latent hardening, the axial and hoop stresses increase at lower shear strains, but decrease at higher shear strains.

The predicted texture of grains for compression tests assumes an orientation given by the ideal  $\{110\}\langle uvw \rangle$  fibre where  $\{110\}$  planes become perpendicular to the loading axis. For simple shear, predictions show the presence of the ideal  $A^*$  ( $\{111\}\langle uvw \rangle$  partial fibre) and  $B^*$  ( $\{hkl\}\langle 110 \rangle$  partial fibre) fibres and  $C$  ( $\{001\}\langle 110 \rangle$ ) orientation, where in this notation, planes are parallel to the shear plane and directions are along the shear direction.

A STUDY OF THE NOTCH SIZE EFFECT ON THE FAILURE MECHANISMS AND STRAIN DISTRIBUTIONS OF ANGLE PLY LAMINATES SUBJECTED TO FATIGUE LOADING USING THE MOIRE INTERFEROMETRY METHOD.

Dr.R.L.Pendleton	Mr.F.C.J.Anigbo	Mr.S.I.Ibekwe
Professor	Graduate Student	Graduate Student
Mech.Engr.Dept.	Mech.Engr.Dept	Mech.Engr.Dept.
S.D.School of Mines	School of Mines	School of Mines.
&Technology	&Technology	&Technology
R.City SD 57701	R.City SD 57701	R.City SD 57701

**Introduction:** The inhomogeneous nature of fibrous polymer composites gives rise to a widely different stress levels within the composite laminate. This makes the analysis of the fatigue behavior of composites difficult. The fatigue failure processes occurring within an individual laminae depend on the basic characteristics of the lamina and its angle of orientation relative to the applied cyclic load [1]. The consequences of gradual deterioration of specimens subjected to fluctuating load is that the strain level in the test coupons may increase as cycling between fixed load limits progresses. Therefore an understanding of both the failure processes and the strain distribution on a composite laminate is necessary.

**Method:** [0/30/60/90/0]<sub>s</sub> and [0/30/60/90/0]<sub>2s</sub> laminates were investigated. Edge notch at the center of the specimens were of the slit type with the notch depth either 3/16th or 5/16th of an inch. Cross grating measuring 1x1 inch was mounted at the center of the specimen ( Fig.5). Two mutually coherent beams of light illuminating the specimens at angles +A and -A interfere to form a virtual reference grating [2]. The specimen grating and reference grating interact to form the desired fringe patterns. The strain values were calculated as in [2]. The specimens were cycled between fixed loads of 603 and 1008 lbs. at a frequency of 10Hz for 55,000 cycles and then removed from the test fixture and analyzed.

**Results:** Using the Moire technique, the initial failure mechanisms observed in both laminates and the two notch depths studied were those of axial cracking in the direction of the applied cyclic load. Subsequent to this was delamination along the axial cracked path. The 3/16th inch notched laminates of the [0/30/60/90/0]<sub>s</sub> were observed to axially split on both sides of the notch with a length equal to twice the width of the notch (2x.0313in.) [3]. The delamination that followed was not very extensive as was observed from the Moire fringe photographs. The 5/16th in. notched specimens of the same composite type had extensive axial cracking measuring about five times the notch width (5x.0313in.) The delamination that followed was equally extensive and was along the axial cracked path. At the notch, digitization was difficult due to the extensive delamination .

The 3/16th inch notched laminates of the [0/30/60/90/0]<sub>2s</sub> exhibited an initial axial splitting which was to the size of the notch width (.0313in.) followed by delaminations. The delaminations were limited to the areas exhibiting axial cracking. A wavy form of fringe pattern was also observed for these laminate type. Similar to the 3/16th's, the 5/16th inch notched laminates exhibited axial cracking equal to twice the size of the notch depth (2x.0313in.). This was followed by delamination. Both the axial cracks and the delaminations were extensive in comparisons to the 3/16th inch notched specimens. Also, a wavy form of fringe pattern was observed. According to Daniel and Pipes[4], this type of fringe pattern is associated with interlaminar shear edge effects.

**Strain Distribution:** Irregular strain variations were obtained for both specimen types and their respective notch depths. The X-displacement strain plot taken at the notch axis for the

[0/30/60/90/0]s laminates shown in Fig. 1 indicated high strain magnitudes around the notch for the 5/16th in. notched specimens. The strain magnitude decreased as strain was plotted away from the notch. The 3/16th in. notched laminates exhibited increasing strain magnitude away from the notch. The Y-displacement strain plot shown in Fig. 2 plotted at points below and above the notch axis again indicated high strain magnitude for the 5/16th in. notched laminates. Due to the extensive delamination observed in the moire fringe patterns, strains at the notch could not be determined. The 3/16th in. notched laminates exhibited peaks of maximum and minimum strain magnitudes but decreased in strain magnitude as we moved further away from the notch.

The X-displacement strain plot for the [0/30/60/90/0]2s shown in Fig. 3 exhibited high strain magnitude for the 5/16th in. notched laminates. The laminate exhibited decreasing strain magnitude half way into the specimen and thereafter increased again. Contrary to this, the 3/16th in. notched laminates exhibited an increasing strain magnitude and an inflation point as we moved away from the notch. The Y-displacement plots shown in Fig. 4 exhibited a much narrower strain range for both notch depths. The 3/16th in. notched laminates exhibited strain peaks before decreasing towards zero strains, while the 5/16th in. notched laminates exhibited lower strain magnitudes close to the notch but thereafter increased gradually to a maximum before falling to almost zero strain.

Conclusion: Composite degradation due to cyclic loading was dependent on the notch depth, the thickness of the laminate and the number of cycles. The various peaks recorded for the strain magnitudes were due mainly to material inhomogeneity at the surface of composite laminates and errors due to digitization. Finally, Moire interferometry is an effective and efficient method for the determination of the surface strains due to gradual deterioration in composite laminates.

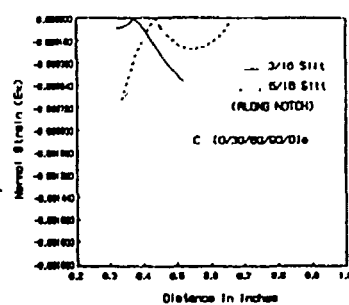


Fig. 1 Notch size effect on the same stacking sequence after 65,000 cycles at 10081ib

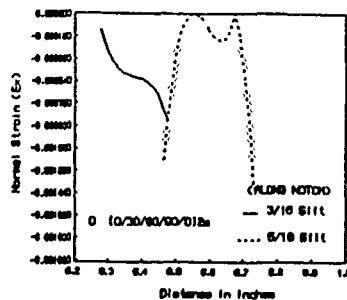


Fig. 3 Notch size effect on the same stacking sequence after 65,000 cycles at 10081ib

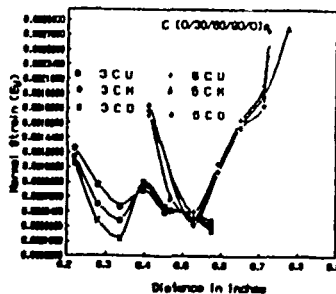


Fig. 2 Notch size effect on the same stacking sequence after 65,000 cycles at 10081ib

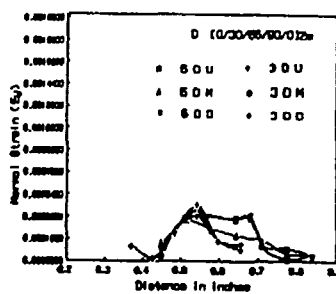


Fig. 4 Notch size effect on the same stacking sequence after 65,000 cycles at 10081ib

u) .07 in above notch a) at notch d) .07 in below notch u) .07 in above notch a) at notch d) .07 in below notch

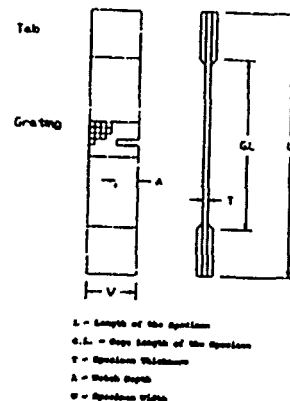


Fig. 5. Design of the notched tensile specimen, showing the geometry for moire analysis.

1. Morley, J. G., "High Performance Fiber Composites", Academic Press Publisher, 1987, p 216.
2. Post, D. "Moire for Interferometry" Manual on Experimental Method for Mechanical Testing of Composites R.L.Pendleton, and M.E.Tuttle, Eds., S.E.M., Inc. 1989.
3. Anigbo, F.C.J., "Investigations on the Failure Mechanisms and The Strain Distribution of Notched and Unnotched Composite Laminates Subjected to both Tensile and Fatigue Loading Using The Moire Interferometry Method" a Ph.D. Dissertation Submitted to the School of Mines and Technology, R. City, South Dakota, 1991.
4. Pipes, R.B. and Daniel, I.M., "Moire Analysis of The Interlaminar Shear Edge Effects in Laminated Composite." Journal of Composite Materials, Vol.5, April 1971, pp 255-259.

# VEHICLE STRUCTURAL COMPONENTS CRASH SIMULATION by USING NONLINEAR FINITE ELEMENT APPROACH

De-Shin (Scott) Liu  
Associate Professor  
Department of Mechanical Engineering  
National Chung-Cheng University  
Chia-Yi, Taiwan

## ABSTRACT

For the automotive industry , to have a newly developed vehicle meet the crashworthiness requirements is time consuming and expensive . Therefore the use of computer-based , analytical methods to provide quick and inexpensive design iterations has become a fundamental part of the design process .

This paper focuses on vehicle structural components crash simulation . Three example problems have been analyzed by employing the dynamic nonlinear finite element crash simulation code "DYNA3D" . The three example problems include :

- 1) front upper rail crash simulation .
- 2) rear bumper low speed impact simulation .
- 3) knee impact simulation .

In all three problems , very reasonable correlations between analysis and experiment have been observed .

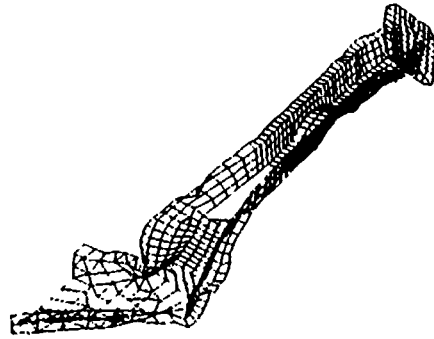


Figure 1. Deformed Shape of The Rear Rail .

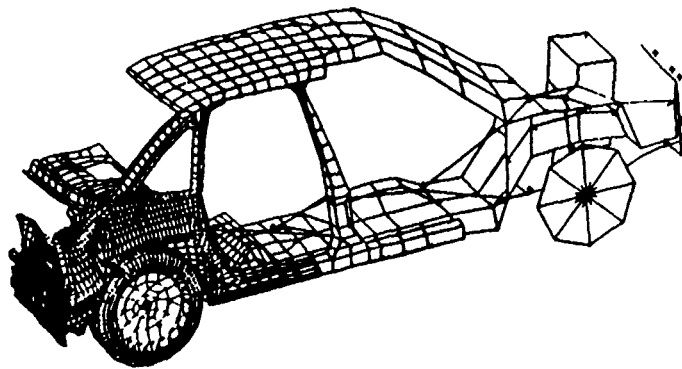


Figure 2. Failure Mode of The Full Vehicle at 50 ms .

# THREE DIMENSIONAL PLANE WAVE ANALYSIS FOR PIEZOELECTRIC MATERIALS USING FINITE ELEMENTS

N. M. Sallah, Department of Industrial Engineering  
G. R. Buchanan, Department of Civil Engineering  
Tennessee Technological University  
Cookeville, Tennessee 38505

## ABSTRACT

The theory of plane waves is presented in numerous textbooks, such as [1,2]. The solution is in the form of a progressive wave travelling in the direction of a unit vector  $n_i$  perpendicular to the plane wave. The phase velocity vector  $V_i$  is perpendicular to the wave plane and has magnitude  $V$ . When the propagation direction is varied the end of the phase velocity vector describes a three dimensional surface that is referred to as the velocity surface. At any point on the velocity surface the velocity can be analyzed as three types, a quasi-longitudinal wave velocity  $V_1$  and two quasi-shear wave velocities  $V_2$  and  $V_3$ . Normally, the longitudinal wave has greater magnitude than the shear waves. The wave velocities are obtained by solving the eigenvalue problem that is associated with free vibration.

The equations governing free vibration of piezoelectric materials are given in [3]. There are four coupled partial differential equations and in subscript tensor notation can be written as;

$$C_{ijkl}(u_{k,li} + u_{l,ki})/2 + e_{kij}\phi_{,ki} = \rho \partial^2 u_j / \partial t^2 \quad (1)$$

$$e_{ikl}(u_{k,li} + u_{l,ki})/2 - \epsilon_{ij}\phi_{,ki} = 0 \quad (2)$$

The terms in Eqs. (1) and (2) are defined as follows;

$C_{ijkl}$ - elasticity tensor,	$e_{kij}$ - piezoelectric tensor,
$\epsilon_{ik}$ - permittivity tensor,	$\rho$ - material density,
$u_i$ - displacement vector,	$\phi$ - electric potential,
$t$ - time,	$( ),_i$ - spatial differentiation.

A solution for Eqs. (1) and (2) can be obtained by assuming appropriate functions for  $u_i$  and  $\phi$  such that

$$u_j = U_j e^{(k_i x_i - \omega t)}, \quad \phi = \Phi e^{(k_i x_i - \omega t)}. \quad (3)$$

where  $k_i$ ,  $\omega$  and  $x_i$  are the wave number vector, circular frequency and position vector, respectively. The wave number can be defined as  $k_i = (\omega/V)n_i$ . Substituting into Eqs. (1) and (2) gives an equivalent set of algebraic equations.



$$C_{ijkl}n_i n_j U_k + e_{mij} n_i n_m \Phi = \rho V^2 U_i \quad (4)$$

$$e_{ikl} n_i n_l - \epsilon_{mij} n_i n_m \Phi = 0 \quad (5)$$

Equations (4) and (5) are solved using the finite element method.

The finite element equations are written as follows and additional details are given in [3].

$$[[B_U]^T [C] [B_U] - V^2 [N_U]^T [\rho] [N_U]] (U) + [B_U]^T [e] [B_\Phi] (\Phi) = 0 \quad (6)$$

$$[[B_U]^T [e] [B_\Phi]]^T (U) - [B_\Phi]^T [\epsilon] [B_\Phi] (\Phi) = 0 \quad (7)$$

The [B] matrices are defined as follows;

$$[B_U] = [L_U] [N_U], \quad [B_\Phi] = [L_\Phi] [N_\Phi]. \quad (8)$$

with

$$[L_U] = \begin{bmatrix} n_1 & 0 & 0 \\ 0 & n_2 & 0 \\ 0 & 0 & n_3 \\ 0 & n_3 & n_2 \\ n_3 & 0 & n_1 \\ n_2 & n_1 & 0 \end{bmatrix}, \quad [L_\Phi] = \begin{bmatrix} n_1 \\ n_2 \\ n_3 \end{bmatrix} \quad (9)$$

The shape functions  $[N_U]$  and  $[N_\Phi]$  correspond to any one, two or three dimensional element that is to be used for the analysis. The finite element operators contain partial derivatives but they are functions of the direction cosines ( $n_1, n_2, n_3$ ). One finite element, defined by any shape function, is sufficient to solve for the phase velocity of the wave for any crystal type. For example, to obtain the phase velocity in the z direction, let  $n_3=1$  and  $n_1=n_2=0$  and compute the corresponding result.

Results are computed for various materials and presented as polar plots of the phase velocity as a function of angle of orientation. The effect of polarization is studied for piezoelectric materials by comparing phase velocities when piezoelectric effects are included to phase velocities when the effect is omitted. Phase velocities are presented for representative materials, such as, Si, TiO<sub>2</sub>, GaAs, TeO<sub>2</sub>, ZnO and LiNbO<sub>3</sub>. These results are also tabulated in [4].

#### REFERENCES

1. Dieulesat, E. and Royer, D., *Elastic Waves in Solids*, John Wiley & Sons, New York (1980)
2. Perelomova, N. V. and Tagieva, M. M., *Problems in Crystal Physics with Applications*, Mir Publishers, Moscow (1985)
3. Sallah, M., *Finite Element Analysis of Microelectronic Materials with Application to Field Effect Transistors and Waveguide Convolvers*, PhD Dissertation, Tennessee Technological University, Cookeville (1989)
4. Sallah, N. M. and Buchanan, G. R., "Finite element analysis of plane waves in piezoelectric materials", 7th International Conference on Computer-Aided Production Engineering, Tennessee Technological University, Cookeville, August (1991)

LOCAL STRESSES IN PIPING AT WELDED ATTACHMENTS  
BY FINITE ELEMENT METHOD

C. Basavaraju, Bechtel Power Corporation, Gaithersburg, Maryland  
S. R. Kalavar, Bechtel Power Corporation, Gaithersburg, Maryland  
C. Y. Chern, Bechtel Power Corporation, San Francisco, California

In the Power Generation Industry Integral Welded Attachments (IWA) are often used to support piping systems. The local stresses at the IWA locations are commonly evaluated using Bijlaard's method per WRC-107 approach. The finite element analysis (FEA) method is very effective and one of the most powerful tools but is costly, time consuming and is not convenient to apply on a production basis. On the other hand, the Bijlaard's method is relatively simple to use but has limitations in terms of the attachment and pipe size (i.e.,  $\beta$  and  $\gamma$  parameters). In this paper, the FEA, using 3-D solid brick elements and shell elements, was utilized to assess the conservatism present in Bijlaard's method and also to evaluate stresses when Bijlaard's method cannot be applied due to the exceedance of limits of  $\beta$  and  $\gamma$  parameters. Extensive parametric studies utilizing FEA method covering various pipe and attachment sizes were undertaken. The results were presented as reduction factors to be applied to WRC-107 results. Methods to evaluate attachments on elbows and odd shaped attachments were also addressed. These results are considered to be of benefit to the industry at large in evaluating many practical situations where  $\beta$  parameter exceeds the limits of Bijlaard's method without actual recourse to FEA method for commonly encountered pipe sizes.

# General Limit Analysis of Plane-Strain Extrusion Using Finite Element Method

Kuo-Hsiao Liu

General Motors Corporation  
CPC Engineering  
Warren, MI 48090

## Abstract

A general limit analysis algorithm for plane-strain problems has been developed. The theoretical foundation of this algorithm is a duality theorem which equates the least upper bound to the greatest lower bound. Minimizing the upper bound approach is chosen in this study. Unlike the classical upper bound methods which assume the kinematic function of the flow field, the algorithm automatically converges to the correct mode (a correct mode if it is not unique) by an iterative scheme. The advantage of this general method is most evident for problems with complex geometry and boundary conditions for which the correct deformation field will be difficult to assume.

The extrusion problems with square dies and wedge-shaped dies are studied. In addition, the friction effect between die face and the extrudate is taken into consideration. The results obtained are compared whatever possible with the classical solutions. Good agreement is found for this comparison.

# ENERGY CHANGES CAUSED BY DEFECT GROWTH IN PIEZOELECTRIC SOLIDS

H. A. SOSA

Mechanical Engineering and Mechanics Department, Drexel University, Philadelphia, Pa 19104

Piezoelectric ceramics are anisotropic insulators possessing a remarkable property: They deform under the effect of an electric field and conversely, they induce an electric voltage when subjected to mechanical loads. Because of this dual effect, piezoceramics have become the key component in a multitude of electromechanical devices which range from medical instrumentation to deep submersion acoustics. More recently, they play an important role as components of "smart structures". The increasing number of applications is also being reflected in the severity of the loads to which these materials are being exposed. In fact, experimental observation has shown that mechanical and electrical effects are responsible for the development of high stress concentrations in the neighborhood of existing defects such as cracks and holes. Thus, it is not surprising that questions related to the mechanical failure and electrical degradation of piezoceramics have become of great concern. Consequently, it is clear that the mechanical strength of piezoelectric ceramics is a factor that must be considered in the design of electromechanical devices. The causes of failure can be understood through fracture analysis. Such an analysis could suggest solutions to avoid fracture based on design changes, material selection or manufacturing modifications.

In a series of papers, the author and co-worker have developed analytical models describing the interaction of electroelastic phenomena with defects. For the particular case of the crack-like defect, the distribution of the electromechanical fields in the neighborhood of the crack tip have been deduced. Furthermore, fracture parameters addressing both mechanical and electrical effects were introduced and their use was illustrated by means of several examples.

In this work the fracture mechanisms that occur in piezoelectric materials are addressed from a different point of view. The approach consists of the evaluation of the change in the total potential energy owing to defect growth. Towards this end, the total potential energy functional,  $\Pi$ , of a linear piezoelectric material is defined in terms of the elastic strain energy, the electrostatic energy (as a function of the electric field),

as well as in terms of the external work associated with surface traction and total surface charge.

An expression for the change in total potential energy,  $\Delta\Pi$ , caused by the growth of an arbitrary cavity is deduced. In the particular case of a crack, a piezoelectric energy release rate,  $G_P$ , is defined as the negative limit of the ratio of  $\Delta\Pi$  to change in crack length, as this length tends to zero. A closed form expression for  $G_P$  is obtained in terms of applied electromechanical load, crack geometry and material properties. Examples are provided to show that for a given tensile stress,  $G_P$  can increase or decrease depending on the direction and intensity of the applied field. It is found, however, that the levels of electric voltage necessary to produce crack growth may exceed the limitations imposed by the material to avoid dielectric breakdown.

### References

- SOSA H. A. and PAK, Y. E. [1990a]: *Int. J. Solids Structures*, **26**(1), pp. 1-15.
- SOSA H. A. and PAK, Y. E. [1990b]: *Mechanical Modellings of New Electromagnetic Materials*, pp. 305-312, ed. Hsieh, R. K., Elsevier.
- SOSA, H. A. [1991]: *Proceedings of the Second Pan American Congress of Applied Mechanics*, pp. 151-154.

A Note on the Compatibility of Thermal Stress Analysis  
By Finite Element Method

Zhou Ming and Huang, C.L.D.  
Department of Mechanical Engineering  
Durland Hall  
Kansas State University  
Manhattan, KS 66506-5106

Finite Element Method (FEM) has developed very rapidly, and it has been applied to many fields in engineering. Many commercial FEM packages for general purpose and/or special purposes are now available to users. Occasionally, because of the limitations of the packages themselves; or the limitations of the user's background about FEM and its field of application, the use of the packages might result in an unsatisfactory solution or it might take too much CPU time to achieve accurate solutions. In some special cases, an unacceptable solution might be obtained if the weight function of the finite element model is improperly chosen. Particularly in application of FEM to the structural thermal stress analysis, compatibility problems of choice of element models are encountered. In this paper, some compatibility conditions of thermal stress analysis are investigated and imposed, which can help to obtain solutions of thermal stress problems more accurately and economically with usage of FEM packages.

The uncoupled thermal stress problems are considered in two phases: the temperature field and the displacements, which yield the thermal stresses. Two kinds of FEM models are required, namely thermal element (or temperature element) models and structural element (or displacement element) models. It is reasonable to use the same geometrical mesh for both phases (i.e. uniform mesh). For a uniform mesh thermal stress analysis, different kinds of models can be used for thermal elements and structural elements, based on the physically modeling. The order of an element model is defined as the order of the complete polynomials in the shape functions of the element. If both the thermal element model and structural element model are of the same order, a *full-model* process is called. A *reduced-model* process is defined that has the order of temperature element model one less than that of the displacement one. It can be shown that the reduced model process gives the best solution in predicting thermal stress for a given uniform mesh.

The thermal stress problem is considered as an initial strain problem, with the strain-stress relation defined as  $\sigma_{ij} = D_{ijkl}(\epsilon_{kl} - \epsilon_{kl}^T)$ , where  $\epsilon_{kl}$  is the total strain tensor, which depends on the derivatives of displacement,  $\epsilon_{kl} = \frac{1}{2}(u_{k,l} + u_{l,k})$ , and  $\epsilon_{kl}^T$  is the thermal strain tensor which is the linear function of temperature,  $\epsilon_{kl}^T = \alpha T \delta_{kl}$ . So the error of thermal stress ( $e''$ ) depends on the difference of the error of  $\epsilon_{kl}(e')$  and the error of  $\epsilon_{kl}^T(e'^T)$ . The relation is,  $e'' \sim e' - e'^T$ . Thus, the reduced model process results in the uniformity of order of errors  $e'$  and  $e'^T$ . Furthermore, it can be shown, that  $e'$  and  $e'^T$  always have the same sign, the uniformity of the error orders minimizes the error difference ( $e' - e'^T$ ), which yields the optimum solution of thermal stresses for the given uniform mesh.

Numerical examples show that the linear full-model process converges very slowly as the element approaches infinitesimal size. Thus, if Wilson's non-conforming element is used for the structural analysis, the corresponding thermal element model should be linear to be compatible. The Wilson element has an order of 2 although the same number of nodes in the uniform mesh are used in the linear element. Numerical examples by FEM are given. The correctness and significance of the compatibility condition are illustrated. The following table shows the thermal stresses at points of the interior surface of a infinite long circular cylinder for three types of different uniform meshes. The number of elements of each of the meshes are 4, 10, and 40, respectively.

MODEL MESH	FULL-MODEL			REDUCED MODEL		
	Value	Error	Time	Value	Error	Time
MESH I	72.2008	4.56%	11.2	67.9269	1.63%	10.9
MESH II	69.9362	1.28%	44.4	68.8263	0.33%	40.3
MESH III	69.3269	0.40%	851.1	69.0424	0.01%	847.1
EXACT SOLUTION	69.0516					

For thermal stresses in shells, in spite of the descretization error as it was discussed before, there is another kind of error, the Shell Modeling Error (SME). The uniformity of order of thermal SME and structural SME is also a key factor in the finite element analysis of thermal stresses. Generally, the structural SME is much smaller than the thermal SME, so a higher order temperature shell element (in thickness direction) is required corresponding to the commonly used Kirchhoff or Mindlin structural shell elements which are linear in the thickness direction. Numerical results show that the linear temperature shell element might give unacceptable solutions of thermal stresses, and a quadratic temperature shell element usually yields a fairly good result of thermal stress if the shell is not too thick.

# ON THE ANALYSIS OF SUPERHARMONIC OSCILLATIONS USING A GENERALIZED HARMONIC BALANCE METHOD

Julian J. Wu  
US Army Research Office  
Research Triangle Park, NC 27709

## ABSTRACT

It is well known that nonlinearities can cause sub- and super-harmonic excitations in vibratory systems. The analytical understanding of such phenomena is often difficult to obtain. It has been shown that the method of multiple scales can be used to solve such problems as demonstrated in several papers by Nayfeh. However, the procedures involved are quite complicated and require recursive solution of differential equations, the elimination of secular terms and reconstitution, all of which are nontrivial procedures. Recently, in a series of papers by Noble, Hussian and Wu, a generalized harmonic balance method (GHB) was introduced as an alternative to the method of multiple scales. This variant of the harmonic balance method consists of two parts: first, to derive the form of solution using only the basic of multiple scales, and then, solve for the coefficients of various harmonics. It was shown that GHB is equivalent to the multiple scales method in terms of getting all the pertinent information. Yet, the steps involved in GHB appear to be more straightforward than those of the multiple scales method. In this paper, examples will be given for the obtaining of superharmonic excitations. A quite general nonlinear ordinary differential equation with several nonlinear terms is considered. A specific case of superharmonic oscillations of order 2 will be investigated. Like the case for subharmonics, the form of the solution is first derived, which is then plugged into the original differential equation. Using an iterative scheme, equations of various harmonics are then obtained which include a new, nonlinear ordinary differential equation of a slow varying function compared with the original dependent variable. This same equation will be shown to yield the steady state solutions. Results are presented for some specific set of parameters.



# ON THE USE OF ARTIFICIAL SPRINGS IN THE FREE VIBRATIONAL ANALYSIS OF SYSTEMS COMPRISING SEVERAL DISTINCT COMPONENTS

J. Yuan and S. M. Dickinson  
Department of Mechanical Engineering  
The University of Western Ontario  
London, Ontario, Canada  
N6A 5B9

## INTRODUCTION

In 1943, Courant[1] included in his address to the American Mathematical Society a discussion of the use of the Rayleigh-Ritz method for solving problems with rigid boundaries by treating them as limiting cases of free boundary problems, for which the choice of admissible functions can be simpler. The technique proposed was to introduce what amounted to 'artificial' springs at the otherwise free boundaries and permitting their stiffnesses to become sufficiently high that the required rigid boundaries were approximated. This technique was subsequently used by a number of researchers, sometimes to solve rigid boundary problems (for example see references [2,3]) and sometimes as limiting cases of studies on spring supported systems (for example, see references [4,5]).

The present authors have recently proposed and demonstrated that this approach may be used effectively to solve problems of systems comprised of straight and/or curved beams[6,7] and of rectangular plates[8]. For such cases, appropriate artificial springs are introduced between the constituent members and at the boundaries of the system and the admissible functions are chosen simply to satisfy the free conditions at the boundaries of each component. The necessary boundary and continuity conditions between components are enforced by permitting the stiffnesses of the appropriate springs to become very high compared with the stiffness of the components. In the event that the system has flexible boundaries and/or flexible joints between components, then each artificial spring is simply assigned the actual stiffness of the appropriate boundary or joint.

In the present paper, the analytical procedure is described for application to the study of systems comprised of beams, plates and shells, with several particular systems being treated to illustrate the versatility and accuracy of the approach.

## OUTLINE OF PROCEDURE

The following steps are employed:

- (i) The system under consideration is decomposed into its individual components, each of which must be amenable to analysis in the 'free' condition by means of the Rayleigh-Ritz method.
- (ii) The admissible functions are chosen for each component, satisfying the geometrical free edge or end conditions for the component.
- (iii) Assuming that the system will vibrate with simple harmonic motion, the maximum kinetic and strain energies for each component are evaluated and summed over the whole 'free' system.
- (iv) Appropriate artificial springs are introduced at the system boundaries and joints between the components and the maximum strain energy stored in the springs evaluated.
- (v) Summing both the component and spring strain energy, the Rayleigh-Ritz minimization procedure is carried out to yield the eigenvalue equation for the flexibly jointed and supported system.
- (vi) Should the real system have flexible joints or flexible supports at a boundary, then the appropriate artificial springs assume the actual stiffness of the joint or boundary support. For rigid connections between components or at the boundaries, these are approximated by allowing the appropriate spring stiffnesses to become very high.

## ILLUSTRATIVE EXAMPLES

In order to demonstrate the applicability of the approach, several systems are considered, including structures composed of circular plates and cylindrical shells. Comparisons are made with results from the literature, where available, and close agreement is shown to be achieved.

## REFERENCES

1. Courant, R., Bulletin of the American Mathematical Society, Vol.49, pp.1-23, 1943.
2. Kao, R., International Journal of Solids and Structures, Vol.11, pp.21-31, 1975.
3. Mizusawa, T., Journal of Sound and Vibration, Vol.62, No.2, pp.301-308, 1979.
4. Warburton, G. B. and Edney, S. L., Journal of Sound and Vibration, Vol.95, No.3, pp.537-552, 1984.
5. Kim, C. S., Young, P. G. and Dickinson, S. M., Journal of Sound and Vibration, Vol.143, No.3, pp.379-394, 1990.
6. Yuan, J. and Dickinson, S. M., Canadian Society of Mechanical Engineers Forum, Toronto, Vol.IV, pp.127-131, 1990.
7. Yuan, J. and Dickinson, S. M., Journal of Sound and Vibration, provisionally scheduled for January, 1992.
8. Yuan, J. and Dickinson, S. M., 13th Canadian Congress of Applied Mechanics (CANCAM'91), Winnipeg, Alberta, June 1990.

# VIBRATIONS OF RECTANGULAR MEMBRANES SUBJECTED TO SHEAR AND NON-UNIFORM TENSILE STRESSES

Arthur W. Leissa and Amir Ghamat-Rezaei  
Department of Engineering Mechanics  
The Ohio State University  
Columbus, Ohio 43210

Although the free vibrations of membranes is a subject that has been studied for more than a century, virtually all problems investigated have been for membranes stretched uniformly in tension in all directions. Two important questions arise: (1) What effects would a variation in the tension have upon the frequencies and mode shapes? (2) What effects would additional shear stress have?

The present work investigates the vibration characteristics of rectangular membranes subjected to possible combinations of constant plus linear variations in normal stresses, and constant shear stress; that is,

$$\sigma_x = C_1 + C_2y, \quad \sigma_y = C_3 + C_4x, \quad \tau_{xy} = C_5 \quad (1)$$

where proper restrictions are placed upon the coefficients  $C_1, \dots, C_5$  so that the normal stress in all directions and at all points does not become compressive, to avoid wrinkling. The Ritz method is used to solve the free vibration problems. Transverse displacements are assumed to be a double series of trigonometric functions. A convergence study is made to establish that  $8 \times 8 = 64$  terms in the series is sufficiently accurate for most purposes.

Using such solutions, the first 10 frequencies are found for a square membrane subjected to uniform and equal tensile stresses with added shear stress ( $C_1 = C_3, C_2 = C_4 = 0$ ). Contour plots of mode shapes are also shown for  $C_5/C_1 = 0, 0.2, 0.5, 0.85$  and 1. It is found that the addition of moderate shear stresses ( $C_5/C_1 = 0.2$ ) cause only small changes in the frequencies (4.6% maximum change among the first 10 frequencies). However, as  $C_5/C_1$  approaches unity, (on the verge of wrinkling), the stress field becomes one of diagonal tension, and frequencies and mode shapes change rapidly. As the limiting value  $C_5/C_1 = 1$  is approached, all frequencies decrease markedly, and node lines (lines of zero displacement in the mode shapes) become parallel to the diagonal and closely spaced, near the diagonal. Frequencies for rectangular membranes of aspect ratio 2 are also given.

Finally, the effects of nonuniformity in the tensile stress ( $C_1 = C_3$ ,  $C_2 = C_4$ ,  $C_5 = 0$ ) upon the frequencies and mode shapes are studied. The effect of nonuniformity is also to decrease all frequencies, but less severely than the decrease caused by shear stress.

Rather comprehensive sets of tables of frequencies and contour plots of mode shapes have been recently published for the two types of problems described above [1].

#### REFERENCE

1. Arthur W. Leissa and Amir Ghamat-Rezaei, "Vibrations of Rectangular Membranes Subjected to Shear and Nonuniform Tensile Stresses," Journal of the Acoustical Society of America, vol. 88, pp. 231-238, 1990.

# DYNAMIC BEHAVIOR OF AN INELASTIC SYSTEM TO HARMONIC AND RANDOM EXCITATIONS

N.C. Nigam

Director, I.I.T. Delhi, New Delhi (INDIA)

In the inelastic regime, the dynamic behavior of structural systems is nonlinear. Under simultaneous action of two, or more, excitations it may involve significant inelastic interactions (1). We consider a symmetrical frame (Fig.1) having two-degree-of-freedom and subjected to harmonic and random base excitations in two orthogonal directions. Assuming inelastic interactions in bending only, the elastic and inelastic behavior of the frame in the force-space is shown in Fig.2. It may be expressed by the equations

$$\ddot{u}_i + p_i \dot{u}_i = -r\ddot{z}_i(\tau), \quad i = 1, 2, \quad (1)$$

$$p_i = u_i - u_{oi} \quad \text{if } p_1^2 + p_2^2 < 1, \text{ or if } p_1^2 + p_2^2 = 1, \text{ and } \dot{w}_p < 0, \quad (2)$$

$$\begin{Bmatrix} \dot{p}_1 \\ \dot{p}_2 \end{Bmatrix} = \begin{bmatrix} p_2^2 & -p_1 p_2 \\ -p_1 p_2 & p_1^2 \end{bmatrix} \begin{Bmatrix} \dot{u}_1 \\ \dot{u}_2 \end{Bmatrix}, \quad \text{if } p_1^2 + p_2^2 = 1, \text{ and } \dot{w}_p \geq 0 \quad (3)$$

in which,  $\tau = \omega_0 t$ ,  $u_i = x_i/x_y$ ,  $p_i = Q_i/Q_y$ ,  $a_y = Q_y/m$ ,  $r = a/a_y$ ,  $\omega_0$  is the natural frequency  $u_{oi}$  the current position of elastic equilibrium and  $\dot{w}_p$  is the rate of plastic work.

**HARMONIC EXCITATION:** For harmonic excitation:  $\ddot{z}_1 = \sin \alpha\tau$ ,  $\ddot{z}_2 = \sin(\alpha\tau + \rho)$ , the steady-state elastic response is given by

$$p_1 = u_1 = b \sin \alpha\tau, \quad p_2 = u_2 = b \sin(\alpha\tau + \rho) \quad (4)$$

where  $b = r/(1-\alpha^2)$ , and  $r < (1-\alpha^2)/(1+\cos \rho)^{1/2}$ . For  $0 \leq \rho \leq \pi/2$ , the response is partly-elastic and partly-plastic. For

$\rho = \pi/2$  and  $r \geq (1-\alpha^2)$ , steady-state response is completely plastic and the frequency response equation can be expressed as

$$r^2 \cdot b^2 \alpha^4 + 2\alpha^2 = 1, \text{ and } b_p = 1/\alpha_p = 1/(1-r^2)^{1/2}, \quad (5)$$

which represents the locus of peak amplitude. Plots of frequency response equation and locus of peak amplitude is shown in Fig.3 for  $r = 1.0$  and  $0.7$ . Plots for elastic behavior (E), elastic-plastic behavior, with interaction effects neglected (EP), and results of numerical computation are also shown in Fig.3.

**RANDOM EXCITATION:** For random excitation  $\ddot{z}_1, \ddot{z}_2$  are modeled as correlated, zero mean, white noise with

$$\phi_{\ddot{z}_j \ddot{z}_k}(\omega) = \phi_{jk} \phi_0, \quad \phi_{jk} = 1, \text{ if } j=k, \quad 0 \leq \phi_{jk} \leq 1, \text{ if } j \neq k, \quad j, k = 1, 2. \quad (6)$$

the response is partly-elastic and partly-plastic. Assuming the plastic excursion is a rare event, the expected value of the fraction of time spent in plastic state can be expressed as

$$E[D(T)] = 1 - \frac{1}{T} \int_0^T \frac{1}{(2\sigma_1^2 \sigma_2^2 (1-\rho_{12}^2))} \left\{ \int_0^1 \exp(-\alpha s) I_0(\beta s) ds \right\} dt$$

where  $\alpha = (\sigma_1^2 + \sigma_2^2) / 4\sigma_1^2 \sigma_2^2 (1-\rho_{12}^2)$ ,  $\beta = (\sigma_1^2 - \sigma_2^2 + 4\rho_{12}^2 \sigma_1^2 \sigma_2^2) / (4(1-\rho_{12}^2) \sigma_1^2 \sigma_2^2)$  (7)

$I_0$  is the modified Bessel function of the first kind. If interaction effect is neglected, and  $\sigma_1 = \sigma_2 = \sigma$ ,  $x_y = n\sigma$ ,  $E[D(T)]$  is given by (2):

$$E[D(T)] = 2 \operatorname{erfc}(n/\sqrt{2}) \quad (8)$$

Fig.4 shows the plot of fractional occupation time for different levels of correlation with interaction (EPI), and without interaction (EP). Numerical simulation results using artificial earthquakes are also shown. RESULTS: Effects of interaction on inelastic response are significant for both harmonic and random excitation. Theoretical results match the simulation results closely in both cases.

#### REFERENCES

1. Nigam, N.C. "Yielding in framed structures under dynamic loads. Proc. ASCE, J. Engg. Mech. Div., 96(EM5), 1970, p.637-707.
2. Nigam, N.C., Introduction to Random Vibrations. The MIT Press, 1983.

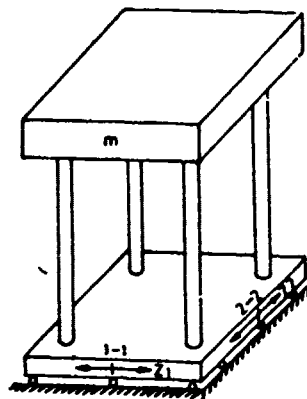


Fig.1 A Simple Frame

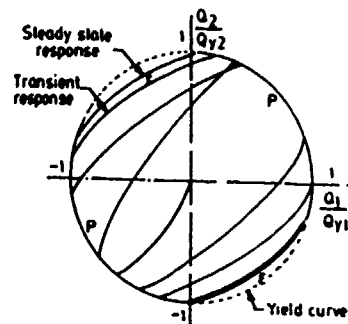


Fig.2 Response In Force-Space

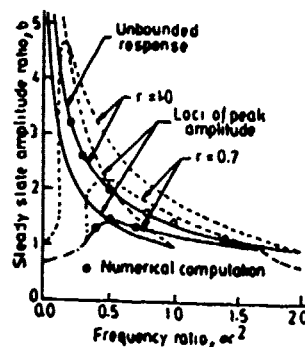


Fig.3 Frequency Response Curve  
(~ FPI, ..., EP)

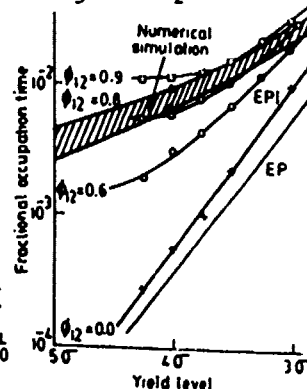


Fig.4 Fractional Occupation Time vs Yield Level

# POISSON EFFECT ON THE FREE VIBRATION OF LAMINATED COMPOSITE BEAMS

K. Chandrashekhara and Kiran M. Bangera\*  
Department of Mechanical and Aerospace Engineering  
and Engineering Mechanics  
University of Missouri - Rolla  
Rolla, MO 65401 USA

## ABSTRACT

Free vibration characteristics of laminated composite beams are studied based on a higher order shear deformation theory. The Poisson effect, which is often neglected in one-dimensional laminated beam analysis, is incorporated in the formulation of the beam constitutive equation. A finite element beam model is developed to demonstrate the influence of Poisson effect and boundary conditions on the frequencies of laminated composite beams.

## MATHEMATICAL FORMULATION

Fiber-reinforced composite beams are finding increasing applications in a variety of structural components, such as helicopter blades, turbine blades, and robot arms. A survey of recent developments in the vibration analysis of laminated composite beams has been compiled by Kapania and Raciti [1]. Exact solutions for the free vibration analysis of symmetrically laminated composite beams with various boundary conditions has been recently reported by Chandrashekhara *et al.* [2]. The results presented in [2] are based on a laminated beam theory in which Poisson effect is neglected. In the present work, equations of motion are derived for laminated composite beams based on a higher order plate theory [3], and the Poisson effect is incorporated in one-dimensional beam model. The laminated beam constitutive equations can be expressed as [4]

$$\begin{Bmatrix} N_x \\ M_x \\ P_x \end{Bmatrix} = \begin{bmatrix} \bar{A}_{11} & \bar{B}_{11} & \bar{E}_{11} \\ \bar{B}_{11} & \bar{D}_{11} & \bar{F}_{11} \\ \bar{E}_{11} & \bar{F}_{11} & \bar{H}_{11} \end{bmatrix} \begin{Bmatrix} \epsilon_x^0 \\ \kappa_x^1 \\ \kappa_x^2 \end{Bmatrix} \quad (1)$$

$$\begin{Bmatrix} Q_{xz} \\ R_{xz} \end{Bmatrix} = \begin{bmatrix} A_{66}^* & D_{66}^* \\ D_{56}^* & F_{56}^* \end{bmatrix} \begin{Bmatrix} \epsilon_{xz}^* \\ \epsilon_{yz}^* \end{Bmatrix}$$

It should be noted that the coefficients  $\bar{A}_{11}$ ,  $\bar{B}_{11}$ , etc. in Eq. (1) account for the Poisson effect or y-direction strains.

\*Currently at EGS, Inc., Detroit, MI

## RESULTS AND DISCUSSIONS

A finite element beam model, with the in-plane displacement ( $u$ ), transverse displacement ( $w$ ), bending slope ( $dw/dx$ ), and normal rotation ( $\phi$ ) as the nodal variables, is developed based on Eq. (1). The details of the finite element formulation can be seen from reference [4]. Table I shows the non-dimensional frequencies of symmetrically layered cross-ply and angle-ply beams. It is noted that the cross-ply results are in good agreement with the exact solutions presented in [2]. However, the angle-ply results deviate significantly from the exact solutions. This is due to the fact that the laminated beam theory considered in [2] neglects the Poisson effect. Table II shows the effect of ply orientation on the first five natural frequencies. Of the three lamination schemes considered, the cross-ply beam exhibits the highest frequency.

## REFERENCES

1. R. K. Kapania and S. Raciti, "Recent Advances in Analysis of Laminated Beams and Plates, Part II: Vibrations and Wave Propagation", AIAA Journal, Vol. 27, pp. 935-946 (1989).
2. K. Chandrashekhara, K. Krishnamurthy, and S. Roy, "Free Vibration of Composite Beams Including Rotary Inertia and Shear Deformation", Composite Structures, Vol. 14, pp. 269-279 (1990).
3. J. N. Reddy, "A Simple Higher Order Theory for Laminated Composite Plates", Journal of Applied Mechanics, Vol. 51, pp. 745-752 (1984).
4. K. Chandrashekhara and Kiran M. Bangera, "Free Vibration of Composite Beams Using a Refined Shear Flexible Beam Element" (Under Review).

TABLE 1. Comparison of Natural Frequencies ( $\bar{\omega} = \omega L^2 \sqrt{\rho/E_1 h^2}$ ) of Symmetrically Laminated Beam ( $E_1 = 144.80$  GPa,  $E_2 = 9.65$  GPa,  $G_{23} = 3.45$  GPa,  $G_{12} = G_{13} = 4.14$  GPa,  $\nu_{12} = 0.3$ ,  $\rho = 1389.23$  kg/m<sup>3</sup>,  $L/h = 15$ )

Boundary Conditions	[0/90/90/0]		[45/-45/-45/45]	
	FSDT Exact [2]	Present HSDT	FSDT Exact [2]	Present HSDT
SS	2.4978	2.5023	1.5368	0.8295
CC	4.6602	4.5940	3.1843	1.8472
CS	3.5446	3.5254	2.3032	1.2855
CF	0.9231	0.9241	0.5551	0.2965

TABLE 2. Effect of Ply Orientation on the Non-Dimensional Frequencies ( $\bar{\omega}$ ) of an Unsymmetric Clamped-Clamped Beam

Mode No.	[0/90/0/90]	[45/-45/45/-45]	[30/50/30/50]
1	3.7244	1.9807	2.2526
2	8.9275	5.2165	5.8624
3	15.3408	9.6912	10.7609
4	22.3940	10.5345	11.9506
5	24.3155	15.0981	16.5747



## FLEXURAL BEHAVIOUR OF TAPERED LAMINATED GRAPHITE/EPOXY BEAMS

S.C.YEN and P.GOPAL  
Department of Civil Engineering and Mechanics  
Southern Illinois University  
Carbondale, IL-62901

The creation of contours is a very important aspect in laminated composite structural fabrication, not only because of the strength and stiffness design parameters, but also because of the need to meet the demands of certain non-structural aspects like aerodynamics. Ply termination at appropriate spots, appears to be an easy and simple method to achieve the contours in structural composites. It is obvious that ply termination will give rise to a change in laminate thickness. In addition to this, ply termination can result in a region of stress concentration.

As part of this research, two basic types of tapered laminates were fabricated, namely the externally stepped laminate (E.S.T.L) and the internally stepped laminate (I.S.T.L). A variation of the I.S.T.L, hereby referred to as the S.I.S.T.L was also studied. A sketch of these laminates is shown in fig.1. The essential difference between the E.S.T.L and I.S.T.L lies in the lay-up of the terminated plies.

Graphite/Epoxy tape (T300/934) was used to fabricate all the specimens. A compression molding procedure was also adopted for curing, with suitable modifications to the mold. Only symmetric cross-ply lay-up was used in the above mentioned three categories of tapered laminates. This was done to keep the material usage and lay-up, the same in a given set of specimens, irrespective of the type of ply termination. The laminates were fabricated with taper angles of  $1^\circ$  and  $2^\circ$ . Microscopic observation and three-point bend tests were carried out to evaluate and compare the three categories of tapered laminated beams.

Three-point bending test results showed that the stiffness of corresponding specimens of the three categories were practically the same. However, the mode of failure of the E.S.T.L was found to be that of step by step delamination

while the I.S.T.L and S.I.S.T.L failed by the tensile mode. A photograph of a delaminated E.S.T.L beam is shown in fig. 2. The I.S.T.L beams, withstood loads of the order of 2.5 times higher than that taken up by the corresponding E.S.T.L beams. The theoretical bending deflection and normal strains, predicted using the laminated beam theory, agreed reasonably well with the experimental results. Figs.3 and 4 show typical variations of experimental and theoretical deflections and normal strains at various cross-sections of the tapered beam.

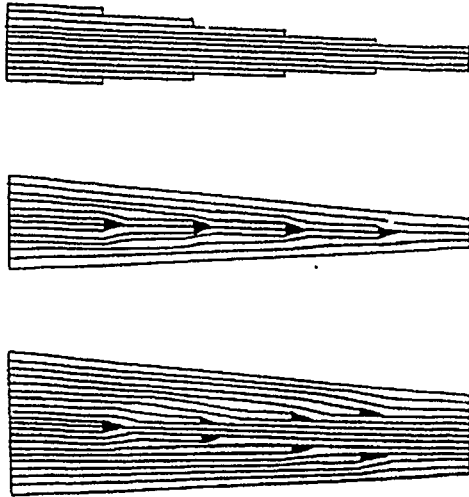


Fig.1. Cross-sections of typical E.S.T.L (top), I.S.T.L (middle) and S.I.S.T.L (bottom).



Fig.2. Delaminations in an E.S.T.L beam.

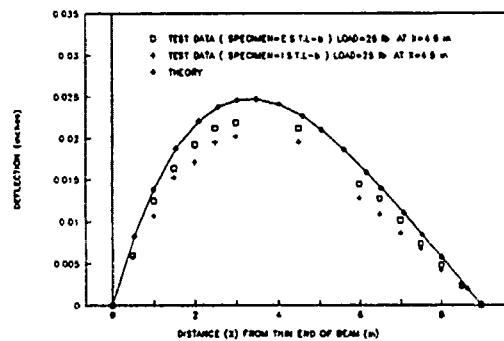


Fig.3. Experimental and theoretical deflections.

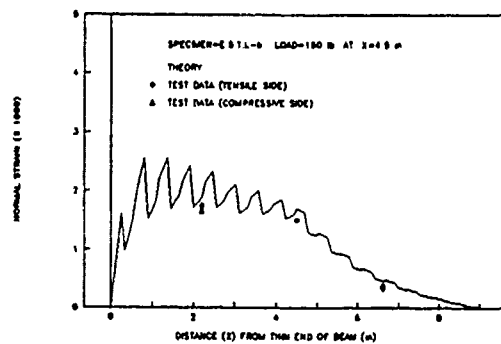


Fig.4. Experimental and theoretical normal strains.

## THE EFFECT OF DELAMINATIONS ON THE VIBRATIONAL CHARACTERISTICS OF COMPOSITE BEAMS

K. Bhalla, D. J. Jennings and R. H. Lance, Department of Theoretical  
and Applied Mechanics, Kimball Hall, Cornell University, Ithaca NY  
14850

Laminated composite materials are used widely in light-weight, high-strength structures. Such materials, however, are particularly vulnerable to in-service damage in the form of delaminations. Delaminations can also be present as a result of improper fabrication procedures. Delaminations can clearly affect the integrity of the structure in which they occur and must thus be detected when it is suspected that they exist.

The zones of delamination that lie on or near the surface of a laminate are generally visible and thus can be easily detected by eye. Internal delaminations, on the other hand, are usually invisible and must be found by other, preferably non-destructive, methods.

Our research, which consisted of an analytical phase and an experimental phase, has been directed at the quantitative characterization of the effect of delaminations on the dynamic characteristics of model beams. Our overall intent was to develop a reliable, non-destructive method for determining the location and extent of delaminations in beam, plate and shell structures. The method proposed here is based on the changes of mode shapes and frequencies induced in beams by built-in delaminations.

In the experimental phase of our work, we studied the vibrational characteristics of cantilever beams made from sheets of Polymethyl Methacrylate (PMMA). This material was chosen because it is easy to fabricate beams from it with controllable zones of delamination. Specifically, we built beams with thickness-to-width-to-length ratios approximately 1:4:10, with two classes of delamination. The beams were built by partially gluing together two layers of PMMA. Figure 1 is a sketch of a typical experimental beam.

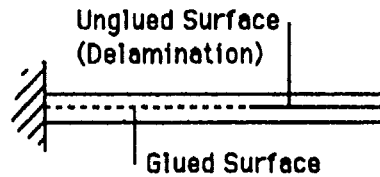


Fig. 1 Delaminated Cantilever Beam

If the two layers of PMMA from which the beam was fabricated were of equal thickness, we called the delamination "symmetric;" if they were unequal the delamination was called "unsymmetric." We built beams with both symmetric and unsymmetric delaminations, and with a variety of lengths of delamination, and measured their vibrational characteristics, including the mode shapes and frequencies of vibration of the first three modes of vibration, with conventional vibration-measuring devices.

In the analytical phase of our study, we calculated the frequencies and the mode shapes of delaminated beams using two different models. For beams with symmetric delaminations, we found that a simple "split beam" model predicted the experimental behavior with sufficient accuracy. A split beam model is one in which a "reduced bending rigidity" is used in the delaminated portion of the beam. The reduced bending rigidity is calculated by assuming that the delaminated portion of the beam is two identical, half-thickness beams, compared to the undelaminated portion of the beam.

The predictions of the vibrational frequencies for unsymmetrically delaminated beams using the reduced bending rigidity model were unsatisfactory. We thus have developed a new method for analyzing such beams that accounts for longitudinal inertia of the beams undergoing vibration. We believe this is the first time such a model has been proposed. The predicted frequencies of unsymmetric beams, using this model, are quite close to the experimentally measured ones.

Thus, we are able to demonstrate that there is a close correlation between delaminations in a beams and their vibrational behavior. We believe this is a mechanically sound basis for further studies in this area leading to a reliable method for non-destructively testing structures made of composite materials to determine whether delaminations are present, and the extent and location of such delaminations.

# High Speed Fracture Behavior of Glass-Cloth/Epoxy Composite

Kensuke Ichinose

Dept. of Mechanical Engineering, Tokyo Denki University,  
Kanda-nishikicyo 2-2, Chiyodaku, 101 Tokyo JAPAN

Goro Suzuki

Dept. of Mechanical Engineering, Tokyo Denki University,  
Kanda-nishikicyo 2-2, Chiyodaku, 101 Tokyo JAPAN

Teruo Kaneda

Dept. of Electronic Engineering, Tokyo Denki University,  
Kanda-nishikicyo 2-2, Chiyodaku, 101 Tokyo JAPAN

## INTRODUCTION

Usually, pendulum-type or Charpy impact testing machine is used for the impact fracture tests. However, it is difficult to apply the constant loading speed to the specimens by these testing machines.

In this research, the electro-hydraulic high speed impact testing machine was developed, which could apply tensile load to the specimens with the speed of 0.1 - 10.0m/s.[1] High speed fracture tests of the glass-cloth/epoxy laminated composite material ( standard compact specimens ) were carried out by using this impact testing machine. The fracture process was observed by a high speed image converter camera. The influences of the loading speed on the maximum load and the absorbed energy were investigated.

## TESTING MACHINE AND SPECIMEN

The developed high speed testing machine is shown in fig. 1. This machine is controlled by an electro-hydraulic feed-back servo system, and it is possible to pull specimens at a given speed in the range from 0.1 to 10.0m/s. Pressurized oil of 200kgf/cm<sup>2</sup> is saved in the large accumulator (3). This high pressure oil is controlled by the servo-valve (2), and the actuator (1) is driven. The output voltage of the stroke sensor (7) is controlled as a feed-back signal. Applied force is measured by the load cell (6). In the case of the faster pull loading more than 7.0m/s, the speed was too fast to measure the force because of the stress wave reflection from the end of the load cell and the testing machine. Photographs during loading were taken by the image converter camera; its shutter speed could be up to 10<sup>7</sup> frame/s.

Figure 2 shows the shape and dimensions of tested CT specimen. The specimens were made of the glass-cloth/epoxy laminated composite plate and the notch tip was machined carefully with a special tool. The direction of the horizontal fiber of the composite is the same as the direction of the machined notch as shown in Fig.2. The notch tip radius is 0.1mm.

## EXPERIMENTAL RESULTS

Figure 3 shows the photographs of the surface of CT specimens during the

loading. The shutter speed was 0.1ms. The maximum load was applied at the time of No.6 photograph in Fig. 3(a), and No.2 in Fig. 3(b). The effects of the loading speed on the maximum load and absorbed energy are shown in Table 1. From these results, the maximum load increases as the loading speed becomes faster. However, the amount of the absorbed energy decreases as the loading speed increases.

## CONCLUSIONS

The electro-hydraulic high speed impact testing machine was developed. High speed fracture tests of the glass-cloth/epoxy laminated composite material (standard compact specimens) were carried out by using this testing machine. The effects of the loading speed on the maximum failure load and absorbed energy were investigated.

## REFERENCES

- (1) K. Ichinose, G. Suzuki and T. Kaneda, Journal of Material Testing Research, Association of Japan, Vol.36, No.1, pp.35-42 (1991) (in Japanese)

Table 1 The influence of the loading speed on the maximum load and absorbed energy.

loading speed(m/s)	1	3	5	7	10
maximum load (t)	0.811	0.913	1.154	1.213	(0.954)
absorbed energy(J)	0.187	0.174	0.167	0.197	(0.277)

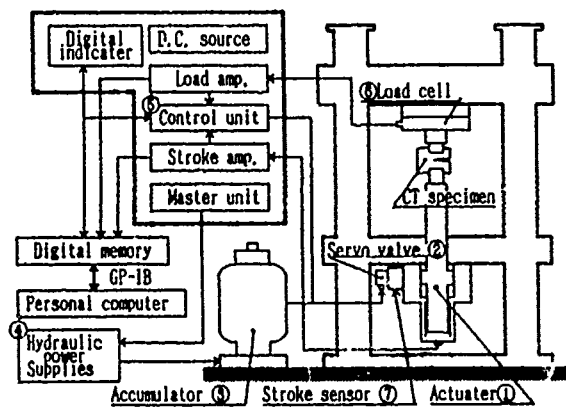


Fig. 1 Schematic figure of high speed impact testing machine.

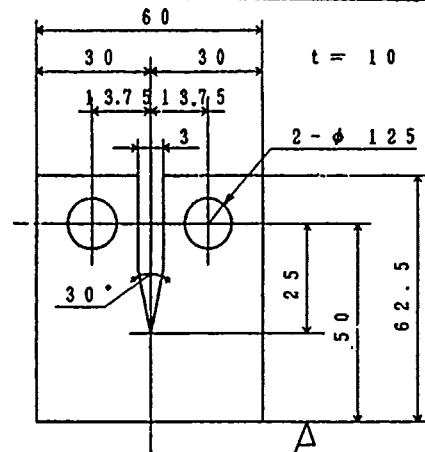
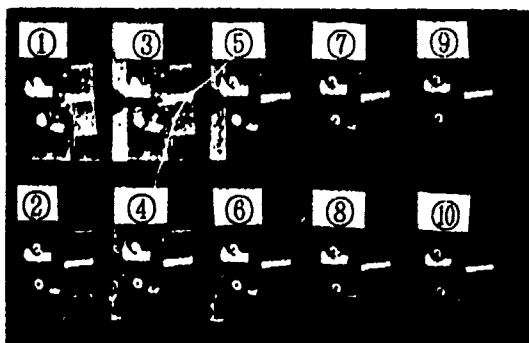


Fig. 2 Size and shape of GFRP CT specimen.



(a) 1.0 m/s



(b) 5.0 m/s

Fig. 3 The photographs of specimens during the loading.

# DYNAMIC RESPONSE OF MULTILAYER BEAMS CONTAINING POROELASTIC ELEMENTS

Akihiro Okuno  
Mazda Motor Corporation,  
Yokohama, Japan

Herbert B. Kingsbury  
Department of Mechanical Engineering  
University of Delaware, Newark DE. 19716

This paper explores the dynamic response of multilayer beams containing fluid-filled porous elastic solid (poroelastic) elements. Beams with polymer foam layers are examples of such structures. Two types of multilayer beams are considered; a two layer beam consisting of a thin metal plate to which is attached a flexible poroelastic layer, and a three layer beam with metallic face layers and a poroelastic core. Although damping of multilayer beams containing viscoelastic elements have been extensively studied, the authors are unaware of any investigations which directly explore internal flow induced damping in porous layers of such structures.

The analyses employ Biot's formulation of the equations three dimensional poroelasticity (1,2) to model the solid phase deformation and the three dimensional fluid flow in the poroelastic layer. These equations are combined with a beam theory formulation of the other layers to derive the systems of equations governing the motion of the structures.

The governing equations for the two layer beam are phrased in terms of two coupled equations involving the lateral displacement and the pressure distribution in the poroelastic layer. Series solutions are formulated which satisfy simple support beam boundary conditions and poroelastic layer pressure boundary conditions corresponding to sealed upper and lower surfaces with free flow at the ends and sides. The beam is center excited with a harmonically time varying force.

These solutions yield a complex frequency response function which is the ratio of center beam displacement to exciting force ( the complex admittance). This frequency response function contains expressions which may be interpreted as complex moduli in bending and extension of the poroelastic layer. From these, expressions for the frequencies,  $\Omega_c$ , at which the energy dissipation is maximum and the values of the loss moduli  $K''$  at these frequencies are obtained.

$$\text{Bending:} \quad \Omega_c = 10.6 \frac{n^* M}{h^2 b} \quad K'' = 0.40 \alpha^2 M$$

$$\text{Extension:} \quad \Omega_c = 10.28 \frac{n^* M}{d^2 b} \quad K'' = 0.41 \alpha^2 M$$

M and  $\alpha$  are poroelastic material constants (Ref. 2),  $n^*$  the porosity, b the resistivity, and n the beam mode number. h is the layer thickness and l and d the beam length and width.

Sample calculations for an aluminum beam with polyurethane foam-air systems show that the unconstrained poroelastic layer contributes only a small amount of damping to the system.

The three layer beam consists of a flexible poroelastic core combined with relatively stiff and heavy facing layers. The model assumes that thickness change, rather than beam bending, is the primary mode of core deformation so that as the entire structure deforms, the upper face acts as a seismic mass for the core layer. During deformation, fluid flows within the core layer as well as across its side and end faces. A system of three coupled equations are derived which govern the lateral bending displacements of the two face layers and the pressure distribution in the core. A solution to these equations is obtained for the case of a free-free beam excited by a harmonically time varying force applied to the center of the lower face. Again, series solutions satisfying the appropriate boundary conditions are assumed for each of the variables leading to an expression for the complex ratio of lower layer center beam displacement to driving point force. This complex frequency response function contains an expression for a complex modulus resulting from the fluid-solid interaction in the poroelastic layer.

$$\Omega_c = 3.90 \frac{n^* M}{d^2 b} \quad K'' = 0.41 \alpha^2 M$$

In order to obtain maximum energy dissipation in the system, it is necessary to adjust the system parameters so that both the frequency of maximum fluid damping and the core thickness change resonant frequency equal the excitation frequency. Numerical examples show the major factors affecting the system damping characteristics. These factors include the stiffness and mass of the face plate, and the resistivity of the core layer. Driving point admittance frequency response curves for several combinations of face and core properties corroborate the predictions of the analysis that core damping is maximized by tuning the core thickness resonance mode and the maximum poroelastic damping frequency to the exciting frequency. Finally, in contrast to the two layer system, the three layer system provides substantial energy dissipation because of more effective deformation of the core layer.

#### References:

1. Biot, M.A., 1956, "Theory of Propagation of Elastic Waves in Fluid Saturated Porous Solids: Low Frequency Range." J. of Acous. Soc. of America, Vol 28, pp 168-178.
2. Biot, M.A., and Willis, D.G., 1957, "The Elastic Coefficients and the Theory of Consolidation," ASME J. of Applied Mechanics, Vol. 24, No. 79, pp 594-601.



# DISSIPATION OF MECHANICAL POWER IN THERMOPLASTIC UNIDIRECTIONAL COMPOSITES - EQUIVALENT ISOTROPIC MATERIAL

I.T.Georgiou and C.T.Sun  
School of Aeronautics and Astronautics, Purdue University  
West Lafayette, Indiana 47906

The class of thermodynamically simple continuous solids that deform elastically and inelastically (plasticity, viscosity) dissipate part of the mechanical power that the environment exerts on them. Irreversible thermodynamics [1] defines the rate of the internal dissipation density  $\delta$  to be the difference between the densities of the least upper bound of the heating and the heating itself. In [1] it is shown that  $\delta$  is identical to the Fréchet-derivative of the free energy which is a function of the histories of strain  $\epsilon_{ij}$  and temperature  $T$ .  $\delta$  is not only a scalar functional of the history of  $(\epsilon_{ij}, T)$  but also a scalar function defined over the group of material symmetries. For instance, if the group of material symmetry is identical to the group of orthogonal unimodular tensors, then  $\delta$  is an isotropic scalar function [2]. In this paper we are interested in the functional form of  $\delta$  when the group of material symmetry is orthotropic.

For orthotropic material symmetry,  $\delta$  must be a scalar function of the invariants of the tensor  $\epsilon_{ij}^t$  (or  $\sigma_{ij}^t$ ) and of the Euler angles  $\psi_i$  orientating the orthogonal coordinate system (to which all tensors are referred to) to a reference orthogonal coordinate system coincident with the axes of material symmetry:

$$\delta = \delta(\epsilon_{ij}^t, T^t; \psi_i) = \delta(E_i^t, T^t; \psi_i), \quad i, j = 1, 2, 3 \quad (1)$$

$$\epsilon_{ij}^t \equiv \epsilon_{ij}(t-s); \quad 0 < s < \infty, \quad t \text{ is the time} \quad (2)$$

where  $E_i^t$  are the invariants of the history of  $\epsilon_{ij}$ . In what follows we suppress the dependence of  $\delta$  on  $T^t$ .

We claim that there exists a nonsingular linear orthotropic transformation  $A_{ijmn}$  that transforms the space of symmetric tensors to itself such that  $\delta$  becomes an isotropic scalar function of the transformed tensors, thereby justifying the introduction of the term equivalent isotropic material.

For specified sinusoidal stress  $\sigma_{ij}$  (of frequency  $\omega$ ) about a mean stress  $\sigma_{ij}^{(0)}$ , the argument of the dissipated mechanical work (over a cycle)  $\delta_c$  becomes  $(\Delta\sigma_{ij}^{(k)}, \sigma_{ij}^{(0)}, \omega)$  provided that the material exhibits smooth memory [3].  $\Delta\sigma_{ij}^{(k)}$  ( $\Delta\sigma_{ij}^{(0)} \equiv \Delta\sigma_{ij}$ ) are the amplitudes of the time derivatives of the transformed stress  $\sigma_{ij}$ :

$$\overline{\sigma_{ij}^{(k)}} = A_{ijmn} \sigma_{mn}^{(k)}, \quad i, j, m, n = 1, 2, 3, \quad k = 0, 1, 2, \dots; \quad \sigma_{ij} = \sigma_{ij}^{(0)} + (\Delta\sigma_{ij}) \cos(\omega t) \quad (3)$$

In the transformed stress space  $\delta_c$  becomes a function only of the invariants  $(\overline{\Delta I_1^{(k)}}, \overline{I_1^{(0)}})$  of the corresponding transformed tensors in the argument of  $\delta_c$ .

We have verified experimentally that the transformation  $A_{ijmn}$  exists: Off-axis specimens of AS4/PEEK thermoplastic composite were subjected to sinusoidal stress and  $\delta_c$  was measured as a function of  $\Delta\sigma_0$  (amplitude of the applied uniaxial stress). For plane stress, only the restriction of  $A_{ijmn}$  to the 3-D Euclidean space is involved. Its existence is equivalent to the requirement that the transformation  $A_{ijmn}$  corresponds the graphs of the experimentally obtained set of functions ( $\delta_c(\Delta\sigma_{00}, \omega)$ ,  $\delta_c(\Delta\sigma_{45}, \omega)$ ,  $\delta_c(\Delta\sigma_{70}, \omega)$ ,  $\omega = 10\pi, 20\pi, 30\pi, 50\pi, 60\pi$  ( $\frac{\text{rad}}{\text{s}}$ )) to the graph of an isotropic scalar function  $\delta_{ic}(\Delta\sigma_{ij}, \omega)$  defined over the transformed stress space (Fig.1). We have developed a method that uses experimental data to verify that such a correspondence exists, thereby determining numerical values of the restriction of  $A_{ijmn}$ . For the tested thermoplastic fiber composite, this isotropic function turns out to be a function only of the second invariant of  $\Delta\sigma_{ij}$ . When transformed by the inverse transformation  $A_{ijmn}^{-1}$ ,  $\delta_{ic}$  predicts the mechanical power dissipated in any off-axis uniaxial specimen. In Fig. 2, the predicted  $\delta_c$  is compared to the one obtained experimentally, the agreement being exceptional. Moreover, because the anisotropy of the dissipative properties of the material has been eliminated, we say that the original orthotropic material has been replaced by an equivalent isotropic one. Indeed, there exists an off-axis specimen of fiber orientation  $\theta^*$  endowed with the dissipative properties of the equivalent isotropic material.

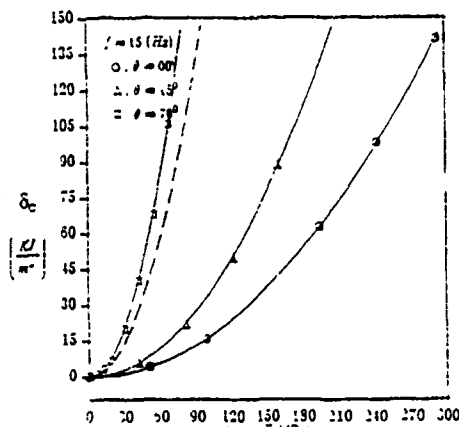


Fig.1 - Dissipated mechanical work(experiment) as function of stress amplitude and fiber orientation. — graph of isotropic dissipation function over transformed stress space.

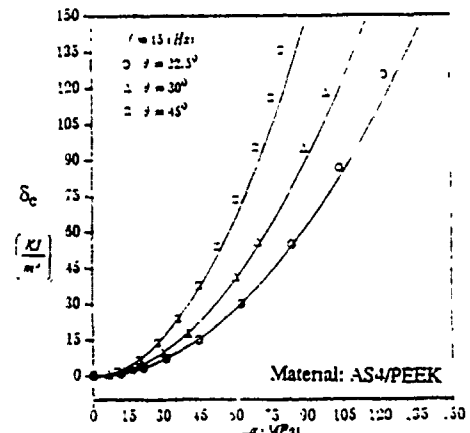


Fig.2 - Dissipated mechanical work predicted by isotropic dissipation function. various symbols: experimental data.

**Acknowledgements** - This work was supported by NASA Langley Research Center under Grant No. NA G-1-825 to Purdue University.

## References

1. Truesdell, C., "Rational Thermodynamics," McGraw-Hill, New York (1969).
2. C.-C. Wang, "On Representations for Isotropic Functions," *Arch. Rat. Mech. Anal.*, 33 (1968) 249-267.
3. A. Cemal Eringen, "Mechanics of Continua," John Wiley & Sons, New York (1967).

# IMPROVED MODEL FOR ANALYZING STRESS DISTRIBUTION FOR COMPOSITE LAMINATES WITH CENTRAL HOLE \*

Stanley N. Ihekweazu  
Department of Mechanical Engineering Technology  
South Carolina State College, Orangeburg, SC 29117

## Introduction

Whitney and Nuismer<sup>2</sup> investigated the "Uniaxial Failure of Composite Laminates Containing Stress Concentrations". Their investigations were based on what is known as the hole size effect, that is, for tension specimen containing various sized holes, larger holes cause greater strength reduction than do small holes. Their explanation of the hole effect is based on the concept that the normal stress distribution from a uniform stress state is considerably more concentrated near the hole boundary in the case of a small hole. They developed two criteria for the strength of notched composite materials. The first criterion is based on the stress at a point a fixed distance away from the notch and referred to as the point stress criteria (psc). The second criterion is based on the average stress over some fixed distance ahead of the hole, referred to as the average stress criterion (ASC).

The Whitney and Nuismer PSC was initially used to analyze the stress distribution of three types of composite laminates containing circular holes or an edge notch. The prepreg material of the laminates were obtained from the Fiberite corporation.

Ihekweazu and Pendleton revealed some limitations with Whitney and Nusimer PSC, noting, that although their PSC in its basic form is good for analyzing specific laminates, it needed to be modified in order to be a general model.

This paper presents an improved or versatile model for analyzing stress distribution for composite laminates with central hole.

## EXPERIMENTAL

The materials tested are:

- MXM - 7714/120 A fabric prepreg consisting of woven kevlar 49 reinforce-impregnated with fiberite 250 F curing 7714 epoxy resin. (Material 1)
- HMF - 2448A1e 250 F curing epoxy resin impregnated graphite fabric. (Material 2)
- HYE - 24481E 250 F curing epoxy resin impregnated unidirectional graphite tape. (Material 3)

Specimen were fabricated according to ASTM standard D 3039. Principal material Hookian constants were provided by Fiberite.

---

\*Paper shortened by the editors

Experiment was conducted to verify the values provided by Fiberite. Results are shown on table 1. Additional specimen were made for determining stress distribution near a central hole for a composite material in pure tension.

TABLE 1. Summary of the Material Properties of the 3 Materials at Room Temperature

MATERIAL TYPE	STACKING SEQ.	NO. OF LAYERS	E1	E2	V12	V21	G12	SULT
MXM-7714/120 KEVLAR 49 FABRIC	FABRIC UNIDIRECT- IONAL	10	3.8 <sub>6</sub> x10 <sup>6</sup> Psi	3.8 <sub>6</sub> x10 <sup>6</sup> Psi	.33	.33	.143 <sub>6</sub> x10 <sup>6</sup> Psi	63 Ksi
HYE-2448AIE GRA. UNI. DIR. TAPE	UNIDIRECT- IONAL TAPE	10	19.89 x10 <sup>6</sup> Psi	1.8 <sub>6</sub> x10 <sup>6</sup> Psi	.28	.025	.8 <sub>6</sub> x10 <sup>6</sup> Psi	206 Psi
HMF-322/74B GRAPHITE FABRIC	FABRIC UNIDIRECT- IONAL	8	8 <sub>6</sub> x10 <sup>6</sup> Psi	8 <sub>6</sub> x10 <sup>6</sup> Psi	.3	.3	.307 <sub>6</sub> x10 <sup>6</sup> Psi	98 Ksi

TABLE 2. Comparison of Stresses Using Whitney-Nuismer' Point Stress Criteria With Stresses Obtained for Experiment.

MATERIAL	$\sigma_e$ (KSi)	$\sigma_{exp}$ (KSi)	Error $\frac{\sigma_e - \sigma_{exp}}{\sigma_{exp}}$	% Error
HYE2448A/E	89.041	82.545	.0790	7.9
MXM7714/120	49.853	20.064	1.4847	147.47
HMF322/74B	56.107	26.800	1.09355	109.35

TABLE 3. Comparison of Stresses Using the Modified Whitney-Nuismer's Point Stress Criteria with Stresses Obtained from Experiment.

MATERIAL	$\lambda \sigma_e$ (KSi)	$\sigma_{exp}$ (KSi)	Error $\frac{\lambda \sigma_e - \sigma_{exp}}{\sigma_{exp}}$	% Error
HYE2448A/E	(3) 89.041	82.545	.0790	7.9
MXM7714/120	(1) 24.428	20.064	0.2175	21.75
HMF322/74B	(2) 26.931	26.800	0.0049	0.49

#### REFERENCES

1. Ihekweazu, S. N. and Pendleton, R. L. "Model for Analyzing Stress Distribution for Composite Laminates with Central Hole" Failure Prevention and Reliability (ASME) DE - Vol.16 Pg. 255-258.
2. Whitney, J. M. and Nusimer, R. J. "Stress Fracture Centering for Laminated Composites Containing Stress Concentration", Journal of Composite Materials, Vol. 8 pp. 253-265.

## VIBRATION OF UNIDIRECTIONAL FIBER - REINFORCED PLANAR FRAME STRUCTURES

GAD EL RAB RAEFI\*

Mechanical Engineering Dept. Technical University  
of Budapest, 1111. Budapest, XI., Muegyetem rkp. 5

In this research work, theoretical and experimental techniques have been used to determine the natural frequencies and natural modes of unidirectional fiber reinforced planar frame structures. Finite element techniques has been applied to construct the mass and stiffness matrices for large structures and degrees of freedom . Jacobi's method provides a convenient scheme to compute all eigenvalues and eigenvectors in case of symmetric real structural matrices . A comprehensive computer program has been established to compute eigenvalues and eigenvectors for a general fiber reinforced composite structure with different design parameter such as concentrated mass , mass moment of Inertia and concentrated spring at any selected boundary condition. A Graphical program has been used to draw the selected eigenmodes . Experimental work has been carried out to measure eigen frequencies and structure loss factor of unidirectional fiber reinforced planar frame structures. Finally a comparison between experimental and numerical results have been presented.

---

\* ( On leave from Department of Mechanical Engineering,  
University of Helwan, Cairo. Egypt. )

## REFERENCES\_

- 1- Y.J.Dudek, " Yong's and Shear moduli of unidirectional composites by resonant beam method " J. Sound & Vib. Vol 4., pp. 232 - 241 , 1970.
- 2- R.B.Abarcar and P.F.Cunniff, " The vibration of cantilever beams of fiber reinforced material " J. Composite Materials Vol.6, pp. 504 - 517 , 1972.
- 3- R.Davis , R.D.Henshel and G.B.Warburton " A Timoshenko beam element " J. Sound & Vib. Vol. 22, pp. 475- 487, 1972.
- 4- D.L.Thomas , J.M.Wilson and R.R.Wilson " Timoshenko beam finite elements " J. Sound & Vib. Vol. 31., pp. 315 - 330 , 1973.
- 5- B.Walter Rosen " Stiffness of fiber composite materials ", J. Composite Materials Jan pp. 16., 1973.
- 6- R.D.Adams and D.G.C.Bacon " The dynamic properties of unidirectional fiber reinforced composites in flexural and torsion." J.Composite Materials Vol.7 , pp. 402., 1973
- 7- L.S.Teoh and .C.Huang " The vibration of beams of fiber reinforced material " J. Sound & Vib. Vol. 51. pp. 433 - 449., 1975.
- 8- K..Bathe and H.Ozdemir " Elastic - plastic large deformation static and dynamic analysis." Comp. & structures. Vol.6 , pp. 81- 92., 1976.
- 9- K.K.Teh and C.C.Huang " The effects of fiber orientation on free vibrations of composite beams " J. Sound & Vib. Vol. 69 (2) ,pp. 327 - 337 , 1980.
- 10- Alex T.Chen and T.Y.Yang " Static and dynamic formulation of a symmetrically laminated beam finite element for a Microcomputer." J. Composite Materials Vol. 19. pp. 459. , 1985.

*On the Mechanics of Materials Susceptible to Cold Drawing*, Bernard D. Coleman and Daniel C. Newman, College of Engineering, Rutgers University, Piscataway, New Jersey 08855-0909, U.S.A.

A procedure is presented for deriving constitutive equations for fibers and film strips of viscoelastic simple materials with long-range gradually fading memory undergoing non-homogeneous stretching. The derived formulae for the tension  $T$  per unit area can be viewed as constitutive equations for unidimensional bodies composed of non-simple materials for which gradients of strain influence  $T$ . From the point of view of the theory of three-dimensional bodies, the formulae are valid to within an error  $O(D^4)$  in the sample thickness  $D$ . The present theory extends to materials with viscoelastic memory previous work on the mechanics of neck formation and cold drawing in elastic materials [*Arch. Rational Mech. Anal.* **83**, 115-137 (1983); *J. Polym. Sci. B, Polym. Phys.* **26**, 1801-1822 (1988)] and materials with viscous stresses [*Comp. Math. Appls.* **11**, 35-65 (1985)]. Material response for various types of histories is discussed and the derived constitutive equation for  $T$  is shown to be consistent with thermodynamical principles. The theory has been employed to calculate the creep response of fibers under static loads. Numerical solutions of the evolution equation for the (unidimensional) strain field show that for an appropriate class of (three-dimensional) constitutive functionals of the BKZ type there is a range of applied loads for which an initially homogeneous deformation evolves into a well defined neck whose edges advance at high speed along the fiber and in so doing transform moderately stretched material into highly stretched (*i.e.*, drawn) material. The calculated fiber profiles and the predicted dynamics of neck formation and growth are in good accord with experimental observations of materials susceptible to cold drawing. A description is given of the circumstances under which one can use instantaneous (*i.e.*, high-speed) response functions to calculate fiber profiles in rapidly growing necks.

# Stability and Localization in Thermo-Plasticity: A Variational Approach

REZA MALEK-MADANI  
DEPT. OF MATHEMATICS  
UNITED STATES NAVAL ACADEMY  
ANNAPOLIS, MD 21402-5002

The system of partial differential equations

$$(1) \quad \begin{aligned} \rho v_t &= \sigma_x, \\ \rho c \theta_t &= \lambda \theta_{xx} + k \sigma v_x, \end{aligned}$$

complimented with the constitutive law

$$(2) \quad \sigma = \hat{\sigma}(\theta, v_x)$$

models simple shearing of a thermo-plastic material. In (1)  $\rho$  is the density,  $c$  is the specific heat and  $\lambda$  is the thermal conductivity of the material. We are interested in the asymptotic behavior of solutions (1)-(2) once initial and boundary conditions are specified. Our primary result concerns the stability of steady-state solutions of (1)-(2) when either stress or velocity boundary conditions are specified at  $x = \pm 1$ . We will first cast the above system in a variational form and classify all constitutive laws for which the right-hand side of (1) is the Euler-Lagrange equations of an appropriate Lagrangian. For this class of nonlinearities we are able to distinguish all steady-state solutions that are minimizers of the nonlinear Lagrangian. Since the Lagrangian defines a Lyapunov functional for the dynamical system (1), these minimizers become nonlinearly stable as solutions of (1) once one proves a global existence theorem for (1).

We show that the right-hand side of (1) are the Euler-Lagrange equations for the functional

$$(3) \quad \begin{aligned} I(\theta, v_x, \sigma_0) &= \int_{-1}^1 \left[ \frac{1}{2} \frac{\sigma}{\kappa} \theta_x^2 + \Sigma(\theta, v_x) - \sigma_0 v_x \right] dx, \\ v(-1) &= 0, \quad \theta(-1) = \theta(1) = 0, \end{aligned}$$

if and only if  $\sigma$  depends on  $\theta$  and  $v_x$  in the form

$$(4) \quad \hat{\sigma}(\theta, v_x) \equiv e^{-\alpha \theta} g(e^{-\alpha \theta} v_x),$$

where  $\hat{\sigma} = \Sigma'$ . The advantage of this variational formulation is that the stability analysis of the steady-state solutions are given a unified treatment in both cases of velocity and stress boundary conditions (cf. Maddocks & Malek-Madani [1991] for details). Specifically we prove the following results:

a) For the case of stress boundary conditions, there is a critical value of  $\sigma_0$  above which there are no steady-state solutions. Below this value of  $\sigma_0$  there are in general a multiplicity of solutions. The number of such solutions depends on the growth nature of  $g$  in (4) and examples exist that demonstrate multiple folds in the bifurcation diagram. When the bifurcation diagram is drawn in the preferred coordinate system of  $(\sigma_0, -I_{\sigma_0})$ , the general theory of Maddocks (1987) is used to deduce the stability of extremals of (3) from the geometry of the bifurcation diagram. In particular, the principle of exchange of energy is shown to hold.

b) In the case of velocity boundary conditions, we show that there is a unique steady-state solution for each  $v_0$  and that this solution is a minimizer of (3).



### References.

- J. H. MADDOCKS & R. MALEK-MADANI, *Stability of localized steady-state shear-bands in thermo-plasticity: Part I: Vanishing Yield Stress*, to appear.
- J.H. MADDOCKS, *Stability and folds*, Arch. Rat. Mech. Anal., 99 (1987), pp. 301-328.

## 22nd MIDWESTERN MECHANICS CONFERENCE

October 6-9, 1991  
University of Missouri-Rolla

Name: ..... Athanasios Tzavaras .....  
Affiliation: ..... Department of Mathematics, University of Wisconsin .....  
Address: ..... Madison, WI 53706 .....  
Office Telephone: (608) 263-3168 ..... E-mail: tzavaras@eunice.cms.wisc.edu .....

### Title & Abstract

#### On the Formation of Shear Bands at High Strain Rates

One of the most striking manifestations of instability in solid mechanics is the localization of shear strain into narrow bands during high speed, plastic deformations of metals. According to one theory, the formation of shear bands is attributed to effective strain-softening response, which results at high strain rates as the combined outcome of the influence of thermal softening on the, normally, strain-hardening response of metals. Our objective is to review some of the insight offered by nonlinear analysis techniques on simple models of nonlinear partial differential equations simulating this scenario for instability. First, we take up a simple system, intended as a paradigm, that describes isothermal shear deformations of a material exhibiting strain softening and strain-rate sensitivity. As it turns out, for moderate amounts of strain softening, strain-rate sensitivity exerts a dissipative effect and stabilizes the motion. However, once a threshold is exceeded, the response becomes unstable and shear strain localization can occur. Next, we present extensions of these results to situations where explicit thermal effects, through the energy equation, are taken into account.

# **The Phenomenon of Shear Strain Localization in Dynamic Viscoplasticity**

By

**T. G. Shawki**

Department of Theoretical and Applied Mechanics  
University of Illinois at Urbana-Champaign  
Urbana, Illinois 61801

## **Abstract**

This article presents a state-of-the-art review concerning the analysis of shear flow localization during high rates of deformation of thermal viscoplastic materials. An overview of several efforts towards an improved understanding of shear band formation is given. Such efforts include the analysis of the pre-localization as well as the post-localization regimes while they implement a variety of techniques: (i) nonlinear a priori estimates, (ii) linear stability theory, (iii) exact solutions and (iv) numerical analysis. This presentation aims at extracting a unified framework towards the analysis of shear band formation for the considered class of deformations. Furthermore, we present a number of rigorous exact solutions for the one-dimensional simple shearing deformation of a general class of thermal viscoplastic materials. These solutions are used as a benchmark for the validity of both analytical and computational procedures. The interactive roles of inertia, rate-sensitivity, heat conduction, perturbation geometry, boundary conditions, thermal softening, strain hardening and constitutive description as regards the initiation and further intensification of flow localization are thoroughly addressed. We also examine the delicate questions concerning the notion of shear localization and the related mathematical characterization, length and time scales as well as the connection between localization and the loss of load-carrying capacity. Finally, we examine possible directions of future research.

# NONHOMOGENEOUS DEFORMATIONS OF A NONLINEAR ELASTIC MATERIAL UNDERGOING MICROSTRUCTURAL CHANGES

Alan Wineman and Hugh E. Huntley, Department of Mechanical  
Engineering and Applied Mechanics, University of Michigan,  
Ann Arbor, Michigan 48109

An assumption which is intrinsically incorporated in the constitutive equation for nonlinear elasticity is that stress arises due to a single microstructural mechanism, namely macromolecular reconfigurations. Recently, a constitutive equation has been introduced for rubbery materials that accounts for change in the microstructural mechanism as deformation progresses. The underlying constitutive assumption is that, during each increment of deformation, a portion of the original material is transformed into a new material with a new microstructural mechanism for generating stress. At each state of deformation, the current material consists of the untransformed portion of the original material and the newly formed material. The total stress is the superposition of the stress in the remainder of the original material, which is determined by its deformation from its initial configuration, and the stress in the newly formed portions, each of which is determined by its deformation from the configuration at which it formed.

In this talk, we present a number of examples which illustrate the interaction of the microstructural changes and nonhomogeneous deformations. These include the determination of regions containing the original and modified material as loading increases, the effects of the new response micromechanism on structural response, the influence of the amount of conversion of original material to new material, and the development of residual stresses and deformation on removal of load.

# ULTRASONIC MEASUREMENT OF STRESS IN WEAKLY ANISOTROPIC THIN SHEETS

CHI-SING MAN

Department of Mathematics, University of Kentucky, Lexington, KY 40506

WEI-YANG LU, QUN GU, & WENLIANG TANG

Department of Engineering Mechanics, University of Kentucky, Lexington, KY 40506

A membrane theory is developed for measurement of stress in weakly anisotropic thin sheets. The thin sheets are modelled as prestressed planar membranes, and the application of horizontally polarized quasishear waves (which correspond to the  $SH_0$  mode in a plate theory) in stress evaluation is studied. The theory presented here would be valid so long as the superimposed small amplitude stress waves could be taken as hyperelastic, irrespective of the origin of the prestress and the thermomechanical history of the specimen in question. In particular it should be applicable to thin metal sheets that have undergone plastic deformations and/or thermomechanical processes such as welding or annealing. To examine the validity of the preceding assertion, a series of experiments were performed on thin aluminum sheets, each of which had undergone inhomogeneous plastic deformations. By using a probe that consisted of three electromagnetic acoustic transducers (one transmitter, and two receivers separated by a rigid spacer of 30 mm), velocities of horizontally polarized quasishear waves were measured, for various orientations of the probe and at various places of each sample sheet, by cross-correlation of signals picked up by the two receivers. There were indications that the present theory and measurement system delivered at each place a good estimate of the local principal surface-stress directions and difference in principal surface stresses. Some of the samples were annealed after the aforementioned experiments were completed. By using the same probe measurements of stress were repeated for the annealed samples. These measurements showed that residual stresses were relieved by the annealing.

# LARGE CYCLIC DEFORMATIONS OF VISCOELASTIC RUBBERLIKE MATERIALS

Arthur R. Johnson  
Army Materials Technology Laboratory  
Watertown, MA 02172-0001

Donald L. Cox\* and Laurent C. Bissonnette\*\*  
Naval Underwater Systems Center

## ABSTRACT

Load-displacement data for large deformations of rubberlike materials typically indicate the presence of viscous and plastic-like effects. In some applications involving cyclic loads repeatable stress-strain hysteresis loops are observed. A stress analysis for these cyclic loads requires the use of finite deformation viscoelastic models. In this effort a recently developed viscohyperelastic Maxwell model is reviewed and used to analyze large cyclic deformations. Previous models based on uniaxial data are extended to include biaxial (flat membrane spherical inflation) data. The model consists of a hyperelastic solid in parallel with viscohyperelastic "fluid-solids". The hyperelastic solid's constitutive equation is determined by fitting relaxed stress-stretch ratio data to constrained forms of a Rivlin expansion. Requirements for material stability are discussed. The flow laws and constitutive equations for the internal fluid-solids are developed from "quick pull" stress relaxation tests. Nonlinear one-dimensional computational models are used to generate numerical data demonstrating a range of material behavior for which the method can be used. An axisymmetric finite element algorithm which implements the viscohyperelastic theory is reviewed. The algorithm uses a penalty method to enforce incompressibility and requires the integration of a system of first order nonlinear differential equations. Cyclic inflation and deflation deformations of axisymmetric viscous rubberlike solids are computed. The advantages and disadvantages of the computational scheme are discussed.

\* New London, CT.

\*\* Newport, RI.

Roberta SBURLATI

Istituto di Scienza delle Costruzioni, Università di Genova  
Via Montallegro, 1 - 16145 Genova - Italy

In classical problems of linear elasticity the assigned boundary values (e.g. the displacement field  $u$  or the traction field  $S(n) = s$ ) are constrained only by regularity requirements.

The situation is completely different when one considers internal constrained material; actually, one cannot freely assign both the boundary values and a functional restriction on the problem; if one considers an incompressible material, for instance, the displacement field  $u$  have to be chosen in such a way that the deformed material will preserve the total volume.

Various contributions are present in the literature; in [1] Rostamian obtains a set of *necessary* conditions for the existence of the elastic solution. These conditions are found by utilizing functional analysis techniques in the case of mixed boundary values problem; more precisely, it is supposed that the elastic body  $\Omega$  admits a boundary  $\partial\Omega$  which can be regarded as the disjoint union of two regions  $\partial_1\Omega$  and  $\partial_2\Omega$  such that the displacement field  $u$  is assigned in the first region while the traction field  $s$  is assigned in the second one.

The aim of the present work is to generalize the result obtained by Rostamian to the so called *contact problem*. More precisely we suppose that  $\partial\Omega = \partial_1\Omega \cup \partial_2\Omega \cup \partial_3\Omega$  and  $\partial_1\Omega \cap \partial_2\Omega = \emptyset$ ,  $\partial_1\Omega \cap \partial_3\Omega = \emptyset$ ,  $\partial_2\Omega \cap \partial_3\Omega = \emptyset$ ; moreover the following requirements are assumed:

$$\left\{ \begin{array}{ll} u = u^* & \text{on } \partial_1\Omega \\ s = s^* & \text{on } \partial_2\Omega \\ (u \cdot n)n = u^* & \text{on } \partial_3\Omega \\ s - n(n \cdot s) = s^* & \text{on } \partial_3\Omega \end{array} \right. \quad (1.1)$$

The field  $u^*$  and  $s^*$  are to be regarded as the prescribed surface displacement and traction fields.

Rostamian observes that by considering the elastic problem in terms of stress one can study constrained problems on the same line of reasoning of ordinary problems since all the new information is described by means of a suitable choice of the compliance tensor. More precisely, in the case of constrained problems the compliance tensor  $K$  is not invertible and the formulation in terms of the displacement field is *not equivalent*. On the contrary, when no internal constraints is present  $K$  admits the inverse elasticity tensor  $C$  and the two formulations are equivalent.

A internal constraint is described by a relation like:

$$c \cdot \nabla u = 0$$

where  $c$  is called the constraint matrix [2]. One can show that this matrix belongs to the so called null space of  $K$ .  $K(c) = 0$ .

Our constrained elastic problem is so formulated: we have to find the elastic state  $[u, E, S]$  satisfying the following equations:

$$\left\{ \begin{array}{ll} \operatorname{div} S = f & \text{in } \Omega \\ E = K(S) & \text{in } \Omega \\ u = u^* & \text{on } \partial_1 \Omega \\ Sn = s^* & \text{in } \partial_2 \Omega \\ (u \cdot n)n = u^* & \text{on } \partial_3 \Omega \\ s - n(n \cdot s) = s^* & \text{on } \partial_3 \Omega \end{array} \right. \quad (1.2)$$

where  $f$  denotes the body force field.

In the present note we use the same functional assumption of [1]: for this reason we suppose that the reader would have previously read this work.

Our main result is contained in the following theorem:

**Theorem.** *A necessary condition for the existence of solution of the elastic problem (1.1) is given by the following requirement on the displacement field:*

$$\int_{\partial_1 \Omega} u^* \cdot S'(n) dA = 0 \quad (1.3)$$

for all the stress fields  $S'$  which verify the following relations:

$$\left\{ \begin{array}{ll} \operatorname{div} S' = 0 \\ K(S') = 0 \\ S'(n) = 0 & \text{on } \partial_2 \Omega \cup \partial_3 \Omega \end{array} \right. \quad (1.4)$$

*Proof.* Assume that  $(S, u)$  is an elastic solution of the problem. Consider the equation which is a simple consequence of the Green formula:

$$\begin{aligned} 0 &= \int_{\Omega} K(S') \cdot S d^3x = \int_{\Omega} S' \cdot E d^3x \\ &= \int_{\partial \Omega} S'(n) \cdot u dA - \int_{\Omega} \operatorname{div} S' \cdot u \\ &= \int_{\partial_1 \Omega} S'(n) \cdot u^* dA + \int_{\partial_2 \Omega} S'(n) \cdot u dA + \int_{\partial_3 \Omega} S'(n) \cdot u dA \end{aligned} \quad (1.5)$$

The term  $\operatorname{div} S'$  vanish in view of our assumption (1.4a) and the last two terms in view of equation (1.4c).

In a next work we shall study a further generalization to the generalized boundary value problem also by taking into account the recent paper of D.N. Arnold and R.S. Falk [3] in which the authors find necessary and sufficient conditions for the well-posedness of constrained elastic problems.

## REFERENCES

1. R. ROSTAMIAN, *Internal constraints in linearly elasticity*, Journal of Elasticity 11 (1981), p. 11-31.
2. A.C. PIPKIN, *Constraints in linearly elastic materials*, Journal of Elasticity 6 (1976), p. 179-193.
3. D.N. ARNOLD and R.S. FALK, *Well posedness of the fundamental boundary value problems for constrained anisotropic elastic materials*, Arch. Rat. Mech. Anal. (1987), p. 143-165.



# WAVES IN COUPLED NON-LINEAR THERMOELASTIC SOLIDS

M.C. SINGH, Professor  
D.V.D. TRAN, Graduate Student  
Department of Mechanical Engineering  
The University of Calgary, Calgary, Alberta, Canada T2N 1N4

## INTRODUCTION

The literatures on the investigation of wave propagation in linear thermoelastic materials is vast and can be viewed in the survey work of Chandrasekharaiah [1]. However, the work on non-linear thermoelastic waves is rarely seen in the literature. The linearized theory can not express the real behaviour of materials which have been proved to disobey the Hooke's law even under small deformations [2]. Recently, Singh and Tran [3] investigated waves in non-linear non-conducting thermoelastic materials. In this paper, the basic equations for uniaxial wave motion in a coupled non-linear thermoelastic material are presented and analysis of temperature response along a cast iron rod subject to a constant velocity impact is given. The study also includes stress, velocity, temperature and heat flux responses of different non-linear thermoelastic materials under various impact loadings.

## BASIC EQUATIONS AND JUMP CONDITIONS

Consider a uniaxial thin semi-infinite non-linear coupled thermoelastic rod which is assumed to be initially at rest and at reference temperature  $T_0$ . The modified Fourier's law of heat conduction is employed to consider the finite speed of thermal wave. Wave propagation in such a rod can be represented by the following basic equations:

$$\rho \frac{\partial v}{\partial t} - \frac{\partial \sigma}{\partial x} = 0 \quad \text{equation of motion ,} \quad (1a)$$

$$\frac{\partial}{\partial t} \left\{ \left( \frac{\sigma}{\mu} \right)^n + \alpha \theta \right\} - \frac{\partial v}{\partial x} = 0 \quad \text{compatibility equation ,} \quad (1b)$$

$$\tau_0 \frac{\partial q}{\partial t} + q + K \frac{\partial \theta}{\partial x} = 0 \quad \text{modified heat conduction ,} \quad (1c)$$

$$\alpha T_0 \frac{\partial \sigma}{\partial t} + \rho C_\sigma \frac{\partial \theta}{\partial t} + \frac{\partial q}{\partial x} = 0 \quad \text{conservation of energy .} \quad (1d)$$

The auxiliary conditions are given as:

$$v(0,t) = v_0, \quad \theta(0,t) = 0; \quad t > 0, \quad (2a,b)$$

$$v(x,0) = \sigma(x,0) = \theta(x,0) = q(x,0) = 0; \quad x > 0. \quad (2c,d,e,f)$$

Jump conditions along and across the leading and lagging wave fronts are given by the following equations:

$$[\sigma] = -\rho v_i [v], [q] = \frac{K}{\tau_o v_i} [\theta], [q] = \alpha T_o v_i [\sigma] + \rho C_o v_i [\theta], \quad (3a,b,c)$$

$$-\rho v_i \frac{d[v]}{dt} + \frac{d[\sigma]}{dt} + \frac{\rho}{\alpha T_o \gamma} (C_o \gamma - v_i^2) \frac{d[\theta]}{dt} + \frac{\rho \tau_o v_i}{K \alpha T_o \gamma} (C_o \gamma - v_i^2) \frac{d[q]}{dt} + \frac{\rho \tau_o}{K \alpha T_o \gamma} (C_o \gamma - v_i^2) [q] = 0, \quad (3d)$$

in which the bracket  $[\ ]$  denotes the jump,  $v_i$  ( $i=1,2$ ) denote the velocities of leading and lagging wave fronts, respectively. Values of  $v_i$  and  $\gamma$  depend on the local stress  $\sigma$ . Equations (3d) are recognized as the characteristic conditions along the leading and lagging wave fronts.

### RESULTS AND DISCUSSION

Figure 1 represents the temperature response along the cast iron rod at two elapsed times. The numerical computation is based on the new approach of the characteristic method developed recently by the authors, which is able to locate the wave fronts as well as estimate the magnitude of jumps. It may be noted that the temperature response along the rod is negative with respect to the reference temperature, it is because the rod is subject to a tensile impact loading condition.

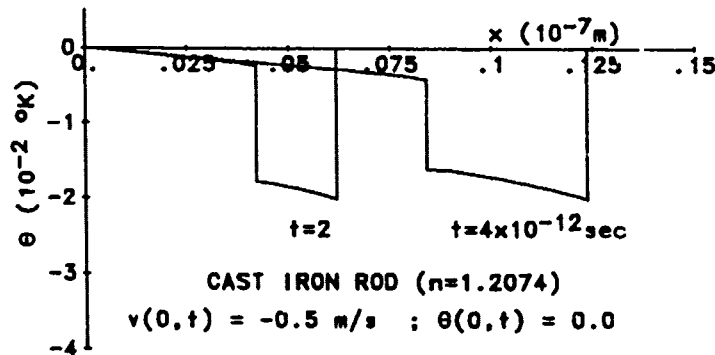


Fig.1 Temperature response along a cast iron rod.

### REFERENCES

1. Chandrasekharaiah, D.S., 1986, " Thermoelasticity with Second Sound: A Review ", *Appl. Mech. Rev.*, Vol. 39, pp. 355-376.
2. Bell, J., 1973, " The Experimental Foundations of Solid Mechanics ", in *Encyclopedia of Physics*, S. Flugge, Ed., Vol. VIa/1, Springer Verlag, Berlin.
3. Singh, M.C. and Tran, D.V.D., 1991, " Wave Propagation in Non-Conducting Non-Linear Elastic Solids ", *Proceeding of the Second Pan American Congress of Applied Mechanics (PACAM)*, Valparaiso, Chile, pp. 748-751.

# SHOCK WAVES IN UNIAXIAL NON-LINEAR ELASTIC SOLIDS

M.C. SINGH, Professor

D.V.D. TRAN, Graduate Student

Department of Mechanical Engineering

The University of Calgary, Calgary, Alberta, Canada T2N 1N4

## INTRODUCTION

Shock waves as well as simple waves have been widely discussed in the area of gas dynamics. In solids the shock waves are studied mostly in plastic materials subject to high velocity impact or explosions. According to Bland [1] shock waves in elastic materials depend not only on the geometric non-linearity but also on the nature of boundary conditions. Herein material non-linearity of an elastic uniaxial body is considered. The nature of shock and the wave speed are found to depend not only on the material non-linearity but also on nature of the impact. When the wavelets behind the wave front have a velocity greater than that of the wave front, they catch up with the front, effecting the magnitude of the wave front and causing a shock. When the wavelets behind the wave front have a velocity smaller than that of the wave front, they do not catch up with the front, the jump at the wave front remains constant, this is the case of a simple wave. In this study, shock waves in uniaxial non-linear elastic materials are considered. The condition for the occurrence of shock waves in non-linear elastic materials has been determined and shock evolution analysed. The results are obtained by the method of characteristics and compared with those obtained by a mixed finite element and finite difference technique.

## BASIC EQUATIONS

Propagation of waves in a uniaxial semi-infinite non-linear elastic rod is represented by the following system of equations [2]:

$$\frac{\partial \sigma}{\partial x} = \rho \frac{\partial v}{\partial t} \quad \text{equation of motion ,} \quad (1a)$$

$$\frac{\partial \epsilon}{\partial t} = \frac{\partial v}{\partial x} \quad \text{compatibility relation ,} \quad (1b)$$

$$\frac{\partial v}{\partial x} = \frac{\partial}{\partial t} \left[ \left( \frac{\sigma}{\mu} \right)^n \right] \quad \text{constitutive relation .} \quad (1c)$$

The boundary and initial conditions are assumed :

$$\sigma(x = 0, t > 0) = \sigma_0 t^\delta ; v(x, 0) = \sigma(x, 0) = \epsilon(x, 0) = 0 ; x > 0 . \quad (2a, b, c, d)$$

The wave speed travelling in this material is found to be:

$$v = \frac{dx}{dt} = \sqrt{\frac{\mu^n}{\rho n} \sigma^{1-n}} \quad (3)$$

Taking derivative of  $V$  given by equation (3) with respect to time  $t$  and employing the prescribed boundary condition (2a), the variation of wave speed along the  $Ox$ -axis can be expressed by:

$$\frac{dv}{dt} = \frac{\delta(1-n)}{2} \left\{ \frac{\mu^n}{\rho n} \sigma_o^{1-n} \right\}^{\frac{1}{2}} \left\{ t^{\frac{\delta(1-n)}{2}-1} \right\} \quad (4)$$

Examining the sign of equation (4) allows us to draw some important conclusions: (i) simple waves or shock waves propagating in the medium are dependent not only on the mechanical properties of such materials but also on the prescribed boundary conditions, i.e. values of  $\delta$  and  $n$ , (ii) Under a constant impact ( $\delta=0$ ) applied to the boundary, there are always simple waves travelling in the material irrespective of the value of  $n$ , and (iii) in linear elastic materials, i.e. when  $n$  equals unity, the disturbed region must be a simple wave region regardless of the boundary conditions.

#### TREATMENT OF SHOCK WAVES

In the presence of a shock wave, the shock path is independent of the characteristic curves. The following system of equations are employed on the basis of jump conditions for the study of shock front:

$$\|\sigma\| = -\rho U_s \|\dot{v}\| ; \quad U_s = \sqrt{\frac{\|\sigma\|}{\rho \|\epsilon\|}} ; \quad \|\epsilon\| = \left\| \left( \frac{\sigma}{\mu} \right)^n \right\| , \quad (5a,b,c)$$

$$2U_s \frac{d\|\epsilon\|}{dt} + \|\epsilon\| \frac{dU_s}{dt} = U_s^2 \left\| \frac{\partial \epsilon}{\partial x} \right\| - \frac{1}{\rho} \left\| \frac{\partial \sigma}{\partial x} \right\| , \quad (5d)$$

where  $U_s$  is the intrinsic velocity of the shock front.

The results obtained have shown that under a loading condition ( $\delta > 0$ ), simple waves and shock waves propagate in the rubber-like material ( $n=1.6$ ) and leather-like material ( $n=0.7545$ ), respectively. The situation is reversed when an unloading condition ( $\delta < 0$ ) is applied, i.e. shock waves occur in the rubber-like material and simple waves in the leather-like material. The numerical simulations were processed by using the finite element and characteristic methods, and they show a good agreement on comparing the results. The growth of shock waves in those two materials are also studied.

#### REFERENCES

1. Bland, D.R., 1969, Nonlinear Dynamic Elasticity, Blaisdell Publishing Company, Waltham, Massachusetts.
2. Prydrychowicz, W. and Singh, M.C., 1985, "Group Theoretic Technique for the Similarity Solution of a Non-Linear Elastic Rod Subjected to Velocity Impact", Theoretical mechanics, Warsaw, Vol.23, pp. 19-37.

ANALYTICAL AND FINITE ELEMENT STUDY OF THE THERMAL SHOCK PROBLEM  
OF A HALF-SPACE WITH VARIOUS THERMOELASTIC MODELS

Mihály Balla, assistant professor, Technical University of Budapest  
Faculty of Mechanical Engineering, Department of Technical Mechanics  
H-1111 Budapest, Műegyetem rkp 5, HUNGARY

The dynamic propagation of mechanical and thermal disturbances in solids and structures has been given considerable interest in research activities during the last forty years. The early investigations were based on classical thermoelasticity theory, which allows thermal disturbances to propagate with infinite velocity. To eliminate this physically unrealistic behaviour, there have been proposed generalized thermoelasticity theories to allow for so-called "second sound" effects. Though such effects in elastic solids are generally small and short-lived, widespread interest has recently been directed toward these theories, mainly due to the design of nuclear reactors, space vehicles, high-speed aeroplanes and laser technologies. In the common engineering practice, however, there is usually no need for the use of fully coupled governing equations of the classical or generalized thermoelasticity theory. In many cases, we can obtain adequate results using various simplified models. In technical literature, three different thermoelastic models have become general, both in classical and generalized cases. These models are: 1. uncoupled quasistatic model, 2. uncoupled dynamic model, 3. coupled dynamic model.

The class of thermoelastic problems which can be solved analytically is very small. Closed-form solutions can be obtained for the simplest problems only, especially when we use coupled models. The problems of practical interest, however, usually involve structures of complicated geometry and complex loadings. In such cases, numerical techniques have to be applied in order to gain approximate solutions. Therefore, much effort has been made during the last two decades to develop numerical methods for solving thermoelastic problems. After initial attempts, the finite element method has by now become the most generally used numerical technique. However, the developed finite element programs can reliably be employed in practice only if they have been tested very thoroughly by comparing numerical results with existing analytical solutions. Thus, it is very important to determine some analytical reference solutions, over and above their theoretical significance, in order to validate FEM programs.

Because of its relative simplicity, the thermal shock problem of an elastic half space seems to be suitable for getting such reference solutions. Ana-

lytical solutions of this problem have been reported by several authors since the first solution including inertia effects was reported by Danilovskaya in 1950. Most of the investigations have been based on Laplace transform. Closed-form solutions in the whole time domain have only been gained for the simplest classical uncoupled models. In case of more complicated models, authors usually gave long time and wavefront approximations of temperature-, displacement- and thermal stress fields and studied discontinuities and their propagations. These investigations are very important because they provide a lot of information about the nature of thermally induced waves, but their results can't be used for checking computer programs.

Papers, dealing with the numerical solution of the problem, have been reported from the late sixties on. For want of exact solutions, the authors compared their own results to previously published numerical results. Of course, this method alone is not sufficient for a thorough program testing. Though some authors have recommended their results for typical bechmark tests, it is evident that there is a real need for exact solutions.

The main purpose of this work is to determine such reference solutions for all of the above-mentioned six thermoelastic models. Laplace transform is employed on time and the transform solutions are retransformed by means of Durbin's numerical inversion technique. Beside the sudden surface heating condition, the more realistic ramp-type surface heating condition is also taken into consideration and the results gained for both heating cases are compared. For the sake of completeness, a brief summary of the existing closed-form solutions is also included.

The first part of the lecture prescribes the investigated half-space problem both in time and transform domains. This is followed by the presentation of transform solutions for each of the six models. Next long and short time approximations are determined, and subsequently the properties of the elastic and thermal waves are studied in details and some wrong conclusions of earlier published investigations are pointed out. It is shown how results of adequate accuracy can be obtained by means of numerical inversion of Laplace transforms. The curves of dimensionless field variables as a function of time are given in a very useful form for testing programs. The finite finite element solution of the problem is also demonstrated and the FEM results are compared with the developed reference solutions. Finally, the results are summarized and the importance of the gained solutions is emphasized by the analysis of previously reported finite element solutions.

CONSERVATION LAWS AND DUAL CONSERVATION LAWS  
FOR CRACK PROBLEMS IN HOMOGENEOUS  
ISOTROPIC CONDUCTIVE SOLID

XU LI

Department of Engineering Mechanics, Tsinghua University, Beijing, China

Abstract

In this paper three conservation laws and three dual conservation laws are presented for the 3-dimensional cases in the homogeneous isotropic conductive solid in which the steady current flows. The physical models for the conservation laws are considered.

Several years ago Rice (1) (1968) discovered a path-independent integral associated with plane elastostatics fields. Some new path-independent integrals in elastostatics have recently been discovered by Knowles and Sternberg (2) (1972). The derivation of conservation laws in these articles is based on the existence of the elastic strain energy density function.

Three dual conservation laws in elastostatics have been discovered by Li (3) (1988) with the aid of a version of Noether's theorem on invariant variational principle in conjunction with the principle of stationary complementary potential energy.

In this study, three conservation laws and three dual conservation laws for crack problems in homogeneous isotropic conductive solid are given under the assumption of the existence of the electric energy density function and the complementary electric energy density function.

The Rice integral and the Knowles-Sternberg integrals in elastostatics are

$$\hat{J}_i = \int_S (\hat{U} n_i - T_k u_{k,i}) dA, \quad (1.1)$$

$$\hat{L}_i = \int_S \epsilon_{ijk} (\hat{U} x_k n_j - T_p u_{p,j} x_k + T_j u_k) dA, \quad (1.2)$$

$$\hat{M} = \int_S (\hat{U} x_i n_i - T_k u_{k,i} x_i - \frac{1}{2} T_k u_k) dA, \quad (1.3)$$

where  $S$  is a closed surface with outer normal  $n_i$ ,  $\hat{U}$  is the elastic strain energy density,  $T_k$  is the stress vector acting on the outer side of  $S$ ,  $\epsilon_{ijk}$  is the alternating tensor.

The dual path-independent integrals in elastostatics are

$$\hat{J}_i^* = \int_S (\hat{U}^* n_i - \sigma_{kj,i} n_j u_k) dA, \quad (1.4)$$

$$\hat{L}_i^* = \int_S \epsilon_{ijk} (\hat{U}^* x_k n_j - \sigma_{pl,j} n_l u_p x_k - \sigma_{pj} n_k u_p - T_j u_k) dA, \quad (1.5)$$

$$\hat{M}^* = \int_S (\hat{U}^* x_i n_i - \sigma_{kj,i} n_j u_k x_i - \frac{3}{2} T_k u_k) dA, \quad (1.6)$$

where  $\hat{U}^*$  is the complementary strain energy density.

In three dimensions the path-independent integrals for crack problems in homogeneous isotropic conductive solid are

$$J_i = \int_S (U n_i + I_j n_j \phi_{,i}) dA, \quad (1.7)$$

$$L_i = \int_S \epsilon_{ijk} (U x_k n_j + I_l n_l \phi_{,j} x_k) dA, \quad (1.8)$$

$$M = \int_S (U x_i n_i + I_j n_j \phi_{,i} x_i + \frac{1}{2} I_j n_j \phi) dA \quad (1.9)$$

where  $U$  is the electric energy density function.

The dual path-independent integrals which may be taken to be the counterparts of the integrals  $J_i$ ,  $L_i$ ,  $M$  are

$$J_i^* = \int_S (U^* n_i + I_{j,i} n_j \phi) dA, \quad (1.10)$$

$$L_i^* = \int_S \epsilon_{ijk} (U^* x_k n_j + I_{l,j} n_l \phi x_k + I_j n_k \phi) dA, \quad (1.11)$$

$$M^* = \int_S (U^* x_i n_i + I_{j,i} n_j \phi x_i + \frac{3}{2} I_j n_j \phi) dA, \quad (1.12)$$

where  $U^*$  is the complementary electric energy density function.

In this paper, these conservation laws are related to energy release rates associated with cavity or crack extension, rotation and expansion rates.

In (1.7) — (1.12),  $I_i$  are the components of the current density vector,  $\phi$  is the electric potential.

Acknowledgement—This research was supported by grants from the National Natural Science Foundation of China.

#### References

- (1) Rice, J.R. (1968). A path independent integral and the approximate analysis of strain concentration by notches and cracks. J. Appl. Mech. 35, 379-386.
- (2) Knowles, J.K. and Sternberg, E. (1972). On a class of conservation laws in linearized and finite elasticity. Arch. Ration. Mech. Anal. 44, 187-211.
- (3) Li, Xu (1988). Dual conservation laws in elastostatics. Engng Fracture Mech. 29, 233-241.
- (4) Saka, M. and Abé, H. (1983). A path-independent integral for 2-dimensional cracks in homogeneous isotropic conductive plate. Int. J. Engng Sci. 21, 1451-1457.
- (5) Zienkiewicz, O.C. (1977). The Finite Element Method in Engineering Science. McGraw-Hill, London.
- (6) Budiansky, B. and Rice, J.R. (1973). Conservation laws and energy-release rates. J. Appl. Mech. 40, 201-203.



## RECENT DEVELOPMENTS IN BOUNDARY ELEMENT METHODS FOR ELASTIC WAVE-SCATTERING FROM VOIDS

P. J. Schafbuch  
Fisher Controls International  
Engel Technical Center  
Marshalltown, Iowa 50158

Yijun Liu and F. J. Rizzo  
Dept. of Theoretical and Applied Mechanics  
University of Illinois  
Urbana, Illinois 61801

This paper is concerned with scattering of time-harmonic elastic waves from a single void or several voids in an otherwise unbounded linearly elastic medium. The formulas for solution are in terms of boundary integrals, and the boundary element method is used for solution of the integral equations.

It is well known that the conventional Cauchy-singular integral equations for such problems suffer from the so-called fictitious eigenfrequency difficulty. This difficulty is that the integral equations exhibit a multiplicity of solutions at frequencies which correspond to certain modes of vibration of (fictitious) elastic bodies of the size and shape of the void scatterers. However, if a linear combination of the Cauchy-singular integral equations and another set of equations, which are hypersingular, is used, the combination is free of the mentioned difficulty. The presence of the hypersingularity presents nontrivial problems of both an analytical and numerical nature, but the combined equations do have a unique solution. Results based on a simpler version of this formulation, for acoustic (rather than elastic) scattering from a single void, are presented in the paper along with a report on progress to obtain comparable results for the (vector) elastic case.

Because of the mentioned hypersingularity, attention must be given to higher order boundary elements in solving the equations, i.e. elements having sufficient smoothness at collocation points for the hypersingular integrals to exist. Figure 1 depicts the boundary element solution, versus the analytical one, for normalized scatter as a function of radial direction due to an incident plane acoustic wave at  $180^\circ$  on a spherical void. Three types of elements, with varying degrees of sophistication and ease of implementation, are compared (number of elements  $M$ , number of algebraic equations  $N$ ) showing computer time for comparable accuracy. As expected, the Overharser spline elements, which are the most sophisticated and smooth but the most difficult to implement, turn out to be the most efficient. Of overriding importance, however, is the fact that the formulation, regardless of the elements used, has a unique stable solution at the eigenfrequency  $ka = 2\pi$ .

In cases of scattering from multiple voids, attention is focused on the conventional formulation for elastic scattering, and work is restricted to known nontroublesome frequencies. Emphasis here is on the efficiency and accuracy of an approximate iterative solution scheme which relates terms in a series to the number of interactions between scatterers. The idea is to reduce and simplify the computational burden of dealing with multiple scatterers all at once. With the iterative scheme, higher-order interactions between scatterers, which are often negligible, need not be calculated.

Also, the sizes of the largest matrices in the solution process correspond to individual scatterers rather than the union of these scatterers; thus numerical work is considerably reduced.

For multiple scattering, results are shown in Figure 2 for a measure of the scattered field, specifically a quantity  $\sigma$  called the Total Cross Section, for two (10:10:1) spheroids parallel to each other and subjected to an incident wave coaxial with the small semi-axes. The quantity  $\sigma$  relates the total power in the scattered field to the power flux in the incident field. The dimension 'a' is the major semi-axis length and the separation distance ranges from one to six 'a' units. Note that the truncated series approximations are compared to the converged solution. The most interesting behavior at small separation distances is that the lower order partial sums do not converge monotonically.

The 10:1 aspect ratio of the mentioned spheroids is enough for these shapes to display cracklike behavior when considered as isolated scatterers. However, it is not clear whether these finite thickness crack models have near field behavior similar to zero-thickness crack models. Such issues are part of our ongoing research.

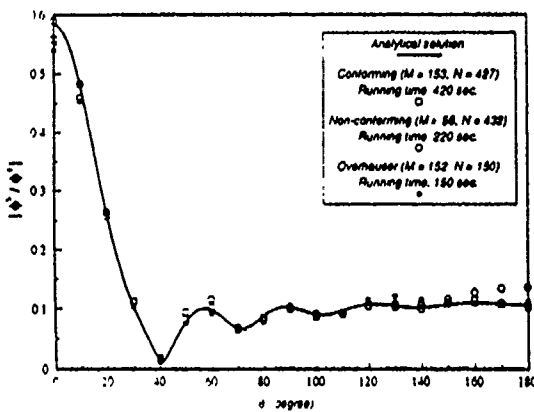


Fig. 1. Element comparison at wavenumber  $ka = 2\pi$ , for comparable accuracy.

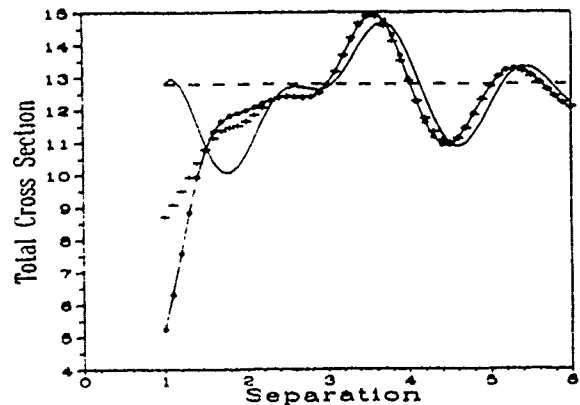


Fig. 2. Total scattering cross section of two oblate (10:10:1) spheroidal voids at  $ka = \pi/2$  for coaxial incidence as a function of separation distance  $d$ : Comparison of first (---), second (—), third (o), and converged (+) approximations for the scatterer interaction.

## ACKNOWLEDGEMENT

Thanks are due the NDE Center at Iowa State University, The National Science Foundation, Y. Rajapakse at the Office of Naval Research, and Dr. W. S. Hall for their support of and contributions to this research.

## REFERENCES

1. Y. Liu and F. J. Rizzo, 'Application of Overhauser  $C^1$  Continuous Boundary Elements to "Hypersingular" BIE for 3-D Acoustic Wave Problems', Proc. of 13th International Conference on the Boundary Element Method, Tulsa, Oklahoma, August 1991 (to appear).
2. P. J. Schafbuch, 'Application of the Boundary Element Method to Elastic Wave Scattering Problems in Ultrasonic Nondestructive Evaluation', Ph.D. Dissertation, Iowa State University, Ames, Iowa (1991).

**SURFACE AND INTERNAL BUCKLING OF ELASTOMERIC COMPONENTS:  
SEALS, SHOCK ABSORBERS, GASKETS\***

Joe Padovan\*\*

Farhad Tabaddor†

Don Cummings\*\*

\*\* Dept. of Mechanical and Polymer Engineering, The University of Akron, Akron, Ohio 44325

† Uniroyal Goodrich Co.

\* Partially supported under NSF grant MSS-0915467

## ABSTRACT

The presentation will develop finite element schemes to handle the analysis of elastomeric components (seals, gaskets), undergoing large deformations leading to potential surface folding-wrinkling-stretching, as well as localized bifurcations. Since significant element degeneracies occur in the vicinity of such behavior, specialized procedures are developed to define the ensuing deformation morphology. For instance, this includes the modelling of the complex mechanical fields in the apex region of the folding collapse zone along with the associated self contact. Checks are developed to monitor local-global system stability, solution conditioning, as well as kinematic motion leading to self contact in wrinkle zones. These initiate the concomitant remesh cycle. To generalize the results, the eigenvalue properties of the tangent stiffness are formally investigated. Here the main emphasis is to define the occurrence of shifts in definiteness leading to bifurcations on the element, regional and global levels. To benchmark the scheme, a series of examples will be considered. These include seals, switches and shock absorbers. Since Mooney-Rivlin and Ogden generalized models are employed, energy based criteria are also developed to monitor the potential for multiple states resulting from load histories generated path dependencies.

# FLAW DETECTION IN ELASTOSTATICS WITH BOUNDARY ELEMENTS

by

Luciano M. Bezerra and Sunil Saigal  
Department of Civil Engineering  
Carnegie Mellon University  
Pittsburgh, PA 15213

## ABSTRACT

A boundary integral formulation is presented for the detection of flaws in planar structural members given the boundary displacement measurements and the applied loading. Such inverse problems usually start with an initial guess for the flaw location and size and proceed towards the final configuration in a sequence of iterative steps. A finite element formulation will require a remeshing of the object corresponding to the revised flaw configuration in each iteration making the procedure computationally expensive and cumbersome. No such remeshing is required for the boundary element approach. The inverse problem is written as an optimization problem with the objective function being the minimization of the sum of the square of the differences between the measured displacements and the computed displacements for the assumed flaw configuration. The geometric condition that the flaw lies within the domain of the object is imposed using the internal penalty function approach in which the objective function is augmented by the constraint using a penalty parameter. A first order regularization procedure is also implemented to modify the objective function in order to minimize the numerical fluctuations that may be caused in the numerical procedure due to errors in the experimental measurements for displacements. The flaw configuration is defined in terms of geometric parameters and the sensitivities with respect to these parameters are obtained in the boundary element framework by the implicit differentiation approach developed earlier by the second author. A series of numerical examples involving the detection of circular and elliptical flaws are solved using the present approach. Good predictions of the flaw shape and location are obtained.

Acknowledgments: The work by L. Bezerra was supported by the CNPq - The Brazilian Research Council. The support for S. Saigal from the National Science Foundation Presidential Young Investigator Grant No. MSS-9057055 is also gratefully acknowledged.

# A Comparison of Various Methods for A-Posteriori Error Estimation in Finite-Element Approximations

T. Strouboulis † and K. A. Haque ††  
Department of Aerospace Engineering  
Texas A & M University/System  
College Station, Texas 77842

## SUMMARY

In this work we review several methods for a-posteriori estimation of the error in finite-element solutions of elliptic boundary-value problems. Several error estimates were implemented for various adaptive finite-element approximations of elliptic model problems and for the equations of plane-elastostatics; finite-element approximations are constructed using:

1. h-adaptive meshes of bilinear and biquadratic quadrilateral elements.
2. r-h-p adaptive meshes of triangular elements with variable order of local interpolation in each element ( $1 \leq p \leq 7$ ).

A-posteriori error estimates for elliptic boundary-value problems were introduced in the pioneering work of Babuska and Rheinboldt [1]. Extensions of these estimates to general multidimensional approximations of elliptic and parabolic boundary-value problems were presented by Oden, Demkowicz and co-workers [2], Bank and Weiser [3]; these estimates are based on local calculations of the element and interelement residuals and are classified as **residual estimates**. A-priori error estimates were also employed for error estimation by Diaz, Kikuchi & Taylor [4], Demkowicz, Devloo & Oden [5] and Eriksson & Johnson [6]; such estimates are often referred to as **interpolation-type estimates**. The analysis and implementation of several estimates for general h-p-approximations in three-dimensional domains was presented by Oden and co-workers [7]. Zienkiewicz and Zhu [8] presented a different class of error estimates which employed an extracted flux based on global smoothing procedures introduced by Oden and Brauchli [9] two decades ago. Such estimates are referred to as **flux-projection estimates** and may be easily incorporated into existing commercial codes. Recent numerical experiments by Shephard and co-workers [10] and by Strouboulis and Haque [11] point out that flux-projection estimates may lead to very poor predictions of the error for even-order finite-element approximations.

---

† Assistant Professor

†† Graduate Research Assistant

We will present a detailed account of our recent experiences with a-posteriori error estimation techniques namely element-, subdomain-residual and flux-projection methods combined with several local and global post-processing techniques for extracting approximate fluxes. It will be demonstrated that flux-projection methods, as presented in [8], lead to divergent error estimates when they are used with even-order approximations; in particular it is demonstrated that such flux-projection error estimation methods may lead to very poor estimates of the error in biquadratic finite-element approximations in plane elastostatics. A full description of the various methods and numerical results with conclusions of this study are given in [11].

### ACKNOWLEDGMENT

The financial support of grants TATP-70120 and TARP-70410 by the Texas Advanced Research and Technology Program is gratefully acknowledged.

### REFERENCES

1. Babuska, I., and Rheinboldt, W. C., "Reliable Error Estimation and Mesh Adaptation for the Finite Element Method," in **Computational Methods in Nonlinear Mechanics**, J. T. Oden, ed., Chapter 3, pp. 67-108, North Holland Publishing Co., Amsterdam, 1980.
2. Oden, J. T., Demkowicz, L., Strouboulis, T., and Devloo, P., "Adaptive Methods for Problems in Solid and Fluid Mechanics," in **Accuracy Estimates and Adaptive Refinements in Finite Element Computations**, I. Babuska, O. C. Zienkiewicz, J. Gago, and E. R. de A. Oliveira ( eds.), Chapter 14, pp. 249-280, J. Wiley and Sons, New York, 1986.
3. Bank, R. E., and Weiser, A., "Some A Posteriori Error Estimators for Elliptic Partial Differential Equations," *Math. Comp.*, Vol. 44, No. 170, pp. 283-301, 1985.
4. Diaz, A. R., Kikuchi, N., and Taylor, J. E., "A Method of Grid Optimization for Finite Element Methods," *Comput. Meths. Appl. Mech. Engrg.*, Vol. 41, pp. 29-45, 1983.
5. Demkowicz, L., Devloo, P., and Oden, J. T., "On an h-Type Mesh-Refinement Strategy Based on Minimization of Interpolation Errors," *Comput. Meths. Appl. Mech. Engrg.*, Vol. 53, pp. 67-89, 1985.
6. Eriksson, K., and Johnson, C., "An Adaptive Finite Element Method for Linear Elliptic Problems," *Math. Comp.* Vol. 50, No. 182, pp. 361-383, 1988.
7. Oden, J. T., Demkowicz, L., Rachowicz, W., and Westermann, T. A., "Toward a Universal h-p Adaptive Finite Element Strategy; Part 2, A Posteriori Error Estimates," *Comput. Meths. Appl. Mech. Engrg.*, Vol. 77, pp. 113-180, 1989.
8. Zienkiewicz, O. C., and Zhu, J. Z., "A Simple Error Estimator and Adaptive Procedure For Practical Engineering Analysis," *Internat. J. Numer. Meths. Engrg.*, Vol. 24, pp. 337-357, 1987.
9. Oden, J. T., and Brauchli, H. J., "On the Calculation of Consistent Stress Distributions in Finite Element Applications," *Internat. J. Numer. Meths. Engrg.*, Vol. 3, No. 3, pp. 317-325, 1971.
10. Shephard, M. S., Niu, Q., Baehmann, P. L., "Some Results Using Stress Projectors for Error Indication and Estimation," in **Adaptive Methods for Partial Differential Equations**, J. E. Flaherty, P. J. Paslow, M. S. Shephard, J. D. Vasilakis ( eds.), Chapter 7, pp. 83-99, SIAM 1989.
11. Strouboulis, T., and Haque, K. A., "Recent Experiences with Error Estimation and Adaptivity in h-, r- and h-p Finite-Element Approximations," in preparation.

# NUMERICAL SIMULATION OF LOW-REYNOLDS-NUMBER VISCOUS FLUID FLOW AROUND CYLINDRICAL ARCS

Chang-Sheng Lin  
Department of Physics  
Inner Mongolia Teacher's College of the Nationalities  
Tongliao, 028043, P.R.CHINA

The numerical simulations of the low-Reynolds-number viscous fluid flow around the cylindrical arcs have been made by using Boundary Element Method (BEM) in this paper. The method based on an idea of the fundamental solution of Stokes equations as Green's function to convert the Navier-Stokes equations to boundary integral equations as follows

$$c(\vec{X})v^k(\vec{X}) = \oint_{\Gamma} n_i(\vec{X}_0)T'_{ij}(\vec{W}^k(\vec{X}-\vec{X}_0))v_j(\vec{X}_0)d\Gamma_0 - \oint_{\Gamma} n_i(\vec{X}_0)T_{ij}(\vec{V}^k(\vec{X}_0))w_j^k(\vec{X}-\vec{X}_0)d\Gamma_0 \quad (1)$$

$$c(\vec{X})p(\vec{X}) = \oint_{\Gamma} q^k(\vec{X}-\vec{X}_0)T_{ki}(\vec{V}(\vec{X}))n_i(\vec{X}_0)d\Gamma_0 + \frac{1}{R_0} \oint_{\Gamma} \frac{\partial q^k(\vec{X}-\vec{X}_0)}{\partial x_{j0}}v_k(\vec{X}_0)n_i(\vec{X}_0)d\Gamma_0 \quad (2)$$

where  $T_{ij}(\vec{V})$  and  $T'_{ij}(\vec{W}^k)$  are stress tensor correlate with  $\vec{V}$  and  $\vec{W}^k$ . The fundamental solution  $w_j^k$  and  $q^k$  are given<sup>(1)</sup> by

$$w_j^k(\vec{X}-\vec{X}_0) = -\frac{1}{4\pi} \left[ \delta_{ij} \ln \frac{1}{|\vec{X}-\vec{X}_0|} + \frac{(x_j-x_{j0})(x_k-x_{k0})}{|\vec{X}-\vec{X}_0|} \right]$$

$$q^k(\vec{X}-\vec{X}_0) = \frac{\partial}{\partial x_k} \left[ \frac{1}{2\pi} \ln \frac{1}{|\vec{X}-\vec{X}_0|} \right] = -\frac{1}{2\pi} \frac{x_k-x_{k0}}{|\vec{X}-\vec{X}_0|^2}$$

The boundary integral equations can be discretized and solved numerically the surface-stress force and pressure on the boundaries and velocity fields in the flow domain. In order to show an effectiveness of the method, we study a problem of low-Reynolds-number viscous fluid flow around the cylindrical arc with various angles of circumference. We calculated numerically the distributions of surface-stress force and pressure on the surface of arcs. The velocity fields of numerical simulation show in Figure 1(a,b,c,d). There is a vortex pair within the concavity of the cylindrical arc when the angle of circumference is  $7\pi/9 \leq \phi \leq 5\pi/3$ . Moreover, two rotatory vor-



texes are in opposite direction as show in figures. The distance between two vortex centres are obtained. By comparison, the numerical results are in good agreement with the experimental ones (2). The numerical investigations show that the method is very effective in researching and solving unbounded problem and studying the phenomena of vortex, and has some advantages of computational convenience, the superior accuracy. The question of especial importance is the method not only is more suitable for the complex geometry of body than other method but also can be treated the problem of the flow past multibody as well.

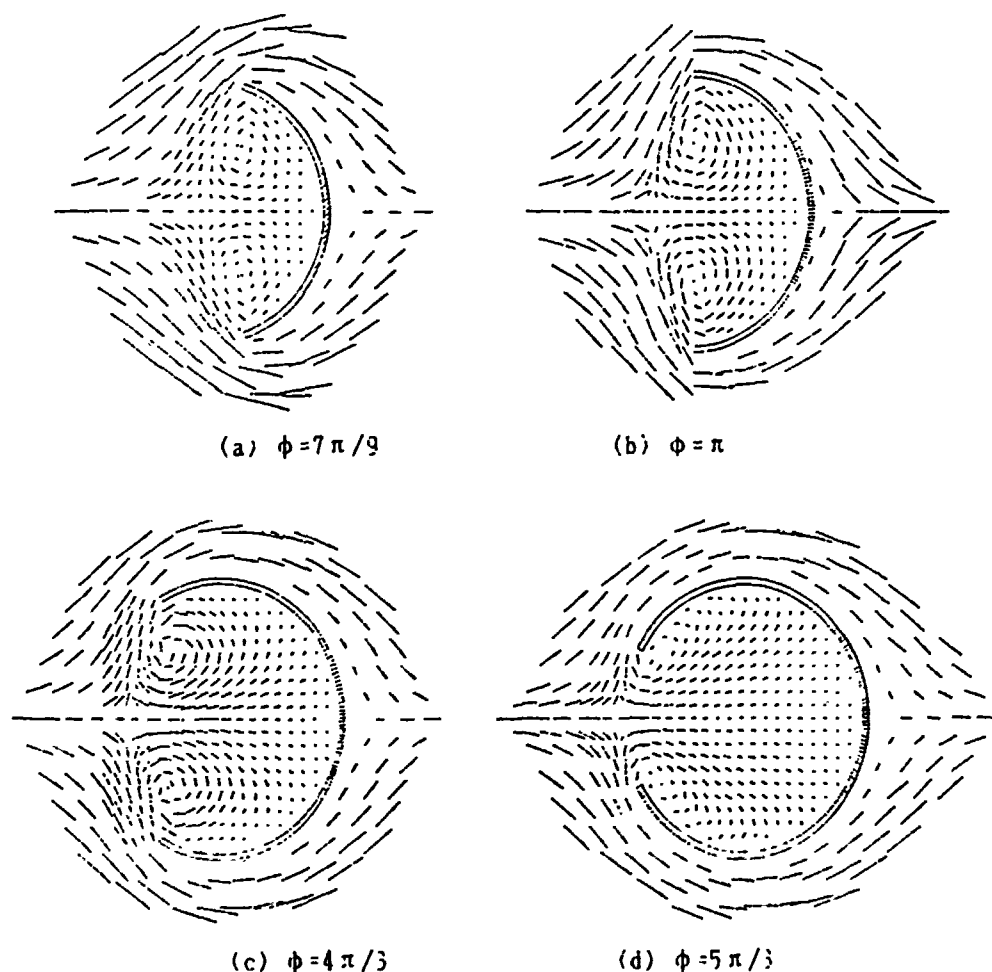


Figure 1. The velocity fields of the flow around the cylindrical arcs

#### REFERENCES

1. J. Mu, Acta Mechanica Sinica, 5(1984), 425.
2. S. Taneda, J. Phys. Soc. Japan, 6(1979), 1935.

# THE STRESS FIELD AROUND A CYLINDRICAL INTERFACE DISLOCATION

I. Demir, J.P. Hirth, H.M.Zbib

*Department of Mechanical and Materials Engineering  
Washington State University, Pullman, WA 99164-2790*

The concept of interface dislocations and the stress field in two semi infinite linearly elastic homogeneous materials have been analyzed by many researchers since the original work of Dundurs and Sendeckyj [1]. In general all those calculations are restricted to a straight dislocation of Volterra type in planar cases.

The Somigliana type of ring dislocation has already been introduced in homogeneous isotropic infinite elastic medium [2]. The natural extension of this type of dislocation would be the interface form of the Somigliana ring dislocation. This interface dislocation will extend the previous planar interface dislocation concept to the 3-D cylindrical interface dislocation which has some applications to the fiber matrix interfaces in composite materials and different kind of inhomogeneities in elastic continuum. The dislocation density distribution of this type has already been used to compute stress intensity factors and energy release rates of a cylindrical interface crack in fiber matrix debonding problem [3,4]

The solution is carried out using Love's stress function following the same procedure given in [2,3,4]. Final form of the solution is obtained achieved numerically due to the difficulty of performing some very complicated integrals of the Bessel functions. In order to solve interaction problems between different type of cracks and dislocations, the entire stress field must be known, therefore, the present calculations can be considered as one more important step towards calculating interaction of different singularities in composites.

Combining the entire stress field solutions for cylindrical interface cracks and dislocations, interaction problems involving these type of defects can be analyzed. Moreover, by determining the effective region of similarities between the stress field around cylindrical interface crack and a single dislocation, it could be possible to represent debonding by two super interface Somigliana ring dislocation. This enables one to represent interaction of cylindrical cracks simply by super dislocations depending on the distance between cylindrical cracks and/or dislocations. The solution for interface cylindrical dislocation also enables one to evaluate line force on the dislocation. Using the line force concept on an interface Somigliana dislocation it is possible to analyze stress field around short fiber tips and also interaction of this field with the stress field due to debonding or cracking.

## References

- [1] Dundurs J., Sendeckyj G.P. "Behavior of an Edge Dislocation Near a Bimetallic Interface" J. Appl. Phys., V.36, (1965), pp:3353
- [2] -) Demir I., Hirth J.P., Zbib H.M. "The Somigliana Ring Dislocation", Submitted for publication
- [3] Erdogan F, Ozbek T. "Stresses in Fiber Reinforced Composites with Imperfect Bonding", J Appl. Mech. V.36, (1969), pp:865-869
- [4] Farris T.N., Kokini K., Demir I, " The Cylindrical Crack", J. Appl. Mech. V.56, (1989), pp:981-983

# Crack Tip Displacement Factor – D: Concept and Applications:

Jiping Zhang<sup>1</sup> Al Ghorbanpoor<sup>2</sup>

College of Engineering, University of Wisconsin-Milwaukee  
P. O. Box 784, Milwaukee, WI 53201

## Abstract

A fracture parameter, crack tip displacement factor,  $D$ , is introduced to evaluate the fracture behavior in linear elastic fracture mechanics problems. The introduced fracture control parameters are defined as

$$D_I = \lim_{x \rightarrow a} \frac{COD(x)}{F(x)}$$

$$D_{II} = \lim_{x \rightarrow a} \frac{CSD(x)}{F(x)}$$

$$D_{III} = \lim_{x \rightarrow a} \frac{CTD(x)}{F(x)}$$

where  $COD$ ,  $CSD$  and  $CTD$  are the crack surface relative displacements for the mode I, mode II and mode III fractures, respectively, and  $F(x)$  is a normalized function which usually has the form

$$F(x) = \sqrt{1 - \left(\frac{x}{a}\right)^2}$$

The  $D$  factors may be determined analytically if a mathematical expression can be found for the crack surface relative displacements. For numerical

---

<sup>1</sup>Ph. D. Candidate, Materials Engineering Department

<sup>2</sup>Associate Professor, Department of Civil Engineering and Mechanics

and experimental analyses of the crack problems, the  $D$  factor can be obtained by extrapolating the results from the crack surface to the crack tip. The crack tip displacement factor -  $D$  can be bridged to the stress intensity factor  $K$  and the energy release rate  $G$  by the following equations

$$D_I = \frac{4\sqrt{a}}{E\sqrt{\pi}} K_I$$

$$D_{II} = \frac{4\sqrt{a}}{E\sqrt{\pi}} K_{II}$$

$$D_{III} = \frac{4\sqrt{a}}{(1+\nu)E\sqrt{\pi}} K_{III}$$

and

$$D = \sqrt{D_I^2 + D_{II}^2 + D_{III}^2} = 4\sqrt{\frac{Ga}{\pi E}}$$

The major advantage of this fracture control parameter is that one can obtain it by using the crack surface displacement from a numerical analysis or an experiment, similar to the conventional  $COD$  approach, without the need for considering the stress field at the crack tip. Unlike the  $COD$  method, the introduced fracture parameter can be used for not only the simple opening mode but also for the other two modes as well as for the mixed mode fracture problems. The introduced parameter may be used as a fracture control criterion for crack extension, as it is derived from the displacement field at the crack tip. Although the current discussion in this paper is limited to two-dimensional elastic fracture problems, the extension of this theory to other fracture problems, such as the elasto-plastic fracture mechanics, three-dimensional fracture mechanics, etc., is possible.

# DETERMINATION OF THE NEAR-TIP STRESS FIELDS FOR THE SCATTERING OF P-WAVES BY A CRACK

**Qing Jiang**

**Division of Engineering and Applied Sciences  
California Institute of Technology 104-44  
Pasadena, California 91125 U.S.A.**

## ABSTRACT

Determination of stress fields induced by interaction of elastic waves with cracks remains a challenging problem. In [1], Jiang and Knowles reconsidered the linear elastodynamic problem of the transient scattering of a plane SH-(or anti-plane shear) wave by a semi-infinite crack. They showed that the near-tip stress field can be found directly by using a conservation law, instead of solving the underlying boundary-initial value problem. This paper illustrates a procedure for determination of the near-tip stress fields arising from the scattering of normally incident P-(or plane strain longitudinal) waves by a crack in a homogeneous, isotropic elastic medium, based on a conservation law implied by the relevant field equations [2].

In this paper, the linear elastodynamic problem of the transient scattering of a plane P-wave by a semi-infinite crack is reconsidered. The global solution of this problem was constructed by DeHoop [3] by employing the Wiener-Hopf procedure, however, his solution is too complicated to be used for developing the near-tip stress field, which is of particular interest to the people who concern the opening of the crack. An extensive discussion on this issue can be found in [4]. By using a conservation law reduced from a more generalized one established by

Jiang in [2], the author has found the near-tip stress field for the special case in which the front of the incident wave is parallel to the crack.

## References

- [1] Jiang, Q., Knowles, J.K.: On the direct determination of the near-tip stress field for the scattering of SH-waves by a crack. *International Journal of Fracture*, **41**, 283-288(1989).
- [2] Jiang, Q.: Conservation laws of linear viscoelastodynamics. *Journal of Elasticity*, **16**, 213-219(1986).
- [3] DeHoop, A.T.: Representation theorems for the displacement in an elastic solid and their application to elastodynamic diffraction theory. Doctoral Dissertation, Technische Hogeschool, Delft, The Netherlands(1958).
- [4] Freund, L.B.: **Dynamic Fracture Mechanics**, 72-97, Cambridge: Cambridge University Press, 1990.

# A DISCRETE MODEL ANALYSIS OF MICRO-MACRO CRACK INTERACTIONS IN PARTICULATE COMPOSITES

A. A. Sukere and Anil Misra  
Department of Civil Engineering, University of Missouri  
600 W Mechanic, Independence, MO 64050, U.S.A.

## Introduction

Presence of micro-cracks in the neighborhood of macro-cracks in brittle materials can influence the fracture process. In particulate composites micro-cracks can develop as a result of manufacturing process or loading history. These micro-cracks in the neighborhood of macro-cracks alter the stress and the displacement fields. In order to study the fracture process in such composites it is important to carefully characterize the influence of micro-cracks on these field quantities. Along this line, fracture toughening due to micro-cracks has been investigated by Shum and Hutchinson (1990) for isotropic elastic materials under plane strain conditions. In this paper, we use a discrete modelling scheme to investigate the interaction of micro and macro cracks. The study particularly focusses upon investigating the sensitivity of the method in detecting the interactions.

## Discrete System

The particulate composite is modelled as a discrete material consisting of randomly distributed rigid inclusions embedded in a relatively softer matrix. Under an imposed load, the soft matrix undergoes deformations. In this work, we idealize this load carrying mechanism such that the soft matrix is replaced by a system of springs which connects a rigid inclusion to its interacting neighbors. In the idealized system, the micro-crack is modelled by an interaction point with zero stiffness.

The relative movement between the centroid of two neighboring rigid inclusions causes the deformation of the springs connecting them. The interactions between inclusions  $n$  and  $m$  is given by

$$\delta_i^{nm} = u_i^m - u_i^n + e_{ijk}(\omega_j^m r_k^m - \omega_j^n r_k^n); \quad f_i^{nm} = K_{ij}^{nm} \delta_j^{nm} \dots \dots \dots (1)$$

and

$$\theta_i^{nm} = \omega_i^m - \omega_i^n; \quad \mu_i^{nm} = G_{ij}^{nm} \theta_j^{nm} \dots \dots \dots (2)$$



where  $\delta_i^{nm}$  is the relative displacement between inclusions n and m,  $\theta_i^{nm}$  is the relative rotation between the inclusions,  $u_i$  denotes the displacement of inclusion centroid,  $\omega_k$  denotes the inclusion rotation,  $r_j$  is the vector joining the centroid of the inclusion to the interaction point, superscripts refer to the particles,  $e_{ijk}$  is the permutation symbol,  $f_i^{nm}$  is the force at the interaction point,  $\mu_i^{nm}$  is the moment at the interaction point,  $K_{ij}^{nm}$  is the stretch spring stiffness, and  $G_{ij}^{nm}$  is the rotational spring stiffness.

Considering the equilibrium at the m-th inclusion, the governing equations for the discrete system can be written as (Chang and Misra 1989)

$$F_i^m = \sum_{\alpha} K_{ij}^{m\alpha} [u_j^m - u_j^n + e_{ijk} (\omega_k^m r_l^{m\alpha} - \omega_k^n r_l^{n\alpha})] = \sum_{\alpha} f_i^{m\alpha} \dots \dots \dots (3)$$

and

$$M_i^m = \sum_{\alpha} e_{ijl} K_{jk}^{m\alpha} [u_k^m - u_k^n + e_{kpq} (\omega_p^m r_q^{m\alpha} - \omega_p^n r_q^{n\alpha})] r_l^{m\alpha} + G_{ij}^{m\alpha} [\omega_j^m - \omega_j^n] = \sum_{\alpha} e_{ijl} f_l^{m\alpha} r_l^{m\alpha} + \mu_i^{m\alpha} \dots \dots (4)$$

where m and n are the interacting inclusions at the  $\alpha$ -th interaction point.

### Discussion

The discrete scheme is used to analyze a double cantilever beam specimen (DCB) with a single micro-crack as well as with several micro-cracks placed at various locations and orientations in the neighborhood of the macro-crack. The results show that the introduction of even a single micro-crack alters the stress field near crack tip as well as the crack tip displacement. The discrete model can be potentially employed to investigate micro-crack toughening phenomena and crack tip damage evolution in particulate composites.

### References

- Chang, C.S. and Misra, A. (1989), "Computer simulation and modelling of mechanical properties of particulates", Computers and Geotechnics, Vol. 7, No. 4, 269-287.
- Shum, D.K.M. and Hutchinson, J.W. (1990), "On toughening by micro-cracks", Mechanics of Materials, Vol. 9, 83-91.

# THE ENERGY RELEASE RATE FOR TRANSIENT MODE I CRACK PROPAGATION IN A GENERAL LINEAR VISCOELASTIC BODY

J.M. Herrmann and J.R. Walton†  
Department of Mathematics  
Texas A&M University  
College Station, TX 77843-3368

The analytical study of dynamically propagating cracks in linearly viscoelastic material was begun by the Willis (1967) study which constructed the dynamic steady state stress intensity factor for a propagating semi-infinite, mode III crack in an infinite viscoelastic body modelled as a standard linear solid. Extensions and generalizations of this work have been accomplished by several researchers, most notably Atkinson and Walton. A synopsis of this previous work can be found in the introduction of Herrmann and Walton (1989).

Herrmann and Walton (1989) derived analytical expressions for the stresses, displacements, and stress intensity factor for a semi-infinite mode III crack, initially at rest, which begins to propagate at a constant speed under the action of suddenly applied loads on the crack faces. These loads are completely general and can be time varying. These were the first transient dynamic results for a very general class of viscoelastic material models which includes both the power law and standard linear solid viscoelastic models. Herrmann and Walton (1989) also presented closed form expressions for the Laplace transform of an energy release rate. A Barenblatt type process zone was incorporated into the model behind the crack tip and the energy flux into this damage zone per unit crack advance was derived for loadings which have a particular spatial form which follows the advancing crack tip but are allowed to be time varying. This energy release rate was found to be the product of the response stress in the process zone and an energy integral. An expression for the Laplace transform of each of these functions was derived and the mathematical behavior of the energy release rate was determined through asymptotic methods and by considering the form of the energy release rate when such simplifying assumptions as quasi-static propagation or an elastic material model were introduced. Herrmann and Walton (1988) showed that these formulas could be generalized to the complex plane and thus numerical Laplace inversion along a Bromwich path was valid. The numerous graphs displayed in Herrmann and Walton (1988) showed the effect on the energy release rate of varying the different nondimensional parameters identified in these formulae.

The purpose of this paper is to report our results in extending these models to the more applicable case of transient dynamic mode I crack propagation. Furthermore, these results have allowed the authors to provide an idealized model of the fundamental dynamic fracture experiments described in Ravi-Chandar and Knauss (1982), (1984abc). In these experiments, a large plate with a starter crack had a fixed part of its crack faces loaded by copper strip which provided an opening mode pressure when a capacitor-inductor circuit was discharged through the strip. The size of the plate was chosen large enough such that reflected waves did not interact with the crack tip for the duration of the experiment. Thus, it was possible to simulate an infinite specimen geometry in their experiments. It was discovered that the crack tip advanced at a constant speed even though the stress

---

† Each author gratefully acknowledges the support for this research provided by the Air Force Office of Scientific Research and the National Science Foundation through the NSF Grant No. DMS-8903672.

intensity factor was varying. Furthermore, the initial acceleration phase of the crack tip could not be observed since it occurred in a time period of less than the  $5\ \mu\text{sec}$  that the experiments could resolve. Similarly, no deceleration phase for crack arrest was observed since the arrest also occurred in a time period of less than  $5\ \mu\text{sec}$ . Ravi-Chandar and Knauss concluded from a series of experiments which varied the duration of the loading on the crack faces that "the question of whether a crack will initiate under some applied loading into unstable growth depends not only on the amplitude of the loading, but also on the complete history of load application."

Our mathematical model assumes a general viscoelastic material whose current state of stress depends on the complete history of the strain of the material through Riemann-Stieltjes convolutions of the shear modulus and Lamé modulus  $\lambda$  with the strain. For a semi-infinite mode I crack that begins to propagate at a constant speed less than the glassy shear wave speed, the authors derive expressions for the Laplace transform of the stresses, the displacements, and the stress intensity factor. Furthermore, a Barenblatt type process zone is incorporated behind the crack tip and an expression for the energy flux into this damage zone is determined. This energy release rate is derived for two different loading schemes, the first assumes the load on the crack faces follows the advancing crack tip as in the previous studies Herrmann and Walton (1989), (1988), and the second loading assumes that the crack face tractions remain fixed as the crack tip advances. The energy release rate in each case is found to be the product of the response stress in the damage zone and an energy integral. The Laplace transforms of each of these functions is determined for complex values of the Laplace variable so that numerical Laplace inversion of these expressions is valid. The behavior of these expressions is investigated by asymptotic as well as numerical means. Moreover, the effect of such simplifying assumptions as quasistatic propagation or an elastic material model is also examined. In particular, it is shown that the first loading scheme has the energy release rate quickly and monotonically rise to its steady state value while the second loading scheme has a quick monotonic increase to a peak value and then a monotonic decrease to zero. Note that this behavior of the energy release rate under the second loading scheme, which reflects that found in the experiments of Ravi-Chandar and Knauss, provides an explanation of their observations of an abrupt crack arrest if a critical energy release rate is assumed as the fracture criterion.

Herrmann, J.M. & J. R. Walton, [1989], On the energy release rate for dynamic transient anti-plane shear crack propagation in a general linear viscoelastic body, *J. Mech. Phys. Solids*. **37** No. 5 pp.619-645.

———, [1988], A comparison of the dynamic transient anti-plane shear crack energy release rate for standard linear solid and power-law type viscoelastic materials, *Elastic-Plastic Failure Modelling of Structures with Applications*, Eds. D. Hui and T.J. Kozik, (ASME PVP-Vol 141) pp.1-11.

Ravi-Chandar, K. & Knauss, W.G., [1982], Dynamic crack-tip stresses under stress wave loading—a comparison of theory and experiment, *Int. J. Frac.* **20** pp.209-222.

———, [1984a], An experimental investigation into dynamic fracture: I. Crack initiation and arrest, *ibid.* **25** pp.247-262.

———, [1984b], An experimental investigation into dynamic fracture: II. Microstructural aspects, *ibid.* **26** pp.65-80.

———, [1984c], An experimental investigation into dynamic fracture: III. On steady-state crack propagation and crack branching, *ibid.* **26** pp.141-154.

Willis, J.R., [1967], Crack propagation in viscoelastic media, *J. Mech. Phys. Solids* **15** pp.229-240.

# ON MIXED-MODE FRACTURE CRITERIA OF CRACK INITIATION ANGLE UNDER NON-PROPORTIONAL LOADING

C.L. Chow and T.J. Lu  
Mechanical Engineering, Southern Illinois University  
at Edwardsville, Edwardsville, Il. 62026-1805

## ABSTRACT

The development of modern design methodology imposes increasing importance on reliable and accurate method of predicting fracture toughness and crack growth direction. So far, the practical use of fracture mechanics has been confined to structural components which remain essentially elastic such that the usual assumption of small-scale yielding (SSY) applies. However, the valid range of SSY assumption has been elucidated to be surprisingly small [1] which necessitates the extension of linear elastic fracture mechanics to, say, low strength ductile materials or high strength materials under plane stress, where crack initiation and propagation is usually accompanied by extensive plastic deformation. Beginning from Begley and Landes [2], the J-integral has been postulated as a potential method to determine the fracture toughness (i.e., the onset of crack extension) in ductile materials. The use of J is nevertheless restricted by the underlying assumption of nonlinear elasticity in deriving the HHR (Hutchinson-Rice-Rosengren) singularity fields. It is also difficult to apply J analysis to problems of surface or shallow cracks and to non-coplanar cracks. Furthermore, this approach does not account for the effect of distributed microvoiding and/or microcracking near crack tip on stress and strain fields which has been shown in to be severe [3].

Recently, a phenomenological theory known as continuum damage mechanics (CDM) has emerged as an alternative candidate for elastic-plastic fracture mechanics [3-6]. The theory discusses systematically the effects of irreversible microstructural alterations or material damage on macroscopic mechanical properties of the material such as stiffness and strength, and also the effects of loading, environmental condition as well as damage itself on the subsequent development of damage. The general framework of CDM can be established, after identifying a proper set of internal variables characterizing the irreversible microscopic occurrences together with their conjugated generalized forces, by appealing to the thermodynamic theory of irreversible processes.

In this paper, a symmetric second-order tensor is used to characterize the geometrical and distributive properties of damage. A new matrix formulation of damage effect tensor based on the normative representation of stress and strain [7] is employed to define effective stress and effective strain. For damage-coupled elasticity and plasticity, a new hypothesis of energy equivalence is proposed which extends the more familiar hypothesis of

elastic complementary strain energy equivalence to phenomena other than elasticity. Evolution law of anisotropic damage is constructed using the concept of a damage surface in the space of affinities as well as the principle of maximum damage dissipation. The influence of non-proportionality in stress histories presenting in the crack tip region is accounted for by introducing a dynamic coordinate system of principal damage such that the principal direction of damage rotates in accordance with that of the loading. Numerical algorithms are finally developed to implement the proposed damage model for ductile fracture.

To complete the proposed damage model, two damage fracture criteria are developed for predicting fracture toughness and crack initiation angle. One of them is known as the  $c$ -criterion which may be stated as: a crack will propagate at the direction of the maximum ratio of effective damage equivalent stress/effective plastic equivalent stress, or  $c = \tilde{\sigma}_d / \tilde{\sigma}_p$ , and initiate when the overall damage reaches its critical value, an intrinsic material property. The  $\delta$ -criterion makes use of the difference in angle,  $\delta$ , between the principal damage plane of an element and the radial plane of the element which states that: a crack will initiate at the direction of zero  $\delta$  when the overall damage of an element ahead of the crack tip at that direction reaches the critical value. These criteria are used to predict the threshold condition, i.e. fracture toughness and crack initiation angle, in mixed mode specimens made of aluminum alloy 2024-T3. The thin aluminum alloy plates embedded with an isolated central crack of inclined angle  $\beta = 45, 60, 75^\circ$  are manufactured to simulate the mixed mode ductile fracture. A biaxial loading rig with two orthogonal, hydraulic servo actuators is employed to simulate a set of prescribed non-proportional loading paths.

In addition to  $c$ - and  $\delta$ -criteria, three other criteria postulated with the conventional fracture mechanics theory are examined, namely, the criteria of maximum tangential stress (MTS-criterion), strain energy density (S-criterion) and maximum dilatational strain energy density (T-criterion). The relative merits of all the above listed fracture criteria in predicting fracture initiation load and angle of crack initiation of mixed-mode ductile fracture are compared with experimental measurements. The non-proportional loading condition prescribed should provide one of the most stringent checks on the validity of different fracture criteria which is otherwise inaccessible with routine proportional loading.

## REFERENCES

1. C.L. Chow and T.J. Lu, *Proc. Inst. Mech. Engrs., Part C-Mechanical Engineering Science*, 204 (1990) 219-231.
2. J.D. Landes and J.A. Begley, in *Fracture Analysis*, ASTM STP 560, 1974, pp. 170-186.
3. T.J. Lu and C.L. Chow, *Theor. Appl. Frac. Mech.*, 14 (1991) 187-218.
4. C.L. Chow and T.J. Lu, *Engng. Frac. Mech.*, 34 (1989) 679-701.
5. C.L. Chow and J. Wang, *Engng. Frac. Mech.*, 32 (1989) 601-612.
6. C.L. Chow and J. Wang, *Int. J. Frac.*, 47 (1991) 145-160.
7. C.L. Chow and T.J. Lu, *Theor. Appl. Frac. Mech.*, 12 (1989) 161-187.

## ESTIMATION OF THE $C_t$ -PARAMETER UNDER CREEP-FATIGUE CONDITION

Kee Bong Yoon<sup>1</sup> and Ashok Saxena<sup>2</sup>

<sup>1</sup>Research Engineer, Materials Evaluation Center, Korea Standards Research Institute, P.O. Box 3, Taedok, Republic of Korea

<sup>2</sup>Professor, School of Materials Engineering, Georgia Institute of Technology, Atlanta, GA 30332-0245

### ABSTRACT

The problem of creep-fatigue crack growth under trapezoidal waveshapes has received much attention due to its applicability to remaining life prediction of the power plant components such as steam headers and turbine rotors. As a fracture parameter characterizing the time-dependent crack growth rate during the load hold period,  $C_t$ -parameter seems to be promising. The  $C_t$  estimation equation derived for elastic-secondary creep (EL-SC) material has been used particularly for creep crack growth problems. However, for creep-fatigue problems in which the hold period is relatively short, the previous estimation equation is no longer accurate. Thus, better estimation scheme is required for creep-fatigue problems considering the influence of crack tip plasticity and primary creep.

In this study, finite element simulations of the first three fatigue cycles are conducted. In the first analysis, the constitutive law employed includes elastic deformation, nonlinear kinematic hardening plasticity suitable for cyclic loading and decoupled secondary creep. Cyclic plasticity is included to understand the nature of the crack tip plasticity and the resultant retardation of the creep rate in the crack tip region. In the second analysis, decoupled primary creep is also added to see the significance of the primary creep. Based on the numerical results whose main results are shown in Figure 1, new  $C_t$  estimation equations are proposed.

In order to show the effectiveness of the proposed estimation schemes, creep-fatigue crack growth experiments on compact-type specimens are conducted for 1.25Cr-0.5Mo steel at 538°C. In these experiments, hold times are 98 seconds and 10 minutes. The load line deflection during the load hold period is monitored and the crack length is measured using the potential drop method. The experimental results show that the previous  $C_t$  estimation equation derived for elastic-secondary creep material gives significantly larger values of  $C_t$  than the measured values. It is also shown that the estimation equation based on elastic-plastic-primary creep-secondary creep (EL-PL-PC-SC) analysis gives much closer values to the measured  $C_t$  values than that based on elastic-plastic-secondary creep (EL-PL-SC) analysis. Based on the experimental and numerical results, explanations will be provided on the discrepancies between the measured and the estimated  $C_t$  values.

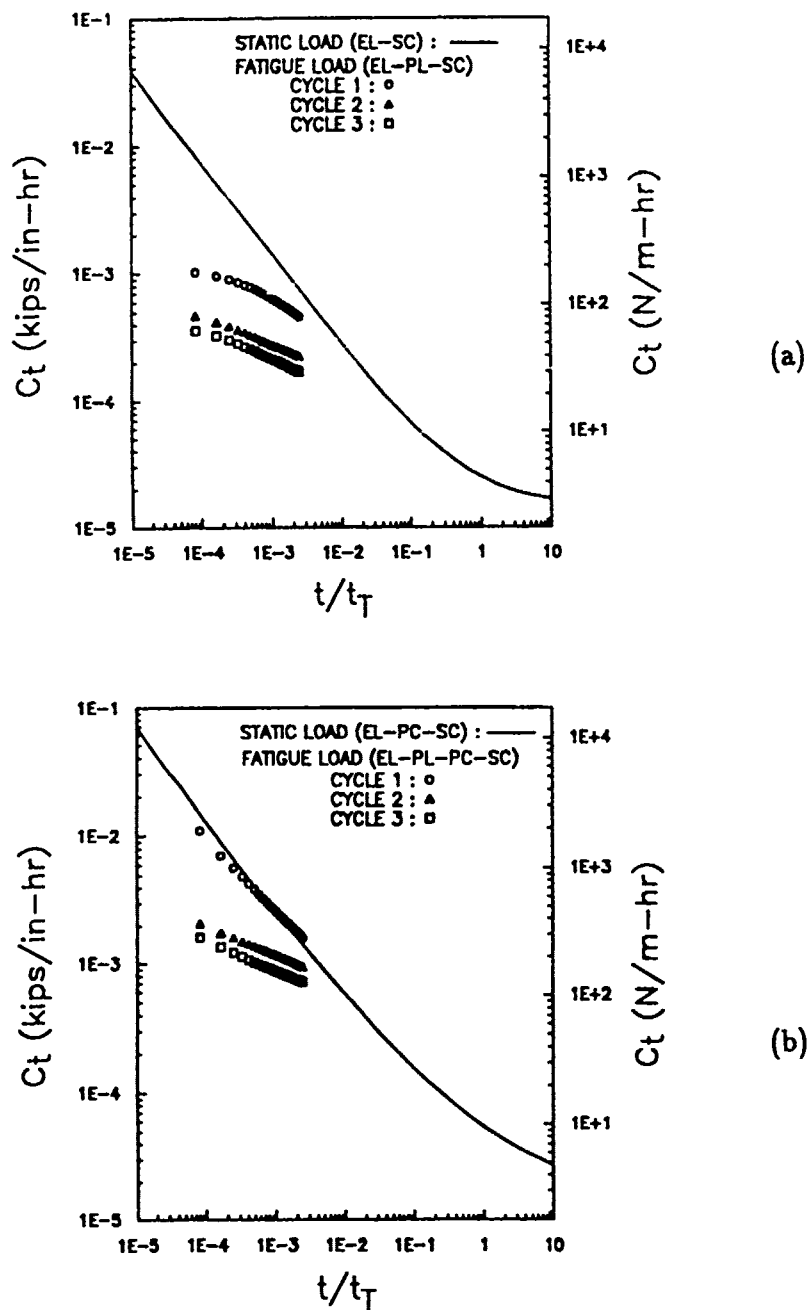


Figure 1:  $C_t$  as a function of time in fatigue analyses with 10 minute hold period. (a) elastic-plastic-secondary creep (EL-PL-SC) material (b) elastic-plastic-primary creep-secondary creep (EL-PL-PC-SC) material

## Mixed Mode Tangential Displacement Fracture Criterion

Liu Pu (Dept. of Naval Architecture & Ocean  
Engineering, Shanghai Jiao Tong University,  
200030, P.R.China)

### Abstract

Tangential displacement, a new mechanical parameter which can reflect the fracture mechanism of materials more evidently, has been proposed as fracture-controlling parameter, and basing upon it a new fracture criterion, namely, mixed mode tangential displacement fracture criterion, has been established in this paper. Researches on mixed mode fracture experiments have been undertaken and they have provided sufficient and necessary evidence for the new criterion.

The spherical coordinate system has been adopted with some point in crack profile as origin. Tangential displacement has been defined as the total displacement in the direction perpendicular to vector  $\vec{r}$ . Tangential displacement fracture criterion has been established basing upon the following two assumptions,

a. The initial growth of mixed mode crack occurs inside the normal plane of crack profile, and the growth orientation is opposite to that along which tangential displacement takes its maximum value.

b. Cracking starts when maximum tangential displacement reaches its critical value.

Applying tangential displacement fracture criterion to various kinds of mixed mode crack, following results have been obtained.

1). For the sliding mode crack, the initial growth direction varies between  $-75^\circ$  and  $-84^\circ$  under plane stress state,  $-71^\circ$  and  $-84^\circ$  under plane strain state, and fracture toughness is  $0.87 \sim 1.1 K_{IC}$  for  $0 < \nu < 0.5$ . The fracture toughness of shear mode crack is  $0.5 \sim 1 K_{IC}$ .

2). For mixed mode I and II crack, the growth direction is in accord with the results from  $\delta$ -criterion and maximum pulling stress criterion. For both mixed mode I, II and I, III crack, the critical fracture state curve lies between those of above two criterions.

3). For mixed mode I, II and III crack, critical load calculated according to the new criterion is a little larger than that deduced from  $\delta$ -criterion if  $K_{II}$  is small compared with  $K_I$  and  $K_{III}$ , and smaller if  $K_{II}$  is small relative to  $K_I$  and  $K_{III}$ .

By adopting Irwin modification under small scale yielding for the opening mode crack, it can be proved that there exists following relation between maximum tangential displacement and open displacement at the original crack tip,

$$u_{tmax} = \frac{1}{2} CTOD$$



Therefore, maximum tangential displacement is an equally appreciable parameter as CTOD for the opening mode crack. CTOD criterion may be considered as a special case of maximum tangential displacement criterion.

Mixed mode brittle fracture experiments have been performed for two kinds of specimen made of spring steel. The first kind of specimen experienced the joint action of tension and shear. Mixed mode loading has been realized through the variation of two directions, of which one is the loading direction relative to crack surface and the other is the specimen direction relative to horizontal. The second kind of specimen bearing both tension and torsion have been used for mixed mode I and III fracture experiments.

Critical fracture points of specimen have formed a narrow scatter strip surrounding the fracture curve described by the tangential displacement criterion. It's appropriate to conclude that the new criterion is available.

#### Reference

1. Sih, G.C., Strain energy density factor applied to mixed mode crack problems, *Int. J. Fracture*, Vol. 10, 1974
2. Palaniswamy, K., Crack propagation under general inplane loading. Ph.D. Thesis, California Institute of Tech., 1972
3. Nuismer, R.J., A energy release rate criterion for mixed modes fracture. *Int. J. Fracture*, Vol. 11, 1975
4. G.A. Papadopoulos, Crack initiation under biaxial loading, *Engng. Fracture Mech.*, Vol. 29., no. 5, 1988
5. Grigoriu, M., etc., Mixed mode fracture initiation and trajectory prediction under random stresses. *Int. J. Fracture*, Vol. 45, no. 1, 1990
6. S.E. Swartz and N.M. Taha, Mixed mode crack propagation and fracture in concrete, *Engng. Fracture Mech.* Vol. 35, no. 1, 1990

# THE ANALYSIS OF SOME NONLINEAR SYSTEMS USING ABEL'S IDENTITY

by

T. L. Caipen, Lt Col  
Gary J. Butson, Lt Col

and

S. E. Jones, Visiting Professor  
Department of Engineering Mechanics  
U. S. Air Force Academy, CO 80840

Abel's Identity is a valuable tool for constructing solutions to linear differential equations, as well as a fundamental building block for theoretical developments (e. g. , Ince [1]). An extension of Abel's Identity to a wide class of nonlinear differential equations was recently given by Jones and Butson [2, 3]. The equations to which the identity applied were cast in the form of first order systems.

$$\dot{x} = F(x, y, t) \quad (1)$$

$$\dot{y} = G(x, y, t) \quad (2)$$

which satisfy

$$\frac{\partial F}{\partial x} + \frac{\partial G}{\partial y} = f(t) \quad (3)$$

It was shown that the general solution

$$x = x(t, \alpha, \beta) \quad (4)$$

$$y = y(t, \alpha, \beta) \quad (5)$$

where  $\alpha$  and  $\beta$  are the arbitrary constants of integration, satisfies

$$W = \frac{\partial x}{\partial \alpha} \frac{\partial y}{\partial \beta} - \frac{\partial x}{\partial \beta} \frac{\partial y}{\partial \alpha} = W_0 \exp \left\{ \int_{t_0}^t f(t) dt \right\} \quad (6)$$

In this equation,  $W_0 = W_0(t_0, \alpha, \beta)$  and  $t_0$  is some convenient lower limit.

Equation (6) is actually an integral of the motion of (1), (2). The form of this integral is unconventional and extracting useful information was the subject a paper by Jones, Butson, and Lemmers [4].

In this paper, we explore in detail several of the general solutions presented in [4]. Among the systems discussed is the nonlinear damped oscillator

$$\ddot{x} + \mu \dot{x} + 2/9 \mu^2 x + \epsilon x^3 = 0 \quad (7)$$

where  $\mu$  and  $\epsilon$  are constants.

#### References

1. E. L. Ince, Ordinary Differential Equations, New York, Dover Publications (1956).
2. S. E. Jones and Gary J. Butson, "The Use of Abel's Identity for the Solution of Problems in Nonlinear Oscillation Theory," Abstract, Proceedings of the Eleventh U.S. National Congress of Applied Mechanics, Tucson, AZ (1990)
3. S. E. Jones and Gary J. Butson, "On Abel's Identity, Part I: Nonlinear Differential Equations," to appear in the Journal of Sound and Vibration
4. S. E. Jones, Gary J. Butson, and Patrick Lemmers, "On Abel's Identity, Part II: The Integration of a Nonlinear Nonconservative System," to appear in the Journal of Sound and Vibration.

# SMALL DENOMINATORS AND THE PROBLEM OF EIGENVECTOR STABILITY IN STRUCTURAL DYNAMICS

D. Afolabi  
Purdue University  
Indianapolis, Indiana 46202.

B. Alabi  
University of Ibadan  
Ibadan, Nigeria.

## ABSTRACT

Perfectly symmetric systems have degenerate eigenvalues. Various kinds of imperfections destroy perfect symmetry, converting degenerate eigenvalues to pathologically close eigenvalues. This gives rise to small denominators, leading to inaccurate prediction of corresponding eigenvectors when using classical perturbation methods.

## INTRODUCTION

The influence of small denominators in mechanics has been discussed in considerable detail by V. I. Arnol'd, in his celebrated papers [1-2] on celestial mechanics.

In structural dynamics, classical perturbation methods are used in sensitivity analysis, structural redesign, optimization, etc. The literature in this area is vast, for which [3-6] represent a sample. In the cited references, it is implicitly assumed that small changes in the eigenmatrix of a linear structure induces only small order perturbation in the eigenvalues and eigenvectors. It is shown in this paper that the above is not true in the regime of small denominators. The practical importance of the foregoing seems not be sufficiently appreciated in the structural dynamic community at present.

## SMALL DENOMINATORS

Small denominators arise when the divisor in a computation tends to zero. Unless the numerator also goes to zero at a comparable rate, the resulting ratio becomes almost infinite. This is the case in classical first order perturbation eigenvalue problem, for which the following formulas (1) - (3) are well known.

$$Au_i = \lambda_i; \quad A^{(0)}u_i^{(0)} = \lambda_i^{(0)}; \quad A = A^{(0)} + A^{(1)}; \quad \lambda_i = \lambda_i^{(0)} + \lambda_i^{(1)}; \quad u_i = u_i^{(0)} + u_i^{(1)}. \quad (1)$$

Here superscript (0) denotes reference system; while superscript (1) denote first order correction terms, which are presumed to be small—but this is not always true in the case of eigenvectors. Unsuperscripted symbols denote the perturbed system. The first order corrections to the  $i$ th eigenvalue and vector, respectively, are

$$\lambda_i^{(1)} = \frac{u_i^{(0)T} \cdot [A^{(1)}] \cdot u_i^{(0)}}{\|u_i^{(0)}\|_2}. \quad (2)$$

$$u_i^{(1)} = \sum_{j=1}^N q_{ij} u_j^{(0)}; \quad q_{ij} = \frac{1}{\lambda_i^{(0)} - \lambda_j^{(0)}} \cdot \frac{\langle A^{(1)} u_i^{(0)}, u_j^{(0)} \rangle}{\langle u_i^{(0)}, u_i^{(0)} \rangle}; \quad i \neq j; \quad q_{ii} = 0. \quad (3)$$

where  $\langle \cdot \rangle$  denotes inner product of two real vectors. It is emphasized that the eigenvalues of the systems being considered here are all *distinct*, although some may be pathologically close.

The "small denominators",  $\lambda_i^{(0)} - \lambda_j^{(0)}$ , which are present in equation (3) for almost equal but distinct eigenvalues gives rise to large correction terms in the eigenvectors. Thus  $u_i^{(1)}$  is not small, unless  $\lambda_i^{(1)}$  is equal to zero or very small. This, therefore, introduces large errors. Second and higher order perturbation formulas do not lead to more accurate prediction. In fact, they introduce larger errors, since the small denominators are now raised to higher powers.

### NUMERICAL EXAMPLE

For an illustration, we use a very simple 3 d.o.f cyclic system. A whole range of examples for realistic engineering structures having larger matrix size may be easily constructed. Let

$$A^{(0)} = \begin{bmatrix} 200 & -95 & -95 \\ -95 & 201 & -95 \\ -95 & -95 & 200 \end{bmatrix}; \quad A^{(1)} = \begin{bmatrix} -0.2 & 0 & 0 \\ 0 & -0.2 & 0 \\ 0 & 0 & 0.4 \end{bmatrix}; \quad A = \begin{bmatrix} 199.8 & -95 & -95 \\ -95 & 200.8 & -95 \\ -95 & -95 & 200.4 \end{bmatrix} \quad (4)$$

The eigenvectors of  $A^{(0)}$  and  $A$  are, respectively,

$$U^{(0)} = \begin{bmatrix} 1 & 1 & -5 \\ 1 & 0 & 1 \\ 1 & -1 & -5 \end{bmatrix}; \quad U = \begin{bmatrix} 1 & 1 & -21 \\ 1 & -32 & 1 \\ 1 & -68 & -78 \end{bmatrix}; \quad (5)$$

It seen that the perturbation  $A^{(1)}$  is very small indeed, by any matrix norm, compared to the reference matrix  $A^{(0)}$ . Yet, the error it creates in the eigenvectors is not small. Thus, a 'small' perturbation of a matrix with large elements, does not necessarily imply that eigenvector corrections will be small. Moreover, under several arbitrary choices of  $A^{(1)}$  all of which are small, very different corrections  $u_i^{(1)}$  are obtained, some small others very large.

In the foregoing developments, only self-adjoint matrices have been considered.

### REFERENCES

1. Arnol'd, V. I., "The classical theory of perturbations and the problem of stability of planetary systems", *Soviet Math. Dokl.*, vol 3, pp 1008-1011, 1962.
2. Arnol'd, V. I., "Small denominators and problems of stability of motion in classical and celestial mechanics", *Russian Math Surveys*, vol 18, #6, pp85-192, 1963.
3. Chen, J. C., and Wada, B. K., "Criteria for Analysis-Test Correlation of Structural Dynamic Systems", *J. Appl. Mech.*, vol 45, pp 471-477, 1975.
4. Meirovitch, L., and Ryland, G., "Response of slightly damped gyroscopic systems", *J. Sound Vib.*, vol 67, pp 1-19, 1979.
5. Murthy, D. V., and Haftka, R. T., "Derivatives of eigenvalues and eigenvectors of a general complex matrix" *Int J Numer Meth Eng*, vol 26, pp 293-311, 1988.
6. Plaut, R. H. and Huseyin, K., "Derivatives of eigenvalues and eigenvectors in non-self adjoint systems", *AIAA Journal*, vol 11, #2, pp 250-251, 1973.
7. Afolabi, D., "The stability of eigenvectors under arbitrary perturbation", *Proc. 61st Shock & Vib Symp.*, vol II, pp. 93-102, Pasadena, CA, October, 1990.

# SMOOTHING AND PARTIAL DERIVATIVES OF TWO-DIMENSIONAL SURFACES USING REGRESSIVE HARMONIC SERIES

José Roberto F. Arruda

Visiting Scholar, Dr.

Department of Mechanical Engineering  
Virginia Polytechnic Institute & State University  
Blacksburg, Virginia 24061-0238  
on leave of the University of Campinas (Brazil)

The problem of smoothing surfaces which can be described as scalar functions of a two-dimensional domain is classical in image processing. Smoothing techniques can be applied to experimental modal analysis whenever a large number of transducer locations is used. Smoothing can give a better image of the mode shapes. Also, it is essential when spatial partial derivatives are sought. Those derivatives are directly related to angular deflections and can be useful when verifying Finite Element model predictions. Smoothing techniques can include transformation and median filtering. The latter does not lead to a mathematical description of the surface and hence is not appropriate for partial derivative extraction, although it can be used for pre-processing the data when non-Gaussian type of noise is present. Transformation filtering techniques are based on discrete linear transforms, most frequently the Discrete Fourier Transform (DFT). The DFT can be efficiently computed using various fast algorithms.

For two-dimensional surfaces  $x(\xi, \eta)$  the two-dimensional DFT applies and it can be defined as:

$$X_{kl} = \frac{1}{M} \frac{1}{N} \sum_{m=0}^{M-1} \sum_{n=0}^{N-1} x_{mn} W_M^{-km} W_N^{-nl} \quad ; k = 0, M-1 ; l = 0, N-1. \quad (1)$$

where  $x_{mn}$  is the discretized data with constant resolution  $\Delta\xi$  and  $\Delta\eta$ ,  $W_M$  and  $W_N$  are the  $M^{th}$  and  $N^{th}$  root of unity respectively and  $X_{kl}$  are the bidimensional Euler-Fourier coefficients. Conversely, the data can be expressed as:

$$x_{mn} = \sum_{k=0}^{M-1} \sum_{l=0}^{N-1} X_{kl} W_M^{mk} W_N^{ln} \quad ; m = 0, M-1 ; n = 0, N-1. \quad (2)$$

Equation (2) shows that a particular two-dimensional Discrete Fourier Series (DFS) with period  $M$  in  $m$  and period  $N$  in  $n$  is the mathematical model used to interpolate  $x_{mn}$ . This *periodization* effect introduces high-frequency components that account for the sharp edges present in the *wrapped-around* data. This phenomenon is known as *leakage*. In the smoothing process leakage is prejudicial as it causes distortion in the borders of the low-pass filtered data.

Two techniques are presented in this paper to overcome this problem. The first consists of calculating the two-dimensional DFT with a two-step procedure where in each step one-dimensional DFTs are computed:

$$Y_{nk} = \frac{1}{M} \sum_{m=0}^{M-1} x_{mn} W_M^{-km} \quad ; k = 0, M-1 ; n = 0, N-1. \quad (3)$$

$$X_{kl} = \frac{1}{N} \sum_{n=0}^{N-1} Y_{nk} W_N^{-ln} \quad ; k = 0, M-1 ; l = 0, N-1. \quad (4)$$

case	method $\rightarrow$	DFT	RHS
case 1 $M = 16, \mathcal{M} = 24$ $N = 32, \mathcal{N} = 48$ $p = 2, q = 4$	max error relative to max exact value [%]	57%	4.4%
	computation cost [MFLOPS]	1.09	0.12
case 2 $M = 32, \mathcal{M} = 48$ $N = 64, \mathcal{N} = 96$ $p = 2, q = 4$	max error relative to max exact value [%]	84%	5.3%
	computation cost [MFLOPS]	3.96	0.40

Table 1: Comparison of the two proposed methods: DFT and RIIS.

To avoid leakage in the one-dimensional DFTs different methods can be used. In this paper the one-dimensional data were padded with splines on both extremities so that smooth *wrapped around* periodic sequences could be generated. Smoothing is then achieved by low-pass filtering  $Y$  and  $X$  before performing the inverse DFTs:

$$Y_{nk} = 0 \ ; k = p+2, p+3, \dots, M-p. \text{ and } X_{kl} = 0 \ ; l = q+2, q+3, \dots, N-q. \quad (5)$$

Note that the lines  $M-p+1, \dots, M$  and  $N-q+1, \dots, N$  correspond to the first  $p$  and  $q$  negative frequencies in  $\xi$  and  $\eta$  respectively and should not be discarded. The partial spatial derivatives are obtained by differentiating Eq. (2) with respect to  $\xi = m\Delta\xi$  and  $\eta = n\Delta\eta$ . Mathematically this can be shown to be equivalent to multiplying  $Y_{nk}$  by  $\frac{i2\pi k}{M\Delta\xi}$  and  $X_{kl}$  by  $\frac{i2\pi l}{N\Delta\eta}$  before computing the inverse DFTs.

The second technique also consists of representing the data by a two-dimensional Regressive Harmonic Series (RHS). Unlike the DFT, now the original size (length) of the data is not assumed to be equal to the period and nor does the number of frequency lines:

$$x_{mn} = \sum_{k=-p}^p \sum_{l=-q}^q X_{kl} W_{\mathcal{M}}^{mk} W_{\mathcal{N}}^{ln} + \epsilon_{mn} \ ; m = 0, M-1 \ ; n = 0, N-1. \quad (6)$$

The length of the data in  $\xi$  is  $M\Delta\xi$  but the period of the RHS is  $\mathcal{M} > M$  and  $p \ll M$ . In the  $\eta$  direction  $\mathcal{N} > N$  and  $q \ll N$ . It should be noted that  $\Delta\xi$  and  $\Delta\eta$  do not need to be constant in this case. The RHS is an approximation instead of an interpolation of  $x_{mn}$  and the Euler-Fourier coefficients cannot be calculated by the DFT. Rewriting Eq. (6) in matrix form:

$$\mathbf{x} = W_{\mathcal{M}} X W_{\mathcal{N}} + \epsilon \quad (7)$$

The least-squares (LS) solution is given by:

$$X = (W_{\mathcal{M}}^H W_{\mathcal{M}})^{-1} W_{\mathcal{M}}^H \mathbf{x} W_{\mathcal{N}}^H (W_{\mathcal{N}} W_{\mathcal{N}}^H)^{-1} \quad (8)$$

where the matrices to be inverted have a very small size,  $(p \times p)$  and  $(q \times q)$  respectively. The smoothed shape  $\mathbf{x}^{(s)}$  is obtained from:

$$\mathbf{x}^{(s)} = W_{\mathcal{M}} X W_{\mathcal{N}} \quad (9)$$

The spatial partial derivatives in  $\xi$  and  $\eta$  can be easily obtained by multiplying  $X_{kl}$  by  $\frac{i2\pi k}{M\Delta\xi}$  and  $\frac{i2\pi l}{N\Delta\eta}$  respectively before using Eq. (9). Both techniques were applied to simulated data with added Gaussian noise. Illustrative results are summarized in Table 1. The RIIS method gives more precise results at a much lower computational cost. The computational cost was estimated using the number of floating point operations (FLOPS).

# VARIATIONAL FORMULATIONS FOR MINIMUM SURFACES IN CYLINDRICAL COORDINATE SYSTEMS

*Y. Xiong*

*Postdoctoral Fellow*

*Department of Mechanical Engineering*

*The University of British Columbia*

*2324 Main Mall, Vancouver, B.C.*

*Canada V6T 1W5*

*B. Tabarrok*

*Professor*

*Department of Mechanical Engineering*

*University of Victoria*

*P. O. Box 3055, Victoria, B.C.*

*Canada V8W 3P6*

The problem of finding a surface of the minimum area bounded by a given closed curve in space was first cast into a variational statement by Lagrange with the following functional:

$$A = \iint_D \sqrt{1 + w_x^2 + w_y^2} dx dy, \quad (1)$$

where  $w(x, y)$  represents a surface covering a domain  $D$  on the projected  $(x, y)$  plane. If the surface is axisymmetric, the problem may be further simplified as a one-dimensional formulation as

$$A = 2\pi \int_a^b r \sqrt{1 + r_z^2} dz, \quad (2)$$

where  $z$  is the axis of symmetry and  $r(z)$  is the radius function in the range  $(a, b)$ . That is, a cylindrical coordinate system is utilized in eq. (2) for an axisymmetric problem.

It is known that the formulation in Cartesian coordinate system, eq. (1), is not convenient to be used for problems with free boundaries, e.g., a full catenoid surface, because  $w(x, y)$  in eq. (1) must be a single-valued function on  $(x, y)$  plane, while eq. (2) is only for axisymmetric surfaces.

In the present study, a general minimum surface problem, with or without free boundaries, is cast into a variational statement in cylindrical coordinate system. The functional is written as

$$A = \int_{\alpha_1}^{\alpha_2} \sqrt{r^2 + r_\theta^2} dx \int_a^b \sqrt{1 + r_z^2} dz, \quad (3)$$

where the radius function  $r(\theta, z)$  is defined in a range  $(a, b)$  on  $z$ -axis extending an angle from  $\alpha_1$  to  $\alpha_2$ . The statement  $\delta A = 0$  leads to the following equation and boundary conditions:



In the domain

$$\frac{\partial}{\partial \theta} \left( \frac{r_{,\theta} \sqrt{1 + r_{,z}^2}}{\sqrt{r^2 + r_{,\theta}^2}} \right) + \frac{\partial}{\partial z} \left( \frac{r_{,z} \sqrt{r^2 + r_{,\theta}^2}}{\sqrt{1 + r_{,z}^2}} \right) - \frac{r \sqrt{1 + r_{,z}^2}}{\sqrt{r^2 + r_{,\theta}^2}} = 0, \quad (4)$$

On the boundary  $S_1$  where  $r$  is not prescribed

$$\frac{r_{,\theta} \sqrt{1 + r_{,z}^2}}{\sqrt{r^2 + r_{,\theta}^2}} n_\theta = 0, \quad \frac{r_{,z} \sqrt{r^2 + r_{,\theta}^2}}{\sqrt{1 + r_{,z}^2}} n_z = 0, \quad (5)$$

where  $n_\theta$  and  $n_z$  are the normal cosines on the boundary.

Following a similar procedure outlined in Tabarrok and Xiong (1991), a complementary "energy" formulation is derived with a functional as

$$\hat{A} = \int_{\alpha_1}^{\alpha_2} \int_a^b M_z \sqrt{M_\theta^2 + Q^2 - 1} d\theta dz, \quad (6)$$

where various quantities are related to the function  $r(\theta, z)$  as

$$M_\theta = \frac{r_{,\theta} \sqrt{1 + r_{,z}^2}}{\sqrt{r^2 + r_{,\theta}^2}}, \quad M_z = \frac{r_{,z} \sqrt{r^2 + r_{,\theta}^2}}{\sqrt{1 + r_{,z}^2}}, \quad Q = \frac{r \sqrt{1 + r_{,z}^2}}{\sqrt{r^2 + r_{,\theta}^2}}. \quad (7)$$

Similarly, a set of equation and boundary conditions complementary to eqs. (4-5) are derived from the statement  $\delta \hat{A} = 0$ .

Using the functionals developed, finite element analysis may be carried out following conventional procedures. By incorporating some constraints into the basic functionals, by means of Lagrange multipliers, the formulations may be further generalized and some mixed formulations may be developed. This work is presently under study.

### Reference

Tabarrok, B. and Xiong, Y., 1991, "Some Variational Formulations for Minimum Surfaces," to appear in *Acta Mechanica*.

# PERTURBATION METHOD FOR THE EIGENVALUE PROBLEM OF LIGHTLY DAMPED SYSTEMS

Moon K. Kwak

Department of Engineering Science and Mechanics  
Virginia Polytechnic Institute and State University  
Blacksburg, VA 24061

## 1. Introduction

The motion of mechanical systems is in general described by second-order matrix differential equations containing symmetric mass, stiffness, and damping matrices. In the dynamic analysis of structures, the eigenvalue problem of the system is to be solved a priori in order to avoid the resonance or to define the natural vibration characteristics, in which the effect of damping is often ignored. For the calculation of the response of the damped system, the damping matrix is generally assumed to be a diagonalizable matrix, which implies that the eigenvalues are complex but the eigenvectors are still real. To take non-diagonalizable property of the damping matrix into consideration, we need to transform the second-order matrix differential equation into the so-called state equation which is a first-order matrix differential equation. The undamped eigenvalue problem is characterized by symmetric mass and stiffness matrices resulting in real eigenvalues and real eigenvectors readily solvable by various algorithms. By contrast, the eigenvalue problem of the state equation, characterized by unsymmetric matrices, results in complex eigenvalues and complex eigenvectors requiring extensive additional computations. To avoid the computational complexity in the case of light damping and nonproportional damping, a perturbation method has been used (Refs. 1-4). However, the algorithms developed in Refs. 1-4 lack expressions for the higher-order terms.

In this paper, an efficient algorithm for the eigensolution of a lightly damped system is developed. To this end, a perturbation technique is introduced in which light damping is regarded as a first-order term in magnitude. Once the eigenvalue problem of the undamped system, which in fact is a zero-order problem, is solved, the higher-order terms which reflect the effect of damping can be obtained from the matrix equations. It is shown that those matrix equations can be further reduced to simple algebraic equations.

## 2. Perturbation Method

Let us consider the free vibration of a multi-degree-of-freedom mechanical system as

$$M\ddot{x} + \varepsilon C\dot{x} + Kx = 0 \quad (1)$$

where  $x$  represents the displacement vector,  $M$  is an  $n \times n$  symmetric mass matrix,  $C$  is an  $n \times n$  damping matrix and  $K$  is an  $n \times n$  symmetric stiffness matrix, and  $\varepsilon$  represents a small coefficient. The eigenvalue problem described by Eq. (1) can be written in the form

$$MU\Omega^2 + \varepsilon CU\Omega + KU = 0 \quad (2)$$

where  $\Omega$  is an  $n \times n$  diagonal matrix, whose diagonals represent the eigenvalues and  $U$  is an  $n \times n$  matrix containing the eigenvectors in each column corresponding to each eigenvalue. Light damping implies that the eigensolution of the damped system differs only slightly from that of the undamped system, implying that the eigensolution of the lightly damped system can be expressed in terms of an infinite series expanded from the eigensolution of the undamped system. Thus, we can write

$$U = \sum_{i=0}^{\infty} \epsilon^i U_0 (E_i + i F_i), \quad \Omega = \sum_{i=0}^{\infty} \epsilon^i \Omega_0 (G_i + i H_i) \quad (3a, b)$$

where  $i = \sqrt{-1}$  and  $U_0$  and  $\Omega_0$  represent the eigenvector and eigenvalue of the zero-order eigenvalue problem which amounts to the eigenvalue problem of the undamped system and also satisfying the orthogonality relationships;  $U_0^T M U_0 = I$ ,  $U_0^T K U_0 = \Omega_0^2$ . In expressing Eqs. (3), the matrices  $E_i$  and  $F_i$  are assumed to have zero diagonals and the matrices  $G_i$  and  $H_i$  are assumed to be diagonal matrices. Because  $U = U_0$  when  $\epsilon = 0$ , it can be concluded that  $E_0 = H_0 = I$  and  $F_0 = G_0 = 0$ .

Considering the  $n$ th order equation, the following equations for the higher order perturbed terms can be derived:

$$\Omega_0^2 E_n - E_n \Omega_0^2 - 2\Omega_0^2 H_n = P_n, \quad \Omega_0^2 F_n - F_n \Omega_0^2 + 2\Omega_0^2 G_n = Q_n \quad n \geq 1 \quad (5a, b)$$

where

$$P_n = - \sum_{i=1}^{n-1} \Omega_0^2 (G_i G_{n-i} - H_i H_{n-i}) - \sum_{i=1}^{n-1} \sum_{j=0}^{n-i} [E_i \Omega_0^2 (G_j G_{n-i-j} - H_j H_{n-i-j}) - F_i \Omega_0^2 (G_j H_{n-i-j} + H_j G_{n-i-j})] - \sum_{i=0}^{n-1} U_0^T C U_0 (E_i \Omega_0 G_{n-i-1} - F_i \Omega_0 H_{n-i-1}) \quad (6a)$$

and

$$Q_n = - \sum_{i=0}^{n-1} \Omega_0^2 (G_i H_{n-i} + H_i G_{n-i}) - \sum_{i=1}^{n-1} \sum_{j=0}^{n-i} [E_i \Omega_0^2 (G_j H_{n-i-j} + H_j G_{n-i-j}) + F_i \Omega_0^2 (G_j G_{n-i-j} - H_j H_{n-i-j})] - \sum_{i=0}^{n-1} U_0^T C U_0 (E_i \Omega_0 H_{n-i-1} + F_i \Omega_0 G_{n-i-1}) \quad (6b)$$

Due to the matrix properties mentioned above, Eqs. (5) can be reduced to simpler algebraic equations.

### 3. Summary and Conclusions

In this paper, an efficient algorithm is derived by means of a perturbation technique for the eigensolution of mechanical systems which contain light damping. Compared to previous algorithms developed by various researchers, the new algorithm is simpler to use and can cope with higher-order terms.

### 4. References

1. Meirovitch, L. and Ryland, G. H., "Response of Slightly Damped Gyroscopic Systems", *Journal of Sound and Vibration*, Vol. 67, 1979, pp. 1-19.
2. Meirovitch, L., *Computational Method for Structural Dynamics*, Noordhoff Sitjhoff, 1980.
3. Chung, K. R. and Lee, C. W., "Dynamic Reanalysis of Weakly Non-Proportionally Damped System", *Journal of Sound and Vibration*, Vol. 117, 1986, pp. 37-50.
4. Cronin, D. L., "Perturbation Approach for Determining Eigenvalues and Eigenvectors for Nonproportional Damped Systems", *Proc. of the 6th International Modal Analysis Conference* Feb. 1988, Kissimmee, Florida, pp. 23-29.

**A Perturbation Technique That Works  
Even When the Nonlinearity is Not Small**

**M. Senator  
Davidson Laboratory  
Stevens Institute of Technology, Hoboken, N.J 07030.**

**C. N. Bapat  
Department of Mechanical Engineering  
The City College of New York, New York, N.Y 10031.**

The problem of extending the Poincare-Lindstedt technique to large nonlinearities has been studied by Shohat,[1] Bellman and Waters,[2] Jones,[3] Mickens,[4] and Rahman and Burton [5]. Eminhizer, Helleman, and Montroll [6] appear to have first explicitly stated a successful idea, which is adding balanced linear terms starting at the zeroth level on the response side of the equations and at the first level on the forcing side. Hayashi [7] and Stoker[8] also used the same idea. Since Eminhizer, Helleman, and Montroll used a computer to do their algebra, they had no need to find solutions that were accurate at low order. Here we are interested in preserving the intuition-guiding features of the Poincare-Lindstedt technique, which means that we have to adjust the technique so that it gives high-accuracy approximations at low-order.

We extend the Lindstedt-Poincare small-linearity-based perturbation scheme to strongly nonlinear systems. This extended technique can be used to find optimum low-order hand-derivable periodic solutions at all nonlinearity magnitude. The extended technique starts from a physically nonexistent neighboring linear system. This system is created by adding an optimal linear spring term to the system side of each linear differential equation starting at the zeroth level, and balancing that term by adding an equal one to the forcing side one level down. Unlike the Ritz method, which also works for strongly nonlinear systems, results can be obtained beyond the first level without resorting to numerical techniques. Thus, this method keeps the intuition-guiding straightforwardness of the perturbation method while giving accurate, beyond-first-level, hand-derivable numerical results. Examples are presented for free vibrations with cubic and antisymmetric-quadratic nonlinearities and for harmonic solutions of the undamped Duffing equation. The forms of the solutions allow the regions of validity of the expansions to be estimated. An internal method of estimating accuracy of the perturbation

solutions is developed and checked with the free vibration examples, whose exact solutions are available. This method is then used to estimate the accuracy of the new solutions to the Duffing equation. These new Duffing equation solutions seem to be accurate in all regions where stable harmonic solutions are known to exist. In particular, they seem to be accurate at and near the vertical tangent to the resonance curve, a region where Hayashi's existing amplitude-based perturbation solution necessarily breaks down.

We start by studying the problems of free undamped vibrations of masses on springs with pure cubic, pure antisymmetric quadratic, linear/cubic, and linear/antisymmetric quadratic characteristics. These systems are inherently strongly nonlinear, while the third and fourth can be made so by the proper choice of a parameter. Yet these systems are simple enough so that third level (second level for the quadratic springs) perturbation solutions to these problems can conveniently be found by hand and used to point toward a general optimization scheme. Since the exact solutions to these problems are known, the accuracy of the optimum solutions can be judged. However, more importantly, because the Poincare-Lindstedt technique allows us to analyze the errors in frequency and in displacement vs. time response independently, we can develop an internal method of estimating accuracy that doesn't rely on knowing exact solutions. We then use the technique to find optimum harmonic solutions for the system consisting of a mass with harmonic forcing moving within the origin-centered potential well of a linear/cubic spring (the undamped Duffing equation), with neither the nonlinearity magnitude nor the forcing magnitude required to be small. The two new hand-derived, parameterized, third level, optimum harmonic solutions that are found are in forms that allow their ranges of validity to be estimated. When the accuracy estimating procedure developed with the free vibrating systems is applied to these solutions it is found that they are accurate at and near the vertical tangent to the resonance curve, region in which Hayashi's varying amplitude perturbation solution [7] necessarily breaks down.

#### REFERENCES

1. J. Shohat, Journal of Applied Physics, 15, 568-574, July, 1944.
2. R. Bellman, Quarterly of Applied Mathematics, 13, No. 2, 195-200, 1955.
3. S. E. Jones, Int. J. Non-linear Mechanics, 13, 125-128, 1978.
4. R. E. Mickens, Journal of Sound and Vibration, 111(3), 515-518, 1986.
5. Z. Rahaman and T. D. Burton, Journal of Sound and Vibration, 110(3), 363-380, 1986.
6. C. R. Eminhizer, R. H. G. Helleman, and E. W. Montroll, Journal of Mathematical Physics, 17, No. 1, 121-140, January, 1976.
7. C. Hayashi, Nonlinear Oscillations in Physical Systems, McGraw-Hill, New York, 1964, 19-21.
8. J. J. Stoker, Nonlinear Vibrations in Mechanical and Electrical Systems, Interscience Publishers, New York, 1950.

# Shock Wave and Solitary Wave in the Nonlinear Lattice

(Duan Wen Shan)

Department of Physics, North-Western Normal University,  
Lan Zhou, 730070, The People's Republic of China

## Abstract

The analytical results of small amplitude solitons have been obtained in nonlinear lattice approximately. The soliton solution have been given in Morse nonlinear lattice particularly. The numerical studies of the propagation of longitudinal shock wave in Morse lattice also have been given. From particle velocity trajectories of this lattice we find that the leading pulses of shock profile tends to evolve into a sequence of extremely well defined excitations (solitons) and reach a constant amplitude of approximately  $2U_p$  as shock propagates. We have compared the shape amplitude and velocity between the analytical soliton solutions and the solitons of numerical results in the leading pulses of the shock profiles. We find that for the weak shock wave both are in good agreements. The relationship between shock velocity and piston velocity have been obtained for the weak shock wave.

# PROCESSING AND MECHANICAL PROPERTIES OF SiC WHISKER REINFORCED MULLITE MATRIX COMPOSITE

De-Yin Jeng and Mohamed N. Rahaman  
Ceramic Engineering Department  
University of Missouri-Rolla  
Rolla, MO 65401

## ABSTRACT

Mullite matrix composites reinforced with SiC whiskers were fabricated using a sol-gel process followed by sintering or hot-pressing. Composites containing 15 v% whiskers with a green density of 0.45 of the theoretical were sintered to a density of 0.85 after 1 h at 1550 °C in an argon atmosphere. Dense composites for mechanical property measurement were formed by hot-pressing. For these composites, both the flexural strength and the fracture toughness increased significantly with the whisker content up to ~ 30 v% whiskers and then decreased for higher whisker content. The flexural strength was 420 Mpa and the fracture toughness was 5.7 Mpa·m<sup>1/2</sup> for the composite with 30 v% whiskers, compared to values of 260 Mpa and 2.0 Mpa·m<sup>1/2</sup> for the strength and fracture toughness, respectively, of the unreinforced mullite. Crack/microstructure interactions were investigated by Vickers indentation of polished surfaces and observed by scanning electron microscopy. The dominant toughening mechanisms were crack deflection and whisker pull-out. The relative contributions of these two mechanisms were estimated from toughening models.

## FAILURE MODES IN METAL MATRIX COMPOSITES

D. M. Harmon  
McDonnell Douglas Corporation  
McDonnell Aircraft Company  
St. Louis, Missouri

Elevated temperature applications for advanced hypersonic aircraft and advanced fabrication techniques such as diffusion bonding and superplastic forming have brought renewed interest in metal matrix composites for aircraft structures. To predict the strength and durability of metal matrix composites, it will be necessary to predict the mode in which failure occurs, such as net section failure, or shear along the fiber.

Fatigue failure modes of unidirectional reinforced aluminum matrix composites have been compared with those found in titanium matrix composites. The comparison was based upon the results of tests performed under two Air Force contracts, "Durability of Continuous Fiber Reinforced Metal Matrix Composites" (F33616-83-C-3219) and "Thermomechanical Load History Effects in Metal Matrix Composites" (F33615-87-C-3219). These tests included detailed optical and scanning electron microscope studies of failures in aluminum and titanium matrix composites.



**THE EFFECT OF TEMPERATURE AND IMPERFECT BONDING  
ON THE MECHANICAL PROPERTIES  
OF WHISKER REINFORCED CERAMICS**

Douglas R. Carroll  
Basic Engineering Department  
University of Missouri-Rolla  
Rolla, Missouri 65401

L. R. Dharani  
Department of Mechanical and Aerospace Engineering  
and Engineering Mechanics  
University of Missouri-Rolla  
Rolla, Missouri 65401

## **I. INTRODUCTION**

Ceramic materials are chemically and thermally stable at high temperatures, and this would seem to make them legitimate candidates for high temperature structural components. However, the brittle nature of the materials makes them unsuitable for use in applications requiring bending or tensile strength. Reinforcing the ceramic material with whiskers, or with continuous fibers, improves the mechanical properties and seems to offer the best hope of developing reliable high temperature ceramic materials. From a manufacturing viewpoint, whiskers are the most attractive means of reinforcing a ceramic to improve its mechanical properties. Any component which can be made from a monolithic powder can be made with equal ease from a whisker reinforced powder. Continuous fibers provide better reinforcement, but greatly complicate the manufacturing process. Intricate parts simply cannot be made with continuous fiber reinforcement. This paper focuses on the whisker reinforced ceramics. Before these materials can be used reliably, the mechanical properties must be well understood, and this requires both experimental and analytical work.

## **II. EXPERIMENT**

An experimental investigation was done measuring the ultimate strength and modulus of cordierite and cordierite reinforced with SiC whiskers. Four point bend tests were performed over a range of temperatures from 25°C to 1300°C. At room temperature the whiskers provided very effective reinforcement, improving the strength and modulus by more than a factor of two. This improvement degraded rapidly as the temperature was raised. At high temperatures, there was little difference between the mechanical properties of the cordierite and those of the whisker reinforced cordierite. The experimental results are summarized in Table 1.

Table 1. Experimental Results for Cordierite								
	Ultimate Strength (MPa)				Modulus (GPa)			
Temperature (°C)	25	1000	1200	1300	25	1000	1200	1300
Cordierite	55 60	63 84	61 85	72*	45 55	32 50	10 25	0*
Cordierite with 30% Whiskers	160 180	121 162	81 105	52*	110 130	40 55	8 18	0*
*Considerable viscous flow at 1300°C.								

### III. ANALYTICAL MODELING

Two analytic models were developed to explain why the mechanical properties of the whisker reinforced materials are degraded at high temperatures. In the modeling it was assumed that a friction bond existed between the matrix and the whiskers. Thus, the bond strength would be limited by the coefficient of friction multiplied by the normal stress. Ceramics are processed at high temperatures, and the normal stress comes from the thermal expansion mismatch between the whiskers and matrix when the material is cooled. Because of this, the friction bond is strong at low temperatures and weak at high temperatures. It is the reduction in the bond strength which causes the mechanical properties to be degraded at high temperatures.

A cylindrical geometry was used in developing the model, as illustrated in Figure 1. Due to symmetry only half the whisker length was modeled. The load  $P$  is applied to the matrix and transferred across the interface to the whisker. Slipping occurs along portion  $l_1$  and no slipping occurs along portion  $l_2$ . The first model developed was based on a mechanics of materials approach with an empirical constant. In developing the second model, a more rigorous approach was used for the mechanics and the empirical constant was eliminated. Both models agree favorably with the experimental data. Parametric studies were done with both models to show how each parameter affects the mechanical properties. Figure 2 shows the effect of the processing (or heat treatment) temperature on the modulus of a whisker reinforced ceramic. The modulus ratio plotted is the composite modulus divided by the matrix modulus. Note that the high temperature performance of the material is greatly improved by raising the processing temperature. This suggests that the material should be heat treated to as high a temperature as possible without destroying the microstructure.

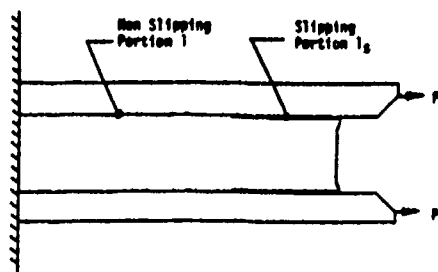


Figure 1. Model Schematic.

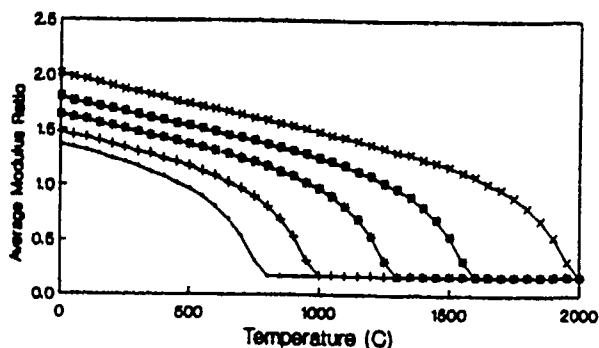


Figure 2. Effect of Processing Temperature on Modulus.  
(• 800°C, + 1000°C, □ 1300°C, ◇ 1600°C, × 2000°C)

# COMPARISON OF INTERPHASE MODELS FOR A FRACTURE PROBLEM IN COMPOSITE MATERIALS <sup>1</sup>

Autar K. Kaw<sup>2</sup>  
Alex Selvarathinam<sup>3</sup>  
Glen H. Besterfield<sup>2</sup>

Mechanical Engineering Department,  
University of South Florida,  
ENG 118, 4202 E. Fowler Avenue,  
Tampa, FL 33620-5350.

The behavior of a composite material depends on the properties of its constituents, namely the fiber, the matrix, and the interphase between the matrix and the fiber. The strength and the stiffness of the composite are determined by the fiber, while the matrix determines much of the shear and compressive properties. The interphase determines the off-axis properties and how the loads are transmitted from the matrix to the fiber.

The requirements on the strength of the interphase are conflicting in nature. For example, a strong interphase is a requirement for high shear strength of the composite. On the other hand, in the case of brittle fibers, for improved fracture toughness it is desirable that the interphase is weak enough so that the fiber cracking is followed by debonding from the matrix. A strong interphase may allow the crack in the fiber to continue across the interphase and into the matrix. One hence needs to fully understand the effect of the interphase on the mechanical performance of a composite.

The interphase/interface between the fiber and matrix has been modeled as a perfect bond (Gupta, 1973), distributed and uncoupled normal and shear springs (Gecit and Erdogan, 1978, Kaw and Goree, 1990.a,b), distributed shear springs only, homogeneous (Gecit and Erdogan, 1978) and nonhomogeneous continuum (Delale and Erdogan, 1988). In this study, the interphase is modeled as a nonhomogeneous continuum.

The geometry of the composite consists of an infinite strip (fiber) bonded to two half planes (matrix) through an infinite strip (interphase). The three materials are linearly elastic, isotropic and dissimilar. The fiber and the matrix are homogeneous, while the

---

<sup>1</sup> Unlimited use of IBM 3090 supercomputer at USF, Tampa is acknowledged.

<sup>2</sup> Assistant Professor

<sup>3</sup> Graduate Student

interphase is considered to be nonhomogeneous. The interphase material properties namely Young's modulus and Poisson's ratio are assumed to vary exponentially along the thickness of the interphase. The properties may be continuous at the interfaces at the fiber and the matrix. The fiber is assumed to have a symmetric crack. The perturbation problem of a uniform pressure on the crack is solved by using the Fourier transform techniques. The resulting solution is obtained in terms of a Cauchy singular integral equation, where the slope of the crack opening displacement is the unknown variable.

For the nonhomogeneous interphase, the influence of interphase thickness, crack length, fiber radius, moduli of the matrix and the fiber, on parameters like the stress intensity factor, the normal and shear stresses at the interfaces, and the load diffusion along the length of the fiber are studied. It is found that the stress intensity factor decreases as a function of the interphase thickness, if the fiber is stiffer than the matrix. The stress intensity factor increases as a function of the interphase thickness, if the matrix is stiffer than the fiber. Also, if the matrix is stiffer than the fiber, the cleavage stresses in the matrix initially increase as a function of the interphase thickness. This result is important in understanding that thin interphases may cause high cleavage stresses in the matrix, and perhaps assist in continuing the crack across the interphase.

The results from the nonhomogeneous model are then compared with other models mentioned above, namely the perfect bond, the shear and normal springs, the shear springs only, and the homogeneous continuum. In the case of a crack in a fiber stiffer than the matrix, the continuum interphase models give distinctly higher values for the interface cleavage stresses and lower values for the stress intensity factor, than the spring model interphase models. Correspondingly, in the case of a crack in a fiber less stiff than the matrix, the continuum and spring interphase model results are quite similar.

## REFERENCES

- Delale, F. and Erdogan, F., 1988, "On the Mechanical Modeling of The Interfacial Region in Bonded Half-Planes," ASME Journal of Applied Mechanics, Vol. 55, pp. 317-324.
- Gecit, M.R. and Erdogan, F., 1978, "The Effect of Adhesive Layers on the Fracture of Laminated Structures," ASME Journal of Engineering Materials and Technology, Vol. 100, pp. 2-9.
- Gupta, G.D., 1973, "A Layered Composite With a Broken Laminate," International Journal of Solids and Structures, Vol. 9, pp. 1141-1154.
- Kaw, A.K. and Goree, J.G., 1990a, "The Effect of Interleaves on Fracture of Laminated Composites: Part I - Analysis," ASME Journal of Applied Mechanics, Vol. 57, pp. 168-174.
- Kaw, A.K. and Goree, J.G., 1990b, "The Effect of Interleaves on Fracture of Laminated Composites: Part II - Solution and Results," ASME Journal of Applied Mechanics, Vol. 57, pp. 175-181.

# STRUCTURAL RESPONSE OF COMPONENTS USING VISCOPLASTIC MODELS

V. K. ARYA  
(University of Toledo)  
NASA-Lewis Research Center  
Cleveland, Ohio 44135, USA.

## ABSTRACT

Finite element solution technology developed for use in conjunction with advanced viscoplastic models is described. The development of such solution technology is necessary for performing structural and life analyses of engineering structural problems where the complex geometries and loadings make the conventional analytical solutions difficult. The versatility of the solution technology is demonstrated by applying it to viscoplastic models possessing different mathematical structures and encompassing isotropic and anisotropic materials. The models selected for demonstrational purpose are those developed by Robinson (1982), Freed (1988) and Robinson (1990). The computational results are shown (wherever possible) to qualitatively replicate deformation behavior observed in experiments on prototypical structural components.

The observed interaction between creep and plastic deformation at high temperatures has led to the development of a number of viscoplastic models. These models treat all inelastic strain as a single time-dependent quantity, and thus, automatically include creep, relaxation and plasticity interactions. Viscoplastic models are intended to provide realistic descriptions of high temperature, time-dependent, inelastic behavior of materials. Their mathematical structure, however, may be very complex. The highly nonlinear and mathematically "stiff" nature of the constitutive equations makes closed-form analytical solutions virtually impossible. It is, therefore, of the utmost importance that suitable (finite element or other numerical) solution technologies be developed to make these models adaptable for realistic structural and life analyses of these components.

This paper illustrates the application of some of these solution technologies with regard to the three viscoplastic models. These models have different mathematical structures and encompass both isotropic and anisotropic (for example, metal-matrix composite) materials. The intent of the paper is to familiarize the researchers and designers in the industries with the applicability of these models in engineering structural problems. It is expected that the results from the present work will stimulate the use of realistic viscoplastic models for better and more rational designs of components.

The finite element analyses for the uniaxial and multiaxial problems were performed using the finite element program MARC (1988). The nonlinear constitutive relationships of the viscoplastic models are implemented through the user subroutine, HYPELA. The stiff nature of the constitutive equations requires smart and efficient time-integration strategies for their integration. The integration strategy employed for the present computations is described in Arya et al. (1986).

Several uniaxial and multiaxial problems were analyzed. Good agreement between the experimental and predicted hysteresis loops for uniaxial thermomechanical loadings confirms the correct finite element implementation of the viscoplastic models. Using this 'validated' implementation, finite element analyses were performed for the multiaxial problems. It is seen that viscoplastic models are capable of describing thermal/mechanical phenomena observed in experiments. The versatility of the finite element solution technique described is demonstrated by applying it successfully to three different types of viscoplastic models.

#### REFERENCES

Robinson, D.N. and Swindeman, R.W. (1982) : Unified creep-plasticity constitutive equations for 2-1/4Cr-1Mo steel at elevated temperature. ORNL/TM-8444.

MARC General Purpose Finite Element Program (1988). MARC Research Analysis Research Corporation, Palo Alto, CA.

Robinson, D.N. (1990) : A continuum theory of thermoelastic/viscoplasticity for a NARloy-Z/W composite.

Freed, A.D. and Verrilli, M.J. (1988) : A viscoplastic theory applied to copper. NASA TM-100831.

Arya, V.K.; Hornberger, K. and Stamm, H. (1986) : On the numerical integration of viscoplastic models. KfK-4082.

## STRESS ANALYSIS OF SILICON RIBBON CRYSTAL GROWTH

Oscar W. Dillon, Jr., Department of Engineering Mechanics,  
University of Kentucky, Lexington, KY., 40506

When silicon crystals are produced in the form of very thin sheets, called ribbon, they frequently look like the common potato chip. This buckled shape occurs because there are non-uniformly distributed residual in-plane stresses in the very thin plates. The stresses in turn developed because the nonuniform temperature fields used to cool the material from the molten state cause the material to exceed the local yield stress. The material is modeled as a viscoplastic substance with an internal variable (dislocation density). The model needs to be applicable to a wide range of rates and temperatures.

While in metals dislocations are considered helpful because their interaction causes the material to work harden, in semiconductor applications they are harmful to the electrical performance of the device. Thus the control of the internal variable used in the response function is of very great value in another context as well. Since the dislocation density must be low, the values of this parameter are considerably below the domain represented by those encountered in metals. In turn this means that the dislocation density changes that are encountered are very large compared to the initial values and must be considered.

It is assumed that the silicon solidifies with a very low dislocation density. A complex stress field develops that far exceeds the local yield condition which in turn causes the dislocation density to multiply and the plastic strain rate to increase. It is found that a new type deformational instability develops, when one considers this changing microstructure. This instability limits the width of crystal that can be grown with a prescribed cooling profile.

This presentation will be an overview of the mechanics considerations of this problem. It is probably significant to note that LARGE scale commercial applications of this technology are being contemplated by two industrial giants as solar power sources "even as we speak".

This work was sponsored by the Department of Energy via subcontracts from the Jet Propulsion Laboratory and the Solar Energy Research Institute. Many colleagues have contributed to the research that is summarized in this presentation.

## TIME RATES OF GENERALIZED STRAIN TENSORS

Mike Scheidler

US Army Ballistic Research Laboratory  
Aberdeen Proving Ground, Maryland 21005-5066

Generalized Lagrangian and Eulerian strain tensors of the type introduced by Hill [1] are considered. We present some new formulas, both approximate and exact, for the time rate of change of these strain tensors in terms of the stretching and spin tensors. These general results, when applied to the logarithmic strain tensors, yield improved versions of approximate formulas due to Hill[1] and Gurtin and Spear[2], and a class of exact formulas which include those of Hoger[3]. As an application of the approximate formulas, we discuss the error in the approximate rate form for isotropic elastic materials used in many hydrocodes.

- [1] R. Hill. Aspects of invariance in solid mechanics. In C.-S. Yih, editor, *Advances in Applied Mechanics*, volume 18, pages 1-75. Academic Press, New York, 1978.
- [2] M. E. Gurtin and K. Spear. On the relationship between the logarithmic strain rate and the stretching tensor. *International Journal of Solids and Structures*, 19:437-444, 1983.
- [3] A. Hoger. The material time derivative of logarithmic strain. *International Journal of Solids and Structures*, 22:1019-1032, 1986.



# A CONTINUUM DAMAGE MODEL FOR RIGID POLYURETHANE FOAM\*

M.K. Neilsen<sup>1</sup> and H.L. Schreyer<sup>2</sup>

<sup>1</sup>Senior Member of Technical Staff, Engr. and Struct. Mechanics Div.  
Sandia National Laboratories, Albuquerque, New Mexico 87185

<sup>1</sup>Doctoral Student, <sup>2</sup>Professor, Dept. of Mechanical Engineering  
University of New Mexico, Albuquerque, New Mexico 87131

## SUMMARY

Rigid polyurethane foams consist of interconnected polyurethane struts or plates which form cells. These foams are often used in impact limiters for shipping containers which protect the contents from damage during accidents. During a shipping container accident, the foam is expected to absorb a significant amount of energy by undergoing large inelastic volume reductions. A continuum damage model for polyurethane foams that can be used in finite element analyses of shipping container accidents has been developed.

Polyurethane foam behaviors have been both analytically and experimentally evaluated (Gibson and Ashby, 1988). A typical load-displacement curve for polyurethane foam subjected to uniaxial compression is shown in Figure 1a. The initial elastic regime is followed by a plateau regime in which the load required to crush the material remains nearly constant. As the foam is crushed, cell walls are damaged, large permanent volume changes are generated, and the elastic stiffness of the foam decreases. As additional load is applied, the cell walls are compressed against neighboring cell walls, and the stiffness of the foam actually increases and approaches a value equal to the stiffness of solid polyurethane.

A number of researchers (Gibson and Ashby, 1988, and Warren et al., 1989) have studied the elastic behavior of foams using a micromechanical approach. In these studies, equations were developed that related the elastic constants to parameters that defined the geometry of a typical cell (i.e., the thickness of the cell wall and length of a typical cell wall section). Equations that define the critical load beyond which the behavior is no longer linear elastic were also developed by these researchers. Significant extensions to these micromechanical approaches would be needed to investigate inelastic behavior.

\* This work, performed at Sandia National Laboratories in Albuquerque, New Mexico, was supported by the United States Department of Energy under Contract DE-AC04-76DP00789.

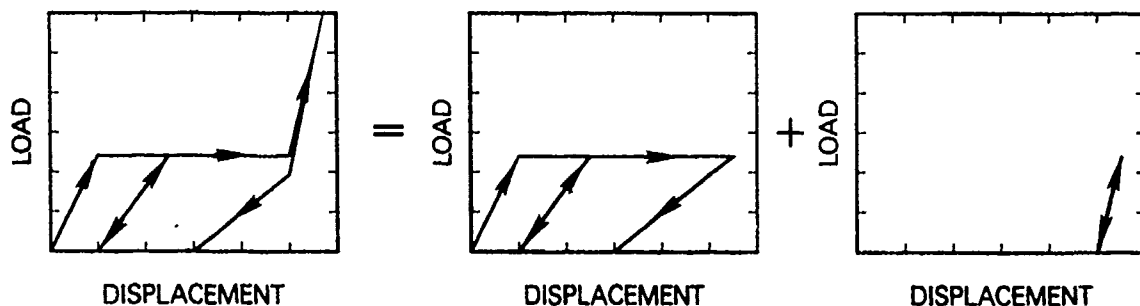


Figure 1a. Foam Response. Figure 1b. Skeleton Response and Polymer/Air Response.

A plasticity model for polyurethane foam (Neilsen et al., 1987) was developed using a phenomenological approach to capture not only the elastic response of foam but also the permanent deformation generated when these materials are subjected to crushing loads. However, this model was not able to capture the stiffness variations that are generated; thus, a foam model based on continuum damage mechanics was recently developed.

Continuum damage models have been used to describe the behavior of a wide variety of materials from concrete to metals. A complete description of continuum damage models can be found in Kachanov, 1986, or Krajcinovic, 1989. Here a continuum damage approach is used to capture not only the elastic response of a foam but also the permanent deformation and damage that are generated during crush. The foam model is based on a decomposition of the foam into two parts: a skeleton and a diffuse continuum in parallel (Figure 1b). The continuum is not activated until the voids present in the foam are closed. A continuum damage model is used to describe the behavior of the skeleton. This damage model is expressed in terms of principal stresses. As the skeleton is crushed, the cell walls are damaged resulting in both permanent deformations and a reduction in the stiffness of the skeleton. At some strain level the volume fraction of solid material approaches 1.0, and the continuum part of the model begins to carry a significant amount of load. Thus, the foam stiffness actually increases even though the skeleton stiffness continues to decrease. The new model was implemented in both static and dynamic finite element codes. Finite element analyses of a shipping container accident will be presented.

## REFERENCES

- Gibson, L.J. and Ashby, M.F., *Cellular Solids*, Pergamon Press, 1988.
- Kachanov, L.M., *Introduction to Continuum Damage Mechanics*, Martinus Nijhoff Publishers, 1986.
- Krajcinovic, D., *Damage Mechanics*, Mechanics of Materials, 8, 1989.
- Neilsen, M.K., Morgan, H.S. and Krieg, R.D., *A Phenomenological Constitutive Model for Low Density Polyurethane Foams*, SAND86-2927, Sandia National Laboratories, 1987.
- Warren, W.E., Kraynik, A.M. and Stone, C.M., *A Constitutive Model for Two-dimensional Non-linear Elastic Foams*, Journal of the Mechanics and Physics of Solids, 37, 1989.

# A STRAIN-STRESS FORMULATION OF THE CONSTITUTIVE LAW FOR INCOMPRESSIBLE, HYPERELASTIC SOLIDS

Janet A. Blume and David Reynolds  
Division of Engineering  
Brown University  
Providence, Rhode Island 02912

## Abstract

In a usual constitutive formulation for nonlinearly elastic materials, one prescribes stress as a function of strain, through a stress-response function. The constitutive response for a class of materials may be described instead by a *strain-response function*, which gives the right Cauchy-Green strain tensor as an algebraic function of the 2<sup>nd</sup> Piola-Kirchhoff stress tensor. Such materials are referred to as *stress-determined materials*. This type of material characterization proves to be an effective way of handling the constraint of incompressibility.

Stress-determined materials which do not dissipate energy in any stress cycle are said to be hyperelastic, and this implies that the strain-response function is the tensor-gradient of a scalar function of the 2<sup>nd</sup> Piola-Kirchhoff stress. Incompressible materials in this class are those for which the right Cauchy-Green strain-response function evaluates to tensors with unit determinant for all values of its argument. Conditions on the strain-response function and the generating scalar potential that are necessary and sufficient for incompressibility are derived. These conditions are in the form of restrictions on the way these functions depend upon their arguments. For the subclass of incompressible materials with *invertible* strain-stress relations, it is shown that the motion determines the stress in a constitutive sense only to within an arbitrary pressure field. The existence of this undetermined pressure field is generally assumed in a traditional formulation of incompressible hyperelastic materials.

## **Eshelby's Tensor in Materials of Grade 2**

Marcelo Epstein\* and Gérard A. Maugin\*\*

The theory of material uniformity can be used as a framework for the geometric description of continuous distributions of dislocations. Within such a framework it is possible [1, 2] to obtain a measure of the forces associated with the inhomogeneities in terms of a rigorously defined tensor of Eshelby. It appears, however, that as long as the analysis is restricted to simple elastic materials, continuous distributions of disclinations would be ruled out. In the present work we, therefore, extend the formulation to grade 2 materials and show that, associated with the appearance of a new field of material isomorphisms, a new Eshelby tensor can be naturally defined. This new tensor is then shown to satisfy an identity which is a generalization of its counterpart as presented in [1, 2].

### **References**

1. Epstein, M. and Maugin, G.A., C.R. Acad. Sci., Paris, 310, II, 1990, p. 675-678.
2. Maugin, G.A. and Epstein, M., "The Electroelastic Energy-Momentum Tensor", Proc. Royal Soc., London (in press).

\* Department of Mechanical Engineering, The University of Calgary, Calgary, Alberta T2N 1N4 Canada

\*\* Laboratoire de Modélisation en Mécanique, U.R.A. CNR9 229, Université Pierre et Marie Curie, Tour 66, 4 Place Jussieu, 75252, Paris, Cedex 05 France

FOR PRESENTATION AT THE MIDWEST MECHANICS CONFERENCE  
UNIVERSITY OF MISSOURI - ROLLA OCTOBER 6 - 9, 1991

**DERIVATION OF HIGHER ORDER GRADIENT CONTINUUM THEORIES  
FROM DISCRETE MICROSCOPICAL MODELS**

By:

Nicolas Triantafyllidis  
Aerospace Engineering Dept.  
The University of Michigan  
Ann Arbor, MI 48109 - 2140

A wide range of solids exhibits localization of deformation (in the form of shear bands) when adequately stressed. Within the classical continuum mechanics framework, where the strain depends solely on the deformation gradient, the onset of localization is characterized by the loss of ellipticity of the governing equations for the corresponding boundary value problem. The classical nonlinear continuum models provide no size for the localization of deformation zone, thus rendering the numerical study of the postlocalization behavior difficult and strongly dependent on the employed finite element mesh.

One way to correct the aforementioned shortcomings in order to permit the study of the postlocalization behavior for these solids is to introduce a higher order gradient in the model, thus abandoning the classical local action hypothesis. Various such phenomenological continuum models have been proposed which give a satisfactory description of the evolution of the postlocalization behavior for the solids in question. The purpose of this work is to provide a consistent method to derive those higher order gradient continuum models from the corresponding microscopical models.

In this presentation a one dimensional microscopical model of nonlinear springs is "averaged up" in order to provide the corresponding nonlinear continuum theory with the higher order gradients in the displacement. The resulting continuum model where only up to second order displacement gradients have been retained, is employed to solve the boundary value problem of the stretching of a finite length bar. The results are compared to the solution of the discrete model with the same length. An excellent agreement is found between the exact discrete model and the second order gradient continuum model up to the full development of the localized deformation zone. The continuum model encounters difficulties in modelling the propagation of the localized zone past a certain strain for a class of materials.

## **HYPER-ELASTIC BODIES WITH COUPLE STRESSES**

**Gautam Batra  
212 Bancroft Hall  
Department of Engineering Mechanics  
University of Nebraska-Lincoln  
Lincoln, NE 68588-0347**

In ordinary applications of continuum mechanics, one frequently assumes that all torques arise as moments of forces. It is possible to allow greater generality in assumption by supposing that the action of part of a body on one side of an imagined surface on the part of the body on the other side of it is equipollent to the action of a traction field as well as a field of couples. This field of couples gives rise to couple stresses. In polarized media an electromagnetic field, say, may exert couples which are independent of forces, thus supplementing body forces by body couples.

We review results from the recent literature on this subject. Variational formulations and the effects of internal constraints are emphasized.

EFFECT OF INJECTED BUBBLES ON LIQUID FLOW  
VELOCITIES IN AN AGITATED MIXING VESSEL

Gary K. Patterson, Chemical Engineering Department  
University of Missouri-Rolla

Comparisons of experimental measurements of liquid velocities in the presence of bubbles and of numerical simulations of the same systems showed close correspondence of the effects of the bubbles. The measurements were made by laser-Doppler anemometry in a stirred vessel with gas sparged in through small holes below a radial flow (Rushton) impeller. At the bubble density where reliable measurements could be made, the effects on liquid velocities were small but evident. The effects in the simulations were very similar. Simulations at much higher bubble densities (higher gas injection rates) showed very strong effects on liquid velocities, particularly near the vessel wall. Where the bubbles are in high concentration, their upward movements drag liquid upward at increased velocities.

Even though detailed liquid velocities from experiment were not available at the high gas injection rates, correlations of experimental gas bubble distributions and of total gas bubble holdup in the vessel were compared with the predictions from the simulations. The holdup levels were of approximately correct values, but the variations with gas injection rate did not have the correct slope. Future simulations must better account for bubble-bubble interactions in order to improve this aspect.

# A NUMERICAL SOLUTION FOR TWO-DIMENSIONAL FLOW PAST A FINITE STEP

**Bashar S. AbdulNour**  
Assistant Professor  
Department of Mechanical Engineering  
University of Wyoming  
Laramie, WY 82071-3295

The steady, viscous, incompressible, two-dimensional, confined flow past a finite step is considered in this study. The problem is modeled as a laminar flow in the entry region of a rectangular channel with uniform inlet velocity upstream and a fully-developed parabolic profile downstream, as illustrated in Fig. 1. Flows in the presence of obstructions are identified with separation. When a finite step is fixed to the channel's lower boundary, distinct separated regions with pronounced eddies of recirculating fluid are developed on both sides. The main purpose of this investigation is to provide a detailed description of the flow field by solving the describing equations of motion.

The solution can be obtained numerically by considering the continuity and the Navier-Stokes equations along with the appropriate boundary conditions. The vorticity-stream function formulation is selected for the treatment of the problem. For two-dimensional flows, the z-component of the vorticity vector is defined as  $\zeta(x,y,t) = \partial v / \partial x - \partial u / \partial y$ , and the stream function  $\psi(x,y,t)$  is introduced through:  $u = \partial \psi / \partial y$  and  $v = -\partial \psi / \partial x$ , where  $u$  and  $v$  are the velocity components in the  $x$ - and  $y$ -directions, respectively. This approach is attractive since it reduces the number of equations to be solved from three to two; and, second it ensures that the continuity equation is automatically satisfied. From substituting the above definition for  $\psi$  into the expression of  $\zeta$  and the Navier-Stokes equation, we obtain the Poisson-type *stream function equation* and the  $z$ -component *vorticity equation*, respectively, i.e.,

$$\frac{\partial^2 \psi}{\partial x^2} + \frac{\partial^2 \psi}{\partial y^2} = -\zeta, \quad \frac{\partial \zeta}{\partial t} + \frac{\partial \psi}{\partial y} \frac{\partial \zeta}{\partial x} - \frac{\partial \psi}{\partial x} \frac{\partial \zeta}{\partial y} = \frac{1}{\text{Re}} \left( \frac{\partial^2 \zeta}{\partial x^2} + \frac{\partial^2 \zeta}{\partial y^2} \right)$$

where the Reynolds number  $\text{Re} = HU/\nu$ ;  $H$  is the channel height,  $U$  is the velocity at the inlet, and  $\nu$  is the kinematic viscosity. The result is a nonlinear system of two dimensionless partial differential equations which involve the two unknowns  $\zeta$  and  $\psi$ . The time derivatives are retained in the equations since the time marching numerical methods require the presence of the time derivatives. In such a case, the time is fictitious and each time step is equivalent to an iteration. The solution of the unsteady equations for large time is considered to be the solution to the steady-flow problem.

To obtain a solution to the above describing equations, we must prescribe the appropriate initial and boundary conditions. In dimensionless terms, the inlet is identified to exist at  $x = 0$ , the lower boundary at  $y = 0$ , and the upper boundary at  $y = 1$ . The location of the downstream boundary is chosen at  $x \geq L_e$ , where  $L_e$  is the entrance length defined as the distance from the inlet to the point where the centerline velocity reaches 99% of the fully-developed parabolic centerline value. The initial conditions are derived from the quiescent state; they are given in terms of the stream function and the vorticity as  $\psi(x,y,0) = y$  and  $\zeta(x,y,0) = 0$ . The velocity boundary conditions are the prescribed velocities upstream and far downstream, and the no-slip boundary conditions on both the lower and upper boundaries. The boundary conditions on  $\zeta$  and  $\psi$  are derived from the known velocity boundary conditions. These boundary conditions are summarized below.

$$\begin{aligned} \psi(0,y,t) &= y, & \psi(x,y,t) &= 3y^2 - 2y^3, & \psi(x,0,t) &= 0, & \psi(x,1,t) &= 1, \\ \zeta(0,y,t) &= 0, & \zeta(x,y,t) &= 12y - 6, & \zeta(x,0,t) &= -\frac{\partial^2 \psi}{\partial y^2}, & \zeta(x,1,t) &= -\frac{\partial^2 \psi}{\partial y^2}. \end{aligned}$$

In the presence of a step, boundary conditions on the lower boundary must be modified. While  $\psi$  on the lower boundary remains equal to zero, the vorticity on the upstream and downstream faces of the step becomes  $\zeta(x,y,t) = -\partial^2 \psi / \partial x^2$ . The advantage gained by eliminating the pressure and its boundary conditions from the describing equations shows up as a difficulty in expressing the boundary conditions on the vorticity. On the lower and upper boundaries, these boundary conditions are not known explicitly. However, they are modified for subsequent use in the numerical solution by expanding in a Taylor series to express the second order derivatives at the wall in terms of the stream function and vorticity at nodal points adjacent to the wall. The above procedure yields the well known *Woods' condition*.



The finite-difference approximation is selected to solve the describing equations numerically. The finite-difference equations are obtained from the partial differential equations of motion using second-order discretizations. After expressing the initial and boundary conditions in finite-difference form, a solution to the system of equations can be pursued to yield the vorticity and the stream function. From this information the velocity field can be calculated. The Alternating-Direction Implicit (ADI) method is used to solve the vorticity equation while the iterative Successive Over-Relaxation (SOR) method is used to solve the stream function equation. The present numerical solution is second-order accurate in its entirety since both the difference equations and boundary conditions have second-order accuracy. For large Reynolds numbers, however, it is essential to ensure the stability of the numerical solution by maintaining the diagonal dominance of the system of equations. An upwind differencing applied to the convective terms in the vorticity equation helps avoid numerical instability. Second-order accuracy is then recovered at convergence via a correction technique. The power of this ADI/SOR computational scheme lies in the structure of the difference equations, which for all Reynolds numbers, yields a diagonally dominant system of linear algebraic equations. The use of accelerating parameters artificially inserted into the difference equations, can further improve the convergence characteristics of the numerical procedure; such parameters expand the domain of convergence and improve the computational speed as well. The optimum values of these parameters depend on the shape of the computational domain, mesh size, and the Reynolds number. They are determined primarily by numerical experimentation.

A computational grid is constructed with a mesh size carefully selected since the total number of nodal points is limited by the available computer capabilities. A rectangular grid with lines parallel to the  $x$ - and  $y$ -axes, is superimposed to exactly fit the geometry of the flow problem. The vorticity, stream function, and velocity components are calculated at each nodal point for Reynolds numbers ranging between 20 and 2000. A uniform grid with a spacing size  $h = 0.05$  is used. To ensure that the solution is not influenced by the downstream boundary condition, we select the location of the downstream boundary sufficiently larger than  $L_2$  such that the solution at the downstream end does not depend on  $x$ ; the number of meshes in the  $x$ -direction is equal to  $Re/(20h)$ . Convergence is attained by advancing the solution in time until it no longer varies significantly. An error criterion is used to decide whether additional time steps are necessary; a tolerance error  $\epsilon = 10^{-6}$  is selected as a condition for convergence. The finite step of variable height and length is defined to exist between the streamwise locations  $x = X_1$  and  $x = X_2$  along the lower boundary. As a result, the flow becomes separated before and aft of the step. The size of these separated regions depends on the Reynolds number, the height ( $B$ ), and length ( $D$ ) of the step; the separated region upstream of the step is considerably smaller in size than that aft of the step.

Results demonstrated that for a fixed step location  $X_1$  in the range of  $Re$  considered, the length  $L_1$  of the separated region in front of the step appears to be uninfluenced by an increase in  $D$  while the length  $L_2$  of the separated region aft of the step is slightly decreased with an increase in  $D$ . Conversely, increasing the height of the step causes the size of the aft separated region to increase, as expected. In both of the above cases, the length of the front separated region is observed to be somewhat fixed with value  $L_1 \approx 0.10$ . The size of the separated regions is unaffected by the streamwise location of the step. This result is confirmed by placing the step further upstream and in the fully-developed flow region. The increase in the  $Re$  is accompanied by an increase in the length of the separated region aft of the step. The size of the separated region upstream of the step, however, seems to be relatively independent of the Reynolds number. Vorticity contours show that the changes in the flow field are most pronounced in the vicinity around the step. Velocity vectors also emphasize that the velocity gradients are high in the vicinity of the step as exhibited by the direction of the vectors. In addition, streamwise velocity profiles reveal that the presence of a step has an upstream effect on the shape of the velocity profile and that the velocity distribution becomes parabolic at a sufficient distance downstream. A typical flow streamlines exhibiting the separated regions are shown in Fig. 2 (AbdulNour, 1990†).

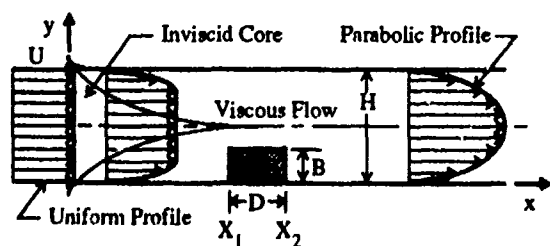


Figure 1. The flow problem in a two-dimensional channel with a finite step.

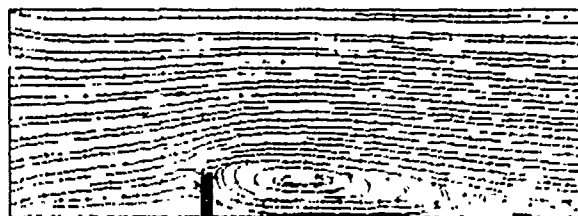


Figure 2. Flow separation due to a finite step;  $X_1 = 1.0$ ,  $B = 0.20$ ,  $D = 0.05$ ,  $Re = 200$ .

† AbdulNour, B. S., 1990, "The Numerical Solution of Confined Laminar Flow Past a Moving Boundary", Ph.D. Dissertation, Department of Mechanical Engineering, Michigan State University, East Lansing, MI.

# TURBULENT PIPE FLOW OF A PARTICULATE SUSPENSION

Manohar Gadiraju,<sup>1,2</sup> John Peddieson, Jr.,<sup>2</sup>  
and Sastry S. Munukutla<sup>2,3</sup>

<sup>1</sup>Bristol Babcock, Inc., Watertown, Connecticut 06795

<sup>2</sup>Department of Mechanical Engineering and <sup>3</sup>Center for Electric Power, Tennessee Technological University, Cookeville, Tennessee 38505

This paper deals with fully developed, steady, vertical, turbulent flow of a particulate suspension in a circular pipe of radius  $a$  due to a pressure gradient  $G$  and a gravitational force per unit mass  $g$ . The particle phase exhibits a small volume fraction and a uniform in-suspension density  $\rho_p$ . The fluid phase is an incompressible liquid of density  $\rho$  and dynamic viscosity  $\mu$  (or kinematic viscosity  $\nu = \mu/\rho$ ). The suspension exhibits a linear interphase drag mechanism characterized by a momentum relaxation time  $\tau$ .

The flow problem described above was simulated by solving the boundary value problem

$$((1+\nu_t)rv')'/r + \kappa\alpha(v_p - v) = 4(\lambda - 1), ((\beta + \nu_{p,t})rv_p')'/r + \alpha(v - v_p) = 4\lambda \quad (1)$$

$$v'(0) = v_p'(0) = v(1) = v_p(1) = 0 \quad (2)$$

In (1) and (2)  $r$  is a radial coordinate (normalized by  $a$ ), a prime denotes differentiation with respect to  $r$ ,  $v$  and  $v_p$  are the velocities of the fluid and particulate phases (normalized with respect to the characteristic velocity  $v_c = Ga^2/(4\mu)$ ) respectively,  $\beta$  is the particle phase kinematic viscosity (normalized by  $\nu$ ),  $\nu_t$  and  $\nu_{p,t}$  are the kinematic eddy viscosities of the fluid and particulate phases (also normalized by  $\nu$ ) respectively, and

$$\alpha = a^2/(\nu\tau), \kappa = \rho_p/\rho, \lambda = \rho g/G \quad (3)$$

Equations (1a,b) are the axial balances of linear momentum for the fluid and particulate phases respectively, (2a,b) are the centerline symmetry conditions, and (2c,d) are the wall no-slip conditions ((2d) being used tentatively due to lack of definitive information about particle phase surface conditions). The boundary value problem consisting of (1) and (2) was solved by an iterative finite difference approach.

Numerical solutions were obtained using four different algebraic two phase turbulence models reported in the literature ([1],[2],[3],[4]). Predictions of velocity profiles and friction factors were found to exhibit considerable model dependence, indicating a need for further work in two-phase turbulence modeling. The numerical method was found to work well for all models.

Figures 1 and 2 show some typical velocity profiles computed using the Melville-Bray model. Here the velocities  $v$  and  $v_p$  are normalized by their mean values  $\bar{v}$  and  $\bar{v}_p$  respectively and  $Re_m = (2a\bar{v}_c/\nu)\bar{v}$ . As expected, the degree of equilibrium between the phases increases with the inverse stokes number  $\alpha$ . It is interesting that the velocity profiles of both phases become less uniform as the particle loading  $\kappa$  is increased.

#### REFERENCES

- [1] P.R. OWEN, J. Fluid Mech. 39, 407 (1969).
- [2] W.K. MELVILLE and K.M.C. BRAY, Int. J. Heat Mass Trans. 22, 647 (1979).
- [3] Y.D. CHOI and M.K. CHUNG, ASME J. Fluids Engr. 105, 329 (1983).
- [4] K.B. LEE and M.K. CHUNG, Int. J. Multiphase Flow 13, 275 (1987).

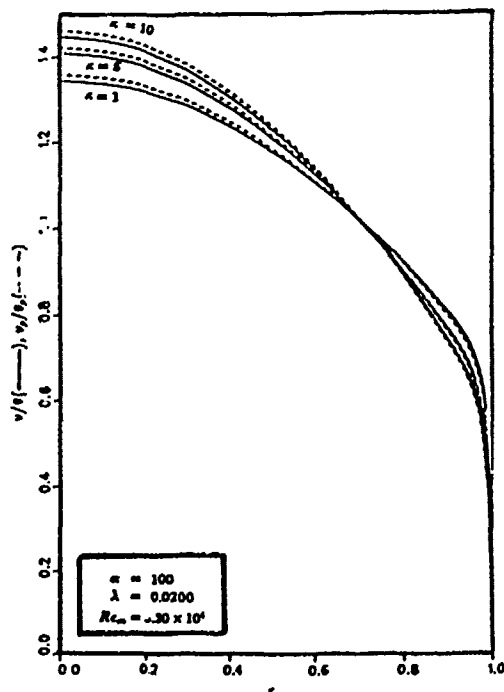


Figure 1. Normalized Velocity Profiles using Melville-Bray Model

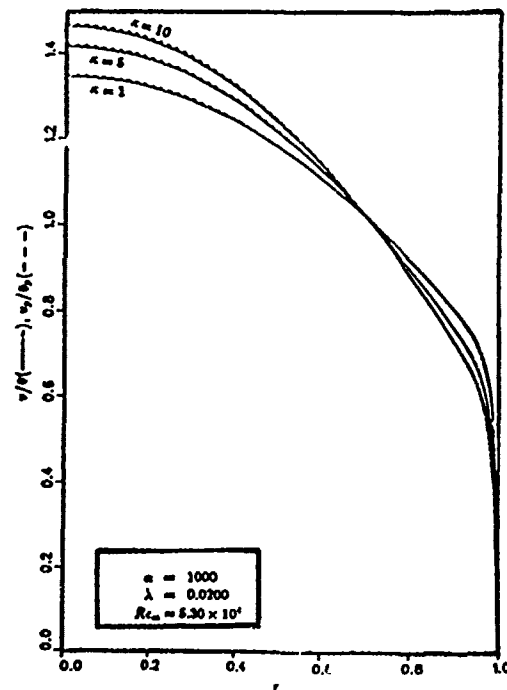


Figure 2. Normalized Velocity Profiles using Melville-Bray Model

# STEADY VISCOUS LAMINAR FLOW IN AN ANNULAR HELICOIDAL PIPE

*H. C. Topakoglu and H. P. Mohamadian  
Mechanical Engineering Department  
Southern University, Baton Rouge, LA 70813*

The solution of the secondary flow stream function in a helicoidal pipe of circular annular cross section based on the first term of the expansion of secondary flow is obtained. For a selected set of parameters of the flow, the stream lines are plotted. It is found that in four different regions of the cross section, different types of stream lines are developing. These regions and the types of stream lines are discussed.

## Introduction

A literature survey including Berger, Talbot & Yao [1] and Kakac, Shah & Aung [2] indicates that the solution of the secondary flow stream function in a helicoidal pipe of annular cross section is not presently available in engineering publications. The subject, besides its obvious scientific interest, has considerable engineering applications especially in heat exchangers using helicoidal annular pipes. In the case of an ordinary curved pipe of annular cross section, the secondary flow stream function and the shape of the stream lines have been given by Topakoglu [3]. In this paper, the torsion effects on the secondary flow stream function for a helicoidal annular pipe in addition to the curvature effect are presented.

## Analysis

The basic formulation and analysis of a viscous flow in a helicoidal pipe of full circular cross section is presented by Topakoglu and Lee [4]. In that work, the flow parameters; the primary flow dimensionless velocity component  $w$ , and the secondary flow dimensionless stream function  $\psi$  are expanded in terms of a combined parameter of curvature and torsion ( $\lambda$ ) as

$$w = w_0 + \lambda w_1 = \lambda_2 w_2 + \dots \text{ and } \psi = \lambda \psi_1 + \lambda^2 \psi_2 + \dots \text{ where } \lambda = (1/\sigma)\cos^2\alpha \quad (1)$$

in which  $\sigma$  and  $\alpha$  are dimensionless radius and the helix angle of the center line helix of the helicoidal pipe, respectively. Following the formulation of reference [4] the first term of the expansion of the dimensionless secondary stream function after separating the torsion part as

$$\psi_1 = \phi_1 + \chi_1 \tan\alpha \quad (2)$$

satisfies the following set of differential equations:

$$\nabla^4 \phi_1 = (w_0^2)_x, \quad \nabla^4 \chi_1 = 2\nabla^2 w_0 \quad (3)$$

where  $w_0$  indicates the dimensionless velocity for a straight pipe of annular cross section and  $\nabla^2$  and  $\nabla^4$  represent the Laplacian and Bilaplacian operators in the plane of the cross section of the helicoidal pipe, respectively. The subscript  $x$  indicates the partial differentiation with respect to this variable  $x$  which represents the dimensionless vertical rectangular coordinate in the plane of the cross section. The solutions of the Equ. (3) are subjected to the following boundary conditions: for  $r = 1$   $\phi_1 = 0$ ,  $\partial\phi_1/\partial r = 0$  and  $\chi_1 = 0$ ,  $\partial\chi_1/\partial r = 0$  (4)

in which  $r$  indicates the dimensionless radial coordinate in the cross section of the helicoidal pipe.

The solutions of Equ. (3) under the specified boundary conditions (Equ. 4) are obtained as

$$\phi_i = g_i(r) \sin \theta \quad \text{and} \quad \chi_i = c_i(r) \quad (5)$$

where  $\theta$  represents the polar coordinate in the plane of the cross section and  $g_1(r)$  is a function identical to the dimensionless stream function of a curved pipe as given in the reference [3]. The part  $\chi_1$  represents the torsion effect on the stream function and is equal to

$$e_1 = -(ke/8)(1-r^2)^2 \quad (6)$$

in which  $Re$  represents the Reynolds Number of the flow as defined in the reference [3].

## Results and Discussion

On the basis of the obtained functions  $\phi_1$  and  $\chi_1$  typical secondary flow stream lines are plotted and presented in Figure 1. The following selected parameter were used:

Centerline helix angle  $\alpha = 45^\circ$ ;  
Dimensionless core radius  $\omega = 0.2$ ; Reynolds  
number  $Re=100$ .

It has been found that the torsion effect is completely modifying the symmetrically arranged quadruple secondary flow vortices of an ordinary curved pipe [3] into a non-symmetric configuration, in which the cross section is divided into four distinct regions. In the first region immediately next to the core the streamlines are circle like closed lines enclosing the core. The second region contains a group of major vortices which are positioned above the core. The next region, the streamlines again exhibit circle like closed lines enclosing the major vortices and the core. In the remaining region of the cross section which is positioned below the core a group of minor vortices are formed. The orientation of the cross section in Figure 1 is such that the vertical direction corresponds to the axial direction of the cylinder on which the helicoidal pipe is based.

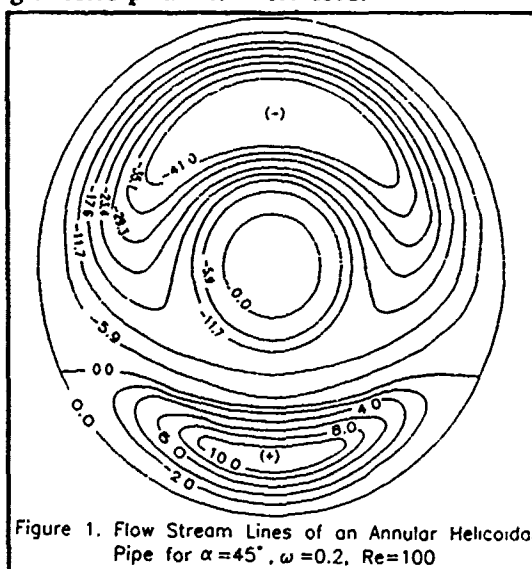


Figure 1. Flow Stream Lines of an Annular Helicoidal Pipe for  $\alpha=45^\circ$ ,  $\omega=0.2$ ,  $Re=100$

## Acknowledgement

The result presented in this paper were obtained in the course of research sponsored by The National Science Foundation, Washington, D.C., under the grant R11-8305297 to Southern University and its precursor.

## References

1. Berger, S., Talbot, L., & Yao, L., *Ann. Rev. Fluid Mech.* 15, 1983.
2. Kakac, S., et al, *Handbook of Single-Phase Conv. H.T.*, John Wiley & Sons 1987
3. Topakoglu, H.C., *J. Math. Mech.* 16; 1321-38, 1967.
4. Topakoglu, H.C., & C.F. Lee, *Int. J. Energy Fluid Mech.* (Submitted for publication, 1991)

# "BURGERLENT" CONCENTRATION SPECTRA IN THE HIGH WAVENUMBER REGIME FOR $Sc = 0.1, 1.0, 10$

Weiguo Zheng and X B Reed, Jr., Chemical Engineering Department  
University of Missouri-Rolla, Rolla, MO 65401-0249

Kolmogorov's universal statistical equilibrium hypotheses prevail at sufficiently high turbulence Reynolds numbers. The behavior of the high wavenumber part of the fluctuating velocity measurements is  $k^{-\frac{5}{3}}$ , as predicted for the inertial subrange; the behavior of the viscous cutoff at still higher wavenumbers is somewhat less clear. High wavenumber temperature and concentration spectra can not be measured because of inadequate spatial and temporal resolution at high  $Re$ . They can not be computed with sufficient resolution on the current generation of supercomputers, either. Consequently, it is not possible to decide amongst the theories (which depend upon  $Pr/Sc$  in the two spectral ranges) of Batchelor, Batchelor, Howells, and Townsend, and Gibson.

Burgers' equation has been studied widely in theoretical turbulence as a one-dimensional paradigm for the Navier-Stokes equations [1 - 3 and references therein]. We consider a random passive additive field, here called  $c$  for concentration, convected by random solutions to Burgers' equation

$$u_t + uu_x = Re^{-1} u_{xx} \quad (1)$$

in the following two versions,

$$c_t + uc_x = Pe^{-1} c_{xx}, \quad c_t + (uc)_x = Pe^{-1} c_{xx} \quad (2),(3)$$

in which  $Pe = ScRe$ . Initially,  $Re = 400$ , and two values of the Schmidt number are considered,  $Sc = 0.1$  and  $Sc = 10$ . The concentration spectrum  $E_{cc}(k)$  at  $Sc = 1$  is the same as the energy spectrum  $E(k)$  for Eq.(2), which for Burgers' equation is  $k^{-2}$  in the inertial subrange<sup>(1)</sup> and which has an exponential viscous cutoff<sup>(2)</sup>.

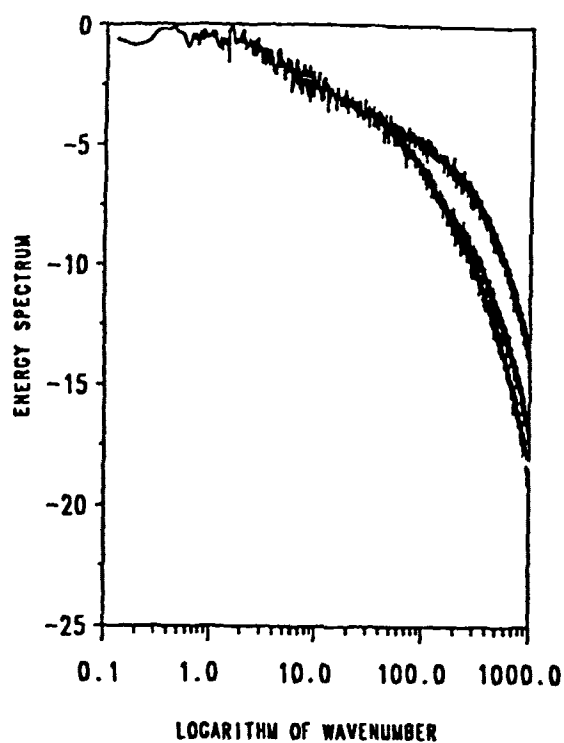
If  $Sc < 1$ , the  $E_{cc}(k)$  should fall away from  $E(k)$  before the viscous cutoff ( $Sc = 0.1$ , log-log), whereas if  $Sc > 1$ , then  $E_{cc}(k)$  should roll off before  $E(k)$  ( $Sc = 10$ , log-log). By the same token,  $E_{cc}(k)$  for  $Sc < 1$  should be lower than  $E(k)$  in the diffusive cutoff and is ( $Sc = 0.1$ , log-semi) and should be higher for  $Sc > 1$  and is ( $Sc = 10$ , log-semi). The analogs of the arguments of Corrsin and Obukhov would suggest  $E_{cc}(k) \sim k^{-2}$ , but we show here that  $E_{cc}(k)$  has an exponential cutoff for  $Sc \geq 1$ , as well as for  $Sc = 1$ .

(1) Y.-C. Shih and X B Reed, Jr., "Solution to the Piecewise Linear Continuous Random Initial Value Problem for Burgers' Equation", *Phys. Fluids* 28, 2088-2099 (1985)

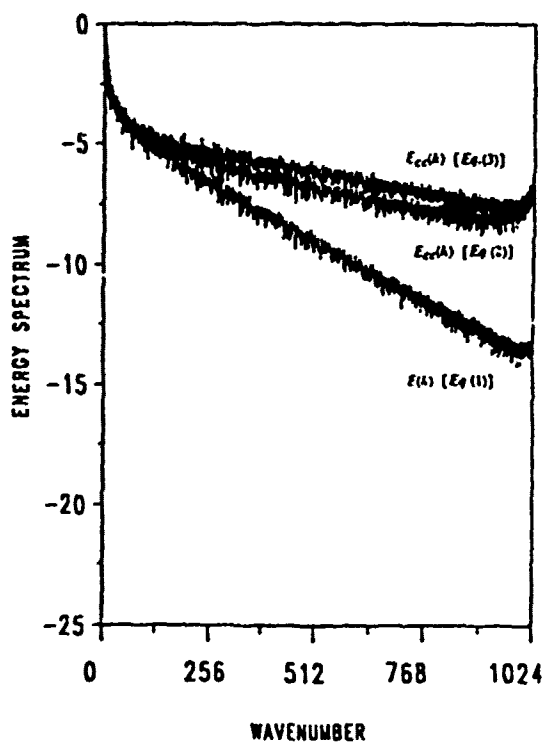
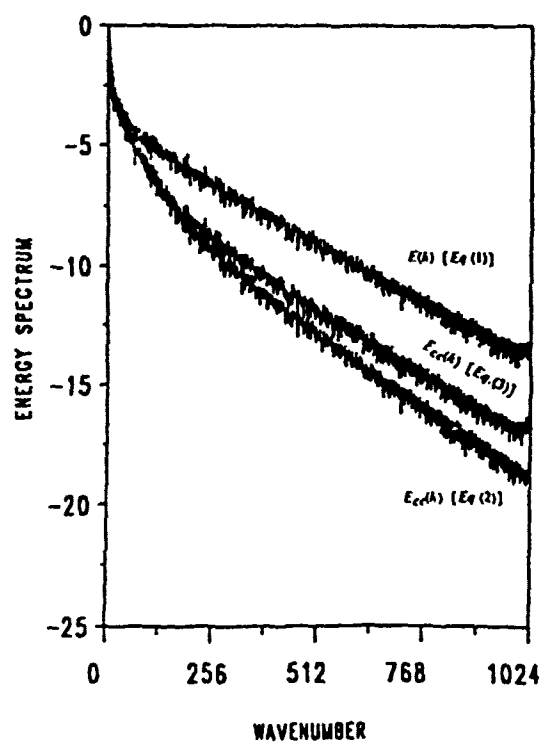
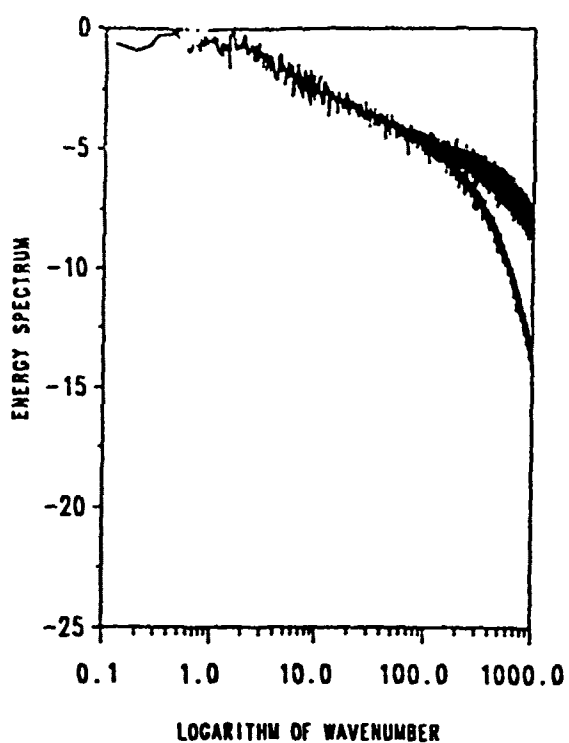
(2) S. Keleti and X B Reed, Jr., "Spectral Properties of Exact Random Solutions to Burgers' Equation for Modified Thomas Initial Conditions", *Computers & Fluids*, Vol. 16, No.2, pp.147-173, (1988)

(3) W. Zheng and X B Reed, Jr., "Some Observations of Bispectral Behavior of Large Ensembles of Exact Solutions to Burgers' Equation for Random Initial Conditions", accepted by *Phys. Fluids*

ENERGY SPECTRUM FOR SC-01, T-101, RE-400



ENERGY SPECTRUM FOR SC-10, T-101, RE-400



# A HIGH-PRECISION FCT FINITE ELEMENT METHOD FOR SHOCK CAPTURING

Tony W.H. Shyu, Hsin-Chuan Kuo

Institute of Naval Architecture, National Taiwan University,  
73 Chou-Shan Rd., Taipei, Taiwan, R. O. C.

## ABSTRACT

A Flux-Corrected Transport Finite Element Method (FCT-FEM) is presented for obtaining high resolution shock solution. The investigated FCT techniques are based on those proposed by Boris et al. and Zalesak. The simulation is currently addressed on one-dimensional analysis. The computed results for inviscid Burgers equation, shock tube and blasting waves problems are all agreed well with analytic solutions.

## INTRODUCTION

Numerical capturing of shocks in high speed gas dynamic flowfield has been successfully made, at least in the context of finite difference method, using TVD [1] etc. schemes. The present work is addressed on incorporating FCT technique to Taylor-Galerkin weak formulation that discontinuities can be accurately captured.

## BASIC FORMULATION

One dimensional Euler equations [1] are analyzed. The resulting implicit weak Taylor-Galerkin discretization equations for  $\underline{U} = [\rho, \rho u, \rho e]^T$  can be represented by  $\underline{M} \partial \underline{U} = \underline{R}$ . The expressions of  $\underline{M}$  and  $\underline{R}$  can be found in [2]. Harten's artificial viscosity [1] in  $\underline{R}$  is employed for obtaining high and low-order solutions which are required in FCT anti-diffusive technique. Both Boris [3] and Zalesak [4] FCT algorithms were conducted.

## NUMERICAL RESULTS

The computed solution at  $t = 1.1$  for inviscid Burgers equation  $u_t + (1/2 u^2)_x = 0$  is illustrated in Fig.1 where the investigated initial condition is  $u(0, x) = 1/4 + 1/2 \sin(\pi x)$ . The computed solution at  $t = 0.24$  for shock tube problem is illustrated in Fig.2. The investigated initial condition is  $\underline{U}(0, x) = [1, 0, 2.5]^T$ ,  $x \in [0, 0.5)$  and  $\underline{U}(0, x) = [0.125, 0, 0.25]^T$ ,  $x \in [0.5, 1.0]$ . The computed solution at  $t = 0.038$  for two interacting blast waves is illustrated in Fig.3. The blast waves are initially defined by  $\underline{U}(0, x) = [1, 0, 2.5]^T$ ,  $x \in [0, 0.1)$ ;  $\underline{U}(0, x) = [1, 0, 0.25]^T$ ,  $x \in [0.1, 0.9)$ ;  $\underline{U}(0, x) = [1, 0, 250]^T$ ,  $x \in [0.9, 1]$ .

## CONCLUSIONS



The developed FCT-FEM computer code can accurately capture the discontinuities in the three investigated benchmark problems. The extension of present formulation to two-dimensional analysis is on-going.

## REFERENCES

- [1] A. Harten, High resolution schemes for hyperbolic conservation laws, J. Comput. Phys., 49, 357-393, 1984.
- [2] Hsin-Chuan Kuo, A FCT finite element analysis for compressible Euler equations, Master thesis, Institute of Applied Mechanics, National Taiwan University, R. O. C., June 1990.
- [3] J. P. Boris, and D. L. Book, Flux-corrected transport I: SHASTA, A fluid transport algorithm that works, J. Comput. Phys., 11, 248-283, 1973.
- [4] S. T. Zalesak, Fully multidimensional flux-corrected transport algorithm for fluids, J. Comput. Phys., 31, 335-362, 1979.

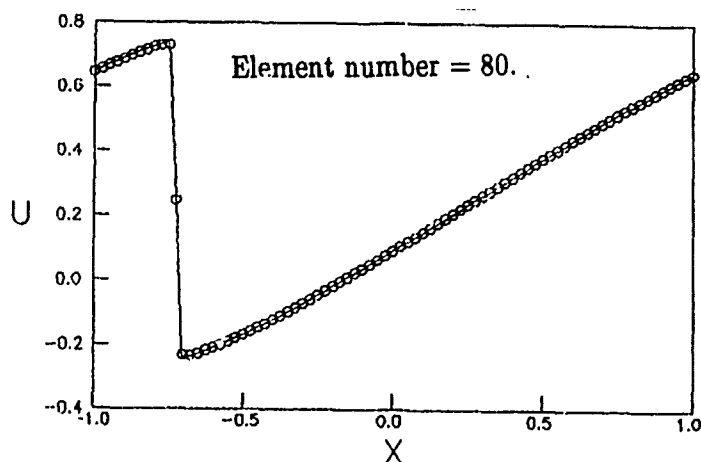


Fig.1 Computed velocity distributions  
(•) by Boris's FCT technique  
and analytic data (—).

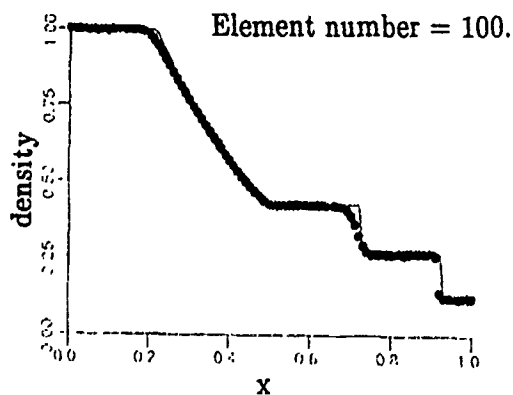


Fig.2 Computed density distributions  
(•) by Zalesak's FCT technique  
and analytic data (—).

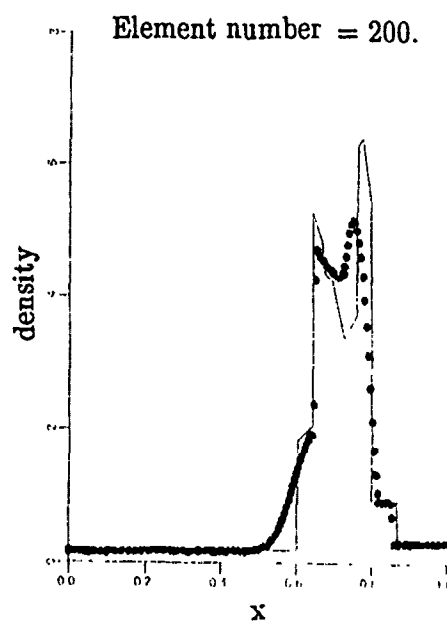


Fig.3 Computed density distributions  
(•) by Zalesak's FCT technique  
and analytic data (—).

# VIBRATING ROD IN A CYLINDRICALLY BOUNDED, VISCOUS, COMPRESSIBLE FLUID

Jörg WAUER

Institut für Technische Mechanik, Universität Karlsruhe  
Kaiserstraße 12, W-7500 Karlsruhe 1

Dynamic fluid structure interaction is involved with interesting phenomena, e.g., flutter instabilities for fluid flow past flexible structures or added mass effects for vibration problems. While flow problems are commonly dealt with by a spatial (Eulerian) approach, the interaction of structural members coupled with finite fluid regions, in which the fluid initially is in rest, represents a category where a material (Lagrangian) description is adequate.

Liquid or gas storage tanks and off-shore structures surrounded by water are typical engineering applications of this second sphere. But the complex geometry then requires purely numerical investigations. In contrast, a centrally supported, cylindrical bar in a cylindrically confined fluid region which is analyzed here, is the basic example to investigate the most aspects of the vibrational behaviour analytically.

Supplementing results recently found by Weidenhammer (1975) for the corresponding case of a non-viscous fluid, in the present contribution the much more complicated free transverse vibrations of bars in a viscous fluid are studied. Occasionally, this influence has already been discussed by Yang and Moran (1979), but they neglected the compressibility of the fluid and performed a numerical FE-analysis. Here, the compressibility is included and a semi-analytical approach in connection with generalized Galerkin procedures is preferred. Since only small vibrations of the two interacting subsystems are considered, a linear theory is sufficient and a distinction between a spatial and a material description has no consequences. Starting with the single equation of motion for the transversely vibrating rod, the linearized Navier Stokes equations (together with the continuity equation and an appropriate thermodynamic state equation) for the compressible fluid annulus and corresponding boundary and transition conditions, a modal truncation governing the first mode vibrations leads to the corresponding eigenvalue equation to be solved numerically. In detail, three calculation steps have to be carried out. First, a solution for the displacement field of the fluid is assumed in such a form that all kinematical boundary and transition conditions are satisfied. Subsequently, Galerkin's method is applied to the field equations of the fluid. Finally, the solution is fitted to the equation of motion of the rod.

The variations of vibration frequencies and damping properties with the different system parameters are examined. Special cases, e.g., a vibrating rod in an incompressible, viscous fluid and a compressible non-viscous fluid, are likewise deduced.

## REFERENCES

- Weidenhammer, F. (1975). Eigenfrequenzen eines Stabes in zylindrisch berandetem Luftraum. ZAMM 55, T187-190.
- Yang, C.-I., and Moran, T.J. (1979). Finite-element solution of added mass and damping of oscillation rods in viscous fluid. J. Appl. Mech. 46, 519-523.

# REYNOLDS DILATANCY AND QUASI-STATIC YIELD OF GRANULAR ASSEMBLAGES

J. D. Goddard

Department of Chemical Engineering  
University of Southern California  
Los Angeles, California 90089-1211

The yield behavior of granular media and dense particulate suspensions is often dominated by the effects of volume-coupled shape change (Reynolds dilatancy), which in a continuum sense represents an internal kinematic constraint. As evident from the early micromechanical theory of O. Reynolds (1885, *Phil. Mag.* **20**, 469) and elucidated further here, dilatancy is by its very nature an  $n$ -body problem, with  $n \geq d + 1$  in space dimension  $d$ . The present work provides new theoretical estimates for dilatancy in monodisperse and polydisperse sphere assemblages, together with comparisons to experiment and computer simulations.

R. Gudhe\*, M. Massoudi<sup>+</sup>, K.R. Rajagopal\*

\* Department of Mechanical Engineering  
University of Pittsburgh  
Pittsburgh, PA 15261

<sup>+</sup> U.S. Department of Energy  
Pittsburgh Energy Technology Center  
P.O. Box 10940  
Pittsburgh, PA 15236

In recent years, there has been considerable interest in understanding the behavior of granular material as it has relevance to several technological problems. This includes the handling of such substances as coal, agriculture products, metal ores, rocket propellants, fertilizers, sand and other particulate solids, fluidization, pneumatic and hydraulic transport of particles, and the mechanics of avalanches and other natural disasters which involve the flow of powders and bulk solids. Many situations, such as discharge through bin outlets, flow through hoppers and chutes, pneumatic transport of coal, etc., require information on material properties of these particles, flow patterns, and concentration profiles [Rajagopal and Massoudi (1990)].

A considerable amount of research has been devoted to the mechanics of flowing granular materials and their flow characteristics [Savage (1984)]. In a number of applications, these materials are also heated prior to processing, or cooled after processing [Patton, et al. (1986)]. Very little fundamental work, from a mathematical point of view, has been devoted to these types of heat transfer in granular materials. These contact dominated (dense phase) flows have applications in certain industrial equipment designed to heat, cool, or dry granular materials [Uhl and Root (1967)]. Moreover, granular materials exhibit phenomena like normal stress differences in simple shear flow, a characteristic of non-Newtonian fluids and non-linearly elastic solids. One approach used in the modeling of granular materials is the continuum approach, which assumes that the material properties of the ensemble may be represented by continuous functions so that the medium may be divided infinitely without losing any of its defining properties.

The governing equations are the conservation of mass, linear momentum and energy. In the present study, the granular material is treated as a continuum, and its stress tensor is modelled as [Cowin (1974), Rajagopal and Massoudi (1990)]

$$\underline{T} = [\beta_0(v) + \beta_1(v) \nabla v \cdot \nabla v + \beta_2(v) \text{tr } D] \underline{1} + \beta_3(v) D + \beta_4(v) \nabla v \otimes \nabla v \quad (1)$$

where  $\beta_0$  is similar to pressure in a compressible fluid and is given by an equation of state,  $\beta_2$  is akin to the second coefficient of viscosity in a compressible fluid,  $\beta_1$  and  $\beta_4$  are the material parameters that reflect the distribution of the granular material, and  $\beta_3$  is the viscosity of the material. The volume fraction  $v$  is related to the bulk density of the material through

$$\rho = \gamma v \quad (2)$$

where  $\gamma$  is the actual density of the grains ( $0 \leq v < 1$ ). The rate of stretching  $D$  is given by

$$D = \frac{1}{2} [(\nabla u) + (\nabla u)^T] \quad (3)$$

where  $\nabla$  denotes the gradient operator and  $\underline{u}$  is the velocity vector. In equation (1),  $\underline{1}$  is the identity tensor and  $\otimes$  indicates the outer product.

In this problem, we consider the steady one dimensional flow of an incompressible granular material (i.e.,  $\gamma = \text{const}$ ) down an inclined plane where the angle of inclination is  $\alpha$ . The surface of the inclined plane is at a higher temperature than the temperature of the surrounding environment, and as a result, there is transfer of heat. The coupled non-linear equations of motion are solved and volume fraction, velocity, and temperature profiles are presented.

#### References:

- Cowin, S.C. Powder Technology, Vol. 9 (1974), p. 61
- Rajagopal, K.R., M. Massoudi. Topical Report, U.S. Department of Energy, DOE/PETC/TR-90/3 (1990).
- Patton, J.S., R.H. Sabersky, and C.E. Brenner, Int. J. Heat Mass Transfer, Vol. 29 (1986), p. 1263.
- Savage, S.B., Advances in Applied Mechanics, Vol. 24 (1984), p. 289.
- Uhl, V.W., and W.L. Root, Chem. Eng. Prog., Vol. 63 (1967), p. 81

# AN EVALUATION OF NON-DARCY EFFECTS IN POROUS AND VISCOUS/POROUS FLOW PROBLEMS<sup>1</sup>

D. K. Gartling and C. E. Hickox  
Fluid, Thermal and Structural Sciences Department  
Sandia National Laboratories  
Albuquerque, New Mexico 87185

There is an increasing interest in the use of extended forms of Darcy's law for the study and analysis of flow problems in saturated porous media. Though Darcy's law is a well known and justifiable description for many porous flow applications, it has been extensively criticized for shortcomings in several particular applications. Often cited limitations include: an inability to specify no-slip velocity boundary conditions on bounding surfaces, uncertain interface conditions for merging a viscous flow description with a saturated porous layer in conjugate problems and poor representation of high Reynolds number flows in porous layers.

Modifications to Darcy's law that address inertial and boundary effects have been proposed in numerous forms, the most popular being variations of the Forchheimer-Brinkman model. Specifically, the Forchheimer extension adds a drag term that is quadratic in the velocity, thereby allowing the low Reynolds number restriction to be lifted. The Brinkman modification includes a second order viscous term that permits boundary and interface conditions similar to those encountered in Navier-Stokes problems to be added to a porous flow description. Though these modifications have received considerable attention and use in the literature, they have generated considerable controversy as to their range of applicability and correctness in representing physical phenomena.

Many authors have advocated the use of the Brinkman model<sup>1,2</sup> in order to satisfy a no-slip boundary condition on a solid wall or enforce continuity of the stress components at a viscous fluid/porous layer interface. Nield<sup>3</sup> argues that if the Brinkman term is included, then an appropriate variation in the porosity near a wall must also be specified; this feature has not often been employed in previous work. Nield also points out that the Brinkman model cannot really be justified for porosities less than  $\phi < 0.60$ . He also notes that the preferred method for describing interface conditions employs a Darcy law with a velocity slip condition proposed by Beavers and Joseph.<sup>4</sup> This approach is generally not favored by those doing numerical simulations. The work of Cheng<sup>5</sup> suggests that when

---

<sup>1</sup>This work was performed at Sandia National Laboratories which is supported by the U. S. Department of Energy under contract DE-AC04-76-DP00789.

the Brinkman model is employed, along with a variation of porosity near a boundary, dispersion effects should also be modeled. Again, little attention has been paid to this proposal. In terms of accommodating higher Reynolds number flows, the debate centers on the form of the inertial terms in the Forchheimer-Brinkman model. Some authors advocate the replacement of the advective acceleration terms with a quadratic drag term, while others retain both the advective acceleration and quadratic drag terms.

The present study was undertaken in an attempt to clarify the controversial and confused state of non-Darcy flow models. Extending the work presented in earlier contributions<sup>6,7</sup> a series of numerical simulations have been carried out to evaluate the relative importance of each term in the extended forms of Darcy's law. Also tested were proposed variations in material and flow properties, such as porosity near a wall and the inclusion/exclusion of dispersion. Several simple geometries were selected for evaluation including a conjugate problem that allowed several types of interface conditions to be studied. The results of the study have provided insights into which effects are important in commonly encountered porous flows and which terms are only significant for extremes in porosity.

## References

1. K. Vafai and S. J. Kim, "Fluid Mechanics of the Interface Region Between a Porous Medium and a Fluid Layer - An Exact Solution," *Int. J. Heat Fluid Flow*, **11**, pp. 254-256, 1990.
2. C. Beckermann, S. Ramadhyani and R. Viskanta, "Natural Convection Flow and Heat Transfer Between a Fluid Layer and a Porous Layer Inside a Rectangular Enclosure," *J. Heat Transfer*, **109**, pp. 363-370, 1987.
3. D. A. Nield, "The Limitations of the Brinkman-Forchheimer Equation in Modelling Flow in a Saturated Porous Medium and at an Interface," *Int. J. Heat and Fluid Flow*, accepted for publication, 1991.
4. G. S. Beavers and D. D. Joseph, "Boundary Conditions at a Naturally Permeable Wall," *J. Fluid Mech.*, **30**, pp. 197-207, 1967.
5. P. Cheng and C. T. Hsu, "Applications of Van Driest's Mixing Length Theory to Transverse Thermal Dispersion in Forced Convective Flow Through a Packed Bed," *Comm. Heat and Mass Transfer*, **13**, pp. 613-625, 1986.
6. C. E. Hickox and D. K. Gartling, "Non-Darcy Effects in Porous Media Natural Convection," *Proc. 10th U.S. National Congress of Applied Mechanics*, University of Texas, Austin, Texas, Section T2, 1986.
7. D. K. Gartling, "A Finite Element Formulation for Incompressible, Conjugate, Viscous/Porous Flow Problems," *Proc. Int. Conf. on Computational Methods in Flow Analysis*, Vol. 1, H. Niki and M. Kawahara, Eds., Okayama, Japan, pp. 619-626, 1988.

## Rapid Granular Flow Down Inclines

James T. Jenkins

Department of Theoretical and Applied Mechanics

Cornell University, Ithaca, NY 14853-1503

We analyze rapid, steady, fully developed flows of idealized granular materials that are driven by gravity down inclines. The grains are assumed to be identical spheres that interact through inelastic, frictional collisions. We employ field equations that are derived using methods from the kinetic theory of dense gases and boundary conditions that result from a consideration of the rate of transfer of momentum and energy at several types of boundaries. These include flat frictional walls, frictional bumpy boundaries, and interfaces within the granular material on which the mean shear is discontinuous. The predictions of the theory are compared with existing experimental results on steady flows in chutes and rotating drums.



## MATHEMATICAL MODELS: THEORY AND PRACTICE

Barna A. Szabó  
Center for Computational Mechanics  
Washington University  
St. Louis, MO 63130

Procedures by which the integrity of mathematical models can be established, and errors in their numerical solution estimated, in the setting of practical engineering problem-solving are discussed. Two essential requirements must be satisfied in establishing the reliability of computed information:

1. The mathematical model used for representing a physical system or process must account for all essential attributes of the system or process;
2. The numerical approximation of the solution of the mathematical model must be sufficiently accurate so that decisions based on the approximate solution are essentially the same as the decisions based on the (unknown) exact solution.

There has been a great deal of progress in the development of methods for controlling errors in the numerical solution of mathematical problems, called *discretization errors*, especially for problems of the elliptic type. Today it is possible in principle, and in many cases in industrial practice as well, to guarantee that errors in the data of interest are within prespecified tolerance ranges. The main points of this development are described in a recently published textbook [1]. Examples for the estimation and control of discretization errors have been presented in a number of papers, see, for instance, [1-4].

If computers are to be used for generating data on which engineering decisions can be based then, in addition to the errors of discretization, the errors of *idealization* must be controlled also. Clearly, it is not meaningful to know that the approximate solution to a mathematical problem is accurate to within one or two percent relative error (the error must be measured in terms of the quantities of interest) if it is not known with a high degree of certainty that no essential phenomena have been overlooked in formulating the mathematical problem itself. One of the interesting and important problems for research in the 1990's is the problem of proper formulation of mathematical models.

Construction of mathematical models for structural plates and shells is a classical problem as well as one of great practical importance. Plate and shell models should be viewed as three-dimensional bodies, one dimension of which happens to be much smaller than the other two. Thus the quality of a plate or shell model must be judged on the basis of how well its exact solution approximates the exact solution of the problem of three-dimensional elasticity. Of course, the exact solution depends not only on the choice of the model but also on the topology, material properties, loading and constraints. The desired degree of approximation depends on the goals of analysis. For these reasons models have to be chosen adaptively. Hierarchic sequences of models make adaptive selection of the model which is best suited for the purposes of a particular analysis possible.

The essential features of the hierarchic models are as follows:

1. The exact solutions of the hierarchic models  $\tilde{u}_{HM|i}$  ( $i = 1, 2, \dots$ ) converge to the exact solution of the problem of elasticity ( $\tilde{u}_{EL}$ ) for a fixed thickness:

$$\lim_{i \rightarrow \infty} \|\tilde{u}_{EL} - \tilde{u}_{HM|i}\|_E = 0 \quad (1)$$

where  $\|\cdot\|_E$  is the energy norm. The rate of convergence depends on the smoothness of  $\tilde{u}_{EL}$ .

2. The exact solution of each hierarchic model converges to the same limit as the exact solution of the problem of elasticity with respect to the plate/shell thickness ( $h$ ) approaching zero:

$$\lim_{h \rightarrow 0} \frac{\|\tilde{u}_{EL} - \tilde{u}_{HM|i}\|_E}{\|\tilde{u}_{EX}\|_E} = 0 \quad i = 1, 2, \dots \quad (2)$$

and, when the solution is smooth, the rate of convergence increases with  $i$ .

These requirements are important because, typically, the solution of the problem of elasticity in the interior regions of the domain can be approximated well by the lowest in the hierarchic sequence of models but near the boundaries higher models are needed.

The construction of hierarchic models for homogeneous isotropic plates and shells was discussed by Szabó and Sahrman in [5]. Additional discussion and examples are available in [6]. The principles governing the derivation of a hierarchic sequence of models for laminated composites are presented in [7].

## REFERENCES

- [1] Szabó, B. A. and Babuška, I., *Finite Element Analysis*. John Wiley & Sons, New York, (1991).
- [2] Szabó, B. A., "On Reliability in Finite Element Computations" *Computers and Structures*, to appear in 1991.
- [3] Andersson, B. and Falk, U., "Self-Adaptive Analysis of Three-Dimensional Structures Using the p-Version of the Finite Element Method", Technical Report FFA TN 1987-31, The Aeronautical Research Institute of Sweden, Bromma (1987).
- [4] Babuška, I. and Rank, E., "An Expert-System-Like Feedback Approach in the hp-Version of the Finite Element Method", *Finite Elements in Analysis and Design*, Vol. 3, pp. 127-147 (1987).
- [5] Szabó, B. A. and Sahrman, G. J., "Hierarchic Plate and Shell Models Based on p-Extension", *International Journal for Numerical Methods in Engineering*, Vol. 26, pp. 1855-1881 (1988).
- [6] Szabó, B. A., "Hierarchic Plate and Shell Models Based on p-Extension", in *Analytical and Computational Models of Shells*, edited by A. K. Noor, T. Belytschko and J. C. Simo, Society of Mechanical Engineers, New York, Vol. 3, pp. 317-331 (1989).
- [7] Babuška, I., Szabó, B. and Actis, R., "Hierarchic Models for Laminated Composites", Report WU/CCM-90/4, Center for Computational Mechanics, Washington University, St. Louis, MO 63130 (1990). To appear in the *International Journal for Numerical Methods in Engineering*.

# Mechanics of Polymer Crystallization: Theoretical Modeling

Mehrdad Negahban, Department of Engineering Mechanics and the Center for Materials Research and Analysis, University of Nebraska-Lincoln, Lincoln, NE 68588-0347

Many common polymers like polyethylene, poly(vinyl chloride), polycarbonate, and natural rubber can crystallize. This crystallization is accompanied by a change in mechanical properties. For example, the stress in a stretched sample of natural rubber at  $-25^{\circ}\text{C}$  will relax in a manner similar to that seen in viscoelastic materials [1], but this relaxation is accompanied by a 100 fold increase in the elastic modulus [2,3]. In this case, Gent [1] has shown that for each value of stretch there is a linear relation between the change in volume and the amount of stress relaxed. Since the change in volume is closely related to the amount of crystallization, this suggests that the crystallization can be the main cause of this relaxation. This assumption is further supported by the fact that there is a large increase in the modulus.

Crystallization in polymers is a gradual process. Depending on the polymer and the loading conditions, the process of crystallization might take from minutes to years to be completed. This process is normally accelerated by stretching. A rate equation is developed to model the rate of crystallization.

A multi-dimensional, fully nonlinear model has been developed to characterize the changes seen in the stress response during the process of crystallization. This equation combined with the equation for the rate of crystallization and the equation of motion can be used to solve initial and boundary value problems.

The solution to several problems will be presented to show how the model can capture both qualitative and quantitative characteristics of crystallization.

## References:

- [1] Gent, A. N., "Crystallization and the Relaxation of Stress in Stretched Natural Rubber Vulcanizates," *Trans. Faraday Soc.*, vol. 51, pages 521-533 (1954).

- [2 ] Leitner, M., "Young's Modulus of Crystalline, Unstretched Rubber," *Trans. Faraday Soc.*, pages 51, 1015 (1955).
- [3 ] Stevenson, A., "The Influence of Low-Temperature Crystallization on the Tensile Elastic Modulus of Natural Rubber," *Journal of Polymer Science: Polymer Physics Edition*, vol. 21, pages 553-572 (1983).

# A DYNAMICAL SYSTEM APPROACH FOR DETERMINING ALL THE ZEROS OF A NONLINEAR VECTOR FUNCTION

RAMESH S. GUTTALU  
Department of Mechanical Engineering  
University of Southern California  
Los Angeles, CA 90089-1453, USA

PEDRO J. ZUFIRIA  
GTI, ETSI de Telecomunicación  
Polytechnic University of Madrid  
28040 Madrid, Spain

There is a great need for numerical tools in mechanics area for determining *all* the solutions to a system of nonlinear algebraic equations. Such tools are helpful in determining equilibria, fixed points, and periodic solutions of nonlinear dynamical systems, for obtaining inverse-kinematic relations in robotics, and for solving optimization problems. In this article we summarize the results obtained by the authors on an approach for finding all the zeros of a vector function  $f(\mathbf{x})$ . It is based on the idea of constructing a dynamical system. One form of continuous-time dynamical system studied extensively in the literature is

$$\begin{aligned}\dot{\mathbf{x}}(t) &= \mathbf{F}(\mathbf{x}) = -\mathbf{J}^{-1}(\mathbf{x})\mathbf{f}(\mathbf{x}), \quad \mathbf{x} \in \mathbb{R}^N, \\ \mathbf{F} : \mathbb{R}^N &\rightarrow \mathbb{R}^N, \quad \mathbf{J} = \frac{\partial \mathbf{f}}{\partial \mathbf{x}},\end{aligned}\tag{1}$$

where  $\dot{\mathbf{x}}$  is the time derivative of the unknown vector  $\mathbf{x}(t)$ . For details regarding the properties of (1) and for its use in homotopic and continuation methods for locating zeros, see references [1,2,3]. A discrete counterpart of (1) given by  $\mathbf{x}(n+1) = \mathbf{x}(n) + \mathbf{F}(\mathbf{x})$ ,  $n \in \mathbb{Z}$ , and its dynamic properties are studied in [4].

The basic idea here is to follow the trajectories of (1) and to ascertain their long time behavior. Global behavior of the dynamical system (1) has been explored by the authors in references [4,5,6,7]. First one needs to establish a relationship between the zeros of  $\mathbf{f}$  and the equilibria of the system (1) (equivalently, the zeros of  $\mathbf{F}$ ). The equilibria of (1) are asymptotically stable. They correspond with the locations of the zeros of  $\dot{\mathbf{x}}$ . However, the converse need not be true. The function  $\mathbf{F} = -\mathbf{J}^{-1}\mathbf{f}$  need not be defined when the  $\mathbf{J}(\mathbf{x})$  is singular at a zero of  $\mathbf{f}$ . The stability of equilibria is established by a Lyapunov function  $V = \mathbf{f}^T \mathbf{f}$  which also provides an estimate of the domain of attraction associated with each equilibria. This domain may be used as a region of initial guesses with iterative techniques

for converging to a zero of  $f$ . It has also been established that no periodic solutions of the dynamical system (1) can exist when all the zeros of  $f$  are isolated implying that (1) cannot possess complicated dynamics such as chaotic behavior even in higher dimensions.

It has been identified that the *singular manifolds* where  $\det J(x) = 0$  play a crucial role in determining the global behavior of (1). Several results have been established relating the *barrier manifolds* (singular manifolds which the trajectories of (1) do not cross), *isolated regions* (regions separated by barrier manifolds), and domains of attraction. Every trajectory of (1) which starts in a particular isolated region evolves only within that region. The role of singularities of  $J(x)$  has been further explored in [7] with a particular reference to pathological cases.

Computational algorithms based on cell-to-cell mapping analysis for finding singular manifolds and zeros are developed in [6]. Several examples are illustrated therein including the computation of fixed points of a two degrees of freedom damped mechanical system subjected to impulsive loads.

## References

1. F. H. Branin (1973), Widely convergent method for finding multiple solutions of simultaneous nonlinear equations, *IBM Journal of Research and Development*, Vol. 16, pp. 504-522.
2. H. B. Keller (1978), Global homotopies and Newton methods, in "Symposium on Recent Advances in Numerical Analysis" (Editors: C. de Boor and G. H. Golub), Academic Press, New York.
3. C. B. Garcia and W. I. Zangwill (1981), *Pathways to Solutions, Fixed Points, and Equilibria*, Prentice-Hall, Englewood Cliffs, New Jersey.
4. P. J. Zufiria (1989), *Global Behavior of a Class of Nonlinear Dynamical Systems: Analytical, Computational and Control Aspects*, Ph.D. dissertation, University of California, Los Angeles.
5. P. J. Zufiria and R. S. Guttalu (1990), On an application of dynamical systems theory to determine all the zeros of a vector function, *Journal of Mathematical Analysis and Applications*, Vol. 152, pp. 269-295.
6. P. J. Zufiria and R. S. Guttalu (1990), A computational method for finding all the roots of a vector function, *Applied Mathematics and Computation*, Vol. 35, pp. 13-59.
7. R. S. Guttalu and P. J. Zufiria (1990), On a class of nonstandard dynamical systems: singularity issues, in *Advances in Control and Dynamic Systems* (Editor: C. T. Leonides), Vol. 34, pp. 279-324, Academic Press, New York.

# A Survey of Modern Applications of Conformal Mapping

by Patricio A.A.Laura

Professor, Dept. of Engineering  
Universidad Nacional del Sur

and

Director  
Institute of Applied Mechanics  
(CONICET - SENID - ACCE)  
8000 - Bahía Blanca  
A R G E N T I N A

## Abstract

According to Caratheodory's classical treatise [1] Ptolemy was the first mathematician who used conformal transformation when dealing with the representation of the celestial sphere. His transformation is the stereographic projection of the sphere, it maps the sphere conformally into a plane. The fact that one usually remembers Ptolemy's name only in connection with his wrong theory of the Universe is certainly unfair.

Classical applications of conformal mapping to many stationary problems of mathematical physics go back over a century and a half and continue to the present. These applications deal, in general, with solutions of Laplace's equation which remains invariant if the real plane is subjected to a conformal transformation.

Applications of conformal mapping techniques to the mathematical theory of elasticity are considerable more complex. On the other hand they are treated in well known textbooks.

It is the purpose of the present paper to briefly discuss non - classical applications of conformal mapping to several fields of applied science and technology [2], e.g.

- acoustics and vibrations
- electromagnetic theory
- viscous flows
- unsteady diffusion situations.

One may conclude that from Ptolemy's conformal transformation developed almost 2000 years ago to sophisticated determinations of mapping functions and their applications to complex scientific and technological problems in a wide variety of fields, Man has accomplished significantly in this respect.

It is to be expected that Man will learn more about conformal mapping in the next 20 centuries !

#### References

1. C.Carathéodory. Conformal Representation. Cambridge at the University Press, 1932.
2. R.Schinzinger and P.A.A.Laura. Modern Applications of Conformal Mapping, Elsevier, 1990.



## ACOUSTIC EMISSION STUDIES OF DAMAGE IN COMPOSITES\*

W. O. Soboyejo  
McDonnell Douglas Research Laboratories  
P.O. Box 516, St. Louis, MO 63166

The results of recent studies of damage evolution in composites will be presented for monotonic and cyclic loading conditions. These include the use of acoustic emission techniques to determine crack initiation and propagation components in fiber-reinforced titanium matrix and ceramic matrix composites. The paper will discuss the effects of interfaces and matrix microstructure on the evolution of damage in the  $\beta$  Ti-15V-3Cr-3Al-3Sn/SCS9 composite, and the potential for using acoustic emission techniques to monitor the onset, location, amplitude, and progression of damage in composite systems. The potential for increasing microcracking stresses in ceramic matrix composites via hybrid reinforcement of cordierite with various combinations of alumina whiskers and nicalon fibers will also be examined. Microcracking stresses determined by acoustic emission techniques will be compared to those obtained from whisker-reinforced or fiber-reinforced composites and the effects of reinforcement-matrix interfaces and matrix microstructure on microcracking stresses and damage propagation will be elucidated. The paper will highlight the degradation in tensile strength and fatigue resistance that can occur due to coarsening of the fiber-matrix interface and matrix microstructure transformations during thermal exposure. It will also illustrate the use of acoustic emission techniques to distinguish between crack initiation and propagation during tensile and low cycle fatigue/high cycle fatigue tests.

\*Research conducted under the McDonnell Douglas Corporation  
Independent Research and Development program.

THE MECHANICAL PROPERTIES OF  
TIGHTLY WOVEN CARBON-CARBON COMPOSITES

Abdullah Ozturk, Rollie Dutton and Robert E. Moore  
Department of Ceramic Engineering  
222 McNutt Hall  
University of Missouri-Rolla  
Rolla, MO 65401

The mechanical properties of a tightly woven carbon-carbon composite were investigated. The composite consists of a graphite fiber reinforced graphite matrix. Flexural strength tests were performed in three point bending at room and elevated temperatures in air and argon. Flexural strength increases slightly with increasing temperature in argon, but decreases significantly in air as the temperature increases.

Optical microscope observation of the specimens broken in flexure revealed that the composite failed in a tension/shear mixed mode rather than in tension. Propagation of cracks perpendicular to the plane of the cloth layer and delamination of the cloth layers were observed. Scanning Electron Microscopy (SEM) fractographs indicated microcracking of the matrix, debonding of fiber-matrix interfaces, pull-out of fibers from the matrix, fiber bridging and separation of the matrices.

Fracture toughness tests were conducted at room and elevated temperatures in air and in argon using the Single Edge Notch Bend (SENB) test. It was observed that the critical stress intensity factor ( $K_{Ic}$ ) of these composites decreases with increasing temperature in air, but remains almost the same in argon.

Tension-tension cyclic fatigue tests were performed to determine the effect of fluctuating stresses on the mechanical properties of these composites at ambient laboratory conditions. The numbers of fatigue cycles to failure were determined as a function of the applied stress levels. Results of composite behavior are discussed in terms of the relationship of the fatigue life of these composites as well as the effects of applied stress levels. The maximum stress at which specimens do not fail after  $10^6$  cycles is approximately 80% of the ultimate tensile strength. Fatigue failure did not occur for the specimens tested below this stress level. Specimens tested between 80% and 90% of the ultimate tensile strength either failed during testing or survived after  $10^6$  cycles. This range of stress levels is considered as a critical range for cyclic fatigue of these composites. All specimens fatigue tested at

stress levels greater than 90% of the ultimate tensile strength failed during testing. The average residual strength of the specimens after  $10^6$  cycles was comparable to the average ultimate tensile strength of unfatigued specimens.

Fatigue tests were interrupted at  $10$ ,  $10^2$ ,  $10^3$ ,  $10^4$ , and  $10^5$  cycles to measure the composite elastic modulus and hence to determine whether any structural deterioration had occurred with increasing numbers of cycles. It was observed that composite elastic modulus decreases slightly within the first 100 cycles and then remains almost unchanged through  $10^6$  cycles. The change in the composite elastic modulus was also seen in stress-strain hysteresis loops of these composites. The stress-strain hysteresis loops become progressively narrower coincident with a smaller elastic moduli as the number of cycles increases. The reduction of elastic moduli is attributed to the development of damage modes in the composite due to the fatigue loading.

Results of mechanical testing were correlated with SEM analysis to explain observed fatigue effects. The SEM analysis of fatigue tested specimens revealed the evidence of textural changes associated with increasing number of fatigue cycles. These occurred in the matrix regions. A comparison of the matrix regions of tensile and fatigue tested specimens suggested that the matrix regions of fatigue tested specimens are different from the tensile tested specimens. The fracture surface of the matrix of a tensile tested specimen is flat and smooth while the fracture surface of the matrix of a fatigue tested specimen is rough. The striations which indicate the advance of crack growth after each cycle are also observed on the fracture surfaces of the fatigue tested specimens.

A series of fatigue tests were also conducted to determine the influence of cyclic fatigue on the fracture toughness of these composites.  $K_{Ic}$  of these composites remains unchanged with increasing number of cycles at the stress levels of 80% of the ultimate tensile strength; however,  $K_{Ic}$  decreased with increasing number of cycles at higher stress levels.

# EFFECT OF CONSTRAINT ON DENSIFICATION OF CERAMIC MATRIX COMPOSITES

L. R. Dharani and W. Hong  
Department of Mechanical and Aerospace  
Engineering and Engineering Mechanics  
University of Missouri-Rolla  
Rolla, MO 65401-0249

## Introduction.

Ceramic matrix composites can offer important performance advantages in that they may have a higher fracture toughness and creep resistance at elevated temperatures compared to single phase ceramics. The potential for improved performance is, however, offset by the increased difficulties in pressureless processing of these materials. The free sintering of single phase polycrystalline ceramic matrices is significantly hampered by the presence of a dispersed particulate inert, rigid phase. Some factors that have been put forward to explain the reduction in densification rates of ceramic matrix composites, such as viscoelastic stresses originating in densification incompatibilities between the matrix and the dispersed second phase and the adverse effects of microcrack and crack-like defects promoted by the constraint of the dispersed inclusions. Isothermal sintering has attracted a special concern by isolating the temperature effect. The special situation of the isothermal sintering is that the instantaneous free strain rate as well as the material properties is density dependent and the density of the constrained sintering matrix is not known apriori. Moreover, the deformation is large due to the large range experienced by changing densities. So this problem has nonlinear relationships in both material and geometry. Since the exact solutions are mathematically intractable, this problem is approached by using the finite element method in an incremental fashion.

## Results.

A single inclusion case (10% volume fraction of inclusion) is considered by assuming that the interactions among inclusions are quite small at low volume fraction and can be neglected. The average relative density of the constrained matrix against the unconstrained matrix  $v$  as calculated and compared with the experimental data. The result reconfirms Scherer's theory in that viscoelastic stresses are too small to account for the drastic reduction in densification rates of ceramic matrix composites.

The multiple inclusion model seems more realistic than single inclusion model in spite of idealization of uniform size and distribution of inclusions in the matrix. Without loss of generality we considered a symmetric composite geometry, in which only a sectional of the problem needed to be considered. The size of the inclusions and

distance between them are arranged to match the inclusion volume fraction. The difference in the predicted relative densities for the two cases, single and multiple inclusions, is very minimal as shown in Fig. 1. The results indicate that effects of relevant non-mechanical factors, such as mass diffusion, grain surface energy minimization and grain growth, on the viscoelastic constitutive relations of the matrix material during sintering should be considered.

An interesting phenomenon from the results is that the variation of density is not sensitive to the viscosity coefficient but quite so to the poisson's ratio. It agrees with results from a viscoelastic analysis that no volumetric strain except elastic part exists if the poisson's ratio is constant throughout the process.

#### Acknowledgements.

This work is being supported by Electronics and Material Sciences Division, Air Force Office of Scientific Research. The experimental results were provided by Dr. Rahaman, University of Missouri-Rolla.

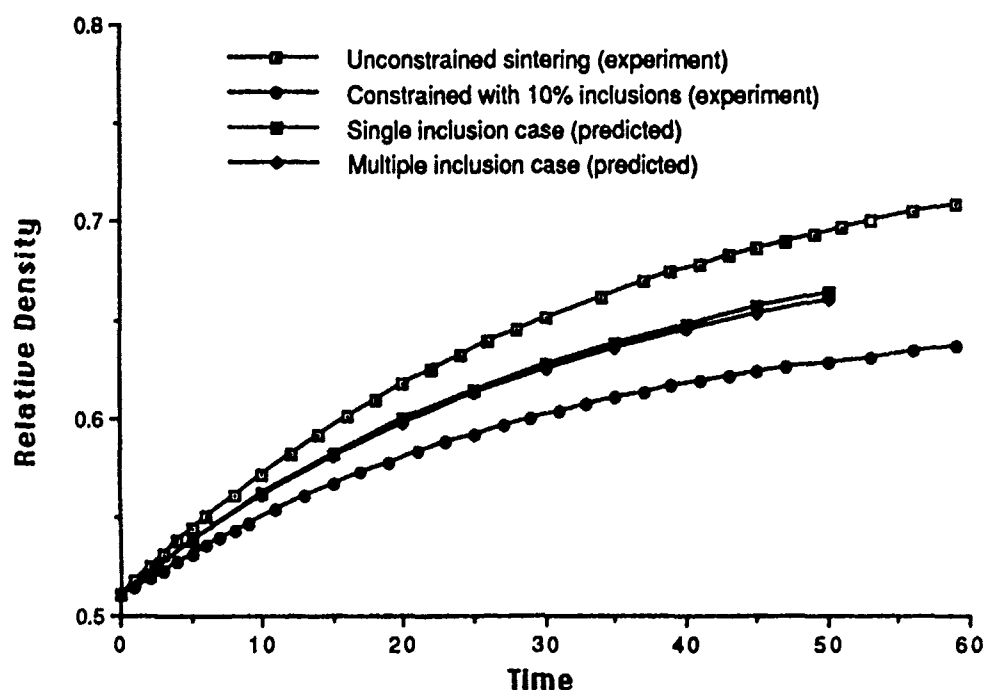


Fig. 1 Predictions for matrix with 10% volume fraction inclusions.

# INTERFACE MECHANICS IN CERAMIC AND GLASS MATRIX COMPOSITES

V.S. Gopalaratnam\*

## Abstract

Monolithic ceramic and glass components are generally very brittle and often fail catastrophically when subjected to tensile loads. One of the ways in which their brittleness and low fracture toughness can be improved, is through the incorporation of fibers or whiskers to yield a two-phase composite. The resulting composite called ceramic or glass matrix composite has markedly superior resistance to crack propagation and improved fracture toughness.

Fibers provide toughening through various energy dissipation processes during crack advance in such composites. The toughening mechanisms that are related to fiber addition include fiber pull-out, crack deflection, crack bridging, crack bowing or pinning, and thermal mismatch toughening. The first three are influenced to a large extent by the mechanical characteristics of the fiber-matrix interface. A thorough understanding of the failure modes and toughening mechanisms in such composites is not possible without a good understanding of the mechanics of interfacial stress transfer.

The classical fiber pull-out problem is solved assuming that the fiber and the matrix remain elastic during the entire pull-out process. The interface is idealized as an elastic linear-softening material. Although it is intuitively speculated that the actual local interface load-slip response will exhibit exponentially decaying post-elastic stress transfer capacity with a nominal mechanical frictional component at very large slips, it is shown that the linear softening idealization provides a representative

---

\* Assistant Professor of Civil Engineering, University of Missouri-Columbia, Columbia, Missouri 65211.

and mathematically convenient simplification. Solutions to the fiber axial force and interfacial shear stress along the embedded length of the fiber have been obtained by applying appropriate boundary and continuity conditions. The stability of the debonding process has been investigated by varying the fundamental characteristics of the fiber-matrix interface, the fiber embedment length and the fiber diameter. Energy based solutions are obtained for predicting the residual slip and stiffness degradation in cyclic pull-out (unloading/reloading). The influence of the radial stresses due to the combined effect of elastic and thermal mismatch is incorporated by making the interface softening parameter a function of  $\sigma_{rr}$  and  $\sigma_{\theta\theta}$ . The validity of this kind of a modification appears justified from the results reported by previous investigations on elastic mismatch, as well as the thermal mismatch in the pull-out problem. A functional relationship is used for incorporating the effects due elastic and thermal mismatch problem, thus essentially retaining the one-dimensional and axisymmetric nature of the pull-out problem.

The analytical model is successfully validated for a glass matrix composite system using experimental pull-out results from displacement controlled pull-out tests. The parametric study of the model parameters offers useful insights for the analysis and design of superior short-fiber brittle-matrix composites.

# COMPUTATIONAL METHODS FOR STATIC PROBLEMS INVOLVING CONTINUUM DAMAGE MECHANICS WITH SOFTENING

H.L. SCHREYER<sup>1</sup>, Z. CHEN<sup>2</sup> and M.K. NEILSEN<sup>3</sup>

<sup>1</sup>Professor, <sup>3</sup>Doctoral Student, Dept. of Mechanical Engineering,

<sup>2</sup>Research Engineer, New Mexico Engineering Research Institute  
Univ. of New Mexico, Albuquerque, NM 87131

## SUMMARY

There exist two major difficulties for nonlinear structural analysis involving softening. One consists of the ill-conditioning of the tangent stiffness matrix near critical points, and the other is the choice of a suitable constraint to obtain the solution path. In an attempt to make failure simulation a routine procedure, a new solution procedure is proposed in which a local constraint condition is used in an iterative solution algorithm. The procedure is described in the context of continuum damage mechanics which yields a secant stiffness matrix. However, the solution procedure is even more efficient if the initial elastic stiffness matrix is used because only one decomposition is necessary. Numerical solutions have been obtained for both plane strain and plane stress to show that snap-back and snap-through associated with shear band formation can be efficiently predicted.

The existence of structural softening has been demonstrated conclusively by a number of experimentalists using displacement controlled devices. Furthermore, if the displacement measurement used for load control is made across a softening zone, a reversal or "snap-back" in the space of load versus structural displacement can be exhibited. To predict such phenomena it is necessary to introduce constitutive models that exhibit softening with a nonlocal feature to limit the size of the failure zone or to use a cracking model in which the softening is given directly in terms of traction versus crack opening. With either approach, there are formidable computational problems in that the governing tangent stiffness matrix becomes singular at a bifurcation or limit point, and multiple solution paths exist beyond these critical points [de Borst, 1987; Crisfield and Willis, 1988; Chen and Schreyer, 1990a and 1990b]. The successful existing solution procedures are very inefficient so only a handful of numerical solutions exist.

To illustrate the proposed procedure, consider a static problem in which the spatial discretization process yields the secant stiffness matrix  $[K]$  based on the current value of the components of the elasticity tensor, and the load vector  $\{q\}$  is assumed to be applied proportionally, i.e., if  $m$  is the magnitude of the load, then

$$\{q\} = m\{q^*\} \quad \{q^*\}^T \{q^*\} = 1 \quad (1)$$

The problem is to solve the nonlinear matrix equation



$$[K]\{u\} = \{q\} \quad [K] = [K\{u\}] \quad (2)$$

in which the dependence of the secant stiffness on the displacement vector  $\{u\}$  is emphasized. Suppose the load parameter is to be incremented. To begin the iterative process, let  $[K]_I$  denote the secant stiffness from the previous iteration. Determine the new displacement field  $\{u^*\}_{I+1}$  associated with the unit force,  $\{q^*\}$ :

$$[K]_I\{u^*\}_{I+1} = \{q^*\} \quad (3)$$

Then if the magnitude of the force,  $m$ , is known, the actual displacement field will be  $\{u\} = m\{u^*\}$ . However, instead of prescribing  $m$ , suppose the magnitude,  $c$ , of a constraint condition is specified:  $c = \{c\}^T\{u\} = m\{c\}^T\{u^*\}$  where  $\{c\}$  is a vector of the type  $\{c\}^T = \langle 0, \dots, 0, 1, 0, -1, 0, \dots, 0 \rangle$  which is used merely to relate two or more of the degrees of freedom of the problem. Then the magnitude of the force vector is determined indirectly from the relation:  $m = c/(\langle c \rangle^T\{u^*\})$ . The displacement field is the product of  $m$  and  $\{u^*\}$ , both of which are known. The equilibrium relation (3) is satisfied unless additional damage is predicted from the level of damage computed in the previous iteration in which case the secant matrix must be updated and the sequence of equations solved again for  $\{u^*\}$ ,  $m$ , and  $\{u\}$ .

To obviate the need for a decomposition of a stiffness matrix with every iteration and load step, suppose (2) is replaced with  $[K]_0\{\delta u\}_I = \{g\}_{I-1}$  in which  $[K]_0$  can be the original, secant, or other stiffness matrix chosen for convenience. The out-of-balance force vector  $\{g\}_{I-1}$  incorporates the nonlinear behavior associated with the displacement field. The force vector includes the load increment  $\Delta m_I$  which is adjusted so that the localized constraint criterion is satisfied. Iterations continue until norms of the increment of both the displacement and out-of-balance force vectors are sufficiently small.

There are two significant advantages to the approach. First, the constraint criterion can be identified with that point in the body which is undergoing the highest rate of damage. That point usually changes during the loading process. Second, the artificial or secant stiffness is not singular at critical points as defined through the use of the tangent stiffness matrix so the algorithm is particularly robust. Softening with snapback can routinely be predicted.

## REFERENCES

- de Borst, R., 1987, "Computation of post-bifurcation and post-failure behavior of strain-softening solids," Computers and Structures, 25, 211-224.
- Crisfield, M.A. and J. Wills, J., 1988, "Solution strategies and softening materials," Computer Methods in Applied Mechanics and Engineering, 66, 267-289.
- Chen, Z. and Schreyer, H.L., 1990a, "Failure-Controlled Solution Strategies for Damage Softening with Localization," Proceedings of the International Conference on Micromechanics of Failure of Quasi-Brittle Materials, Albuquerque, NM, 6-8 June 1990, Elsevier Applied Science, NY, 135-145.
- Chen, Z. and Schreyer, H.L., 1990b, "A Numerical Solution Scheme for Softening Problems Involving Total Strain Control," Computers and Structures, Vol. 37, No. 6, 1043-1050.

## IMPLEMENTATION OF THE NONLOCAL MICROPLANE CONCRETE MODEL WITHIN AN EXPLICIT DYNAMIC FINITE ELEMENT PROGRAM

William F. Cofer  
Department of Civil and Environmental Engineering  
Washington State University  
Pullman, Washington 99164-2910

The finite element modeling of concrete is necessary for the design and response analysis of many structures that are subjected to shock loading. Much of the current analysis is performed using the well known explicit dynamic finite element code, DYNA3D. The concrete material model that is presently available in this program is based upon plasticity theory with a Drucker-Prager yield surface, a tension cutoff for tensile loading, and a cap to limit hydrostatic strength. However, plasticity theories for concrete are basically phenomenological models in which previously accepted techniques for metals are modified to represent macro-behavior. Fracture is not a natural ingredient of the theory. Indeed, research has shown that concrete does not fracture abruptly but, rather, displays softening behavior due to the formation of microcracks prior to fracture. Thus, many widely varying approaches have been considered, none of which are universally accepted.

In contrast, microplane models are derived on the basis of the actual behavior of the components of the material. At each point of interest, the response to the strain tensor on arbitrarily oriented surfaces (i. e., microplanes) is considered [Bazant, 1984]. This response could be elastic or it could involve the formation, opening, closing, or sliding of cracks. Simple stress-strain laws are applied in the directions perpendicular and parallel to the planes. The macroscopic material behavior is then composed of the sum of the effects.

Recently, Bazant and Prat [1988] extended the microplane method to enable it to consider the general triaxial response of concrete. For each microplane, the strain tensor was divided into normal deviatoric (i. e., the normal component minus volumetric strain), volumetric, and shear components, each of which was considered independently. The use of volumetric strain allowed the model to include the effects of confining stress. Macroscopic effects, such as smooth brittle ductile transition, hydrostatic stiffening, and strain softening in compression as well as in tension were all described by the model.

However, without modification, the microplane material model is subject to mesh dependence. This is due to the fact that cracking tends to localize to the width of a single element, causing the amount of energy that is dissipated to vary accordingly. The actual width of a crack is a material property and, if the elements are smaller than the crack width, provision must be made to ensure that the crack encompasses a band of several elements. That is, a localization limiter must be invoked.

The nonlocal continuum method is one of several types of localization limiters in which, for a particular point within a finite element, the stress is not computed from the resulting strain at that location, but from an averaged value of strain in a surrounding region. In this way, large strain variations and, hence, crack widths, are smoothed to a given characteristic width. To date, this method has mainly been applied to continuum damage mechanics, for which strain softening is represented by a damage variable or tensor. Bazant and Pijaudier-Cabot [1988] have reported that accurate results are obtained if only the damage variables are based upon nonlocal (or averaged) strain while all elastic stress contributions are computed from local strain. This idea should be directly applicable to any material if the variables that cause strain softening are developed in terms of nonlocal strain. For the microplane model, softening is accomplished through stress modifiers on each microplane in conjunction with a secant elastic relationship. The stress modifiers are thus defined on the basis of nonlocal strain.

In a practical sense, the nonlocal strain values are obtained via Gauss quadrature, using the same sampling points as those used for integrating the finite element stiffness. It involves a two stage process, in which the local strain for all elements is computed and stored. Then, for each integration point of each element, all points within a given characteristic radius are identified and the strain is extracted, modified by a weight factor, and summed to obtain the nonlocal values. Boundaries of the model and planes of symmetry must also be considered.

The strain averaging procedure has been implemented into DYNA3D. However, this method is only applicable to cases in which the element size is less than roughly 1/3 of the characteristic length [Bazant and Mazars, 1990], which is reported to be approximately 2.7 times the maximum aggregate size [Bazant and Pijaudier-Cabot, 1988]. For large elements, the strain automatically reverts to the local value and the resulting crack width will equal that of an element. As further research, methods are being investigated to include the effects of crack formation within an element and provide a technique that is applicable to meshes of any size.

Research sponsored by the Air Force Office of Scientific Research/AFSC, United States Air Force, under Contract F49620-88-C-0053. The United States Government is authorized to reproduce and distribute reprints for governmental purposes notwithstanding any copyright notation hereon.

Bazant, Z. P., "Microplane Model for Strain-Controlled Inelastic Behavior," *Mechanics of Engineering Materials*, C. S. Desai and R. H. Gallagher, eds., Wiley, 1984.

Bazant, Z. P. and Mazars, J., "France-U. S. Workshop on Strain Localization and Size Effect due to Cracking and Damage," *Journal of Engineering Mechanics*, ASCE, Vol. 116, No. 6, 1990, pp. 1412-1424.

Bazant, Z. P. and Pijaudier-Cabot, G., "Nonlocal Continuum Damage, Localization Instability and Convergence," *Journal of Applied Mechanics*, Vol. 55, 1988, pp. 287-293.

Bazant, Z. P. and Prat, P. C., "Microplane Model for Brittle Plastic Material: I. Theory," *Journal of Engineering Mechanics*, Vol. 114, No. 10, 1988, pp. 1672-1688.

## THE STRUCTURE OF SHEAR BANDS IN IDEALIZED GRANULAR MATERIALS

J.P. Bardet and J. Proubet  
*Civil Engineering Department,  
University of Southern California, Los Angeles, CA 90089-2531*

In the last decade, two different approaches have been proposed to study the thickness of shear bands in materials. Aifantis (1984 and 1987), Zbib and Aifantis (1989), Vardoulakis and Aifantis (1989) and Zbib and Aifantis (1989) introduced a second order strain gradient into the constitutive equation of plasticity, whereas Mühlhaus and Vardoulakis (1987) and Vardoulakis (1989) used the micropolar (Cosserat) theory.

The present paper focuses on the micropolar approach. Mühlhaus and Vardoulakis (1987) and Vardoulakis (1989) introduced couple stresses into the constitutive equations of the deformation and flow theories of plasticity, and successfully predicted the emergence, inclination and thickness of the shear bands in sands. They determined the thickness of shear bands after assuming that the linear stability analysis remains valid in the post-localization range. The linear stability analysis is appropriate to investigate the emergence and initial inclination of strain localization within homogeneously strained and stressed solids. However, its application in the post-bifurcation range requires additional assumptions about the uniformity of stress and strain, which need to be verified.

Mühlhaus and Vardoulakis (1987) and Vardoulakis (1989) found that the shear bands thickness decreases during the straining of the materials modelled with the deformation theory of plasticity but increases for those modeled with the flow theory of plasticity. They did not calibrate the parameters controlling the effects of couple stresses from test results but obtained them by using two micromechanical models referred to as the kinematical and statical models. They did not examine the structure of shear bands as Aifantis (1987) and Zbib and Aifantis (1989) had, due to the lack of experimental data on the localized deformation patterns in soils.

Recently, Bardet and Proubet (1990) examined the structure of persistent shear bands by numerically simulating an idealized assembly of two-dimensional particles. They showed the displacement, volumetric strain, void ratio, particle rotations and those of their neighborhoods inside the shear bands. They replaced the periodic boundaries used by Cundall (1989) with a flexible boundary similar to the rubber membranes of triaxial tests. In contrast to a periodic boundary, the stress-controlled boundary does not constrain the motion of particles inside the shear bands. Periodic boundaries are not appropriate to simulate the localized deformations that have very long spatial periods.

The main objective of the present work is to assess the assumptions and limitations of the theories of Mühlhaus and Vardoulakis (1987) and Vardoulakis (1989) based on the results of the numerical simulations on idealized granular media.

## REFERENCES

- Aifantis, E.C., 1984, "On the microstructural origin of certain inelastic models," ASME, *J. Engr. Mater. Tech.*, 106, pp.326-330.
- Aifantis, E.C., 1987, "The physics of plastic deformation, *Int. J. Plasticity*, 3, pp.211-247.
- Bardet, J.P., and J. Proubet, 1990, "A numerical investigation of the structure of persistent shear bands in granular materials," *accepted for publication in Géotechnique*.
- Cundall, P.A., 1989, "Numerical experiments on localization in frictional materials, *Ingenieur-Archiv*, Vol.59, No.2, pp.148-159.
- Mühlhaus, H.B., and I. Vardoulakis, 1987, "The thickness of shear bands in granular materials," *Géotechnique*, 37, pp.271-283.
- Vardoulakis, I., 1989, "Shear-banding and liquefaction in granular materials on the basis of a Cosserat continuum theory," *Ingenieur-Archiv*, Vol.59, No.2, pp.106-114.
- Vardoulakis, I., 1980, "Shear band inclination and shear modulus of sand in biaxial tests," *Int. J. Num. Anal. Meth. in Geomech.*, 4, pp.103-119.
- Vardoulakis, I., and E.C. Aifantis, 1989, "Gradient dependent dilatancy and its implications in shear banding and liquefaction," *Ingenieur-Archiv*, Vol.59, No.3, pp.197-208.
- Zbib, H.M. and E.C. Aifantis, (1988). On the structure and width of shear bands. *Scripta Metallurgica*, Vol.22, pp.703-708.
- Zbib, H.M. and E.C. Aifantis, (1989). A gradient-dependent flow theory of plasticity: Application to metal and soil instabilities. *Applied Mechanics Review, Pan-American Congress of Applied Mechanics*, Vol.42, 11, pp.295-304.

## FAULT GROWTH IN GRANITE UNDER CONFINING PRESSURE

J. Byerlee and D. Lockner  
U.S. Geological Survey  
345 Middlefield Road, MS/977  
Menlo Park, CA 94025

The failure process in a brittle granite was studied using acoustic emission (AE) techniques. The AE arrival times were inverted to obtain three dimensional locations of the microfracturing events. During a creep experiment the nucleation of faulting coincided with the onset of tertiary creep, but the development of the fault could not be followed because the failure occurred catastrophically. A technique has been developed that enabled the failure process to be stabilized by controlling the axial stress to maintain a constant AE rate. As a result the post failure stress-strain curve was followed quasi-statically, extending to hours the fault growth process that normally would occur violently in a fraction of a second. The results from the controlled experiment showed that the fault plane nucleated at a point on the sample surface after the stress-strain curve reached its peak. Prior to nucleation the microcrack growth was distributed evenly throughout the sample. From the nucleation site the fault plane grew across the sample accompanied by a gradual drop in stress. AE locations showed that the fault propagated as a fracture front (process zone) with dimensions of 1 to 3 cm. As the fracture front passed, the AE from a given region would drop to a low level. When allowed to progress until the fault bisected the sample the stress dropped to the frictional strength. These observations are in agreement with the behavior predicted by Rudnicki and Rice's bifurcation analysis and in disagreement with experiments suggesting that shear localization in brittle rocks like granite starts while the material is still hardening.

SECOND-ORDER EFFECTS IN AN ELASTIC HALF SPACE  
ACTED UPON BY A NON-UNIFORMLY DISTRIBUTED LOAD

J. Guo and P.N. Kaloni  
Department of Mathematics and Statistics  
University of Windsor  
Windsor, Ontario N9B 3P4, Canada.

In the theory of finite elasticity of compressible materials, the problem of finding second-order solutions, in the sense of successive approximations, correspond to the solution of a classical linear elasticity problem with body force. In general, analytic solutions to find second-order effects become quite difficult because particular integrals for the body-force can not be obtained easily in explicit form. Here by using a transformation technique, we discuss and present solutions to a second-order elastic problem when an elastic half-space undergoes deformation owing to a non-uniformly distributed normal surface load. We find closed form expressions for displacements, stresses etc., in several special cases and also present the limiting solutions for incompressible materials.

# ON THE FORM OF THE INTERNAL-ENERGY FUNCTION FOR AN INCOMPRESSIBLE, ISOTROPIC, HYPERELASTIC MATERIAL

Donald E. Carlson  
Department of Theoretical and Applied Mechanics  
University of Illinois at Urbana-Champaign  
Urbana, IL 61801

According to contemporary thinking, the stress  $T$  in an internally constrained material is written as the sum of an active stress  $T^A$ , given in terms of appropriate kinematical variables through a constitutive equation, and a reactive stress  $T^R$ , which has zero power in any motion that satisfies the constraint. As a consequence of this latter condition, the general form of the reactive stress is determined by the constraint to within a scalar-valued multiplier, which is determined in a particular situation through the balance equations and the boundary and initial conditions. In the incompressible case, motions are constrained to be volume preserving, and the reactive stress is a pressure:  $T^R = -\pi I$ . Here,  $\pi$  is a scalar-valued function of position and time, and  $I$  is the identity tensor.

Since

$$T = T^A + T^R,$$

it is pointless to include in the constitutive equation for the active stress  $T^A$  any additive terms which are of the same form as the indeterminate reactive stress  $T^R$ . A natural way to ensure that this not happen is to give the linear space of symmetric tensors  $\text{Sym}$ , where the stress  $T$  lives, the orthogonal direct sum decomposition

$$\text{Sym} = \mathcal{R} \oplus \mathcal{R}^\perp,$$

where  $\mathcal{R}$  is the linear space whose elements are the reactive stresses  $T^R$ , and then to require that

$$T^A \in \mathcal{R}^\perp.$$

This condition is called the *normalization*, and it is important to understand that there is no loss of generality in imposing it. In the incompressible case,

$$\mathcal{R} = \{T: T = \alpha I, \alpha \in \mathbb{R}\}, \quad \mathcal{R}^\perp = \{T \in \text{Sym}: I \cdot T = \text{tr} T = 0\},$$

and the normalization is



$$\text{tr} T^4 = 0.$$

For an incompressible, isotropic, hyperelastic material, it is well-known that the internal-energy function is a function of the first and second invariants of the left deformation tensor. Here, it is shown that the above normalization requires that the internal-energy function reduce to a function of a single invariant -- the second invariant divided by the square of the first invariant.

# RECENT DEVELOPMENTS IN THE MECHANICS OF FRACTURED AND MICROFRACTURED CONTINUA

GIANPIETRO DEL PIERO

Istituto di Meccanica, Università di Udine  
Viale Ungheria 43, 33100 Udine, Italy

In this communication I present some results of a research still in progress, made jointly with D.R.Owen [1],[2], and devoted to the construction of a mathematical theory of fractured and microfractured continua. Our first goal was to describe mathematically the deformation of continuous bodies in the presence of fractures. For this purpose we introduced a class of simple deformations, consisting of piecewise  $C^1$  functions with discontinuities concentrated over surfaces of finite area. When completing this class with respect to a suitable metric, we found that the elements of the completed space were not any more functions, but objects whose nature depends on the metric chosen for the completion. We called these objects structured deformations.

Here I refer to the completion with respect to a  $L^\infty$  norm, in which a structured deformation is a triple  $(\kappa, g, G)$ , with  $\kappa$  a null set included in  $\Omega$ , the region of space occupied by the body,  $g$  a  $C^1$  vector field on  $\Omega \setminus \kappa$ , and  $G$  a continuous tensor field over the same set. The set  $\kappa$  is the site of the macroscopic fractures created by the structured deformation, and  $g$  is the function which maps points of the reference configuration into points of the deformed configuration. If  $\{g_h\}$  is a Cauchy sequence of simple deformations with respect to the chosen metric, then  $g$  is the limit of  $\{g_h\}$  and  $G$  is the limit of the sequence of the derivatives  $Dg_h$ . In view of their definition,  $G$  and  $Dg$  are interpreted as the deformation of the body as a continuum and as the macroscopic deformation, respectively. The inequality  $Dg \neq G$  reveals the presence of microfractures diffused in  $\Omega \setminus \kappa$ . They are measured by the difference  $Dg - G$ .

Diffused microfractures can be used in describing plastic deformation, the dilatancy of soils, the deterioration of the internal material structure occurring in damage, or the microcracking occurring in solids which do not support tension, such as masonry or stone. In

classical Continuum Mechanics, these effects are described by internal variables. A peculiarity of the proposed theory consists in describing them all as kinematical objects of the same nature. What changes from case to case is the constitutive equation relating the microscopic deformation gradient to the stress. For some one-dimensional examples see [3].

More sophisticated types of structured deformations, obtained by different procedures of completion, allow for the presence of microfractures concentrated over singular surfaces interior to the body [4]; they can be employed, for instance, to describe concentrated plastic flow.

#### REFERENCES

- [1] DEL PIERO, G., & D.R. OWEN, New Concepts in the Mechanics of Fractured Continua, Proc. 10th National Congress AIMETA, Pisa 1990.
- [2] DEL PIERO, G., & D.R. OWEN, in preparation.
- [3] DEL PIERO, G., & R. SAMPAIO, A Unified Treatment of Damage and Plasticity Based on a New Definition of Microfracture, Proc. 4th Meeting Unilateral Problems in Structural Analysis, Capri 1989. Publ. Birkhäuser Verlag, 1991.
- [4] DEL PIERO, G., A New Function Space for the Mathematical Theory of Plasticity, Proc. 2nd Internat. Symp. on Plasticity and Its Current Applications, Tsu, Japan, 1989. Publ. Pergamon Press, 1989.

## Gibbs Bivectors - Theory and Applications

M. Hayes

Mathematical Physics  
University College Dublin  
Belfield, Dublin 4, Ireland.

The combination of two real vectors  $\mathbf{a}$  and  $\mathbf{b}$  in the form  $\mathbf{a} + i\mathbf{b}$  where  $i^2 = -1$ , is called a bivector. Gibbs [1] associated an ellipse with each bivector. If the scalar product  $\mathbf{C} \cdot \mathbf{D}$  of two bivectors  $\mathbf{C}$  and  $\mathbf{D}$  is zero then the planes of the ellipses of  $\mathbf{C}$  and  $\mathbf{D}$  may not be orthogonal, in general [2]; also the orthogonal projection of the ellipse of  $\mathbf{C}$  upon the plane of the ellipse of  $\mathbf{D}$  is similar (same aspect ratio) and similarly situated (major axes parallel) to the ellipse of  $\mathbf{D}$  when rotated through a quadrant [1]. If  $\mathbf{C} \cdot \mathbf{C} = 0$  the bivector is said to be isotropic, the corresponding ellipse being a circle. Because inhomogeneous plane waves such as Rayleigh or Love waves in mechanics and  $TE$  and  $TM$  waves in electromagnetism are described in terms of two bivectors - the amplitude and slowness bivectors - the theory of bivectors finds ready application in wave propagation problems in mechanics [2] and optics [3].

### References

- [1] Gibbs, J.W., *Elements of Vector Analysis*, 1881 (privately printed)  $\equiv$  pp. 17-90, Vol. 2, Part 2 Scientific Papers, Dover Publications, New York 1961.
- [2] Hayes, M., *Inhomogeneous Plane Waves*. Archive for Rational Mechanics and Analysis **85** (1984) 41-79.
- [3] Boulanger, Ph. and Hayes, M., *Electromagnetic Plane Waves in Anisotropic Media*. Phil. Trans. Roy. Soc. A. **330** (1990) 335-393.

# SPATIAL DECAY ESTIMATES FOR COMPRESSIBLE FLOWS IN A CHANNEL HAVING CONSTANT SECTION

Mariarosaria Padula

Dipartimento di Matematica dell'Università,  
via Machiavelli 35, 44100 Ferrara, ITALY

Consider a stationary compressible viscous fluid in the infinite channel  $\Omega = \{x \in \mathbb{R}^3 : x_3 > 0, x' \equiv (x_1, x_2) \in \Sigma\}$ , where  $\Sigma$  is a smooth, bounded domain of  $\mathbb{R}^2$ . Denoting by  $\Gamma$  the lateral surface of  $\Omega$ , i.e.  $\Gamma = \{x \in \mathbb{R}^3 : x_3 > 0, x' \in \partial\Sigma\}$ , we take  $\rho = \rho_0$  and  $v = v_0$ , where  $v_0$  is the velocity field associated to the Poiseuille of an incompressible flow, as a basic solution of the steady problem corresponding to an ascribed flux  $\Phi$ . For  $\rho = \rho_0 + \sigma$ ,  $v = v_0 + u$  the density and velocity fields associated with a given steady motion, we assume that  $v \equiv 0$  a  $\Sigma$  and that the flux

$$\Phi = \int_{\Sigma} \rho v \cdot n$$

is prescribed. The problem is then to investigate the decay rate at which  $\rho(x)$ ,  $v(x)$  approach  $\rho_0$ ,  $v_0$  at infinity. Such a question represents the compressible counterpart of the incompressible problem in fluid-dynamic cf. Horgan & Wheeler (1978) who, however, consider a different version of the problem where  $\Omega$  is bounded, this amounting to suppose that the fully developed Poiseuille flow takes place at a finite value  $l$  of the  $x$ -coordinate. They then prove that if the Reynolds number  $\mathcal{R}$  satisfies  $\mathcal{R} < R$ , for a suitable positive constant  $R$ , the quantity

$$G(l, x_3) \equiv \int_{x_3}^{\infty} \left( \int_{\Sigma} |\nabla(v - v_0)|^2 d\Sigma \right) dx_3$$

decays exponentially to zero as  $x_3 \rightarrow \infty$ . However, their estimates no longer hold if  $l \rightarrow \infty$ . Moreover, very recently, Galdi proved, among others, that if

(i)  $\mathcal{R}_c$  satisfies (1) with  $R$  critical Reynolds number for the energy stability of the Poiseuille flow  $v_0$ ; (ii) for some  $M > 0$ ,  $G(z, 0) \leq Mz^{\frac{2}{3}}$ . Then,  $G(\infty, 0) < \infty$  and the exponential decay holds, i.e. there exist constants  $A, B, C > 0$  such

(i)  $G(\infty, x_3) \leq AG(\infty, 0) \exp(-Cx_3)$ , for all  $x_3 > 0$ ,

(ii)  $|D^\alpha(v - v_0)| \leq BG(\infty, 0) \exp(-Cx_3)$ , for all  $x_3 > d > 0$ ,

where  $D^\alpha$  is an arbitrary derivative of order  $\alpha \geq 0$ .

In this paper, setting

$$\mathcal{E}(l, x_3) \equiv \int_{x_3}^l \int_{\Sigma} [|\nabla(v - v_0)|^2 + \sigma^2] d\Sigma dx$$

we prove the following theorem.

**Theorem- Assume:**

(i)  $\mathcal{R}_c$  satisfies (1) with  $R$  critical Reynolds number for the energy stability of the Poiseuille flow  $v_0$

(ii) for some  $M > 0$ ,

$$\mathcal{E}(z, 0) \leq Mz^{\frac{2}{3}}. \quad (2)$$

Then,

$$\mathcal{E}(\infty, 0) < \infty$$

and there exist constants  $A, B, C > 0$  such that

$$\mathcal{E}(\infty, x_3) \leq A\mathcal{E}(\infty, 0) \exp(-Cx_3), \text{ for all } x_3 > 0.$$

#### REFERENCES

Horgan, C.O. & Wheeler, L.T. (1978) *Spatial Decay Estimates for the Navier-Stokes Equations with Applications to the Problem of Entry Flows*, SIAM J. Appl. Math., 35, 97.

Galdi, G.P., (1991), *Decay estimates for steady viscous flows in a semi-infinite channel*, 22-nd Midwestern Mechanics Conference, Rolla october, 6-9/1991.

## FORMULATION OF CRACK PROBLEMS

R. N. DUBEY, M. SINGH and G. GLINKA

Department of Mechanical Engineering,  
University of Waterloo, N2L 3G1, Canada.

### Introduction

The governing equations for finite deformation of a body can be described in a compact form in terms of either (a) the true or Cauchy stress,  $\sigma_{ij}$ , or (b) the nominal or 1st Piola-Kirchhoff stress,  $s_{ij}$ . The true stress is related to the current area and hence it is based on the deformed geometry; the associated formulation is labelled Eulerian. The nominal stress is based on the undeformed geometry, it is obtained with the help of the initial area; the corresponding formulation is called Lagrangian. Suppose that a prescribed loading deforms the body from its given initial configuration  $B_0$  into the final configuration  $B$ . The volume, boundary surface and the density of the body in two configurations are denoted  $V_0$ ,  $S_0$ ,  $\rho_0$  and  $V$ ,  $S$  and  $\rho$ , respectively. Let  $X_i$  be the coordinates of a particle in  $B_0$ . The Lagrangian formulation is mathematically expressed in terms of the equations of equilibrium

$$\frac{\partial s_{ij}}{\partial X_i} + \rho_0 f_j = 0 \quad \text{in } V_0 \quad (1)$$

and the boundary conditions

$$\begin{aligned} t_j &= N_i s_{ij} \quad \text{on } S_0^t \\ u_i &= U_i \quad \text{on } S_0 - S_0^t \end{aligned} \quad (2)$$

On the other hand, the Eulerian formulation uses the current position  $x_i$  of the particle in the equations of equilibrium

$$\frac{\partial \sigma_{ij}}{\partial x_i} + \rho f_j = 0 \quad \text{in } V \quad (3)$$

The boundary conditions are stated in the form

$$\begin{aligned} t_j &= n_i \sigma_{ij} \quad \text{on } S^t \\ u_i &= U_i \quad \text{on } S - S^t \end{aligned} \quad (4)$$

In the two formulations,  $N_i$  and  $n_i$  represent the unit external normals to the initial and the current boundaries, respectively, and  $f_i$  is the body force. In addition, the equilibrium condition for the moment requires that

$$\sigma_{ij} = \sigma_{ji} \text{ in } V, \text{ or} \quad (5)$$

$$\frac{\partial x_i}{\partial X_k} s_{kj} = \frac{\partial x_j}{\partial X_k} s_{ki} \text{ in } V_0 \quad (6)$$

In the infinitesimal theory, it is assumed that  $x_i \sim X_i$  and the current boundary in the Eulerian formulation is approximated by the initial boundary of the Lagrangian formulation. As a result, one obtains only an approximate solution of the boundary-value problem.

In the case of finite deformation, such an approximation may not be valid. It is then necessary to use the Lagrangian formulation in order to employ the prescribed traction kinematic constraints on the undeformed boundary. In the Eulerian formulation, a correct formulation of the boundary conditions requires the use of the deformed boundary, especially those involving traction.

### Application

This paper presents a solution for the boundary value problem involving an infinite plate with an initial crack and subject to uniaxial loading. The material behaviour has been assumed isotropic elastic and the formulation used is Eulerian. Therefore, the prescribed boundary conditions must be expressed in terms of the deformed boundary surface.

The solution suggests that the cracks open and the tip radius is no longer zero. The radius can in fact be calculated from the displacement field which also helps relate the deformed boundary to the prescribed initial crack geometry. It is also found that the stress at the tip is finite. It depends on the elastic modulus and is independent of the applied far-field stress. It follows that the concentration factor is finite and its value depends on Young's modulus and the far-field stress.

In the case of a notch, the solution yields the concentration factor of three provided the deformed opening is a circle.

### Acknowledgement

Authors gratefully acknowledge the partial support of NSERC grants.



EARLY TRANSIENT RESPONSE DURING CRACK PROPAGATION  
IN A WEAKLY-COUPLED THERMOELASTIC SOLID

L.M. Brock  
Engineering Mechanics  
University of Kentucky  
Lexington, KY 40506

P. Matic and V.G. DeGiorgi  
Code 6382  
Naval Research Laboratory  
Washington, DC 20375

Various results [1] indicate that significant temperature rises can occur during fracture. Because 90% of plastic deformation energy goes into heat [2] these temperature rises are associated with inelastic zones at crack edges.

Studies often treat steady-state crack growth e.g. [3]. In some contrast, we are here interested in rapid, nearly-brittle fracture under dynamic loading during the period right after initiation. A rudimentary inelastic zone acts as a heat flux site in a weakly-coupled [4] thermoelastic solid. The solid is unbounded and the dynamic loading is provided by stress wave diffraction. The inelastic zone has a Dugdale [5] geometry, and causes crack blunting. However, the zone heat flux is not a priori fixed, and the fracture and heat energies are not necessarily the same. A transient 2D analysis is performed, and nearly exact results obtained for short times after fracture/zone growth initiation. As a first step, a simple heat flux model and constant crack and zone extension rates are treated.

Two cases are considered: In the first case the crack is initially undisturbed while, in the second, an inelastic zone

exists in equilibrium with a uniform tension field prior to stress wave loading. Analyses show that, for step-stress waves, the stress level must exceed that predicted in a non-thermal analysis for inelastic zone growth. Temperatures rise in the zone extremely rapidly before leveling off at values that are inversely proportional to zone growth rate. The analysis also shows that allowing the yield stress to vary with temperature produces an inelastic zone temperature rise that is initially different from that associated with a constant yield stress, but not markedly so.

#### Acknowledgement

This work was partially supported by NSF Grant MSM 89117944 to LMB, and the basic analysis was performed while he was a 1990 Navy/ASEE Summer Research Faculty Fellow at the Naval Research Laboratory, Washington, DC.

#### References

1. Zehnder, A.T. and Rosakis, A.J. 1989 "On the temperature distribution at the vicinity of dynamically propagating cracks in 4340 steel," SM 89-2, Pasadena: California Institute of Technology.
2. Taylor, G.I. and Quinney, M.A. 1934 "The latent energy remaining in a metal after cold working," *Proceedings of the Royal Society* A143, pp. 307-322.
3. Rice, J.R. and Levy, N. 1969 "Local heating by plastic deformation at a crack tip," in Physics of Strength and Plasticity (A.S. Argon, ed.) Cambridge, MA: MIT Press.
4. Boley, B. and Weiner, J.H. 1960 Theory of Thermal Stresses, New York: Wiley.
5. Dugdale, D.S. 1960 "Yielding of steel sheets containing slits," *Journal of the Mechanics and Physics of Solids* 8, pp. 100-104.

# PRESSURE-SENSITIVE YIELDING ON FRACTURE

J. Pan

Mechanical Engineering and Applied Mechanics  
The University of Michigan  
Ann Arbor, Michigan 48109

Many materials such as zirconia-containing ceramics and some polymeric materials exhibit appreciable pressure-sensitive yielding and macroscopic volume changes under large deformation. Crack-tip fields for these pressure-sensitive materials are examined. Mode I loading and plane-strain conditions are considered. The yield criterion is chosen to be a linear combination of the shear effective stress and the hydrostatic stress, and the plastic flow follows the normality rule. For power-law hardening materials, HRR-type crack-tip fields are obtained by asymptotic analysis based on a stress function for  $\mu < \mu_{lim}$  where  $\mu$  is a pressure sensitivity parameter and  $\mu_{lim}$  is the limit value of  $\mu$  for each hardening exponent  $n$  (Li and Pan, *J. Appl. Mech.*, 1990). The numerical method used by Li and Pan is based on the Runge-Kutta integration scheme and the shooting method to satisfy the boundary conditions. As  $\mu$  increases and approaches  $\mu_{lim}$ , the stress state ahead of the crack tip approaches hydrostatic tension, which is at the vertex of the yield surface in the stress space, and the numerical method based on the stress function diverges.

An accurate finite element method of a deformation plasticity nature is formulated to investigate the asymptotic crack-tip behavior for  $\mu > \mu_{lim}$ . The finite element results confirm the asymptotic results for  $\mu < \mu_{lim}$ . The finite element results also show the existence of HRR-type crack-tip fields for  $\mu > \mu_{lim}$ . In addition, the finite element results show that as  $\mu$  increases from  $\mu_{lim}$ , the stress state ahead of the tip remains in hydrostatic tension. Plastic zones are also given for different values of the pressure sensitivity parameter  $\mu$  and the hardening exponent  $n$ . The pressure sensitivity parameter  $\mu$  and the hardening exponent  $n$  have significant effects on the plastic zone sizes and shapes. The plastic zone sizes and shapes differ significantly from those of the generalized effective stress contours from asymptotic analyses. The finite element results show that the contribution of the hydrostatic stress in the yield function causes the plastic zone boundary in front of the crack tip to extend much farther than that in a pressure-insensitive material. Implications of pressure-sensitive yielding on toughening are discussed.

## SOME ASPECTS OF CREEP STABILITY ANALYSIS\*

P.G. Glockner  
Professor of Civil and Mechanical Engineering  
The University of Calgary  
Calgary, Alberta, Canada

W. Szyszkowski  
Professor of Mechanical Engineering  
The University of Saskatchewan  
Saskatoon, Saskatchewan, Canada

The continuing emphasis on preservation of the environment and conservation of natural resources has focused attention on increased use of many natural materials or the use as a new structural material of abundantly available indigenous materials heretofore largely ignored, such as ice, rock and other natural materials. A material like ice is very much time and temperature dependent and therefore creep behaviour becomes important in the design and analysis of any structure involving elements made of such a material. The emphasis on time dependent response of structures is further underlined by recent introduction and general acceptance of new 'synthetic' structural materials such as plastics and fibre-reinforced resins. This emphasis brought about research and development with significant advances in our understanding of the behaviour of time dependent materials and leading to improved constitutive models which, in turn, resulted in more realistic predictions of the behaviour of structures and structural components made of such materials. We have seen significant advances in specialized areas such as the stability and post-buckling behaviour of columns made of materials undergoing creep and a clarification of concepts associated with such behaviour. Thus, new definitions and important parameters like the 'safe-load-limit',  $P_v$ , and the 'safe-service-period',  $t_s$ , were introduced and closed-form expressions obtained for them for linear materials. In the case of nonlinear materials convenient numerical and computational solution techniques are now available for their determination. When dealing with creep stability problems the engineer is interested primarily in determining these two key design parameters since a load level  $P < P_v$  ensures stable behaviour for all times. For load levels  $P_v < P < P_e$ , where  $P_e$  denotes the classical Euler load, the safe-service-life is of interest and its determination may have significant effects on the economic feasibility of the proposed design.

In this paper we will briefly review some of our work in this area [1-7] pointing out its relevance to the everyday design process and generally placing its significance and importance in perspective. Particularly and after reviewing briefly the key features of our

---

\* The results presented were obtained in the course of research sponsored by the Natural Sciences and Engineering Research Council of Canada, Grants No. A-2736 and A-5676.

material model underlying most of our results, we will discuss the significance of the safe-load-limit,  $P_v$ , and the manner in which this design parameter is affected by material and/or geometric nonlinearities and imperfections. We will also briefly describe a semigraphical solution technique introduced in [2,6] which can be used conveniently to determine this parameter for a column made of a nonlinear time-dependent material.

Next we discuss the viscoelastic instability domain and the manner in which material and geometric imperfections influence the safe-service-period,  $t_s$ . We will show that imperfections influence  $t_s$  more significantly than short duration or transient disturbances, and that these imperfections can be and should be treated as permanent disturbances.

Finally we will discuss structural configurations involving compression members which exhibit unstable post-buckling characteristics and which have associated imperfection sensitivity. The structural designer has to be aware of such imperfection sensitivity and of the effects such small imperfections can play in structures made of time-dependent materials, imperfections which normally are of no significance in the overall behaviour and response of elastic structures. In the case of structures made of time-dependent materials, such small imperfections can lead to significant reductions in the load carrying capacity and the safe-service-period of a structure which is undergoing creep, thereby underscoring the importance of time as an ever-present destabilizing parameter. The paper also discusses the significance of the safe-load-limit and points out that, as opposed to the two stability domains of Hookean columns, there are three basic stability domains of columns made of time-dependent materials namely an absolutely stable domain for loads  $P < P_v$  in which the response of the structure is bounded for  $t \rightarrow \infty$ ; a creep stability domain for  $P_v < P < P_c$  in which the response is unbounded for  $t \rightarrow \infty$ ; and a dynamically unstable domain for  $P > P_c$  with instantaneous indeterminate unbounded response.

## References

- [1] Dost, S. and Glockner, P.G., "On the Dynamic Stability of Viscoelastic Perfect Columns", *Int. J. Solids Structures*, **18**, 1982, pp. 587-596.
- [2] Glockner, P.G. and Szyszkowski, W., "On the Stability of Columns Made of Time-Dependent Materials", Chapter 23 in Vol. 1, 'Structures' of *Encyclopedia of Civil Engineering Practice*, P.N. Cheremisinoff, et al. (eds.), Technomic Publishing Co. Inc., 1987, pp. 577-626.
- [3] Szyszkowski, W. and Glockner, P.G., "The Stability of Viscoelastic Perfect Columns: A Dynamic Approach", *Int. J. Solids Structures*, **21**, 1984, pp. 545-553.
- [4] Szyszkowski, W. and Glockner, P.G., "The Imperfect Linearly Viscoelastic Column", *Int. J. Engg. Sci.*, **23**, (10), 1985, pp. 1113-1120.
- [5] Szyszkowski, W. and Glockner, P.G., "On the Static Stability Analysis of Viscoelastic Perfect Columns", *CSME Transactions*, **9**, 1985, pp. 156-163.
- [6] Szyszkowski, W. and Glockner, P.G., "On the Safe Load Limit of Columns Made of Time-Dependent Materials", *Acta Mechanica* **65**, 1986, pp. 181-204.
- [7] Szyszkowski, W. and Glockner, P.G., "Further Results on the Stability of Viscoelastic Columns", *CSME Transactions*, **11**, No. 3, 1987, pp. 179-194.

## **MATERIAL MODELING FOR PROCESS MODELING AND FAILURE ANALYSIS**

**R. E. Smelser and R. Becker  
Fabricating Technology Division  
Alcoa Laboratories, Alcoa Center, PA 15069**

The demand for improved processing and utilization of materials requires a deeper understanding of the evolving material microstructure and damage during complex loading histories. To achieve this understanding, quantitative descriptions of the evolving microstructure are necessary. Various levels of material description are required depending on the type of information being sought. These descriptions may range from the variation of hardness, microporosity or crystallographic texture throughout a manufactured part to the effects of voids and second phase particles on ductile fracture during the life of the part. Detailed macromechanical process models as well as micromechanical material models are needed to gain a quantitative understanding of material performance.

The complexity of the process models and material models usually requires that numerical techniques be used for their solution. This presents a challenging task for both the numerical technique and the solution algorithm. The numerical technique must be able to address nonuniform geometries, large deformations and complex loading histories. The numerical technique must also allow the implementation of history dependent constitutive behavior with internal state variables and the modeling of complex interface behavior. The solution algorithms must be accurate and robust. The finite element method offers the flexibility to satisfy these requirements.

The capability of including evolving microstructure at the level of an amorphous continuum material model is given by internal state variable constitutive models [see e.g. Sample and Lalli, 1987 and their references]. The inclusion of this type of constitutive behavior in a process model allows one to obtain a prediction of the material microstructure throughout the deformed piece. An example of the predicted microhardness distribution and an experimentally measured microhardness distribution in a hot rolled plate has been given by Smelser and Thompson [1987]. Such process simulations provide a means for assessing process modifications to obtain a desired distribution of material structure in the product.

The inclusion of multiple phases in the material microstructure becomes important when trying to predict the failure of materials. The ductile failure of many structural materials occurs by the growth and coalescence of voids [e.g. Edelson and Baldwin, 1962]. Continuum models of ductile failure have been developed [e.g. Saje et al. 1982]. These models address the failure of materials by introducing a region of material which contains a higher volume fraction of voids than the surrounding material. Such models predict failure strains which are isotropic using unrealistically large void volume fractions.

The failure of materials is usually not isotropic [e.g. Speich and Spitzig, 1982]. The modeling of the anisotropy of fracture requires detailed micromechanical models of the material. A model of the experiments of Speich and Spitzig has been developed by Becker et al. [1989a]. The failure predictions from this micromechanical model predict the fracture

strain to within a factor of two. The void growth predicted from this type of micromechanical model can also be incorporated into the continuum models mentioned previously. A method for this has been given by Becker et al. [1989b].

A final example of the inclusion of material modeling in process modeling is given by the development of plastic flow localization in the bending of a polycrystalline sheet [Becker, 1990]. The polycrystal model of Asaro and Needleman [1985] has been used to model the material constitutive behavior. The polycrystal constitutive model develops a vertex at the loading point of the yield surface. This facilitates the development of shear band type bifurcations [Needleman and Rice, 1978]. The comparison of the predicted flow localization with that measured experimentally was accurate and encouraging.

The development and use of detailed material models has been shown to give good predictions of the material microstructure and failure predictions in process models. The use of such detailed constitutive models has been made possible by the development of increasingly sophisticated numerical techniques, increasingly robust numerical algorithms and the development of powerful computers to carry out the calculations. The continued development of detailed constitutive models for materials presents an opportunity for realistic process simulations and failure predictions.

### References

- R. J. Asaro and A. Needleman, 1985, Texture Development and Strain Hardening in Rate Dependent Polycrystals, *Acta Metallurgica*, Vol. 33, 923-953.
- R. Becker, 1990, An Analysis of Shear Localization During Bending of A Polycrystalline Sheet, in *Microstructural Evolution in Metal Processing* PED-Vol. 46, E. S. Geskin and I. V. Samarasekera eds, American Society of Mechanical Engineers, New York, 35-45.
- R. Becker, R. E. Smelser, O. Richmond and E. J. Appleby, 1989a, The Effect of Void Shape on Void Growth and Ductility in Axisymmetric Tension Tests, *Metallurgical Transactions A*, Vol. 20A, 853-861.
- R. Becker, R. E. Smelser and O. Richmond, 1989b, The Effect of Void Shape on the Development of Damage and Fracture in Plane-Strain Tension, *Journal of the Mechanics and Physics of Solids*, Vol. 37, 111-129.
- B. I. Edelson and W. M. Baldwin, Jr., 1962, The Effect of Second Phases on the Mechanical Properties of Alloys, *Transactions of the ASM*, Vol. 55, 230-250.
- A. Needleman and J. R. Rice, 1978, Limits to Ductility Set by Plastic Flow Localization, in *Mechanics of Sheet Metal Forming - Material Behavior and Deformation Analysis*, D. P. Koistinen and N.-M. Wang eds, Plenum Press, New York, 237-265.
- M. Saje, J. Pan and A. Needleman, 1982, Void Nucleation Effects on Shear Localization in Porous Plastic Solids, *International Journal of Fracture*, Vol. 19, 163-182.
- V. M. Sample and L. A. Lalli, 1987, Effects of Thermomechanical History on the Hardness of Aluminum, *Materials Science and Technology*, Vol. 3, 28-35.
- G. R. Speich and W. A. Spitzig, 1982, Effect of Volume Fraction and Shape of Sulfide Inclusions on Through-Thickness Ductility and Impact Energy of High-Strength 4340 Plate Steels, *Metallurgical Transactions A*, Vol. 13A, 2239-2257.
- R. E. Smelser and E. G. Thompson, 1987, Validation of Flow Formulation for Process Modelling, in *Advances in Inelastic Analysis* AMD-Vol. 88, PED-Vol. 28, S Nakazawa et al. eds, American Society of Mechanical Engineers, New York, 272-283.

# FLOW FORMULATION OF THE RATE EQUILIBRIUM EQUATIONS APPLIED TO ELASTIC, VISCOPLASTIC MATERIALS

Lung Tsai  
Erik G. Thompson

Department of Civil Engineering  
Colorado State University  
Fort Collins, CO 80523

Steady-state, finite-element analyses of metal forming processes can provide valuable and accurate information. However, such analyses normally require that the elastic response of the process be neglected. When the elastic behavior of the material is included in the standard flow formulation, numerical instabilities occur. Recently, Yu and Thompson [1,2] developed a steady-state flow formulation which is stable for high elastic responses. They used the technique for the analysis of drawing of elastic, perfectly plastic materials.

Yu and Thompson attributed the numerical instabilities associated with the standard flow formulation to the presence of the gradient of stress in the Eulerian formulation of the constitutive equation. They noted that this gradient does not appear in the governing equation for momentum balance if the rate of equilibrium equation is used rather than the equilibrium equation itself. The rate equilibrium equation is obtained by specifying the material derivative of the equilibrium equation to be zero. Thus it can easily be shown [2] that

$$\frac{D}{Dt} \left[ \frac{\partial \sigma_{ij}}{\partial x_i} \right] = \frac{\partial}{\partial x_i} \left[ \frac{D\sigma_{ij}}{Dt} - \frac{\partial u_i}{\partial x_k} \sigma_{kj} + \frac{\partial u_k}{\partial x_i} \sigma_{kj} \right] = 0$$

where  $\sigma_{ij}$  is the Cauchy stress and  $u_i$  is the velocity. The terms in the bracket represent the material derivative of the first Piola-Kirchhoff stress.

An elastic, viscoplastic material can be represented using a constitutive equation having the form:

$$(D_{ij} - \delta_{ij} D_{kk}) = \frac{1}{2\mu} S_{ij} + \frac{1}{2G} \mathcal{D}_t (\sigma_{ij} - \delta_{ij} \sigma_{kk})$$

$$D_{kk} = \frac{1}{3K} \frac{D\sigma_{kk}}{Dt}$$

where  $D_{ij}$  is the rate of deformation,  $\mathcal{D}_t(\cdot)$  represents an appropriate stress rate,  $G$  and  $K$  are elastic constants, and  $\mu$  is the effective viscosity for plastic deformation.



Two stress rates have been investigated: the Jaumann rate,

$$\mathcal{D}_t(\sigma_{ij}) = \frac{D\sigma_{ij}}{Dt} - \omega_{kj}\sigma_{ik} - \omega_{ki}\sigma_{jk}$$

and the upper convective Oldroyd rate,

$$\mathcal{D}_t(\sigma_{ij}) = \frac{D\sigma_{ij}}{Dt} - u_{i,k}\sigma_{kj} - u_{j,k}\sigma_{ik}$$

When either of these rates is used, the resulting weak formulation of the problem is void of stress gradients.

Recent efforts to extend the procedure developed in [2] to include elastic, viscoplastic materials has revealed that the gradient of stress might not be the sole source of the trouble associated with the equilibrium approach. It has been found that the rate of equilibrium approach becomes unstable as the viscous response of the material is increased. When this phenomenon was investigated, a mathematical similarity between the two approaches was noted which might explain the unstable behavior found in both methods.

This paper will discuss the current state of the research and will focus on some new methods to stabilize both the equilibrium and the rate-of-equilibrium approaches. Application will be to drawing and rolling of elastic, viscoplastic materials.

## REFERENCES

- [1] S.-W. Yu and E.G. Thompson. A direct Eulerian finite element method for steady state elastic plastic flow. In E.G. Thompson, R.D. Wood, O.C. Zienkiewicz, and A. Samuelsson, editors, *NUMIFORM89*, pages 95-103. A.A.Balkema, 1989.
- [2] E.G. Thompson and S.-W. Yu. A flow formulation rate equilibrium equations. *Int. J. for Num. Meth. in Eng.*, 30:1619-1632, 1990.

## A BEM/FEM Framework for Simulation of a Workpiece Deformed by an Elastic Tool

A. J. Beaudoin, S. Mukherjee, and P. R. Dawson  
Cornell University, Ithaca, NY

**Introduction.** A solution methodology is developed for the simulation of a plastic workpiece deformed by an elastic tool. The solution procedure for tool displacements is based on the Boundary Element Method. The plastic response of the workpiece is computed using the Finite Element Method with the material configuration advanced through an updated Lagrangian procedure. At each update increment, tool deflections (BEM) are recomputed based on surface tractions developed in the previous iteration for the workpiece stresses (FEM). The updated tool geometry correspondingly modifies the contact constraint applied in the FEM plasticity solution over the subsequent time step.

**Contact Algorithm.** Contact between the tool and the workpiece results in a normal traction which is assumed to follow an invertible relationship of the form (Eggert and Dawson, 1991)

$$T_n = f(\hat{s}, s_o, T_o) \quad (1)$$

where  $T_n$  is the normal traction,  $\hat{s}$  is the separation distance from the tool, and  $s_o$  and  $T_o$  are characteristic distances and tractions, respectively. The contact penalty constraint is introduced by adding the equation

$$\{\bar{T}_n\}^T \left[ \int_{S_c} [N]^T (\hat{\dot{s}} - \dot{s}) dS \right] = 0 \quad (2)$$

to the system of equations resulting from the FEM formulation. Here,  $\bar{T}_n$  are nodal point normal tractions,  $\hat{\dot{s}}$  is the rate of separation distance developed from Equation 1,  $N$  are shape functions, and  $S_c$  is the segment of workpiece surface in contact with the tool. The separation distance  $\dot{s}$  must be computed from the current geometric configuration of the tool and the workpiece.

**Tool Description.** Tool deflections are computed using a two-dimensional plane strain formulation based on the Boundary Element Method. Quadratic shape functions were used to form the elements. Consistent with this choice of shape functions, the tool surface was described parametrically by a table of normalized distances  $0 \leq s_i \leq 1$  along the tool surface. As described above, development of the contact constraint for the deforming material (FEM solution) requires the evaluation of the minimum distance to the tool surface. Using the parametric description, and for a particular point on the FEM domain, the functional form of this distance measure may be written

$$r = f(s) \quad (3)$$

The minimum distance from a point on the FEM domain to the tool is obtained by minimization of this function. This is carried out by first conducting a linear search to locate the element on which this minimum value lies, and then performing bisection on the element.

**Solution Algorithm.** The above are compiled into the following iterative solution procedure.

1. Tool is advanced
2. FEM solution for plastic deformation of workpiece
3. Traction are computed
4. BEM solution for tool deflections
5. Workpiece and tool configurations are updated

**Results.** The above algorithm has been used to simulate the deformation of a material obeying a strain hardening constitutive relationship. Initial simulations were performed for a cylindrical tool deforming a rectangular slab. This choice enabled comparison of tool stresses with available closed form solution. Results were also compared to a non-deforming circular tool. The expected "flattening" of the round tool upon contact with the workpiece was observed. Tools with convex and concave contacting surfaces are currently under investigation.

**References** Eggert, G.M. and Dawson, P.R. (1991) A Consistent Penalty Method for Rigid Contact, in preparation.

## OPTIMIZING DIE DESIGN AND PROCESING CONDITIONS FOR SUPERPLASTIC FORMING WITH FEA\*

E. C. Flower, D. J. Nikkel, Jr., D. D. Sam, and P. J. Raboin  
Mechanical Engineering Department  
Lawrence Livermore National Laboratory  
Livermore, CA 94550

Superplasticity refers to the ability of a metal to undergo extensive uniform tensile elongation (potentially greater than 1000% strain) prior to failure. Materials which are capable of exhibiting superplastic behavior can do so only for specific ranges of temperature and strain rate. Superplastic forming refers to a process which utilizes this material phenomena to form complex near net shapes. Thin sheets can be formed by placing the sheet over a heated die cavity that is sealed on the periphery and applying an inert gas pressure to the top. Pressures are generally low to keep the material rate of deformation in the superplastic range which is usually between  $10^{-4}$  and  $10^{-2}$  per second. Because of the need to keep the strain rate within known bounds, a critical aspect of the forming process is the pressure time history applied to the part. Another aspect of this which is critical to the economics of the process is the need to form at the highest rate possible without losing the superplastic properties of the material.

One potential problem with the process described above is that the blank may experience too much thinning at the polar region of a part. One way to overcome this is to use a reverse blow forming process in which the blank is first formed into one side of a two sided die which is designed to cause pre-straining of the material away from the polar region. The pressure is then reversed forming the blank into the other side of the die which is of the desired final shape. Critical to the success of this process is the design of the die.

We present a numerical method which accurately models the superplastic forming of a thin sheet into a hemispherical shape using a reverse blow forming process. Finite element modeling and analysis (FEA) using the large deformation implicit code NIKE2D is used to optimize the pressure time history and die design.

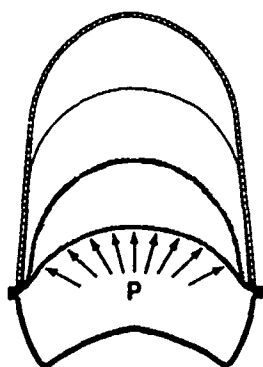
Central to the FE analysis is the constitutive model that determines the material response. To accurately model a material which can exhibit superplastic behavior requires an inelastic constitutive model which is both temperature and strain rate dependent. Moreover, in order to accurately predict the material behavior which occurs during the reverse blow forming process requires a model which keeps track of the inelastic components of the strain and can take into

---

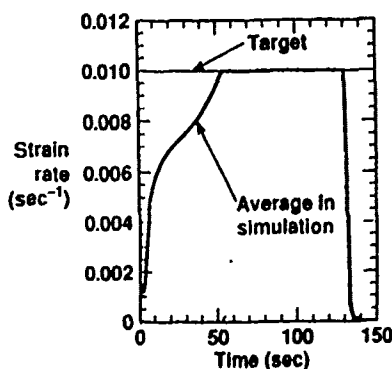
\* Work performed under the auspices of the U.S. Department of Energy by the Lawrence Livermore National Laboratory under contract number W-7405-ENG-48.

account such a complex deformation path. We used Bammann's rate and temperature dependent plasticity model in our calculations as it meets these criteria and provides quite a bit of flexibility in specifying material properties. The inelastic part of this constitutive model contains six temperature dependent parameter functions, the functional form of which is fixed, and which involve a total of twelve material constants. These functions are related to the rate-independent yield stress, the rate sensitivity of the material, the hardening, and the static and dynamic recovery. One additional material constant governs the adiabatic heating. The isothermal case involves only six constants.

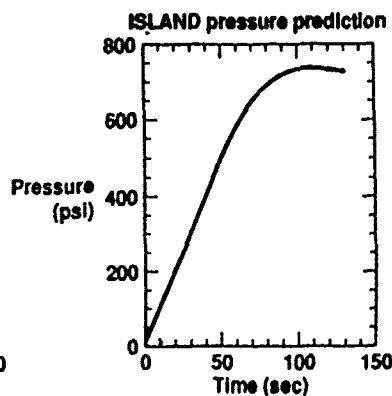
Apart from the issue of an appropriate constitutive model for superplastic materials, modeling the reverse blow forming process provides a number of numerical challenges by itself. The deformations are large, material surfaces come into and go out of contact, and the blank undergoes a very nonlinear *snap-through* process when the pressure is reversed. All of these issues combine to make this a hard process to model, and make the problem of optimizing processing conditions very difficult. We have exploited a new adaptive solution control feature of the NIKE2D code, known as ISLAND, which allows for this problem to be accurately modeled, and enables the processing conditions to be optimized in a straight forward manner. Rather than having to specify boundary conditions and convergence criteria *a priori*, ISLAND allows such conditions to be altered as a calculation proceeds based upon a variety of criteria involving the current value of field variables. By prescribing an adaptive scheme in which the pressure is adjusted so that the maximum strain rate experienced by material elements is a particular value, the calculation determines the appropriate pressure history for keeping the material within the superplastic range as a part of the solution.



ISLAND controls applied pressure to achieve target deformation rate in superplastic material



Trial and error is eliminated by ISLAND strategy



Optimum pressure processing conditions

# DYNAMIC RESPONSE OF A ROTATING DISK WITH VARIABLE THICKNESS AND A STATIONARY TRANSVERSE LOAD

Fred Barez  
Mechanical Engineering Department  
San Jose State University  
San Jose, CA 95192-0087

## ABSTRACT

This paper presents the results of an investigation on the effects of thickness uniformity and a transverse load on the stability of a rotating elastic disk such as that used in a computer disk file.

## INTRODUCTION

In a computer disk file, magnetic recording is accomplished by the relative motion of a magnetic recording head and a magnetic media. An air bearing separates the recording head from the disk and the head is attached to an external supporting member by means of a flexible mounting. The storage capacity of computer disk files can increase due to a reduction in this air bearing separation, so-called head to disk flying height. The current technology requires a head to disk spacing of about 0.1  $\mu\text{m}$  and it must be maintained under a wide range of operating conditions without contact. This will impose severe constraints on the design of both the head and the disk. This research addresses the dynamic response of the disk. Finite element analysis was carried out to model the disk and the effect of the head in the form of a stationary transverse load. The effects of the disk thickness uniformity is also studied. The finite element model results are compared to the analytical ones using membrane theory.

## FINITE ELEMENT MODEL

The disk and head combination model consists of an elastic, homogeneous, circular disk clamped at an inner radius  $a$  of a spindle and free at an outer radius of  $b$ . The transverse load is a stationary point load located at a radius of  $C$ . The disk is a 20 mm inner radius, 65 mm outer radius and 1.9 mm thick made of 5586 aluminum alloy. The transverse load of 0.15 N is applied at a radius of 27 mm. The disk is rotating at an angular speed of 3600 RPM. The finite element model shown in Fig. 1 is formed using isoparametric thin shell elements for the disk and concentrated load for the transverse loading. Disk thickness variation is introduced by specifying different thickness variation in the model.

## GOVERNINIG EQUATIONS OF THE ROTATING DISK

The equations of motion of the disk is governed by the classical membrane theory in which the effects of the rotatory inertia and shear deformation of the disk are not taken into account. Further, it is assumed that the disk transverse deflections are small compared to the disk thickness[1,2]. In the case of a rotating undamped uniform thickness disk anaytical solutions of the resonant frequency are obtained by means of the classical theory. However, in case of a rotating undamped disk of variable thickness and the inclusion of the rotatory inertia and the shear deformation, the frequencies need to be obtained numerically since closed-form solution is not available. Mindlin theory is applied in analyzing this problem in the presence of the rotatory inertia and shear deformation[3].

## RESULTS AND DISCUSSIONS

Finite element analysis results for the resonant frequencies of the rotating disk with uniform thickness are determined and compared to those derived from the classical membrane theory. For the variable thickness disk, the resonant frequencies determined by finite element analysis are compared to the numerically calculated ones. These resonant frequencies are also compared to the ones associated with those of the disk where the rotatory inertia and shear deformation have been taken into account. Transfer Matrix method[4] is employed using the Runge-Kutta-Gill integration appraoch[3] to calculate the numerical values. The effect of the transverse load due to the head loading on the disk is quite negligible compared to the harmonically induced accelerations in the transverse direction. The effect of the element size in the radial direction on the values of resonant frequency are also discussed.

## REFERENCES

1. Lamb. H. and Southwell, R. V., "The Vibrations of a Spinning Disk." Proceedings of the Royal Society, London, Vol. 99, 1921. PP. 272-280.
2. Barasch, S. and Chen, Y. "On the Vibration of a Rotating Disk." ASME Journal of Applied Mechanics, Vol. 39, 2972, pp. 1143-1144.
3. Irie, T., Yamada, G., and Aomura, S., "The Steady-State Response of a Rotating Damped Disk of Variable Thickness," ASME Journal of Applied Mechanics, Vol. 47, December 1980, pp.896-900.
4. Ehrich, F. F., "A Matrix Solution for the Vibration Modes of Nonuniform Disks." ASME Journal of Applied Mechanics, Vol. 23, 1956. pp. 109-115.

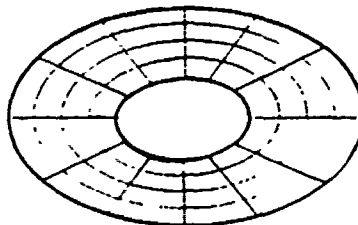


Fig. 1

## ANALYSIS OF PLATES ON ELASTIC FOUNDATIONS: A NEW APPROACH

C.V. Girija Vallabhan, Professor, Dept. of Civil Engineering,  
Texas Tech Univ., Lubbock, TX  
W. Thomas Straughan, Associate Professor, Dept. of Civil Engineering,  
Univ. of New Orleans, New Orleans, LA  
Y.C. Das, Visiting Professor, Dept. of Civil Engineering,  
Texas Tech Univ., Lubbock, TX

The classical problem of the analysis of plates on elastic foundations has been recognized by engineers as a complex soil-structure interaction problem. Practicing engineers continue to use the Winkler model for the analysis of beams and plates resting on elastic foundations despite the disclosure of some of the inconsistencies of the use of the Winkler model by many researchers in the past. To use the Winkler model, the engineer has to determine the value of the modulus of subgrade reaction,  $k$ , representing the soil continuum. The most important behavioral inconsistency of this model is that the analysis of plates carrying a uniformly distributed lateral load or a uniformly varying load, will result in a rigid body displacement of the plate with zero bending moment and transverse shear force within the plate. Recognizing the inherent difficulties in determining the value of  $k$  for a foundation, several researchers such as Biot, Vesic, Filonenko-Borodich, Hetényi, and Pasternak have attempted to make the Winkler model more realistic. All these works are summarized by Scott (1981) in his book on foundation analysis. Using Boussinesq equations and finite elements, Cheung and Zienkiewicz (1965) modeled plates on elastic foundations, assuming that the soil is a semi-infinite elastic continuum, an assumption that may not be realistic, because it may lead to conservative displacements, bending moments and shear forces, etc., in the plate.

Vlasov and Leont'ev (1966), recognizing the difficulty in determining values of  $k$  for soils, as well as the behavioral inconsistency in the Winkler model, postulated a two-parameter model using a theoretical approach to represent the soil continuum. Vlasov's model provided for the effect of the neglected shear strain energy in the soil and the subsequent shear forces on the plate edges as a result of the soil displacement. The disadvantage of this model is that it introduced a parameter,  $\gamma$ , that describes the distribution of the vertical displacement in the soil medium, whose value has to be estimated and no mechanism was provided for computing its value. Jones and Xenophontos (1977) derived the relationship between the  $\gamma$  parameter and the surface displacements, and recent work by Vallabhan and Das (1988, 1989, 1991) showed how  $\gamma$  can be calculated numerically for beams on elastic foundations but stopped short of developing computational techniques for plates.

Using variational calculus and the principle of minimum potential energy theorem, here a mathematical model for the analysis of rectangular plates on elastic foundations is developed. The soil is assumed to be layered having a thickness equal to  $H$  and resting on a rigid rock base, with linear elastic properties. The modulus of elasticity of the soil medium can be either constant or linearly varying with depth. The governing equation of the plate on elastic foundation becomes:

$$D \nabla^4 w - 2t \nabla^2 w + kw = \bar{q} \text{ in the domain of the plate.}$$

with usual definitions for  $w$ ,  $D$ ,  $\bar{q}$ , etc., as used in the Kirchhoff theory of plates. The parameters such as  $k$  and  $t$  are related to the material properties and geometry of the soil continuum for a given plate and the loading on it. A third parameter  $\gamma$  is introduced that depends on the



distribution of the vertical displacement in the soil medium from the top of the soil surface to the bottom. This parameter is directly related to the deflected shape of the plate, and thus is not known apriori; in other words, it depends on the soil depth  $H$ , plate size, stiffness of the plate and the distribution of the loading. Computing a consistent value of the parameter  $\gamma$  for a given problem is necessary for the accurate analysis of the plate. This computation is internally made possible by a simple iterative procedure. The major advantage in this model is the incorporation of the edge shear forces and corner reactions created by the soil surrounding the plate, a necessary set of elastic reactions from the soil continuum, that is neglected in the classical Winkler model. The solution of the governing biharmonic differential equation is achieved by creating a numerical computer model using the finite difference method. At present, only rectangular plates of uniform thickness can be solved by this computer model. Straughan (1990) solved numerous plate problems involving different depths of soil medium, different loading cases such as uniformly distributed load, concentrated loads and line loads. It is quite easy to note that the values of the parameters  $k$  and  $t$  vary depending on the depth of the soil, size and stiffness of the plate, and the distribution of the loading. The model can handle variation of the elastic modulus of the soil in the vertical direction, even though the model is at present developed for a constant or linear variation of the elastic soil modulus. It is believed that a linear variation can approximately model most of the layered soil media very well. The quest for a single value of the modulus of subgrade reaction  $k$  for the soil continuum is thus shown to be futile and can lead to less conservative and erroneous soil-structure interaction analysis.

## REFERENCES

- Cheung, Y.K., and Zienkiewicz, O.C. (1965). "Plates and tanks on elastic foundations: an application of the finite element method" *International Journal of Solids and Structures*, Vol. 1, pp. 451-461.
- Jones, R., and Xenophontos, J. (1977). "The Vlasov foundation model," *International Journal of Mechanical Science*, Vol. 19, pp. 317-323, Pergamon Press.
- Scott, R.F., (1981). "Foundation Analysis," Prentice Hall, Inc., Englewood Cliffs, NJ.
- Straughan, W.T. (1990). "Analysis of plates on elastic foundations," Doctoral Dissertation submitted to the Dept. of Civ. Engrg., Texas Tech Univ., Lubbock, Texas (May).
- Vallabhan, C.V.G., and Das, Y.C. (1988). "A parametric study of beams on elastic foundations," *Proceedings of the American Society of Civil Engineering, Journal of Engineering Mechanics Division*, pp. 2072-2082.
- Vallabhan, C.V.G., and Das, Y.C. (1989). "Beams on elastic foundations: A new approach," *Proceedings of the American Society of Civil Engineers Conference on Foundation Engineering: Current Principles and Practices*, June 25-29, 1989.
- Vallabhan, C.V.G., and Das, Y.C., (1991). "Analysis of circular tank foundations," *Journal of the Engineering Mechanics Division, ASCE*, Vol. 117, No. 4, pp. 789-797, April 1991.
- Vlasov, V.Z., and Leont'ev, N.N. (1966). "Beams, plates, and shells on elastic foundations," Translated from Russian, *Israel Program for Scientific Translations*, Jerusalem.

# FREE VIBRATION OF POINT SUPPORTED ORTHOTROPIC PLATES

by

D.J. Gorman, Professor  
Department of Mechanical Engineering  
University of Ottawa  
770 King Edward Ave., K1N 6N5 Ottawa

## INTRODUCTION

A number of accurate analytical type solutions have now been developed for the free vibration of isotropic, rectangular plates resting on discrete point supports. Significant recent papers are referred to in reference [1]. The subject of this paper is the extension of the superposition method, as discussed in [1], to the problem of point supported orthotropic plates. The plates are considered to possess rectangular orthotropy, i.e., the principal directions of orthotropy run parallel to the plate edges. In the analysis conducted here, each plate is considered to be supported by four discrete point supports symmetrically distributed about the plate central axis. This model conveniently lends itself to discussion, but it will be apparent that solutions are readily achievable regardless of the number of support points or their distribution if a judicious choice of building blocks is made.

## ANALYTICAL PROCEDURE

Because we choose to consider plates with a symmetrical distribution of point supports, it will be obvious that all modes of free vibration will be fully symmetric about the central axis, fully anti-symmetric about this axis, or symmetric about one axis and anti-symmetric about the other axis. Here, due to space limitations, we will discuss the fully symmetric modes only.

Because of symmetry, we will analyze a quarter of the plate only, as shown on the left hand side of Figure 1. The forced vibration building blocks utilized on the right hand side of the figure are essentially identical to those described for isotropic plate analysis as described in Ref. [2]. Two small circles adjacent to an edge imply slip-shear conditions, i.e., no vertical edge reaction and zero slope taken normal to the edge. The first two building blocks are driven by distributed harmonic bending moments which are expanded in a Fourier cosine series. There is zero vertical edge reaction along the driven edges. The third building block is driven by a concentrated harmonic force. It is at this point that we wish to have zero net displacement.

Because the analysis is conducted in a manner identical to that described in Ref. [2] for isotropic plates, only the slight differences will be pointed out here.

The governing differential equation for the first building block is now written as

$$\frac{\partial^4 W(\xi, \eta)}{\partial \eta^4} + 2 \frac{H}{D_y} \phi^2 \frac{\partial^4 W(\xi, \eta)}{\partial \xi^2 \partial \eta^2} + \frac{D_x}{D_y} \phi^4 \left\{ \frac{\partial^4 W(\xi, \eta)}{\partial \xi^4} \right\} - \lambda^4 W(\xi, \eta) = 0 \quad (1)$$

FREE VIBRATION OF LAMINATED PLATES OF RECTANGULAR PLANFORM  
WITH MULTIPLE INTERMEDIATE LINE SUPPORTS

Serge Abrate  
Department of Mechanical and Aerospace Engineering  
and Engineering Mechanics  
University of Missouri-Rolla  
Rolla, MO 65401

In many applications, laminated composite plates of rectangular planform are supported by a number of intermediate line supports and constraints on the lowest natural vibration frequency must be satisfied. An accurate method for determining the natural frequencies of such plates is necessary in order to determine the optimal layup that will maximize the fundamental natural frequency. The same problem for isotropic plates was studied by Azimi, Soedel and Hamilton [1] using the receptance method and later by Kim and Dickinson [2] who used the Rayleigh-Ritz variational method. A recent survey of publications on optimal design of laminated plates and shells [3] indicates that this problem has not been considered in the literature.

In this investigation, the free vibrations of symmetrically laminated plates are studied including twisting-bending coupling in the formulation. Natural frequencies and mode shapes are obtained using the Rayleigh-Ritz method. Approximation functions for the transverse displacements are taken as

$$\Phi_{mn}(x,y) = \phi_m(x) \cdot \mu_n(y) \quad (1)$$

where  $\phi_m(x)$  and  $\mu_n(y)$  are polynomial functions satisfying the essential boundary conditions in the  $x$  and  $y$  directions respectively. Here two approaches are taken in order to deal with intermediate line supports. First, the conditions of zero displacement at intermediate displacements along the lines  $x = \alpha_s$  with  $s = 1, S$  are included in the displacement functions

$$\phi_m(x) = x^{i+m} \cdot (x-\alpha_1)(x-\alpha_2)\dots(x-\alpha_S)(x-1)^j$$

where  $i$  and  $j$  account for the support conditions at both ends and are taken as  $-1$  for a free edge,  $0$  for a simple support and  $1$  for a clamped edge. Here, the equations have been nondimensionalized so that the plate extends from  $0$  to  $1$  in both directions and the  $\alpha$ 's are between  $0$  and  $1$ . Increasing the value of  $m$ , Eq. (2) gives a complete set of functions and the  $\mu$ 's are of the same form. Using the Rayleigh-Ritz method with these approximation functions, definite integrals of  $\phi_i'' \cdot \phi_j''$ ,  $\phi_i'' \cdot \phi_j'$ ,  $\phi_i' \cdot \phi_j'$  and  $\phi_i \cdot \phi_j$  as  $x$  varies from  $0$  to  $1$  must be evaluated. This is done using a symbolic manipulation package and simple expressions are obtained for each of those terms. This method works well for a small number of intermediate supports parallel to the edges of the plate but calculations become cumbersome as the number of intermediate supports increase.

A second approach consists of taking the approximation functions so that only the essential boundary conditions along the edges of the plate are satisfied. The conditions of zero displacements on the intermediate supports are then enforced using the Lagrange multiplier method. With this approach, the approximation functions are the same regardless of the number of intermediate supports. Point supports and oblique line supports can also be handled. Results are obtained for all combination of boundary conditions along the edges and up to three line supports in the  $x$  and  $y$  direction. The influence of fiber orientation is studied, expressing the plate rigidities in terms of stiffness invariants and lamination parameters. For a given material system, the variation in natural frequencies is plotted as the lamination parameters vary over their allowable ranges.

#### REFERENCES

- 1- Azimi S., Hamilton J.F., Soedel W., "The Receptance method Applied to the Free Vibration of Continuous Plate Structures," J. Sound and Vibration, Vol 93, pp 9-29, 1984
- 2- Kim C.S., Dickinson S.M., "The Flexural Vibration of Line Supported Rectangular Plate Systems," J. Sound and Vibration, Vol 114, No 1, pp 129-142, 1987
- 3- Abrate S., "Optimal Design of Laminated Plates and Shells," Submitted for publication

# VIBRATION OF CIRCULAR PLATES WITH V-NOTCH CORNER STRESS SINGULARITIES

A.W. Leissa<sup>1</sup>, O.G. McGee<sup>2</sup>, and C.S. Huang<sup>1</sup>

<sup>1</sup>Dept. of Engineering Mechanics, <sup>2</sup>Dept. of Civil Engineering  
The Ohio State University, Columbus, Ohio 43210, U.S.A.

No known theoretical results exist in the published literature for the free vibration of circular plates having an exterior V-notch which cause significant stress singularities [1]. The present work analyzes circular plates, where such stress singularities occur. The analysis uses the Ritz method to determine free vibration frequencies and mode shapes. Transverse displacement functions of two types are assumed, namely, products of polynomials and trigonometric functions, and corner functions. The algebraic polynomials and trigonometric functions assumed are well known and are mathematically complete in the circular plate region. The corner functions were derived for plane elasticity and plate bending problems approximately four decades ago [2,3] to study the nature of the stress singularities which occur at sharp interior corners, and are widely used in stress analysis at crack tips.

Consider the completely free, circular plate of radius  $k$  depicted in Figure 1. A V-notch having its vertex located a distance " $c$ " from the center is cut into the plate. For free vibration the transverse displacement ( $w$ ) of the circular plate is sinusoidal in time:  $w(x,y,t)=W(x,y)\sin\Omega t$ , where  $\Omega$  is a natural frequency. Further, admissible displacements for the symmetric modes are taken as  $W_p=W_{ps}+W_{cs}$ , where  $W_{ps}=A_{mn}r^m\cos n\theta+A_{ij}r^i\cos j\theta$  and ( $m=0,2,\dots,M_1$ ;  $n=0,2,\dots,m$ ;  $i=1,3,\dots,I_1$ ;  $j=1,3,\dots,i$ ), and where  $W_{cs}$  is a sum of corner functions:  $W_{cs}(x,y)=B_uW_u(x,y)+C_vW_v^*(x,y)$  and ( $u=1,2,\dots,U$ ;  $v=1,2,\dots,V$ ), where  $W_u$  and  $W_v^*$  are the real and imaginary parts of the symmetric complex eigenfunctions [2] satisfying the free-free boundary conditions of the V-notch, that is, along the radial lines ( $\theta=\alpha/2$ ) and ( $\theta=-\alpha/2$ ) (see Figure 1). The admissible displacements for the antisymmetric modes are taken as  $W_p=W_{pa}+W_{ca}$ , where  $W_{ca}$  is a sum of antisymmetric corner functions and  $W_{pa}=D_{mn}r^m\sin n\theta+D_{ij}r^i\sin j\theta$  ( $m=2,4,\dots,M_2$ ;  $n=2,4,\dots,m$ ;  $i=1,3,\dots,I_2$ ;  $j=1,2,\dots,i$ ). Substituting the above assumed displacements into the appropriate energy functionals [1] and minimizing according to the Ritz method, accurate upper bounds on the free vibration frequencies are obtained.

Nondimensional frequencies for a completely free circular plate with a 30 degree notch ( $\alpha=330^\circ$ ) cut one-fourth of the way across the plate ( $c/R=0.5$ ) (Figure 1 is drawn to these dimensions) are listed in Table 1. Convergence using various numbers of admissible functions  $W_p$  and corner functions  $W_c$  is observed. It is seen that poor convergence is obtained if insufficient corner functions are used. Comparing the first four frequencies of the plates with those of a

plate with no notch, one finds that the notch reduces them by 8.8, 1.3, 2.6, and 15.3 percent. Thus, the frequencies corresponding to the antisymmetric modes are most greatly affected by the V-notch.

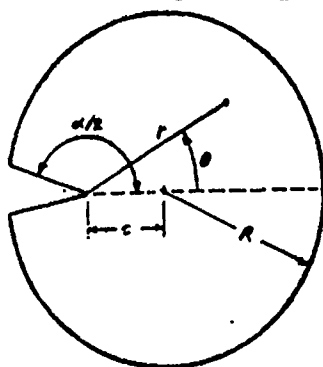


Figure 1. Completely free circular plate with V-notch

Table 1. Frequencies  $[\Omega R^2(\rho/D)^{1/2}]$  for a completely free plate with a V-notch ( $\alpha=330^\circ$ ,  $c/R=0.5$ ,  $\mu=0.3$ )

Mode No. <sup>+</sup>	No. of Corner Functions ( $W_C$ )	Number of Polynomial Terms ( $W_p$ )			
		9	25	36	49
1 (A)	0	5.320	5.318	5.315	5.312
	1	5.064	5.021	5.021	5.006
	5	4.959	4.949	4.942	4.937
	15	4.898	4.892	4.889	4.887
2 (S)	0	5.488	5.484	5.478	5.471
	1	5.317	5.310	5.305	5.302
	5	5.304	5.300	5.298	5.297
	15	5.293	5.291	5.290	5.289
3 (S)	0	9.030	9.022	9.014	9.005
	1	8.802	8.794	8.789	8.786
	5	8.789	8.785	8.782	8.780
	15	8.773	8.770	8.769	8.768
4 (A)	0	12.326	12.317	12.307	12.298
	1	11.155	11.073	11.004	10.949
	5	10.785	10.745	10.718	10.701
	15	10.571	10.551	10.541	10.534

+(A)=antisymmetric mode, (S)=symmetric mode

#### REFERENCES

1. A.W. Leissa, Vibration of Plates, U.S. Government Printing Office, 353 pp. (1969).
2. M.L. Williams, "Surface stress singularities resulting from various boundary conditions in angular corners of plates under bending", Proc. U.S. Nat. Cong. of Appl. Mech., 325-329, (1951).
3. M.L. Williams, "Stress singularities resulting from various boundary conditions in angular corners of plates in extension", J. Appl. Mech., 526-528, (1952).

Huang-Yih                      Sheng-Yao  
 (Xian Institute of Metallurgy and Construction Engineering)  
 People's Republic of China

### I. Basic Theory

On the bases of literature (1), (2), the bending problem of thick plate on the two-parameter elastic foundation is reduced to solve the following differential equations (Fig. 1):

$$\nabla^4 F - 2r^2 \nabla^2 F + S^4 F = 2 \frac{C}{D(c+2t)}, \quad \nabla^2 f - 2d^2 f = 0 \quad (1-1)$$

where,  $F(x, y)$ ,  $f(x, y)$  is displacement function, respectively,

$d^2 = C/\mu^* D$ ,  $\mu^* = 1 - \mu$ ,  $D = Eh^3/12(1-\mu^2)$ ,  $C = SEh/2(1+\mu)$ ,  $2r^2 = (2C + kD)/D(c+2t)$ ,  $S^4 = k^2 c/D(c+2t)$ ,  $k, t$ , are v.v. vlasov's foundation modulud. If the  $F(x, y)$ ,  $f(x, y)$  are obtained, the components of displacement and stress resultant of plate have also been obtained by expressions concerned (2).

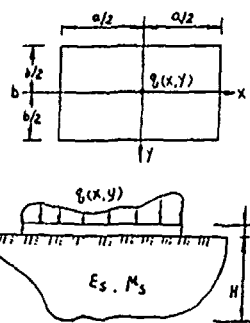


Fig. 1  
(1-2a)

The solutions of equation (1-1) are written as following form:

$$F(x, y) = F_p(x, y) + \sum_{m=1}^{\infty} [A_m \phi_{1m}(y) + B_m \phi_{2m}(y) + C_m \phi_{3m}(y) + D_m \phi_{4m}(y)] (\cos \alpha_m x \text{ or } \sin \alpha_m x)$$

$$f(x, y) = \sum_{m=1}^{\infty} (a_m \sinh \lambda_m y + b_m \cosh \lambda_m y) (\sin \alpha_m x \text{ or } \cos \alpha_m x)$$

$$F(x, y) = F_p(x, y) + \sum_{n=1}^{\infty} [A_n \phi_{1n}(x) + B_n \phi_{2n}(x) + C_n \phi_{3n}(x) + D_n \phi_{4n}(x)] (\cos \alpha_n y \text{ or } \sin \alpha_n y)$$

(1-2b)

$$f(x, y) = \sum_{n=1}^{\infty} (a_n \sinh \lambda_n x + b_n \cosh \lambda_n x) (\sin \alpha_n y \text{ or } \cos \alpha_n y)$$

in which,  $\alpha_n = 2m\pi/a$ ,  $\alpha_n = 2n\pi/b$ ,  $F_p(x, y)$  is a particular solution, we can take the double trigonometric series as the particular solution, therefore, we only give the homogeneous solution.  $A_m, B_m, C_m, D_m, a_m, b_m, A_n, B_n, C_n, D_n, a_n, b_n$  are arbitrary constants, the function  $\phi_{im}(y)$  ( $i=1, 2, 3, 4$ ) have the following form:

$$\phi_{1m}(y) = \cosh \tau_m y \cos \gamma_m y, \quad \phi_{2m}(y) = \sinh \tau_m y \cos \gamma_m y$$

$$\phi_{3m}(y) = \sinh \tau_m y \sin \gamma_m y, \quad \phi_{4m}(y) = \cosh \tau_m y \sin \gamma_m y$$

(1-3)

$$\tau_m^2 = \frac{1}{2} (\alpha_m^2 + \alpha_m'^2 + r^2), \quad \gamma_m^2 = \frac{1}{2} (\alpha_m^2 - \alpha_m'^2 - r^2)$$

$$\lambda_m^2 = \alpha_m^2 + r^2 + \alpha_m'^2 + S^4, \quad \lambda_m = (2d^2 + \alpha_m'^2)^{\frac{1}{2}}$$

The quantities with subscript n are obtained from the corresponding quantities with subscript m replacing n and interchanging b and a. So, we will only define the quantities with subscript m.

The following boundary conditions are of importance to solution of the complicated boundary condition problem, for example,  $x = a/2$ , simply supported edge (SSE):

$$w(\frac{a}{2}, y) = M_{xy}(\frac{a}{2}, y) = M_x(\frac{a}{2}, y) = 0 \quad (1-4a)$$

slip edge (SE):

$$\tau_x(\frac{a}{2}, y) = M_{xy}(\frac{a}{2}, y) = Q_x(\frac{a}{2}, y) = 0 \quad (1-4b)$$

generalized simply supported edge (GSSE):

$$M_x(\frac{a}{2}, y) = M_{xy}(\frac{a}{2}, y) = 0, \quad w(\frac{a}{2}, y) = \bar{w}, \quad (1-4c)$$

generalized slip edge (GSE):

$$M_{xy}(\frac{a}{2}, y) = Q_x(\frac{a}{2}, y) = 0, \quad \tau_x(\frac{a}{2}, y) = \bar{\tau}_x, \quad (1-4d)$$

### II. Basic Solutions

For the bending problem of the plate, we can always divide it in the combination of the different states of the deformation: the doubly symmetric deformation (ss); the doubly antisymmetric deformation (aa); the symmetric-antisymmetric deformation (sa); the antisymmetric-symmetric deformation (as). In order to obtain its solution, we need to focus our attention on only a quarter segment of plate. Using the

expression (1-2) and boundary conditions (1-4), the following basic solutions are derived out which have satisfied the boundary conditions shown in Fig. 2

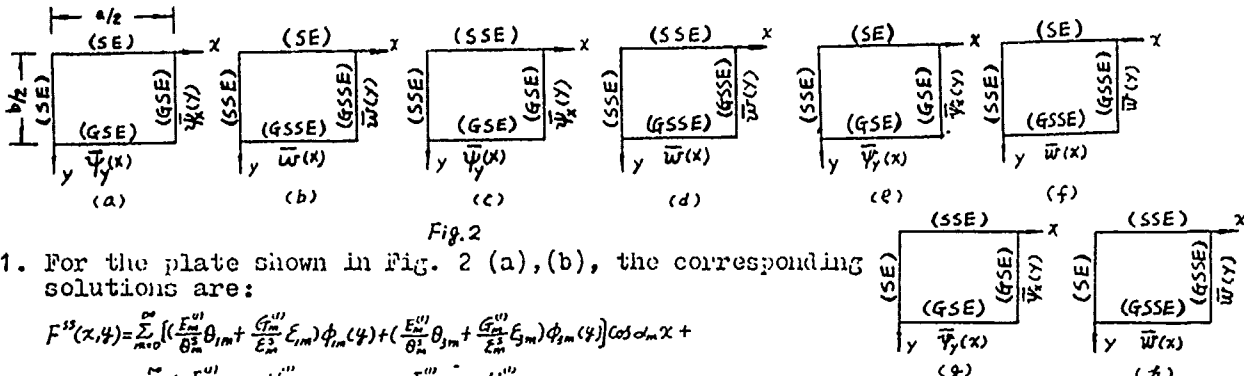


Fig. 2

1. For the plate shown in Fig. 2 (a), (b), the corresponding solutions are:

$$F^{(1)}(x, y) = \sum_{m=0}^{\infty} \left[ \left( \frac{E_m^{(1)}}{\theta_m^2} \theta_{1m} + \frac{G_m^{(1)}}{\varepsilon_m^2} \varepsilon_{1m} \right) \phi_{1m}(y) + \left( \frac{E_m^{(1)}}{\theta_m^2} \theta_{2m} + \frac{G_m^{(1)}}{\varepsilon_m^2} \varepsilon_{2m} \right) \phi_{2m}(y) \right] \cos \alpha_m x + \sum_{n=0}^{\infty} \left[ \left( \frac{F_n^{(1)}}{\theta_n^2} \theta_{1n} + \frac{H_n^{(1)}}{\varepsilon_n^2} \varepsilon_{1n} \right) \phi_{1n}(x) + \left( \frac{F_n^{(1)}}{\theta_n^2} \theta_{2n} + \frac{H_n^{(1)}}{\varepsilon_n^2} \varepsilon_{2n} \right) \phi_{2n}(x) \right] \cos \alpha_n y + F_p^{(1)}(x, y) \quad (2-1)$$

$$f^{(1)}(x, y) = \sum_{m=1}^{\infty} \left( \eta_{1m} E_m^{(1)} + \frac{\xi_{1m}}{\varepsilon_m^2} G_m^{(1)} \right) \text{sh} \lambda_m y \sin \alpha_m x - \sum_{n=1}^{\infty} \left( \eta_{2n} F_n^{(1)} + \frac{\xi_{2n}}{\varepsilon_n^2} H_n^{(1)} \right) \text{sh} \lambda_n x \sin \alpha_n y$$

in which,  $E_m^{(1)}, G_m^{(1)}, F_n^{(1)}, H_n^{(1)}$  are undetermined coefficients,  $\theta_m^2, \varepsilon_m^2, \dots, \xi_{2n}$  are the quantities concerning the eigen-roots of Equ. (1-1) and the geometric dimensions of plate.

2. In like manner, for the plate shown in Fig. 2 (c), (d), (e), (f), the general solutions are written below, respectively.

$$F^{(2)}(x, y) = \sum_{m=1}^{\infty} \left[ \left( \frac{E_m^{(2)}}{\theta_m^2} \theta_{1m} + \frac{G_m^{(2)}}{\varepsilon_m^2} \varepsilon_{1m} \right) \phi_{1m}(y) + \left( \frac{E_m^{(2)}}{\theta_m^2} \theta_{2m} + \frac{G_m^{(2)}}{\varepsilon_m^2} \varepsilon_{2m} \right) \phi_{2m}(y) \right] \sin \alpha_m x + \sum_{n=1}^{\infty} \left[ \left( \frac{F_n^{(2)}}{\theta_n^2} \theta_{1n} + \frac{H_n^{(2)}}{\varepsilon_n^2} \varepsilon_{1n} \right) \phi_{1n}(x) + \left( \frac{F_n^{(2)}}{\theta_n^2} \theta_{2n} + \frac{H_n^{(2)}}{\varepsilon_n^2} \varepsilon_{2n} \right) \phi_{2n}(x) \right] \sin \alpha_n y + F_p^{(2)}(x, y) \quad (2-2)$$

$$f^{(2)}(x, y) = \sum_{m=1}^{\infty} \left( \eta_{1m} E_m^{(2)} + \frac{\xi_{1m}}{\varepsilon_m^2} G_m^{(2)} \right) \text{ch} \lambda_m y \cos \alpha_m x + \sum_{n=1}^{\infty} \left( \eta_{2n} F_n^{(2)} + \frac{\xi_{2n}}{\varepsilon_n^2} H_n^{(2)} \right) \text{ch} \lambda_n x \cos \alpha_n y$$

$$F^{(3)}(x, y) = \sum_{m=1}^{\infty} \left[ \left( \frac{E_m^{(3)}}{\theta_m^2} \theta_{1m} + \frac{G_m^{(3)}}{\varepsilon_m^2} \varepsilon_{1m} \right) \phi_{1m}(y) + \left( \frac{E_m^{(3)}}{\theta_m^2} \theta_{2m} + \frac{G_m^{(3)}}{\varepsilon_m^2} \varepsilon_{2m} \right) \phi_{2m}(y) \right] \sin \alpha_m x + \sum_{n=0}^{\infty} \left[ \left( \frac{F_n^{(3)}}{\theta_n^2} \theta_{1n} + \frac{H_n^{(3)}}{\varepsilon_n^2} \varepsilon_{1n} \right) \phi_{1n}(x) + \left( \frac{F_n^{(3)}}{\theta_n^2} \theta_{2n} + \frac{H_n^{(3)}}{\varepsilon_n^2} \varepsilon_{2n} \right) \phi_{2n}(x) \right] \cos \alpha_n y + F_p^{(3)}(x, y) \quad (2-3)$$

$f^{(3)}(x, y) = \sum_{m=1}^{\infty} \left( \eta_{1m} E_m^{(3)} + \frac{\xi_{1m}}{\varepsilon_m^2} G_m^{(3)} \right) \text{sh} \lambda_m y \cos \alpha_m x + \sum_{n=1}^{\infty} \left( \eta_{2n} F_n^{(3)} + \frac{\xi_{2n}}{\varepsilon_n^2} H_n^{(3)} \right) \text{ch} \lambda_n x \sin \alpha_n y$   
The solution  $F^{(2)}(x, y), f^{(2)}(x, y)$  are extracted from  $F^{(3)}(x, y), f^{(3)}(x, y)$  by interchanging the variable  $x$  and  $y$ .

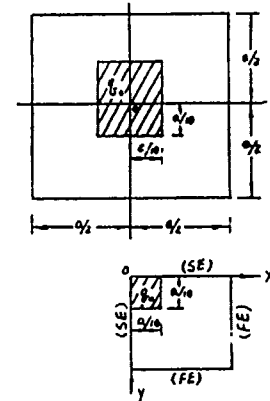


Fig. 3

### III. Application. Numerical Example.

As the application, an example of square plate with four free edges (Fig. 3) is given.  $E = 2 \times 10^6 \text{ T/m}^2, \mu = 0.167, h = 0.2 \text{ m}, E_s = 4 \times 10^6 \text{ T/m}^2, \mu_s = 0.4, \gamma = 1.55, a = 1 \text{ m}, \rho_s = 100 \text{ T/m}^2$ . This problem is a doubly symmetric deformation. Along the section of symmetric axes the antisymmetric rotation angle and shearing force equal zero, these edges along the symmetric axes can be regarded as slip edge (SE). From expression (2-1) and using boundary condition:  $x = a/2, M_x = 0, \theta_x = \bar{\theta}_x^{(1)}$ ;  $y = a/2, M_y = 0, \theta_y = \bar{\theta}_y^{(1)}$ , the  $E_m^{(1)}, F_n^{(1)}, G_m^{(1)}, H_n^{(1)}$  can be determined, and then the displacements and stress resultants can be also obtained. The calculation results are listed in Table 1 and Table 2.

Table 1. Deflection values for plate  $H=0.6$  Table 2. Deflection values for plate  $H=0.0$

$x \backslash y$	0	$a/8$	$a/4$	$3a/8$	$a/2$
0	0.2586	0.2538	0.2470	0.2425	0.1842
$a/8$	0.2538	0.2057	0.2455	0.2417	0.1768
$a/4$	0.2470	0.2455	0.2424	0.2396	0.1614
$3a/8$	0.2425	0.2417	0.2396	0.2377	0.1430
$a/2$	0.1842	0.1768	0.1614	0.1430	0.0320

$x \backslash y$	0	$a/8$	$a/4$	$3a/8$	$a/2$
0	0.3167	0.3119	0.3051	0.3006	0.2317
$a/8$	0.3119	0.3088	0.3036	0.2998	0.2257
$a/4$	0.3051	0.3036	0.3005	0.2977	0.2095
$3a/8$	0.3006	0.2998	0.2977	0.2958	0.1700
$a/2$	0.2317	0.2259	0.2095	0.1700	0.0671

### Reference

- (1). Hu Hai-Chang, ACTA MECHANICA SINICA, No. 6. 1965
- (2). Huang-Tih, ACTA MECHANICA SINICA, No. 1. 1986
- (3). Selvadurai, A. P., Elastic Analysis of Soil-Foundation Interaction, Elsevier Scientific Publishing CO. 1979



# A LAYER-WISE PLATE BENDING FINITE ELEMENT FOR COMPOSITE LAMINATES

D. H. Robbins and J. N. Reddy  
Department of Engineering Science and Mechanics  
227 Norris Hall  
Virginia Polytechnic Institute and State University  
Blacksburg, VA 24061 USA

In the conventional, equivalent single-layer plate theories used to describe the kinematics of composite laminates, the material properties of individual layers are *averaged* by integrating the stress field through the laminate thickness. Since the displacements are expressed in terms of a single expression through the thickness, the computed transverse strains are continuous, causing the transverse stresses to be discontinuous at layer interfaces (because of different elastic coefficients at layer interfaces). Noting these restrictions of the conventional plate theories, Reddy ('Generalization of two-dimensional theories of laminated composite plates,' *Commun. Appl. Numer. Meth.* 3, 173-180, 1987) proposed a layer-wise theory for plates which can be used to accurately represent interlaminar and free edge stress fields.

In the layer-wise theory of Reddy the displacements are interpolated through the thickness first to reduce the 3-D elasticity equations to differential equations in the  $x$  and  $y$  coordinates (in the plane of the laminate):

$$u_i(x,y,z) = \sum_{J=1}^{N_i} U_i^J(x,y) \phi_J^i(z)$$

where  $i = 1,2,3$ ,  $N_i$  is the number of mathematical subdivisions (e.g., finite-element discretization) through the thickness of the laminate, and  $\phi_J^i$  are known functions (e.g., global finite element interpolation functions) of the thickness coordinate,  $z$ . The functions  $\phi_J^i$  are layer-wise continuous functions, defined only on two adjacent layers. Because of this local nature of  $\phi_J^i$  the displacements are continuous through the thickness but their derivatives with respect to  $z$  are not continuous. This allows a discontinuous representation of the transverse strains at layer interfaces, leaving the possibility that the interlaminar transverse stresses computed from the layer constitutive equations are continuous. The theory requires only 2-D finite elements (in the  $xy$ -plane), but with many degrees of freedom per node. Consequently, the element aspect ratio is restricted to only 2-D considerations. The number of degrees of freedom per node in the thickness as well as the  $x$ - $y$  plane is three ( $u,v,w$ ), like in a 3-D finite element. It is possible to use the sublaminar concept to include several physical layers into a mathematical layer, and a physical layer can be subdivided into several mathematical layers.

In the present paper a reformulation of the layer-wise theory of Reddy is represented and element development is described. Numerical results of interlaminar and free edge stress fields obtained with the present element are discussed in light of three-dimensional elasticity solutions. It is found that the layer-wise finite element yields stress fields, computed from the constitutive relations, that agree with the 3-D elasticity solutions for thin and thick composites.

#### Acknowledgement

The authors gratefully acknowledge the support of this research from the NASA Langley Research Center (Grant NAG-1-1030).

# MULTI-FIELD FINITE ELEMENT FORMULATIONS FOR MODERATELY THICK LAMINATED COMPOSITE PLATES

Ali M. Alghothani  
Ventura Engineering, Inc.  
7610 Olentangy River RD  
Columbus Ohio 43235

Closed form solutions to the vibration of laminated plates are quite limited. With the advent of digital computers, numerical methods such as finite element method that can handle a problem of complex boundary conditions in a straightforward manner are indispensable. Although the finite element method in theory and by definition has no disadvantages or limitations, in practice some disadvantages and/or limitations may be transferred to the finite element models by the theory used or variational approximation employed in the analysis. For example, Galerkin's method does not provide an effective means of handling boundary conditions. Meanwhile, the choice of an appropriate penalty function plays a very important role in using the penalty method.

The present work is based on a comprehensive general theory developed earlier (1) for the dynamics of bending and extension of laminated plates with an arbitrary stacking of layers based on layer-wise theory using variational principles. Here the multifield finite element mixed models are derived from multivariable variational principles which leads to the field equations as well as boundary conditions. The domain of the governing function is completely defined by the displacement variables and the interlaminar stresses. The in-plane displacement field within each layer is assumed to vary linearly over the thickness where the transverse displacement is assumed to be constant.

$$u_a^k(x, t) = v_a^k(z_\beta, t) + (x_3 - h_{k-1}) \varphi_a^k(x_\beta, t)$$

$$u_3^k(x, t) = w^k(x_\beta, t)$$

Setting up the field variable in term of a layer interpolation functions as

$$v_{ae} = \{H_v\}_e^T \{v_a\}_e; \varphi_{ae} = \{H_r\}_e^T \{\varphi_a\}_e; N_{a\beta e} = \{H_n\}_e^T \{N_{a\beta}\}_e; M_{a\beta e} = \{H_m\}_e^T \{M_{a\beta}\}_e; Q_{ae} = \{H_q\}_e^T \{Q_a\}_e; \sigma_e = \{H_3\}_e^T \{\sigma\}_e$$

The above interpolating functions must be differentiable up to first order. However, they do not have to satisfy any of the boundary conditions. Utilizing the assumed field variables in the governing functional and applying variational principles yields the following equation in matrix form (1)

$$[M]\{U\} + t*[K]\{U\} = \{R_0\} + t*\{R\}$$

where

$$[M] = \begin{bmatrix} [M_v] \sum_{k=1}^n P^k & [M_w](R^1 + t_1 \sum_{k=2}^n P^k) & \dots & [M_w](R^i + t_i \sum_{k=i+1}^n P^k) & 0 \\ & [M_r](I^1 + t_1 \sum_{k=2}^n P^k) & \dots & [M_r](I^i + t_i \sum_{k=i+1}^n P^k) & 0 \\ & \dots & \dots & \dots & \dots \\ \text{Symm} & & & [M_r](I^i + t_i \sum_{k=i+1}^n P^k) & 0 \\ & & & & [M_w] \sum_{k=1}^n P^k \end{bmatrix}$$

$$[K] = \begin{bmatrix} \sum_{k=1}^n [K_v]^k & [K_{vb}]^1 + t_1 \sum_{k=2}^n [K_{vb}]^k & \dots & [K_{vb}]^i + t_i \sum_{k=i+1}^n [K_{vb}]^k & 0 \\ & t_1 t_1 \sum_{k=2}^n [K_{rb}]^k + [K_{rb}]^1 & \dots & t_i \sum_{k=j+1}^n [K_{rb}]^k + t_i [K_{rb}]^i & [K_{rw}]^1 \\ & \dots & \dots & \dots & \dots \\ & \text{symm.} & & t_{ii} \sum_{k=i+1}^n [K_{rb}]^k + [K_{rb}]^i + [K_{rb}]^i & [K_{rw}]^i \\ & & & & \sum_{k=1}^n [K_{ww}]^k \end{bmatrix}$$

$$\{U\}^T = \{v_e^{-1}, \phi_e^1, \dots, \phi_e^i, \dots, w\}$$

$$\{R_o\}^T = \{ \{H_1\} \sum_{k=1}^n X^k, \dots, \{H_2\} Z^1 + t_1 \{H_2\} \sum_{k=2}^n X^k, \dots, \{H_2\} \sum_{k=1}^n Y^k \}$$

$$\{R\} = \begin{bmatrix} \{R_j\} + \sum_{k=1}^n \{R_w\} + \{H_1\} \sum_{k=1}^n F_e^k \\ \dots \\ \{R_j\} + \sum_{k=1}^n \{R_w\} + \{H_2\} \sum_{k=1}^n F_e^k + \{H_2\} G_e^1 \\ \dots \\ \{R_j\} + \sum_{k=1}^n \{R_w\} + \{H_3\} \sum_{k=1}^n F_3^k \end{bmatrix}$$

Some of the advantages of the layer-wise theory are firstly, it accurately models laminates made of dissimilar material layers. Secondly, boundary conditions are properly satisfied if they are not the same for all layers. Thirdly, it requires only 2-D finite elements. However, finite elements of a laminated plate which consists of a large number of layers might become intractable due to economical barriers. This difficulty can be overcome by dividing the laminate into "local" and "global" parts with the assumption of  $\phi^k \neq \phi^{k+1}$  over the local parts and  $\phi^i = \phi^{i+1}$  over the global parts.

#### REFERENCES

1. Algothani, A.M., "A Unified Approach to The Dynamics of Bending and Extension of Moderately Thick Laminated Composite Plates." Ph.D. Dissertation, The Ohio State University, Columbus, Ohio, June 1986.

# A NEW FINITE ELEMENT APPROACH TO ANALYSIS OF RANDOM COMPOSITES USING TESSELLATION METHODS

Somnath Ghosh  
Department of Engineering Mechanics  
Ohio State University, Columbus, Ohio

## Abstract :

In this paper a new finite element formulation has been developed for composites, in which second phase particulates or unidirectional fibers are randomly dispersed in a matrix. It involves the introduction of an unique mesh that accounts for the randomness in location, shape and size of the second phase materials. Motivation for the use of the present method comes from the limitations of the conventional finite element meshes in modeling the above class of composite materials. For example if a composite domain with a random second phase distribution were to be discretised by traditional mesh generators, the resulting element boundaries could interfere with the second phase, thus allocating parts of the same inclusions to different elements. Also each element in such cases could consist of a varying number of inclusions. These situations may therefore lead to excessive difficulties in analysis phase due to the fact that the volume and shape fractions of each inclusion in the sharing elements have to be recorded in addition to the varying number of inclusions in each element.

The deficiencies of the conventional meshes can be overcome by introducing an alternate mesh that has been proposed in this paper. The method is based on Dirichlet tessellation of a domain into a number of convex polygons, called Voronoi polygons, each containing only one inclusion. In this paper these Voronoi polygons are assumed to serve as elements in the finite element analysis of composites.

Indeed, Voronoi polygons make rather unconventional finite elements. A hybrid assumed stress formulation has been invoked in order to accommodate elements with varying number of nodes. Elimination or suppression of hourglass modes by utilization of appropriate techniques have been implemented. The effect of the second phase material has been incorporated by decomposition of the non-homogenous problem into two parts, a homogenous part and a deviation part and the introduction of a transformation strain. Numerical examples elucidating the effectiveness of the above model have been executed.

A MIXED VARIATIONAL PRINCIPLE AND ITS APPLICATION TO THE  
NONLINEAR BENDING PROBLEM OF ORTHOTROPIC TUBES

Avinoam Libai  
Department of Aerospace Engineering  
Technion, Haifa 32000, Israel

Charles W. Bert  
School of Aerospace and Mechanical Engineering  
University of Oklahoma  
Norman, OK 73019

A mixed variational principle based on the intrinsic formulation of the shell equations is presented and applied to the problem of the geometrically nonlinear bending of a circular cylindrical tube. The principle is formulated within the scope of small-strain, moderate-rotation theory of shells under the Kirchhoff hypothesis, and its applicability is demonstrated for shallow and for circular cylindrical shells.

The variational functional basically contains the strain energy of bending and the complementary energy of the membrane force resultants. It is formulated in terms of curvature and stress functions and its Euler-Lagrange equations are those of normal equilibrium and Gauss (incremental) compatibility. Both may be nonlinear.

Using the mixed principle as a starting point, approximate equations for the nonlinear bending of orthotropic circular cylindrical tubes (extended Brazier effect) are developed. The semi-membrane approximation is used in the analysis, plus some added restrictions (in the Rayleigh-Ritz sense) on the curvature and stress fields. The resulting equations can be used for problems involving finite-length tubes subjected to variable beam-type moments and shear forces with miscellaneous beam and shell type boundary conditions. Membrane-type shear deformations are included in the formulation.

As an example, numerical results are given for the deformation of a clamped finite-length tube subjected to pure bending. (The shear deformation is neglected in the example.)

### Selected References

1. Brazier, L. G. "On the Flexure of Thin Cylindrical Shells and other "Thin" Sections," Proc. Royal Society of London, Ser. A., Vol. 116, pp. 104-114 (1927).
2. Simmonds, J. G. and Danielson, D. A., "Nonlinear Shell Theory with Finite Rotation and Stress-Function Vectors," J. Appl. Mech., Vol. 39, pp. 1084-1090 (1972).
3. Stephens, W. B., Starnes, J. H., and Almroth, B. O., "Collapse of Long Cylindrical Shells under Combined Bending and Pressure Loads," AIAA Journal, Vol. 13, pp. 20-25 (1975).
4. Calladine, C. R., Theory of Shell Structures, Chap. 16, Cambridge University Press (1983).
5. Axelrad, E. I. and Emmerling, F. A., "Elastic Tubes," Applied Mechanics Reviews, Vol. 37, pp. 891-897 (1984).
6. Libai, A. and Simmonds, J. G., Nonlinear Elastic Shell Theory, Academic Press (1988).

Effect of the Thermo-visco-plastic Flow Law  
on  
Adiabatic Shear Band Morphology  
in  
One Dimension.

John W. Walter Jr.  
US Army Ballistic Research Laboratory  
Aberdeen Proving Ground, Maryland 21005-5066

Previous results [1, 2] indicate that extremely large strain rates ( $\dot{\gamma} > 10^6/\text{s}$ ), strains ( $\gamma \gg 1$ ), and temperatures ( $\theta > \theta_{\text{melt}}$ ) may occur during shear band formation. In order to model this phenomenon accurately, it is important to employ a flow law which represents, at least qualitatively, the real material response over relevant ranges of these variables. Recent experimental results [3, 4] indicate that the strong increase in the flow stress,  $s$ , of some pure metals at high strain-rates ( $\approx 10^3/\text{sec}$ ) is due to increased rate sensitivity of the evolution of internal structure (i.e., of strain hardening) rather than to increased rate sensitivity of the flow stress at constant internal structure. Previous numerical studies of shear bands have relied primarily on viscoplastic laws of the "overstress" type for which the rate sensitivity parameter,  $m = \partial(\ln s)/\partial(\ln \dot{\gamma})$ , must be of order unity to fit this high strain rate data. Analysis by Wright [5] shows that, other things being equal, larger values of  $m$  will hinder adiabatic shear band formation. This analysis, taken together with experimental evidence that adiabatic shear localization becomes more severe with increased strain rate, suggests that the overstress type flow law is not appropriate for modeling shear bands in these situations. In contrast, an appropriate internal-variable flow law such as the Mechanical Threshold Stress (MTS) model of Follansbee and Kocks [3] can be fit to this same high strain rate data with much smaller values of  $m$ . With this motivation, we compare the kinetics of adiabatic shear band formation for the MTS flow law and for the Litoński-type model used previously in the context of unidirectional shearing of a slab. These one-dimensional numerical simulations are considered to simulate tests of the "pressure-shear" type [4] and, somewhat less precisely, the thin-wall tube torsional Kolsky bar test [6].

Specifically, for a body under going simple shear

$$x = X + u(Y, t), \quad y = Y, \quad z = Z, \quad (1)$$

the equations of balance and of elastic response are

$$\begin{aligned} \text{Momentum:} \quad \rho v_{,t} &= s_{,y}, \\ \text{Energy:} \quad \rho c_v \theta_{,t} &= K \theta_{,yy} + s \dot{\gamma}_p, \\ \text{Elasticity:} \quad s_{,t} &= \mu (v_y - \dot{\gamma}_p), \end{aligned} \quad (2)$$

where  $v$  is the velocity,  $\theta$  is the temperature,  $s$  is the shear stress,  $\dot{\gamma}_p$  is the plastic strain rate,  $\rho$  is the mass density,  $K$  is the thermal conductivity,  $c_v$  is the heat capacity at constant volume,  $\mu$  is the shear modulus and a subscript  $t$  or  $y$  following a comma indicates the respective partial derivative. The complete system of field equations is obtained by augmenting (2) with a flow law and evolution equations for any internal variables it contains. The flow law used previously [2] has the form

$$s = \mathcal{G}(\theta, \psi, \dot{\gamma}_p) = \kappa(\psi) g(\theta) f(\dot{\gamma}_p), \quad (3)$$

in which  $\kappa$ ,  $\psi$  are the stress and plastic strain measured in a slow, isothermal shear at ambient temperature and  $g$ ,  $f$  are dimensionless.  $\psi$  was used as the internal variable and an evolution equation for it was obtained



by assuming that strain hardening evolved according to total plastic work done, regardless of rate so that

$$\dot{\psi}_t = W_{p,t}/\kappa(\psi) = s\dot{\gamma}_p/\kappa(\psi), \quad (4)$$

where  $W_{p,t}$  is the rate of plastic work. While (3) and (4) do comprise an internal variable model, the latter specifically excludes the sort of strain rate history effects which the MTS model attempts to capture. Moreover, in our previous computations [2, 7] the strain rate sensitivity,  $m$ , was assumed to be constant.

In this work we shall not consider the MTS model in full generality but rather use the form appearing in [3]. In that work the primary intent was to account for the influence of *thermal activation controlled* dislocation glide on the evolution of internal structure (i.e., on strain hardening). In this case and for a pure, polycrystalline metal with face-centered cubic lattice the MTS flow law takes the form

$$s = \hat{s}_a + (\hat{s} - \hat{s}_a) \left\{ 1 - \left[ \frac{k\theta \ln(\dot{\gamma}_p/\dot{\Gamma}_0)}{e_0 \mu b^3} \right]^{1/q} \right\}^{1/p}, \quad (5)$$

in which  $\hat{s}$  is the *mechanical threshold stress* (flow stress at 0° K in the absence of any drag or momentum effects),  $\hat{s}_a$  is its athermal component, and  $k, \dot{\Gamma}_0, e_0, b, p, q$  are constants. The evolution equation for  $\hat{s}$  takes the form

$$\hat{s}_t = \dot{\gamma}_p N_0(\dot{\gamma}_p) [1 - F(\mathcal{X})], \quad (6)$$

where  $\mathcal{X}$  is given by

$$\mathcal{X} = \frac{\hat{s} - \hat{s}_a}{\hat{s}_s(\theta, \dot{\gamma}_p) - \hat{s}_a}. \quad (7)$$

Here  $N_0$  is the "Stage II" hardening rate and  $\hat{s}_s$  is a *saturation* value of the threshold stress used to model the decrease in the rate of strain hardening at larger strains (i.e., "Stage III" dynamic recovery). A three-parameter Arrhenius expression is suggested *ibid* for  $\hat{s}_s$  and is used together with an empirical selection of the functions  $F$  and  $N_0$  to fit strain hardening rate data for a specific f.c.c. metal.

- [1] Thomas W. Wright and John William Walter, Jr. Adiabatic shear bands in one dimension. In J. Harding, editor, *Mechanical Properties of Materials at High Rates of Strain 1989*, number 102 in Institute of Physics Conference Series, pages 119-126. Institute of Physics, Bristol and New York, 1989.
- [2] John William Walter, Jr. Numerical experiments on adiabatic shear bands. Submitted to *International Journal of Plasticity*, 1991.
- [3] Paul S. Follansbee and U. F. Kocks. A constitutive description of the deformation of copper based on the use of the mechanical threshold stress as an internal variable. *Acta Metallurgica*, 36(1):81-93, 1988.
- [4] Rodney J. Clifton. High strain rate behavior of metals. *Applied Mechanics Reviews*, 43(5):S9-S22, 1990. Supplement, Part 2.
- [5] Thomas W. Wright. Approximate analysis for the formation of adiabatic shear bands. *Journal of the Mechanics and Physics of Solids*, 38(4):515-530, 1990.
- [6] K. A. Hartley, J. Duffy, and R. H. Hawley. Measurement of the temperature profile during shear band formation in steels deforming at high strain rates. *Journal of the Mechanics and Physics of Solids*, 35(3):283-301, 1987.
- [7] Thomas W. Wright and John William Walter, Jr. On stress collapse in adiabatic shear bands. *Journal of the Mechanics and Physics of Solids*, 35(6):701-720, 1987.

## ANALYSIS OF SHEAR BANDS IN PLANE STRAIN DEFORMATIONS

R. C. Batra  
Department of Mechanical and Aerospace  
Engineering and Engineering Mechanics  
University of Missouri - Rolla  
Rolla, MO 65401-0249

During the last few years, Batra and his co-workers (Liu, Zhu, and Zhang) have studied the initiation and growth of shear bands in a thermally softening viscoplastic body undergoing overall adiabatic plane strain deformations at a nominal strain-rate of 5,000  $\text{sec}^{-1}$ . The problem formulation has included the effect of inertia forces and the heat generated due to plastic deformations. The thermal softening of the material has been described by either an affine function of the temperature rise or an exponentially decaying function of the temperature. A material defect in the body has been modeled by introducing at the site of the defect (i) a temperature perturbation, (ii) a weak material, (iii) a void, or (iv) a rigid inclusion. It is found that the initiation and growth of shear bands in a two-dimensional problem differs significantly from that in a one-dimensional simple shearing problem because of the constraining effects offered by the relatively strong material enclosing the softened material within the band. In each case, as the band grows, the temperature at the band center rises sharply. However, in the two-dimensional problem, the rate of temperature rise at the band center slows down considerably, resulting in a concave downward curve. The speed of propagation of the contours of constant principle logarithmic strain depends upon the state of deformation at the band center; contours of different values of the principle logarithmic strain propagate at different speeds. The finite element meshes have not been fine enough to obtain mesh-independent results. However, the qualitative nature of the results seems to be independent of the mesh used. The on-going and completed work will be briefly discussed.

### References

1. R. C. Batra and D.-S. Liu, Adiabatic Shear Banding in Plane Strain Problems, *J. Appl. Mechs.*, 56, 527-534, 1989.
2. R. C. Batra and Z. G. Zhu, Dynamic Adiabatic Shear Band Development in a Bimetallic Body Containing a Void, *Int. J. Solids Structures*, 27, 1829-1854, 1991.
3. R. C. Batra and X.-T. Zhang, Shear Band Development in Dynamic Loading of a Viscoplastic Cylinder Containing Two Voids, *Acta Mechanica*, 85, 221-234, 1990.

**ON THE ROLE OF INTERNAL VARIABLES, ANISOTROPY, SPIN, AND  
STRAIN GRADIENTS ON SHEAR BANDING: THEORY AND  
APPLICATION**

by

**Hussein M. Zbib  
Department of Mechanical and Materials Engineering  
Washington State University,  
Pullman, WA 99164-2920**

and

**Elias C. Aifantis  
Department of Mechanical Engineering and Engineering Mechanics  
Michigan Technological University  
Houghton, MI 49931**

**ABSTRACT**

In this work we investigate the problem of finite viscoplastic deformation and the associated phenomena of anisotropic hardening, texture and shear banding. A general theory incorporating the effect of higher order strain gradients, deformation induced anisotropy and material rotation is developed. The theory is then employed to examine the phenomenon of shear banding. The problem is treated analytically by resorting to a linear stability analysis and the influence of material rotation and anisotropy on the onset of shear bands is examined. The nonlinear problem is solved using the finite element method. It is shown that internal stresses (deformation induced anisotropy) along with strain rate effects influence the size of the shear band. Moreover, the material rotation (plastic spin) is shown to have a significant effect on the development of severe localization. An increase in plastic spin seems to delay severe shear banding.

## ON THE FORMABILITY/INSTABILITY EXPERIMENTAL MECHANICS OF SHEET METAL FORMING

Abdel E. Bayoumi

*Department of Mechanical and Materials Engineering  
Washington State University, Pullman, WA 99164-2920 USA*

Stretch forming is a significant component in many sheet metal processes such as cupping and deep drawing and is extensively used in the aircraft, automobile and electronic industries to produce parts with large radius of curvature. These manufacturing processes involve a large amount of straining which, in turn, may lead to plastic instabilities; including tensile necking, slip formation or shear banding. Understanding the instability phenomenon requires the development of the constitutive description of material characterizing the plastic instability and the post-uniform deformation behavior. As is well-known, a very widely used method for instability and/or formability characterization, both in uniform and post-uniform deformation regions, is the gridded specimen technique. The post-uniform deformation in the uniaxial tension test, starting with diffuse necking and continuing to localized necking and shear banding before fracture, is a well known phenomenon. Although a great deal of effort has been devoted to the understanding of the onset of this phenomenon, only a little attention and a limited amount of theoretical work to explain the post-localization behavior exists. There was a great need to obtain an accurate measurements of stress-strain behavior where the strain measurement is sensitive to gage length and to location along the gage length as the deformation proceeds.

Theoretical investigation on plastic instability of materials, conducted by many researchers, usually lacks the experimental verification of the theoretical models. This may be owing to the complexity involved in designing a suitable experimental methodology for accurate measurements of strain in the locally deforming zone as the deformation progresses rather rapidly once the local neck sets in. Several techniques were used in measuring large deformations. Optical techniques are not as laborious as conventional metrological ones, however they suffer from two drawbacks. The interferometric methods have stringent stability requirements which limit their applicability to the research environments. Speckle photography, Moire and White-light Speckle have less stringent requirements, however, the data processing requirements in obtaining the desired information is laborious, qualitative and time consuming. The surface gridding technique coupled with ordinary photography, is widely used in analyzing metal forming processes.

Recording the strain data has been advanced and moved a very long way from that of using a travelling microscope, a rear projection digitizing system to finally the use of digital image processing. Similarly, photography of deformation has moved from a manual camera, a motor-driven camera, a computer controlled camera, a high speed camera to a video camera.

Although researchers have developed computerized procedures to simplify the data reduction process, the gridding technique is still laborious since it involves measurement of large number of points, which form the grid pattern. This logically led to use computers for the measurement of strain and strain rate at numerous locations in rapidly evolving nonuniform deformation field. The special purpose computers that can process binary pictures in reasonable time have let to the use of digital image processing (DIP) as a powerful research and application too, in many areas of engineering.

An in-depth review of the important methodologies that were and are used in studying instability of sheet metal forming will be presented. Results obtained by the author and other investigators will also be presented. A brief presentation will be given on the theoretical verifications of the experimental work.

# **UNSTEADY INHOMOGENEOUS MOTIONS OF NON-LINEARLY ELASTIC SOLIDS**

**K.R. Rajagopal  
Department of Mechanical Engineering  
University of Pittsburgh  
Pittsburgh, PA 15261**

## **Abstract**

**I will discuss several unsteady inhomogeneous motions within the context of specific constitutive theories, for both compressible and incompressible isotropic solids.**

# UNIVERSAL MOTIONS FOR A CLASS OF VISCOELASTIC MATERIALS OF DIFFERENTIAL TYPE

Millard F. Beatty  
Department of Engineering Mechanics  
University of Nebraska-Lincoln  
Lincoln, NE 68588-0347

Universal quasi-static motions for a class of incompressible, viscoelastic materials of differential type are examined. These time dependent motions are similar to corresponding static universal deformations well-known for incompressible, isotropic elastic materials described in Truesdell and Noll [1]. Carroll [2] later extended these ideas to the general class of simple materials. The present paper, which is based on work by Beatty and Zhou [3], however, is less ambitious; we consider a special viscoelastic solid of differential type.

Here we appeal to simplicity of a nonlinearly elastic, linearly viscous material to derive specific formulae for the stress distributions in quasi-static, universal motions for this class of materials. In consequence, some physical results are made evident and these are shown to be consistent with familiar ideas of creep and recovery effects. We focus attention on some universal quasi-static deformations possible in every incompressible, viscoelastic material of this type. These time dependent motions are similar to corresponding static universal deformations well-known for homogeneous, compressible and incompressible, isotropic elastic bodies [1,4]. The general details are illustrated for the pure torsion problem, and specific results and physical effects are provided for the viscoelastic Mooney-Rivlin model. The results obtained here are useful in analysis of vibrations of a variety of mechanical devices. This was first illustrated in [5] for homogeneous shearing oscillations of a load supported by shear springs. Application of the present study to a vibrating mechanical system will be presented as time permits.

**Acknowledgement:** This work was supported by grants from the National Science Foundation.

## REFERENCES

- [1] Truesdell, C., and Noll, W., The Nonlinear Field Theories of Mechanics. Flugge's Handbuch der Physik III/3, Springer-Verlag, Berlin, Heidelberg, New York, (1965).
- [2] Carroll, M. M., Controllable deformations of incompressible simple materials. Int. J. Engng. Sci. 5 (1967), 515-525.
- [3] Beatty, M.F., and Zhou, Z., Universal motions for a class of viscoelastic materials of differential type. Continuum Mechanics and Thermodynamics (In press).
- [4] Beatty, M. F., Topics in Finite Elasticity: Hyperelasticity of Rubber, Elastomers, and Biological Tissues — with Examples. Appl. Mech. Revs. 40, Part 2 (1987), 1699-1734.
- [5] Beatty, M.F., and Zhou, Z., Finite amplitude, free vibrations of a body supported by incompressible, nonlinear viscoelastic shear mountings. Int. J. Solids Struc. 27 (1990), 355-370.



THE THEORY OF CONTINUA WITH VOIDS AS A BASIS  
FOR THE STUDY OF AERATED LUBRICATION

G. Capriz & P. Giovine  
Dipartimento di Matematica  
Università di Pisa  
Via Buonarroti 2  
PISA

The theory of continua with voids was proposed on the basis of some ad hoc assumptions (Nunziato & Cowin [1]) but can be considered also as a special instance of a general theory of continua with microstructure (Capriz & Podio-Guidugli [2]). Such 'top down' reference offers the advantage of understanding the origin of essential terms in the balance equations.

When one considers, in particular, liquids (i.e., linearly viscous incompressible fluids) with finely dispersed bubbles of air, which do not diffuse appreciably but are carried along with the liquid, the microstructural variable (i.e., the void fraction) gives an extra freedom exactly compensating the constraint of incompressibility, and one can say that the continuum has a very special type of 'latent' microstructure (Capriz [3]). It can be studied as a compressible fluid, with a rather peculiar response to expansion/compression, but otherwise classical.

Thus, for instance, the theory of lubrication with compressible lubricants (Gross [4]), appropriately adapted, offers the tools for the study of phenomena of lubrication

with aereated lubricants (Tønder, [5]). The paper deals with this question in detail, to illuminate the general remarks above.

## References

- [1] J.W. Nunziato & S.C. Cowin, A nonlinear theory of elastic materials with voids.  
Arch. Rat. Mech. An., 72 (1979), 175-201.
- [2] G. Capriz & P. Podio-Guidugli, Materials with spherical structure.  
Arch. Rat. Mech. An., 75 (1981), 269-279.
- [3] G. Capriz, Latent microstructure, in Continuum models of discrete systems (A.J.M. Spencer, ed.), (1987), 159-161.
- [4] W.A. Gross, A gas film lubrication study.  
IBM Journal Res. Dev., 3 (1959), 237-255.
- [5] K. Tønder, Parallel surfaces lubricated via bubbly oil.  
Wear, 35 (1975), 23-34.

# THE TORSION PROBLEM FOR A MATERIAL WITH A NONCONVEX STORED ENERGY FUNCTION

Roger Fosdick  
University of Minnesota  
Dept. of Aerospace Engineering and Mechanics  
107 Akerman Hall  
110 Union St. S.E.  
Minneapolis, MN 55455

This work is motivated by an old observation of Badar and Nadai [1,2], who reported on the morphology of the cross sectional deformation that is associated with the gross plastic deformation of highly twisted steel cylinders. Badar and Nadai noted that after the yield stress was exceeded in the twisting of mild steel bars, an etching of the cross section revealed a star-like pattern of flow layers or markings. This pattern consists of a regular distribution of narrow triangle-shaped regions each of which has its base on the periphery of the cross section and tip facing inward toward the center. The distribution of markings is more dense with increasing torque, and coincidentally the triangle tips grow longer until eventually, as the torque approaches an ultimate limit, they very nearly trace out the loci of the ridges of the fully plastic stress surface that is given by the sand-hill analogy. For a circular cross section this trace consists of just the center point.

Here, we investigate a similar equilibrium pattern in nonlinear elasticity theory for a twisted incompressible bar of circular cross section and for a stored energy function that is not convex. A minimizing sequence gives rise to a limit in which for moderate torques the region outside of a certain special radius (this radius decreases with increasing applied torque) consist of a two-phase mixture of both large and small states of shear whose relative concentration lies in the interval  $(0,1)$  and depends on the particular radial position. In a core inside the certain special radius noted above, the minimizing sequence limits to a simple classical torsion field.

This work was done in collaboration with Ying Zhang.

## References:

- [1] Badar, W. and A. Nadai, Die Vorgänge Nach der Überschreitung der Fliessgrenze in verdrehten Eisenstäben. Z. Ver. deut. Ing., 10, 317 (1927).
- [2] Nadai, A., Theory of Flow and Fractures of Solids, Vol. I, 2nd ed, New York, McGraw-Hill, 1950.

## SEPARATION BEHAVIOR OF STRATIFIED FLOW PAST BLUFF BODIES

William R. Lindberg  
Department of Mechanical Engineering  
University of Wyoming  
Laramie, WY 82071-3295

The separation behavior for stably stratified fluid flowing past bluff bodies will be discussed. For the case of stable stratification, the relevant non-dimensional parameters are the Reynolds number,  $Re$ , and the internal Froude number,  $Fi$ ,

$$Re = \frac{U_o L}{\nu}$$

$$Fi = \frac{U_o}{NL}$$

where  $U_o$  is the free stream velocity which will be taken to be uniform,  $L$  is a characteristic length-scale of the bluff body,  $\nu$  is the kinematic viscosity and  $N$  is the buoyancy frequency:

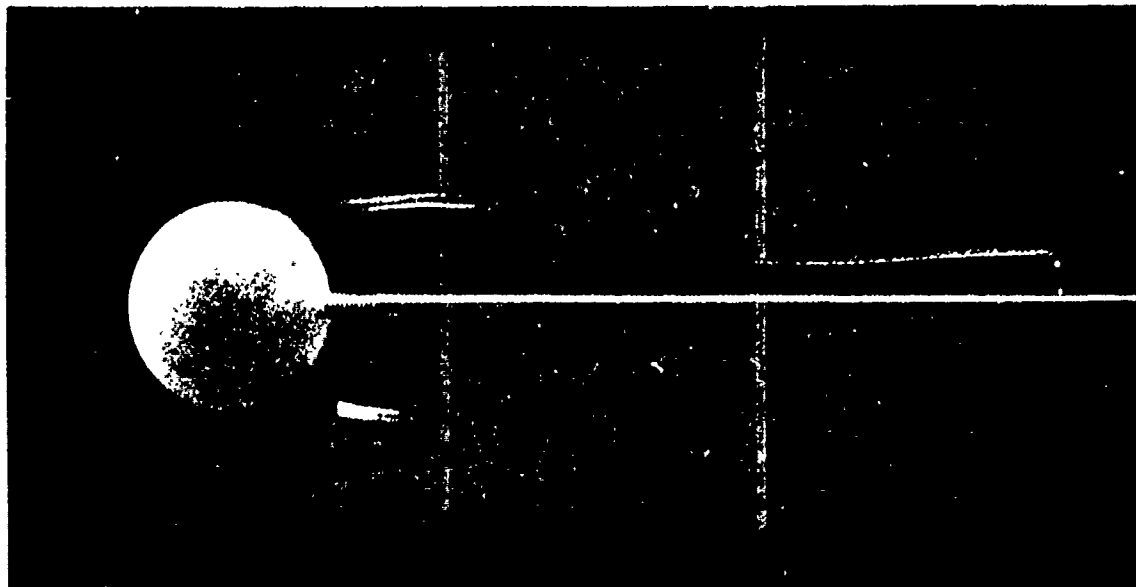
$$N = \left[ -\frac{g}{\rho_o} \frac{\partial \rho}{\partial z} \right]^{\frac{1}{2}}$$

In a recent paper, Lin et al. (1991) describe the observations of flow past a sphere in a linearly stratified fluid over a wide range of  $Re$ ,  $Fi$ . An important result of that study was the identification of flows which exhibited almost complete suppression of downstream flow separation due to a resonance of the internal wave structure with the size of the body. This resonance occurs at values of  $Fi \sim 0.4$  and was independent of  $Re$  (over the parameter space which was examined).

For increasing values of  $Fi > 0.4$ , a double wake structure was observed to occur, as shown in the photograph on the next page, which is a view of the horizontal flow pattern adjacent to the sphere. This separation/wake structure has no counterpart in the flow of a homogeneous fluid past spheres. In order to clarify these observations, physical arguments are presented which are based on the concepts suggested by Lighthill (1963); which include topological structures, surface stress vectors and vorticity line behavior.

The separation criteria of vanishing vorticity may be applied to the topological flow patterns adjacent to the surface to show that the double wake formation is a consequence of induced streamwise vorticity in the vicinity of the aft end of the sphere. This streamwise vorticity is a result of the larger velocities adjacent to the equatorial plane in comparison to the flow velocities over the sphere in the vertical centerplane and the baroclinicity of the boundary layer flows. These effects are shown to cause a

distortion of the lines of surface vorticity to the extent that they bifurcate, forming two nodal points as a limiting case. Physically, the surface flow exhibits a substantial secondary flow, which diverts the flow toward the two nodal (separation) points.



Double wake structure as viewed from above the sphere; the flow is from left to right;  $Re=284$ ,  $Fi=0.583$ . The flow visualization is with illuminated reflective flakes.

The sequence of surface flow topography which leads to this separation will be presented, where the usefulness of the Poincaré-Bendixson Theorem is demonstrated. This kinematic/topologic approach to the examination of separation behavior has proven itself useful in interpreting stratified flows past complex bodies [Hunt et al (1978)] and has the potential for providing insight into separating flow in other contexts as well.

#### REFERENCES

- Hunt, J.C.R. 1978. "Kinematical studies of the flows around free or surface-mounted obstacles; applying topology to flow visualizations," *J. Fluid Mech.*, Vol. 86, Part 1, pp. 179-200.
- Lin, Q, Lindberg, W.R., Boyer, D.L. and Fernando, H.J.S. 1991. "Stratified Flow Past Spheres," Submitted to *J. Fluid Mech.*
- Lighthill, M.J. 1963. In *Laminar Boundary Layers*, L.Rosenhead, ed. Oxford Univ. Press.

# STUDY OF FORCED UNSTEADY SEPARATION AND ITS CONTROL

K. GHIA AND U. GHIA<sup>o</sup>

Department of Aerospace Engineering and Engineering Mechanics  
o Department of Mechanical, Industrial and Nuclear Engineering  
Computational Fluid Dynamics Research Laboratory  
University of Cincinnati  
Cincinnati, Ohio 45221

Flow separation of boundary layers on moving surfaces and in fully separated flow has been and is being studied vigorously by researchers experimentally, theoretically, as well as numerically. The primary goal of many of these studies is to better understand the dynamics of the separated boundary layers that become unsteady, leading to nonlinear interactions, and ultimately to the breakdown of laminar flow. Although the theoretical foundations of steady separation are well established, [see Smith (1989)], this is not the case for unsteady separation. In many engineering applications, unsteady separation phenomena have a significant influence on the resulting flow structure; two applications of present interest are (i) use of unsteady aerodynamics for the design of components of flight vehicles operating in the post-stall regime and (ii) high-lift aids, and design of more effective control surfaces. In this study, the unsteady Navier-Stokes (NS) analyses developed earlier by the authors and their colleagues are used to simulate the detailed results for two flow configurations. These flow problems are briefly discussed here.

## Flow Past a NACA 0012 Airfoil Undergoing a Constant-Rate Pitch-Up Motion

The unsteady NS analysis, in terms of vorticity and stream function, is used to study the role of unsteady separation in the formation of the dynamic stall vortex for a NACA 0015 airfoil undergoing constant-rate pitch-up maneuvers at Reynolds number  $Re=10,000$  and  $45,000$ . A clustered conformal mesh with C-grid topology is developed and includes attempts to resolve the disparate length scales of the separated flow problem, without the use of any turbulence model. The nonlinear unsteady NS equations are solved using alternating-direction-implicit block-Gaussian elimination (ADI-BGE) method. As the airfoil undergoes a pitch-up motion, a separation bubble forms near the leading edge. This bubble, with its counterclockwise spinning fluid within the boundary layer, grows and eventually erupts, ejecting the boundary layer fluid from the wall in the inviscid flow as well as in the leading-edge free shear layer, to form the energetic dynamic stall vortex as described by K. Ghia et al. (1991). The resulting normal pressure gradients set up strong inviscid-viscid interactions. For both flow cases examined, a four-vortex structure is observed just prior to the roll up of the leading-edge free shear layer into the dynamic stall vortex and, for  $Re=10,000$ , it is shown in Fig. 1. The time-dependent pressure field and wall shear stress results analyzed lead to understanding unsteady separation and its role in the dynamic stall phenomenon.

## Flow Inside a Backstep Channel with a Control Flap Mechanism

Separated flow inside a backstep channel with an oscillating flap embedded within the primary separation bubble is studied using the unsteady NS equations, again, in terms of vorticity and stream function. The unique feature of the analysis of U. Ghia et al. (1990) used here for this two-body problem, one fixed and the second oscillating, is that the coordinate system is fixed with respect to the basic channel flow. Thus, the coordinates deform in the proximity of the oscillating body so as to always remain aligned with the bounding surface. Results obtained for this flow without the oscillating flap compared satisfactorily [K. Ghia et al. (1989)] with available experimental data for low  $Re$ . At higher  $Re$ , for persistently unsteady flow, experimental data reveals that the flow is three-dimensional and, hence, the length of the primary bubble is

considerably smaller in comparison with the value for the corresponding 2-D flow. With the present 2-D analysis, results obtained with the flap oscillating at prescribed nondimensional frequencies also show significant reduction in the length of the primary separation bubble, as shown in Fig. 2. These results are further analyzed using the balance of vorticity fluxes in the separated zone, since the flap affects the separation region via two possible mechanisms, namely, it prevents vorticity from entering the primary separated-flow region or it enhances the rate of removal of vorticity from this region.

## References

1. Ghia, K.N., Yang, J., Osswald, G.A. and Ghia, U., (1991), "Study of the Dynamic Stall Mechanism Using Simulation of Two-Dimensional Navier- Stokes Equations," *AIAA Paper* 91-0546.
2. Ghia, K.N., Osswald, G.A. and Ghia, U., (1989), "Analysis of Incompressible Massively Separated Viscous Flows Using Unsteady Navier-Stokes Equations," *International Journal for Numerical Methods in Fluids*, Vol. 9, pp. 1025-1050.
3. Ghia, U. and Ghia, K.N., (1990), "Analysis and Control of Low-Speed Forced Unsteady Flows," *Nonsteady Fluid Dynamics*, Editors: J.A. Miller and D.P. Telonis, FED-Vol. 92, pp. 321-328.
4. Smith, F.T. (1989), "Bursting in Separating Flow and in Transition," *Lecture Notes in Engineering*, Editor: T.J. Mueller, Vol. 54, Springer-Verlag, pp. 93-103.

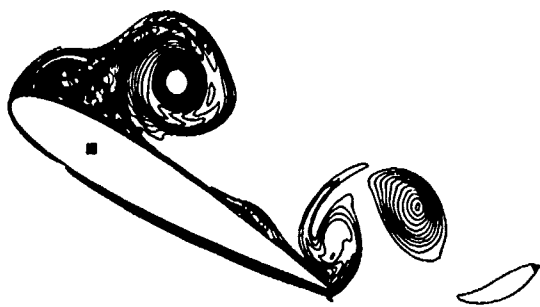
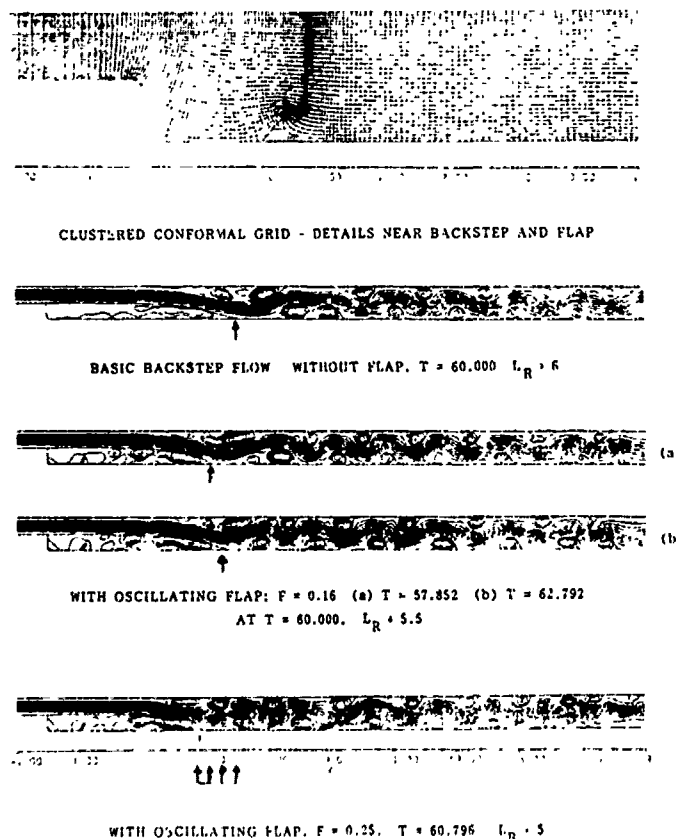


Fig.1. Evolution of Dynamic Stall Showing Four-Vortex Structure for NACA 0015 Maneuvering Airfoil;  $Re=10000$ , Time=2.6.

Fig.2. Active Control of Separated Flow in Backstep Channel Using Forced Unsteadiness;  $Re=2000$ , (375 x 35) Grid.



# NAVIER-STOKES SOLUTIONS OF SEPARATED FLOWS: Mean Flow Past a Circular Cylinder

I. Celik<sup>1</sup> and F. D. Shaffer<sup>2</sup>

<sup>1</sup> Mechanical and Aerospace Engineering Department  
West Virginia University, Morgantown, WV 26506-6101

<sup>2</sup> United States Department of Energy  
Pittsburgh Energy Technology Center, Pittsburgh, PA 15236

## Abstract:

Recent Navier-Stokes solutions of the mean flow past circular cylinders are reviewed and compared with results from the present work. Predictions from various sources with essentially the same turbulence models and numerics, as well as the experiments differ from each other significantly. The solutions are dependent on the grid fineness and distribution in the boundary layer. At high Reynolds numbers the transitional nature of the flow in the boundary layer must be taken into account. By imposing transition to turbulence in the shear layers down stream of the separation point the critical behavior of the flow around the cylinder in the range  $1 \times 10^5 < Re < 3 \times 10^5$  can be predicted. Comparison of the predictions from conventional turbulence models with those from more sophisticated turbulence models such as the large eddy simulation (LES) show that there still remains many questions as to the fine tuning of the model constants and the cost effectiveness of each model for engineering applications.

## Introduction

The flow past a circular cylinder represents a good example of separated flows, and it is a good test case for computational fluid dynamics (CFD). Previous studies [2,3,4,7] have shown that in the subcritical flow regime,  $Re < 10^5$ , the mean flow quantities can be predicted with a good degree of accuracy using Navier-Stokes solvers. Near  $Re = 2 \times 10^5$  (with negligible surface roughness and free stream turbulence) the transition occurs at or close to the separation point [1]. This causes the flow to reattach and then separate again further downstream. The regime characterized by this laminar-separation turbulent reattachment is known as the critical regime. Here the flow is sensitive to any disturbance, hence quite different results can be observed from experiment to experiment or prediction to prediction. This paper focuses attention to this and the supercritical flow regimes. The present simulations were performed using the PHOENICS CFD code [6]. The governing equations are solved using a finite volume approach and the SIMPLE algorithm [8]. The standard k- $\epsilon$  model is utilized for turbulence closure. For more details the reader is referred to Celik and Shaffer [3,4].

## Results

In Figure 1 the predicted pressure coefficient distribution from this work is compared with the experimental data of Fage and Falkner [5]. The experiments exhibit a subcritical flow regime at  $Re = 1.06 \times 10^5$ . The results for the same  $Re$  with less blockage (diameter = 2.93 in.) show that there is still



some influence of blockage. The predictions are theoretically with no blockage. By increasing the Reynolds number to  $2.12 \times 10^5$  or by increasing the free stream turbulence level (Case with  $Re = 1.08 \times 10^5$ ) it was possible to push the flow into the critical flow regime; see pressure distribution with small plateaus near 90 deg.. A completely laminar model (lam6nb5) overpredicts the base pressure but the predicted location of separation is close to the experimental value of 90 deg. The fully turbulent calculation (tur6nb5) gives a supercritical flow behavior. When transition is imposed in the model after separation the critical flow regime is obtained which leads to a good agreement between experimental and predicted pressure distribution. Similar trends are seen when the measured and predicted skin friction coefficients are compared (Fig. 2). More examples and discussion shall be presented in the full paper.

**Aknowlegements:** This work was sponsored by the U.S. DOE Pittsburgh Energy Technology Center in conjunction with the Oak Ridge Associated Universities Part Time Faculty Participation Program.

### References

1. Bloor, S.M. (1964), "The Transition to Turbulence in the Wake of a Circular Cylinder," J.F.M. 19, 291-304.
2. Celik, I. (1986) "Analytical Modeling of Mean Flow over Circular Cylinders: A Review," ASCE Conference on Advancements In Aerodynamics, Fluid Mechanics and Hydraulics, Minneapolis, Minnesota, June 3-6.
3. Celik, I. and Shaffer, F.D. (1991) "Calculation of the Mean Flow Past Circular Clinders Using a Navier-Stokes Solver," U.S. DOE Rept. in Prep.
4. Celik, I. and Shaffer, F.D. (1991) "Analysis of Numerical Simulations of Mean Turbulent Flow Past a Circular Cylinder," ASME-JSME Fluids Engineering Conference, Portland, Oregon, June 23-28.
5. Fage, A.R.C. and Falkner, B. (1931) "Further Experiments on the Flow Around a Circular Cylinder," Aeronautical Research Committee Reports and Memoranda No. 1369 (Ae. 496), London.
6. Ludwig, J.C., Qin, H.Q., and Spalding, D.B. (1989) "The PHOENICS Reference Manual," TR/200, CHAM Ltd., Bakery House, 40 High st. Wimbledon Village, London SW19 5AU, England
7. Majumdar, S. and Rodi, W. (1985) "Numerical Calculation of Turbulent Flow Past Circular Cylinders," 3rd Symp. on Physical Aspects of Aerodynamic Flows, Long Beach, California, Jan. 21-24.
8. Patankar, S.V. (1980) Numerical Fluid Flow and Heat Transfer, Hemisphere Publ., Corp. New York.

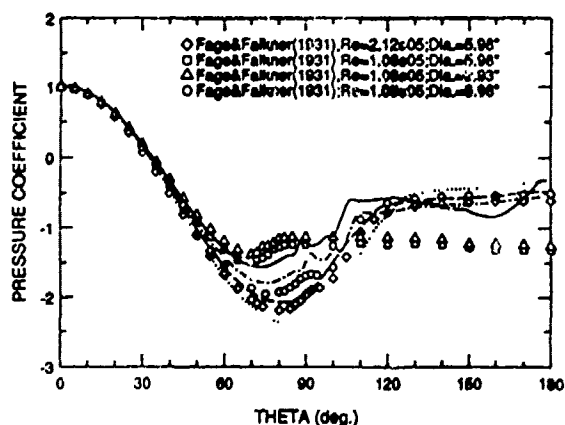


Fig 1 Pressure distribution; Present work: — lam6nb5, --- tur6nb5

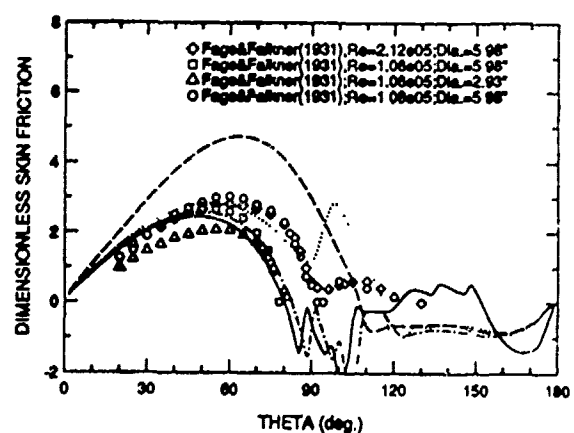


Fig.2 Skin friction distribution; Present Work: — lam6nb5, --- tur6nb5

# PROPERTIES OF THE VORTICITY FIELD IN PLANAR SHEAR LAYERS

John F. Foss, Professor  
Department of Mechanical Engineering  
Michigan State University  
East Lansing, Michigan

An extended effort to develop the capability to execute time resolved transverse vorticity:  $\omega_z = (\partial v / \partial x - \partial u / \partial y)$ , measurements over a small ( $1\text{mm}^2$ ) sample domain has resulted in a definitive probe (Haw, et. al. [1989]) and algorithm (Foss and Haw [1990]). The probe is shown in Fig. 1.

This measurement capability was employed in a program of comparative measurements in a two-stream shear layer, Lang and Dimotakis [1985], Balint, et. al. [1989], Kim [1989], and Foss and Haw [1990].

The outcome of this comparative measurements program was to reassure the various investigators of the viability of the four rather different techniques given the good agreement between the various methods. In addition, the systematic variations, that were observed in the results obtained in the independent studies, clearly suggest the important role of probe size effects.

The comparative measurements program will be briefly discussed for its reference value. The balance of the presentation will focus on recent results wherein the low Reynolds number ( $\Delta U \theta / \nu = 4.8 \times 10^3$ ) two stream shear layer of the comparative study can be set in contrast to the MSU high Reynolds ( $U_0 \theta / \nu = 78 \times 10^3$ ) single stream shear layer.

A dramatic "two scale" behavior of the vorticity field is evidenced at the high Reynolds number condition as shown in Fig. 2 from Foss [1991]. This and other stochastic results from the two shear layers will be discussed.

Conditionally sampled results for the instantaneous ( $uv$ ) and the ( $\omega_z$ ) values will also be presented. These computations show that large  $\omega_z$  values are associated with a tendency toward local isotropy of the fluid motion.

## References:

Balint, J.L., Wallace, J.M., and Vukoslavcevic [1989] "The

Statistical Properties of the Vorticity Field of a Two-Stream Turbulent Mixing Layer," Advances in Turbulence 2, Ed. Fernholz, H. and Fiedler H., Springer-Berlag, Heidelberg.

Foss, J.F. [1991] "Vorticity Considerations and Planar Shear Layers," Experimental Heat Transfer, Fluid Mechanics and Thermodynamics, 1991, Ed. Keffer, Shah, Ganic', Elsevier, p. 240.

Foss, J.F. and R.C. Haw [1990] "Transverse Vorticity Measurements Using a Compact Array of Four Sensors" Symposium on the Hueristics of Thermal Anemometry, Ed. D.E. Stock, ASME, June.

Foss, J.F. and R. C. Haw [1990] "Vorticity and Velocity Measurements in a 2:1 Mixing Layer," Forum on Turbulent Flows, Ed. W. W. Bowers, ASME, FED v. 94, June.

Haw, R.C. Foss, J.K. and Foss, J.F. [1989] "Vorticity Based Intermittency Measurements in a Single Stream Shear Layer," Proceedings Second European Turbulence Conference, Advances in Turbulence 2, Ed. H. H. Fernholz and H.E. Fiedler, Springer Verlag.

Kim, J.-H. [1989] Wirbelstärkmessungen in Einer Turbulenten Scherschicht, Dr. Ing Thesis, Technical University Berlin, (Prof. Dr. H. Fiedler).

Lang, D. B. and P.E. Dimotakis [1985] "Laser Doppler Velocity and Vorticity Measurements in Turbulent Shear Layers," Final Report NSF MEA 8022945 Cal. Inst. Tech.

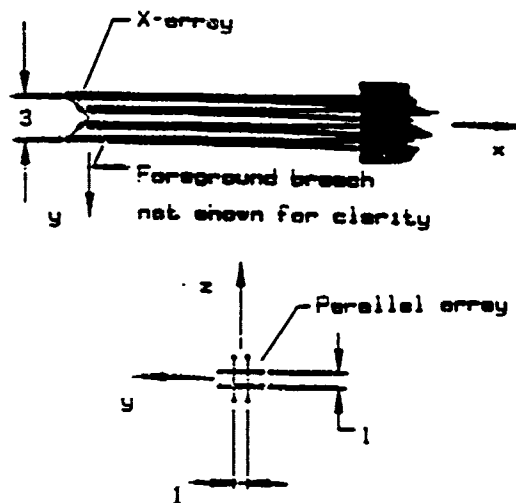


Fig. 1 Transverse Vorticity Probe

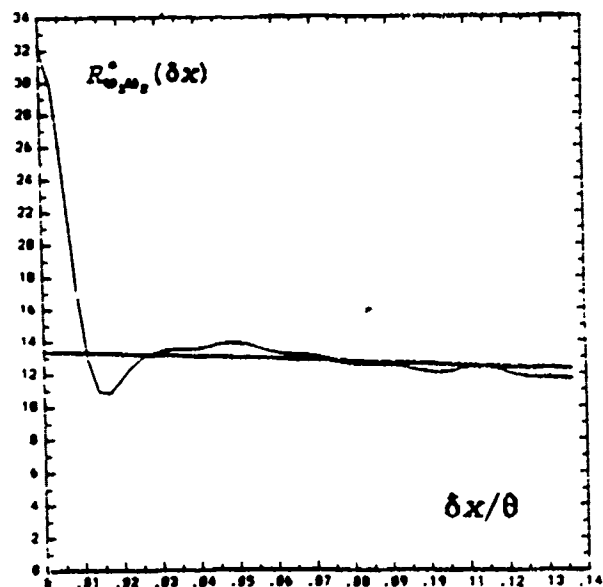


Fig. 2 Autocorrelation of  $[\omega_z \theta / U_0]$  at  $[y - y_{1/2}] / \theta = 0.11$ ,  $R_0 = 78 \times 10^3$ . Note,  $R \rightarrow 0$  at  $(\delta x / \theta) = 2.5$ .

## Structure of Turbulence Using PIV in a Wall-Bounded Shear Flow\*

C. E. Wark<sup>†</sup>, P. W. Offutt<sup>‡</sup> and R. J. Adrian<sup>‡</sup>.

<sup>†</sup> MAE Dept., Illinois Institute of Technology, Chicago IL, 60616

<sup>‡</sup> TAM Dept., University of Illinois, Urbana IL, 61801

Many recent investigations have focused on the statistics and structure of turbulence with emphasis on the Reynolds numbers dependence. Most of the experimental investigations have relied upon single-point measurements<sup>1</sup>; whereas, Direct Numerical Simulation (DNS) results provide full-field information in a three-dimensional grid for various turbulent shear flows; however, these results are limited to very low Reynolds numbers. A promising technique for obtaining high Reynolds number, full-field information is Particle Image Velocimetry (PIV)<sup>2</sup>.

A turbulent pipe flow in air at  $Re_D = 50,000$  was investigated using PIV. The laser system used consisted of a pair of Nd-YAG lasers with approximately 60 mJ of energy per pulse. Each laser was pulsed at 50 Hz, with a 46  $\mu$ sec time delay between the two pulse trains. The photographs were double exposed and recorded using a 4 by 5 view camera. The flow was seeded with atomized olive-oil droplets approximately 1 to 5  $\mu$ m in diameter.

Two-dimensional instantaneous velocity field information will be presented for the x-y plane. Each instantaneous realization (photograph) spans 1800 wall units in the streamwise direction and extends from  $10 \leq y^+ \leq 500$  (the centerline of the pipe corresponds to  $y^+ = 1300$ ). Eleven photographs were analyzed with each yielding velocity measurements at more than 9000 points; the results from a 15 by 25 mm section of a photograph is shown in Figure 1. The average of all 11 photographs gives excellent agreement with the log-law velocity profile (Figure 2). Both instantaneous structure and various statistics will be presented.

\*Supported by ONR under contract N00014-90-J-1415 and AFOSR under contract AFOSR-90-0171.

## References

<sup>1</sup>Naguib, A.M. and Wark, C.E., 1991. An Investigation of Wall-layer Dynamics Using a Combined Temporal Filtering and Correlation Technique. In Review, *J. of Fluid Mechanics*.

<sup>2</sup>Adrian, R. J., 1991. Particle-Imaging Techniques for Experimental Fluid Mechanics. *Annual Review of Fluid Mechanics*, Vol. 23.

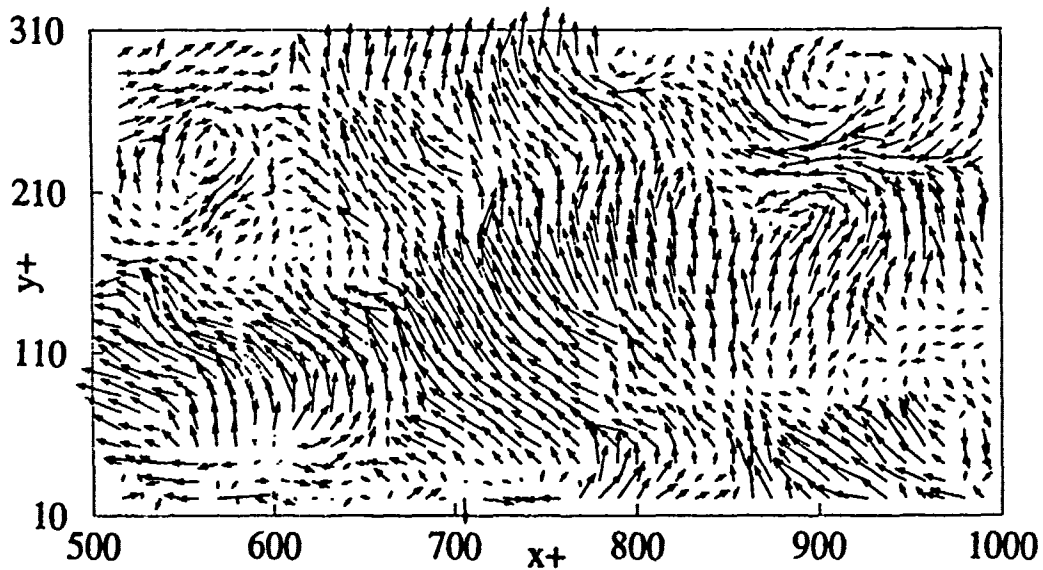


Figure 1. A section of one photograph, depicting instantaneous velocity vectors.

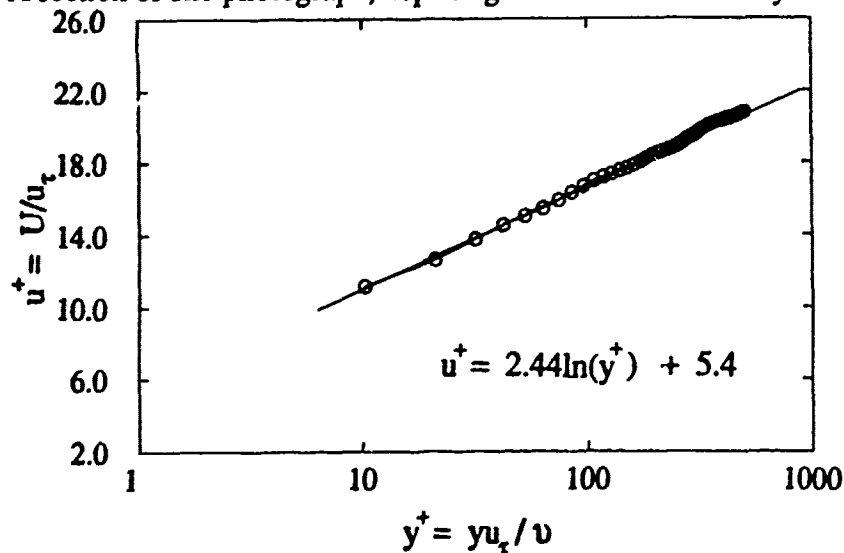


Figure 2. Comparison of Log-Law fit to velocity results averaged over 11 photographs.

## **BENDING EFFECTS ON SHEET FORMING SIMULATIONS**

**J.K. Lee <sup>1)</sup> and R. H. Wagoner <sup>2)</sup>**

**The Ohio State University**

**<sup>1)</sup> Department of Engineering Mechanics**

**<sup>2)</sup> Department of Material Science and Engineering  
155 W. Woodruff Ave., Columbus, Ohio 43210, USA**

Finite element methods for sectional analyses of sheet forming operations have been developed. Two types of elements are available; one based on the membrane theory and the other based on nonlinear shell theory. Both elements are implemented using the updated Lagrangian scheme in an implicit form. The sheet material is modelled by Hill's new theory and an exponential hardening law with the strain rate sensitivity. The tools are assumed to be rigid and interface friction is modelled by using a modified Coulomb's law permitting sliding nodal contacts.

Effects of bending on sheet forming are studied here through a sequence of numerical experiments. Comparisons are made between the membrane and bending formulations. The pros and cons of each formulation are discussed and numerical results are shown by comparing with experimental data. Numerical convergence characteristics and computing time requirements are discussed. Numerical simulations of complex auto body panel forming are presented and results are compared with measured data.

# **AN EXACT REPRESENTATION OF FRICTIONAL SLIDING FOR ELASTOPLASTIC FLOW IN DEFORMATION PROCESSING**

**Y. K. LEE**

**The George W. Woodruff School of Mechanical Engineering  
Georgia Institute of Technology  
Atlanta, GA 30332-0405  
(404) 853-9342**

## **Abstract**

Problems of concern in metal forming analyses have been associated with (1) the difficulty in imposing actual boundary conditions for the frictional sliding that occur at the interface between the contact surfaces of the die and workpiece, and (2) the inability of predicting material failure that may incur during deformation processing.

Over the past years, a finite elastoplasticity model and its computational scheme have been developed to solve the class of problems cited above. The elastoplasticity model is formulated for problems of the generalized Mises type with compressibility. The model accounts for both dilation and shear banding and provides an analysis capability for detecting material defects that may occur during deformation. The criterion for material instability has an invariant form and is embodied exclusively in the constitutive relation.

Based on the model, a set of equations for the interface sliding is derived. These equations satisfy both the kinematic constraints and the equations of motion at the interface. The derivation treats the interface friction as a natural response of the deformation process. Consequently, the formulation provides an intrinsic means for describing the actual sliding condition at any instantaneous state of deformation. The equations are deformation sensitive and are dependent of the local configuration and its rate changes.

With the above bases, a computational scheme is developed for problem solving. The scheme adopts a finite element method of the least squares type, which is insensitive to the changing characters of the field equations and remains valid even in the absence of work-hardening. The scheme provides means to impose intrinsically the required interface conditions for analysis.

As an illustration, upset forging of a block of mild steel is analyzed. The analysis results give us insight into the evolution of the frictional responses at the die-workpiece interface during deformation. In the analysis, it is demonstrated that the frictional sliding at the die-workpiece interface is a bulk phenomenon. Under the influence of bulk deformation, both the normal pressure and the frictional traction along the interface change drastically during deformation.

In addition, the analysis results also demonstrate that both the onset and the subsequent progressive damage of the deforming material can emerge as the natural outcome of the analysis. The results mimic the development of void growth and shear bands, as those observed experimentally in the open literature. Furthermore, the resulting load-deflection curve exhibits a unique feature of the analysis capability and, as expected, it delineates an upper-and-lower yield phenomenon. These results make apparent the efficacy of the solution method in treating metal forming problems.

Submitted for presentation at the 22nd Midwestern Mechanics Conference  
University of Missouri Rolla, 7-9 October 1991.



## ON 3-D SHEET FORMING ANALYSIS USING A BENDING-MEMBRANE FLOW FORMULATION

S. Roy and J. K. Lee  
Engineering Mechanics Department  
The Ohio State University  
Columbus, Ohio 43201

Sheet metal products have found their use at numerous places in automobiles, aircrafts, pressure vessels, cans etc. The properties that made them so attractive are their light weight, good surface finish, formability etc. With the advent of high speed digital computers and the development of a strong numerical tool like the finite element method, sheet forming analysis in the recent years has become a major thrust area for research in several disciplines in engineering. Several researchers have carried out intensive research in this field using various approaches. Different kinds of sheet forming operations like stretching, drawing, flanging, bending etc. have been studied by these researchers. However, different assumptions had been made by them to make reasonable simplifications in order to obtain numerical results for problems which otherwise are very cumbersome and difficult to solve numerically.

The present work is an extension of the work carried out by Lee et al. [1]. These authors used a finite element analysis to simulate two-dimensional sheet forming processes using an updated Lagrangian formulation with fully non-linear shell theory. A strain-controlled elastic-plastic model was used to describe material behavior, the material being assumed to be rigid-plastic after yielding. Modified Coulomb's law was used to model the interfacial friction. However, a sheet forming process with a general geometry demands a three-dimensional analysis. Important effects like material anisotropy can be modelled only by using a three-dimensional analysis. Also an updated Lagrangian formulation is more time intensive compared to a flow formulation.

In this study, an 18 degrees of freedom (d.o.f.) triangular shell element is used for the spatial discretization. It is constructed by the superposition of two elements. A 9 d.o.f. plate bending element based on the discrete Kirchhoff theory [2] to approximate flexural strains and a 9 d.o.f. plane stress element from a degenerate linear strain triangle [3] to approximate the membrane strains. The simplicity in construction, convergence characteristics and total-performance test results as shown by Carpenter et al. [3] are the primary reasons for choosing this element for our study.

The flow formulation used here is a simple and effective method which has been used for metal forming analysis over the years. The primary unknowns in the finite element formulation are the nodal velocities. The sheet geometry and boundary are updated using the solution at each time step and the process restarted. Strain hardening effects and interfacial friction are incorporated into the algorithm in a simple manner.

### References

1. Lee, J. K. and Chaudhry, S., Plane Strain Finite Element Analysis of Sheet Forming Processes with Bending Effects, Report No. ERC/NSM-S-89-34, Engineering Research Center for Net Shape Manufacturing, The Ohio State University, 1989.
2. Batoz, J. L., Bathe, K. J. and Ho, L.W., "A Study of Three-Node Triangular Plate Bending Elements," International Journal for Numerical Methods in Engineering, Vol. 15, pp. 1777-1812, 1980.
3. Carpenter, N., Stolarski, H. and Belytshko, T., "A Flat Triangular Shell Element with Improved Membrane Interpolation," Communications in Applied Methods, Vol. 1, pp. 161-168, 1985.

# ON LIMIT VALUES FOR FRICTION FACTORS

A. Azarkhin and O. Richmond

Alcoa Laboratories,  
Aluminum Company of America  
Alcoa Center, Pennsylvania 15069

The friction factor, commonly used in metal forming modeling and tribology to characterize friction at the interface, is defined as a fraction,  $m$ , of the yield shear stress. It takes values between zero and one, depending on the surface and lubrication conditions. In this presentation, we show that the friction factor cannot exceed a certain limit value,  $m_{lim} < 1$ , even under conditions of full stick at the interface. These limit values depend on the deformation state of the interface and its neighborhood, size of the contact area, and the boundary conditions outside the interface. This is demonstrated on the

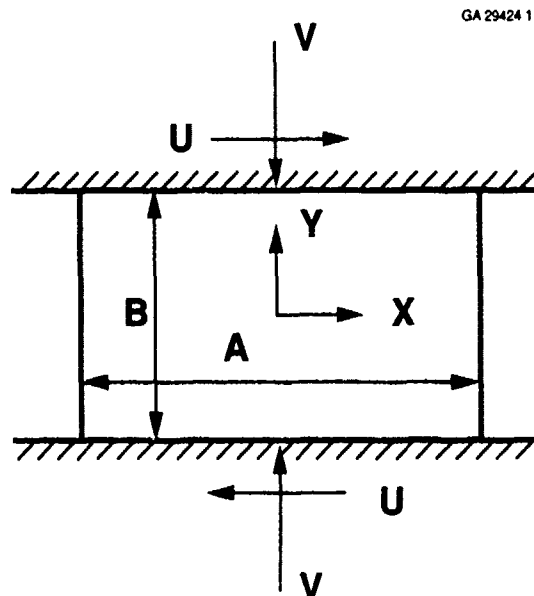


Figure 1. Model of Combined Loading

plane strain problem as shown in Figure 1. Stick conditions are assumed at  $y=\pm B/2$ , and displacements of these surfaces are controlled. Surfaces  $x=\pm A/2$  are stress free. The upper limits for two ratios of  $A/B$  and different ratios of  $e_{xx}/e_{xy}$  are shown in Figure 2. We can see that these limits decrease as  $e_{xx}/e_{xy}$  grows and as the ratio of  $A/B$  decreases. In Figure 2,  $e_{xx}=-e_{yy}$  and  $e_{xy}$  are the average deformations defined respectively as  $2V/B$  and  $U/B$ . These graphs are the examples of results obtained with the use of the earlier developed technique [1] based on a combination of the upper bound method and a finite element representation. Other applications are also discussed.

### References

1. A. Azarkhin and O. Richmond, "Extension of the Upper Bound Method to Include Estimation of Stresses", Trans. ASME, Journ. Applied Mech. (in press).

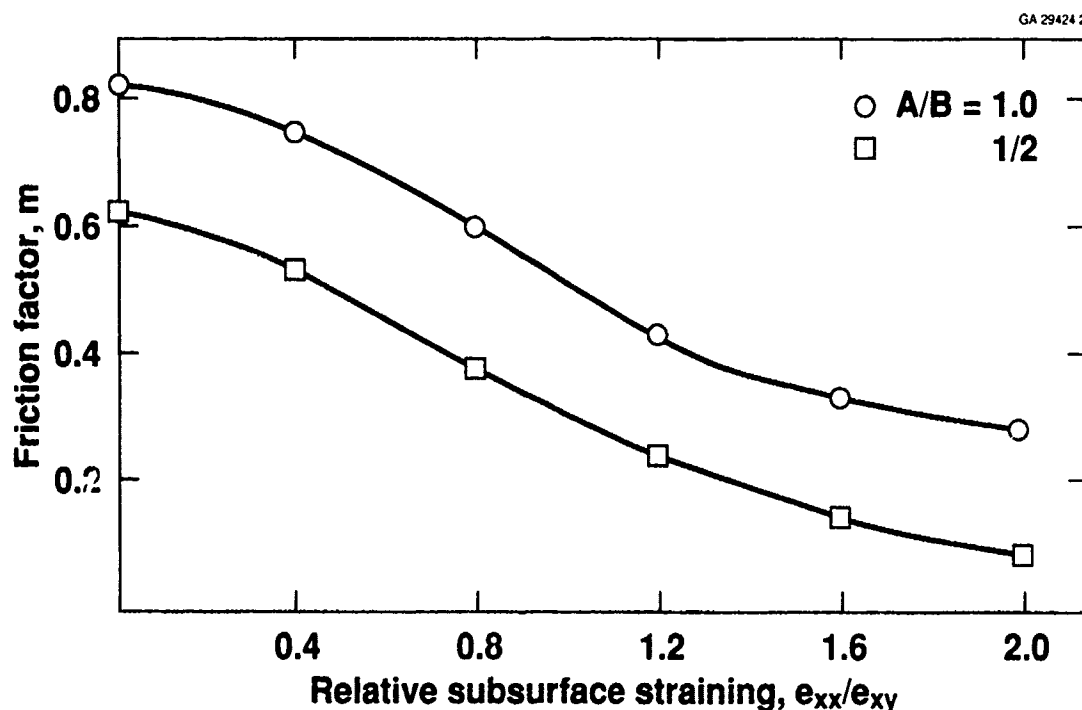


Figure 2. Friction Factors for Combined Loading

# A COMPARISON BETWEEN THE MULTIAXIAL AND THERMOMECHANICAL RESPONSE OF METALS

D. C. Stouffer and V. Bhattachar

Department of Aerospace Engineering and Engineering Mechanics  
University of Cincinnati, Cincinnati OH 45221-0070

## INTRODUCTION

The general objective of the research is to develop a constitutive model for mechanical and thermal loading of nickel base alloys used in gas turbines and rocket engines. This work includes an extensive experimental program; and, the results have produced an accurate model for the uniaxial and multiaxial response of Rene 80 (1,2) that more recently has been extended to thermomechanical cycling. This extension has produced a number of comparisons between nonproportional multiaxial fatigue and uniaxial thermomechanical fatigue that are the subject of this presentation.

## DEFORMATION MECHANISMS IN POLYCRYSTALLINE METALS

The inelastic deformation of crystalline metals at low temperatures (below about 0.8 of the melting temperature) occurs primarily due to the propagation of dislocations through the metal lattice. The slip, or propagation of dislocations, occurs on planes of high atomic density in the close pack directions due to the action of a shear stress. In polycrystalline metals the inelastic slip occurs on the planes most closely oriented to the maximum shear stress. Hardening is associated with the presence of obstacles in the slip plane that slow or pin the propagating dislocations. These obstacles can be grain boundaries, precipitates, or other dislocations. As deformation continues an extensive dislocation structure develops that slows or pins the propagating dislocations, thus a larger shear stress is required to maintain plastic flow and hardening is observed.

At high temperature deformation occurs simultaneously by planar slip and dislocation climb (the movement of dislocations normal to the slip plane). Climb occurs by the diffusion of vacancies or interstitial atoms to or away from the site of a dislocation. The mechanism for positive climb is for a vacancy to diffuse to a dislocation and an extra atom move into the vacant lattice site. Since climb is diffusion controlled it occurs more readily at elevated temperature, and the addition of stress increases the rate of climb.

## MECHANICAL RESPONSE OF METALS UNDER MULTIAXIAL AND THERMAL CYCLING.

In strain controlled proportional multiaxial loading, all the components of strain are proportional for the entire load history. Thus in proportional loading the planes of the maximum shear stress and slip are constant through out the loading. In nonproportional loading the components of strain all vary independently during the loading, and the planes of the maximum shear stress and slip change continuously throughout the loading. A 90 degree out-of-phase tension( $\epsilon$ )/torsion( $\gamma$ ) experiment is a special nonproportional loading defined by  $\epsilon = a_1 \sin \omega t$  and  $\gamma = a_2 \sin(\omega t + \pi/2)$  where the cyclic frequency is  $\omega$ , and  $a_1$  and  $a_2$  are the axial and shear strain amplitudes, respectively.

A recent experimental study (3) shows the combination of responses that can be obtained in nonproportional and thermal cycling. The study compared blocks tension/compression

cycles (proportional) and 90 degree out-of-phase cycles (non-proportional) all at different block temperatures of 316 stainless steel. The results showed:

- Much higher stress amplitudes in nonproportional cycling than in proportional cycling.
- Tension/compression cycling at high temperature influenced the lower temperature response; but, the reverse temperature order had no effect.
- Temperature cycling had little effect on the nonproportional cycling at high temperature.
- Increased strain amplitude increased hardness for all temperatures and load histories.
- Decrease in strain amplitude showed the previous history was not erased except at very high temperature when recovery is important.

These observations suggest extra hardening can occur in both nonproportional and thermomechanical cycling. The extra hardening in the nonproportional loading results because the slip planes change continuously throughout the test. This allows the slip in one slip system to interact with the dislocation structure in another slip system and slow the rate of dislocation propagation. The extra hardening in thermomechanical cycling occurs due to the interactions between dislocation climb at high temperature and planar slip at low temperature. Finally it appears that the maximum hardness obtained the nonproportional and thermomechanical cycling is approximately the same even though the mechanisms are much different. This suggests that there is a maximum or ultimate hardness that can be developed by a dislocation substructure.

#### MODELING OF MULTIAXIAL AND THERMAL CYCLING

If the above postulate is correct, nonproportional cyclic response at high temperature can be modeled without the addition of terms to account for the extra hardness if the constants in the model are determined from uniaxial tests at the same high temperature. In this case the uniaxial constants will include the effect of both the planar slip and climb mechanisms and their interaction. Since the extra hardening from the planar slip/ climb interaction is almost the same as that from intersecting slip planes in the nonproportional loading, the same constants should be successful in predicting the response. The comparison between theory and experiment for Rene 80 verified this assumption. The constants used to predict the nonproportional response were determined only from uniaxial experiments at the same temperature.

It also follows that it is necessary to add extra hardening terms to model uniaxial thermomechanical cycling between high and low temperatures. Constants determined from isothermal experiments will not capture the extra hardening resulting from the interaction between climb at high temperature and planar slip at low temperature. In this case the model was modified by the addition of two variables, one to simulate the presence of climb and the other the activate extra hardening when climb is present. This modification produced a successful model for thermomechanical fatigue of Rene 80.

#### REFERENCES

- (1) Ramaswamy V. G., D. C. Stouffer, and J. H. Lafien, *J. Engrg Mtls Tech* V112, 1990
- (2) Stouffer D. C. et al *J. Engrg Materials and Tech* , V112, pp241, 1990
- (3) Murakami S., Kawai M., and Ohmi Y., *J. Engrg Materials and Tech* V. 111, pp278, 1989

# THERMAL AND MECHANICAL PROPERTIES OF CONCRETE SUBJECTED TO MICROSCOPIC THERMAL STRESS AS A COMPOSITE CHARACTERISTICS

Kazutaka MINAMI, Department of Civil Engineering, The National Defense  
Academy, 1-10-20 Hashirimizu, Yokosuka City, Japan

## 1. INTRODUCTION

The AE signals were detected in concrete specimen by means of Acoustic Emission Method during heating or cooling of concrete. The temperature when the AE signal is detected at first, is lower than that when the dehydration of moisture in concrete takes place. This result suggests that the reason for the change of property of concrete subjected to high temperature cannot be explained only by the dehydration of moisture in concrete. It is the purpose of this paper to point out that the microscopic cracks are developed by the microscopic thermal stress generation due to the difference between the thermal expansion of mortar and coarse aggregate. It was proved from the experimental results that the mechanical properties of concrete subjected to the high temperature are influenced by the generation of microscopic stress and crack.

## 2. EXPERIMENTAL PROCEDURES

Table 1 Condition of Temperature

Ordinary portland cement was used. Two types of aggregates were used as fine and coarse aggregate, and they were hornfels(H) and limestone(L). The compressive strength, modulus of elasticity and thermal expansion strain of mortar and concrete were measured at three conditions shown in table 1.

Type of Test	Method of Heating & Cooling
Normal	Temperature of Test: 20°C
High	Rate of Heating: 20°C
Temperature	Temperature of Test: 200°C
One High	Rate of Heating & Cooling: 20°C/hr.
Temperature	Maximum Temperature: 200°C
Cycle	Temperature of Test: 20°C

## 3. RESULTS AND DISCUSSIONS

When concrete is subjected to high temperature, the stress within concrete is generated at the interface of coarse aggregate by the difference of the thermal strains of mortar and coarse aggregate. These stresses were calculated on the assumption that the inclusion is spherical and the matrix phase is infinite. These formulas are shown as follows.

By the theory of elasticity, the stresses which are generated in the matrix at distance  $r$  from the center of inclusion, are described as follows.

$$\text{Radial Stress: } \sigma_r = P \cdot (R/r)^3 \text{ -----(1)}$$

$$\text{Tangential Stress: } \sigma_t = -P \cdot (R/r)^3 \text{ -----(2)}$$

where,  $R$  is the radius of inclusion and  $r$  is the distance from the center of inclusion. Furthermore,  $P$  is expressed as following equation.

$$P = \frac{(\alpha_m - \alpha_p) \cdot \Delta T}{\frac{1 + \nu_m}{E_m} + \frac{1 - 2 \cdot \nu_p}{E_p}} \quad (3)$$

where,  $\alpha$ ,  $E$  and  $\nu$  show thermal expansion coefficient, modulus of elasticity and Poisson's ratio respectively, and subscripts,  $m$  and  $p$  refer to the matrix and inclusion severally. Moreover,  $\Delta T$  is the difference between the temperature of specimen and the initial temperature.

The results calculated by the equation, are shown in Fig.1. This figure shows the microscopic thermal stress of concrete in the radial directions. The tensile stress is generated in the radial direction of aggregate with an increase of temperature. This stress increases up to a temperature of 100°C, thereafter, decreases by a shrinkage of mortar. Because the microscopic thermal stress which is generated in the radial direction is larger than the bond strength between mortar and coarse aggregate, it seems that the microscopic bond cracks occur.

Fig.2 shows the accumulation of AE count measured in the processes of temperature rise and fall. The beginning of microscopic crack generation is estimated by the increase of AE count with an increase of temperature. In the occasion of temperature drop, the value of AE count becomes larger, and the level of AE signal detected is higher than that at a temperature rise. The microscopic thermal stress in the tangential direction becomes large, and the propagation and connection of microscopic bond cracks are caused at the interface of aggregate by this stress, when the temperature falls.

In Fig.3, it seems that the decreases of compressive strength and modulus of elasticity are in proportion to the increase of accumulation of AE count at temperature rise and down.

#### 4. CONCLUSION

The compressive strength and modulus of elasticity in concrete subjected to high temperature are generally decreasing, and the percentage of decrease of them in concrete subjected to high temperature cycle is especially large. These tendencies differs with the combination of aggregate. It is proved that the evaporations of capillary and gel water are important, in addition, the generation of microscopic crack which is due to the microscopic thermal stress, is also an important factor from this research. This microscopic thermal stress is different by the combination of aggregate, and the state of microscopic crack generation is changed.

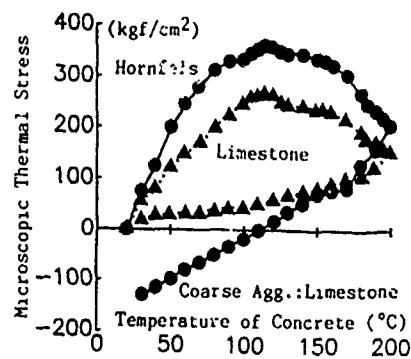


Fig.1 Microscopic Thermal Stress

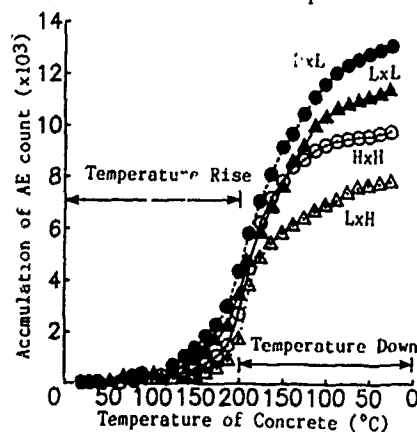


Fig.2 AE Property at Temperature Rise and Down

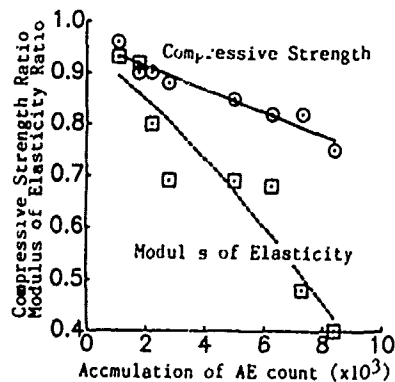


Fig.3 Decrease of Concrete Strength by Crack Generation



# **A CONSTITUTIVE MODEL FOR JOINTED ROCK MASS WITH TWO INTERSECTING SETS OF JOINTS\***

**E. P. Chen**  
**Engineering and Structural Mechanics Division**  
**Sandia National Laboratories**  
**Albuquerque, New Mexico 87185**

## **Abstract**

This investigation involves the development of a general two-dimensional continuum model to describe jointed rock mass. Chen (1986,1989) recently developed a model for the analysis of rock mass containing two orthogonal joint sets. Development of the orthogonal joint set model followed the general formulation of Morland (1974) and the special single joint set implementation of Morland's model by Thomas (1982). Although the orthogonal joint set model has proven useful for analyzing field-scale problems (see Costin and Chen; 1988a,1988b), it remains restrictive in terms of the general field conditions. In this paper, the orthogonal joint set model has been extended to a more general model where the orthogonality restriction has been relaxed. Fundamental approaches remain the same for both models. However, as the general model becomes capable of treating physically more complicated problems, it becomes mathematically more complex. This complexity provides the potential to study more completely the interaction of various parameters representing the characteristics of jointed rock mass behavior. The equation governing the solution of the problem has been given, and example problems have been solved. The behavior of the rock mass predicted by the orthogonal joint set model has been compared to the general model.

This model has been developed to aid in characterizing the site of the repository at Yucca Mountain, Nevada, for the potential geologic disposal of radioactive waste. Disposal of high-level nuclear waste is currently being considered by the Yucca Mountain Project, administered by the Nevada Operations Office of the U. S. Department of Energy.

---

\*This work was performed under the auspices of the U. S. Department of Energy, Office of Civilian Radioactive Waste Management, Yucca Mountain Project, under contract number DE-AC04-76DP00789.

## References

- Chen, E. P., 1986, Two Dimensional Continuum Model for Jointed Media with Orthogonal Set of Joints, Proceedings of the 27th U. S. Symposium on Rock Mechanics, edited
- Chen, E. P., 1989, A Constitutive Model for Jointed Rock Mass with Orthogonal Sets of Joints, Journal of Applied Mechanics, Vol. 56, pp. 25-32.
- Costin, L. S., and E. P. Chen, 1988a, An Analysis of the G-Tunnel Heated Block Experiment Using a Compliant Joint Rock-Mass Model, Proceedings of the 29th U. S. Symposium on Rock Mechanics, edited by P. A. Cundall, R. L. Sterling, and A. M. Starfield, A. A. Balkema, Rotterdam, The Netherlands, pp. 625-632.
- Costin, L. S., and E. P. Chen, 1988b, An Analysis of the G-Tunnel Heated Block Thermo-mechanical Response Using a Compliant Joint Rock Mass Model, SAND87-2699, Sandia National Laboratories, Albuquerque, New Mexico.
- Morland, L. W., 1974, Continuum Model of Regularly Jointed Medium, Journal of Geophysical Research, Vol. 79, No. 2, pp. 357-362.
- Thomas, R. K., 1982, A Continuum Description for Jointed Media, SAND81-2615, Sandia National Laboratories, Albuquerque, New Mexico.

# UNIFIED STRESS-STRAIN MODEL WITH STRAIN-RATES IN CONFINED CONCRETE MATERIALS

Tomonori OHNO, Department of Civil Engineering, National Defense Academy,  
Hashirimizu 1-10-20, Yokosuka, Kanagawa, 239 Japan

## 1. INTRODUCTION

The stress-strain relation in concrete under the condition of static loading was introduced first by using the elastic theory. Then three types of specimens were tested under three different loading speeds to investigate the strain-rate effects on the dynamic properties of confined concrete and to complete the stress-strain relation. The calculated stress-strain curve is compared with the results from three types of tests for circular confined concrete specimens. In tests, the different loading velocity from the range of  $\dot{\epsilon}=10^{-6}/\text{sec}$  to  $10^0/\text{sec}$  in strain-rates were assigned.

## 2. STATIC PROPERTIES OF CONFINED CONCRETE BASED ON ELASTIC THEORY

When the conventional elastic theory and some assumptions are introduced, the maximum stress,  $f_{cm}$ , and the corresponding strain,  $\epsilon_{cm}$ , to  $f_{cm}$ , in the case that the cylindrical concrete is subjected to axial compressive force, can be easily derived as follows.

The relation between the compressive strength of unconfined concrete,  $f_c'$ , and the maximum stress of confined concrete,  $f_{cm}$ , is expressed as

$$f_{cm}/f_c' = 1 + \{(1/\nu - 1)/2\} \cdot p_b \cdot (f_{sy}/f_c') \quad (1)$$

in which  $f_{sy}$  is the yield strength of confining steel,  $\nu$  is the Poisson's ratio and  $p_b$  is the volume ratio of confining steel. The relation of the corresponding strain of maximum stress is obtained as the same type of form as

$$\epsilon_{cm}/\epsilon_{co}' = 1 + \{(1/\nu - \nu)/2\} \cdot p_b \cdot (f_{sy}/f_c') \quad (2)$$

where  $\epsilon_{co}'$  is the strain corresponds to the compressive strength of unconfined concrete. The value of  $\nu$  may be employed by  $1/2.5 - 1/3.5$ . After yielding of materials, the descending branch of gradient after the maximum stress is also influenced by the degree of confinement. The failure strain,  $\epsilon_{su}$ , is defined in this study as the strain when the value of stress becomes zero after descending from its maximum. However, there is no alternative but to estimate the approximate value for  $\epsilon_{su}$  on the basis of stress-strain curves by tests. Then, upon referring test results for static loading, the value of failure strain can be determined as

$$\epsilon_{su} = 5 \cdot \{1 + \{(1/\nu - \nu)/2\} \cdot p_b \cdot (f_{sy}/f_c')\}^2 \cdot \epsilon_{co}' \quad (3)$$

Calculated results by the use of these formulas are compared with test results. It is regarded that good agreement can be obtained by the proposed formulas.



Photo 1  
High-speed testing apparatus.

### 3. TESTS FOR CYLINDRICAL CONCRETE SPECIMENS CONFINED BY CIRCULAR HOOPS

Three types of specimens were used for tests. Type-1 and 2 specimens have the circular hoops arranged between 40mm and 60mm interval, respectively. Type-3 specimen is an unconfined concrete specimen. Tests were conducted in a servo-hydraulic testing apparatus as shown in Photo 1, which has a vertical load capacity of up to 490kN. The loading velocity is variable from 0.0 to 4.0m/sec. Tests were done at three loading rates of  $10^{-6}$  m/s for static loading,  $3 \times 10^{-2}$  m/s for low-speed loading and  $3 \times 10^0$  m/s for high-speed loading.

### 4. FORMULATIONS OF DYNAMIC PROPERTIES OF CONFINED CONCRETE

Based on test results, the dynamic compressive strength,  $d f_c'$ , and the strain,  $d \epsilon_{co}'$ , corresponds to  $d f_c'$  are formulated with respect to the strain-rates as follows:

$$d f_c' / s f_c' = a + b \cdot (\log \dot{\epsilon}) \quad , \quad s \epsilon_{co}' / d \epsilon_{co}' = c + d \cdot (\log \dot{\epsilon}) \quad (4)$$

The yield stress of steel for dynamic loads [1] is given in the form as

$$d f_{sy} = s f_{sy} \cdot (10^{n+0.94}) : n = 0.15 \cdot \log(\dot{\epsilon} \times 10^6) - 1.34 \quad (5)$$

Substituting Eqs.(4) and (5) into Eqs.(1),(2) and (3), the dynamic compressive stress,  $d f_{cm}$ , the strain,  $d \epsilon_{cm}$ , and the failure strain,  $d \epsilon_{su}$ , are then obtained.

Letting the stress-strain relation in confined concrete be a quadratic form up to the maximum stress and the descending gradient after  $d f_{cm}$  be a linear form, the unified stress-strain relation with strain-rates can be expressed as follows and is shown in Fig.1.

$$f = (d f_{cm} / d \epsilon_{cm}) \{ 2\epsilon - (\epsilon / d \epsilon_{cm})^2 \} : \epsilon \leq d \epsilon_{cm}$$

$$f = d f_{cm} (d \epsilon_{su} - \epsilon) / (d \epsilon_{su} - d \epsilon_{cm}) : \epsilon > d \epsilon_{cm} \quad (6)$$

Figure 2 shows the comparison of calculated results with the curves by tests in the case of  $P_b = 3.6\%$  for static and high-speed loadings. In the figure, the broken lines show the calculated results for different Poisson's number,  $m$ . The value of  $m = 3.0$  ( $\nu = 1/3$ ) would be possibly enough upon considering the amount of scatter in tests.

### 5. CONCLUSIONS

- The concluding remarks are as follows:
- (1) The unified stress-strain model with strain-rates is of applicable to predict both the compressive strength and strain at maximum stress of circular confined concrete subjected to either static or dynamic loads.
  - (2) The proposed model has less experimental coefficients in the formulas. It should be noted that good agreement can be achieved when the value of  $\nu = 1/3$  is employed in the model.

### REFERENCES

- 1) Takahashi, Y. et al. : A Flexural Response Analysis Considering Strain-rate Effect of Reinforced Concrete Beams under Impact Load, Proc. of Structural Eng., JSCE, Vol.32A, pp.669-682, 1986.3(in Japanese).

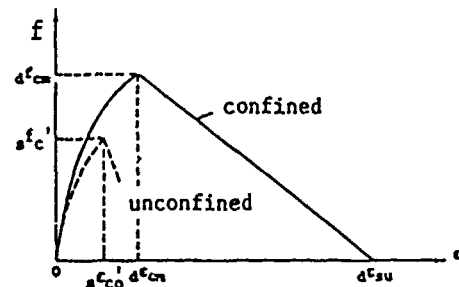


Fig.1 Stress-strain model for confined concrete.

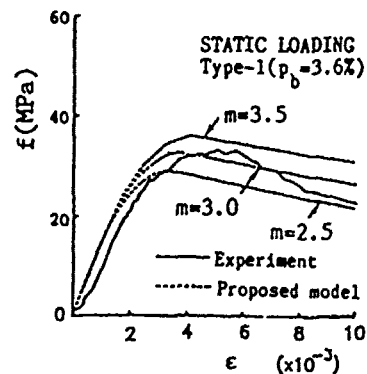
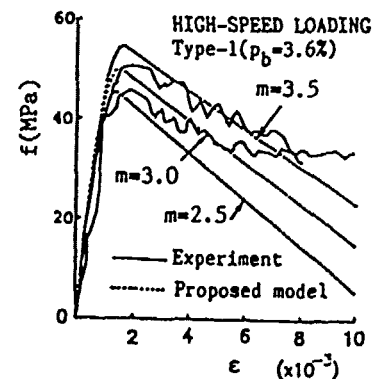


Fig.2 Comparison of stress-strain relationships.

# DYNAMIC INSTABILITY OF A COMPOSITE SHELL SUBJECTED TO COMBINED LOADING

Alan Argento  
Department of Mechanical Engineering  
The University of Michigan- Dearborn  
Dearborn, Michigan 48128

The dynamic instability of composite, circular cylindrical, shell structures subjected to axial loading has recently been studied in [1]-[3]. These works, as well as others not cited here, reveal that statically stable composite structures may become dynamically unstable when subjected to harmonic axial loading; load magnitudes far less than the static buckling load can induce this instability. Similar behavior has been observed in isotropic shells. However in composites mechanical coupling not only complicates the analysis, but also leads to more complex physical behavior. In particular, results in [3] show that for composite shells subjected to axial loading, shear stresses caused by induced mechanical coupling, can significantly effect dynamic instability. The purpose of the present work is to study the effect on dynamic instability, of interaction between harmonic axial and torsional loads.

The shell is taken to be thin, and of circular cylindrical geometry. It is comprised of arbitrarily ordered orthotropic layers, so that the resulting structure has full stiffness property matrices with respect to its natural geometric directions. Axial and torsional loads of the following forms are applied to the shell's ends:

$$P_1 = P_{a_1} + P_{t_1} \cos \Omega_1 t$$

$$P_2 = P_{a_2} + P_{t_2} \cos \Omega_2 t$$

The equations of motion of the shell are linearized by means of perturbation methods, resulting in pre-instability (unperturbed) and perturbed response equations. Unperturbed response quantities appear as coefficients in the perturbed response equations. Upon solution of the unperturbed response, these coefficients are found to be functions of the time dependent loading.

As in [2], spatial dependence in the perturbed response equations is satisfied by means of Fourier series in the axial coordinate, and a complex periodic form in the circumferential coordinate. Clamped boundary conditions are satisfied through proper differentiation of the Fourier series (not term by term). The resulting set of time dependent complex equations are of the form

$$\underline{m} \frac{d^2 \bar{f}}{dt^2} + (\underline{R} - P(t)\underline{S})\bar{f} = 0 \quad (1)$$

Where,  $P(t)$  is a function of the harmonic parts of  $P_1$  and  $P_2$ ,  $\underline{m}$  is a mass matrix,  $\underline{R}$  and  $\underline{S}$  are matrices containing material and geometric constants, and,  $\bar{f}$  is the vector of unknowns. Included in (1) are equations reflecting the boundary conditions.

If  $\Omega_1$  and  $\Omega_2$  are commensurate,  $P(t)$  is periodic and (1) form a set of Hill equations: dynamic instability can then be assessed using techniques for analyzing such equations. Here the monodromy matrix method is used because of its generality. For the special case in which  $\Omega_1 = \Omega_2$ , equations (1) are reduced to a set of Mathieu equations, from which instabilities are determined by Bolotin's method.

Stability diagrams are presented for both the cases  $\Omega_1 = \Omega_2$ , and  $n_1\Omega_1 = n_2\Omega_2$  ( $n_1, n_2$  integers). Dynamic interaction curves are developed to study the mutual effect of the two loads on stability, for both cases. Particular emphasis is placed on the effect of a small component of one load on the stability of the shell, while it is vibrating in a stable mode due to the other load.

## References

- [1] C.W. Bert and V. Birman 1988 *Acta Mechanica* 71, 61-76. Parametric instability of thick, orthotropic circular cylindrical shells.
- [2] A. Argento and R. A. Scott *Journal of Sound and Vibration*, submitted for publication. Dynamic instability of layered anisotropic circular cylindrical shells, Part I: Theoretical development.
- [3] A. Argento and R. A. Scott *Journal of Sound and Vibration*, submitted for publication. Dynamic instability of layered anisotropic circular cylindrical shells, Part II: Numerical results.

# ON THE CONDITIONS OF FINITENESS FOR AXISYMMETRIC STRUCTURES

R.K. JAIN, J.K. Technosoft, Delhi, INDIA  
and  
Y. NATH, Applied Mechanics, IIT-Delhi, INDIA

It is shown numerically that there exists three different boundary conditions at the centre of axisymmetric shallow spherical shells.

## GOVERNING DIFFERENTIAL EQUATIONS

The equations of motion for a cylindrically orthotropic shallow spherical shell supported by elastic media and undergoing moderately large axisymmetric deformation — can be expressed — in terms of nondimensional normal deflection  $\bar{w}$ , stressfunction  $\bar{F}$  [2-3] and the parameters defined therein as :

$$\begin{aligned} & (\int + \delta)^2 \bar{w}_{,\int\int\int} + (\int + \delta) \bar{w}_{,\int\int} - \beta \bar{w}_{,\int} - 12 \left(\frac{L}{h}\right)^2 (\int + \delta) (\bar{F} \bar{w}_{,\int}) \\ & - 12R \left(\frac{L}{h}\right) (\int + \delta)^2 \bar{F} + (\int + \delta) \int_0^1 [(\int + \delta) (\bar{K} \bar{w} - \bar{G} \bar{w}_{,\int\int}) - \bar{G} \bar{w}_{,\int}] d\int \\ & = (\int + \delta) \int_0^1 (\int + \delta) \left[ \left(\frac{L}{a}\right)^3 P - \bar{w}_{,\tau\tau} \right] d\int \end{aligned} \quad (1)$$

$$\begin{aligned} & (\int + \delta)^2 \bar{F}_{,\int\int} + (\int + \delta) \bar{F}_{,\int} - \beta \bar{F} \\ & + \frac{(\beta - \mu^2)(\int + \delta)}{2} [(\bar{w}_{,\int})^2 + 2R (\int + \delta) \left(\frac{h}{L}\right) \bar{w}_{,\int}] = 0. \end{aligned} \quad (2)$$

The domain boundary conditions are :

a) At the outer boundary  $\int = 1$  :

$$\begin{aligned} & \bar{w} = 0, (\int + \delta) \bar{F}_{,\int} - \mu \bar{F} = 0, \\ & \& \bar{w}_{,\int} = 0, \text{ (Clamped) or } (\int + \delta) \bar{w}_{,\int\int} + \mu \bar{w}_{,\int} = 0. \text{ (Simple Support)} \end{aligned} \quad (3)$$

b) Conditions of Finiteness at the centre without hole ( $\delta=0$ )  $\int = 0$  :

$$\begin{aligned} & \bar{F} = 0, \bar{w}_{,\int} = 0 \quad \text{Classical} \quad \text{(Condition I)} \\ \text{or } & \bar{F} = 0, \bar{w}_{,\int\int} = 0 \quad \text{New} \quad \text{(Condition II)} \\ \text{or } & \bar{F} = 0, \bar{w}_{,\int\int\int} = 0 \quad \text{New} \quad \text{(Condition III)} \end{aligned} \quad (4)$$

c) Conditions at the hole ( $\delta \neq 0$ )  $\int = 0$  :

$$\bar{F} = 0, (\int + \delta) \bar{w}, \int\int + \mu \bar{w}, \int = 0. \quad (5)$$

the initial conditions at  $\tau = 0$  are assumed as :

$$\bar{w}(\int, 0) = 0, \bar{w}_{,\tau}(\int, 0) = 0. \quad (6)$$

Equations (1) to (6) form a non-linear boundary and initial value problem. These equations are solved iteratively using Chebyshev polynomials and Houbolt technique in space and time, respectively [1].

## NUMERICAL RESULTS

Influence of three conditions of finiteness at the centre on the maximum central deflection, average deflection, radial membrane, radial bending stress response and their time - periods.

$$Q = qa^4/Bh^4 = 8, \mu = 1/3, b/a = \delta = 0, \bar{R} = 3, \bar{K} = 0, G = 0, \beta = 1$$

Problem Type	Finite-ness	Maximum Central		Maximum Time-Average		Maxm. Radial Membrane Stress				Maxm. Radial Bending Stress				
		Condi-tion No.	Deflec-tion $w(0)_{\max}/h$	period $\tau$	Deflec-tion $w_{\max}$	period $\tau$	at boundary		Time-centre period		at boundary		Time-centre period	
							$\sigma_r^m(1)_{\max}$	$\tau$	$\sigma_r^m(0)_{\max}$	$\tau$	$\sigma_r^b(1)_{\max}$	$\tau$	$\sigma_r^b(0)_{\max}$	$\tau$
Clamped Shell	I	2.6076	0.336	2.7575	0.368	-0.9219	0.234	-1.3131	0.132	10.2924	0.388	-8.8600	0.328	
	II	2.6064	0.336	2.7574	0.368	-0.9220	0.234	-1.3136	0.132	10.2909	0.388	----	---	
	III	2.6076	0.336	2.7575	0.368	-0.9219	0.234	-1.3131	0.132	10.2924	0.388	-8.8598	0.328	
Simply-supported Shell	I	4.1012	0.362	6.7011	0.344	3.4355	0.344	4.5324	0.346	----	---	-8.2688	0.390	
	II	4.1006	0.362	6.7009	0.344	3.4351	0.344	4.5302	0.346	----	---	----	---	
	III	4.1012	0.362	6.7011	0.344	3.4355	0.344	4.5324	0.346	----	---	-8.2687	0.390	

These results clearly show that the deflection and stress response and their time-periods remain the same for each of the three conditions of finiteness employed at the centre for the isotropic spherical shells. It implies that there exists a multiple choices of boundary conditions at the centre of axisymmetric shallow spherical shells.

## REFERENCES

1. Y. NATH and R.K. JAIN, Influence of foundation mass on the nonlinear damped response of orthotropic shallow spherical shells. Int. J. Mech. Sci. 27, 471-479(1985).
2. Y. NATH and R.K. JAIN, Non-linear studies of orthotropic shallow spherical shells on elastic foundation. Int. J. Non-lin. Mech. 21, 447-458 (1986).
3. R.K. JAIN and Y. NATH, Dynamic buckling of orthotropic spherical caps supported by elastic media. AIAA J. 25, 630-633 (1987).



# A Non-Linear Theory of Reticulated Shallow Shells

Nie Guo-hua

Shanghai Jiao Tong University, Department of Naval  
Architecture and Ocean Engineering, Shanghai, 200030, P.R.CHINA

## ABSTRACT

Space latticed structures consisting of beam members, due to their mechanical properties of large space stiffness and reasonable force distribution, commercial properties of low cost, light weight, ease of packaging, transporting, and assembling in space, and structural property of an esthetically pleasing appearance, have received considerable attention for use in engineering for many years.

In this paper, a nonlinear analysis of rectangular reticulated shallow shells is given by using an equivalent continuum model. The investigation is based on five basic assumptions: a) the beam members are placed densely enough in the same shell surface, so that  $L_1 (L_2) \ll$  the sizes of bottom plane of the shell, b) the characteristic size of the cross-section of each member is much smaller than  $L_1 (L_2)$ , so each member is regarded as a long and thin curved beam, c) the members are rigidly connected at the joints, the rotation of each joint is negligible, d) the effect of Poisson's ratio of the material on the transverse bending, twist and axial deformation of each member is neglected, e) the surface of the shell is shallow enough as to make the shallow-shell theory valid, and Kirchhoff-love assumption is useful. (see Fig.1)

According to basic assumption a), the internal forces relation between a typical latticed element and an equivalent continuum element is constructed as follows (see Figs. 2 and 3) [1]

$$\{N_\alpha, N_\beta, N_{\alpha\beta}, Q_\alpha, Q_\beta, M_\alpha, M_\beta, M_{\alpha\beta}\} = \left\{ \frac{N_1}{L_1}, \frac{N_2}{L_2}, \frac{1}{2} \left( \frac{N_{12}}{L_1} + \frac{N_{21}}{L_2} \right), \frac{Q_1}{L_1}, \frac{Q_2}{L_2}, \frac{M_1}{L_1}, \frac{M_2}{L_2}, \frac{1}{2} \left( \frac{M_{12}}{L_1} + \frac{M_{21}}{L_2} \right) \right\}$$

Then, the constitutive equations can be derived by the analysis of the internal forces and deformations of reticulated shallow shell member and the use of the above equivalent relation. Further, the application of a variational principle and large deflection geometrical equations [2] ~ [4] leads to the governing equations and boundary conditions of the problem [5]

$$\frac{E_1 I_1}{L_1} W_{,1111} + \left( \frac{G_1 J_1}{L_1} + \frac{G_2 J_2}{L_2} \right) W_{,1122} + \frac{E_2 I_2}{L_2} W_{,2222} = W_{,11} \phi_{,22} - 2W_{,12} \phi_{,12} + W_{,22} \phi_{,11} + K_1 \phi_{,22} + K_2 \phi_{,11} \\ - f_1 (W_{,11} + K_1) - f_2 (W_{,22} + K_2) - f_{12} W_{,12} - f_\beta W_{,22} + f_\nu$$

$$\frac{L_1}{E_1 A_1} \phi_{,2222} + C \phi_{,1122} + \frac{L_2}{E_2 A_2} \phi_{,1111} = (W_{,12})^2 - W_{,11} W_{,22} - K_1 W_{,22} - K_2 W_{,11} + C_1 W_{,1122} \\ + C_2 (W_{,11} W_{,12})_{,12} + C_3 (W_{,22} W_{,12})_{,12} + \frac{L_1}{E_1 A_1} f_{,12} + \frac{L_2}{E_2 A_2} f_{,21}$$

$$\left. \begin{aligned} N_{\alpha n} &= \bar{N}_{\alpha n}, \quad N_{\beta n} = \bar{N}_{\beta n}, \quad M_n = \bar{M}_n \\ (M_{\alpha\beta,1} + M_{\alpha\beta,2})l + (M_{\alpha\beta,1} + M_{\beta,2})m + W_{,1} N_{\alpha n} + W_{,2} N_{\beta n} + M_{\alpha\beta,3} &= \bar{V}_n + \bar{M}_{n,3} \end{aligned} \right\} \quad \text{on } C_1$$

$$u_1 = \bar{u}_1, \quad u_2 = \bar{u}_2, \quad W = \bar{W}, \quad W_{,n} = \bar{W}_{,n} \quad \text{on } C_2$$

$$\text{Where } M_\alpha = -\frac{E_1 I_1}{L_1} W_{,11}, \quad M_\beta = -\frac{E_2 I_2}{L_2} W_{,22}, \quad M_{\alpha\beta} = -\frac{1}{2} \left( \frac{G_1 J_1}{L_1} + \frac{G_2 J_2}{L_2} \right) W_{,12}$$

$w, \phi$  are the transverse deflection and stress function, respectively, and  
 $N_{\alpha} = \phi_{,22} - f_1$ ,  $N_{\beta} = \phi_{,11} - f_2$ ,  $N_{\alpha\beta} = -\phi_{,12}$ ,  $f_1 = \int f_{\alpha} dx_1$ ,  $f_2 = \int f_{\beta} dx_2$

$$(\bar{N}_{\alpha n}, \bar{N}_{\beta n}, \bar{V}_n) = \int (\bar{F}_{\alpha}, \bar{F}_{\beta}, \bar{F}_n) dv$$

The material constants  $C, C_1, C_2, C_3$  are expressed as follows

$$C = \frac{1}{12} \left( \frac{b_2}{E_1 I_{10}} + \frac{b_1}{E_2 I_{20}} \right), \quad C_1 = \frac{1}{24} \left[ \left( \frac{2}{E_1 I_{10}} + \frac{1}{E_2 I_{20}} \right) (q_1 J_1 K_1 + \left( \frac{1}{E_1 I_{10}} + \frac{2}{E_2 I_{20}} \frac{b_1}{b_2} \right) q_2 J_2 K_2) \right]$$

$$C_2 = \frac{1}{24} \left( \frac{2}{E_1 I_{10}} + \frac{1}{E_2 I_{20}} \right) (q_1 J_1 - E_1 I_1), \quad C_3 = \frac{1}{24} \left( \frac{1}{E_1 I_{10}} + \frac{2}{E_2 I_{20}} \frac{b_1}{b_2} \right) (q_2 J_2 - E_2 I_2)$$

in which  $K_1, K_2$  are curvatures in two directions  $(x_1, x_2)$ , respectively.

The above equations show that the continuum model is an anisotropic shallow shell. Non-linear behaviour can be analyzed by the solution of the partial differential equations with corresponding boundary conditions. It should be pointed that the boundary conditions should be treated independently for a non-rectangular boundary element [6].

## REFERENCES

- [1] Kollár, L., Acta Techn. Acad. Sci. Hung. Vol. 94, No. (3~4), 1982.
- [2] Washizu, K., Variational Methods in Elasticity and Plasticity, Pergamon Press, 1975.
- [3] НОВОЖИЛОВ, В.В., Nonlinear Elastic Mechanics Element, (In Chinese), Science Press, 1959.
- [4] Вольмир, А.С., Flexible plates and shells, (In Chinese), Science Press, 1963.
- [5] Nie Guo-hua, Non-Linear Theory of Reticulated shallow shells, Ph.D. Thesis, Shanghai University of Technology, 1990.
- [6] Liu Ren-hua, Li Dong, Nie Guo-hua, and Chen Zhen-qiang, Non-Linear Buckling of Squarely-Latticed Shallow Spherical Shells, Int. J. Non-Linear Mech., Vol. 26, 1991, (in the press).

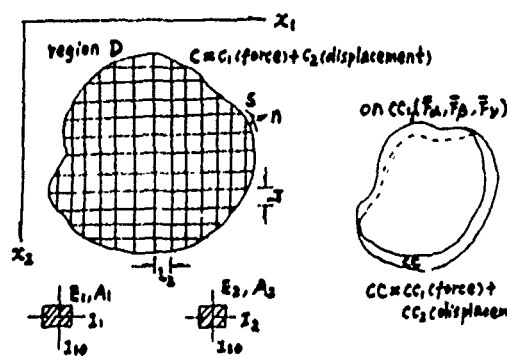


Fig. 1

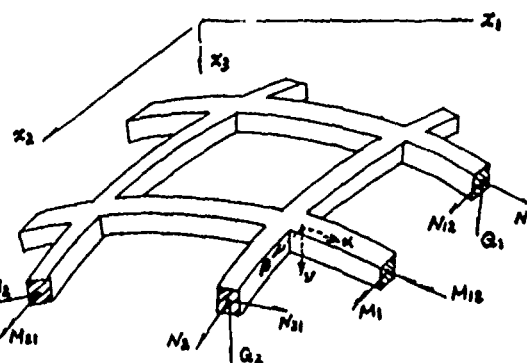


Fig. 2 Typical latticed element

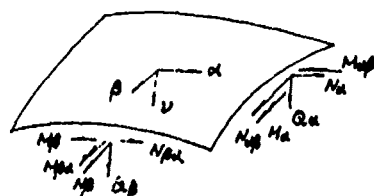


Fig. 3 Equivalent continuum element

# FUNDAMENTAL MODES and ORTHOGONALITY CONDITION FOR ELASTICALLY CONNECTED MULTI-LAYER BEAMLIKE STRIPS or PLATES

U. Yuceoglu, O. Tekinalp and N. Caglayan  
Department of Aeronautical Engineering  
Middle East Technical University, Ankara, Turkey

Composite multi-layer beams or beamlike plate strips are increasingly used in aerospace and flight vehicle structures. In practical applications, composite layers or metal layers are joined by thin adhesive layers or mechanical springs [1,2]. Interlaminar adhesive layers too can be modelled as compression-tension and shear springs.

The purpose of this paper is to investigate the fundamental frequencies, mode shapes and the mode orthogonality conditions for connected multi-layer beamlike strips. The system configuration is shown in Fig.1.

The "Coupled Governing Equations" of n-layer system are:

$$\left\{ \begin{array}{l} D_1 \frac{\partial^4 w_1}{\partial x^4} + m_1 \frac{\partial^2 w_1}{\partial t^2} = -k_1(w_1 - w_2) \\ \vdots \\ D_i \frac{\partial^4 w_i}{\partial x^4} + m_i \frac{\partial^2 w_i}{\partial t^2} = k_{i-1}w_{i-1} - (k_{i-1} + k_i)w_i + k_i w_{i+1} \\ \vdots \\ D_n \frac{\partial^4 w_n}{\partial x^4} + m_n \frac{\partial^2 w_n}{\partial t^2} = k_{n-1}(w_{n-1} - w_n) \end{array} \right. \quad (1)$$

By making use of separable solutions, the free vibration problem is reduced to the classical eigenvalue problem in matrix form:

$$[L] \{w\} = \omega^2 [M] \{w\} \quad (2)$$

where  $D_i$  = bending stiffness,  $w_i(x,t)$  = transverse displacement,  $W_i$  = mode shape,  $m_i$  = mass per unit length,  $\omega$  = eigenfrequency and  $[L]$  and  $[M]$  are the differential operators containing the system characteristics in matrix form and the column matrix  $\{w\}$  is

$$\{w\} = \{w_1, w_2, \dots, w_n\}^T$$

The natural frequencies are obtained by making use of "Transfer and Integrating Matrix Method". For fundamental modes to be an orthogonal set,  $[L]$  and  $[M]$  have to be self-adjoint operators. It can be shown that,

$$\left\{ \begin{array}{l} \int_0^L \{w_r\}^T [L] \{w_s\} dx = \int_0^L \{w_s\}^T [L] \{w_r\} dx \\ \int_0^L \{w_r\}^T [M] \{w_s\} dx = \int_0^L \{w_s\}^T [M] \{w_r\} dx \end{array} \right. \quad (3)$$

After considerable manipulations and operations, the "Orthogonality Condition" for the fundamental modes can be obtained for the elastically connected n-layer system:

$$\int_0^L \{w_r\}^T [M] \{w_s\} dx = 0 \quad (4)$$

or

$$\int_0^L \left( \sum_{i=1}^n m_i w_{ir} w_{is} \right) dx = 0 \quad (r \neq s) \quad (5)$$

where "i" stands for i-th layer, "r" and "s" denote the mode numbers for each beamlike strips.

It is interesting to observe here that, in discrete mass-spring systems, the "Orthogonality Condition" is

$$\sum_{i=1}^n m_i A_{ir} A_{is} = 0 \quad (r \neq s) \quad (6)$$

where A's are the amplitudes. It can be concluded from equations (5) and (6) that, in a way, orthogonality conditions for discrete and for continuous systems are analogous. The 3rd and 4th modes are shown in Fig.2.

#### References

- [1] U.Yuceoglu and D.P. Updike, "Stress Analysis of Bonded Plates and Joints", ASCE Jour. of Eng. Mech. Div., Vol.106, No.EM.1, pp. 37-56, 1980.
- [2] U. Yuceoglu, O. Tekinalp and N. Caglayan, "Vibrations of Two-Layer Orthotropic Strips Connected by Mechanical Springs", Recent Developments in Composite Material Structures, An ASME Publication, AMD-113(AD-19), pp. 67-72, Nov. 1990.

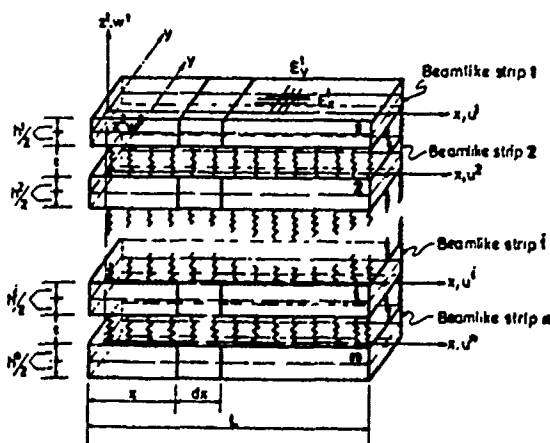


Fig.1. System Configuration.

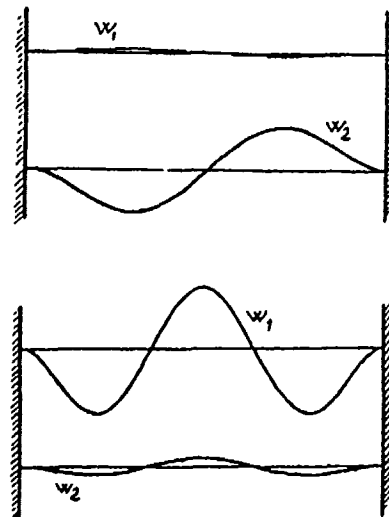


Fig.2. The 3rd and 4th modes.

# BUCKLING LOADS AND DESIGN CONSIDERATION FOR THIN-WALLED BEAM-COLUMNS

Nesrin YARDIMCI  
Department of Civil Engineering  
Istanbul Technical University

## 1- Introduction

For the design of thin-walled beam-columns the interaction of the axial load and the bending moment should be considered. In the present study, the buckling problem of simply supported beam-columns, having wide-flange cross-sections and subjected to equal end moments or uniformly distributed load in addition to the axial load is investigated. Accordingly interaction curves of above mentioned loads are obtained. In the solution of the problem the energy method is used. For the uniformly loaded beam-columns the nonlinear parts of the strain components are considered.

## 2- Solution

In this study, the cross-section of the beam-column is considered to be composed of the elements having all of the plate and membrane displacements. The energy expressions are expressed in terms of these displacement components and the load parameter ( $k$ ) which depends on the external loads. The load parameter ( $k$ ) is composed of two components: one depending on the axial load and the other on the moment which is obtained separately and shown, respectively as ( $k_N$ ) and ( $k_M$ ).

Computing the energy expressions of each element and summing them up, the energy expression for the entire cross-section is determined. Then according to the minimum energy principle, the buckling load is obtained. The buckling load parameter ( $k_{cr}$ ), having the smallest value of ( $k$ ), satisfies the equation (1) at the end of the calculation.

$$\det(\mathbb{S}-Q(k))=0 \quad (1)$$

Here  $\mathbb{S}$  and  $Q(k)$  are stiffness and external load matrices respectively. If beam-column is uniformly loaded, some other terms should be added to the stiffness matrix which depend on the nonlinear parts of the strain components and the uniform load. In this case  $Q(k)$  matrix is a function of the axial load only. ( $k_{cr}$ ) is the critical axial load parameter corresponding to a specific moment value (or vice versa). This parameter gives the local or overall buckling load depending on the dimensions of the cross-section and the magnitudes of the external loads.

### 3- Conclusions

The load parameters  $(k_N)$  and  $(k_M)$  of the I cross-section are investigated as functions of the beam-column's span-to-height ( $a/h$ ) ratios for various thickness-to-height ( $t/h$ ) values. Accordingly using these functions, interaction curves of the load parameters are obtained for the same ( $t/h$ ) ratios. As an example one of these curves is shown in Fig.1.

Considering the yield point of the material and the safety factor, these curves can be used in the design of beam-columns. Comparing the different loaded beam-columns, it can be seen that the equal end moment case can be used instead of the other loading cases by using correction factors for the loads.

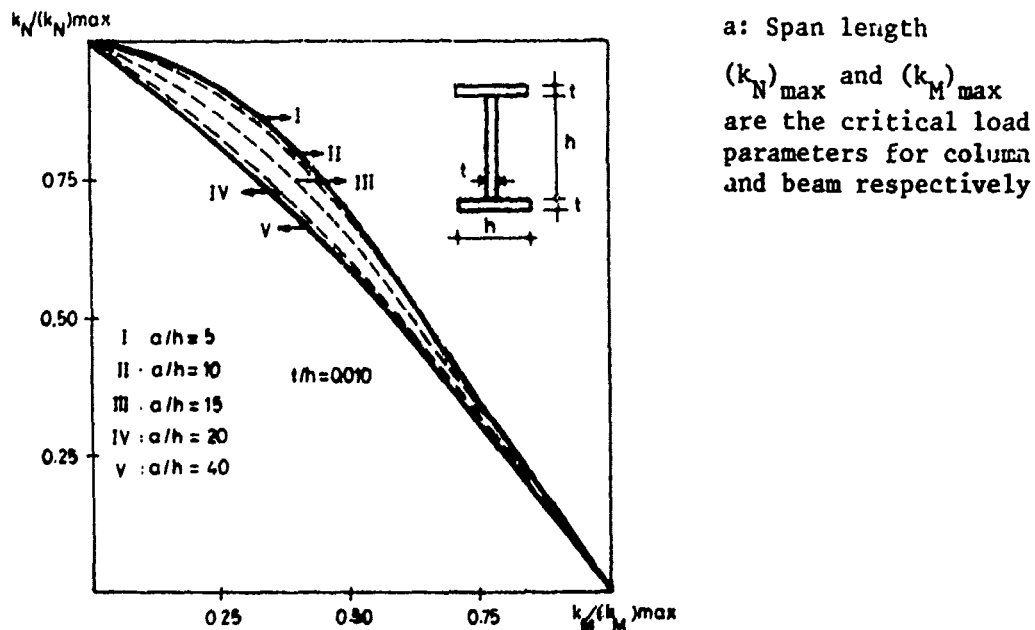


Fig.1- Axial load and bending moment interaction curves

### References:

- [1] YARDIMCI, N.: "Design of Beam-Columns Under the Consideration of Buckling Loads", Journal of the Istanbul Technical University, Vol.48, No.1, 1990, pp.59-68. (in Turkish)
- [2] YARDIMCI, N.: "Buckling of Beam-Columns Subjected to the Axial and Uniformly Distributed Loads", Journal of the Istanbul Technical University, Vol.48, No.2, 1990, pp.1-10. (in Turkish)

# A SEMI-MICROMECHANIC ANALYSIS OF INTERLAMINAR DEFORMATIONS IN SIMPLY-CURVED COMPOSITE BEAMS

D. Joh and K.Y. Byun  
Department of Mechanical and Aerospace Engineering and  
Engineering Mechanics  
University of Missouri-Rolla, Rolla, Missouri 65401-0249

Delamination in laminated composite plates has been recognized as one of the most critical failure mechanisms in advanced composite structures, as composite laminates are not reinforced in the through-the-thickness direction. With a growing employment of curved-plate geometry in composite structures, the study on interlaminar strength and delaminations has received more attention [1]. Due to the limited capabilities of conventional methods of experiments, post-delamination observations have been the main approach for the analysis of these phenomena, whereas the study of deformations prior to delaminations is essential to understanding of the mechanical response of the materials, and eventually, to development of new materials and designs.

A relatively new concept of quantitative nondestructive evaluation is presented. High-sensitivity moiré interferometry is used to measure the highly localized strains varying through the thickness of curved beams at the region of maximum curvature. Whole-field contour maps of deformations were obtained in a semi-micromechanic scale, as shown in Figure 1.

The parametric study shows that the stress is dominated mostly by the geometry of structures rather than the elastic constants of the materials. Deformations of the structures, however, are dominated also by a certain elastic constant as strongly as by the geometry. In particular, the radial deformation is almost inert to the variation of elastic constants other than  $E_3$ .

The experimental results of deformations were compared with those obtained by using the analytical methods. The stress fields determined by the closed-form solution of Lekhnitskii [2] and the NASTRAN finite element code were converted to strain and displacement fields by using the classical lamination theory. The Young's modulus  $E_3$  in the thickness direction was assumed to be equal to  $E_2$ . The hoop strains were the same for all the methods employed. However, the actual radial deformation measured experimentally was significantly larger than those of analytical solutions, as shown in Figure 2. This result indicates that the true value of the Young's modulus  $E_3$  would be smaller than the value assumed in engineering practice. By the parametric study with the elasticity solution and the experimental results, the new value of  $E_3$  was determined. The curves of radial strains imply that the Young's modulus  $E_3$  may vary along the radial axis  $r$ .

## REFERENCES

1. Ko, W.L., "Delamination Stresses in Semicircular Laminated Composite Bars," NASA TM-4026, 1988.
2. Lekhnitskii, S.G., "Theory of Elasticity of an Anisotropic Elastic Body," Mir Publishers, 1981.

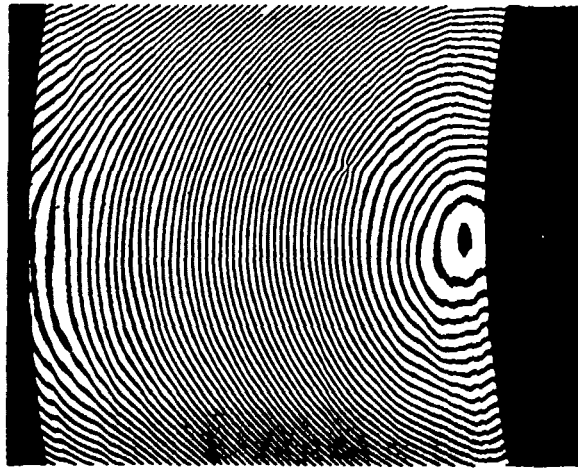


Figure 1. Moire-interferometry fringe pattern of radial displacement field in a semi-circularly unidirectional composite beam.

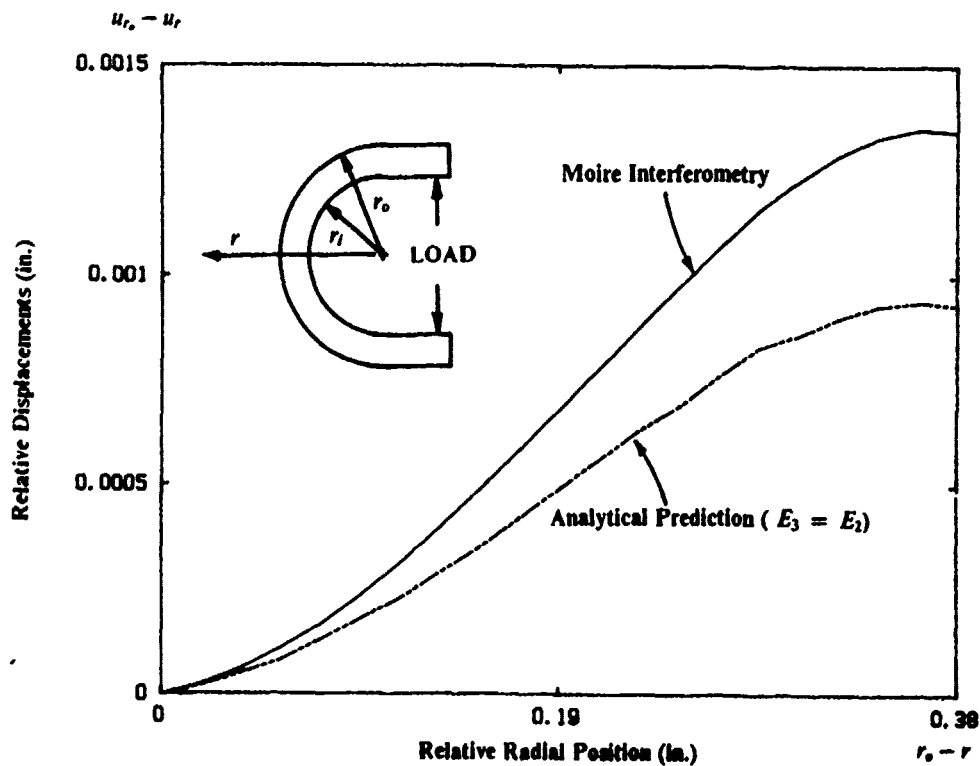


Figure 2. Relative displacements in the radial direction obtained from experiments and the analytical solutions in which  $E_3$  is assumed equal to  $E_2$ .



# INFLUENCE OF RESIN RICH ZONES ON THE ELASTIC RESPONSE OF GRAPHITE/EPOXY COMPOSITE LAMINATES USING MOIRE INTERFEROMETRY.

Dr. R. L. Pendleton  
Professor  
Mech. Engr. Dept.  
S.D. School of Mines  
& Technology  
Rapid City SD 57701

Mr. S. I. Ibekwe  
Graduate Student  
Mech. Engr. Dept.  
School of Mines  
& Technology  
Rapid City, 57701

Mr. F. C. J. Anigbo  
Graduate Student  
Mech. Engr. Dept.  
School of Mines  
& Technology  
Rapid City, 57701

## Introduction.

Graphite/epoxy is finding more and more uses in the aerospace and sporting goods industries because of the attractive mechanical properties. Resin-rich zones are one type of defect that occurs during prepreg preparation and laminate lay up and cure, especially when molded parts have bends and contours, and care is not taken to maintain fiber matrix density there. In literature, several nondestructive testing procedures have been used to identify such flaws [1,2].

Laminates for this work were fabricated by hand lay-up process from Fiberite HYE-2448A1E which is a 948A1 250°F (121.1°C) curing epoxy resin impregnated with 24E Asahi-Nippon graphite fibers. During the lay up process, a group of fibers (1/8 in. or 3.175mm width of prepreg) were pulled out before the layer of prepreg was laid down and the backing material removed as shown in Figure 1. The void created was filled with the epoxy resin during the curing process. This defect was created in different layers for the two types of laminates -  $[0]_8$  and  $[0/+45/-45/90]_5$  constructed. Six different  $[0]_8$  and five different  $[0/+45/-45/90]_5$  specimen coupons each measuring 10 in. (25.4 cm.) long and 1 in. (25.4 mm.) wide were tested.

Optical moire interferometry utilizes diffraction and interference of light principles to measure in plane displacements on specimen surfaces. It is a whole field method that is adaptable to isotropic, anisotropic, elastic or plastic materials because of its geometric nature. The set up used here is the four-beam optical system as shown in Figure 2. Using carrier fringes to enhance the load induced fringes, specimens were tested under a uniaxial tensile load of 200 lbs (889.6 N.). A collimated beam from He-Ne laser interrogated the specimen grating having a frequency of 30, 690 l/in (1200 l/mm.). A contour map of displacement resulted giving displacements as :

$$U = (1/f) N_x ; \text{ and } V = (1/f) N_y .$$

From small deformation relationship for strain,

$$\epsilon_x = \delta U / \delta x = (1/f) \delta N_x / \delta x , \quad \epsilon_y = \delta V / \delta y = (1/f) \delta N_y / \delta y$$

Where U = displacement component in the x-direction

V = displacement component in the y-direction

$N_x, N_y$  = fringe orders in x & y displacement fields resp.

$\epsilon_x, \epsilon_y$  are normal strains in x & y resp.

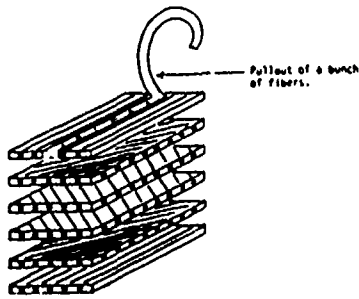


Figure 1. Laminate showing fiber pullout and resin rich zone.

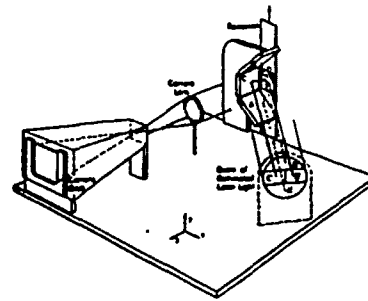


Figure 2. Four beam optical system [3].

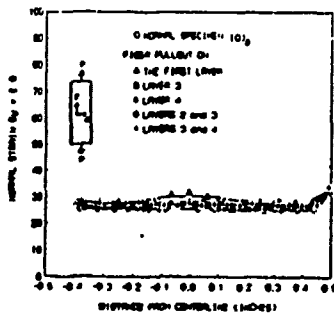


Figure 3. Normal strain  $\epsilon_y$  across  $[0]_8$  laminate.

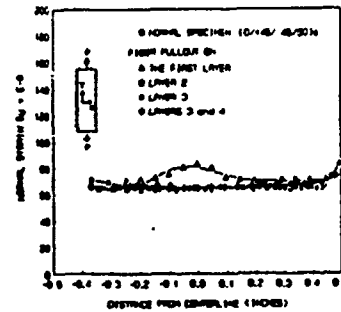


Figure 4. Normal strain  $\epsilon_y$  across  $[0/+45/-45/90]_S$  laminate.

## Results.

At a mean fracture stress of 197.2 ksi (1.36 Mpa), the fracture stress of  $[0]_8$  laminate decreased by 6.1% compared to normal unflawed specimens. The location of the flaw did not further influence the behavior. For  $[0/+45/-45/90]_S$  laminate with resin rich zone on the 1st layer ( $0^\circ$  layer) the decrease of fracture stress was 9.5%. The defect on the other layers  $\pm 45^\circ$  and  $90^\circ$  did not affect fracture stress. Normal strain,  $\epsilon_y$  increased by about 20% in the resin rich zone of  $[0]_8$  laminate with defect on 1st layer and dropped back to the nominal strain as shown in Figure 3. Specimen with defect on 3rd layer showed about 4% increase in  $\epsilon_y$  over the flaw zone. Moiré method measured only the in-plane deformations on the surface. So only perturbations as a result of this that gets to the surface was measured.  $\epsilon_y$  for  $[0/+45/-45/90]_S$  specimen with defect on  $0^\circ$  layer increased by 29% over the flaw region as shown in Figure 4. Since this layer is in the load direction, any defect affects the elastic response more than those of other layers. Similar response were recorded for transverse strain  $\epsilon_x$  for  $[0]_8$  and  $[0/+45/-45/90]_S$  laminates.

## References.

1. Rose, J.L. and Shelton, W., "Damage Analysis in Composite Materials," *Composite Reliability*, ASTM STP 580, American Society for Testing and Materials, 1975, pp. 215-226.
2. Owston, C.N., *British Journal of Nondestructive testing*, January 1973, pp. 2-11.
3. Post, Daniel, "Moiré Interferometry for Composite", *Manual on Experimental Methods for Mechanical Testing of Composites*, R.L. Pendleton, and M.E. Tuttle, Eds., Society of Experimental Mechanics, Inc. Bethel, Connecticut, 1989, Section IV A-2, pp. 67-80.

## DAMAGE MICROMECHANICS STUDY OF A TOUGHENED EPOXY

G.K.Hu D.Baptiste D.François  
Laboratoire MSS-MAT URA 850 CNRS  
Ecole Centrale Paris  
Grande voie des vignes  
92295 Châtenay Malabry Cedex (France)

### *Abstract*

Crazes initiation and propagation in adhesives and polymers play an important role for toughness gain of these materials. Rubber is usually used for this purpose. We have studied one adhesive (epoxy) toughened by rubbery particles. The toughening mechanism is experimentally examined by simple tension test inside a SEM, and craze initiation and evolution are then modelled by micromechanical method.

The in-situ tensile test made inside a SEM, shows the damage mechanisms of our adhesive consist of the following steps:

- (1) crazes initiation at the pole of rubbery particles perpendicular to the tension direction(Fig.1).
- (2) crazes evolution(Fig.2)
- (3) macrocrack formation by crazes coalescences.

Tanaka-Mori micromechanical model is used to calculate the stresses field around a rubbery particle. A local criterion based on the observations, is proposed as the craze initiates when the normal interfacial stress between the matrix and the rubbery particle reaches a critical value. As a result, at a macroscopical level, the craze initiation not only depends on the mean stress but also on the principal stress.

Crazes evolution is modelled in absence of the rubbery particles in the case of simple tension. The crazes are considered as penny-shape inclusions which have a viscoelastic behavior. The crazes density evolution is assumed to follow a power law of the stress and the time. The iteration method is used by discretization of the time. In each incremental step, the relaxation modulus of the crazes and their density are calculated. With the Tanaka-Mori model, the relation between the stress increments and the strain increments can be obtained(Fig.3). In the end, the total stress and strain curve can be derived(Fig.4). The macroscopical behavior is then related to the microstructural parameters.

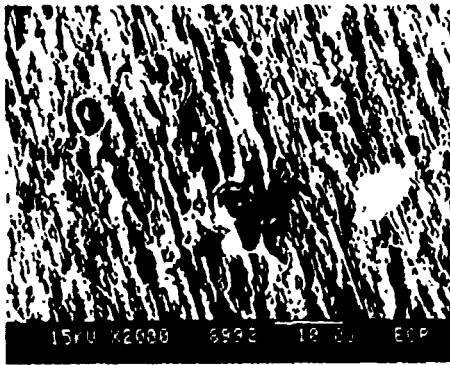


Fig.1 Craze initiation



Fig.2 Craze evolution

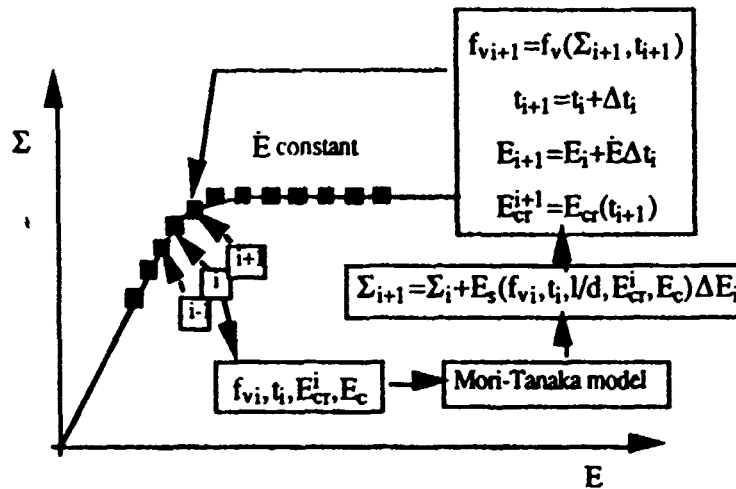
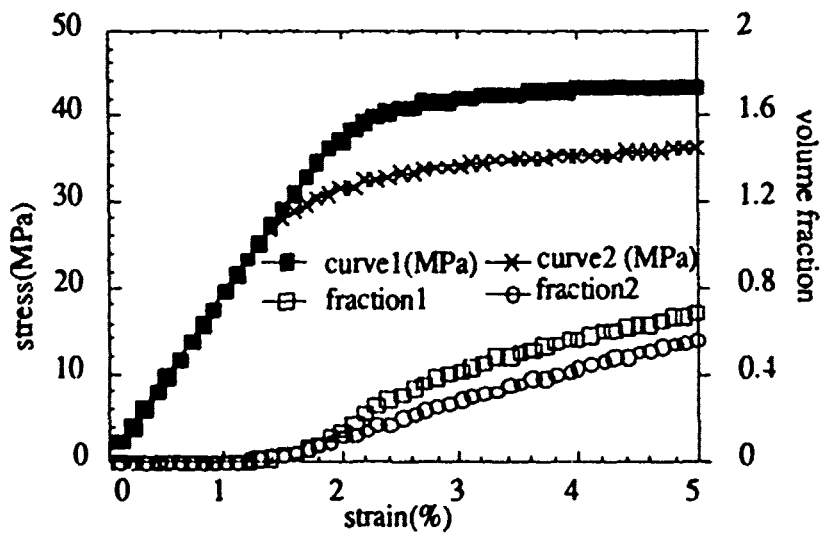


Fig.3 Schematic of the method



curve1: tension rate  $10^{-3}/s$  curve2: tension rate  $10^{-4}/s$

Fig.4 Modelization results

CONTACT OF COMPOSITE LAMINATES BY  
CYLINDRICAL INDENTORS

Enboa Wu<sup>1</sup>, Jey-Chung Chao<sup>2</sup> and Ching-Shih Yen<sup>2</sup>  
Institute of Applied Mechanics  
National Taiwan University  
Taipei, Taiwan 10764 ROC

An analytical method is developed within the scope of linear anisotropic elasticity to investigate the contact behavior between a laminated composite plate and a rigid cylindrical indenter. The indenter is of infinite long, thus a plane strain condition is assumed. In the analysis, we first adopted the exact solution of Pagano (1969) for a lateral loading of arbitrary type applied normally to composite laminates with simple supports, and use an approximate Green's function to find the displacement field at arbitrary point of the plate. This Green's function is then used to simulate the contact loading. Thus, we can find the pressure distribution as well as the contact length.

Although this method can be applied to the investigation of contact behavior between a laminated plate and indentors of arbitrary shapes, we are now focused on that between a laminate plate and a cylindrical indenter. Parameters studied are for the effect of span, stacking sequence of the laminates and the size of the indentors. A series of results are obtained included force-indentation and force-deflection relationships, pressure distribution underneath the indenter and the contact length, as well as the stress distribution near the contact zone in the laminate plate. Further, the effect due to off-center of the location of the indenter is also investigated. It is found that, due to existence of a very tiny off-center distance of the indenter, the force-indentation relation deviates significantly from that contact right at the center position. In addition, the pressure distribution underneath the indenter also becomes asymmetric, which looks differently from the Hertzian distribution.

---

<sup>1</sup> associate professor

<sup>2</sup> graduate students

# TRANSIENT DYNAMIC RESPONSE OF FIBER-REINFORCED COMPOSITE BEAM

\*

GADELRAH RAAFAT

Mechanical Engineering Dept. Technical University  
of Budapest, 1111. Budapest, XI., Muegyetem rkp.5

In this research work, transient dynamic response of simply supported composite beams is investigated. Finite element formulation is used to construct mass and stiffness matrices. Damping process is considered on the basis of Rayleigh damping. Newmark  $\beta$ - method is used to the direct time integration of discretized equation of motion . A finite element program is established in IBM compatible computers for solving beam and planar frame composite structures under different loads in time ( unit step, sine, cosine, and ramp type excitation ). Analytical solutions of the considered problems are also developed and they are compared with the finite element results. A graphical program is established to show the dynamic displacements, dynamic forces and moments respectively at any given time step or degrees of freedom. The numerical results show very good agreement with the analytical ones.

---

\* ( On leave from Department of Mechanical Engineering,  
University of Helwan, Cairo, Egypt.)

## REFEERENCES

- 1- R.S.Dunham, " Integration operators for transient structural response ", Comp. & Structures, Vol.2, pp. 1-15. 1972.
- 2- V.H.Neubert and V.P.Rangaiah, " The prediction of transient response of beams by transform techniques.", J. Sound & Vib.53 (2), pp. 173-181, 1977.
- 3- T.J.R.Hughes and W.K.Liu, " Implicit - Explicit finite elements in transient analysis: Implementation and numerical examples ", J. of Applied Mechanics, Vol.45, pp. 375, 1978.
- 4 Jon Braekhus and Janole Aasen, " Experiments with direct integration algorithms for ordinary differential equations in structural dynamics ", Comp. & Structures, Vol.13.. pp. 91-96, 1981.
- 5- W.L.Wood, " A further look at Newmark, Houbolt, etc., time - stepping formulae." Int. J. Numerical method in Engineering , Vol.20 , pp. 1009-1017, 1984.
- 6- FrankL. Stasa, " Applied finite elements for engineering " CBS Publishing , 1985.
- 7- O.C.Zienkiewicz and S.Nakazawa, " Dynamic transient analysis by a mixed iterative method ." Int. J. for Numerical method in engineering, Vol.23, pp. 1343-1353, 1986.
- 8- Z.Loizina, " A comparison of harmonic acceleration method with the other commonly used methods for calculation of dynamic transient response " , Comp. & Structures , Vol.29, No.2, pp. 227-240, 1988.

# INTERLAMINAR STRESS ESTIMATION IN LAMINATES THROUGH FINITE ELEMENTS

A.V.KRISHNA MURTY, K.VIJAYAKUMAR, R.GOVINDARAJAN, P.V.RAGHURAM  
Department of Aerospace Engineering  
Indian Institute of Science  
Bangalore 560 012, India.

Laminated fibre reinforced plastics are finding extensive application in several engineering areas. In view of the low strength of interlaminar zone in a laminate, the interlaminar stresses play a key role in the design of laminated components. It is well known that these stresses are the primary cause of damages such as delaminations. Also certain defects such as small voids and/or micro cracks are unavoidable at manufacturing stage itself and they may grow during service and affect the performance of structural elements. Thus, the estimation of interlaminar stresses becomes an essential requirement to design laminates.

The complex nature of the stress field in laminates defies possibilities of simple engineering design methodologies. While the 3D approach is desirable, it is often impractical due to limitations from computer costs. On the other hand, simpler approaches based on first order theories are attractive for computational work. It should be noted that they may not be adequate in critical local regions where the solution needs to be reworked in greater detail. However the solutions based on simpler elements are useful in providing some idea of the critical regions and directing the solution approach to evaluate damage tolerance.

Recognizing that currently there are several elements for the analysis of laminates in the literature, as also in standard softwares, it is desirable to examine the performance of some of these elements for estimating interlaminar stresses. Broadly, there are two approaches. The first one consisting of devising an independent numerical scheme based on the data of inplane stresses from a conventional element. In the second approach, the interlaminar stresses are obtained by integration of the local equilibrium equations. The second approach could be more consistent, because it allows the use of analytical derivatives to the required level. The scheme could be implemented only on high precision elements, whose shape functions admit derivatives to the required order. The high precision element developed by Bose & Kirkhope [1] is one such element. In this paper, we present an adaptation of this element for estimation of interlaminar stresses.

Some typical results are presented here illustrating the capability of this element. A 3 layered ([0/90/0]) cross ply square plate under a sinusoidal transverse load is considered. Thickness wise distributions of interlaminar stresses obtained by the FEM are plotted and compared



with the exact CPT solutions. While the distributions of interlaminar shear stresses obtained show a remarkable accuracy, the interlaminar normal stress variation is not quite as expected. The error is largely due to discretization. While the local equilibrium equations are satisfied through integration, the laminate equilibrium equations are only satisfied approximately through finite elements. The unusual normal stress variation is however corrected with reference to the known surface values (thus ensuring the satisfaction of laminate equilibrium equations) along with linear interpolation at ply level. The modified distribution is found to be quite accurate. The thickness wise distributions of the interlaminar stresses are shown in figures 1, 2 & 3.

#### REFERENCES :

1. C.Jeyachandrabose & J.Kirkhope, "A High Precision Triangular Laminated Anisotropic Shallow Thin Shell Element", Computers & Structures, Vol.21, No.4, p.701-723, 1985
2. N.J.Pagano, "Exact solutions for rectangular bidirectional composites and sandwich plates", J. of Composite Materials, Vol.24, Jan'1970, p.20
3. N.J.Pagano & S.J.Hatfield, "Elastic behavior of Multi-layered Bi-directional Composites", AIAA Journal, Vol.10, No.7, 1972, p.931-933

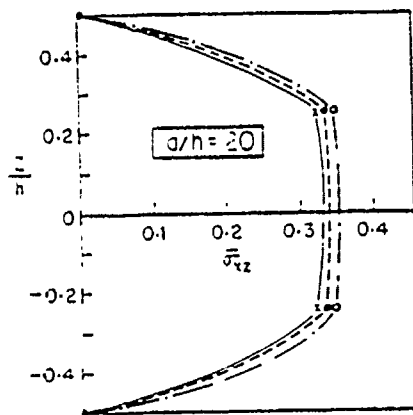


Fig. 1. Variation of  $\bar{\sigma}_{xz}$  through the thickness

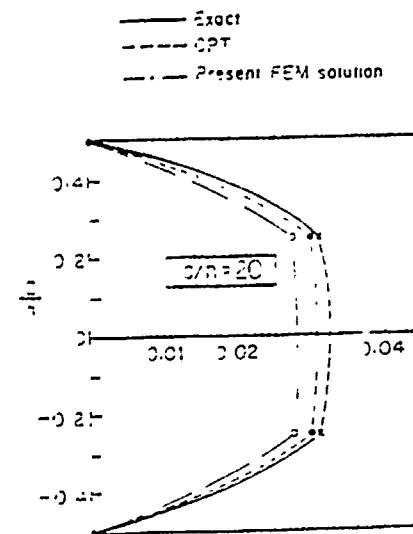


Fig. 2. Variation of  $\bar{\sigma}_{yz}$  through the thickness

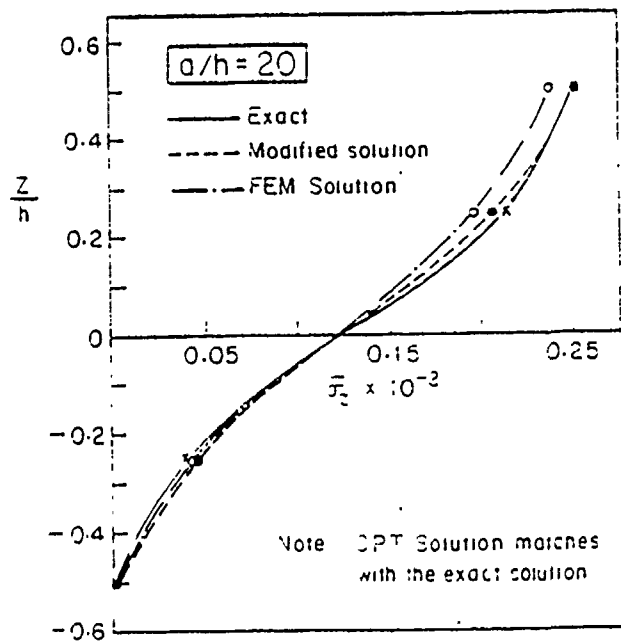


Fig. 3. Variation of  $\bar{\sigma}_z$  through the thickness

# NATURAL VIBRATIONS and the ORTHOGONALITY CONDITION in ROTATING COMPOSITE MULTI-LAYER BEAMS and BLADES

U. Yuceoglu, O. Tekinalp and A. K. Yavuz  
Department of Aeronautical Engineering  
Middle East Technical University, Ankara, Turkey

Composite multi-layer beams joined by interlaminae adhesive layers are increasingly used in aerospace and flight vehicle structures and mechanical components. Some of these applications in which the multi-layer beam rotates are propeller and helicopter blades, robot arms, satellite armlike components [ 1, 2, 3 ].

The dynamic, coupled "Governing Differential Equations" of elastically connected n-layer "Timoshenko Shear Beams" are reduce to the following form (see Fig. 1) :

$$\left\{ \begin{array}{l} -J_i \frac{\partial^2 \psi_i}{\partial t^2} + E_i I_i \frac{\partial^2 \psi_i}{\partial x^2} + k_i A_i G_i \left( \frac{\partial w_i}{\partial x} - \psi_i \right) = 0 \\ -m_i \frac{\partial^2 w_i}{\partial t^2} - k_{s_i} (w_i - w_{i+1}) - k_{s_{i-1}} (w_i - w_{i-1}) \quad (i = 1, 2, \dots, n) \quad (1) \\ + k_i A_i G_i \left( \frac{\partial w_i}{\partial x^2} - \frac{\partial \psi_i}{\partial x} \right) + \frac{1}{2} m_i \Omega^2 \frac{\partial}{\partial x} \left[ (L^2 - x^2) \frac{\partial w_i}{\partial x} \right] = 0 \end{array} \right.$$

where  $EI$  = bending stiffness,  $w$  = transverse displacements,  $\psi$  = angle of rotation,  $m$  = mass per unit length,  $J$  = rotary moment of inertia,  $kAG$  = Timoshenko shear stiffness,  $k_s$  = mechanical spring constant,  $\Omega$  = angular velocity.

By making use of seperable solutions and eliminating the time variable and after some manipulations the free vibration problem of the rotating composite n-layer beam or blade is reduced to the classical eigenvalue problem,

$$[\mathcal{L}] \{\phi\} = \omega^2 [\mathcal{M}] \{\phi\} \quad (2)$$

where  $\omega$  is the eigenfrequency and  $\{\phi\}$  is a coloumn matrix of dependent variables and the operator  $[\mathcal{M}]$ ,

$$\{\phi\} = \{\psi_1, w_1 | \psi_2, w_2 | \dots | \psi_n, w_n\} \quad (3)$$

$$[\mathcal{M}] = \text{diag} \{ J_1, m_1 | J_2, m_2 | \dots | J_n, m_n \} \quad (4)$$

and the operator  $[\mathcal{L}]$  is a square matrix which includes differential operators, geometric and material constants.

The natural frequencies are obtained by making use of "Integrating Matrix Method" [ 2 ] for n-layer rotating beams or blades. Then, fundamental mode shapes and mode interactions of the coupled system are found. Furthermore, it can be shown that operators  $[\mathcal{L}]$  and  $[\mathcal{M}]$  are

self-adjoint operators such that,

$$\int_0^L \{\phi_r\}^T [\mathcal{L}] \{\phi_s\} dx = \int_0^L \{\phi_s\}^T [\mathcal{L}] \{\phi_r\} dx \quad (5)$$

$$\int_0^L \{\phi_r\}^T [\mathcal{M}] \{\phi_s\} dx = \int_0^L \{\phi_s\}^T [\mathcal{M}] \{\phi_r\} dx \quad (6)$$

By employing the aboveproperty of operators the "Orthogonality Condition" of fundamental modes become :

$$\int_0^L \{\phi_r\}^T [\mathcal{M}] \{\phi_s\} dx = 0 \quad (r \neq s) \quad (7)$$

or,

$$\int_0^L \sum_{i=1}^n (J_i \psi_{ir} \psi_{is} + m_i w_{ir} w_{is}) dx = 0 \quad (r \neq s) \quad (8)$$

This condition differs from that of Euler-Bernoulli multi-layer beam in which  $J_i$  terms don't appear. Fig. 2 shows 4th and 5th mode shapes.

### References

- [1] U.Yuceoglu and D.P. Updike, "Stress Analysis of Bonded Plates and Joints", ASCE Jour. of Eng. Mech. Div., Vol.106, No.EM.1, pp. 37-56, 1980.
- [2] W. F. Hunter, " Integrating Matrix Method for Determining Natural Vibration Characteristics of Propeller Blades", NASA Tech. Note NASA TN D-6064, Dec. 1970.
- [3] J. L. Lipeless, " Vibrations of a Rotating Beam", Jour. of Amer. Helicopter Soc. Vol. II, No. 4, pp. 17-24, 1966.

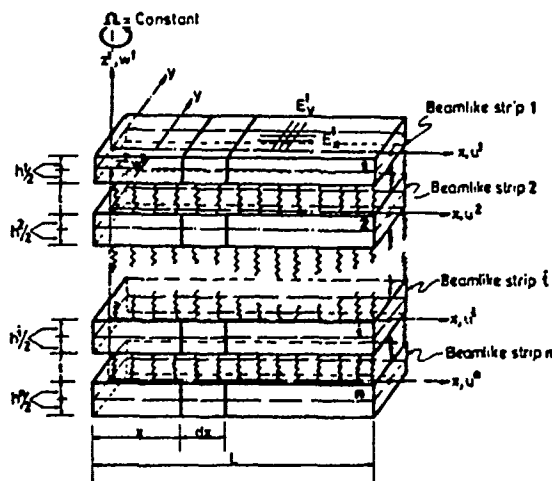


Fig. 1. System Configuration.

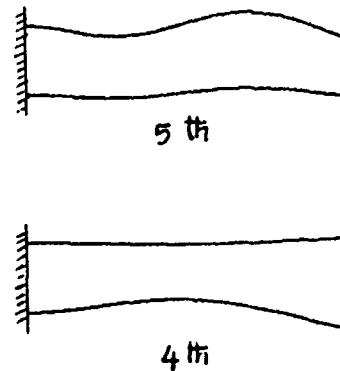


Fig. 2. 4th and 5th mode shapes.

# THE EFFECT OF GEOMETRIC SIZES OF ANISOTROPIC COMPOSITE UNSYMMETRIC CROSS-PLY LAMINATED PLATE ON ITS NONLINEAR FLEXURAL FORCED VIBRATION

Li Hua, Yuan Dongping

Department of Engineering Mechanics  
Wuhan University of Technology  
Wuhan, Hubei, 430070  
P.R.of China

The basic problem of the nonlinear flexural forced vibration(NFFV) of the anisotropic composite unsymmetric cross-ply laminated plate(ACUCPLP) that this paper studies consists of the nondimensional general governing eqns of the NFFV of the ACUCPLP under the harmonic force of uniform distribution and S4, one of the boundary conditions of the four edges simply supported(Ref.3). The ACUCPLP we consider here is a rectangular elastic thin plate with the same thickness all over. The plate satisfies Kirchhoff's hypothesis.

Take nondimensional trial functions(Ref.3) for the above-mentioned problem as follows:

$$\begin{cases} W(\zeta, \eta, \tau) = \sum_m \sum_n W_{mn}(\tau) \sin m\pi\zeta \sin n\pi\eta \\ F(\zeta, \eta, \tau) = \sum_p \sum_q F_{pq}(\tau) (\operatorname{ch} \alpha_p \zeta - \cos \alpha_p \zeta - \nu_p (\operatorname{sh} \alpha_p \zeta - \sin \alpha_p \zeta)) \times \\ \quad \times (\operatorname{ch} \alpha_q \eta - \cos \alpha_q \eta - \nu_q (\operatorname{sh} \alpha_q \eta - \sin \alpha_q \eta)) \end{cases}$$

Based on Galerkin's method and the software we have and used, we analyze separately the NFFV of the ACUCPLP composed of glass-epoxy composite material( $E_1/E_2=3$ ,  $G_{12}/E_2=0.6$ ,  $\nu_{12}=0.25$ ), boron-epoxy composite material ( $E_1/E_2=10$ ,  $G_{12}/E_2=1/3$ ,  $\nu_{12}=0.22$ ) and graph'-e-epoxy composite material ( $E_1/E_2=40$ ,  $G_{12}/E_2=0.5$ ,  $\nu_{12}=0.25$ ) under the nondimensional loads of magnitude  $Q_0=q_0 b^4/(A_{22} h^3)=10$  and when  $\lambda=a/b$ , the aspect ratio of rectangular laminated plate is separately  $\lambda=1.0$ ,  $1.5$  and  $2.0$ . In the calculation, the ply-lamina number of all the laminated plates is two. After the calculation by means of our programme, we get the illustrative amplitude-frequency relationship(AFR) under various conditions, as shown in Fig.1, Fig.2 and Fig.3. By these figures and calculations, we can discuss as follow:

In Ref.2, based on the discussion, we know that the conspicuous effect of the change of the ply-direction angle of laminated plate upon the AFR appears only when the laminated plate is in a low-frequency vibration. Here, in the three figures, we can see that the conspicuous effect of the change of the aspect ratio of rectangular laminated plate upon the AFR always appears no matter what vibration state it is in. Meanwhile, we can also see that the effect of the aspect ratio of laminated plate in a low-frequency vibration on the AFR is stronger than that in a fairly-high-frequency vibration and that the effect of the aspect ratio

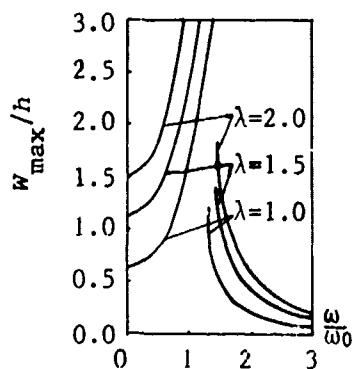


Fig. 1 The NFFV of the ACUCPLP composed of glass-epoxy composite material.

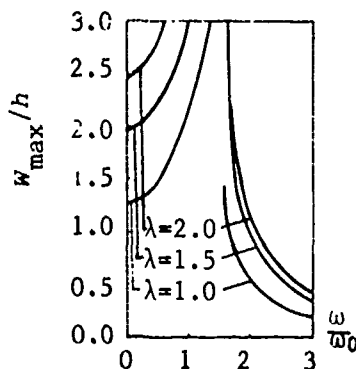


Fig. 2 The NFFV of the ACUCPLP composed of boron-epoxy composite material.

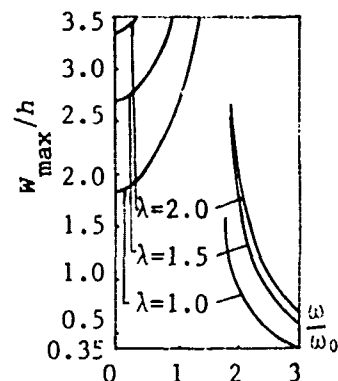


Fig. 3 The NFFV of the ACUCPLP composed of graphite-epoxy composite material.

of the high-modulus laminated plate on the AFR is stronger than that of the low-modulus laminated plate. So, the aspect ratio of rectangular laminated plate is an important factor affecting the AFR. Comparing results in Ref.1, Ref.2 and that of this paper, we conclude that: when considering the effects of the ply-lamina number, the ply-direction angle and the aspect ratio etc. of laminated plate on the AFR of the NFFV of laminated plate, the aspect ratio is comparatively a more important factor which, in consideration, must be given first place.

By comparing the three figures, we know that, for the same boundary conditions and the same amplitudes,  $\omega/\omega_0$ , the ratio of the nonlinear frequency to the linear natural frequency of high-modulus laminated plates is smaller than that of the low-modulus laminated plates. However, for the same amplitudes, the nonlinear frequency of high-modulus laminated plates is higher than that of the low-modulus laminated plates because of different linear natural frequency as a result of the use of laminated plates made of different composite material.

#### REFERENCES

1. Li Hua and Shen Darong, Analysis of Nonlinear Forced Vibration of Anisotropic Composite Unsymmetrically Laminated Plates, COMPOSITE STRUCTURES 5 (Proceedings of 5th International Conference), ELSEVIER SCIENCE PUBLISHERS LTD (1989).
2. Li Hua, Nonlinear Forced Flexural Vibration of Anisotropic Composite Material Symmetrically Laminated Plates, Proceedings of 6th International Conference on Mechanical Behaviour of Materials (ICM-6, 29 July-2 August, 1991, Kyoto Japan), PERGAMON PRESS (1991).
3. Chia Chuen-Yuan, Nonlinear Analysis of Plates, McGraw-Hill (1980).
4. Robert M. Jones, Mechanics of Composite Materials, McGraw-Hill (1975).

# **Knowledge Based Design of Rigging Systems for Light Alloy Sand Castings**

**James L. Hill, Professor and Head,  
Department of Engineering Mechanics  
University of Alabama  
Tuscaloosa, Alabama 35487**

## **ABSTRACT**

The quality of cast metal parts is very dependent upon the design of the rigging system (down sprue, runners, gates, and risers). Historically, methods engineers have designed rigging systems based upon some fundamental concepts of fluid flow and heat transfer tempered with extensive foundry experience. The dependence of the design process upon the accumulation of design experience makes this activity a prime candidate for a knowledge based or expert system. Some advantages of a knowledge based design system for the design of rigging systems include:

1. Knowledge of foundry methods engineers will be recorded and saved so that the knowledge becomes a growing asset of the foundry.
2. Young engineers could use such a system to make expert design decisions for riggings of new castings.
3. The design system would cut costs and development time by reducing the number of trial and error cycles to produce a successful rigging.
4. An expert design system would produce a preliminary design of the rigging of the casting to be used in a numerical simulation model.

A prototype knowledge based system for the design of rigging systems for light alloy castings has been developed. Preliminary knowledge acquisition involved reviewing the literature on rigging, interviewing expert methods engineers and studying actual tooling. The computer software system is called RDEX for Rigging Design Expert. This work has been supported by the US NSF funded CADCAST Project.

AN INTEGRATED ENVIRONMENT FOR FEATURE-BASED  
DESIGN AND PROCESS PLANNING FOR TURNED COMPONENTS.

Seshumohan Sayani  
Juan Lazcano  
Prakash Krishnaswami  
Rodney Howell  
Kansas State University  
Manhattan, KS 66506

The tasks of engineering design and process planning were traditionally done independently by different groups of engineers. The undesirability of this distributed approach is now well known and in recent years much attention has been given to the problem of integrating design and process planning. This paper describes one such effort to tighten the link between design and manufacturing for the specific domain of turned components. The underlying idea behind this work is to provide a single computer environment within which both design and process planning can be done in an interactive or semi-automated manner. An integrated environment of this kind streamlines the transfer of information from the design stage to the manufacturing stage and eliminates the need for data translation which could result in errors or information loss. Such an environment also allows the process planner to make minor changes to the design in order to improve manufacturability. Furthermore, if the user of the environment is suitably qualified, he or she may simultaneously design the component and the process plans for its manufacture. This makes it possible for the user to take manufacturing considerations into account during the design process and vice-versa.

The environment is based upon a feature-based representation for the turned components and a directed acyclic graph (DAG) representation for the process plan. In other words, the component is described in terms of features whereas the process plan is described by a DAG. The features that are currently implemented include STEP, TAPER, THREAD, CHAMFER, GROOVE, etc. Using these features and the editing facilities provided by the environment, the user may define and modify designs very easily. Additional feature classes can be added to the system as needed.

In the DAG representation of the process plan, each node represents an initial, final or intermediate geometry of the component during the manufacturing process. An edge from one node to another indicates that there is manufacturing step whereby the

geometry at the tail node of the edge can be converted to the geometry corresponding to the node at the tip.

The DAG representation offers several advantages. First of all, it gives a formal mathematical structure to a process plan that can be used as a basis for further studies and development. Secondly, interactive process planning can be handled conveniently through standard graph traversal and graph modification algorithms. Most significantly, the DAG representation allows us to convert process planning problems into graph problems for which solutions are often readily available. For example, the problem of finding all the finished products that can be made from a given blank is equivalent to finding the transitive closure of a suitable subgraph of the process plan network. This is a well-known problem in graph theory for which efficient algorithms already exist. Other examples of process planning problems that can be solved by conversion to equivalent graph problems are the following:

- a) Find all blanks from which a specified final product can be made.
- b) From an intermediate node, if the order for the current final product is canceled, what other final products can be made?
- c) What is the most 'flexible' path to a final product?
- d) What is the smallest set of blanks from which all the final products can be made?

There are many other such questions that can be answered automatically by using suitable graph algorithms. Another advantage is that most graph algorithms lend themselves to formal proofs of correctness as well as complexity analysis. Thus, an implementation based on DAG's can be expected to leave a high degree of robustness and efficiency.

The geometry of each component created using the feature-based modeler is stored as a linked list of features. It is also possible to define a linked list of such components. When the DAG for the process plan is created, each node is assigned a pointer to the component geometry corresponding to that node. This permits the process planner to access the geometry at any node in the network. This access makes it possible to display, query or modify the geometry during the process planning step.

The integrated environment described here is only a starting point. It can be enhanced in many ways, such as extension to larger classes of components. It is also desirable to build some expert system capability into the system to raise the level of automation in process planning. The current environment provides a good platform on which further developments along these lines can be based.



## State of the Art in Tool Monitoring

Saeid Motavalli, Behnam Bahr  
Wichita State University  
Wichita KS 67208

### ABSTRACT

This paper describes the state of the art techniques used in tool monitoring. Both direct and indirect techniques have been discussed. Included are tool monitoring using; cutting force, power, vibration, acoustic emission, cutting temperature, electrical resistance, workpiece dimensions, and monitoring the tool using vision system. Research based and commercial systems are described.

### INTRODUCTION

Advances in automated manufacturing has created the need for unmanned machining of the manufacturing parts. The unmanned machining requires sensory feedback and automatic control of machining conditions and parameters. An important parameter in the machining operation is the condition of the machine tool. In the traditional manufacturing environment, the condition of the tool is monitored by an skilled operator who uses experience and frequent visual inspection of the tool surface to assess the usability of the tool. In automated manufacturing, manual tool monitoring is not acceptable; it is time consuming and sometimes erroneous. These errors can cause considerable damage to the workpiece and machine tool. Tool monitoring techniques can be divided into two main categories; Indirect and Direct.

#### Indirect Methods for Tool Monitoring

Thrust Force, Torque and Power. The cutting force changes as the machine tool wears out, thus by monitoring the amount of force requirements the condition of the tool can be predicted. Tool monitoring systems based on force measurement often use one of the force components such as the thrust force or the cutting torque [1].

Vibration. Machining with a worn tool increases the fluctuation of forces acting on the tool because of local welding of the tool and the workpiece and also as a result of internal fractures of the tool. The force fluctuations, increases the vibration level in the system. Therefore by monitoring the level of vibration using accelerometers, the drill condition can be assessed [2].

Temperature. As the cutting tool wears, the temperature developed at the cutting edge increases due to increased forces caused by local welding. Therefore tool wear can be detected by monitoring the cutting edge temperature. Rapid increase in temperature would indicate tool wear [3].

## Direct Methods of Tool Monitoring

Radioactive Emission Measurement. Tools can be made radioactive by radiation in atomic reactors. Worn tool material are transferred into the chip while drilling. By monitoring the amount of radioactive material deposited into the chips, the wear in tool can be assessed [3].

Measuring Electrical Resistance. As a cutting tool wears, the area of contact with the workpiece increases. Therefore if an electrical current flows through the junction of the tool and the workpiece, the resistance to the electric flow increases. This effect can be utilized to measure tool wear. In practice the resistance of the material also changes with temperature, cutting force changes, and also by the natural "emf" produced as the result of the operation [3].

Measuring WorkPiece Dimensions. It is observed that as the tool wears, the size of the finished workpiece changes. Therefore by monitoring the workpiece dimensions, condition of the tool can be assessed [4]. The dimensional measurements can be done by a CMM machine, or the use of a vision system. This procedure can not be used as an on-line method of tool monitoring, because hole sizes are monitored between operations.

Tool Monitoring Using Vision System. As tool wears out, the cutting surface of the tool is deformed. Therefore by analyzing the image of a drill head, it's condition can be assessed [5].

## CONCLUSION

Automatic tool monitoring is an essential element of unattended machining. As explained there are several different methods for tool monitoring most of which have given promising results under laboratory conditions. The techniques that have had commercial success are based on measuring cutting force, power, or acoustic emission.

## REFERENCES

1. Subramanian, K., Cook, N.H., "Sensing of Drill Wear and prediction of Drill Life", J. Eng. Ind. Trans. ASME 103, 1977, pp. 295-301.
2. Kanai M., Kanda Y., "Statistical Characteristics of Drill Wear and Drill Life for the Standardized Performance Tests", Annual CIRP 27, 1978, pp. 61-66.
3. Jetly, S. "Measuring Cutting Tool Wear On-line: Some Practical Considerations", Manufacturing engineering, Vol. 93, July 1984.
4. Yee K. W., Blomquist, D. S., "An On-Line Method for Determining Tool wear by Time-Domain Analysis", SME Paper No. MR 82-901, 1982.
5. Motavalli S. and B. Bahr, "Tool Monitoring by Machine Vision", Proceedings of the Kansas Conference on Excellence in Manufacturing, pp 5A-1 - 5A-7, 1991.

# Heat Source Identifications in Two-Dimensional Steady Heat Conductions

Katsuhiko Hojo, Hiroshi Masuda and Futoshi Shirai

Department of Mechanical Engineering  
Osaka Institute of Technology  
Omiya, Asahi-ku, Osaka, 535, Japan

Electronic instruments with integrated circuits often generate heat in the inside. Such a evolution of heat is observed frequently in the other instruments at work. And, thermal stresses due to heat generation have direct effects on the performances of various instruments. Especially, electronic parts are thermolabile.

If it is possible to identify both the magunitude and the location of a heat source, it would be able to keep efficiently local temperature increase under control. Therefore, heat source identifications in two-dimensional steady conductions are treated in this study. Because the goal of this study is to estatablish an identification method and to examine the accuracy of it, a square plate model which has both two isothermal sides adjacent to each other and two isolated sides was selected as a object of this study.

In this study, the values of temperatures and heat fluxes at boundaries of a model have been determined by such an ordinary analysis as finite diference method. Sequentially, both the magnitude and the location of the heat source were identified by a reverse analysis using two kinds of parameters obtained in the ordinary analysis. In the analysis, two kinds of the boundary integrations which are no need to iterate were accomplished. One of them is a least square method, and the other one is

Gauss's integration method. We have investigated the following to know what remarkably affected the accuracy of identifications.

- Number of data used in both boundary integrations
- Order of polynomial approximations used in the least square method
- Number of points used in Gauss's integration
- Location of a heat source in the model

# EFFECTS OF ACTIVE COOLING ON PERFORMANCES OF SCRAMJET ENGINE

Y. Tsujikawa, T. Onoda and S. Fujii  
Department of Aeronautical Engineering  
University of Osaka Prefecture  
Sakai 591, JAPAN

## EXTENDED ABSTRACT

### 1. Introduction

The design of efficient scramjet engines, where the primary mode of combustion occurs in a supersonic rather than subsonic air streams, requires special consideration in a number of areas. Particularly, the geometry of this engine, for example, the area contraction ratio of the inlet-diffuser and the cross-sectional area between combustor inlet and exit and area distribution of the combustor must be selected to meet the low Mach number performance requirements yet permit good engine performance at the high Mach number cruise condition. Geometric optimization, therefore, is urged. In the present study, the scramjet engine is regarded as a system which consists of a number of subsystems (components.) The operating state is expressed by the parameters which govern such subsystems. The optimization of criteria, for example, specific impulse, thrust coefficient and total pressure recovery factor can be treated as non-linear programming problem. Using the multiplier method, the optimum values of parameters can be calculated in a short time.

The numerical calculation of the turbulent mixing and chemical kinetics of combustion reaction in the supersonic flow through a scramjet combustor is a computational problem of considerable interests. The introduction of detailed chemical reaction mechanisms into theoretical analyses of complex turbulent mixing flows often results in excessive computer run times and storage requirement. In the present study, therefore, some simplifications have been employed. A related concept involves the assumption that the fuel and oxidizer react instantaneously and form reaction products in chemical equilibrium.

Further, for hypersonic vehicles, many structures will be subjected to severe thermal, acoustic and pressure loadings. The primary coolant that will be used for hypersonic vehicle actively cooled structures will be the vehicles's fuel, hydrogen. Therefore, the present study includes the effect of active cooling with hydrogen.

### 2. Description of analytical model

The scramjet engine used in this study is a generic derivation of some recent scramjet powered vehicle concepts. For simplicity, and to be consistent with some of the engine configurations that have been proposed, it is also assumed that the scramjet inlet is located beneath the main body and sufficiently far aft that the effects of forebody compression are negligible. The air capture ratio is fixed to unity in the present analysis. Multi-oblique shock external compression inlet is adopted.

The combustion chamber must be designed to match the mixing process which is gradual and stable because the flow is supersonic. The main requirements of a scramjet of this type is that the reaction rates which control the chemical reactions be very fast so that the mixing of fuel and oxidizer can be a much slower process and, therefore, be a rate-determining process. The turbulent mixing at supersonic speed range is affected

by the method of fuel injection and accompanied with the complicated shock structure and intense interferences by air. The analytical study is very difficult, so that the data obtained from experiments must be fed back into the analysis. The two-dimensional (2D) axisymmetric flow model is made up. Solutions of parabolic partial differential equations for transport of momentum, energy and mass are accomplished by the finite-difference technique. Two more equations are solved for the transport of turbulence kinetic energy  $k$  and of the dissipation rate of turbulence kinetic energy  $\epsilon$ . In the present study, the axisymmetric geometry is selected, boundary to the flow is chosen to be wall and a choice of  $H_2$  injection can be made. Only profiles of temperature, axial velocity, pressure, and  $H_2$  mass fraction are required. In the nozzle, the calculations were made for frozen-nozzle expansions—i. e., the composition in the expansion process is fixed at that corresponding to equilibrium at the combustor exit.

### 3. Results and discussions

In the present study, since only the external compression is adopted, much better pressure recovery can be realized by taking advantage of characteristics of shock waves: for a given Mach number, a series of weak shocks produce much less stagnation pressure loss than one strong shock. The pressure recovery factor versus combustor-inlet Mach number with the number of oblique shocks as parameter and the axial length of inlet are obtained. The further gains are obtained by introducing more oblique shocks. The penalty in weight due to more complicated mechanics, however, is inevitable.

The combustion reaction is assumed to proceed entirely in supersonic speed range. Figure 1 shows the development of the velocity and temperature profiles along the duct. The jet reaches the pipe wall about 59 jet diameters from the start and by reaching there the velocity profile looks generally like that in pipe flow. However the temperature is rather non-uniform there, more than 100 jet diameters combustion is virtually complete.

The completion of combustion is rather difficult to be decided. In the present study, it is determined as the axial distance where temperature profile has non-uniformity (difference between peak temperature and that of centerline) less than some ten percent.

The completion of combustion is affected significantly by initial hydrogen temperature which represents the effects of cooling. For fixed equivalence ratio, hydrogen temperature is raised with increase of jet velocity. It is shown in Fig. 2.

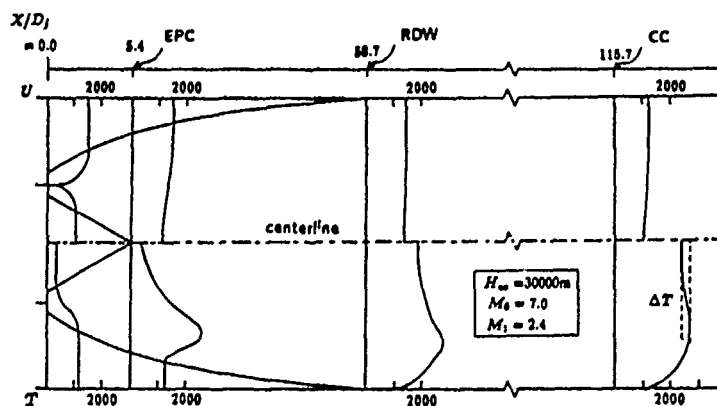


Fig. 1 Velocity and temperature profile.

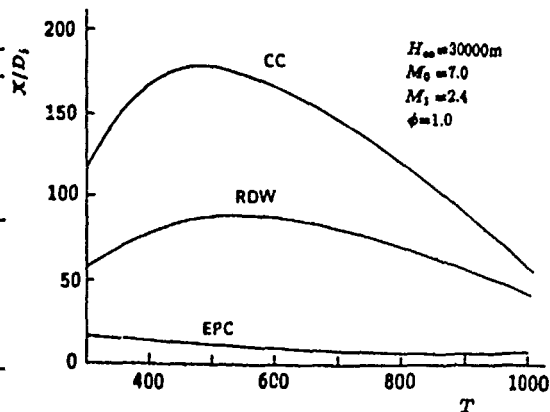


Fig. 2 Effects of active cooling.

# **A SIMPLIFIED DYNAMIC MODEL OF THE EFFECT OF INTERNAL DAMPING ON ROLLING RESISTANCE IN PNEUMATIC TIRES**

D. S. Stutts and W. Soedel  
Ray W. Herrick Laboratories  
School of Mechanical Engineering  
Purdue University  
West Lafayette, Indiana 47907  
U.S.A.

The phenomenon of steady-state rolling resistance in automotive tires has long been recognized to be a function of structural damping or hysteresis and the associated energy losses [1 - 4]. A more recent experimental effort to measure and quantify rolling resistance was made by Keffe and Koralek in 1982 [5]. However, there have been few attempts to mathematically model it. Evens [6] proposed the first model of rolling resistance in 1954. Later, Clark [7] proposed the first analytical model to quantify rolling resistance which also addressed the change in contact region geometry as a function of speed. In this model, Clark predicted an asymmetric growth in the contact region as speed increases. Clark's model predicted a relative forward shift of the contact region which results in a net resistive moment due to the unbalance of vertical displacement forces. In a more recent attempt to explain rolling resistance, Soedel [8] proposed a rolling resistance model based on modal expansion.

The authors' current attempt to understand the mechanics of rolling resistance is undertaken in a vein similar to Clark's efforts, but with a few differences. Whereas Clark's model was based on modeling the tread band as a ring with bending stiffness, with certain assumptions about the nature of the foot print, the present model seeks to extract the fundamental relationship between rolling resistance and equivalent viscous damping by way of a two point boundary value problem where the boundary locations are treated as the unknown variables. Since one of the objectives of this study was to obtain the simplest mathematical model which still predicts the essential rolling resistance behavior, the final model consists only of a perfectly flexible band in tension supported by a viscoelastic foundation. In the current study, the viscous parameter is varied to show its effect upon both the contact region geometry and rolling resistance.

The derivation of the current model is based upon certain simplifying geometric insights regarding the boundaries of the contact region, and the assumption of a relatively small shift of the contact region. Furthermore, the present model demonstrates that rolling resistance can be obtained directly by integrating the product of the radial displacement and the radial elastic stiffness around the circumference of the tire, and resolving the resultant forces into their vertical and horizontal components.

The validity of treating a tire as what amounts to a string rapped around a viscoelastic foundation is supported by the experimental findings of Keffe and Koralek [5] who investigated several tire constructions and determined that the tread band and belt portions of the tire had the greatest effect on rolling resistance. Although it is well known that there are several damping or

loss mechanisms at work in a tire, including bending related damping, it is of course simpler to lump these effects into one viscous foundation factor. This factor more accurately models the damping associated with purely radial compression of the tread rubber and the side walls. The review paper written by Schuring [4] compares the experimental results obtained by Collins et al, [9] and Willett [10, 11], which identify the contribution of the individual parts of a tire to the total rolling loss. These studies show that compression of the tread rubber accounts for a large portion of the total loss – in some cases the largest percentage. These results also agree with the findings of Keefe and Koralek [5], and further support the relevance of studying such a simple model as the one presented here in an effort to isolate the most important physical parameters.

## REFERENCES

1. G. B. Roberts 1959 *International Rubber Conference Nov 8-13* Washington D. C. Power wastage in tires.
2. J. D. Walter and F. S. Conant 1974 *Tire Science and Technology* 2, 235-260. Energy losses in tires.
3. D. J. Schuring 1976 *Tire Science and Technology* 4, 3-15. Energy loss of pneumatic tires under freely rolling, braking and driving conditions.
4. D. J. Schuring 1980 *Rubber Chemistry and Technology* 53, 631-634. The rolling loss of pneumatic tires.
5. R. L. Keefe and A. S. Koralek 1982 *Symposium on Tire Rolling Resistance* Chicago, IL 1, Precision measurement of tire rolling resistance.
6. I. Evans 1954 *British Journal of Applied Physics* 5, 187. The rolling resistance of a wheel with a solid rubber tyre.
7. S. K. Clark 1965 *SAE Mid Year Meeting May 17-21* Chicago Ill. The rolling tire under load.
8. W. Soedel 1980 *ASTM Tire Symposium* Akron, OH Modal analysis applied to tire vibrations.
9. J. M. Collins, W. L. Jackson and P. S. Oubridge 1964 *Transactions of the Institution of the Rubber Industry* 40, 239. Relevance of elastic and loss moduli of tyre components to tyre energy losses.
10. P. R. Willett 1973 *Rubber Chemistry and Technology* 46, 425. Hysteretic losses in rolling tires.
11. P. R. Willett 1974 *Rubber Chemistry and Technology* 47, 363. Heat generation of tires due to viscoelastic properties of elastomeric components.



# THE OPTIMIZATION METHOD OF MULTILAYER MOULD GEOMETRICAL PARAMETRES

Radosław Grzymkowski, DrSc

Silesian Technical University

Math. Phys. Fac., Inst. of Mathematics

Zwycięstwa 42, 44-100 Gliwice, Poland.

The course of solidification process in the casting volume is determined first of all by the conditions of heat exchange between mould and casting subareas. In the case as a multilayer mould is considered and thermophysical parameters of mould segments are known, it is possible to optimize the solidification process: /e.g. solidification time/ by suitable choice of mould layers thicknesses /facing sand, backing sand, etc./.

In the paper a certain algorithm realizing an optimum selection of successive mould layers dimensions will be presented. The upper bound of the problem results from the assumption concerning the maximum mould thickness.

Presented algorithm bases on the inverse geometrical problem solution for thermal conduction equation. The inverse problem solution allows to determine the mould layers thicknesses, if a solidification time is assumed. Here the optimization methods have been utilized.

The mathematical description of heat transport in the system has been supplemented by a certain functional of quality, i. e. criterion of parameters quantities searching. In order to find the functional minimum the gradient methods have been used.

The successive steps of algorithm require a numerical solution of non-linear boundary problem, these ones have been obtained by FDM. In a final part of the paper the exemplar of numeric l computations have been shown.

# THE IDENTIFICATION OF BOUNDARY CONDITIONS IN THE PROCESS OF PRODUCTION OF SINGLE CRYSTAL BY THE VERNEUIL METHOD.

Rodosław Grzymkowski, Dr sc  
Silesian Technical University  
Math. Phys. Fac., Inst. of Mathematics.  
Zwycięstwa 42, 44-100 Gliwice, Poland.

One of the most complex physical processes is directional crystallization. This is caused a number of difficulties in the search for optimum technology to obtain through this method materials, including high quality mono-crystals. These difficulties intensity in the event of using one of the oldest methods: The Verneuil method. In the papers [1, 2] the mathematical and physical model on the basis of which the numerical model was worked out had been presented. Because of the empirical information in the range of boundary conditions is not complete, so the presented model is simplified one. The further investigations in this range show that modelling of boundary conditions the inverse method of heat transfer can be used. It is possible to determine e.g. the cooling condition on the surface of crystal on the basic of information about the situation of crystallization front in the volume of crystal. During the production of crystal in the Verneuil installation the pseudo-stationary temperature field  $T = T(r, z)$  in the volume of crystal is generated. This field in the immovable coordinate system the following equations describe

$$\begin{aligned} c_i \gamma_i \nu \partial_z T &= r^{-m} \partial_r (r^m \lambda_i \partial_r T) + \partial_z (\lambda_i \partial_z T), (r, z) \in D_i, i = \overline{1, 2} \\ T(r, 0) &= T^0, 0 \leq r \leq r^* \\ \partial_{zz}^2 T(r, z^*) &= 0, 0 \leq r \leq r^* \\ T[\zeta(z), z] &= T^*, 0 < z \leq z^* \\ \lambda_2 [\partial_r T(\zeta(z)+0, z) - \partial_z T(\zeta(z)+0, z) \zeta'(z)] + \\ -\lambda_1 [\partial_r T(\zeta(z)-0, z) - \partial_z T(\zeta(z)-0, z) \zeta'(z)] &= \kappa \gamma_2 \nu \zeta'(z), 0 \leq z \leq z^{**} \end{aligned}$$

where  $r = \zeta(z)$  - determined the known position of the crystallization front,  $c_i, \gamma_i, \lambda_i$  - thermophysical parameters,  $v$  - pulling rate of crystal,  $\kappa$  - heat of crystallization,  $T^*$  - solidification point,  $T^0(r)$  - the function determining the course of temperature, liquid state  $D_1 = \{(r, z): 0 < r < \zeta(z), 0 < z < z^{**}\}$ , solid state  $D_2 = \{(r, z): (\zeta(z) < r < r^*, 0 < z < z^{**}) \cup (0 < r < r^*, z^{**} < z < z^*)\}$ . In the mathematical description the boundary conditions on the surface of crystal have not been formulated. The temperatures, heat fluxes or heat transfer coefficients on the surface  $r = r^*$  have not been known. It is possible to show that determining of these quantities in actual.

The inverse problem by the equivalent one of the functional minimum calculation can be substituted.

$$J(\phi) = \int_0^{z^{**}} [\zeta(z) - \chi(z)]^2 dz$$

where the function  $\chi(z)$  describe the crystallization front which was calculated by the auxiliary boundary problem with "a priori" determined function  $\phi(z)$  is a boundary condition e.g.  $T(r^*, z) = \phi(z)$ , or  $-\lambda_i \partial_r T(r^*, z) = \phi(z)$ ,  $0 < z < z^*$ , or  $-\lambda_i \partial_r T(r^*, z) = \phi(z)[T(r^*, z) - T_\infty]$ , where  $T_\infty$  is the ambient temperature.

In order to find the functional minimum  $J(\phi)$  an iterative gradient method [3] can be used. Assuming the first approximation  $\phi^{(0)}(z)$  we determine the successive approximations:

$$\phi^{(n+1)}(z) = F \left( \phi^{(n)}(z) - \alpha^{(n)} \nabla J[\phi^{(n)}(z)] \right)$$

at the same time  $F$  is the projector,  $\alpha^{(n)}$  the step of the method and  $\nabla J$  the functional gradient.

#### References:

1. Grzymkowski R., and al; J. Crystal Growth, 61, 629 - 636 (1983)
2. Grzymkowski R., and al; J. Crystal Growth, 73, 529 - 536 (1985)
3. C  a J.; Optimization: Th  orie et Algorithmes, Dunod (1971).

## PRODUCTION CONTROL OF FLEXIBLE MANUFACTURING CELLS

dr eng. Małgorzata Dolińska  
Technical University of Lublin - WZ IPT  
ul. Nadbystrzycka 38, PL 20-618 Lublin  
POLAND

The control of operations complex - that is scheduling in real time defines for a particular period of time, which operations will be performed, on which elements and by which specified work stations or Flexible Manufacturing System ( FMS ) cells. If static scheduling is used in practice, then during disturbances in realizing of manufacturing processes, for example when a single work station or the FMS breaks down, the total production system has to stop. This problem can be solved during dynamic part scheduling. This problem I have elaborated in the research programme within the range of planning, control and operation of FMS, which is realized by Lublin Technical University.

During dynamic part scheduling, then the synthetic network of processings variable routes must be worked out for collection of the analysed machine elements in the determined enterprise. For every machine element there are chosen from the synthetic network all possible manufacturing process routes of the element execution. The synthetic network of processes routes for collection of parts and every network of processes routes for single analysed part are placed in the computer store and can be made use of them during the optimization of the production scheduling in real - time. All variants of the operation in the network of the alternative processes for every analysed machine element are designed exactly and are also located in the computer memory, in the adequate place. These data are updated after the implementation the new production methods or new products in the analysed enterprise. Dynamic scheduling systems must use the distributed base:

During the static optimization, then are analysed all alternatives of manufacturing processes in total. The dynamic optimization enables reduction of the quantity of analysed solutions on every, successive stage of the production scheduling. On every stage are eliminated these solutions, which are impossible to execution in current time, by reason of the limited quantity of accessible resources in practice; for example limited available standard hours of FMS cell in analysed period of time. Moreover the dynamic optimization enables to introduce changes for the better, during realization of the production scheduling in practice, and only into this stage of the manufacturing processes, on which disturbances are occurring at present.

The dynamic scheduling makes possible the more effective utilization of actual the work resources ( more uniform working load of work stations in determined time ). The system of the dynamic scheduling must work in real - time to support almost random manufacture and then must be available actual informations about accessibility of resources, about alternative solutions, which are possible at present in practice.

The analysis of scheduling processes in FMS cells has shown, that the dynamic programming of R. Bellman is this mathematical method, which suits the structure of the optimization of this problem the best. From here in accordance with principles of this method application in practice I have had to build the network model of the alternatives of processing routes. The using of this method in practice requires that the model of optimization problem

owns properties of the Markow process, that is - " timely state of the process is depended on this state, which is immediately in front of it and isn't depended on the history of this process ".

On every following stage, during the dynamic optimization of production scheduling, there are analysed alternatives of machining operations, which are executed on the determined FMS cells and also the auxiliary operations like washing etc. or inspection operations. From here every knot of the alternative processings network determines the alternative of the part state and every activity determines the alternative of the manufacturing operation.

The alternatives of processing for the analysed machine element are chosen from the synthetic network model and are read in the computer memory as the alternatives of the manufacturing process of this element working out.

The dynamic optimization is realized in real - time on every, successive stage of the designing schedule and for the analysed FMS cell. This optimization leads to reduction of the alternatives solutions number, which can be analysed on the next stages of dynamic optimization of the schedule designing.

The network of the processings alternatives can also be applied during improving the solutions on selected stages of the production schedule or during change the schedule by reason of the different disturbances in realizing of it in practice. The production schedule, which is designed on the successive stages and during the dynamic optimization enables planning of the most effective working load of possessed FMS cells and other work stations, and also reduction of buffer stocks.

Moreover during stage optimization it is possible the application for choice of optimum solution the following criterions: shortest processing time, shortest stock time, minimum cost, minimum stocks, earliest due time and etc. The form of the single criterion function, which possess the properties of Markow process, that is MIN cost and shortest processing time are defined in my doctor thesis on the subject " The Dynamic Optimization of Technology Processes for Collection of the Machine Elements ". I also owns 12 publications within the range of the optimization and flexibility of manufacturing processes and also planning and control of them.

The dynamic optimization of the production schedule causes more effective exploitation of the work stations and the disclosing of hidden production reserves, that gives the possibilities of shortening the interruptions during the production realization and the shortening of the production cycles for analysed parts collections. Thanks to this, the realizing of extra production is possible. These solutions bring the enterprises the additional profits.

The structure of synthetic network model is updated and extended in real - time, as the automated system for dynamic production scheduling " learns " more and more about the production limit and rules during designing and realizing of the system in practice.

The synthetic network of the manufacturing processes has been built for collection of machine elements - shaft type, which are produced in about 180 different assortments in the determined enterprise. This network has been used during dynamic optimization of production schedule for the little and middle production batches of shafts and for the work stations in the analysed enterprise, that is for numerically controlled machines and for conventional machines.

## SHEAR MODULUS OF SLIPED FIBER OUT OF CONCRETE

S. A. HAMOUSH AND M. REZA SALAMI

Assistant Professors, Civil Engineering Department, North Carolina A. & T. State University  
Greensboro, North Carolina 27411

### ABSTRACT

An analytical experimental model is developed to predict the interfacial slip between the concrete and the fiber and to determine the interfacial bond shear modulus of fiber-reinforced concrete. The analytical analysis is developed based on the physical representation of the pulled-out fiber from the surrounding concrete. The model assumes an elastic behavior for both the concrete and the fibers. The analytical model predicts the total displacement of the fiber when pull-out loads are applied at the fiber end. Experimental analyses are used inside the analytical model to determine the value of the bond shear modulus. Numerical examples are presented to compare the results obtained by this paper with that available in the literature. The comparison demonstrates the existence of an interfacial slip between the fiber and the surrounding concrete.

### INTRODUCTION

The slip and the interfacial bond of fiber reinforced concrete have received a considerable attention in the recent research studies<sup>1-3</sup>. The interactions between fibers and the concrete are extremely complex. The first attempt to explain the reinforcing effect of the fibers was based entirely on elastic interactions. Cox<sup>3</sup> considered elastic fibers reinforcing an elastic matrix, and assumed that the shears generated at the fiber-matrix interface could always be withstood. Nammur et al<sup>4</sup> derived an analytical bond-slip relationship of fiber reinforced composite. In the model, it was assumed that a constant value of the normal strain in the cross section of the matrix and a linear relation between the slip and the shear stress. Hamoush and Salami<sup>5</sup> developed an analytical model to find the total strain energy release rate when interfacial cracks existed at the interface between the fiber and the concrete.

### SIGNIFICANCE OF RESEARCH

In the design of fiber reinforced concrete, it is very important to understand the interfacial behavior of the fiber with the concrete. This understanding of the interaction behavior gives the designer more tools for establishing confidence in the over all behavior of the member. The proposed analytical model is established to provide the needed tools to determine the interfacial behavior of a straight fiber with the surrounding concrete. The obtained value for the bond modulus by using the combined analytical-experimental approach provides the basic factor in determining the fracture behavior and the crack propagation in fiber reinforced concrete members.

### ANALYTICAL MODEL

The total fiber displacement under the pull-out applied load was found by Hamoush and Salami<sup>5</sup> to be the combination of three factors. These factors are the displacement due to embedded portion of the fiber, the displacement due to the concrete deformation and the displacement due to interfacial slip of the fiber. These displacements are given in equations 1,2 and 3 respectively.

$$u_1 = p \left\{ \left[ -\left( \frac{1}{q - \alpha k} - \frac{1}{q} \right) \cosh(kL) + \frac{1}{q} \coth(kL) + \frac{\sinh(kL)}{q - \alpha k} - \frac{\sinh(kL)}{q} + \frac{(kL)}{q} + \frac{1}{q} \left[ \frac{1}{\sinh(kL)} \right] + \left( \frac{1}{q - \alpha k} - \frac{1}{q} \right) \left[ \frac{\cosh(kL)}{\sinh(kL)} \right] \right\} \quad (1)$$

$$u_2 = -\frac{pr^2}{n^2 E_f} \left\{ -\left[ \left( \frac{k}{A_f} - \frac{k}{\frac{\alpha}{E_f} + A_f} \right) \cosh(kL) + \frac{1}{\frac{\alpha}{E_f} + A_f} \right] [\coth(kL)] + \left[ \frac{k}{A_f} - \frac{k}{\frac{\alpha}{E_f} + A_f} \right] \sinh(kL) \right\} \quad (2)$$

$$u_3 = \frac{pr}{2T} \left[ \left( \frac{k}{A_f} - \frac{k}{\frac{\alpha}{E_f} + A_f} \right) \cosh(kL) + \frac{k}{\frac{\alpha}{E_f} + A_f} \right] [\coth(kL)] - \frac{r}{2T} \left[ \frac{k}{A_f} - \frac{k}{\frac{\alpha}{E_f} + A_f} \right] \sinh(kL) \quad (3)$$

where  $r$  is the fiber radius,  $R$  is the surrounding concrete radius and depends on the fiber packing<sup>5</sup>,  $E_f$  is the fiber modulus of elasticity,  $A_f$  is the cross-section area of the fiber,  $L$  is the the length of the embedded portion of the fiber,  $T$  is the bond shear modulus,  $E_c$  is the concrete modulus of elasticity,  $\nu_c$  is the concrete Poisson's ratio, and

$$q = (\alpha k + A_f E_f k), \quad n^2 = \frac{E_c}{(1 + \nu_c) E_f \ln \frac{R}{r}}, \quad k^2 = \frac{\left( \frac{\alpha}{E_f} + A_f \right)}{\left[ \frac{\beta r}{2} + \alpha \left( \frac{2rT}{n^2 E_f} + 1 \right) \right] \frac{n^2 E_f}{r^2}}$$

$$\alpha = \pi E_c (R^2 - r^2), \quad \text{and} \quad \beta = \frac{\pi^3}{2(1 + \nu_c)} \left[ \frac{R^2}{2r^2} - \frac{1}{2} - \ln \frac{R}{r} \right].$$

In equations, 1, 2 and 3, the only unknown is the shear modulus  $T$  where the material properties and the fiber packing ratio are given. The procedure used to find the shear modulus ( $T$ ) is obtained by the iteration method. This method is summarized as following: i) Assuming an initial value for the shear modulus ( $T$ ), ii) Obtaining the value of analytical displacement ( $u_1 + u_2 + u_3$ ). iii) Equating the experimental fiber free end displacement to the analytical displacement (Equations 1,2 and 3) leads to a new value of the shear modulus ( $T$ ). By repetition of step ii and iii in the above procedures, a final stable value for the shear modulus ( $T$ ) can be achieved. The experimental data obtained in this study were used to determine the incremental shear bond modulus of the fiber reinforced concrete. The fibers used in this study were a very smooth surfaced fibers.

### CONCLUSION

An analytical experimental model is developed to predict the interfacial shear bond modulus of fiber reinforced concrete and to prove the existence of the interfacial slip at the fiber concrete interface. The proposed model is based on the analytical solution for the physical representation of fibers embedded in the concrete. Experimental results in the literature are used inside the analytical model to predict the interfacial shear bond modulus.

It can be concluded from this model that: (1) unlike most of the theories which say that the bond between the concrete and the fiber is perfect and there is no interfacial slip, it is proven that the interfacial slip exists at the interface. (2). For given material properties of both the concrete and fiber, the bond modulus can be considered as a material property.

### ACKNOWLEDGEMENTS

The authors gratefully appreciate the support by the North Carolina A & T State University.

### REFERENCES

1. Goto, Yukimasa, "Cracks formed in concrete around deformed tension Bars," ACI Journal Proceedings, V. 68, No. 4, Apr 1971, pp. 244-251.
2. Nilson, Arthur H., Internal Measurement of Bond Slip," ACI Journal Proceedings, V. 69, No. 7, July 1972, pp. 439-441.
3. Cox, H. L., "Analysis of effect of orientation of fibers on stiffness and strength," Brit. J. Appl. Phys., V.3, March 1952, PP.72-79.
4. Nammur, G. and Naaman, A. E. "Bond Stress Model for fiber reinforced concrete based on bond stress-slip relationship", ACI Material Journal, Jan.- Feb. 1989, pp.45-57
5. Hamoush, A. S. and Salami, M. R., "Interfacial Strain Energy Release Rate of Fiber-Reinforced Concrete Based on Bond Stress-Slip Relationship", ACI, Structural Division, Vol. 87, November-December 1990, pp. 679-686.

# NUMERICAL MODELING OF NONLINEAR FRACTURE IN CONCRETE

Vellore S. Gopalaratnam and Binsan Ye

Department of Civil Engineering  
University of Missouri-Columbia  
Columbia, Missouri 65211

## ABSTRACT

The growth and development of the fracture process zone in plain concrete has been investigated. A fictitious-crack model based noniterative numerical scheme is developed to study the fracture characteristics of specimens of different sizes and geometries. Results from numerical studies on four different geometrically similar specimen sizes and two different specimen geometries are reported and discussed.

The finite element program developed accommodates linear as well as nonlinear softening laws for the post-cracking response of concrete. For the linear  $\sigma$ - $\omega$  model, parametric study has been completed for three different tensile strengths ( $f_t$ ), and five different critical crack-widths ( $\omega_c$ ). The critical crack-width is observed to play an important role in the growth and development of the process zone. It is observed that the process zone reaches a steady state length which is geometry dependent. Specimen size dependence observed in fracture experiments have been duplicated. As long as the process zone is allowed to develop to its steady state length, the energy absorbed in the process zone appears to be size and geometry independent.

Results from tests on three-point bending specimens reported by Jenq and Shah (Load vs. CMOD and Load vs. Deflection) and compact tension specimens reported by Ratanalert and Wecharatana (Load vs. CMOD) have been compared with the numerical solutions obtained in this investigation. The comparison shows that the numerical model successfully reproduces many of the experimentally observed fracture characteristics of plain concrete.



where  $H$ ,  $D_x$  and  $D_y$  are orthotropic plate flexural rigidity parameters and other symbols are as given in Reference [2].

Because of the Betti reciprocal theorem, we may relate  $v_x$  and  $v_y$  as  $v_x D_y = v_y D_x$ . The solution differs from that of the isotropic plate only in that here it can take on three distinct formulations. The solution procedure parallels that of the isotropic plates as all three building block solutions are superimposed and an eigenvalue matrix is obtained by enforcing the conditions of zero net bending moment along the plate outer edges and zero net displacement at the location of the concentrated harmonic load. Correct Poisson ratios must be employed when formulating bending moments along the edges. Solutions for fully antisymmetric modes, etc., are obtained by using slightly different, but appropriate building blocks.

### COMPUTED RESULTS

Eigenvalues are tabulated for a range of plate orthotropy and geometry. Accurate free vibration mode shapes are readily available. The effects on plate free vibration behaviour of deviations of plate flexural parameters from the isotropic case become apparent. It will be obvious that an entire orthotropic plate with any distribution of point supports can be analyzed by adding, to Figure 1, two building blocks with moment driven edges at  $\eta=0$ , and  $\epsilon=0$ , respectively, and one building block for each additional concentrated force.

### DISCUSSION AND CONCLUSION

In addition to the problem of the mounting of solar panels, a strong interest in the behaviour of such plates has arisen in connection with maximizing the fatigue life of electronic circuit boards. This appears to be the first accurate comprehensive analytical solution for this important structural problem.

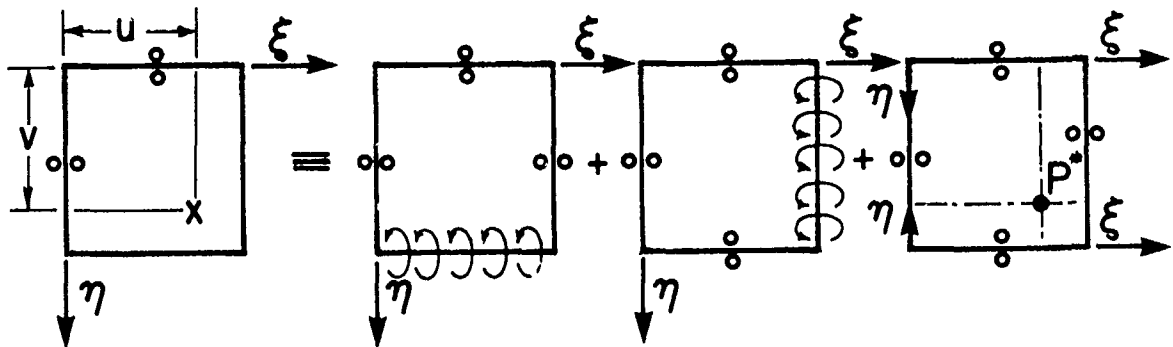


Fig. 1. Building Blocks Utilized in Theoretical Analysis

### REFERENCES

- [1] Gorman, D.J., "A Note on the Free Vibration of Rectangular Plates Resting on Symmetrically Distributed Point Supports", J. of Sound & Vibration, 131(3), pp. 515-519, 1989.
- [2] Gorman, D.J., "An Analytical Solution for the Free Vibration Analysis of Rectangular Plates Resting on Symmetrically Distributed Point Supports", J. of Sound & Vibration, 79, pp.561-574, 1981.

# THEORETICAL ANALYSES OF ULTRASONIC TESTING OF POST-TENSIONING DUCTS IN CONCRETE

Xiaofeng Shen

Ph.D, Dept. Mechanical Engineering,  
Jiaoting University, Shanghai, P.R.China

## 1. INTRODUCTION

The detection of voids in grouted ducts is one of interesting works in nondestructive evaluation for concrete. The purpose of theoretical analyses is to give some quantitative information to a certain extent for ultrasonic testing of post-tensioning ducts in concrete.

## 2. THEORY AND RESULTS

White's researchs [1] dealt with the scattering of compressional elastic waves incident obliquely on an infinitely long cylindrical elastic discontinuity in an isotropic solid.

Let us consider the scattering of normally incidence elastic waves at a void or grouted cylindrical scatterer in concrete.

The computed distributions in angle of scattered waves for the different frequencies of incidence waves at void and grouted cylindrical scatterer are plotted in Fig.1. They show the distribution of the intensity of the scattered wave in angle. Total scattered power (cylindrical scattering) as a function of  $ka$  is given in Fig.2. It shows that the scattered power is in direct proportion with the frequency of incidence waves. Fig. 3 shows the comparison of scattered compressional wave between void and grouted discontinuities. It is found that the scattered wave amplitudes from void discontinuity are larger than from the grouted discontinuity. The differences in the both amplitudes depend on the incidence frequency and the angle of the scattered waves .

## 3. CONCLUSIONS

One of special characteristics of ultrasonic wave propagation in concrete is that the attenuation of energy of elastic waves in concrete is larger than in metal material and the wave propagation in concrete has poor directionality.

There are the unregular reflection and refraction at the random discontinued interfaces. As the sizes of components of concrete vary in great ranges from 1  $\mu$ m to 5-10 mm. The power of scattered waves is very large in high frequency.

-----  
at present inst. f. Massivbau, TH Darmstadt, Germany

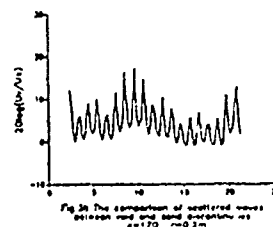
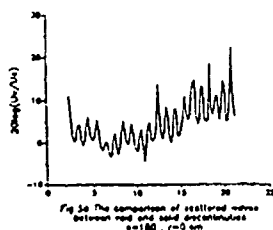
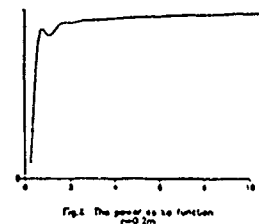
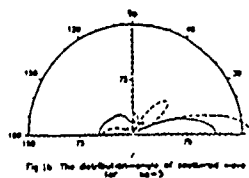
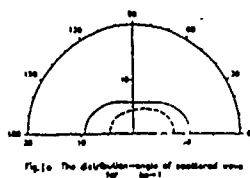
In order to extend the distance of propagation of ultrasonic wave, the ultrasonic wave of the lower frequency is used in testing. But the directionality of propagation is poor. As shown in Fig.1, the directionality of ultrasonic wave is in inverse proportion to the frequency of wave. For very long wavelength (low frequency), the area of distribution of scattered wave in angle is very large. Moreover, when the incidence wave comes, the particulate matters of concrete produce spherical wave and make the directionality of wave poor.

In testing, if the ultrasonic wave of lower frequency is used, it has the characteristics of less attenuation, long distance of progration, but poor directionality and sensitivity. If the ultrasonic wave of higher frequency is used, it has the characteristics of good directionality and sensitivity, but great attenuation of energy. So, Consideration of frequency of ultrasonic wave must be given to both less attenuation of energy and the good directionality and sensitivity in wave propagation. It is suggested that the range of frequency in ultrasonic testing of concrete is 100 KHz -- 200 KHz. The value of  $ka$  correspond to above frequency are approximately 1.5 -- 3 for pebbles and reinforcements.

In Fig.3, It is shown that the differences of scattered compressional wave between void and grouted discontinuities. This differences depend on the incidence frequency and the angle of the scattered wave. In the range of frequency 100 KHz -- 200 KHz, it is found that the scattered wave amplitudes from void discontinuity are larger than from the grouted discontinuity. According to the amplitude of signal received, we can easily judge which signal passes through hollow duct or through grouted duct.

#### REFERENCES

1. R. M. White, Elastic Wave Scattering at a Cylindrical Discontinuity in a Solid, J. Acoust. Soc. Am., Vol.30,1958



EFFECT OF GASKET MATERIALS AND ITS DIMENSIONS  
ON BOLT STRESSES IN THE BOLTED CONNECTION

M. M. EL SAYED \* and M . O. HENDY \*\*

**Abstract**

The type of bolted - Flanged joint represented in this investigation is called the "non - rigid" type, as a joint in which the gasket is located entirely within the bolt circle.

This investigation is concerned to narrow - Faced flanged joint , which is considered as a highly complicated stress system than the full faced gasket joint .

The main purpose of this paper is to study the effect of gasket-materials and its dimensions on the bolt stress variation . A serial of experimental tests has been carried out on the bolted connection ,where the bolt strains were measured by strain gauges . The study shows that the width , thickness and material of the gasket play a major value in the bolt stress variation on the other hand that the bolt is subjected to combined tensile and bending stresses .

One of the promising results is that the bolt stress may decreases with the increase of internal pressure. The rate of decreasing stress( $\alpha$ ) in the bolt has been obtained experimentally and compared with the previous study . According to that comparison, a correction factor ( $k = 2.9$ ) has been proposed . Also it is to be noted that using small value of thickness and width for narrow gasket gives better condition for bolt stresses .

---

\* Assoc . Prof. , \*\* Gradude student in Mech. Design Dept. Faculty of Eng. and Tech., Mataria, Helwan University , Cairo , Egypt .

# INEXTENSIONAL BENDING THIN SPHERICAL SHELL COMPRESSED BY TWO PARALLEL RIGID PLATES

Tian-quan Yun

Department of Mechanics, South China University of Technology  
Guangzhou, 510641, The People's Republic of China

This paper presents an exact solution of axisymmetric deformation of an elastic, inextensional bending thin spherical shell compressed by two parallel rigid smooth plates (Fig.1). The governing equations are 1 :

$$\begin{aligned} & (\Delta/a)[\Psi'' + \cot \xi \Psi' - (\cot^2 \xi - \nu)\Psi - (\cos \beta - \cos \xi)/\sin \xi = \\ & (\Delta/a)[\nu(rV)' + (1+\nu)\cot \xi (rV) - (r^2 p_H)'/\sin \xi - \nu \cot \xi (r^2 p_H)/\sin \xi \\ & (D/a)[\phi'' + \cot \xi \phi' + \cos \beta (\sin \beta - \sin \xi)/\sin^2 \xi - \nu(\cos \beta - \cos \xi)/\sin \xi \\ & + \sin \beta \Psi/\sin \xi = \cos \beta (rV)/\sin \xi \end{aligned}$$

Where  $\phi$  is the meridional angle change of the deformed mid-surface,  $\Psi$  is stress function,  $\beta \equiv \xi - \phi$  is the meridional angle of the deformed mid-surface,  $p_n$  is the normal surface load,  $p_H = -p_n \sin \xi$ ,  $\Delta = 1/(Eh)$ ,  $D = Eh^3/[12(1-\nu^2)]$ ,  $r = a \sin \xi$ ,  $rV = -\int^\xi a^2 p_n \cos \xi \sin \xi d\xi$ ,  $( )' = d( )/d\xi$ ,  $E$  -- Young's modulus,  $\nu$  -- Poisson's ratio.

Boundary conditions:

$$\xi = 0, \pi/2, \quad \phi = \Psi = 0.$$

$$0 \leq \xi \leq \xi_0, \quad w_0(\xi) = a(\cos \xi - \cos \xi_0)$$

Equilibrium condition:

$$P_T = 2\pi \int_0^{\xi_0} r p_v dr.$$

$r_0 = a \sin \xi_0$  is the radius of interface of contact,  $p_v$  is the pressure between the shell and the plate.

For  $\Delta = 0$  (the shell is inextensional), the solution of the above problem is:

$$\begin{aligned} & \phi = 2\xi, \Psi = 0, \quad 0 \leq \xi \leq \xi_0, \\ & \phi = 0, \Psi = -P_T \cot \xi / (2\pi), \quad \xi_0 < \xi \leq \pi/2, \\ & p_v(\xi) = 0, \quad 0 \leq \xi \leq \xi_0, \quad p_v(\xi_0) = P_T / (2\pi r_0) \end{aligned}$$

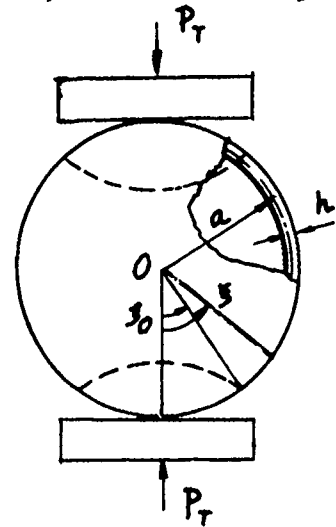


Fig. 1

\* The Project Supported by National Natural Science Foundation of China

This solution shows that: (A). Under certain value of  $P_T$ , axisymmetric dimplings with corresponding radius, which is determined by the principle of virtual work, occur at two poles. (B). The configuration of the dimple part keeps the same shape of a spherical cap but with opposite curvature as shown in Fig. 1 by broken line; the remined part keeps unchange as the undeformed shell. (C). The shell is in contact with the rigid plates only at the edge of the dimplings, no flat contact region occurs.

The relation between  $P_T$  and the turning point  $\xi_0$  is:

$$P_T = 8\pi D(1+\nu)\sin^2\xi_0/[a(1-\cos\xi_0)]$$

The shortness  $S$  of distance between two poles is:

$$S = 2a(1 - \cos\xi_0)$$

The required load  $P_{T0}$  for dimple beginning is:

$$P_{T0} = 16\pi D(1+\nu)/a$$

The range of the above solution available, which is determined by  $(A/a) = 1/(Eha) \rightarrow 0$ ,  $P_{T0} \rightarrow \infty$ , and  $\max \sigma \leq \sigma_0$  (elastic limit), is:

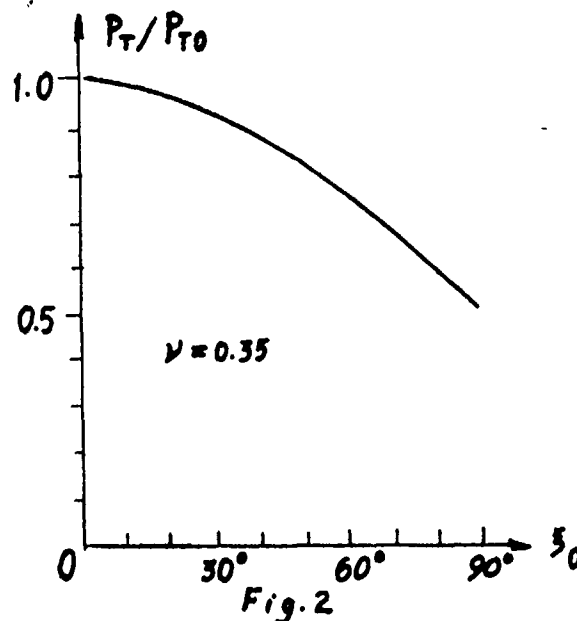
$h/a = (1-\nu)\epsilon_0$  (elastic limit of strain). For steel  $\epsilon_0 = 0.001$ .

The  $P_T - \xi_0$  curve is shown in Fig. 2.

Where  $P_T/P_{T0} < 1$ . This means that

Once the dimple begins, it is unstable, it can be developed to crush under the application of  $P_{T0}$ .

This conclusion is reasonable, since an inextensional bending spherical shell is very thin.



#### References

1. Wan, F.Y.M., Polar Dimpling of Complete Spherical Shells. Proc. of the Third IUTAM Symposium on Shell Theory (Edited by Koiter, W.T. and Mikhailov, G.K., 1980), North-Holland, Amsterdam, 589.
2. Updike, D.P. and Kalnins, A., Axisymmetric Behavior of an Elastic Spherical Shell Compressed Between Rigid Plates, J. of Appl. Mech., (1970), V. 37, 635.

# RESULTS ON BOUNDARY LAYER FLOW OF NON-NEWTONIAN FLUIDS WITHIN/WITHOUT INERTIAL EFFECTS

D. Mansutti

Istituto per le Applicazioni del Calcolo  
(C.N.R.) - Roma

In the recent times, the boundary layer flow of non-newtonian fluids has been often object of interest [1],[2]. This summary is about the interesting experience that we have acquired on boundary layer formation in a flow of a second grade fluid with generalized viscosity.

The issue that we mainly stress is that non-newtonian fluids support sharp boundary layers even in absence of inertial effects. For a newtonian fluid this is impossible, as boundary layers can develop only at large enough Reynolds numbers when the convective acceleration becomes dominant. What we observe in our analysis contradicts the old idea that the boundary layer is an effect of the inertial non-linear term and show the evidence that it might generally be enhanced by any non-linearity present in the mathematical model.

In particular the fluids that we have considered have the following constitutive equation:

being  $\mathbf{v}$ , the velocity vector;  $\mathbf{A}_1$  the deformation tensor and

$$\mathbf{A}_2 = \mathbf{A}_1 + \mathbf{A}_1 (\text{grad } \mathbf{v}) + (\text{grad } \mathbf{v})^T \mathbf{A}_1$$

the expression of the total stress tensor is

$$\mathbf{S} = -p\mathbf{I} + (\mu + \beta (\text{tr}(\mathbf{A}_1^2))^m) \mathbf{A}_1 + \alpha_1 \mathbf{A}_2 + \alpha_2 \mathbf{A}_1^2, \text{ with } \mu, \alpha_i \geq 0, \alpha_1 + \alpha_2 = 0.$$

We have integrated the related equation of motion in the steady case. Although, no memory effect is included, this model supports the two main characteristics of a viscoelastic fluid: shear rate dependent viscosity and normal stress differences. The parameters  $\mu$ ,  $\beta$  and  $m$  relate to the viscosity and scale the shear rate dependency and  $\alpha_1$  and  $\alpha_2$  scale the normal stress dif-

ferences.

Our attention has been mainly focused on two test problems: the creeping flow through a slit and the flow past an infinite porous plate with suction or injection.

In the first case, we have obtained [3],[4] sharp boundary layers for  $\beta = \alpha_1 = \alpha_2 = 0$ . This is the case of a power-law fluid which is used, for example, to represent glycerine and food processing liquids; this model supports only shear thinning and shear thickening effects and boundary layers form when the fluid shear-thins. In the second case, we get to the following conclusions [5]. When on the plate there is suction or injection boundary layers form also when the fluid shear-thickens and, actually, they are sharper than in the case of shear-thinning. The normal stress differences counteract the formation of sharp boundary layers, actually when they grow boundary layers are smoother.

[1]-Beard, D.W., Walters, K., Elastico-viscous boundary layer flows, Proc. Camb. Phil. Soc. 60, 1964

[2]-Rajagopal, K.R., Gupta, A.S., Wineman, A.S., On a boundary layer theory for non-Newtonian fluids, Lett. Appl. Sci. Engng. 18, 1980

[3]-Mansutti, D., Rajagopal, K., R., Flow of a shear thinning fluid between intersecting planes, Intl. Journ. of Non-Lin. Mech. (in print)

[4]-Mansutti, D., Pontrelli, G., Jefferey-Hamel flow of power-law fluids for exponent values close to the critical value, Intl. Journ. of Non-Lin. Mech. (in print)

[5]-Mansutti, D., Pontrelli, G., Rajagopal, K.R., Numerical visco-elatic flows past an infinite porous plate with suction or injection, submitted for publication to Intl. Journ. of Engng. Sci.



A CLASS OF EXACT SOLUTIONS FOR THE MAGNETOHYDRODYNAMIC  
FLOW OF A MICROPOLAR FLUID

by

S.R. Kasiviswanathan and M.V. Gandhi  
Department of Mechanical Engineering  
Machinery Elastodynamics Laboratory  
Michigan State University, East Lansing, MI 48823, USA.

Abstract: The steady magnetohydrodynamic (MHD) flow of a micropolar fluid between two infinite, parallel, non-coaxially rotating disks, is studied. It is observed that for motions characterized by a constant principal relative stretch history, a set of one-parameter family of exact solutions exists, as in Berker's[1] problem for Newtonian fluids, for the velocity and the micro-rotation components. The expressions for the forces and the couples acting on the plates are obtained. Numerical results explaining the effects of various parameters, associated with the flow, are discussed for some interesting special cases. We observe that an increase in the Hartmann number distorts the velocity profile and decreases the boundary layer thickness. The magnitude of the components of micro-rotation vector decreases for an increase in Hartmann number. Although a very few authors have studied the MHD flow of a micropolar fluid, the authors believe that this is the first paper to present a class of exact solutions for the MHD flow of a micropolar fluid.

Reference:

- [1] Berker, R., An Exact Solution of the Navier-Stokes Equation: The Vortex With Curvilinear Axis. International Journal of Engineering Science, 20, 217-230 (1982).

# STEADY FLOWS OF A SECOND GRADE FLUID BY TRANSFORMATION METHODS

A. M. SIDDIQUI and A. BENHARBIT  
Department of Mathematics  
The Pennsylvania State University  
York Campus, York, PA 17403

Known exact solutions of the Navier-Stokes equations are few in number. The basic difficulty in solving these equations is due to the non-linearity introduced by the convective acceleration terms. If the non-linearity also occurs in the viscosity part of equations, as is the case in many non-Newtonian fluids, then the number of exact solutions becomes rare. This is in part so because the equations of motion become highly non-linear partial differential equations. In certain cases, besides the non-linearities, the order of partial differential equations is also increased. It is partly for these reasons that in some situations the transformation methods become attractive in the studies of non-Newtonian fluids.

In general, in the method of transformation, either the system is linearized, the non-linear partial differential equations are reduced to non-linear ordinary differential equations, or some kind of reduction is performed to minimize complexity. Recently we have used hodograph and Legendre transformations to solve steady plane flows of second and third grade fluids [1, 2].

In the present paper we again employ hodograph and Legendre transformations to study some more flow problems in a second-grade fluid. The essence of this technique consists in interchanging of dependent and independent variables and then transforming the governing equations of motion in the hodograph plane, in which the coordinates are the rectangular component of fluid velocity  $u$  and  $v$ . Introducing a function  $L(u,v)$  called Legendre-transform function of the streamfunction  $\psi(x,y)$  we rewrite all the equations in the hodograph plane  $(u,v)$  in terms of this transformed function. The equation this function must satisfy is then determined. On assuming certain forms of the Legendre-transform function  $L(u,v)$ , several illustrations which display the use of the method are considered. A supplementary calculation is then required to determine the streamfunction in the physical plane  $(x,y)$ . Expressions for the velocity distribution and pressure are obtained in the cases considered and these are then compared with the corresponding expressions of linear viscous fluids.

In [1] we establish the theorem which gives the form of the Legendre-transform function  $L(u,v)$  of a streamfunction of the equations of motion governing the plane steady flow of an incompressible fluid of the second grade.

We consider some publications of the above theorem when  $L(u,v) = F(u) + G(v)$  and which  $L(u,v) = vF(u) + G(v)$  and obtain some interesting results. The expression of the streamfunction and pressures are derived in each case.

#### REFERENCES

- [1] A. M. Siddiqui, P. N. Kaloni and O. P. Chandna, "Hodograph transformation methods in non-Newtonian fluids," Journal of Engineering Mathematics 19 (1985) 203-216
- [2] Luisa Moro, A. M. Siddiqui and P. N. Kaloni, "Steady flows of a third grade fluid by transformation methods," Z. Angew. Math. Mech. 70 (1990) 3, 189-198.

# THEORETICAL INVESTIGATION OF NON-LINEAR VISCOUS FLUID LAMINAR FLOW UNDER CONDITIONS OF THE FLOW LOCAL TWIST

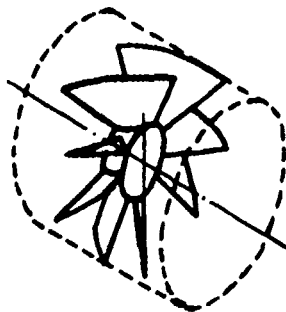
Y.G. Nazmeev, E.K. Vachagina  
Moscow Power Engineering Institute, Kazan  
Branch, 420066 Kazan, Krasnoselskaya str., 51,  
U.S.S.R

One of the method of the convective heat exchange intensification is the application of the flow local twist. Such intensifiers make it possible to reduce essentially the hydraulic resistance. The main difficulty in solving such problems is in obtaining the velocity vector distribution.

Usually, the mathematical model, describing the hydrodynamics of twisted flows of a viscous fluid, is constructed with the help of elliptic equations system. To solve such a system of equations it is necessary to set the boundary conditions over the whole perimeter of the area. But the exact boundary position, where the twist is supposed to damp, is unknown. Such approach to the solution of the problem complicates the calculation algorithm essentially. That is why the statement of the problem and its realization in parabolized equations of motion is of a great interest.

## Statement of the problem

Stationary, laminar flow of non-linear viscous fluid in a round tube with axial-blade twister at the inlet of the tube is considered.



The flow is supposed to be axisymmetric and momentum transfer along the main direction is to be much less than that in transversal direction. Introducing stream function  $\Psi$  and circumferential component of vorticity  $\omega_\varphi$  we transform the system of motion and continuity equations to parabolized form.

Fig. 1. The flow scheme.

$$\frac{\partial \omega_\varphi}{\partial z} \left( -\frac{1}{r} \frac{\partial \Psi}{\partial r} - \frac{1}{\rho} \frac{\partial \mu(I_2)}{\partial z} \right) - \frac{\partial \omega_\varphi}{\partial r} \frac{1}{r} \left( -\frac{r}{\rho} \frac{\partial \mu(I_2)}{\partial r} + \frac{\partial \Psi}{\partial z} - \frac{\mu(I_2)}{\rho} \right) = \frac{\partial^2 \omega_\varphi}{\partial r^2} \frac{\mu(I_2)}{\rho} + \frac{1}{r} \frac{\partial (v_\varphi^2)}{\partial z} - \frac{1}{r^2} \frac{\partial \Psi}{\partial z} \frac{\partial}{\partial r} \left( \frac{1}{r} \frac{\partial \Psi}{\partial r} \right) +$$

$$\frac{1}{\rho} \left\{ \frac{1}{r} \frac{\partial}{\partial r} \left[ r \left( 2 \frac{\partial \mu(I_2)}{\partial r} \frac{\partial}{\partial r} \left( \frac{1}{r} \frac{\partial \Psi}{\partial z} \right) + \frac{\partial \mu(I_2)}{\partial r} \frac{\partial}{\partial r} \left( \frac{1}{r} \frac{\partial \Psi}{\partial r} \right) \right) \right] - \frac{1}{r^2} \mu(I_2) \frac{\partial}{\partial r} \left( \frac{1}{r} \frac{\partial \Psi}{\partial r} \right) - \frac{2}{r^3} \frac{\partial \Psi}{\partial z} \frac{\partial \mu(I_2)}{\partial z} \right\} \quad (1)$$

$$\frac{\partial v_\varphi}{\partial z} \left( \frac{1}{r} \frac{\partial \Psi}{\partial r} + \frac{1}{\rho} \frac{\partial \mu(I_2)}{\partial z} \right) + \frac{\partial v_\varphi}{\partial r} \left[ \frac{1}{r} \frac{\partial \mu(I_2)}{\partial r} - \frac{\partial \Psi}{\partial z} + \frac{\mu(I_2)}{\rho} \right] = \frac{\partial^2 v_\varphi}{\partial r^2} \left( -\frac{\mu(I_2)}{\rho} \right) + \frac{v_\varphi}{r^2} \left( \frac{\partial \Psi}{\partial z} + \frac{r}{\rho} \frac{\partial \mu(I_2)}{\partial z} + \frac{\mu(I_2)}{\rho} \right) \quad (2)$$

$$\frac{1}{r^2} \frac{\partial \Psi}{\partial r} = \frac{1}{r^2} \frac{\partial^2 \Psi}{\partial r^2} - \omega_y \quad (3)$$

The boundary conditions in variables  $\Psi, \omega_y$  will be written as:  
at  $z=0$   $V_y = \tan \beta f_z(r), \Psi = 2\pi \int_0^r f_z(z) r dz, \omega_y = -\frac{\partial f_z(z)}{\partial z}$  (4)

at  $r=R$   $V_y = \frac{\partial \Psi}{\partial r} = 0, \Psi = Q, \text{ at } r=0 \quad V_y = \Psi = \omega_y = 0$  (5)

The generalized model  $\Psi_* = \exp(-\tau_*)$ , where  $\Psi_* = (\Psi_\infty - \Psi)/(\Psi_\infty - \Psi_0)$ ;  $\tau_* = \theta(\tau - \tau_1)/(\Psi_\infty - \Psi_0)$ ;  $\tau = \mu(I_2)\sqrt{I_2}$ ;  $\Phi = 1/\mu(I_2)$ , was used as the rheological constitutive equation. All the equations of the initial system have a similar structure and can be presented as:

$$K_{1i} \frac{\partial y_i}{\partial z} + K_{2i} \frac{\partial y_i}{\partial r} = K_{3i} \frac{\partial^2 y_i}{\partial r^2} + K_{4i} \quad ; \quad i, j = 1, 2, 3 \quad (6)$$

$$K_{ij} = f\left(\frac{\partial^2 \Psi}{\partial r^2}, \frac{\partial^2 \Psi}{\partial z^2}, \frac{\partial \Psi}{\partial r}, \frac{\partial \Psi}{\partial z}, \frac{\partial V_y}{\partial z}, \omega_y\right); \quad y_1 = \omega_y, y_2 = V_y, y_3 = \Psi$$

The system of parabolized motion and continuity equations (6) was solved by numerical method.

The difference method is based on layer by layer transition along  $z$ -axis with the step  $h$  and on successive solution of the equations on each layer  $z^j = jh$  (where  $j=0, 1, \dots, N$ ). To calculate the coefficients  $K_{ij}$  in layer  $z^{j+1}$  the value of hydrodynamic fields and matrices  $\mu(I_2)$  from the preceding layer are used. The calculation of matrices  $I_2$  and  $\mu(I_2)$  with the help of rheological model are made after calculations of hydrodynamic characteristics in layer  $j$ . Then the new values of the coefficients  $K_{ij}$  are calculated. Then again specified values of hydrodynamic characteristics of the flow are calculated. The process is repeated to receive the necessary degree of accuracy.

#### Faedo-Galerkin's method

The approximate solution of the system (6), is searched as:

$$y_i^n = \sum_{j=0}^{n_i} C_{ij} \alpha_j(z) \quad (7)$$

Standard linear functions  $\alpha_j$  of finite element method are used as basis functions. The generalized solution  $y_i(z, z)$  of the system (6) must satisfy the integral relation.

$$\int_0^z \left( K_{1i} \frac{\partial y_i}{\partial z} + K_{2i} \frac{\partial y_i}{\partial r} - K_{3i} \frac{\partial^2 y_i}{\partial r^2} - K_{4i} \right) \alpha_j(z) r dz = 0, \quad j = 1, n_i \quad (8)$$

After introducing (7) into integral relation (8) we have the system of differential equations of the 1-st order with respect to dimensionless coefficients  $C_{ij}(z)$ . The solution of the system is obtained with the help of implicit difference scheme by the factorization algorithm.

#### Main results of calculations

According to the calculation results, the epures of velocity vector components distribution over the length of the tube have been obtained. The segment length of the flow twist damping, depending on Re number, the angles of the twist, the degree of non-newtonian behavior and the magnitude of effective viscosity has been determined.

Nomenclature:  $V_r, V_y, V_z$  - components of velocity vector in cylindrical coordinate system  $(r, y, z)$ ;  $\rho$  - density;  $\Psi$  - stream function;  $\omega_y$  - vorticity component in the direction of  $y$ ;  $\mu(I_2)$  - fluid viscosity;  $I_2$  - second invariant of rate of deformation tensor;  $\tau$  - shear stress;  $\Psi_0, \Psi_\infty$  - fluidity in  $\tau \rightarrow 0$  and  $\tau \rightarrow \infty$ ;  $\theta$  and  $\tau_1$  - measure and limit of structural fluid stability;  $\beta$  - angle of the flow twist;  $h$  - step in the direction- $z$ .

# NUMERICAL SIMULATION OF LOW-REYNOLDS-NUMBER VISCOUS FLUID FLOW AROUND CYLINDRICAL ARCS

Chang-Sheng Lin  
Department of Physics  
Inner Mongolia Teacher's College of the Nationalities  
Tongliao, 028043, P.R.CHINA

The numerical simulations of the low-Reynolds-number viscous fluid flow arounding the cylindrical arcs have been made by using Boundary Element Method(BEM) in this paper. The method based on a idea of the fundamental solution of Stokes equations as Green's function to convert the Navier-Stokes equations to boundary integral equations as follows

$$c(\vec{X})v^k(\vec{X}) = \oint_{\Gamma} n_i(\vec{X}_0)T'_{ij}(\vec{W}^k(\vec{X}-\vec{X}_0))_0 v_j(\vec{X}_0) d\Gamma_0 - \oint_{\Gamma} n_i(\vec{X}_0)T_{ij}(\vec{V}^k(\vec{X}_0))_0 w_j^k(\vec{X}-\vec{X}_0) d\Gamma_0 \quad (1)$$

$$c(\vec{X})p(\vec{X}) = \oint_{\Gamma} q^k(\vec{X}-\vec{X}_0)T_{ki}(\vec{V}(\vec{X}))_0 n_i(\vec{X}_0) d\Gamma_0 + \frac{1}{R_0} \oint_{\Gamma} \frac{\partial q^k(\vec{X}-\vec{X}_0)}{\partial x_{j0}} v_k(\vec{X}_0) n_j(\vec{X}_0) d\Gamma_0 \quad (2)$$

where  $T_{ij}(\vec{V})$  and  $T'_{ij}(\vec{W}^k)$  are stress tensor correlate with  $\vec{V}$  and  $\vec{W}^k$ . The fundamental solution  $w_j^k$  and  $q^k$  are given<sup>(1)</sup> by

$$w_j^k(\vec{X}-\vec{X}_0) = -\frac{1}{4\pi} \left[ \delta_{ij} \ln \frac{1}{|\vec{X}-\vec{X}_0|} + \frac{(x_i-x_{j0})(x_k-x_{k0})}{|\vec{X}-\vec{X}_0|} \right]$$

$$q^k(\vec{X}-\vec{X}_0) = \frac{\partial}{\partial x_k} \left[ \frac{1}{2\pi} \ln \frac{1}{|\vec{X}-\vec{X}_0|} \right] = -\frac{1}{2\pi} \frac{x_k-x_{k0}}{|\vec{X}-\vec{X}_0|^2}$$

The boundary integral equations can be discretized and solved numerically the surface-stress force and pressure on the boundaries and velocity fields in the flow domain. In order to show an effectiveness of the method, we study a problem of low-Reynolds-number viscous fluid flow around the cylindrical arc with various angles of circumference. We calculated numerically the distributions of surface-stress force and pressure on the surface of arcs. The velocity fields of numerical simulation show in Figure 1(a,b,c,d). There is a vortex pair within the concavity of the cylindrical arc when the angle of circumference is  $7\pi/9 \leq \phi \leq 5\pi/3$ . Moreover, two rotatory vor-

textures are in opposite direction as show in figures. The distance between two vortex centres are obtained. By comparison, the numerical results are in good agreement with the experimental ones (2). The numerical investigations show that the method is very effective in researching and solving unbounded problem and studying the phenomena of vortex, and has some advantages of computational convenience, the superior accuracy. The question of especial importance is the method not only is more suitable for the complex geometry of body than other method but also can be treated the problem of the flow past multibody as well.

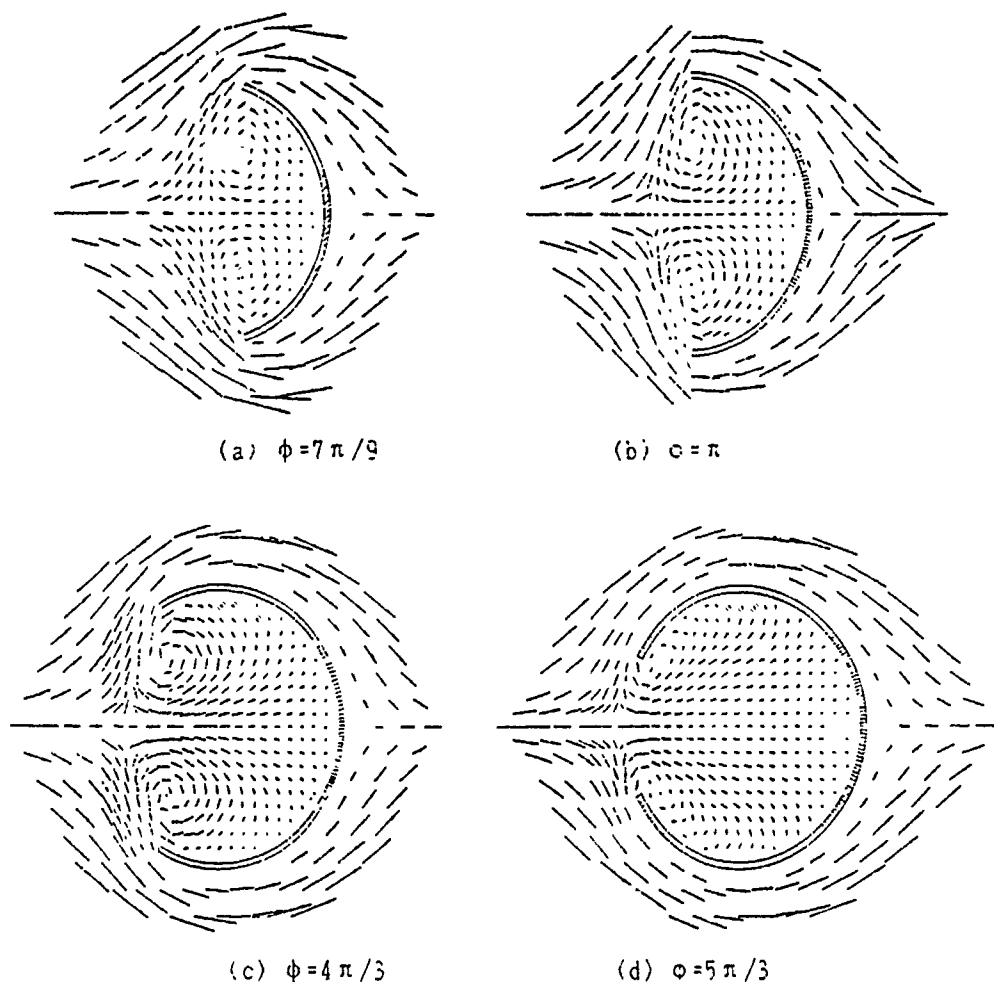


Figure 1. The velocity fields of the flow around the cylindrical arcs

#### REFERENCES

1. J. Wu, Acta Mechanica Sinica, 5(1984), 425.
2. S. Taneda, J. Phys. Soc. Japan, 6(1979), 1935.

# A new pore water pressure equation

Li Yaoming      Yu Maohong

Department of Civil Engineering, Xi'an Jiaotong University,  
Xi'an, Shaanxi 710049, P. R. China

The pore water pressure in soils is a basic problem of soil mechanics. The pore water pressure parameters were first proposed by Skempton(1954):

$$\Delta u = B [ \Delta \sigma_3 + A (\Delta \sigma_1 - \Delta \sigma_3) ] \quad (1)$$

Henkel(1960) extended the Eq.(1) for saturated soils as:

$$\Delta u = \Delta \sigma_{oct} + 3a \Delta \tau_{oct} \quad (2)$$

The Eq (1) is widely applied to the soil engineering problems because it was of a clear physical concept, simple expression and the parameter can be determined by means of triaxial tests. It can't, however, simulated the effect of  $\sigma_2$ . Although the Henkel's equation(2) was simply extended with octahedral stresses, it was a nonlinear expression, and was short of clear and definite proving in mathematics.

In this paper, a new pore water pressure equation is established by analysis of a point of true three-dimension(3-D) stress increment state. The new equation is:

$$\Delta u = B \left[ \frac{\Delta \sigma_2 + \Delta \sigma_3}{2} + A \left( \Delta \sigma_1 - \frac{\Delta \sigma_2 + \Delta \sigma_3}{2} \right) \right] \quad (3)$$

or:

$$\Delta u = B \left[ \frac{\Delta \sigma_1 + \Delta \sigma_2}{2} - A' \left( \frac{\Delta \sigma_1 + \Delta \sigma_2}{2} - \Delta \sigma_3 \right) \right] \quad (3')$$

This equation can be derived from the resolution of the true 3-D stress increment state too. The true stress state can be divided into stress states shown in Fig.1 or Fig.2 when the  $\sigma_2 + \Delta \sigma_2$  is nearing or far from the  $\sigma_3 + \Delta \sigma_3$ . We find that Fig.1 (b), (c) and (d) represent the actions of three principal shear stress increment of  $\Delta \tau_{13} = (\Delta \sigma_1 - \Delta \sigma_3)/2$ ,  $\Delta \tau_{12} = (\Delta \sigma_1 - \Delta \sigma_2)/2$  and  $\Delta \tau_{23} = (\Delta \sigma_2 - \Delta \sigma_3)/2$  respectively; and that Fig.2(b), (c) and (d) express the actions of  $\Delta \tau_{13} = (\Delta \sigma_1 - \Delta \sigma_3)/2$ ,  $\Delta \tau_{23} = (\Delta \sigma_2 - \Delta \sigma_3)/2$  and  $\Delta \tau_{12} = (\Delta \sigma_1 - \Delta \sigma_2)/2$  respectively. It means that the second term in present equation (3) or (3') is the pore pressure developed just by twin shear stress increment  $\Delta \tau_{13} + \Delta \tau_{12}$  or  $\Delta \tau_{13} + \Delta \tau_{23}$  [1][2].

We can observe that equation (3) turns, naturally, to the Skempton's equation while  $\Delta \sigma_2 = \Delta \sigma_3$ . So, the Skempton's is a particular case of the present equation. It is noted that there is a negative sign in front of coefficient  $A'$  in the Eq.(3'). it is just explaining this case of 3-D extension state. When  $\Delta \sigma_1 = \Delta \sigma_2$ , the first term  $B \Delta \sigma_1$  shows the pore pressure produced by loading  $\Delta \sigma_1$  based on the uniform surrounding pressure  $\sigma_1$ , the second term indicates the pore pressure  $A'(\Delta \sigma_1 - \Delta \sigma_3)$  eliminated due to unloading  $\Delta \sigma_3$  after increasing  $\Delta \sigma_1$ . The previous Skempton's equation can not describe this situation.



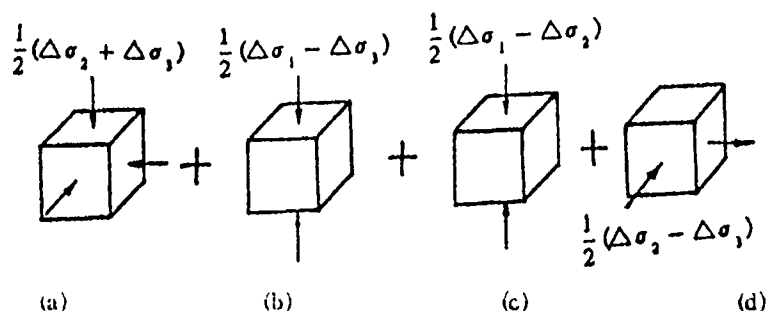


Fig 1 Similar to the compression state when  $\sigma_2 + \Delta\sigma_2 \leq \frac{1}{2}(\sigma_1 + \Delta\sigma_1 + \sigma_3 + \Delta\sigma_3)$

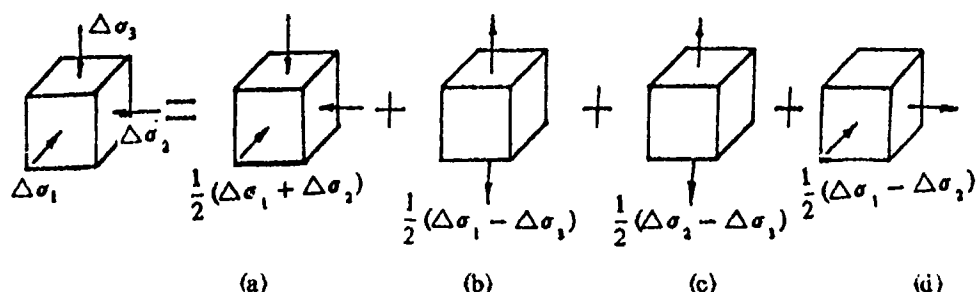


Fig 2 Similar to the extension state when  $\sigma_2 + \Delta\sigma_2 \geq \frac{1}{2}(\sigma_1 + \Delta\sigma_1 + \sigma_3 + \Delta\sigma_3)$

Therefore, if the intermediate principal stress increment is taken into consideration in pore pressure equation, it is very twin shear stress increment in physical concept. The new pore water pressure equation is of two different expression (3) or (3') when intermediate principal stress component is smaller or greater.

The parameter A in present equation could be determined by using the conventional triaxial compression test. The pore pressure variations estimated by three equations with  $\Delta\sigma_2$  from  $\Delta\sigma_3$  to  $\Delta\sigma_1$  show the present results are approaching the Henkel's when the A is smaller and the present results are nearing the Skempton's when the A increases[3].

## References

- (1) Yu Maohong, He Linian, and Song Lingyu, Twin shear stress theory and its generalization, *Scientia Sinica/Science in China* series A, Vol.28(1985), No.11, 1174-1183.
- (2) Yu Maohong, Li Yaoming, The basic ideas of twin shear stress strength theory and its system, *Proc. of 2nd Inter. Conf. on Plasticity and its Current Application*, Tsu, Japan, 1989.
- (3) Li Yaoming, The twin shear stress theory applied to some soil engineering problems, Ph.D thesis of Zhejiang University, 1990.

## NUMERICAL STUDY OF LOCALIZATION IN A MODEL OF GRANULAR FLOW<sup>1</sup>

E. Bruce Pitman  
Department of Mathematics  
State University of New York  
Buffalo, New York

**Abstract** The localization of plastic deformation into shear bands is a fascinating phenomenon in continuum mechanics, and a variety of models have attempted to elucidate the most important factors in shear band formation. Recently, Schaeffer introduced a model system of partial differential equations that incorporates certain aspects of shear band formation and post-critical behavior into the description of flowing granular materials. In this paper, we employ high resolution numerical methods for solving hyperbolic partial differential equations to study Schaeffer's model system. In particular, the equations lose hyperbolicity at the time of shear band initiation; our techniques must overcome this ill-posedness. We shall describe the model equations, discuss well-posedness of the system, explain the numerical techniques, and illustrate our findings.

---

<sup>1</sup>Research supported in part by the Air Force Office of Scientific Research

# CONTINUUM REPRESENTATION OF DISCRETE GRANULAR SYSTEM

Anil Misra, Assistant Professor of Civil Engineering  
University of Missouri, 600 W Mechanic, Independence, MO 64050, U.S.A.

## Introduction

The stress-strain behavior of granular materials is significantly dependent upon the inter-particle interaction and the geometrical arrangement of the particles in space. Continuum models of mechanics of granular media accounting for these factors have been attempted (see for example, Chang and Misra 1990). However, a majority of the continuum models of granular media assume that the deformation fields are uniform within these materials. This assumption has intuitive drawbacks for granular materials. Numerical simulations based on discrete models have substantiated the drawbacks of the uniform strain assumption (Chang and Misra 1990). In light of this, it is desirable to develop an equivalent continuum description of mechanics of granular media which rationally accounts for the inter-particle interaction, the packing structure, and the heterogeneity of the strain field.

## Equivalent Continuum Description of the Granular System

We consider a granular system consisting particles carrying the imposed load at boundary through resistance at discrete contacts between particles. The deformable particles are idealized to be rigid particles connected by spring/slider systems as postulated by the Hertz-Mindlin contact theory (see Misra 1990).

In an equivalent continuum description of the discrete system, each particle is conceptually replaced by a polyhedral continuum element consisting of the particle and associated void space. The discrete interaction at contact points is smeared throughout this cell by defining a local stress and a local strain tensor for the cell.

The increment of local nominal stress tensor  $\Delta \sigma_y^n$  is related to the increment of local strain tensor  $\Delta e_\mu^n$  as

$$\Delta \sigma_{ij}^n = C_{ijkl}^n \Delta \epsilon_{kl}^n \quad (1)$$

where  $C_{ijkl}^n$  is the local stiffness tensor. Thus a discrete granular system can be represented by a collection of continuum cells with a varying stiffness given by  $C_{ijkl}^n$ .

#### Stress-Strain Relationship For Granular Solid

We now consider a volume consisting of a large number of particles such that it is representative of the material behavior of the granular solid. Considering the increment of overall nominal stress  $\Delta \bar{\sigma}_{ij}$  and strain  $\Delta \bar{\epsilon}_{ij}$  to be volume averages of the corresponding local quantities  $\Delta \sigma_{ij}^n$  and  $\Delta \epsilon_{kl}^n$  the overall stress-strain relationship is written as

$$\Delta \bar{\sigma}_{ij} = C_{ijkl} \Delta \bar{\epsilon}_{kl} \quad (2)$$

where the equivalent stiffness tensor  $C_{ijkl}$  is given as a 'weighted' average of the corresponding local quantity by

$$C_{ijkl} = \frac{1}{V} \sum_n V^n C_{ijkl}^n H_{pqkl}^n \quad (3)$$

where  $H_{pqkl}^n$  is a 'concentration' tensor at each particle which accounts for the heterogeneity of the strain field within the representative volume (see Misra 1990).

The derived overall stress-strain law is a function of the contact stiffness, contact frictional strength, particle size, void ratio, coordination number, and packing structure. The packing structure evolution are also accounted by allowing for sliding and separation at inter-particle contacts.

#### References

Chang, C.S. and Misra, A. (1990), "Application of uniform strain theory to heterogeneous granular solids", Journal of Engineering Mechanics, ASCE, Vol. 116, No. 10, 2310-2328.

Misra, A. (1990), "Constitutive relationships for granular solids with particle slidings and fabric changes", Ph.D. dissertation, University of Massachusetts at Amherst.

# METHOD OF ZENO EXTENSION LINES IN STRESS STRAIN ANALYSIS OF GRANULAR MEDIA

A. Sabzevari, Mechanical Engineering Department  
University of Puerto Rico, Mayaguez, P.R. 00708

A. Grahramani, Civil Engineering Department  
Shiraz University, Shiraz, Iran

The failure analysis for granular media has been traditionally based on an assumed simplified stress field without any reference to the deformation field. The medium has been assumed rigid plastic and the upper bound plastic theory is employed to determine the critical load. This simplified classical method does not always give satisfactory results.

To obtain the actual stress field in a granular medium, the deformation field must be first specified, and here is exactly where the present authors method of associated fields has become very useful [1,2,3]. To simplify the computational process of the method of associated fields a new scheme of computational stress-strain analysis named the method of zero extension lines [4,5,6] is developed. In the former method two fields of stress and displacement characteristics are constructed and analyzed separately whereas in the latter, only a simplified strain characteristic field is developed which is applicable to the circular and logarithmic spiral fields.

In the study of load-deformation behavior of soil-structure problems such as retaining walls and foundations, generalized zero extension line fields based on the following stress characteristic equations are developed along the zero extension lines;

$$dS - 2S \tan\phi d\theta = \gamma[-\tan\phi dx + dz] + S[\tan\phi d\phi - \frac{\partial\phi}{\partial\ell^+} \frac{d\ell^-}{\cos\phi}] \quad (1)$$

$$dS + 2S \tan\phi d\theta = \gamma[\tan\phi dx + dz] + S[\tan\phi d\phi - \frac{\partial\phi}{\partial\ell^-} \frac{d\ell^+}{\cos\phi}] \quad (2)$$

which are true on the characteristic directions

$$\frac{dz}{dx} = \tan(\theta - \mu) \quad \text{and} \quad (3)$$

$$\frac{dz}{dx} = \tan(\theta - \mu) \quad (4)$$

respectively. Allowing up to 5% of approximation, the above stress equations along the zero extension lines

$$\frac{dz}{dx} = \tan(\theta - \zeta) \quad (5)$$

$$\frac{dz}{dx} = \tan(\theta - \zeta) \quad (6)$$

are respectively expressed as:

$$dS - 2S\alpha \tan\phi d\theta = \gamma\beta[-\tan\phi dx + \alpha dz] + S[\tan\phi d\phi - \frac{\partial\phi}{\partial d^+} \frac{dd^-}{\cos\phi}] \quad (7)$$

$$dS + 2S\alpha \tan\phi d\theta = \gamma\beta[\tan\phi dx + \alpha dz] + S[\tan\phi d\phi - \frac{\partial\phi}{\partial d^-} \frac{dd^+}{\cos\phi}] \quad (8)$$

In above equations  $\phi$  denotes angle of friction,  $\nu$  is angle of dilation  $\zeta = \pi/4 - \nu/2$  and  $\mu = \pi/4 - \phi/2$ .  $\theta$  is angle between major principal stress and x axes and  $S$  designates the average of major and minor principal stresses, i.e.  $S = (\sigma_1 + \sigma_3)/2$ . The terms  $d\ell^-$  and  $d\ell^+$  are elements of length along negative and positive stress characteristics. Similarly  $dd^-$  and  $dd^+$  are for displacement characteristics.  $\gamma$  is the soil unit weight.

Solutions of equs. (5) through (8) result in values of stresses along the zero extension lines directly. Having the deformation equation

$$du dx + dv dz = 0 \quad (9)$$

where  $u$  and  $v$  are displacements along  $x$  and  $z$  axes the complete load deformation is then obtained by using the zero extension line fields. It should be noted that in this method no zero extension line field is assumed a priori but it is developed by using equations 5 through 8.

In conclusion the results of soil structure problems computed by this method is compared with those obtained through the method of associated fields and close similarity is achieved.

## REFERENCES

1. Sabzevari A. and Ghahramani A.: The Limit Equilibrium Analysis of Bearing Capacity and Earth Pressure Problems in Nonhomogeneous Soil, Journal of Soils & Foundation, JSSMFE, Vol. 12, No. 3, 1972.
2. Ghahramani A. and Sabzevari A.: Theoretical Investigations of Passive Progressive Failure in an Earth Pressure Problem, Journal of Soils & Foundations, JSSMFE, Vol. 13, 1973.
3. Sabzevari A. and Ghahramani A.: On Dynamic Passive Earth Pressure Problem, Journal of Geotechnical Division, ASCE, Vol. 110, No. GT1, 1974.
4. Habibagahi K. and Ghahramani A.: Zero Extension Line Theory of Earth Pressure, Journal of Geotechnical Div. ASCE, Vol. 105, No. GT7, 1979.
5. Ghahramani A. and Clemence S.P.: Zero Extension Line Theory of Dynamic Passive Pressure, Journal of Geotechnical Div. ASCE, Vol. 106, No. GT6, 1980.
6. Jahandish M. and et al: Load Displacement Characteristics of Retaining Walls, Proc. XII Int. Conf. on AMFE de Janeiro, Brazil, Vol. 1, 1989.

# INHOMOGENEOUS GRANULAR SHEAR FLOWS OF NEARLY ELASTIC SPHERES

CHUEN-SHII CHOU  
DEPARTMENT OF MECHANICAL ENGINEERING  
NATIONAL PINGTUNG POLYTECHNIC INSTITUTE  
PINGTUNG, TAIWAN, REPUBLIC OF CHINA

## INTRODUCTION

Significant boundary effects have been demonstrated by the experimental results of Savage and McKeown [1983] and Craig et.al. [1987]. They found that when the shearing surfaces of their device were relatively rough, the stresses induced were considerably higher than those induced when the surfaces were relatively smooth. Employing the constitutive relations of Jenkins and Richman [1985] and boundary conditions of Richman [1988] in the balance equations for mean fields of mass density of flow  $\rho$  or solid fraction  $v$ , velocity  $u$ , and the granular temperature  $T$  (or  $w=\sqrt{T}$ ), we solve the boundary-value problem for the steady inhomogeneous shear flows of identical, smooth, nearly elastic spheres of diameter  $\sigma$  and coefficient of restitution  $e$ . We show all possible circumstances under which the boundary could supply or absorb fluctuation energy. We demonstrate how the resulting profiles of velocity, solid fraction, and granular temperature are affected by changes in the geometry of the boundary as well as predict how the induced stresses vary with the geometry of the boundary.

## INHOMOGENEOUS SHEAR FLOWS

We consider steady and fully developed flow of granular material driven by the relative motion of two identical parallel walls to which hemispherical particles of diameter  $d$  are randomly attached an average distance  $s$  apart. Dimensionless measures of wall geometry are  $r=\sigma/d$  and  $\Delta=s/d$ . In order to ensure that no flow particle ever collides with the flat part of the wall, we insist that  $\Delta$  must be less than  $-1+\sqrt{1+2r}$ . When  $\Delta$  is between 0 and  $-1+\sqrt{1+2r}$ , the boundary may be made effectively rougher either by increasing  $\Delta$  or decreasing  $r$ . The ratio  $E$  is defined  $(1-e)/(1-e_w)$  in which coefficient of restitution  $e_w$  characterizes the energy dissipated in a wall-flow particle collision. In an  $x$ - $y$ - $z$  Cartesian coordinate system the boundaries are located at  $y=\pm L/2$ . The upper boundary moves in the  $x$ -direction with a constant speed  $U$  while the lower boundary moves with the same speed in the opposite direction. The apparent shear rate is then  $2U/L$ . In this steady rectilinear flow the velocity  $u$  in the  $x$ -direction, the solid fraction  $v$ , and the granular temperature  $T$  are function of  $y$  only. In this simple flow, the balance of mass is satisfied identically. In the absence of gravity, the  $x$ - and

y-momentum balances may be integrated to show that both normal stress  $N^*$  and shear stress  $S^*$  are constants throughout the flow.

## RESULTS

In Figure 1, we show the variations of  $E_{\max}$  and  $E_{\min}$  with  $\bar{v}$ . The area above the curve of  $E_{\max}$  corresponds to values of  $E$  for which fluctuation energy can only be supplied to the flows by all possible boundary geometries. The area below the curve of  $E_{\min}$  corresponds to those values of  $E$  for which energy can only be absorbed from the flows, and the area between the two curves corresponds to the values of  $E$  for which energy is either supplied or absorbed. The variations of  $u/U$ ,  $w/U$ , and  $v$  with  $y/L$  are shown in Figure 2 for  $\Delta=0, 0.2, 0.732$ . The middle panel of Figure 2 demonstrates that as  $\Delta$  increases and the slip velocity decreases, the slip work done by the boundary decreases, and the boundary evolves from a fluctuation energy supplier to an absorber. The variation of dimensionless stresses  $N^*$  and  $S^*$  with  $\Delta$  for  $r=2/3$  and  $3/2$  are shown in Figure 3 in which the dashed curves correspond to the solution obtained by Richman [1988]. When  $r=3/2$ , for example, as  $\Delta$  varies between zero to one, the corresponding dimensionless normal stress  $N^*$  nearly doubles from 5.19 to 8.5, while the dimensionless shear stress  $S^*$  more than doubles from 0.88 to 1.85.

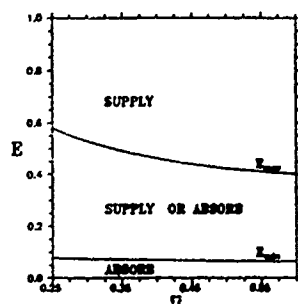


Figure 1

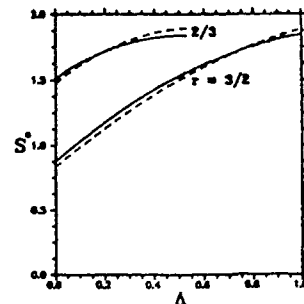
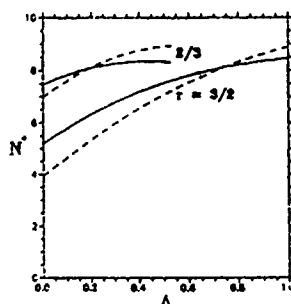
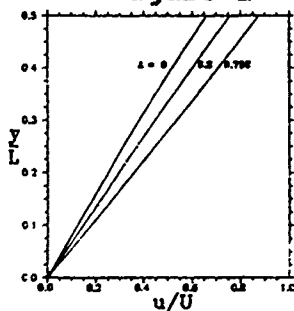


Figure 3

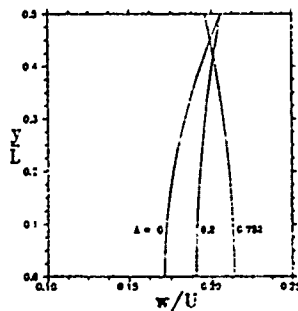
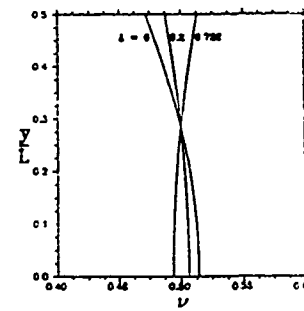


Figure 2



**ACKNOWLEDGEMENT:** The author would like to thank Prof. M.W. Richman of W.P.I. for several helpful discussions.

## REFERENCES

- Craig, K., et.al., 1987. *J. Tribology*, Vol. 109, pp. 232-237.  
 Jenkins, J.T., and Richman, M.W., 1985. *Arch. Rat. Mech. Anal.*, Vol. 87, pp. 355-377.  
 Richman, M.W., 1988. *Acta Mechanica*, Vol. 75, pp. 227-240.  
 Savage, S.B., and McKeown, S., 1983. *J. Fluid Mech.*, Vol. 127, pp. 453-472.



# A THERMAL ANALYSIS OF CHIP COOLING IN AN ELECTRONIC EQUIPMENT USING COMPUTATIONAL FLUID DYNAMICS TECHNIQUE

İbrahim ÖZKOL<sup>1</sup> and C.Ruhi KAYKAYOĞLU<sup>2</sup>

Ph.D. Candidate<sup>1</sup>, Assoc.Prof.Dr.<sup>2</sup>

Istanbul Technical University

Faculty of Aeronautics and Astronautics

Maslak,80626 Istanbul,TURKEY

## ABSTRACT

The prediction of the unsteady flow and temperature fields in a narrow channel containing rectangular blocks has been considered as an important simulation tool in the design of thermal environment in electronic packaging. Integrated circuit devices ,chips,can be idealized as rectangular blocks attached to a single layer substrate. The capability of Computational Fluid Dynamics (CFD) codes to visualize complex flow and thermal fields over PCBs has been reviewed by Nakayama [1].

In this study, an implicit finite difference CFD scheme is developed so as to simulate the heat removal through direct and indirect conduction and direct convection processes.The channel geometry consists of a top layer of finite thickness rectangular block representing device chip and a bottom layer which represents the package. The heat source of rectangular shape with finite thickness is embedded inside the rectangular block. The heat flux of the source can be any function of time. The heat is generated uniformly in the volume of blocks and then is assumed to be transferred from each block to the substrate and to the coolant fluid. The bottom surface temperature is kept constant thus an indirect cooling is applied (see Figure 1a-b). The simultaneous conjugate solution of 2-D Navier Stokes equation in its vorticity-stream function form and the energy equation with a constant source term for fluid and solid predict the coupling between the heat transfer by conduction in the substrate material and convection to the coolant fluid.

An implicit finite difference procedure where the channel, chip and package are discretized into  $M \times N$  rectangular grids is used to solve the equations. Central differencing is applied for all the terms except for the convective terms in the streamwise direction. The Strongly Implicit Procedure (SIP) of Stone [2] is modified and used to obtain the unsteady and steady state solutions. The computation space consists of 409 grid lines in the  $X$  direction, 31 grid lines in the  $Y$ -direction for three chips in line.

The present CFD code is capable of analysing transient, uniform and nonuniform thermal properties of a single homogeneous and multilayer substrate structures. The transient analysis is particularly important for devices operating under a pulsed or switching conditions.

The thermal characteristics of the surface mounted chips were investigated by computer experiments. The transfer of heat from the chip to the coolant fluid is maximum at the front and rear faces where flow forms recirculating zones. It was observed that the convective heat transfer coefficient is almost constant over the top surface of the chip device while it can be strongly influenced by coolant fluid velocity. The flow of dissipated heat from the chip core through the package material can be accelerated by reducing the bottom wall temperature. The characteristics of the recirculation zone downstream of the rectangular block were controlled by the oscillatory coolant fluid to assess reliability of solder joints and the disappearance of nonuniform local hot spots. Figure 2 shows steady state velocity distributions at various channel sections. The steady state temperature contours for a constant chip surface heat flux is shown in Figure 3.

## REFERENCES

- [1] Nakayama, W., "Thermal Management of the Electronic Equipment: A review of Technology and Research Topics", Applied Mech. Rev., Vol. 39, No. 12, 1986, pp 1847-1867
- [2] Stone, H. L., "Iterative solution of Implicit Approximation of Multidimensional Partial Differential Equation", SIAM Journal of Numerical Analysis, Vol. 5, 1968, pp 530-558

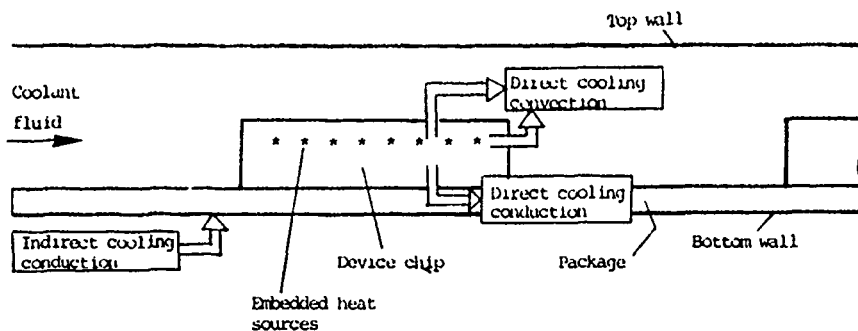


Figure 1a. Simulation Model

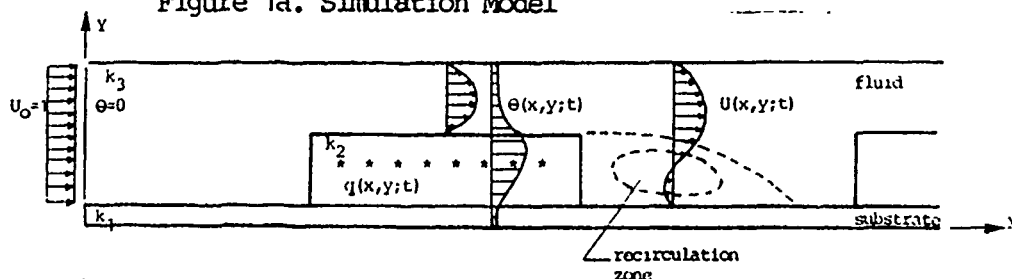


Figure 1b. Velocity and Temperature fields

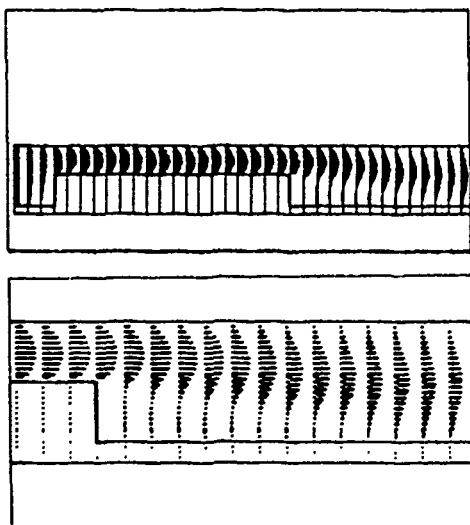


Figure 2. Steady state velocity distribution

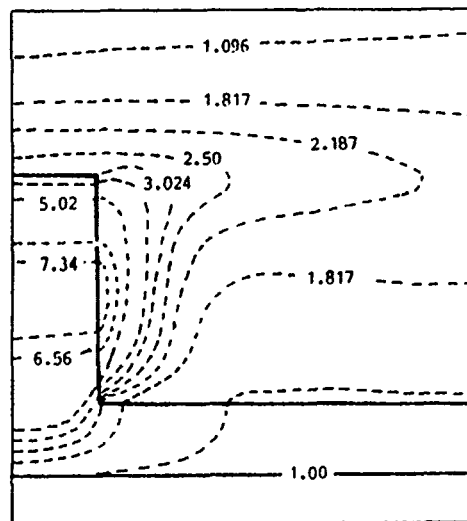


Figure 3. Steady state temperature field behind a chip under constant surface heat flux

## FLOW FORCES IN SPOOL-TYPE HYDRAULIC VALVES

by Dr. Jan Ługowski

Mailing address: ul. Kotuli 5/38, 35-111 Rzeszów, Poland

The theory explaining the origin of the axial flow force  $F$  on the piston was first published by Lee and Blackburn /1/. They computed it from the efflux of momentum:

$$F = \rho \cdot Q \cdot u \cdot \cos \theta \quad (1)$$

At larger valve openings  $x$  the jet angle  $\theta$  was assumed to be  $69^\circ$ .

There exists a simple and reliable way to verify this theory, namely by simultaneously recording the static-pressure distributions both on the piston and on the sleeve. Disregarding friction forces, it is the static pressure that produces the flow force on the piston. Following the theory, a larger radial flow force:

$$F_r = \rho \cdot Q \cdot u \cdot \sin \theta \quad (2)$$

should act on the sleeve.

Figure 1 (a) shows the valve. Both the piston face AB and the sleeve wall EF had 12 measuring slots each connected to pressure gauges. The slots covered the distance of 1.2 mm (0.047 in.) downstream both the piston and sleeve control edges. The piston diameter was 30.28 mm (1.192 in.). Radial clearance was 0.01 mm (0.0004 in.).

Figures 1 (b) and (c) show the recorded static-pressure distributions at a relatively large valve opening  $x$ . All flow parameters, except for valve inlet pressure  $p_i$  and valve outlet pressure  $p_o$ , were the same to provide for the same rate of flow  $Q$  and velocity  $u$  of jet  $u$ , see eqn. (1). The axes of both coordinate systems also show the actual arrangement of piston and sleeve to each other. With pressure  $p_o$  appearing on face CD of the piston, the hatched areas produce the axial flow force acting in a direction to close the valve port. The dotted area produces the axial flow force acting in the opposite direction. Contrary to eqn. (1), the magnitude of the pressure  $p_o$  strongly influenced the magnitude of the computed flow forces  $F$ . No significant decrease of the static pressure was recorded on the sleeve, contrary to eqn. (2).

High pressure peaks appeared on the sleeve only at small valve openings /2/. They were accompanied by only low pressure peaks on the piston. At valve openings exceeding 0.054 mm (0.0021 in.) the pressure peaks abruptly decreased on the sleeve and increased on the piston.

This fluid behavior can be explained by the Coanda effect. Similarly as it provides the lift force on airplane wings, the Coanda effect causes the flow force to appear on the piston. The magnitude of the flow force is influenced by many factors, not only by the magnitude of the efflux of momentum. The Coanda effect makes the issuing jet flow along the walls, not at the angle  $\theta = 69^\circ$ .

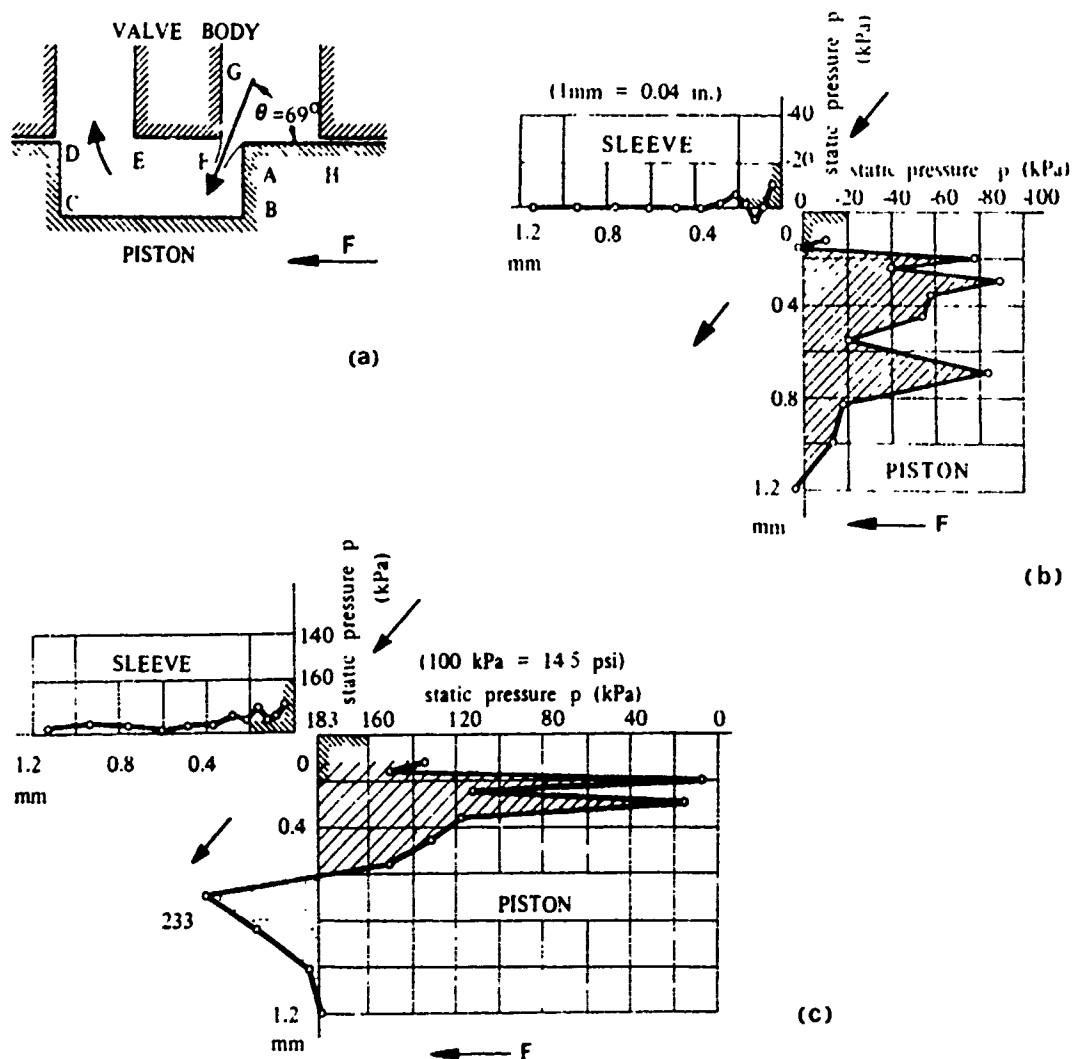


Fig. 1 Static-pressure distributions and computed flow forces at  $x=0.1$  mm (0.004 in.) and  $Q=17.3$  L/min (17.6 in<sup>3</sup>/sec): (a) flow by Lee and Blackburn /1/; (b)  $p_i=853$  kPa (123.7 psi),  $p_o=0$ ,  $F=3.1$  N (0.68 lbf); (c)  $p_i=1040$  kPa (158.8 psi),  $p_o=183$  kPa (26.5 psi),  $F=2.4$  N (0.53 lbf)

#### References:

- /1/ S.-Y. Lee, J.F. Blackburn: "Contributions to Hydraulic Control - 1 - Steady-State Axial Forces on Control-Valve Pistons", Transactions of the ASME, Vol. 74, August 1952, pp. 1005-1011.
- /2/ J. Ługowski: "Flow Forces in Spool-Type Hydraulic Valves", manuscript sent in June 1991 for publication in the Transactions of the ASME, Journal of Fluids Engineering.

## AEROSOL PARTICLE BOUNCING IN CASCADE IMPACTORS

Josef Podzimek, Kakkattukuzhy M. Issac, and Bisma Husen  
Department of Mechanical and Aerospace Engineering and  
Engineering Mechanics and Cloud and Aerosol Science Laboratory  
University of Missouri-Rolla  
Rolla, Missouri 65401-0249

Cascade impactors have been widely used during the past several decades for measuring the size distribution of aerosols generated in the atmosphere and during industrial processes as well. Most of them are designed as cascade impactors in which the particles with the largest inertial mass are impacted onto the first stage substrate and smaller particles are deposited successively on the following stages. Many theoretical studies of the mechanism of particle deposition under a jet or rectangularly shaped nozzle illuminated well the main parameters affecting the motion of the solid particles or droplets under the nozzle and along the substrate sideways. The results of these studies are briefly reviewed and several of the most salient and still unanswered questions formulated. Among these, the particle bouncing at the substrate and its dependence on the flow pattern, state of the particle and of the substrate at different environmental conditions still represent one of the most attractive subjects of particle separation and two-phase flow research.

Most of the particle bouncing investigations in cascade impactors dealt with the jet flow pattern which might be seemingly simpler for the mathematical modeling of particle deposition and comparison of the theoretical results with the experimental work. We used a simple two-dimensional Hiemenz flow model of a boundary layer over a flat plate superimposed to the hyperbolic potential flow describing the particle deposition under a rectangularly shaped long nozzle which can be compared with the particle deposition in the four-stage UNICO impactor frequently used in our laboratory. The main goal was to answer the cardinal question raised by several authors whether the impactor particle bounce errors are caused by the flow pattern and vortice formation around the nozzle's edge or by the back spin caused by some kind of Magnus effect acting on spherical particles in a shear flow close to the impactor's wall.

A simple model of the spherical particle motion in a shear flow close to the impactors wall is discussed and the potential effect of the particle spinning on its deposition assessed. In spite of the fact that this mechanism seems not be predominant in explaining the particle deposition in UNICO impactor, it can help to explain the multiple bouncing zones of the deposited dry salt particles on the sampling glass slide covered with a very thin gelatine layer (Fig. 1). The Liesegang circle (spot test) technique is used for detecting the deposited salt particles (containing chlorides) if they impact a gelatine layer sensitized by a weak solution of silver nitrate (to 8% gelatine solution was added 10% solution of  $\text{AgNO}_3$  in the ratio 20:1). A similar pattern of deposited salt particles shown in Fig. 1 which corresponds to particle deposition in Stage I of UNICO impactor has been found in stages II, III, and IV with some markable deviation in Stage III. It reveals that the "wave length" of the deposited particles is

comparable and does not depend very much on different geometry and different air speed in the individual nozzles of the impactor. For comparison, a similar investigation has been done with insoluble titanium oxide particles impacting a dry glass slide. The difference in a deposited particle pattern is explained by the different state of the sampling substrate, by different environmental conditions, and, possibly, by the different properties of the deposited particles (mainly their aerodynamic diameters).

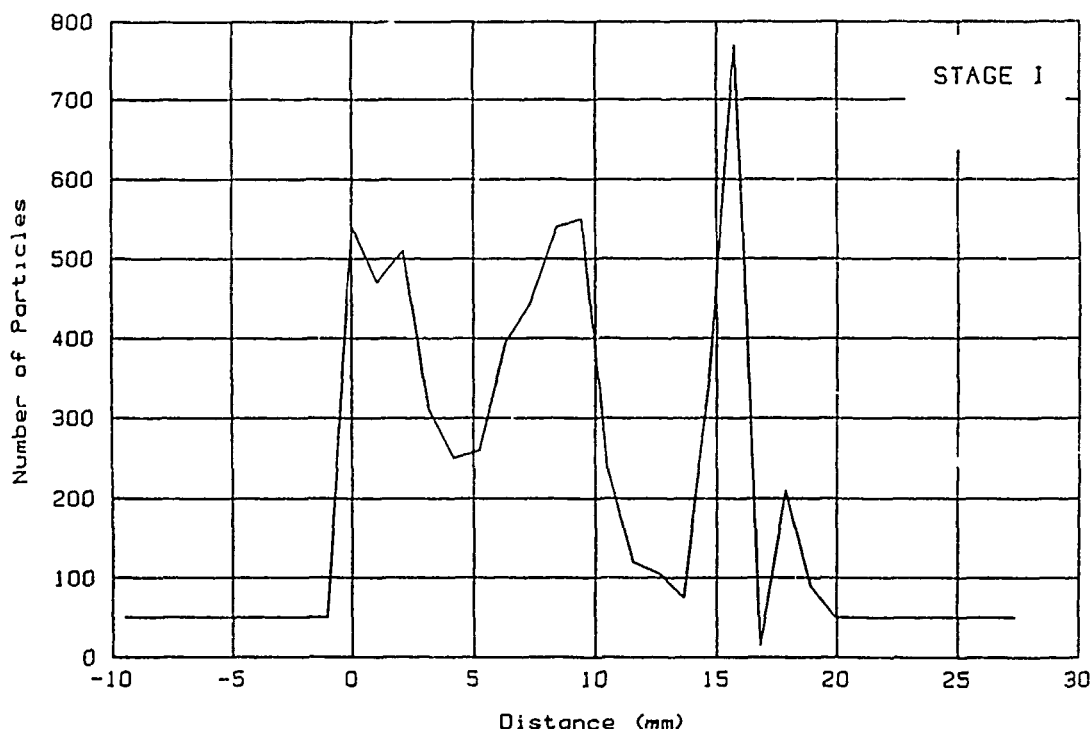


Fig. 1 Number of salt particles deposited at different distances from the nozzle's edge on the gelatine covered slide.

The main effect seems to have, however, the space behind the slightly unsymmetrical nozzle which affects the formation and possibly the releasing of vortices at the sharp edge due to the increasing pressure and bouncing of particles at the subsequent stage. The formulas suggested by several authors for determining the location of a stable vortex at the nozzle's edge from its dimension distance from the sampling substrate and air flow parameters of a jet-impactor is not applicable for UNICO instruments.

In conclusion, we suggest that the air flow conditions in and around the nozzle affect most the particle deposition in UNICO impactor, but that also the particle back spin in a shear flow, state of the particle and of the substrate might explain well the bouncing of the large particles and their deposition on the subsequent (small particle) stages.

# THE NEAR WAKE FLOW REGIME OF SEMI-CYLINDRICAL BODIES IN TURBULENT BOUNDARY LAYERS

B.Tahouri and N.Toy  
Department of Civil Engineering  
University of Surrey, Guildford GU2 5XH, United Kingdom.

## Introduction

Semi-cylindrical bluff bodies immersed in turbulent boundary layers occur in many branches of engineering in the form of barrel vault industrial buildings and surface protrusions on boundaries in either external or internal flows. As in the case of other surface mounted bluff bodies with surface curvature, the boundary layer flow around a horizontal semi-cylinder has received very little attention. The only notable published data, [1,2] illustrated the streamwise extent of the recirculation region in terms of mean velocity profiles. The work presented in this paper is a wind tunnel investigation of the recirculation region in the near wake of semi-cylinders of two types of cross-sectional geometry. Profiles of longitudinal mean velocity and turbulence intensity were obtained by undertaking centre-line point measurements in the region from separation to reattachment on the ground plane. The effects of model surface roughness on the extent of the near wake regions are discussed. In addition, the influence of the flow separation upon the thickness and growth of the highly curved shear layers is examined.

## Summary of experimental details

The wind tunnel used in the investigation had working section dimensions of 1.676 m (height) x 1.372 m (width) x 9.0 m (length). Whilst the effects of different approach boundary layers were examined in the main investigation [3], the data presented here are associated with a naturally developed thin boundary layer, the characteristics of which are given in the following table:

Boundary layer Thickness(mm)	Displacement Thickness(mm)	Momentum Thickness(mm)	Power law exponent, n
98	15.6	11.3	0.158

Two models, denoted as I and II, were used in the experiments, each 95mm high, 380mm long and with cross sections as shown in Figure 1. The cross-section of model I was a complete semi-circle while, having the same surface curvature, model II included a sharp ridge at the top in order to produce fixed flow separation. All the tests were conducted at a Reynolds number of  $6.6 \times 10^4$ , based on the models height and a freestream velocity of 10 m/s. The measurements were initially carried out on models with smooth surfaces. Supercritical flow conditions were simulated by artificially roughening model surfaces, with a roughness ratio of about 0.01, to induce flow separation. The velocity and turbulence measurements were taken using a Pera Instruments pulsed-wire anemometer attached to the sting of a computer-controlled traversing mechanism. Profiles of the longitudinal mean velocity and turbulence intensity were obtained over a two-dimensional grid on the centre-line of the near wake region of each model.

## Results and discussion

Figures 2 and 3 illustrate the longitudinal streamlines on the centre-line downstream of the two models with no surface roughness. They were obtained by integrating the normalised mean velocity profiles to compute the streamfunction in the vertical plane. It can be noted that the flow over model II separates

earlier, at the ridge, forming a shear layer positioned at a greater angle to the ground plane. The distance to reattachment is greater for model II, about 3 heights, as compared to 1.7 heights for model I. The effect of roughness on the wake flow of model II was found to be negligible as expected. For model I, however, it was noted that the rough surface produced an initially slightly thinner shear layer positioned further away from the ground and, consequently, the distance to reattachment was increased to about 2.7 heights. The two different wake regimes of model I with and without surface roughness are presented in Figure 4 as the mean turbulence intensity profiles on the wake centre-line.

#### References

- [1] Sakamoto H., Kiya M. and Arie M. (1977), Trans. JSME 42, 3224-3232.
- [2] Toy N. and Fox T.A. (1984), Proc. Third Int. Conf. Space Structures, 271-276.
- [3] Toy N. and Tahouri B. (1990), AFRC Final Rept. Agreement No. AG90/14.



Figure 1 Cross-section of models

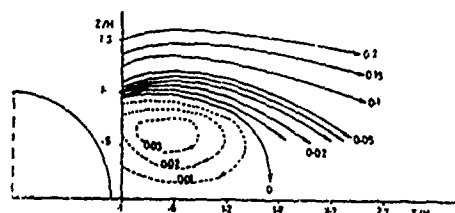


Figure 2 Streamlines for smooth model I

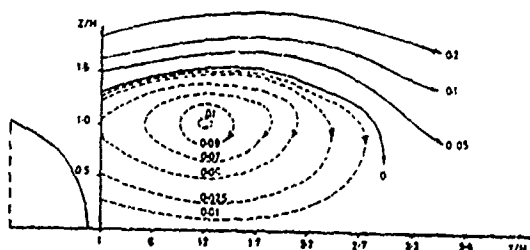


Figure 3 Streamlines for smooth model II

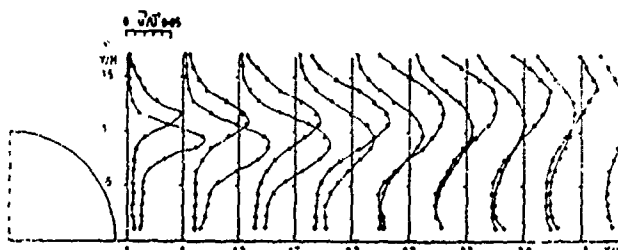


Figure 4 Centre-line turbulence intensity profiles of model I, ●; smooth, ○; rough



# AN NEW KIND OF EXPERIMENTAL FACILITY FOR STUDY OF THE STEADY AND UNSTEADY ROUND JET

Steven P. Schneider, Assistant Professor  
Shucheng Zhang, Graduate Research Assistant  
School of Aeronautics and Astronautics  
Purdue University  
West Lafayette, IN 47907

## Abstract

A round jet emerging into stagnant ambient fluid is a fundamental flow with many applications. As part of an investigation into the control of this flow, an flow-down experimental facility with a maximum jet Reynolds number of  $3 \times 10^5$  has been constructed. The facility is gravity driven, with a 2 inch diameter jet that empties into a test section 48 diameters long. A novel feature of the facility is a computer controlled valve which is used to set and maintain the jet flow rate; the construction and operation of this closed loop feedback system is detailed. The valve can also be used to form unsteady jets.

## General Facility Design and Fabrication

Research inspired by Reynolds' blooming jet work [2] is to be carried out using the heater perturbation technique used in [4]. The first step in the research has been to fabricate an axisymmetric water jet apparatus.

The facility has a 3x3x8 foot horizontal glass test section, into which a 2 inch diameter jet enters at one end. The test section was sized to allow study of the medium-far field of the jet [5]. The glass rests on neoprene gasketing in a welded carbon steel frame. The three 3x8 foot glass sheets are 3/4 inch thick tempered plate glass, designed using [3]. The two 3 foot square ends of the tank are half inch thick tempered plate glass. The top is open.

The jet enters through one end, which has a 6 inch diameter hole in which the jet assembly mounts. A 2 inch exit diameter 16:1 contraction ratio fifth order polynomial axisymmetric nozzle was available from a earlier project [1]. The flow enters the nozzle through an eight inch diameter flow conditioning section placed downstream of the computer controlled valve. This flow conditioning section contains a perforated plate, a honeycomb, and two screens.

The test section overflow is driven by gravity through four 4.5 inch diameter holes in the glass end opposite the jet. The holes are fitted with 4 inch PVC piping which leads to four flexible tubes that feed a plexiglas manifold located on top of the dump tank. The manifold can be raised or lowered using a threaded rod assembly in order to vary the initial height of the water in the test section. When the jet flow starts, the water level rapidly rises, driving flow out of the test

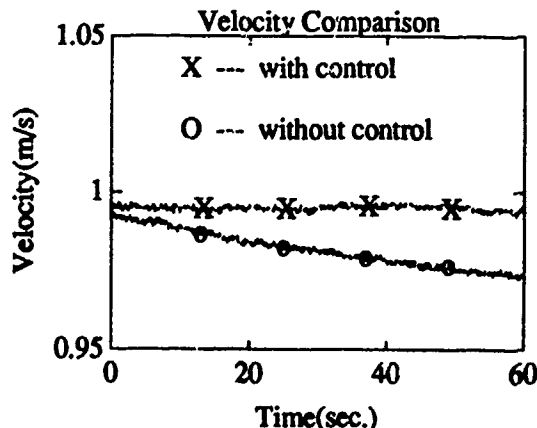
section. The test section water level rapidly reaches an equilibrium between the incoming jet flow and the slow gravity driven outflow through the four large pipes, which are carefully balanced in order to minimally affect the far field behavior of the jet.

500 gallon polyethylene tanks are used as reservoir and dump tanks, providing 140 seconds of run time at the maximum flow rate. The reservoir tank is mounted on a pallet rack 18 feet above the floor, 14 feet above the jet level. A 2 horsepower centrifugal pump allows the reservoir tank to be refilled in about 5 minutes.

### Closed Loop Computer Controlled Flow Control Valve

A computer-controlled valve is used to maintain a constant flow rate in the jet; the control can be modified to allow for unsteady flow experiments. The valve is made from a 4 inch PVC butterfly valve (G.F. Signet) turned by a Compumotor computer controlled microstepping stepper motor. A rotary milling table is used as a transmission. A Compuadd 80386 computer is used to order the opening of the valve; *the data acquisition system of the computer is not used for the constant velocity valve control, leaving the A/D and CPU free for other duties.* The velocity transducer signal is fed to a comparator, which compares it to the output of a voltage reference and outputs a digital open/stop signal to the trigger input of the Compumotor controller. This system is currently being improved; current results are given in the following figure:

The velocity at the 2 inch exit is set to 1.0 meters per second. Without control, the velocity decreases by 1.21% over the course of one minute, due to the dropping water level in the reservoir tank. With control, this velocity reduction is only 0.075%. These results are better if the velocity is higher. The control system is currently being developed further and we expect to report better results at the meeting. The key item seems to be the design of the comparator circuit.



### Acknowledgments

Professor C.H.K. Williamson helped with the design of the glass tank.

### References

- [1] Roger E. Davis. *Secondary Flow and Three-Dimensional Separation in Curved Circular Ducts*. PhD thesis, School of Aeronautics and Astronautics, Purdue University, May 1990.
- [2] P.J. Juvet and W.C. Reynolds. *Entrainment Control in an Acoustically Controlled Shrouded Jet*. Paper 89-0969, AIAA, March 1989.
- [3] G. W. McLellan and Errol B. Shand. *Glass Engineering Handbook*. McGraw-Hill, 1984.
- [4] S. P. Schneider. *Effects of Controlled Three-Dimensional Perturbations on Boundary Layer Transition*. PhD thesis, Graduate Aeronautical Laboratories, California Institute of Technology, March 1989.
- [5] I. Wygnanski and H. Fiedler. Some measurements in the self-preserving jet. *Journal of Fluid Mechanics*, 38:577-612, 1969.

## PRESSURE COEFFICIENT MEASUREMENTS OF A CYLINDER IN CROSSFLOW AT HIGH BLOCKAGE RATIOS

N. Saniei

Mechanical Engineering, Southern Illinois University  
at Edwardsville, Edwardsville, IL 62025-1805

### ABSTRACT

The pressure distribution over a single cylinder in a duct with low and high blockage ratios were investigated. The aspect ratio for all the measurements was 20. Low blockage measurements were performed as a base of comparison with other investigators and to confirm the validity of the experimental results for high blockage cases. For cases of high blockage, the pressure distribution along the confining wall, mean velocity, turbulent intensity, and Strouhal frequency were also measured. At high blockages ( $D/H = 0.3, 0.5, 0.667, 0.73$  and  $0.8$ ), the minimum pressure coefficient decreased with increasing blockage, and the separation point moved downstream at higher Reynolds number. These effects were also observed at higher blockage with a constant Reynolds number. The difference between maximum and minimum pressure along the confining wall increased at a higher blockage ratio. No dominant frequency was recorded for blockages above 0.5.

The heat transfer rates from a circular cylinder in external cross flow have been studied for many years. To interpret heat transfer results, an understanding of the flow field or, at least, the pressure distribution which gives a partial glimpse of the flow field is needed. Several studies have shown that both blockage and aspect ratio strongly influence the pressure distribution, the drag coefficient and the point of separation. West and Apelt (1982) investigated the variation of drag coefficient and base-pressure coefficient with Reynolds number at various low blockage ratios from 2 to 16 percent. At the lower aspect and blockage ratios, a decrease is observed in the pressure distribution around the cylinder. Hiwada and Mabuchi (1982) conducted experiments for a constant Reynolds number of  $4.5 \times 10^4$  and varied blockage ratios from 0.4 to 0.8. As the blockage ratio increased, the pressure coefficient decreased except at the stagnation point. The pressure distribution along the confining walls is needed for a better understanding of the pressure distribution over a cylinder with blockage. A boundary layer develops along its length, and it may be sufficient to interact with the boundary layer developing on the cylinder.

In this study, measurements of static pressure along the confined wall for symmetric cases of high blockage ratio were conducted. Velocity profiles and turbulent measurements were performed upstream of the cylinder and between the confined walls to determine the boundary layer thickness and its nature (laminar, turbulent). The tunnel test section was a rectangular duct,  $1.016 \text{ m} \times 0.609 \text{ m}$ . The velocity profile for the empty tunnel was uniform within 1% at  $Re = 10^5$ , and the turbulent intensity was 0.3%. The cylinder was made of two aluminum alloy tubes (5.06 cm OD, 4.76 cm ID and 47.8

cm long) which were spaced by an acrylic rod 5.08 cm long. The pressure taps were 20 circumferential holes of 2.5 mm ID drilled 0.85 cm deep around the circumference of the acrylic rod at its middle. Two pieces of plywood (101.6 cm x 76.2 cm x 1.27 cm) were used to construct the confining walls. The pressure difference between the stagnation point and each angular position (around the cylinder), pressure along the confining walls, the profile of mean velocity and turbulent intensities, and Strouhal frequencies were measured. Pressure coefficient for the cylinder was defined as:  $C_p = 1 - (P_0 - P_\theta)/(1/2 \rho_a u_\infty^2)$ , and for the confining wall was defined as:  $C_p' = (P_s - P_a)/(1/2 \rho_a u_\infty^2)$ .

To examine the effect of high blockage ratio and the Reynolds number on pressure distribution, a total of ten different cases were considered from which five cases are presented here for discussion (case 1 to 5). A comparison of results for the two Reynolds numbers of 18000 and 39000 at a blockage of 0.8 is discussed first. The position of  $C_{p_{min}}$  was almost independent of the Reynolds number and the  $C_p$  distribution shifts to a lower position with respect to the magnitude and recovers noticeably at a higher Reynolds number. This is due to the difference in interactions of boundary layers in different cases. In the case of a higher Reynolds number, a turbulent boundary layer develops along the wall, and its impingement on the cylinder causes transition on the cylinder and, hence, a delay in separation and a larger pressure recovery. The velocity profile is consistent with a turbulent flow along the confining wall, and the wall boundary layer thickness as the flow approaches the cylinder exceeds the distance between the cylinder and the wall ( $\delta_\tau = 1.219 \text{ cm} > G = 0.635 \text{ cm}$ ). In the case of a low Reynolds number, a laminar boundary layer is expected on the wall, and small recovery and no delay of the separation are observed for the cylinder. Separation shifts slightly downstream at the higher Reynolds number and back pressure is lower at the lower Reynolds number. No dominant frequency was observed in either case since vortex shedding was suppressed due to high blockage. In the case of a higher Reynolds number, pressure along the wall remains constant at the leading edge up to  $X/D = -1.0$  where the presence of the cylinder is not yet felt by the wall boundary layer. Pressure decreases, and the minimum pressure occurs at  $X/D = 0$ . A fairly large recovery follows  $C_{p'_{min}}$ . In the case of lower Reynolds number, a similar pattern is observed; however, after  $C_{p'_{min}}$ ,  $C_p'$  stays almost constant. Obviously, the interaction between the wall boundary layer and the cylinder boundary layer is felt more for the higher Reynolds number as compare to the lower Reynolds number. A higher Reynolds number results in lower  $C_p'$  up to  $X/D = 0.5$  and higher  $C_p'$  thereafter (cross over). The turbulent intensity is higher in case of the higher Reynolds number. The dimensionless velocity profile is fairly constant for the case of higher Reynolds numbers (turbulent boundary layer) and decreases at lower Reynolds numbers close to the wall (laminar boundary layer).

Measurements of  $C_p$  were carried out for a blockage ratio of 0.667 at three Reynolds numbers of 18000, 33700 and 60000 (cases 3, 4, and 5 respectively). Cases 1 and 3 may be selected for a comparison to discuss the effects of change in the blockage ratio at a constant Reynolds number.  $C_{p_{min}}$  shifts downstream as the blockage ratio increases and the magnitude of  $C_{p_{min}}$  is lower in the case of the higher blockage. This is due to the velocity increase and pressure decrease for the higher blockage case. The separation point shifts downstream in the case of higher blockage. The pressure drop is higher at higher blockage due to the flow acceleration, and the location of minimum pressure is almost independent of the blockage ratio.  $C_p'$  patterns look alike in both cases, but higher blockage results in higher  $C_p'$  up to  $X/D = -0.25$  and lower  $C_p'$  thereafter. The turbulent intensity is higher at the higher blockage and the velocity profiles look similar in both cases in the sense that they both increase first and decrease later when the hot wire is moved into the plate boundary layer (this is expected since boundary layer thicknesses are equal in both cases, the same Reynolds number, laminar boundary layers).

## SPATIAL RESOLUTION OF AN ANAMORPHIC OPTICAL PROCESSOR FOR MEASURING SPECKLE PATTERN DISPLACEMENTS

Steven H. Collicott, Assistant Professor  
School of Aeronautics and Astronautics  
Purdue University  
West Lafayette, IN 47907-1282

### ABSTRACT

An anamorphic (non-axisymmetric) optical processor can be used to measure single-component velocity profiles directly from double-exposure speckle photographs. The effect of the unmeasured velocity component is described, as is the spatial resolution in this direction. Analysis shows that a trade-off exists between the tolerance to the unmeasured component and the spatial resolution. An anamorphic optical processor with resolution equivalent to the traditional axisymmetric (2-D Fourier transform) processor has equivalent velocity measurement capabilities and is about two orders of magnitude faster because of the use of 1-D image processing. With small modifications, the anamorphic processor can measure velocity profiles in some flows with much better spatial resolution than is possible with the axisymmetric processor.

### PROBLEM DESCRIPTION

Measurement of displacements in double-exposure speckle patterns has been performed in a variety of manners over the years, from almost entirely digital<sup>1</sup> to almost entirely optical<sup>2</sup>. These techniques all measure two velocity components in a small region, commonly called a point. Often times in fluid mechanics, it is a velocity profile, that is, the distribution of one velocity component in a perpendicular direction, which is of interest. It has been shown that a velocity profile may be measured directly from the double-exposure speckle pattern with an anamorphic optical processor<sup>3</sup> as shown in Figure 1. In the simplest description, one cylindrical lens performs a one-dimensional Fourier transform to produce fringes of frequency proportional to one velocity component, and the other cylindrical lens performs a one-dimensional imaging operation, thereby permitting all the points in a line to be Fourier transformed in parallel. An interrogating sheet is used in place of the interrogating beam found in axisymmetric processors.

The spatial resolution in the Fourier transform direction is set by the sheet thickness, analogous to the beam diameter in the axisymmetric processor. The spatial resolution in the imaging direction is set by the speckle size, the 1-D imaging magnification, and the width of 1-D imaging impulse response. These lengths combine to determine the spatial resolution because of the convolution in the imaging operation. The velocity component in the imaging direction is termed the "cross-flow" velocity, and its primary effect is to reduce fringe modulation. If the cross-flow is larger than the imaging direction spatial resolution in the plane of the double-exposure, then the fringe modulation will be diminished to the extent that the fringe frequency will not be measurable. The optical processor averages in the imaging direction over a distance in the double-exposure given by  $\Delta_{im} = d_{sp} + \lambda f_y (1 + 1/M_y)/L_y$ , see Figure 1 for definitions. Analysis is based on a Fourier Optics description of the processor, and on the statistics of fully-developed speckle patterns. Results of the analysis quantify the degradation of fringe modulation with increasing magnitude of the cross-flow velocity, and shows that the minimum value of  $\Delta_{im}$  is set not by the optical system, but rather by the flow field being measured<sup>4</sup>.

An anamorphic processor with spatial resolution equivalent to a traditional axisymmetric processor will have both the sheet thickness and  $\Delta_{sm}$  equal to the axisymmetric interrogating beam diameter. This implies that the anamorphic processor will tolerate a cross-flow velocity as large as the maximum velocity being measured, that is, it will form fringes at any orientation of the double-exposure. Thus the anamorphic processor will be able to measure both velocity components throughout the double-exposure by scanning the sheet once, rotating the double-exposure by 90 degrees, and scanning through again. In some cases, cross-flow tolerance as large as the maximum velocity may not be necessary. For instance, when an image-shifting device is used to resolve directional ambiguity, or if the flow is predominantly in one direction, then there is a known bias to the displacement field, and a system may be designed to consecutively measure two velocity components with a smaller cross-flow tolerance and thus higher spatial resolution.

## CONCLUSIONS

Anamorphic optical processors may be designed to measure velocity profiles directly from double-exposure speckle patterns. In some cases, this will result in spatial resolution superior to that of the traditional axisymmetric optical processor. When designed to have spatial resolution comparable to that of the axisymmetric processor, the anamorphic processor can measure the same two-dimensional velocity field but in considerably less time. The time savings are a direct result of the use of one-dimensional FFTs or autocorrelations in place of the usual two-dimensional routines. Specifically, the method is faster by a factor of  $N$ , where  $N$  is the number of pixels across the fringes, typically 128 or 256. This permits more creative signal processing algorithms to be implemented to measure the fringe frequencies.

## ACKNOWLEDGEMENTS

This work was partially supported by ONR contract N00014-83-k-0053 under the direction of Professor L. Hesselink at Stanford University.

## REFERENCES

1. C. C. Landreth and R. J. Adrian. "Measurement and refinement of velocity data using high image density analysis in particle image velocimetry", in *Applications of Laser Anemometry to Fluid Mechanics*, Springer-Verlag, 1989.
2. B. Bates and P. C. Miller. "Liquid crystal television in speckle metrology", *Applied Optics*, 27:2816-2817, 1988.
3. S. H. Collicott and L. Hesselink. "Anamorphic optical processing of multiple-exposure speckle patterns", *Optics Letters*, 11:410-412, 1986.
4. S. H. Collicott. *Laser Speckle Velocimetry with Photorefractive Recording and Anamorphic Optical Processing*, Ph.D. Thesis, Stanford University, 1991.

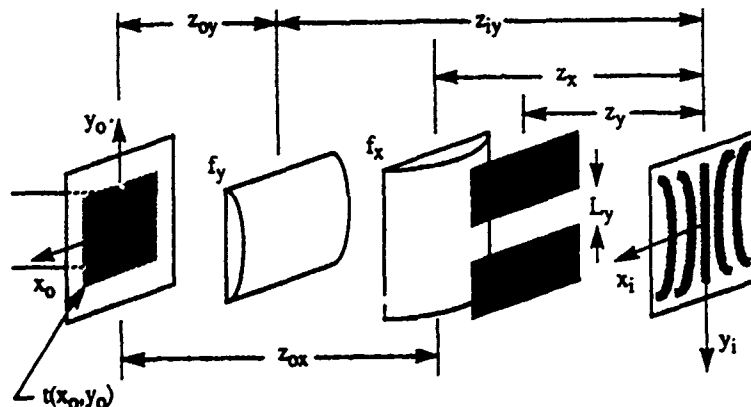


Figure 1. Diagram of anamorphic optical processor. Wavelength of the light is  $\lambda$ , speckle size in the double-exposure is  $d_{sp}$ ,  $f_x$  is the focal length of the Fourier transform lens,  $f_y$  is the focal length of the imaging lens, and the magnification is  $M_y = z_{1y}/z_{0y}$ .  $x$  is the Fourier transform direction.

# TWIN CIRCULAR JETS IN A CROSSFLOW - A COMPARISON OF EXPERIMENTAL TECHNIQUES

N Toy, E Savory and S Ahmed  
Department of Civil Engineering  
University of Surrey, Guildford GU2 5XH, United Kingdom

## Introduction

The single circular jet issuing normally into a crossflow is a classic fluid mechanics problem and, as such, has been the subject of considerable research [1,2]. In contrast, studies of multiple jets in a crossflow are more limited [3,4,5], although these flows are of particular importance in dilution zone mixing inside combustion chambers [6,7]. Investigations concerning two jets, either in-line or side-by-side, have been carried out by other workers [8-12]. However, in many of these multiple jet studies the aim has been to determine overall mixing efficiencies rather than to examine the actual flow fields themselves. In a previous study [13] the present authors demonstrated the application of an image processing technique for quantitative flow visualisation analysis of smoke-seeded, turbulent side-by-side twin jets in a crossflow. In this paper comparisons are now made between those measurements and data obtained recently using a more conventional technique, namely a five-hole pressure probe for determination of local velocity vectors.

## Summary of experimental details

The apparatus and smoke flow visualisation technique used for the twin jet study have been fully described previously [13]. Briefly, a specialised smoke tunnel was utilised with a separate jet rig, located on the tunnel roof, comprising smoke generator, fan, plenum chamber and nozzles. The smoke-seeded jets issued normally through 13.5mm diameter ( $D$ ) nozzles flush with the inside of the tunnel roof. Nozzle centre spacings ( $S$ ) of  $1D$ ,  $3D$  and  $5D$  were utilised in a side-by-side arrangement, for jet velocity ( $U_j$ ) to crossflow velocity ( $U_c$ ) ratios ( $\alpha$ ) of 6, 8 and 10. The smoke jets were illuminated by a single laser beam, whilst a CCD video camera (mounted with the laser outside the tunnel) was used to record the time history of the resulting fluctuating line of smoke-scattered light. Analysis of the data produced the intermittency function along the line ( $I=1$  for fully turbulent flow,  $I=0$  for fully non-turbulent flow). By traversing the laser and camera complete  $YZ$  planes of measurements were obtained over a range of downstream ( $X$ ) locations. A crossflow velocity of  $1\text{m/s}$  was used resulting in a Reynolds number, based on nozzle diameter, of  $9.3 \times 10^3$ . Velocity vector distributions in  $YZ$  planes were obtained using a five-hole pressure probe which had an external diameter of  $2.3\text{mm}$  and an included angle at the tip of  $90^\circ$ . The probe was fully calibrated in pitch and yaw over angular ranges of  $\pm 30^\circ$  in increments of  $2.5^\circ$ , using a similar method to that described in [14]. The five tube pressures, together with the crossflow total pressure, were connected, via a Scanivalve switch, to a pressure transducer referenced against the tunnel static. All data acquisition and analysis, together with traversing of the probe through the flow field, were carried out under computer control. A crossflow velocity of  $6\text{m/s}$  was used for these tests giving a Reynolds number of  $5.5 \times 10^3$ .

## Results and discussion

It is only possible to illustrate in this paper a very limited selection from the data and, for the purposes of discussion, the case with  $\alpha=6$  and  $S/D=5$  will be considered. Figure 1 shows the intermittency contours associated with the twin jets in the  $YZ$  plane located at  $X/D=10$  downstream of the nozzles. The

corresponding projected mean velocity vectors ( $V$  and  $W$  components) are illustrated in figure 2, for half the interaction region only. At this location the largest upwash ( $W$ ) velocities occur in-line with the jet exit and in this region the  $U$  component is reduced to approximately 90% of the freestream value. The centre of the dominant contrarotating vortex, as measured in the plane, is located at about  $Y/D=4.6$  and  $Z/D=5.5$ , whilst earlier experiments for the single jet case [15] give  $Y/D=2.8$  and  $Z/D=7.2$ . The increase in the lateral vortex location for the twin jet is to be expected due to the initial spacing of the two jets, whilst interference between the two closely spaced jets reduces the vertical penetration [4,6]. Comparing figures 1 and 2, the upwash region, which entrains non-turbulent fluid, corresponds to a decrease in the extent of the fully turbulent region in the area immediately in-line with the nozzles, as indicated by the indentation on the wall side of the  $I=1$  contour. For all the planes examined, the vortex centres tend to coincide with the centres of the outer lobes of maximum intermittency in the lateral direction, but with the  $I=0.5$  contour in the vertical direction. Further experimental work is in progress to establish additional correlations between the data obtained using the two techniques.

#### References

- [1] Bradbury L J S (1981), NATO AGARD CP 308
- [2] Hancock G J (1987), *Aero J*, 91, 201-213
- [3] Walker R E and Kors D L (1973), NASA CR-121217
- [4] Kamotani Y and Greber I (1974), NASA CR-2392
- [5] Karagozian A R, Nguyen T T and Kim C N (1986), *J Prop and Power*, 2, 354-360
- [6] Holdeman J D and Walker R E (1977), *AIAA J*, 15, 243-249
- [7] Khan Z A, McGuirk J J and Whitelaw J H (1981), NATO AGARD CP 308
- [8] Ziegler H and Wooler P T (1973), NASA CR-132297
- [9] Schwendemann M F (1973), Northrop Aircraft Div, Hawthorn, CA, USA, Rept NOR 73-98, May
- [10] Makiata T and Miyai Y (1979), *ASME J Fluids Eng*, 105, 91-97
- [11] Isaac K M (1982), PhD Thesis, Virginia Poly Inst and State Univ, Blacksburg, USA
- [12] Isaac K M and Jakubowski A K (1985), *AIAA J*, 23, 1679-1683
- [13] Savory E and Toy N (1991), *ASME J Fluids Eng*, to be published
- [14] Treaster A L and Yocum A M (1979), *ISA Transactions*, 18, 23-34
- [15] Toy N and Savory E (1988), MoD Final Rept, Agreement No 2064/088, November

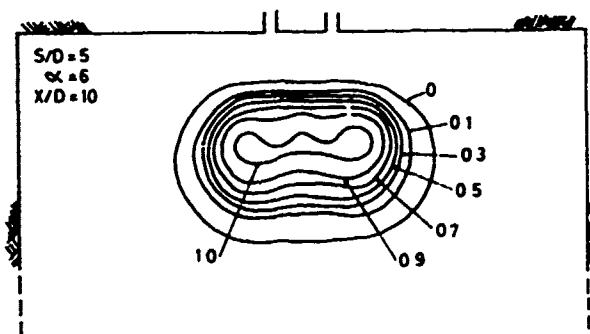


Figure 1 Contours of intermittency in YZ plane at  $X/D=10$

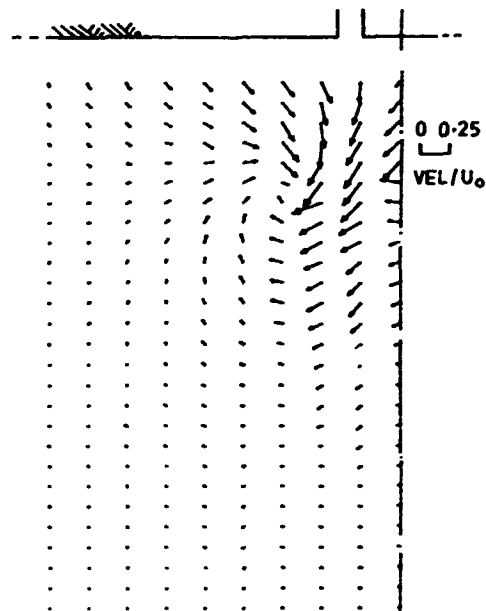


Figure 2 Mean velocity vectors in YZ plane at  $X/D=10$





Northern Jiaotong University  
Beijing China

# THE AERODYNAMIC INTERFERENCE AND STABILITY OF TWO H-SHAPED MEMBERS

Yu Xizhe, Chen Yinjun and Du Qing  
Dept. of Civil Engineering, Northern Jiaotong University  
Mail Code 100044, Beijing, CHINA

## ABSTRACT

The present paper, the aerodynamic interference experiments of two H-shaped members elastically mounted in the wind tunnel are performed. Both tandem and stagger arrangements of members is taken and the angle between the direction and plane of members'axe is changed also in the these tests. The experimental results has indicated that the response of the downstream member is greater than that of the upstream one in the case of most positions. Besides, the experimental investigations also show that the wake field of the member shows overtly turbulent flow.

In this paper according to stochastic theory of aeroelasticity, the stochastic differential equation of system vibration with random factors is established, and then, the vibrating stability and response of the member in wake field corresponding to the turbulence flow excitation are obtained.

The research results demonstrate a good agreements with observational phenomenon.

# THERMALLY INDUCED INTERFACIAL MICRO-CRACKING IN POLYMER MATRIX COMPOSITES

D.L. Hiemstra and N.R. Sottos  
Department of Theoretical and Applied Mechanics  
University of Illinois at Urbana-Champaign  
Urbana, IL 61801

## INTRODUCTION

The structure and properties of internal fiber/matrix interfaces may control many of the thermo-mechanical properties of the overall composite. The interface serves as a critical area where forces are transmitted between fiber and matrix and subsequently where stress concentrations arise due to the abrupt change in material properties. In particular, significant interfacial thermal and residual stresses can develop during manufacturing due to the mismatch of thermal expansion coefficients. Several studies [1,2] have shown that these stresses may become large enough, even in the absence of applied stress, to exceed the failure stress of the matrix and cause micro-cracking in the vicinity of the fiber/matrix interface. Interfacial micro-cracking due to thermal fatigue has also been observed experimentally using SEM stereo-micrographs [3].

At present, there has been no quantitative prediction or measurement of the micro-cracking which might occur due to local thermal stresses. Additionally, no quantitative assessment of the influence of micro-cracks on overall composite failure and performance has been made. In the current study, both experimental and computational methods are utilized to analyze and predict the formation of micro-cracks in polymer matrix composites. In particular, the influence of fiber spacing and local material properties near the interface are investigated.

## COMPUTATIONAL/EXPERIMENTAL STUDIES

Many analytical, computational and experimental techniques have been developed for studying the local thermal stress state in composites. Most of these investigations assume a uniform packing of fibers such as a square or hexagonal array. However, if a cross-section of high volume fraction continuous fiber composite is studied under the microscope, the packing arrangement is highly non-uniform. Many fibers are actually touching. Recent studies by Sottos, et al. [1] have suggested that extremely high thermal stresses develop at the point of fiber-fiber contact. Thus, there is a high probability of micro-cracking initiating at or near touching fibers.

A finite element approach is adopted to first predict the micro-thermal stress state as four fibers are brought into contact in an infinite matrix. A schematic of the unit cell is shown in figure 1. A distinct but uniform region (interphase) is included around the fiber so that the effects of local material properties can also be studied. Thermal stresses are predicted for several values of the inter-fiber spacing,  $d$ , as  $d$  approaches zero. An appropriate failure criterion is then applied to determine the most probable point for micro-cracking to occur. In figure 2, the radial and hoop stresses are plotted as a function of radial distance along the top boundary of the symmetry cell for a value of  $d = 2$  fiber radii. Typical properties of an epoxy matrix and carbon fiber were chosen

for the analysis. Both stress components are constant in the fiber at this spacing and the maximum values of stress occur at the fiber/matrix interface. The existence of a tensile hoop stress tends to craze and crack the matrix.

Experimental investigations to detect micro-cracking are also carried out for the configuration in figure 1. Four carbon fibers are carefully embedded in an epoxy matrix. Optical and electron microscopy is utilized to study the micro-cracks induced by processing. Computational thermal stress predictions are compared with experimentally observed micro-cracking. The influence of both the inter-fiber spacing and the fiber surface treatment are investigated.

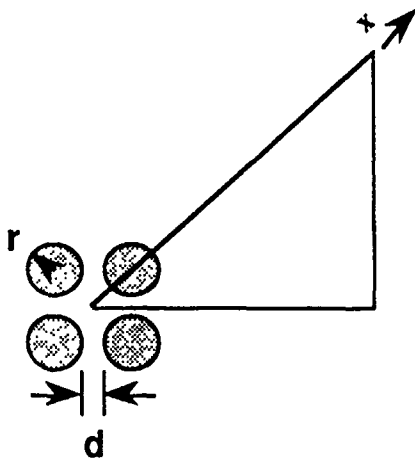


**Figure 1.** Schematic of four fibers in an infinite matrix and representative symmetry cell.

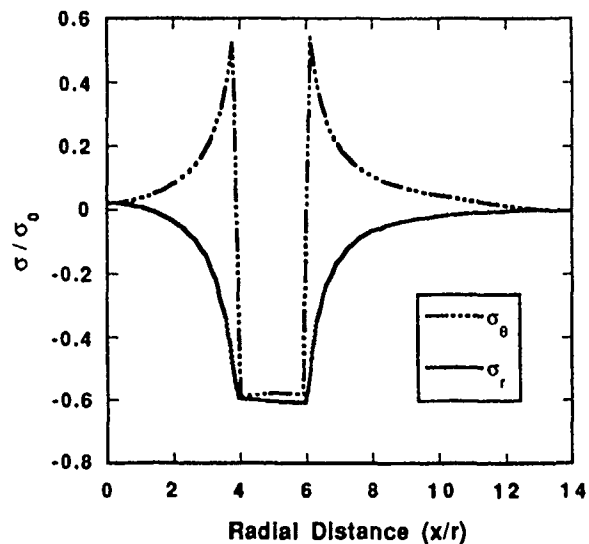


**Figure 2.** Radial and hoop stresses plotted as a function of radial distance along the top boundary of the symmetry cell.

## REFERENCES

1. N.R. Sottos, R.L. McCullough, and S.I. Güçeri, "Thermal Stresses Due to Property Gradients at the Fiber/Matrix Interface." In *Mechanics of Composite Materials and Structures*, Edited by J.N. Reddy and J.L. Teply, ASME Special Volume AMD-100, 1989.
2. D.E. Bowles and O.H. Griffin, "Analysis of Thermal Stresses in Polymer Matrix Composites." In *Proceeding of 34th International SAMPE Symposium*, 1989.
3. W.L. Morris and B.N. Cox, "Thermal Fatigue of Unidirectional Graphite Composites." In *Proceedings of the 6th ICCM/ECCM*, Edited by F.L. Matthews, et al., Vol. 4, 1987.

## THE MECHANICAL RESPONSE OF WOVEN KEVLAR FABRIC\*

W. E. Warren, Org. 1813, Sandia National Laboratories, Albuquerque, NM 87185

Woven Kevlar fabrics exhibit a number of beneficial mechanical properties which include strength, flexibility, and relatively low density. The desire to engineer or design Kevlar fabrics for specific applications has stimulated interest in the development of theoretical models which relate their effective mechanical properties to specific aspects of the fabric morphology and microstructure[1].

In this work we provide a theoretical investigation of the large deformation elastic response of a plane woven Kevlar fabric and compare these theoretical results with experimental data obtained from uniaxially loaded Kevlar fabrics. The theoretical analysis assumes the woven fabric to be a regular network of orthogonal interlaced yarns and the individual yarns are modeled as extensible elastica, thus coupling stretching and bending effects at the outset. The initial unloaded yarn geometry is assumed to be a sequence of alternating circular arcs of constant radius. Yarn stretching is assumed to be linear with applied force since Kevlar yarns remain linear up to fracture. A general development of this nonlinear theory has been presented by Warren [2] who obtains the in-plane linear elastic constants of the woven fabric. This analysis considers the other end of the loading spectrum and investigates the asymptotic elastic behavior for large applied loads. Interestingly enough, the limiting results of this asymptotic analysis for small applied forces provide a very close approximation to the linear elastic response obtained in [2].

Deflection-force relations for the individual yarns are first evaluated and the mechanical response of the fabric is then obtained from the interaction of two individual yarn solutions at the yarn overlap by enforcing equilibrium and compatibility of displacements. This provides expressions for the in-plane displacement-force relations of the fabric in the two principal yarn directions and represents the principal theoretical results of this analysis.

Deflection-force relations for a fabric woven from 400 denier Kevlar yarns has been determined experimentally under conditions of uniaxial loading. These experiments were performed as part of an investigation of parachute fabrics. This particular fabric

\* Supported by the U. S. Dept. of Energy under contract #DE-AC04-76DP00789.

has nominally 30 yarns per inch in the warp direction and 31 yarns per inch in the fill direction. The experimental and theoretical deflection-force relations for loading in the warp and fill directions are shown and compared in Fig. 1. We have denoted the

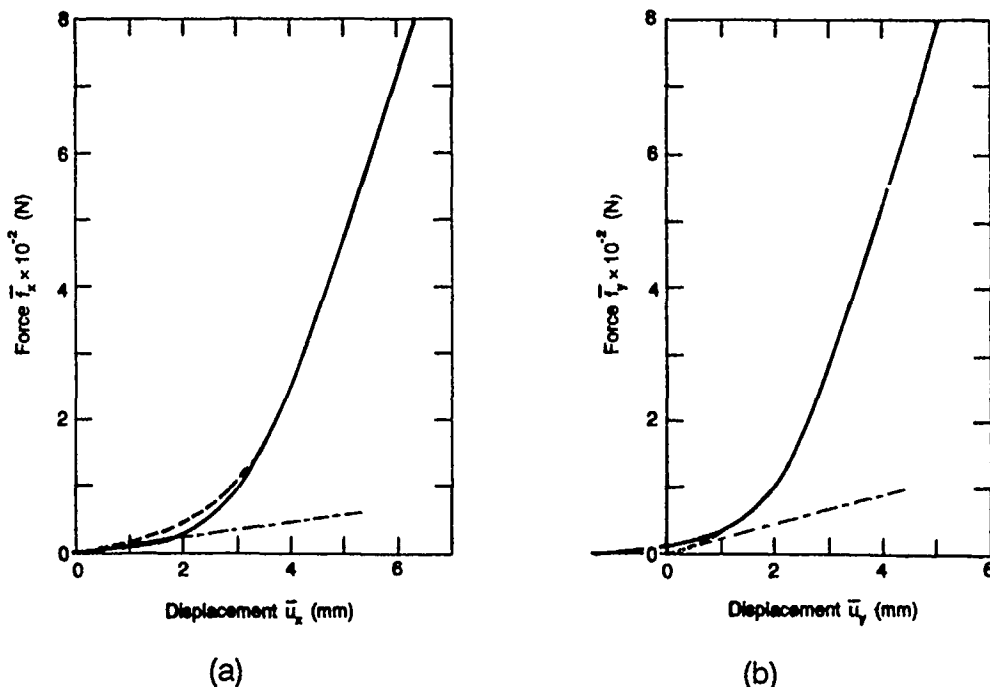


Figure 1 Displacement-force curves for (a)warp, and (b)fill directions. Solid line is experimental, broken line is current theory, - - - - - is linear elastic from [2].

displacement of the specimen measured over a ten inch gage length by  $\bar{u}$  and the total force applied to the one inch wide specimen by  $\bar{f}$ . We have positioned the experimental and theoretical curves in Fig.1 to line up with each other in the large force limit. Figure 1 shows that during initial loading the elastic response is dominated by yarn bending. With increased loading the response goes through a transition from bending to stretching and for large loads is dominated by yarn stretching. This transition is captured by the theoretical model and the difference between bending and stretching effects is significant. The elastic compliance changes by a factor of 20 in the warp direction and a factor of 12 in the fill. These results show that the fabric is stiffer in the fill direction than the warp which is consistent with the initial weave geometry where the crimp height is greater for the warp yarns. Under loading in the fabric plane, more bending deformation is required to straighten out the warp yarns than the fill, and this difference is reflected in Fig. 1. This comparison of experiment with theory indicates that the deformation of woven fabric can be quite accurately predicted by modeling the individual yarns as extensible elastica.

#### REFERENCES

1. Treloar, L. R. G., Physics Today, 30 (1977) 23.
2. Warren, W. E., Poly. Eng. & Science, 30 (1990) 1309.

# High Speed Fracture Behavior of Glass-Cloth/Epoxy Composite

Kensuke Ichinose

Dept. of Mechanical Engineering, Tokyo Denki University,  
Kanda-nishikicyo 2-2, Chiyodaku, 101 Tokyo JAPAN

Goro Suzuki

Dept. of Mechanical Engineering, Tokyo Denki University,  
Kanda-nishikicyo 2-2, Chiyodaku, 101 Tokyo JAPAN

Teruo Kaneda

Dept. of Electronic Engineering, Tokyo Denki University,  
Kanda-nishikicyo 2-2, Chiyodaku. 101 Tokyo JAPAN

## INTRODUCTION

Usually, pendulum-type or Charpy impact testing machine is used for the impact fracture tests. However, it is difficult to apply the constant loading speed to the specimens by these testing machines.

In this research, the electro-hydraulic high speed impact testing machine was developed, which could apply tensile load to the specimens with the speed of 0.1 - 10.0m/s.[1] High speed fracture tests of the glass-cloth/epoxy laminated composite material ( standard compact specimens ) were carried out by using this impact testing machine. The fracture process was observed by a high speed image converter camera. The influences of the loading speed on the maximum load and the absorbed energy were investigated.

## TESTING MACHINE AND SPECIMEN

The developed high speed testing machine is shown in Fig. 1. This machine is controlled by an electro-hydraulic feed-back servo system, and it is possible to pull specimens at a given speed in the range from 0.1 to 10.0m/s. Pressurized oil of 200kgf/cm<sup>2</sup> is saved in the large accumulator (3). This high pressure oil is controlled by the servo-valve (2), and the actuator (1) is driven. The output voltage of the stroke sensor (7) is controlled as a feed-back signal. Applied force is measured by the load cell (6). In the case of the faster pull loading more than 7.0m/s, the speed was too fast to measure the force because of the stress wave reflection from the end of the load cell and the testing machine. Photographs during loading were taken by the image converter camera; its shutter speed could be up to 10<sup>7</sup> frame/s.

Figure 2 shows the shape and dimensions of tested CT specimen. The specimens were made of the glass-cloth/epoxy laminated composite plate and the notch tip was machined carefully with a special tool. The direction of the horizontal fiber of the composite is the same as the direction of the machined notch as shown in Fig.2. The notch tip radius is 0.1mm.

## EXPERIMENTAL RESULTS

Figure 3 shows the photographs of the surface of CT specimens during the

loading. The shutter speed was 0.1ms. The maximum load was applied at the time of No.6 photograph in Fig. 3(a), and No.2 in Fig. 3(b). The effects of the loading speed on the maximum load and absorbed energy are shown in Table 1. From these results, the maximum load increases as the loading speed becomes faster. However, the amount of the absorbed energy decreases as the loading speed increases.

### CONCLUSIONS

The electro-hydraulic high speed impact testing machine was developed. High speed fracture tests of the glass-cloth/epoxy laminated composite material (standard compact specimens) were carried out by using this testing machine. The effects of the loading speed on the maximum failure load and absorbed energy were investigated.

### REFERENCES

- (1) K. Ichinose, G. Suzuki and T. Kaneda, Journal of Material Testing Research Association of Japan, Vol.36, No.1, pp.35-42 (1991) (in Japanese)

Table 1 The influence of the loading speed on the maximum load and absorbed energy.

loading speed(m/s)	1	3	5	7	10
maximum load (t)	0.811	0.913	1.154	1.213	(0.954)
absorbed energy(J)	0.187	0.174	0.167	0.197	(0.277)

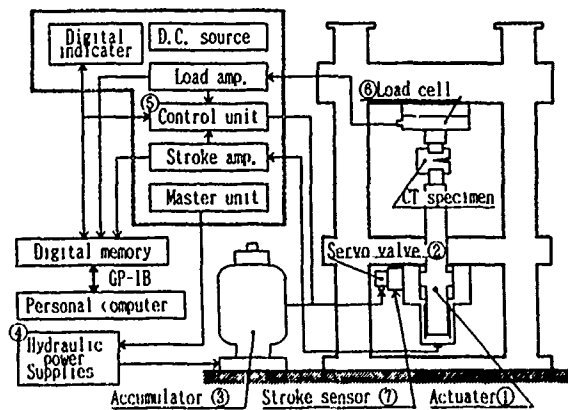


Fig. 1 Schematic figure of high speed impact testing machine.

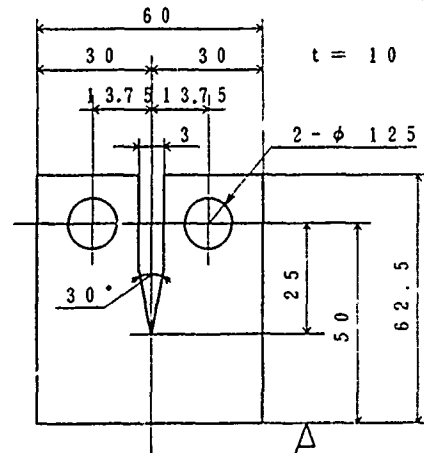
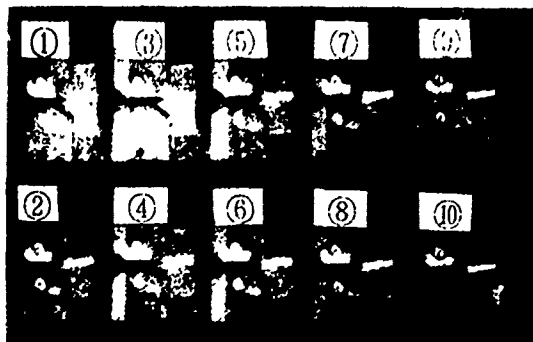


Fig. 2 Size and shape of GFRP CT specimen.



(a) 1.0 m/s



(b) 5.0 m/s

Fig. 3 The photographs of specimens during the loading.

# DETERMINATION OF STIFFNESS PROPERTIES FOR TWISTED CORDS IN RUBBER

R. M. V. Pidaparti

Department of Mechanical Engineering, Purdue University  
IUPUI, Indianapolis, IN 46202, U.S.A.

## Introduction

Cord-rubber composites are widely used in variety of engineering fields for tires, bearings, earthquake equipment etc. For the finite element modeling of rubber composite structures, the stiffness properties of rubber as well as cord are needed. The structure of tire cords are extremely complex. A single cord in cord-rubber composites consists of large number of filaments/yarns twisted together. Experimental determination of cord stiffness properties are extremely difficult as cords should be treated as structures not as solid homogeneous materials [1]. Cord properties measured in rubber are more realistic since the cord-in-rubber is itself a microcomposite consist of cord, adhesive and the surrounding rubber. When a twisted cord is subjected to tensile strain/stress, bending and twisting deformations takes place in addition to the tensile deformation.

Since cord-rubber composites are subjected to a complicated loadings in practice, the axial, bending and twisting stiffnesses of cords are important for accurate analysis of rubber composite structures. The objective of the present paper is an attempt to treat the twisted cords as structures and develop a finite element model to determine the axial, bending and twisting stiffness characteristics.

## Finite Element Model

A typical cord cross-section consists of a number of filaments/yarns surrounded by a layer of rubber material. A twisted cord is modeled using beam elements along the length of the cord and warping elements over the cross-section to model any arbitrary cord shapes [2]. It is assumed that the cross-section of cord and the surrounding rubber layer is modeled using 8-node isoparametric elements each with different isotropic material properties. The material properties for rubber and cord are described by Young's modulus,  $E$  and Poisson's ratio,  $\nu$ . The Young's modulus for the twisted cord is assumed to be [3] as:

$$E_c^i = E_f \cos^4 \beta \cos^2 \alpha \left[ 1 - 1.5 \tan^2 \beta \left( 1 + \frac{2 \log \cos \alpha}{\sin^2 \alpha} \right) \right]$$

where  $E_c^i$  is a contribution by a typical  $i$ th filament and the total cord modulus  $E_c$  is obtained by summing over number of filaments in the cord. In the above equation  $\alpha$  and  $\beta$  are defined as:

$$\tan \alpha = \Pi d \, t_{pi\_yarn} ; \quad \tan \beta = \Pi d^* \, t_{pi\_cord}$$



where  $d$  is the diameter of filament or yarn,  $d^*$  is the distance between the filament centerline and the cord axis, and  $tpi_{yam}$  and  $tpi_{cord}$  are twists per unit lengths of filament and cord, respectively.

### Numerical Results and Discussion

To find the stiffness characteristics of twisted cords, a steel cord with five filaments with diameter  $d = 0.25$  mm,  $d^* = 0.213$  mm,  $tpi_{yam} = 5$ ,  $tpi_{cord} = 5$  and rubber layer thickness of  $0.5d$  was considered. The finite element model consists of two beam elements along the length of the cord and 15, 8-node elements to represent the cross-section of the cord. The material properties used for the rubber and filaments are given as:

Rubber Properties:  $E = 5.0$  Mpa ;  $\nu = 0.5$

Filament properties :  $E = 210.0$  Gpa ;  $\nu = 0.3$

The stiffnesses were calculated by applying a load at free end of a cantilever beam. The three stiffnesses are defined as:

Axial Stiffness (EA) = applied load \* length / axial displacement

Bending Stiffness (EI) = applied load \* length<sup>3</sup> / 3 \* vertical displacement

Torsional Stiffness (GJ) = torsional moment \* length / rotational angle

The calculated stiffnesses are shown in Fig. 1 for various twists per unit length of cord. It can be seen from Fig.1 that all the three stiffnesses decrease as the  $tpi_{cord}$  increases. The rate of decrease is rapid for torsional stiffness as compared to axial and bending stiffnesses. Fig 2. shows the stiffness properties as the surrounding rubber modulus is varied from 5 Mpa to 1000 Mpa. All the three stiffnesses increase as the rubber modulus is increased. The results of stiffness properties obtained indicate that all the three stiffnesses decrease as the  $tpi_{cord}$  is increased, and the stiffnesses increase as the surrounding rubber layer modulus is increased.

### References

- [1] S. Parhizgar et al., Tire Science and Tech., Vol. 16, 1988, 118-126
- [2] S.W. Lee et al., Int. Jr. for Num. Meths. Engg., Vol. 24, 1987, 2327-2341
- [3] S.R. Moghe, Presentation at Fiber Society Meeting, Raleigh, NC, 1982

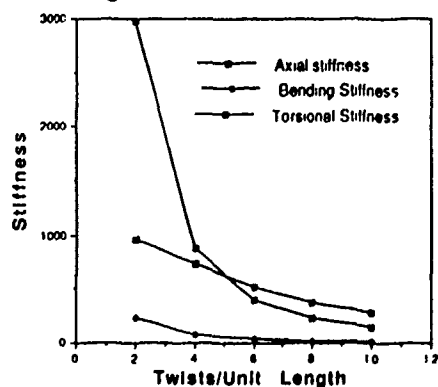


Fig. 1 Variation of Stiffnesses with Twist/unit Length

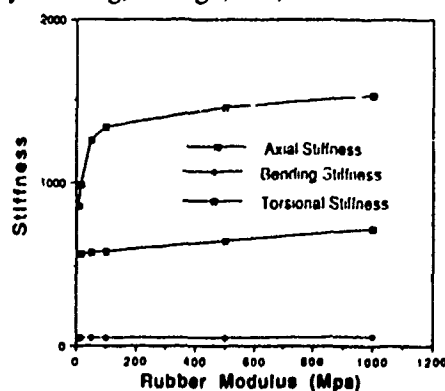


Fig. 2 Variation of Stiffnesses with Rubber Modulus

## CRACK-FACE CONTACT IN A CRACK PARALLEL TO AN INTERFACE BETWEEN DISSIMILAR MATERIALS

Ming-Fa Yang<sup>1</sup> and Kyung-Suk Kim<sup>2</sup>

<sup>1</sup>Department of Theoretical and Applied Mechanics, University of Illinois at Urbana-Champaign, Urbana, IL 61801 and <sup>2</sup>Division of Engineering, Brown University, RI 02912

In this paper, the two-dimensional plane strain problem of a crack parallel to an interface between dissimilar materials, with crack-face contact near one of the crack tips, is studied. This subinterface crack problem is formulated as system of nonlinear Cauchy-type singular integral equations which is solved numerically using Erdogan and Gupta's (1972) method. The physically pathological feature of interpenetration of the crack faces is eliminated in the solution by accounting for the contact of the crack faces.

It is essential to consider the contact of the crack faces. Whenever a shear-stress field is applied, the crack is closed near one of crack tips. Otherwise, owing to the symmetry of the geometry and the loading, half of the crack faces will interpenetrate each other.

The mathematical problem which will be analyzed is shown in Fig. 1. The two materials are taken to be isotropic and linear elastic with Young's moduli  $E_1, E_2$  and Poisson's ratios  $\nu_1, \nu_2$ . Material 2 lies above the interface, which parallel to  $x$ -axis, and material 1 lies below the interface. To simplify the problem without losing generality, the half crack length is normalized to unity.

For a subinterface crack with contact zone, an important phenomenon has been observed in a combined compressive and shear stress field when the distance between the crack and the interface is small. Increasing the level of the compressive stress may result in increases in the stress intensity factor  $K_I$  at one of the crack tips, the maximum value of the crack opening, and the size of the contact zone. When the normal stress is tensile, increasing the level of this tensile stress also results in increasing the stress intensity factor  $K_I$  at one of the crack tips and the maximum value of the crack opening, but shortening of the contact zone. This phenomenon is due to the inhomogeneity of the system of dissimilar materials, and is caused by the shear effect on the symmetric geometry and material system.

The behavior of a subinterface crack depends on both Dundurs parameters  $\alpha$  and  $\beta$  rather than only  $\beta$  for interface crack problems. The crack can be either in material 1 or material 2. When material 1 and 2 are switched, the Dundurs parameters change sign; hence both positive and negative Dundurs parameters need be considered. Whenever a shear stress is applied, if  $\alpha$  and  $\beta$  are positive, the crack may close near the right crack tip; and if  $\alpha$  and  $\beta$  are negative, the crack may close near the left crack tip. The results show that the larger the Dundurs parameters are, the stronger the shear effect on the crack is. Only when both Dundurs' parameters  $\alpha$  and  $\beta$  are zero, the contact of crack faces disappears; the mixed mode of the crack tip fields is separable such that the solution of the subinterface crack reduces to the solution of the Griffith crack in a homogeneous material subjected to the same stress field.

The subinterface crack can be fully closed or opened when the level of compressive stress or tensile stress reaches a certain value, as shown in Fig. 2. This behavior is a result of the interaction of the singularities caused by normal stress and shear stress at the crack tips which are in the naturally mixed mode due to the inhomogeneity. When the crack is fully opened, the problem becomes a linear one.

The distance between the crack and the interface plays an important role in the behavior of cracks parallel to an interface between dissimilar materials. When this distance goes to zero, the solution should converge to the solution of the corresponding problem of an interface crack; and when this distance is large, the solution should reduce to the solution of the corresponding problem of a crack in a homogeneous material. The smaller the distance between the crack and the interface is, the larger the shear effect on the subinterface crack is.

Comparison is made for current results and those of Hutchinson, Mear and Rice's (1987) for a semi-infinite subinterface crack problem. For a crack parallel to the interface between  $Al_2O_3$  and copper and a distance between the crack and the interface of 0.01 in a shear-stress field, the stress intensity factor  $K_I$  is increased 46% in the present results owing to the introduction of crack-face contact.

In conclusion, the cracks parallel to an interface between dissimilar materials may be advanced even in a combined compressive and shear stress field; the predicted level of the stresses causing the crack to advance is smaller than that predicted by Hutchinson, Mear and Rice (1987).

## References

Erdogan, F., and Gupta, G. D., 1972, "On the Numerical Solution of Singular Integral Equations," *Q. Appl. Math.*, Vol. 30, pp. 525-534.

Hutchinson, J. W., Mear, M., and Rice, J. R., 1987, "Crack Paralleling an Interface Between Dissimilar Materials," *J. Appl. Mech.*, Vol. 54, pp. 345-348.

Rice, J. R., 1988, "Elastic Fracture Mechanics Concepts for Interfacial Cracks," *J. Appl. Mech.*, Vol. 55, pp. 98-103.

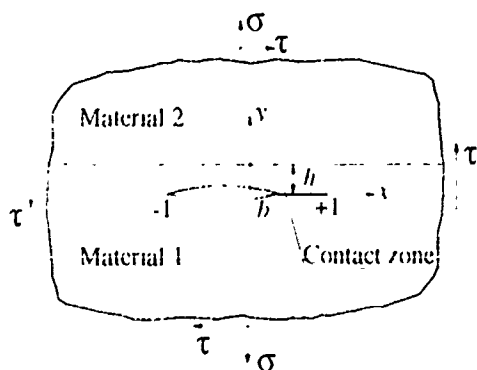


Fig. 1 Subinterface crack with crack face contact.

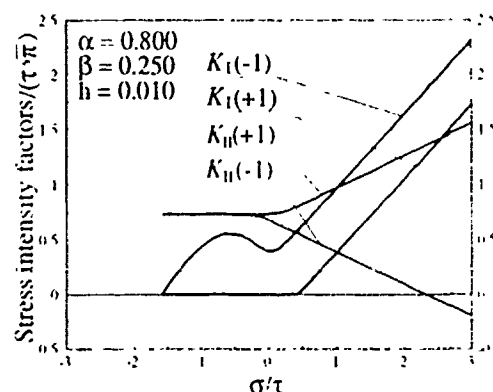


Fig. 2 Stress intensity factors versus the ratio of normal stress to shear stress.

## FIBERS REBONDING IN FIBER REINFORCED COMPOSITE

M. REZA SALAMI AND S. A. HAMOUSH

Assistant Professors, Department of Civil Engineering, North Carolina Agricultural and Technical State University, Greensboro, North Carolina, 27411

### ABSTRACT

An analytical model is proposed to predict the ultimate tensile strength of fiber-reinforced composite when the failure is governed by fiber debonding. The analytical analysis is based on the principle of the compliance method in fracture mechanics with the presence of an interfacial crack between the fiber and the matrix interface. The model is developed based on the assumption that both the matrix and the fiber behave elastically and the matrix strain at a zone far from the matrix fiber interface equals to the composite strain. Also, it is assumed that a complete bond exists between the fiber and the matrix in the unbonded zone, the matrix transfers the loading without yielding and the crack faces are traction free.

### INTRODUCTION

The slip and the interface bond failure in the fiber reinforced composites have received a considerable attention in the recent research studies [1-4]. The interactions between fibers and the matrix are extremely complex. The first attempt to explain the reinforcing effect of the fibers was based entirely on elastic interactions. This was first described by Cox [2]. Piggott [3,4] studied the behavior of short fiber reinforced composites. The study includes the estimation of the strain as well as stress at the bonded interface. The matrix tensile strain was assumed to be constant and equal to the composite tensile strain. It was concluded that the shape of the stress-strain curve is strongly dependent on the fiber aspect ratio, and the adhesion between the fiber and matrix has relatively little effect on the stress-strain curve.

In this paper, the behavior of a singly reinforced composite body is considered to obtain the analytical value of the pull-out strain energy release rate, the analytical value of the strain energy release rate can be used to determine the failure of uniaxial composites.

### FRACTURE MECHANICS APPROACH (COMPLIANCE METHOD)

The reciprocal of the gradient of the load-deflection curve is called a compliance,  $C$ , and governed by

$$C = \frac{u}{P} \quad (1)$$

where  $C$  is the compliance of the body,  $P$  is the applied forces and  $u$  is the boundary displacement in the  $P$  direction. The strain energy release rate,  $G$ , can be shown to satisfy

$$G = \frac{P^2}{8\pi r} \left( \frac{\partial C}{\partial a} \right) \quad (2)$$

where  $a$  is the length of the interfacial crack and  $r$  is the radius of the fiber. In equation (2), the strain energy release rate becomes defined if the function  $(\partial C/\partial a)$  is introduced, the function  $(\partial C/\partial a)$  has been obtained by Hamoush and Salami [1]. These compliances, from Ref. [1], are (1) Compliance of the embedded portion of fiber, (2) Compliance of the free-edge portion of fiber and (3) Compliance due to matrix deformation.

## TOTAL CHANGE COMPLIANCE FOR WHOLE BODY

The total change in compliance for the whole body is given by Hamoush and Salami [1] as

$$\frac{dC}{da} = \frac{S-2}{SA_f E_f} \left[ \frac{1 - \cosh k(L-a)}{\sinh^2 k(L-a)} \right] - \frac{1}{SA_f E_f} + \frac{1}{A_f E_f} + \frac{k^2 r^2}{h^2 E_f} \left[ \frac{S-1}{SA_f} \cosh k(L-a) + \frac{1}{SA_f} \right] \frac{1}{\sinh^2 k(L-a)} \quad \text{where} \quad (3)$$

$$S = (V_f + \frac{1-V_f}{n}) (\frac{1-V_f}{V_f} + n), \quad V_f = \frac{A_f}{A_f + A_m} = \text{volume fraction of fibers,}$$

$$n = \frac{E_f}{E_m} = \text{modular ratio, } A_m, A_f = \text{the areas of matrix and fiber,}$$

$E_f$  = young modulus of fiber,  $E_m, \nu_m$  = young modulus and Poisson's ratio of matrix,

$a$  = length of the interfacial crack,  $L$  = length of the interfacial crack + length of fiber,

$$r = \text{radius of the fiber, } h^2 = \frac{E_m}{(1 + \nu_m) E_f \ln \frac{R}{r}}, \quad \frac{R}{r} = \text{depends on the fiber packing,}$$

$$R = \text{from the fiber surface to a distance, and } k^2 = \frac{h^2}{r^2}$$

The strain energy release rate  $G$ , can be obtained analytically by substituting equation (3) into equation (2).

## CONCLUSION

An analytical model is proposed to predict tensile strength of fiber reinforced cement based composites whose failure is governed by the strength of the fiber matrix interface. The proposed model is based on the concept of fracture mechanics and theory of elasticity.

The debonding is treated as interfacial crack of two dissimilar materials, the total strain energy release rate for interfacial crack is obtained from the concept of compliance method in fracture mechanics, the proposed model is capable of obtaining the strain energy release rate when the interface crack doesn't exist. In the proposed model there is a simplifying assumption made which the interface crack is traction free and no elastic bond slip exists at the interface.

It can be concluded from this model that: (1) For elastic fiber with the ratio  $L/r$  is more than 100, the interface crack and the fiber lengths have no major effect on the pull out strain energy release rate; (2) The interface crack becomes significant if the fiber is rigid; (3) Increasing the fiber spacing increases the strain energy release rate.

## ACKNOWLEDGEMENTS

The authors gratefully appreciate the support by the North Carolina A&T State University.

## REFERENCES

1. Sameer A. Hamoush and M. Reza Salami, "Interfacial Separation of Fibers in Fiber Reinforced Composites", Accepted for Publication in Journal of Composite Science and Technology, (1990).
2. Cox, H. L., Brit. J. Appl. Phys., (1952) 72.
3. Piggott, M. R., "Expressions governing stress-strain curves in short fiber reinforced polymers," Journal of Material Science 13, (1978), pp. 1709-1716.
4. Piggott, M. R., "Load Bearing Fiber Composites", International Series on the Strength and Fracture of Material and Structures, Pergamon Press.
5. Mandel, J. A., Wei, S. and Said, S., "Studies of the Properties of the fiber-matrix interface in steel fiber reinforced mortar; ACI Material Journal, Mar-Apr. 1987, pp. 101-109.

# FINITE STRAIN PLASTICITY AND DAMAGE IN CONSTITUTIVE MODELING OF METALS WITH SPIN TENSORS

George Z. Voyiadjis and Peter I. Kattan  
Department of Civil Engineering  
Louisiana State University  
Baton Rouge, LA 70803

The analysis of damage and plastic deformation in metals is very important towards the full understanding of the various damage mechanisms in these materials. In a general state of deformation and damage, the damage variable was shown to be tensorial [1]. Several authors have then used damage tensors in the mechanical modeling of material damage.

In this work, a coupled theory of damage mechanics and finite strain plasticity is proposed. The theory is based on a sound mathematical and mechanical background and is thermodynamically consistent. It is formulated using spatial coordinates utilizing a von Mises type yield criterion with both isotropic and kinematic hardening. The plasticity model used was recently developed by the authors [2] and used successfully in investigating the problem of finite simple shear.

The derivation is based on the concept of effective stress that was originally proposed by Kachanov [3] for the case of uniaxial tension. In the general case of three-dimensional deformation and damage, the nature and definition of the effective stress become more complex. The plasticity model is first formulated in a fictitious undamaged configuration of the body. Then certain transformation equations are derived to transform this model into a damage-plasticity model in the damaged configuration of the body. Certain assumptions are made in order to make this transformation possible. These assumptions include small elastic strains and the hypothesis of elastic energy equivalence [4].

The model presented here is based on a previous attempt by the authors [5] to provide a coupling between the plasticity theory and the continuum damage mechanics. A considerable portion of the mathematical derivation is devoted to the proper transformation equations for the stresses, strains, strain rates and other relevant quantities. These transformation equations are general (within the context of the assumptions employed) and can be used to formulate other coupled theories of

damage mechanics and different models that describe inelastic behavior, i.e., viscoplasticity, creep, brittle fracture, etc.

The corotational stress rate equations are also discussed since they are used extensively in the constitutive relations. Therefore, the use of spin tensors is also discussed since they play a major role in the definition of the corotational rates. In addition, a modified spin tensor is proposed to be used in the coupled model. Furthermore, the nature of the fourth-rank damage effect tensor is discussed for a general state of deformation and damage. Also, the explicit matrix representation of this tensor is rigorously derived and can be used in future applications to solve plane stress and plane strain problems involving damage.

Finally, the problem of finite simple shear is investigated using the proposed model. It is chosen here for two reasons. First, this problem is widely recognized as a test problem for new constitutive models. The second reason is that the resulting governing differential equations can be solved numerically without the use of finite elements. These equations are solved here using a Runge-Kutta-Verner fifth order and sixth order method. The stress-strain curves are obtained for a certain expression of the modified spin tensor and are compared with other spin tensors. Also, the evolution of the backstress and damage variables is presented. The results obtained compare favorably with previous results.

#### References

1. S. Murakami and N. Ohno, "A Continuum Theory of Creep and Creep Damage," in Proceedings of the 3rd IUTAM Symposium on Creep in Structures, pp. 422-444, Springer, Berlin, 1981.
2. G. Z. Voyiadjis and P. I. Kattan, "Eulerian Constitutive Model for Finite Strain Plasticity with Anisotropic Hardening," Mechanics of Materials Journal, Vol. 7, No. 4, pp. 279-293, 1989.
3. L. M. Kachanov, "On the Creep Fracture Time," Izv. Akad. Nauk USSR Otd. Tekh, Vol. 8, pp. 26-31, 1958 (in Russian).
4. F. Sidoroff, "Description of Anisotropic Damage Application to Elasticity," in IUTAM Colloquium on Physical Nonlinearities in Structural Analysis, pp. 237-244, Springer-Verlag, Berlin, 1981.
5. G. Z. Voyiadjis and P. I. Kattan, "A Coupled Theory of Damage Mechanics and Finite Strain Elasto-Plasticity. Part II: Damage and Finite Strain Plasticity," International Journal of Engineering Science, Vol. 28, No. 6, pp. 505-524, 1990.

## **SURFACE EFFECTS AND MATERIAL LENGTH ESTIMATION**

### **ABSTRACT**

**G. Frantziskonis  
Department of Civil Engineering and Engineering Mechanics  
University of Arizona  
Tucson, Arizona 85721**

A surface can be defined as a physical discontinuity. The consequences of this simple fact are, however, far-reaching; one need only recall that most fractures initiate at surfaces, and that specimens with large surface to volume ratio exhibit anomalous mechanical properties signifying the size (scale) and shape effects. It seems that surface effects have not been understood well. This paper provides theoretical and experimental input on surface effects, their relation to size and shape effects and the related instabilities. The issue of material length estimation is discussed in detail.



## A MARKOV FIELD METHOD FOR PLASTIC FLOW OF RANDOM MEDIA

Martin Ostoja-Starzewski  
Department of Metallurgy, Mechanics and Materials Science  
Michigan State University  
East Lansing, MI 48824-1226

Many engineering and natural materials display spatial randomness of their physical properties. In case of plastic flow of materials this randomness is typically accounted for by either solving a set of deterministic boundary value problems in the Monte Carlo sense, or by solving a single boundary value problem for a medium with average properties. The obstacle in the latter case is the determination of the correct average of random properties so that the solution of a single deterministic problem coincides with the ensemble average solution of a random medium problem. On the other hand, the obstacle in the first case consists in the necessity of performing many solutions; this is often done through brute force computer simulations of large lattices representing discrete media.

In this paper we develop a stochastic method for the determination of plastic flow fields of a medium whose plastic limit  $k$  is a random field of space coordinates. To maintain the generality of the formulation, this underlying random field is taken to be of Markov type. The method is based on an observation that the forward evolution of field quantities - calculation of the net of both (positive and negative) characteristics as well as the stresses on this net - is Markovian. In a given boundary value problem of plastic flow one has to solve an initial value problem, of Cauchy type say, in the  $x,y$ -plane. It follows that the field quantities evolve as a Markovian dynamical system parametrized by the two-dimensional 'time'. The transition probabilities of evolution may be written explicitly in terms of the statistics of the field  $k$ . The entire domain of the medium in  $x,y$ -plane may now be described probabilistically. We end by discussing applications of this method to various boundary value problems such as the problem of instability of earth slopes.

Abstract for  
MID-WERSTERN MECHANICS CONFERENCE

Title:

STRAIN LOCALIZATION ANALYSIS BY ELASTO-VISCOPLASTIC MODEL  
FOR FROZEN SAND WITH STRAIN SOFTENING

Authors:

Fusao Oka, Professor, Department of Civil Engng.,  
Gifu University, Yanagido 1-1, Gifu 501-11, Japan

Toshihisa, Adachi, Professor, Department of Transportation  
Engng., Kyoto University, Kyoto, Japan

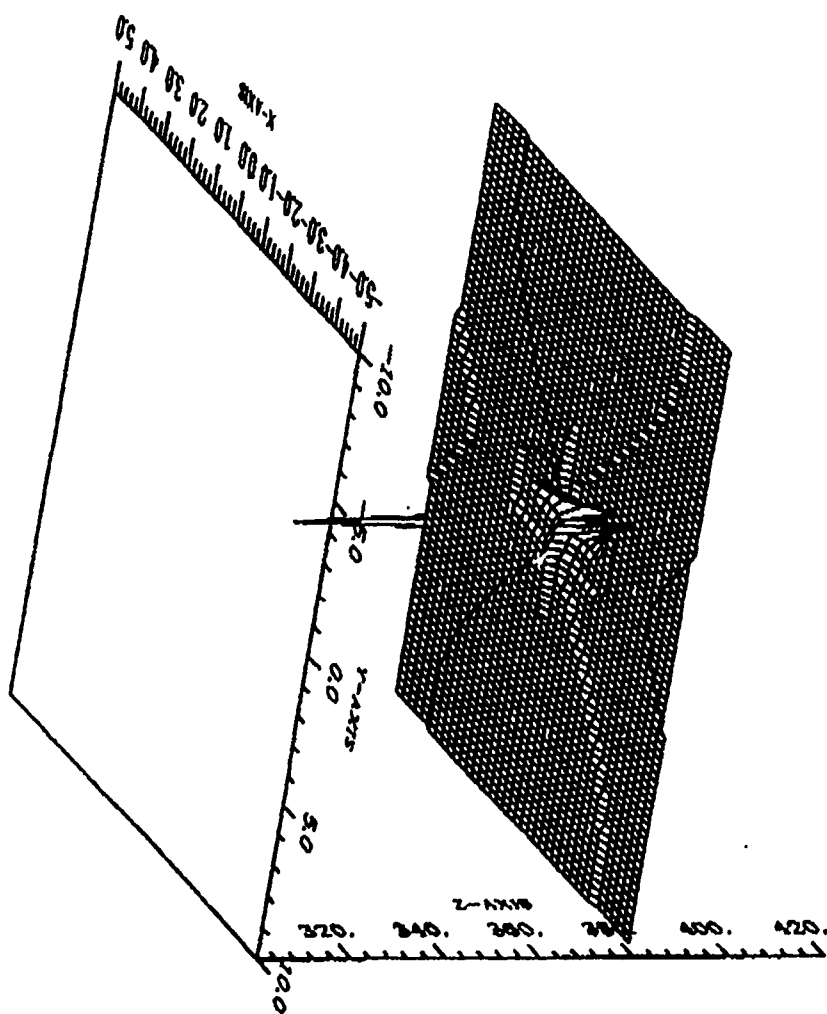
Atsushim, Yashima, Associate Professor, Department of  
Civil Engng., Gifu University, Gifu, Japan

For the last two decades, several constitutive models have been proposed for geomaterials and applied to practical problems. There remain, however, still some outstanding issues to be resolved. One of them is the formation of shear band before and after failure. This problem is deeply connected to the strain localization phenomenon. Recently, the importance of simulation of post localization regime has been pointed out. In the present paper, we have numerically analyzed the behavior of frozen soil by using a viscoplastic constitutive model with strain softening. For the constitutive model for frozen sand, two of the authors (Adachi and Oka) have developed the model introducing the stress history tensor. They have applied it to the triaxial tests results of Tyoura sand with different strain rates. The model is then implemented into FEM code to simulate the behavior under plane strain condition by considering the transport of heat. From the numerical results, it is shown that strain localization like shear banding is observed by use of the proposed model (Fig.1).

Reference

Adachi, T. Oka, F. and H.B. Poorooshasb, 1990, A constitutive model for frozen soil, J. Energy Resources Technology, ASME, Vol.112, 208-212.

# Case(1d.4):2nd invariant of deviatoric stress



Plastic Flow and Shear Instability in Dispersion  
Strengthened Alloys and Particulate Composites

by

J. P. Hirth

Mechanical and Materials Engineering Department  
Washington State University  
Pullman, WA 99164-2920, USA

ABSTRACT

Initial flow in a number of dispersion strengthened alloys and particulate composites follows simple dependences on particulate spacing (and hence on both volume fraction and size of particles) up to a spacing well above those where simple dislocation models should apply. A model is proposed wherein a pinned dislocation subboundary breaks away and initiates a shear band. The tip of the band resembles a superdislocation with an extended core and has line tension. Bowout of the superdislocation between particles gives rise to a dependence of flow stress on particle spacing, analogous to the single dislocation case, that provides an explanation for the observed effect.

SAND91-0337A

## DRAG REDUCTION IN SUSPENSIONS\*

Stephen L. Passman  
Process Research Division  
Sandia National Laboratories  
Albuquerque, New Mexico 87185-5800 USA

A well known but little understood phenomenon in the flow in a pipe of suspensions of particles in fluids is that, even in the most concentrated of such suspensions, fluid is squeezed from the suspension and tends to accumulate near the pipe walls. Often this natural lubrication has the salubrious effect of reducing the power needed to pump the suspension through the pipe. I use two theories for such materials, one quite complicated and the other somewhat simpler, to demonstrate that the phenomenon can be described theoretically, and that the phenomenon is robust enough so that it does not depend delicately on the theory used to describe it. Both theories require a number of constitutive constants and functions. The state of the art has not progressed sufficiently so that these are quantified adequately. It is possible to construct a model that is theoretically crude, but that does not violate any principles of mechanics, and uses the phenomenon of the phenomenon of natural lubrication as an intrinsic part of its simplicity. This model allows for easy first approximation engineering calculations of the decrease in pumping power. I show a good qualitative match with the few dependable experiments. Quantitative matches depend on measurements of high accuracy, and these are just beginning to be made.

---

\*This work was supported by the United States Department of Energy under grant DE-AC04-DP00789 to Sandia National Laboratories. The author also wishes to extend appreciation to the Pittsburgh Energy Technology Center for continued co-operation and encouragement.

# A KINETIC THEORY INVISCID FLOW MODEL FOR PARTICLE-FLUID MIXTURES

Donald A. Drew  
Department of Mathematical Sciences  
RPI, Troy, NY 12180-3590

For many purposes, the flow of a particle-fluid mixture can be described by equations of balance of mass and momentum for each material, i.e., for the particles and the fluid. These equations must be supplemented by constitutive equations for the stresses and the momentum interaction. The stress in the particle component due to the random motions of the particles can be significant in some flows. In addition, the velocity fluctuations of the particles induce velocity fluctuations in the fluid, resulting in a stress there. Moreover, the momentum interaction term is also affected, resulting in a stress-like term. In this paper, I calculate the terms resulting from the particle velocity fluctuations by averaging the flow around a single sphere. The stresses and momentum interaction terms are given in terms of the average velocity and volume fraction fields, and the fluctuation stress for the particles. The particle stress must be given by a separate constitutive assumption. I also give a framework for the particle velocity fluctuations that accounts for the evolution of the particle temperature and the corresponding entropy.

The averaged equation for balance of mass for each component is

$$\frac{\partial \alpha_k \rho_k}{\partial t} + \nabla \cdot \alpha_k \rho_k \mathbf{v}_k = 0 \quad (1)$$

and the averaged equation for balance of momentum for each component is

$$\frac{\partial \alpha_k \rho_k \mathbf{v}_k}{\partial t} + \nabla \cdot \alpha_k \rho_k \mathbf{v}_k \mathbf{v}_k = \nabla \cdot \alpha_k (\mathbf{T}_k + \mathbf{T}_k^{Re}) + \alpha_k \rho_k \mathbf{g} + \mathbf{M}_k, \quad (2)$$

where  $\alpha_k$  is the volume fraction of component  $k$ ,  $\rho_k$  is the density,  $s_k^M$  is the entropy,  $\mathbf{v}_k$  is the velocity,  $\mathbf{T}_k$  is the stress,  $\mathbf{T}_k^{Re}$  is the fluctuation (Reynolds) stress,  $\mathbf{g}$  is the body force density, and  $\mathbf{M}_k$  in the momentum interaction force density.

We also postulate an equation for the balance of fluctuation kinetic energy for each component in the form

$$\frac{\partial \alpha_k \rho_k u_k^{Re}}{\partial t} + \nabla \cdot \alpha_k \rho_k u_k^{Re} \mathbf{v}_k = \alpha_k \mathbf{T}_k^{Re} : \nabla \mathbf{v}_k - \nabla \cdot \alpha_k \mathbf{q}_k^{Re} + W_k - \alpha_k D_k, \quad (3)$$

where  $u_k^{Re}$  is the fluctuation kinetic energy,  $\mathbf{q}_k^{Re}$  is the fluctuation kinetic energy flux,  $W_k$  is the rate of work of the interfacial stresses,  $D_k$  is the rate of energy loss from the mesoscale energy to the microscale energy. In this paper, I do not consider the microscopic, or thermal energy.

The fluctuation entropy inequality is

$$\frac{\partial \alpha_k \rho_k s_k^{Re}}{\partial t} + \nabla \cdot \alpha_k \rho_k s_k^{Re} \mathbf{v}_k \geq -\nabla \cdot \alpha_k \frac{\mathbf{q}_k^{Re}}{\theta_k^{Re}}, \quad (4)$$

where  $s_k^{Re}$  is the entropy per unit mass of component  $k$ ,  $\mathbf{q}_k^{Re}$  is the fluctuation kinetic energy flux, and  $\theta_k^{Re}$  is the fluctuation temperature. Note that there is no body source of fluctuation entropy.

I derive constitutive equations for the stresses in the components, the Reynolds stress in the fluid, the momentum interaction and the interaction work term by averaging the appropriate quantity calculated using the inviscid flow around a single sphere whose velocity is the mean particle velocity plus a velocity perturbation. The averaging process used is a version of ensemble averaging wherein the particle position is assumed to be distributed over the interior of a spherical "cell," and the particle velocities are distributed so that the average of the fluctuation is zero, and the average of the negative of the fluctuation dyad is the particle Reynolds stress.

The fluid stress is given by

$$\mathbf{T}_f = -p_f \mathbf{I}. \quad (5)$$

The momentum interaction force density is given by

$$\begin{aligned} \mathbf{M}_p = & p_{fi} \nabla \alpha_p + \alpha_p \rho_f \left( \frac{1}{2} \left[ \frac{\partial \mathbf{v}_f}{\partial t} - \frac{\partial \mathbf{v}_p}{\partial t} + \mathbf{v}_f \cdot \nabla \mathbf{v}_f - \mathbf{v}_p \cdot \nabla \mathbf{v}_p \right] \right. \\ & \left. - \frac{7}{20} (\mathbf{v}_f - \mathbf{v}_p) \cdot (\nabla \mathbf{v}_f - \nabla \mathbf{v}_p) \right) \\ & - \nabla \left( \frac{4}{5} \alpha_p \rho_f u_p^{Re} \right) - \nabla \cdot \left( \alpha_p \frac{9}{20} \frac{\rho_f}{\rho_p} \mathbf{T}_p^{Re} \right). \end{aligned} \quad (6)$$

where the interfacial averaged pressure is given by

$$p_{fi} = p_f - \frac{1}{4} \rho_f |\mathbf{v}_f - \mathbf{v}_p|^2. \quad (7)$$

The stress in the particle component can also be found; the result is

$$\begin{aligned} \mathbf{T}_p = & -p_{fi} \mathbf{I} + \rho_f \left[ -\frac{9}{20} (\mathbf{v}_f - \mathbf{v}_p)(\mathbf{v}_f - \mathbf{v}_p) + \frac{8}{20} |\mathbf{v}_f - \mathbf{v}_p|^2 \mathbf{I} \right] \\ & - \frac{9}{20} \frac{\rho_f}{\rho_p} \mathbf{T}_p^{Re} + \frac{4}{5} \rho_f u_p^{Re} \mathbf{I}. \end{aligned} \quad (8)$$

The fluid Reynolds stress is found to be

$$\begin{aligned} \mathbf{T}_f^{Re} = & -\frac{1}{20} \alpha_p \rho_f [(\mathbf{v}_f - \mathbf{v}_p)(\mathbf{v}_f - \mathbf{v}_p) + 3(\mathbf{v}_f - \mathbf{v}_p) (\mathbf{v}_f - \mathbf{v}_p) \mathbf{I}] \\ & + \frac{1}{20} \alpha_p \frac{\rho_f}{\rho_p} \mathbf{T}_p^{Re} + \frac{3}{10} \alpha_p \rho_f u_p^{Re}. \end{aligned} \quad (9)$$

## Internal Flows of Vapor Undergoing Film Condensation

A. Narain and R. Kamath  
Department of Mechanical Engineering  
and Engineering Mechanics  
Michigan Technological University  
Houghton, MI-49931.

**ABSTRACT:** Film condensation flows in circular pipe and parallel plate geometries are investigated for laminar flow of liquid condensate and laminar or turbulent flow of the vapor core. A mixed formulation, which employs an integral approach for the vapor flow in the core and retains the scaled local forms of the equations governing the flow of the liquid condensate and conditions at the interface, is used for the above flows. A combined numerical and analytical approach is developed to solve the problem for any admissible model of shear at the interface.

Besides qualitative interpretation of the flows, we assess the performance of some relevant friction factor models and the solution methodology.

**INTRODUCTION:** There is a substantial body of scientific knowledge on the topic of film condensation of pure vapor on surfaces. The knowledge of first principle model equations of non-metallic vapors is fairly complete ([1], [2], [3]) as one can adequately model the interface as a surface of discontinuity and assume thermodynamic equilibrium ([2], [4]) across the interface. A significant open issue is related to a lack of consensus on a good model equation for interfacial shear for flows having a turbulent vapor core and a laminar (or turbulent) film condensate.

**METHOD OF APPROACH:** The above problems are modelled, using an approach similar to that of Narain and Kizilyalli [4], as

$$dy/dx = g(y, f) \text{ for } x \geq 0, f = f(y) \text{ and } y(0) = [0, 0, 1]^T \quad (1)$$

where  $y \equiv [\pi(x), \delta(x), u_{av}(x)]^T$  and the non-dimensional variables  $\pi, \delta, u_{av}, f$  respectively represent average cross-sectional pressure ( $p$ ), location of the interface ( $\Delta$ ), average cross sectional speed ( $u_{av}$ ) of the vapor phase and the stress ( $\tau_i \equiv (1/2) \rho_v u_{av}^2 f$ ) at the interface. The non-linear function  $g$  in (1) is determined by the governing equations of the problem.

Note, however, that (1) usually constitutes a singular initial value problem. Therefore issues of integrability and admissible class of friction factor models in (1) are addressed.

**RESULTS AND DISCUSSIONS:** A solution technique capable of identifying appropriate friction factor models and resolving singular initial conditions encountered in the flow is presented (Fig1). This method is currently being utilized to identify and propose friction factor models which yield predictions, particularly heat transfer correlations, compatible with limited available experimental data for flows in ducts of rectangular



or circular cross sections.

It is shown (c1a and c1b in Fig 1) that the flow of liquid condensate is principally driven by interface shear and insignificantly by the requirement of continuity of tangential velocities at the interface. Furthermore, the same curves (c1a and c1b) demonstrate that the predicted variables (being lower dimensional unknowns) are quite independent of the knowledge of details of vapor velocity profile across the cross section.

## REFERENCES:

1. Delhaye, J. M., 1974. Jump Conditions And Entropy Sources In Two-phase System: Local Instant Formulation. *Int. J. of Multiphase Flow* 1, 395-409.
2. Ishii, M., *Thermo Fluid Dynamic Theory of Two-Phase Flow, Eyrolles* (1975)
3. Moeckel, G.P., 1975, Thermodynamics of an Interface, *Arch. Rat. Mech. and Anal.*, 57 (3), 255-280
4. Narain, A. and Kizilyalli, Y., 1991. Pressure driven Flow Of Pure Vapor Undergoing Film Condensation Between Parallel Plates. (in press) *Int. J. of Non-Linear Mechanics*.

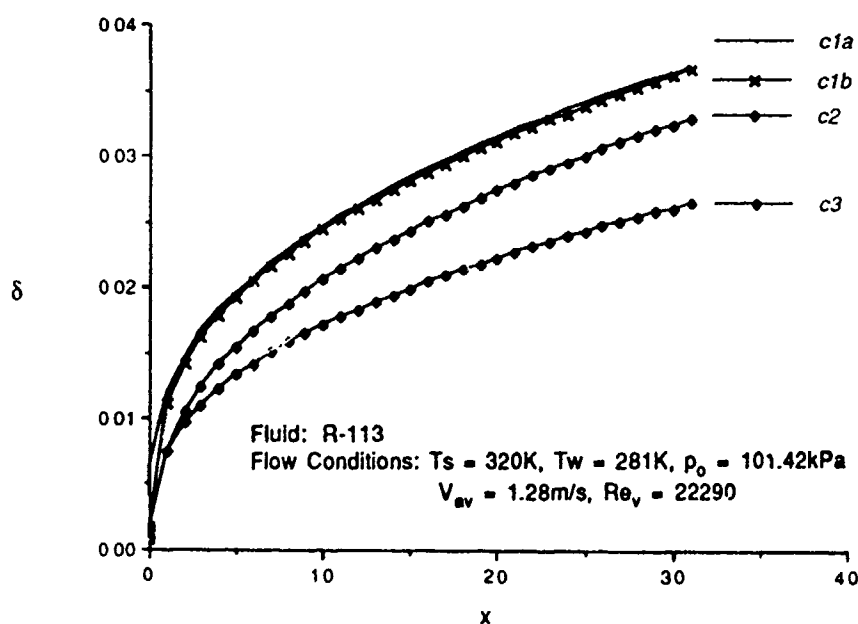


**Fig 1.** The non-dimensional values of film thickness  $\delta$  and distance  $x$  in the figure above are for flow between two horizontal parallel plates a distance  $h$  apart. The vapor condenses on the bottom plate and the flow conditions are described by the saturation temperature of the vapor  $T_s$ , wall temperature  $T_w$ , inlet pressure  $p_0$  and average inlet vapor velocity  $V_{av}$ . The inlet Reynolds number is  $Re_V = (\rho_V V_{av} h) / \mu_V$ .

The curves c1a and c1b correspond to turbulent friction factor  $f = f_0 = 0.06 (Re_V u_{av})^{-0.25}$  where  $u_{av}$  is the non-dimensional average vapor velocity at  $x$ . The curve c1a corresponds to a formulation which assumes vapor velocity to be uniform across the cross-section of the flow. Therefore, for c1a, the tangential components of the vapor and liquid velocities are *not equal* at the interface. Curve c1b is a prediction from a formulation which allows a representative vapor velocity profile at a given  $x$  and *satisfies* continuity of tangential velocities at the interface.

The prediction in c2 is for an  $f$  defined by Wallis correlation;  $f = f_0 [1 + 17.5 Re_V^{0.25} (\rho_l / \rho_v) (\dot{m} / u_{av})]$ , where  $\dot{m}(x)$  represents non-dimensional condensation rate per unit area at the interface and  $\rho_l / \rho_v$  is the ratio of densities of the liquid and the vapor.

The prediction in c3 is for  $f = 3 f_0$  where  $f_0$  is the same as above.

For brevity, we merely state that the solution for  $x \rightarrow 0$  requires explicitly known asymptotic form of  $f$  of the type  $f \sim \dot{m}$  so as to resolve the singularity at  $x=0$

# ON THERMODYNAMICS OF VISCOELASTICITY

I-Shih Liu

Instituto de Matemática  
Universidade Federal do Rio de Janeiro  
Caixa Postal 68530  
21944 Rio de Janeiro, Brasil

In classical theory the behavior of viscoelastic materials is often described by simple rheological models consisting of spring and dashpots with stress-strain relation such as

$$\tau \dot{\sigma} + \sigma = E_1 \epsilon + E_2 \dot{\epsilon}, \quad (1)$$

where  $\tau$ ,  $E_1$ ,  $E_2$  are materials constants, for uniaxial stress of a *standard linear solid*. For general stress and finite deformation, rate-type constitutive relation like this one are often proposed and are analyzed within the framework of thermodynamics.

Recently a different approach to non-equilibrium thermodynamics has received increasing attention. Within this formulation, unlike the usual theories, non-equilibrium thermodynamic fluxes, namely, viscous stress and heat flux, are not considered as constitutive quantities, but are treated as independent field variables, like the basic field variables: the density, the velocity, and the temperature. This approach has been called *extended thermodynamics* and has been applied to classical and relativistic fluids as well as to viscoelastic solids.

The governing equations of extended thermodynamics consist of the usual conservation laws of mass, momentum, and energy and a set of additional equations of balance for the new independent field variables. Their basic structure is motivated by the moment equations of kinetic theory of gases and can be established from the requirement of Galilean invariance of the system.

A theory of isotropic viscoelastic materials, without heat conduction for simplicity, is

presented here within the general scheme of extended thermodynamics. General restrictions for the constitutive functions are obtained, subjected to the requirement of objectivity, material symmetry and the entropy principle. Field equations for the deformation gradient, the temperature and the viscous stress are derived. In particular, the linear equation for viscous stress  $S_{ij}$  can be written as

$$H_{ijkl}\dot{S}_{kl} + V_{ijkl}S_{kl} = \frac{\partial v_i}{\partial x_j}, \quad (2)$$

where  $H_{ijkl}$  and  $V_{ijkl}$  are isotropic functions of the left Cauchy Green tensor and the temperature only. They are positive definite fourth order tensors and must satisfy some further restrictions.

For linear viscoelastic solids, assuming small displacement gradient we obtained the following rate-type stress-strain relation,

$$\begin{aligned} \tau_s \dot{\sigma}_{\langle ij \rangle} + \sigma_{\langle ij \rangle} &= 2\mu \epsilon_{\langle ij \rangle} + 2\tau_s \hat{\mu} \dot{\epsilon}_{\langle ij \rangle}, \\ \tau_b \dot{\sigma}_{kk} + \sigma_{kk} &= 3\nu \epsilon_{kk} + 3\tau_b \hat{\nu} \dot{\epsilon}_{kk}, \end{aligned} \quad (3)$$

where  $\tau_s$  and  $\tau_b$  are relaxation times and  $\mu$  and  $\nu$  are shear and bulk viscosities.  $\sigma_{\langle ij \rangle}$  and  $\sigma_{kk}$  are the deviatoric and the trace part of the total stress  $\sigma_{ij}$ . It reduces to the relation (1) for incompressible body under uniaxial stress. The equation (2) is by no means restricted to small deformations, thus the present results provide a generalization of the linear theory to viscoelasticity of finite deformations.

## APPLICATION OF CONVECTION THEORIES TO GEOLOGY AND GEOPHYSICS

Albert T. Hsui<sup>1</sup> and Daniel N. Riahi<sup>2</sup>

<sup>1</sup> Department of Geology

<sup>2</sup> Department of Theoretical and Applied Mechanics  
University of Illinois, Urbana, IL 61801

Application of convection models to study the dynamics of the atmosphere and the ocean has received much attention during the past century. Using convection theories to study the solid earth, however, represents a relatively recent application. Despite its seemingly rigid appearance, the solid earth is a dynamic system. It is capable of deforming under stress imbalance over geological time scales through solid state creeping processes. The motions of the solid earth can be modeled as convection of viscous fluids. In this paper, applications of various convection theories to study the dynamics of the earth's interior are reviewed. Current status of some modeling techniques and some unsolved problems will be discussed.

The dynamic nature of the earth's surface has been well established since the advent of plate tectonics. Driving mechanism of plate motions is generally attributed to some form of mantle convection. In response to mantle convection, surface morphology, gravity signatures and thermal consequences can be calculated. For example, surface flows driven by topographic variations can be used to study formation of deep oceanic trenches and mountain ranges (Hsui et al., 1990); sea floor topography and oceanic heat flows can be studied through the cooling of a thermal boundary layer (Turcotte and Schubert, 1982 among others). Excellent agreements generally exist between these theoretically predicted results and observations.

Structure of mantle convective cells has been studied by many investigators. Traditionally, mantle convection is perceived as steady flows because of its high viscosity (e.g.  $10^{22}$  Pa-s). Consequently, generation of cells with large horizontal scales (i.e. aspect ratio  $> 4$ ) becomes an important research topic. More recently, however, because of the high Rayleigh number associated with mantle convection (i.e.  $10^6 - 10^8$ ), Hansen et al. (1990) suggest the possible existence of a chaotic and turbulent mantle convective regime based on a two dimensional Cartesian model. This contention seems to be supported by the thermal structure of the mantle as delineated by seismic tomographic studies. One

characteristic feature of a high Rayleigh number flow regime is the production of plumes. These plumes may have important implications to the formation of oceanic islands such as the Hawaiian islands.

The effect of spherical geometry may also play an important role in the determination of flow structure within the mantle. In this paper, some aspects of the pattern of convection in spherical shells generated by bifurcations from basic states that are homogeneous and isotropic with respects to spherical surfaces will be reviewed. This subject is far from being well understood. In a weakly non-linear regime, however, a general theory has begun to emerge (Busse, 1975; Busse and Riahi, 1982, 1984; Riahi et al., 1982; Riahi, 1984; Busse and Riahi, 1988; Riahi and Busse, 1988; Riahi, 1991).

Cellular patterns of convection in spherical shells with spherically symmetric basic states have been studied by an expansion in terms of the amplitude of the bifurcating solution. This method has been applied if the solution in the linear limit is characterized by a single degree  $l$  of spherical harmonics or if the eigenvalues corresponding to bifurcating solutions with different degrees,  $l$  and  $l'$ , nearly coincide. Preferred solutions with various numbers of cells and symmetries have been obtained including those which exhibit symmetries of platonic solids. More recent studies (Riahi, 1991) based on multiple scales and asymptotic techniques in the thin shell limits provide more general information on the planform functions of the convection patterns in spherical shells.

Modeling mantle convection is far from being complete. Many important factors have not yet been taken into consideration. For example, effects of heterogeneity and phase changes have not yet been accounted for. Does double diffusive convection play a role in mantle convection? How do phase changes affect mantle flow structures? These are some of the questions remained to be resolved.

#### References:

- F. H. Busse, *J. Fluid Mech.*, 72, 67, 1975.
- F. H. Busse and N. Riahi, *J. Fluid Mech.*, 123, 283, 1982.
- F. H. Busse and N. Riahi, *J. Tera Cognita*, 4, 240, 1984.
- F. H. Busse and N. Riahi, *J. Nonlinearity*, 1, 379, 1988.
- U. Hansen, D. A. Yuen and S. E. Kroening, *Phys. Fluid*, A2, 12, 2157, 1990.
- A. T. Hsui, M. S. Wilkerson and S. Marshak, *Geophys. Res. Ltr.*, 17, 12, 2421, 1990.
- N. Riahi, G. Geiger and F. H. Busse, *Geophys. Astrophys. Fluid Dyn.*, 20, 307, 1982.
- N. Riahi, *J. Phys. Soc. Japan*, 53, 2506, 1984.
- D. N. Riahi and F. H. Busse, *ZAMP*, 39, 699, 1988.
- D. N. Riahi, *in preparation*, 1991.
- D. L. Turcotte and G. Schubert, *Geodynamics*, 450pp, 1982.

# NONLINEAR PATTERN FORMATION IN THE COUPLED BÉNARD – MARANGONI CONVECTION

Layachi Hadji  
Department of Mathematics, University of Alabama  
Tuscaloosa, AL 35487

D.N. Riahi  
Department of Theoretical and Applied Mechanics,  
University of Illinois  
Urbana, IL 61801

A horizontal layer of a Boussinesq fluid heated from below undergoes a transition to a cellular state when the vertical temperature gradient exceeds some critical value. When the upper surface is open to the ambient air, there are two possible driving mechanisms to the overall convective motion; namely buoyancy and surface-tension forces. The coupling between these two agencies depends on several experimental data, such as the thickness of the liquid layer and the thermal conductivities of the bounding plate and the surrounding air. For a large Prandtl number fluid, the system is described by [1].

$$\nabla^4 \phi - R \theta = 0 \quad (1a)$$

$$\nabla^2 \theta - \nabla_H^2 \phi = \theta_z + \nabla x \nabla x \phi \cdot \mathbf{k} \cdot \nabla \theta \quad (1b)$$

where  $\theta$  is the temperature deviation from the conductive profile,  $\nabla x \nabla x \phi \cdot \mathbf{k}$  is the perturbation of the poloidal component of the solenoidal vector field  $\mathbf{u}$ ,  $\mathbf{k}$  is a unit vector in the vertical direction, and  $R$  is the Rayleigh number. Equations (1) are supplemented by these boundary conditions ( $D = \partial/\partial z$ ):

$$\phi(0) = \phi(1) = D\phi(0) = 0, \quad (2a)$$

$$D^2 \phi(1) = -M \theta(1), \quad (2b)$$

$$D\theta(0) = \beta_p \theta(0), \quad D\theta(1) = -\beta_a \theta(1). \quad (2c)$$

where (2a) is the no-slip condition, (2b) describes the continuity of the tangential stress at the planar air-liquid interface and (2c) represent the thermal boundary conditions at the lower plate and at the interface, respectively.  $M$  is the Marangoni number, and the  $\beta$ 's are heat transfer Biot numbers. The analysis is limited to the case  $\beta_p, \beta_a \ll 1$ . This case corresponds to a liquid having a thermal conductivity that is much larger than that of the plate or air-layer. Under these conditions, the first bifurcation from the static state is stationary and occurs with a very long wavelength [2]. Consider then, following [2], the scaling  $(x, y, z, t) = (X/\epsilon, Y/\epsilon, z, \tau/\epsilon^4)$  and for supercritical Rayleigh and Marangoni numbers,  $R = R_c + \mu\epsilon^2$  and  $M = M_c + \sigma\epsilon^2$ .

Upon scaling and expanding Eq. (1) and boundary conditions (2) in the small parameter  $\epsilon^2$ , the solvability condition at  $O(\epsilon^4)$  yields the following scaled evolution equation for the leading order temperature perturbation  $f$ : ( $\nabla_H = (\partial/\partial X, \partial/\partial Y)$ )

$$f_\tau = -\beta f - 2\nabla_H^2 f - \nabla_H^4 f + \Gamma_1 \nabla_H^2 |\nabla_H f|^2 + \Gamma_2 \nabla_H \cdot \nabla_H f (\nabla_H^2 f) + \nabla_H \cdot \nabla_H f |\nabla_H f|^2 \quad (3)$$

$$\text{where} \quad \Gamma_1 = \psi_3 / \sqrt{\psi_5 \psi_1} \text{ and } \Gamma_2 = \psi_4 / \sqrt{\psi_1 \psi_5}, \quad (4a)$$

$$\psi_1 = (5490 - 4556m - 241 m^2)/41580; \quad \psi_3 = -(35 + 303m + 45 m^2)/630, \quad (4b,c)$$

$$\psi_4 = -(5 + 4m)/90; \quad \psi_5 = (577975 - 1148215m + 574128m^2)/14175. \quad (4d,e)$$

The parameter  $m = Mc/48$ ,  $0 \leq m \leq 1$ , represents the coupled effect between the two agencies causing instability. The limiting values of  $m = 0$  and  $m = 1$  correspond to buoyancy and surface-tension induced convection, respectively.

The regular stationary patterns in the vicinity of the scaled critical wavenumber  $\alpha = 1$  are described by the planform function

$$f(X, Y, \tau) = A(\tau) \cos(aX) \cos(bY) + B(\tau) \cos(Y), \quad (5)$$

where  $a^2 + b^2 = 1$ . For small supercritical deviations, we find that rolls ( $B = 0$ ,  $a = 1$ ) are unstable with respect to inclined disturbances; while Up-Hexagons ( $a = \sqrt{3}/2$ ,  $b = 1/2$ ,  $A = B$ ) are preferred for all values of the coupling coefficient  $m$ . Both Up-Hexagons and Squares ( $B = 0$ ,  $a = b = \sqrt{2}/2$ ) are found to transport more heat than either Rolls or Up-Hexagons. Down-Hexagons are not realizable because they correspond to higher  $\beta$  than that for Up-Hexagons.

For  $O(1)$  supercritical deviations, the fully nonlinear two-dimensional evolution equation with  $\beta = 0$  can be written as,

$$f_\tau = -f_{XX} - f_{XXXX} - \lambda(f_X f_{XX})_X + (f_X^3)_X, \quad (6)$$

where  $\lambda = -(\Gamma_1 + 2\Gamma_2)$ . Eq. (6) is solved numerically for several values of  $\lambda$  [3]. We found that  $\lambda$  increases from  $\lambda = 0.498$  to  $\lambda = 4.3$  as  $m$  increases from  $m = 0$  to  $m = 1$ . Therefore, more rapid motions are driven by horizontal temperature gradients due to an increase in surface-tension effects [3]. The descending cold currents are then compressed into a thin plume.

#### REFERENCES:

1. D.N. Riahi, Int. J. Engng. Sci., 27, 689 (1989).
2. M.R.E. Proctor, J. Fluid Mech. 113, 469 (1981).
3. C.J. Chapman and M.R.E. Proctor, J. Fluid Mech. 101, 759 (1980).

ADAPTIVE GRID COMPUTATIONS FOR COUPLED ODE  
SYSTEM RESULTING FROM SPHERICAL HARMONIC  
DECOMPOSITION OF FORCED CONVECTION BY STOKES FLOW

André Trevor Spears  
X B Reed, Jr.  
Chemical Engineering Department  
University of Missouri-Rolla  
Rolla, MO 65401

For forced convection transport from a solid sphere in steady axisymmetric Stokes flow, the velocity and concentration (or temperature) fields can be represented as expansions in vector and scalar surface spherical harmonics, respectively [1]. Orthonormality can be invoked to obtain a system of coupled ordinary differential equations for the radial functions,  $c_n(r)$  [2,3]:

$$\begin{aligned} Pe \left( \left( \frac{n}{2n-1} \right) \left( f \frac{dc_{n-1}}{dr} + (n-1) \frac{g}{r} c_{n-1} \right) + \left( \frac{n+1}{2n+3} \right) \left( f \frac{dc_{n+1}}{dr} - (n+2) \frac{g}{r} c_{n+1} \right) \right. \\ \left. = \frac{1}{r^2} \frac{d}{dr} \left( r^2 \frac{dc_{n+1}}{dr} \right) - \frac{n(n+1)}{r^2} c_n, \quad 0 \leq n, \right. \end{aligned} \quad (1)$$

in which

$$f = \left( r - \frac{3}{2r} + \frac{1}{2r^2} \right), \quad g = - \left( 1 - \frac{3}{4r} - \frac{1}{4r^2} \right), \quad (2)$$

subject to

$$c_0(r=1) = 1; \quad c_n(r=1) = 0, \quad 1 \leq n; \quad c_n(r \rightarrow \infty) = 0, \quad 0 \leq n \quad (3)$$

The value of the Peclet number  $Pe$  has a significant effect on  $c(r, \theta)$ , with diffusion dominating as  $Pe \rightarrow 0$  [4,5] and with convection dominating as  $Pe \rightarrow \infty$  [6]. There are two major implications of these two limits for a numerical attack on Eqs. (1): as  $Pe$  increases, the total required number of radial modes  $L$  increases, whereas as  $Pe$  decreases, the finite location  $r_\infty$  at which the infinite boundary condition  $c = 0$  is imposed increases.



The role of  $L$  and of  $r_0$  for different  $Pe$  has been studied systematically in the following ranges.

$Pe = 0.05, 0.1, 0.2, 0.5, 1, 2, 5, 10, 20, 50, 100, 200, 500, 100$

$r_0 = 100, 50, 20, 10, 5, 3, 2.75, 2.5$

$L = 16, 32$  and small variations thereabout.

#### References

1. S. S. Bupara, X B Reed, Jr., and L. E. Scriven, "On the Application of Director Vector Methods to the Partial Differential Equations of Fluid Mechanics", AIChE National Meeting, Tampa, Florida, 1968.
2. P. C-H. Chan, D. G. Retzloff, H. Lin, M-S. Razavi, and X B Reed, Jr., "Solution of the Laminar Forced Convection Mass Transfer Problem via Vector Harmonics", pp. 347-350, in International Conference on Mechanics of Two-Phase Flows, June 12-15, 1989.
3. A. T. Spears, X B Reed, Jr., M-S. Razavi, E. J. Bisbis, P. C-H. Chan, D. G. Retzloff, "Forced Convection Heat and Mass Transfer for a Spherical Particle in Slow Flow", Bulletin of the American Physical Society v.35, 2308 (1990).
4. A. Acrivos and T. D. Taylor, "Heat and Mass Transfer from Single Spheres in Stokes Flow", Physics of Fluids 5, 387-394 (1962).
5. H. Brenner, "Forced Convection Heat and Mass Transfer at Small Peclet Numbers from a Particle of Arbitrary Shape", Chemical Engineering Science 18, 109-122 (1963).
6. A. Acrivos and J. D. Goddard, "Asymptotic Expansions for Laminar Forced-convection Heat and Mass Transfer", Journal of Fluid Mechanics 23, 273-291 (1965).

# ON FOURDIMENSIONAL CANTOR-LIKE SETS AND TURBULENCE

M.S. El Naschie  
Sibley School of Mechanical & Aerospace Engineering  
Cornell University  
112 Upson Hall  
Ithaca, N.Y. 14853, U.S.A.

## Abstract

The present discussion attempts to show some abstract connections between chaotic dynamics, fractal sets and dimensionality which may have relevance to physical systems.

The starting point of the analysis is the generally accepted realization that fractals are the carriers of complex strange behaviour. Second we follow Yorke's conjecture that single Cantor sets are somehow the back bone of all strange behaviour. To that we add what is intuitively evident namely that in one dimension the simplest fractal set is Cantor's middle third set with  $d_c = \log 2 / \log 3$ . If we accept this, then we can claim that

in four dimensional phase space a strange set will typically have a Cantor-like fractal dimension  $d_c \approx 4$ . This result is reached using the following scaling argument. The idea is to find the equivalent to a triadic Cantor set in two dimensions. Such a set should be triadic Cantorian in every conceivable direction. It cannot therefore be the Cartesian product of two such sets,  $d_c = \log 4 / \log 2$  nor a Cantor target  $d_c = 1 + \log 2 / \log 3$ . However we know that a unit area  $A$  of an Euclidian manifold is given by  $A = (1)(1) = 1$  and consequently a corresponding quasi area of a Cantor set is  $A_c = (d_c)(d_c)$ . It follows then that in order to normalize  $A_c$  it must be multiplied by the normalization factor  $S_2 = (A/A_c)^2$ . By analogy in  $n$  dimensions we would have  $S_n = (A/A_c)^n$ . Denoting the  $n$ -th Cantor-like fractal dimension in  $n$  dimensional space by  $d_c^{(n)}$  and the dimension of the corresponding Euclidian space in  $n$  dimensions by  $d_E^{(n)} = n$  it follows then that

$$d_c^{(n)} = S_n d_c = d_c / (d_c)^n = (1/d_c)^{n-1} = (d_s)^{n-1}$$

where  $d_s$  is termed the escalation factor. This is the set which we are looking for and the result is now evaluated for  $d_c = \log 2 / \log 3$  in table 1, where we have introduced a new quantity termed co-dimension defined as  $C = d_E^{(n)} - d_c^{(n)}$ . Note that  $C$  could be equally interpreted as the Floquet multiplier of a discrete map

$$d_{(m+1)} = d_{(m)} \cdot \frac{1}{d_{(0)}}$$

where  $n = m + 1$ ,  $d^{(0)} = d_c^{(0)}$  and  $d_s = \partial(d_{(m+1)}) / \partial(d_{(m)})$

Basic assumption	0	$d = 0.63092$	$C = d_E^{(n)} - d_c^{(n)}$
Normality	1	1	
Results	2	1.58496	0.41504
	3	2.51210	0.48790
	4	3.98159	0.01841
	5	6.31067	-1.31067
	6	10.00218	-4.00218
	7	15.85309	-8.85309
	8	25.12655	-17.12655

- TABLE 1 -

There are a few interesting observations here. First  $d_c^{(n+1)}/d_c^{(n)} = d_s$  is the fractal dimension of the Serpenski gasket which is the prototype of fractal lattices with infinite hierarchy of semi loops. Second for all  $n < 4$  we have  $n > d_c^{(n)}$  while for  $n > 4$  we have

$d_c^{(n)} \gg n$ . Only at  $n=4$  we have a Cantor-like structure which comes very near to a space filling set. The two dimensional geometrical analogue of this is the peano curve which is ergodic and shares a few properties with fat fractals. We may say therefore that at  $n=4$  the set is almost ergodic. This point is clearly marked by the co-dimension  $C$  becoming very small and then aproptly changing its sign to negative. The third observation is that for any three successive dimension  $d_c^{(n)} \approx d_c^{(n-1)} + d_c^{(n-2)}$ . This is strongly reminiscent of the Fibonacci numbers [2] and the corresponding dimension will be termed the Fibonacci fractal dimension. Should we insist that  $d_c^{(n)} = d_c^{(n-1)} + d_c^{(n-2)}$  then we find that at  $n=4$  the corresponding Cantor-like dimension is  $d_c = 4.23606$  while the Serpenski gasket is replaced by  $d_s = 1/\phi$  where  $\phi$  is the Golden mean. In fact our table number 1 becomes identical to the table calculated by Cook for Botticelli's venus.

Looking back at table 1, one may be lead to speculate if fully developed turbulence has a fractal dimension  $d \approx 6.3$  and that five dimensional phase space is required to study this phenomina. This would be for instance a nonlinearly oscillating set described by a

phase space  $x, \dot{x}$  and  $\ddot{x}$  representing temporal and spacial oscilation of a state variable  $x$ . In addition we need a spacial fluctuation  $\omega_x$  and a temporal fluctuation  $\omega_t$  as forcing frequencies. This makes them indeed five variables. Another worthwhile observation is that the Fibonacci fractal dimension  $d_c^{(3)} = 1 + 1/(\text{Log } 2/\text{Log } 3) = 2.58496$  is identical to  $d_c^{(3)} = 1/(\text{Log } 2/\text{Log } 6)$  where  $\text{Log } 2/\text{Log } 6$  is clearly a reasonable measure of the fractal dimension at period 3 chaos of a Feigenbaum cuscad. Note also that  $d_c = \text{Log } 2/\text{Log } 6 = 0.387$  is very close to the smallest value found for period 3 chaos of the logistic map ( $d_c = 0.378$ ).

## Three-Dimensional Thermal Convection

Abdelfattah Zebib

Department of Mechanical and Aerospace Engineering  
State University of New Jersey - Rutgers  
Piscataway, New Jersey 08855-0909

Buoyant and/or thermocapillary convective motions in rectangular and cylindrical containers are computed by a finite-volume method which is second-order accurate in space and first-order accurate in time. Two and three dimensional simulations, steady and time-dependent are considered. The numerical results are compared with available experimental data. Examples of transitions to oscillatory buoyant motions through a Hopf bifurcation will be presented. This transition is important in low Prandtl number applications. We find that the critical Grashof number and frequency are sensitive to 3D effects. A model with a free surface indicates that transition from a steady 2D motion to a steady 3D motion occurs at relatively low Marangoni numbers and precedes expected transitions to time-dependent convection.

## IDEAL AND REAL MAGNETICALLY SOFT BODIES

G.L. Viegelahn, M.O. Peach, C.R. Vilmann, C.E. Passerello, S. Yap  
Mechanical Engineering-Engineering Mechanics Department  
Michigan Technological University, Houghton, MI 49931

Maxwell observed<sup>1</sup> that a solenoid carrying a constant current  $I_0$  might be called a rigidly magnetized body, since its magnetization distribution can not be altered by any magnetic force acting on it. Such a solenoid placed in a uniform external field  $H_0$  experiences a torque  $T = CH_0 I_0 \sin \theta$  where  $\theta$  is the angle between the magnetic moment of the solenoid and the field direction and  $C$  is a constant. If we define a normalized torque  $T^* = T/CH_0 I_0$ , the plot of  $T^*$  vs  $\theta$  is a sine curve, denoted by AA in the figures 1 and 2. All ideally hard magnetic bodies give the same plot AA.

We define an ideally soft magnetic body as one which is magnetized to saturation by any field, however small. We can realize such a body by placing a reversing switch in the circuit so arranged as to actuate when  $\theta = 90^\circ$ . All such ideally soft magnetic bodies give the  $T^*$  vs  $\theta$  plot BBBB in the figures.

An ideal linear magnetic body satisfies  $M = kH$ . Since  $M$  is along the solenoid, we set  $H = H_0 \cos \theta$ , and obtain a  $T^*$  vs  $\theta$  plot CC in the figures. (A potentiometer in the circuit can be arranged to vary the current so that  $I = I_0 \cos \theta$ ). All linear bodies produce the plot CC on the  $T^*$  vs  $\theta$  diagram.

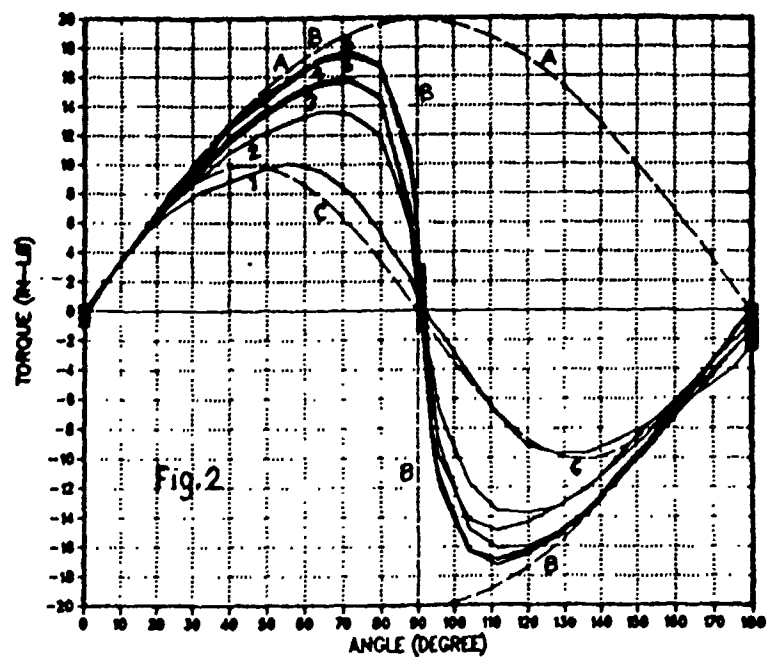
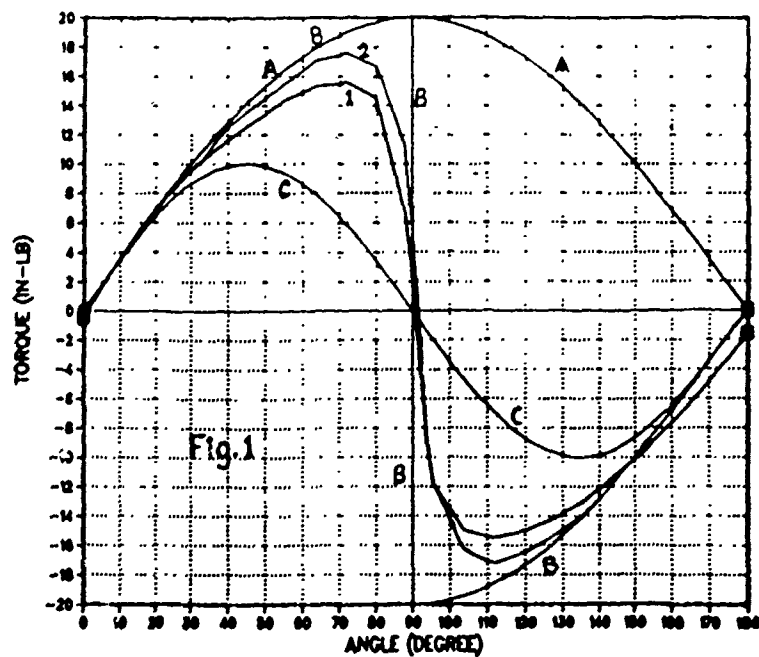
All three ideal bodies give  $T^*$  vs  $\theta$  curves which have the same slope (unity) at  $\theta = 0^\circ$ . Hence the  $T$  vs  $\theta$  curves for real specimens are normalized by setting  $T^* = cT$  where  $c$  is a constant chosen to make the initial slope at  $\theta = 0^\circ$  equal to unity. Experimental data are shown for a structural steel specimen 5" x 0.75 x 0.125".

In Fig. 2 curves labelled 1, 2, ... 7 are for ambient fields of 350, 800, 1200, 1600, 2000, 2400, 2520 Gauss. The specimen was rotated about a centroidal axis parallel to its 0.75 dimension.

In Fig. 1 the ambient field was 2000 Gauss. For curve 1 the rotation axis was parallel to the 0.75" dimension; for curve 2 it was parallel to the 0.125" dimension.

The  $T^*$  vs  $\theta$  experiment provides information complementary<sup>2</sup> to that provided by the classical  $B$  vs  $H$  experiment.

- (1) Maxwell, J.C., A Treatise on Electricity and Magnetism, Oxford Clarendon Press 1904, Art. 424.
- (2) Peach, M.O., Viegelaun, G.L., Dalrymple, J.M., Carlson, S.A., A Complement of Maxwell Constitutive Relation and the Classical Permeability Experiment, Proceedings of the Twenty-first Mid-Western Mechanics Conference.



# AN INCONSISTENCY IN MAXWELL'S CONTINUUM THEORY OF MAGNETOSTATICS

G. L. VIEGELAHN, M. O. PEACH, C. R. VILMANN, C. E. PASSERELLO, S. YAP  
MECHANICAL ENGINEERING - ENGINEERING MECHANICS DEPARTMENT  
MICHIGAN TECHNOLOGICAL UNIVERSITY, HOUGHTON MI 49931

Part III of Maxwell's Treatise, titled "Magnetism", is really restricted to Magnetostatics, since Ampere's Law and Faraday's Law are deferred to Part IV. Although Maxwell uses the word "particle" (and even "molecule, of Art. 380) quite frequently, the theory developed in Part III is continuum theory, and "particle" has the meaning "volume element". It is only much later in Part IV, Art. 638, that Maxwell explicitly refers to "... the method in Part III. in which we regarded the magnet as a continuous and homogeneous body, the minutest part of which has magnetic properties of the same kind as the whole." (Emphasis added.)

Poisson had previously suggested a theory that postulated two kinds of magnetic fluids, in analogy to positive and negative electric charges, and Maxwell rejected it (Art. 380) because "... it enables us to say what would be the properties of a body containing an excess of one magnetic fluid. It is true that a reason is given why such a body cannot exist, but this reason is only introduced as an after-thought to explain this particular fact ..."

In Art. 383, Maxwell says "Let the element  $dx dy dz$  be a particle (emphasis added) of a magnet, and let us assume that its magnetic properties are those of a magnet the strength of whose positive pole  $m$  and whose length  $ds$  ..." A few lines later he proceeds to the limit  $ds \rightarrow 0$ , which of course implies  $dx dy dz \rightarrow 0$  which implies that the actual; structure of magnetic material is being replaced by a continuum approximation.

He then (Art. 385), by the procedures of infinitesimal calculus deduces the formula :

$$V = \iint \frac{\sigma}{r} dS + \iiint \frac{\rho}{r} dx dy dz$$

for the potential  $V$  in term of a surface distribution of density  $\sigma$  and a volume distribution of density  $\rho$ . He notes that the formula is

identical with that for the electric potential due due to a body on the surface of which there is a charge density  $\sigma$  and throughout the volume is a volume charge density  $\rho$ . By analogy  $\sigma$  is a surface pole density and  $\rho$  is a volume pole density. This means that  $\sigma ds$  is pole strength on  $ds$  and  $\rho dxdydz$  is pole strength of the volume element  $dxdydz$ . But he has already rejected Poisson's analogy between electric charge and magnetic pole strength, and he has already said (Art 379) "... we may regard the magnet ... as made up of small particles (i.e. , volume elements) each of which has two equal and opposite poles (i.e., net pole strength equal zero). If we suppose all magnets to be made up of such particles it is evident that since the algebraical quantity of magnetism (i.e., pole strength) in each particle is zero..." (emphasis is added), he should point out that the quantity  $\rho dxdydz$  is always zero, hence  $\rho$  must be set equal to zero in the above formula. Hence the above formula reduces to a surface distribution of poles only.

It may be possible to have a particle model of magnetic material with  $\rho$  not equal to zero, but is certainly not possible in the context of a continuum theory.

## References :

- (1) Maxwell, J.C., A Treatise on Electricity and Magnetism, Oxford Claradon Press 1904.



# WAVE PROPAGATION IN AN ARBITRARY SHAPED PYROELECTRIC SOLID CYLINDER

H.S.Paul and G.V.Raman

Department of Mathematics  
Indian Institute of Technology, Madras  
India

**Abstract :** The flexural and longitudinal wave propagation in a pyroelectric cylinder of arbitrary cross section of crystal class (6mm) is considered. Fourier series collocation method due to Nagaya is applied to satisfy the boundary conditions at the irregular outer boundary. The frequency equation has been derived for stress free, earth connected and thermally insulated outer surface. Numerical results are calculated for polygonal shaped solid cylinder. The results are given for Barium Titanate ceramic.

**Method of Analysis :** Mindlin<sup>1</sup> gave the constitutive equations governing elastic, piezoelectric and thermal behaviour of the pyroelectric material. The equation of motion governing the mechanical, electrical and thermal behaviour for crystal class (6mm) are given in [2] as

$$\bar{T}_{ij,j} = \rho u_{i,t} ; \quad D_{i,i} = 0 ; \quad K_{ij} T_{,ij} = T_0 \sigma_{,t} \quad (1)$$

where  $\bar{T}$ ,  $D$ ,  $\sigma$  are stresses, electrical displacements and entropy respectively. The solutions for the equations (1) can be taken as

$$u_r(r, \theta, z, t) = \sum_{n=0}^{\infty} \epsilon_n \left( \phi_{n,r} + \frac{1}{r} \psi_{n,\theta} \right) \exp j(kz + pt) ;$$

$$u_\theta(r, \theta, z, t) = \sum_{n=0}^{\infty} \epsilon_n \left( \frac{1}{r} \phi_{n,\theta} - \psi_{n,r} \right) \exp j(kz + pt) ;$$

$$u_z(r, \theta, z, t) = j \sum_{n=0}^{\infty} \epsilon_n W_n \exp j(kz + pt) ; \quad V(r, \theta, z, t) = j \sum_{n=0}^{\infty} \epsilon_n V_n \exp j(kz + pt) ;$$

$$T(r, \theta, z, t) = \sum_{n=0}^{\infty} \epsilon_n T_n \exp j(kz + pt) \quad \text{in which } j = \sqrt{-1} \quad \text{and } \epsilon_n = \begin{cases} 1/2 & \text{for } n=0 \\ 1 & \text{for } n \geq 1 \end{cases}$$

where  $\phi_n$ ,  $\psi_n$ ,  $W_n$ ,  $V_n$ ,  $T_n$  are functions of  $r$  and  $\theta$  only. Substituting the solutions in (1) we get the equations of motion in terms of  $\phi_n$ ,  $\psi_n$ ,  $W_n$ ,  $V_n$ ,  $T_n$ . The solutions for the transformed equations can be taken as

$$\phi_n = \sum_{i=1}^4 A_{in} J_i(\alpha_i r) \cos(n\theta) ;$$

$$W_n = \sum_{i=1}^4 d_{in} J_i(\alpha_i r) \cos(n\theta) ;$$

$$V_n = \sum_{i=1}^4 e_{in} J_i(\alpha_i r) \cos(n\theta) ;$$

$$T_n = \sum_{i=1}^4 h_{in} J_i(\alpha_i r) \cos(n\theta) ;$$

$$\psi_n = A_{5n} J_5(\alpha_5 r) \sin(n\theta).$$

It is difficult to satisfy the boundary conditions because of the irregular outer boundary. The assumptions given by Nagaya [3] and Venkatesan [4] are modified for pyroelectric case. The transformed

expressions for the stresses are

$$T_{qq} = (c_{11} \cos^2 \bar{\theta} + c_{12} \sin^2 \bar{\theta}) u_{r,r} + (c_{11} \sin^2 \bar{\theta} + c_{12} \cos^2 \bar{\theta}) (1/r) (u_r + u_{\theta,\theta}) - c_{66} (u_{\theta,r} + (1/r) (u_{r,\theta} - u_{\theta})) \sin 2\bar{\theta} + c_{13} u_{z,z} + e_{31} V_z - \beta_1 T$$

$$T_{qs} = c_{66} \left[ (u_{r,r} - (1/r) (u_r + u_{\theta,\theta})) \sin 2\bar{\theta} + (u_{\theta,r} + (1/r) (u_{r,\theta} - u_{\theta})) \cos 2\bar{\theta} \right]$$

$$T_{qz} = c_{44} \left[ (u_{r,z} + u_{z,r}) \cos \bar{\theta} - (u_{\theta,z} + 1/r u_{z,\theta}) \sin \bar{\theta} \right] + e_{15} \left[ V_{,r} \cos \bar{\theta} - 1/r V_{,\theta} \sin \bar{\theta} \right]$$

where  $T_{qq}$ ,  $T_{qs}$ ,  $T_{qz}$  are normal and shearing stresses respectively and  $\bar{\theta} = (\theta - \gamma_i)$  where  $\gamma_i$  is the angle between the normal to the segment and the reference axis [3]. The coordinate normal to the boundary is  $q$  and  $s$  is the coordinate tangential to the boundary. The boundary conditions are

$$(T_{qi}) = (T_{qs}) = (T_{qz}) = 0 \quad (T_{,qi}) = 0 = (V)_{,i} \quad (2)$$

where  $( )_i$  is the value at the  $i^{th}$  segment of the boundary. Fourier series expansion is taken for (2) along the outer boundary. By eliminating the arbitrary constants  $A_{in}$  we get the frequency equation.

**Numerical Results :** Geometric relation for polygonal cross section is taken from [5]. Material constants are taken for BaTiO<sub>3</sub> ceramic. Roots of the frequency equation are found out by using Newton-Raphson method. The results are given in the table below.

$c \rightarrow$ cb	symmetric case		AntiSymmetric case
	Longitudinal	Flexural	Flexural
0.5	0.2230+10.0016	0.2226+10.0018	0.2004+10.0010
1.0	0.4273+10.0144	0.4444+10.0178	0.4187+10.0147
1.5	0.6502+10.0010	0.6960+10.0022	0.6003+10.0010
2.0	0.8309+10.0011	0.9032+10.0016	0.8131+10.0177

#### References

- [1] R.D.Mindlin, Problems in Continuum Mechanics, SIAM, 282-290 (1961).
- [2] H.S.Paul and G.V.Raman, Acta Mechanica (In Press).
- [3] K.Nagaya, J.Appl.Mech. (ASME), 49, 157-164 (1982).
- [4] H.S.Paul and M.Venkatesan, Int.J.Engng.Sci.27, 847-853 (1989).
- [5] K.Nagaya, J.Acoust.Soc.Am.70, 763-770 (1981).

# IDEAL AND REAL MAGNETICALLY HARD BODIES

G.L. Viegelaahn, M.O. Peach, C.E. Passerello, C.R. Vilmann, S. Yap  
Mechanical Engineering-Engineering Mechanics Department  
Michigan Technological University, Houghton, MI 49931

According to Osborn<sup>1</sup>, the component of  $H$  along any principal axis of an ellipsoid is given by

$$H_i = (H_o)_i - N_i J_i \quad i = x, y, z$$

where  $H_o$  is a uniform applied field,  $N_i$  is a demagnetizing factor, and  $J_i$  is a component of the magnetization  $J$ . The  $x, y, z$  axes are parallel to the  $a, b, c$  semi-axes of the ellipsoid and  $a \geq b \geq c \geq 0$ .

We choose fixed axes  $X, Y, Z$  such that the applied field is parallel to the  $X$ -axis, the  $y$ -axis is identical with the  $Y$ -axis, and the angle between the  $x$  and  $X$  axes is  $\theta$ . See Fig. 1. We then have

$$H_x = H_o \cos \theta - N_x J_x \text{ and } H_z = H_o \sin \theta - N_z J_z$$

Setting  $J_x = K_x H_x$  and  $J_z = K_z H_z$  and solving the resulting two equations for  $H_x$  and  $H_z$  we obtain

$$H_x = (H_o \cos \theta) / (1 + N_x K_x) \text{ and}$$

$$H_z = (H_o \sin \theta) / (1 + N_z K_z)$$

which gives

$$J_x = K_x (H_o \cos \theta) / (1 + N_x K_x) \text{ and}$$

$$J_z = K_z (H_o \sin \theta) / (1 + N_z K_z)$$

Since  $J_x$  and  $J_z$  are uniformly distributed throughout the volume  $V$  of the ellipsoid the  $x, y, z$  components of the magnetic moment of the ellipsoid are  $VJ_x, 0, VJ_z$ . Using the symbols  $\hat{i}_x, \hat{i}_y, \hat{i}_z, \hat{i}_x, \hat{i}_y, \hat{i}_z$  for unit vectors along the positive axes, we can write

$$M = VH_o \{ \hat{i}_x K_x \cos \theta / (1 + N_x K_x) + \hat{i}_z K_z \sin \theta / (1 + N_z K_z) \}$$

for the magnetic moment induced in the ellipsoid by the applied field  $H_0$ . Then the torque exerted on the ellipsoid by the applied field  $\hat{i}_x H_0$  is

$$T = (VH_0^2 \sin \theta \cos \theta) \left( \frac{K_x}{(1 + N_x K_x)} - \frac{K_z}{(1 + N_z K_z)} \right) \hat{i}_y$$

Let us now suppose that the ellipsoid has also a "permanent" magnetization  $J'_x$  along the  $\hat{i}_x$  axis, producing an additional magnetic moment  $M' = \hat{i}_x J'_x V$  and hence an additional torque

$$T' = \hat{i}_y J'_x V H_0 \sin \theta$$

For "hard" magnetic bodies  $T' \gg T$  so that  $T(\theta)$  is a small perturbation of the sine curve  $T'(\theta)$  and passes through zero value at  $\theta = 90^\circ$ . Fig. 2 shows the total torque  $T' + T$  as a function of  $\theta$  for several hard specimens. For one of them we also show  $T'(\theta)$  and  $T(\theta)$  separately.

- (1) Osborn, J.A., Demagnetizing Factors of the General Ellipsoid, Phys. Rev. Vol. 67, Nos. 11 and 12 (1945) pp. 351-357.

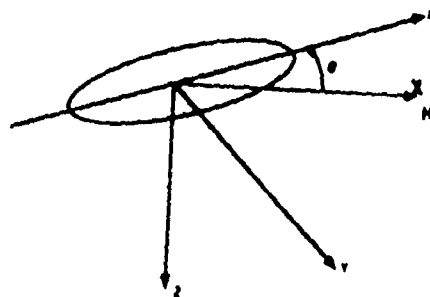


Figure 1

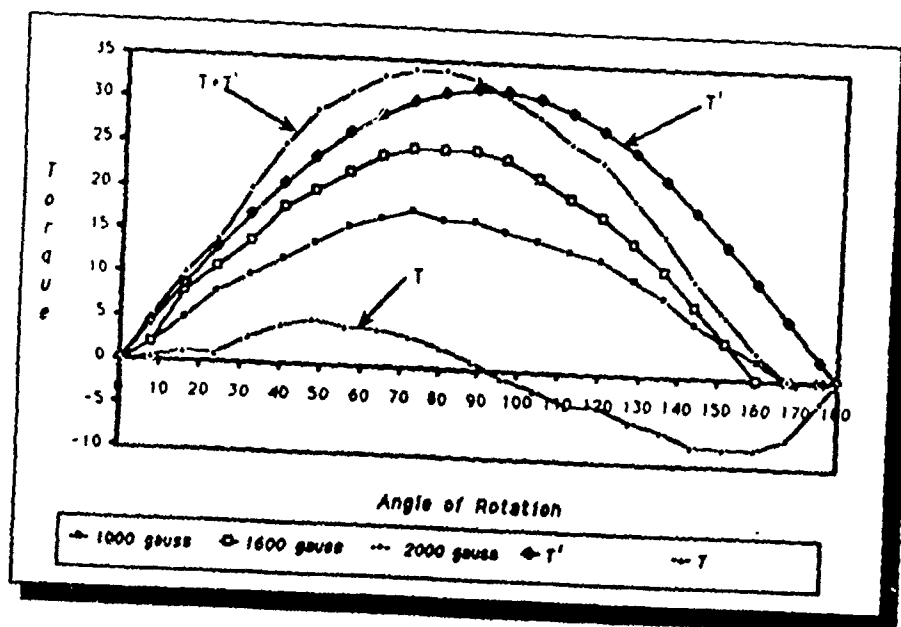


Fig. 2

# FINE STRUCTURE OF THE EDGE EFFECT

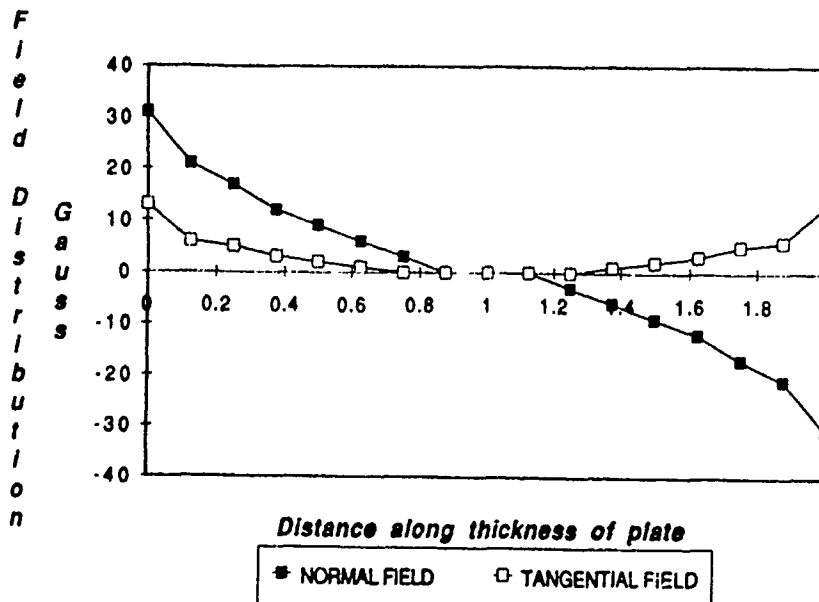
G.L. Viegelaahn, M.O. Peach, C.E. Passerello, C.R. Vilmann, S. Yap  
 Mechanical Engineering-Engineering Mechanics Department  
 Michigan Technological University, Houghton, MI 49931

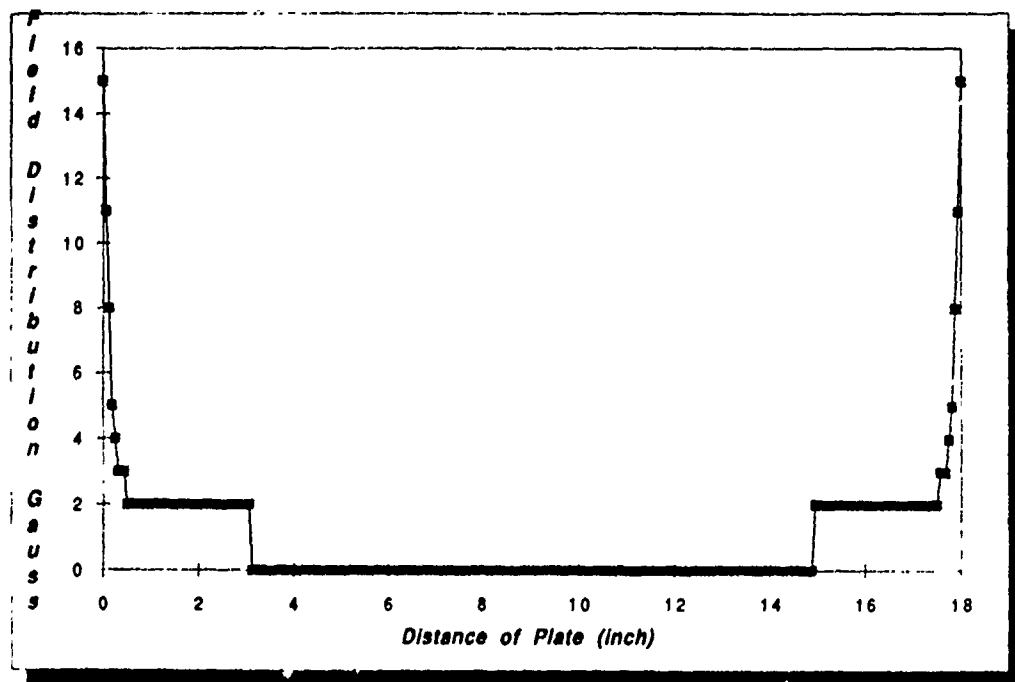
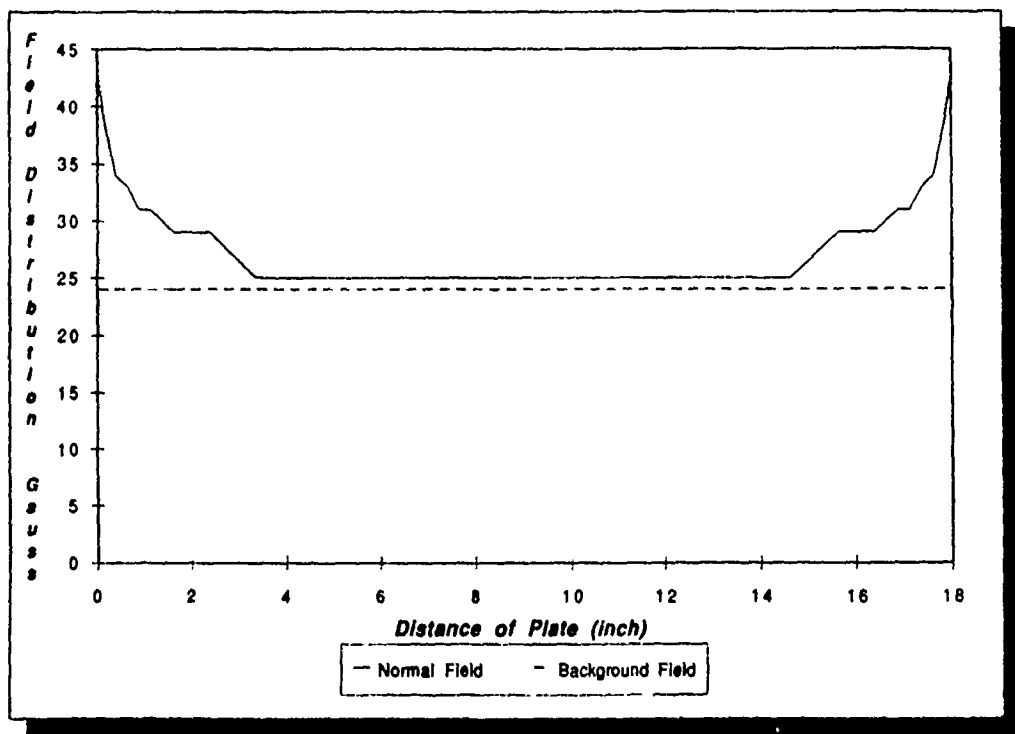
Christopherson's<sup>1,2</sup> doctoral work has called attention to the importance of the magnetic edge effect in magnetoelastic bending and buckling of magnetic plates. Until now, the maximum plate size studied was 0.5 in. thick. For such a plate the edge-effect region extends inward 1.8 in. from the edge, and the region where the theoretical and experimental results disagree extends inward only 0.25 in. Although the latter region is small the magnetic forces acting there are significant, accounting for approximately 30% of the bending moment at all points along the beam-plate. The theoretical solution in this region gives a field which goes to infinity as  $1/r$  where  $r$  is the distance from the edge.

We now have an apparatus which can accommodate plates up to 6 in. thick. We can now get good resolution in measuring the field in the latter region, as well as over the end of the plate, not previously measured.

Experimental results are shown in the figures.

- (1) N.S. Christopherson, M.O. Peach, J.M. Dalrymple, "Magnetostatic Deformation: Bending of a Thin Plate", *Experimental Mechanics*, Dec. 1989, pp. 432-436.
- (2) N.S. Christopherson, J.M. Dalrymple, M.O. Peach, "An Alternate Approach to Magnetic Deformation Problems", *Proceedings of the Twenty-first Mid-Western Mechanics Conference*, p. 257.





# **Transient Temperature Distribution in Rectangular Mounting Plates for Thermal Resistance Applications**

**Arshad Y. Khan and Nellore S. Venkataraman  
Department of Mechanical Engineering  
University of Puerto Rico  
Mayaguez Puerto Rico 00708**

In many thermal analysis and design problems a knowledge of thermal resistance between two objects is necessary. For example during the thermal design of spacecrafts, a spacecraft is divided into a large number of isothermal nodes (not necessarily an infinitesimal node) [1,2]. An energy balance is then performed to account for conduction and radiation heat transfer between these nodes. To calculate the conduction heat transfer between two nodes, thermal resistance is required as an input parameter. Because of numerous difficulties associated in evaluating thermal resistance, it is a common practice to use values based on intuition, judgment and experience.

This work is directed towards establishing a step by step procedure in the estimation of thermal resistance based on transient and steady state temperature distributions in a thin rectangular plate with two arbitrarily located heat sources. These sources acquire a steady state strength after going through a rise time (not necessarily the same for both), so as to closely simulate the heat generating object in actual situation. Isothermal or convective boundary conditions are assumed for the rectangular plate.

Transient and steady state temperature distribution have been obtained, both analytically and numerically. For a plate with isothermal boundaries analytical solution was obtained, however, for convective boundary conditions, only numerical solution was possible. The thermal resistance as a function of time for both the boundary condition cases is determined for several combinations of heat dissipation rate, geometric characteristic of the plate and heat sources and rise time difference. This procedure for thermal resistance estimation can also be used in cooling of

electronic components, where thermal resistance between chip modules has to be calculated in order to design a cooling system for heat dissipation from these chip modules.

A next step in the right direction would be the compilation of this information in form of a look up chart or table which can be easily used by the designers. Compilation of such information requires the analysis of every possible combination of pertinent parameters. Therefore, this study would be used to lead toward a two fold objective: (i) Identification of parameters influencing the thermal resistance, and (ii) Compilation of results in a convenient form for designers.

**References:**

1. "Fundamentals of Spacecraft Thermal Design", J.W. Lucas, Editor, AIAA, 1972
2. "Heat Transfer and Spacecraft Thermal Control", J.W. Lucas, Editor, AIAA, 1971



# BUCKLING AND BENDING OF CYLINDRICALLY ORTHOTROPIC ANNULAR PLATES

Victor Birman  
University of Missouri-Rolla  
Engineering Education Center  
8001 Natural Bridge Road  
St. Louis, MO 63121-4499

George J. Simitzes  
Department of Aerospace Engineering and  
Engineering Mechanics  
University of Cincinnati  
Cincinnati, Ohio 45221-0070

In this paper exact solutions for bending and buckling problems of cylindrically orthotropic circular and annular plates are presented. The loads include a uniformly distributed transverse pressure (bending problem) and compressive stresses associated either with uniform radial mechanical forces or with a uniform thermal field (bending and buckling problems). Effects of in-plane deformations on bending and buckling are disregarded as done in classical solutions for isotropic plates. Arbitrary boundary conditions can be considered. Notably, in the particular case of isotropic circular plates the present solution converges to that published in the literature.

In the case of buckling of a circular plate clamped along the edge a universal curve shown in Fig. 1 represents all possible geometries and materials. In this Figure  $\nu = \sqrt{D_{\theta\theta}/D_{rr}}$  where  $D_{\theta\theta}$  and  $D_{rr}$  denote bending stiffnesses of the plate material in the circumferential and radial directions respectively and  $u_0 = a\sqrt{-N_r/D_{rr}}$  is a parameter that characterizes the critical intensity of the radial loads ( $N_r$ ),  $a$  being the plate radius.

A typical distribution of circumferential and radial strain parameters ( $\bar{\epsilon}_\theta, \bar{\epsilon}_r$ ) in a circular plate subject to bending by a uniformly distributed transverse pressure and radial compression is shown in Fig. 2. ( $\bar{r} = 1$  corresponding to the external edge). Notably, the distribution of strains in Fig. 2 is similar to that in an isotropic plate subject to the same loading.

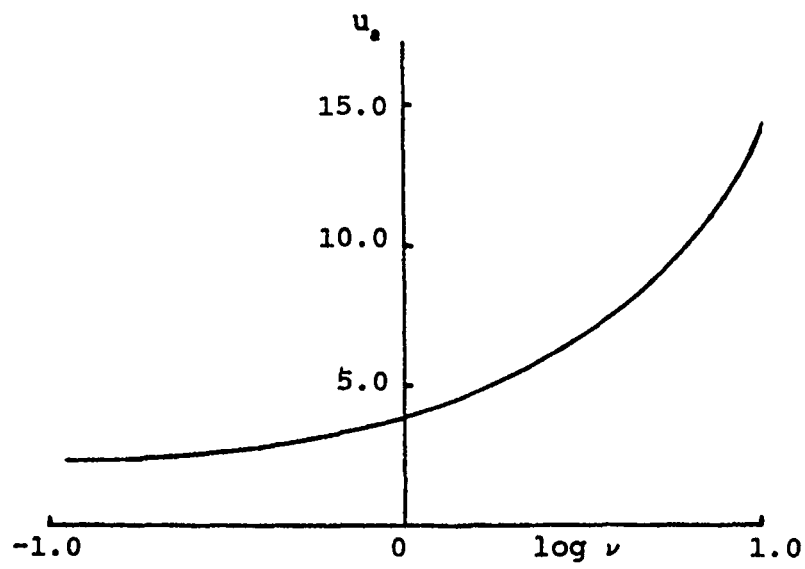


Fig. 1

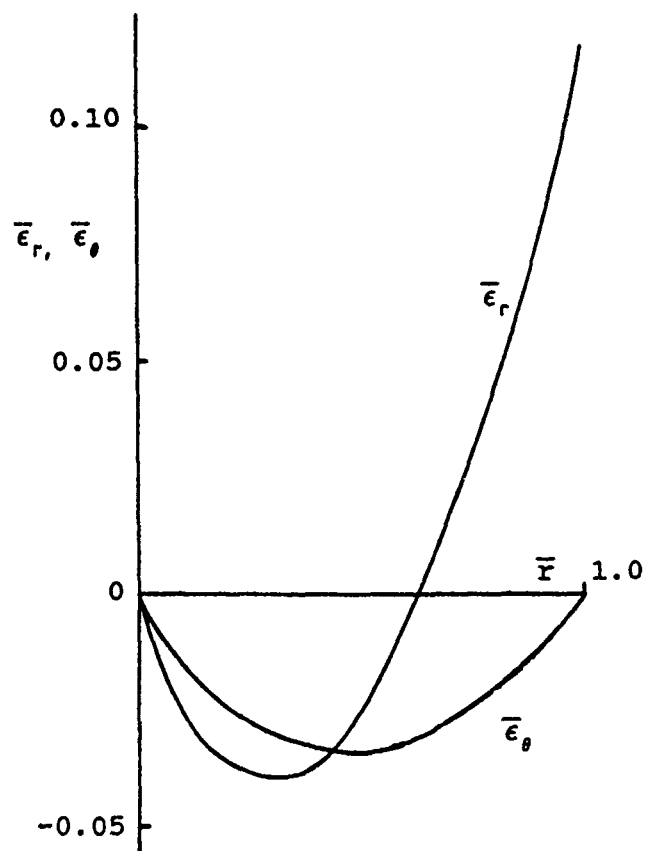


Fig. 2

# VIBRATIONS OF SYMMETRICALLY LAMINATED PLATES

Kenji HOSOKAWA and Toshiyuki SAKATA  
Department of Mechanical Engineering, Chubu University  
1200 Matsumotocho, Kasugai, Aichi, 487 Japan

## 1. Introduction

A numerical approach to the free, forced, and transient vibrations of an orthotropic plate was proposed and applied to a combined system consisting of plate, beam, and damping material [1]. In the present paper, the approach has been applied to symmetrically laminated plate of arbitrary planform and boundary condition. As an example, clamped symmetrically laminated rectangular plate with the structural damping was demonstrated.

## 2. Numerical Approach

By using the classical laminate plate theory, the differential equation governing the bending vibration of the symmetrically laminated plate is given by equation (1).

$$L^*[w^*] + \rho h (\partial^2 w^* / \partial t^2) = q^* \quad (1)$$

where  $h$  is the thickness,  $L^*[\ ]$  is the differential operator for the bending problem of the plate,  $w^*(x, y, t)$  is the deflection,  $q^*(x, y, t)$  is the lateral load acting on the plate,  $t$  is the time variable,  $\rho$  is the density of the plate material. Let us consider the function  $G^*(x, y, \xi, \eta)$ , which satisfies the boundary condition of the plate and the following differential equation,

$$L^*[G^*(x, y, \xi, \eta)] = \delta(x-\xi)\delta(y-\eta) \quad (2)$$

where  $\delta(\ )$  is Dirac's delta function. By dividing the plate into  $N$  pieces of small regions and applying the function  $G^*(x, y, x_n, y_n)$ , one has a frequency equation,

$$\det |\delta_{m,n} - \omega^{*2} \rho h G^*(x_m, y_m, x_n, y_n) \Delta S_n| = 0 \quad (3)$$

$$m, n = 1, 2, 3, \dots, N$$

where  $\delta_{m,n}$  is Kronecker's delta,  $\omega^*$  is a radian frequency, and  $\Delta S_n$  is area of the  $n$ th small region of the plate. For the forced vibration problem, by assuming that the lateral load acting on the plate is a sinusoidally varying force  $q^* = Q_0 \delta(x-a_1) \delta(y-b_1) e^{j\omega t}$  and that the deflection of the plate is  $w^*(x, y, t) = \bar{w}^*(x, y) e^{j\omega t}$ , one has simultaneous equation (4).

$$(\delta_{m,n} - \omega^2 \rho h \sum_{n=1}^N G^*(x_m, y_m, x_n, y_n) \Delta S_n) W^*(x_n, y_n) = Q_0 G^*(x_m, y_m, a_1, b_1) \quad (4)$$

$$m = 1, 2, 3, \dots, N$$

The function  $G^*(x, y, \xi, \eta)$  is assumed in the form

$$G^*(x, y, \xi, \eta) = \sum_{i=1}^I A_i^*(\xi, \eta) \psi(x, y) x^k y^l \quad (5)$$

where  $l$  is determined by  $l$  and  $k$ , and  $\psi(x, y)$  is determined just as the function  $G^*(x, y, \xi, \eta)$  satisfies the boundary condition. Undetermined coefficients  $A_i^*$  can be determined by Galerkin's method or energy method according to boundary conditions.

### 3. Numerical Example

Numerical calculations were carried out for a clamped symmetrically laminated square plate. All layers are assumed of equal thickness. As a typical filamentary composite material, the Graphite/Epoxy is considered. Moduli ratios are assumed to be  $E_1^* = E_1(1+j\eta)$ ,  $E_2^* = E_2(1+j\eta)$ ,  $G_{12}^* = G_{12}(1+j\eta)$ ,  $\nu_{12} = 0.30$ , where  $E_1 = 138 \text{ GPa}$ ,  $E_2 = 8.96 \text{ GPa}$ ,  $G_{12} = 7.1 \text{ GPa}$  [2], and  $\eta$  is structural damping factor. Table 1 shows the lowest three natural frequencies  $\omega_s / \sqrt{D_0 / \rho h a^4}$  of three layered  $(\theta, -\theta, \theta)$  plate, where  $D_0 = E_1 h^3 / 12(1 - \nu_{12} \nu_{21})$ . Figure 1 shows the normalized driving point impedance of three layered  $(45^\circ, -45^\circ, 45^\circ)$  plate.

Table 1 Natural frequencies  $\omega_s / \sqrt{D_0 / \rho h a^4}$  of clamped three layered  $(\theta, -\theta, \theta)$  square plates. ( $I=66$ ,  $N=15 \times 15$ ,  $\eta=0$ )

Fiber angle $\theta$	$\omega_s / \sqrt{D_0 / \rho h a^4}$		
	$s=1$	$s=2$	$s=3$
$0^\circ$	23.853	29.719	41.727
$5^\circ$	23.757	29.771	41.947
$10^\circ$	23.479	29.945	42.622
$15^\circ$	23.050	30.288	43.781
$20^\circ$	22.523	30.857	45.420
$25^\circ$	21.962	31.692	47.435
$30^\circ$	21.439	31.775	49.552
$35^\circ$	21.017	33.998	49.901
$40^\circ$	20.745	35.084	47.980
$45^\circ$	20.651	35.550	47.223

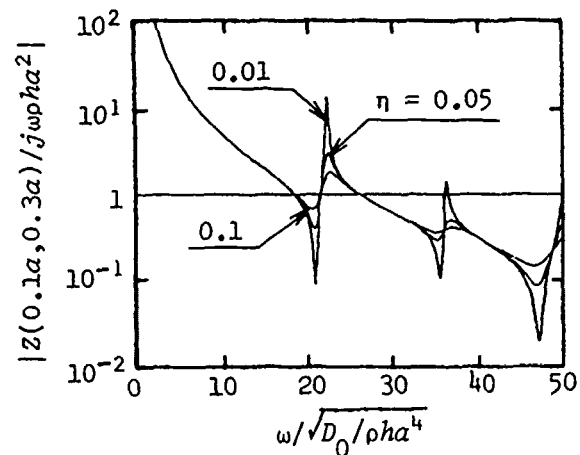


Fig. 1 Normalized driving point impedance of clamped three layered  $(45^\circ, -45^\circ, 45^\circ)$  square plate.

### References

1. Sakata, T. and Hosokawa, K., "Vibrations of Simply Supported Orthotropic Rectangular Plates Reinforced by an Intermediate Beam Support", Dynamics of Plates and Shells - 1989, ASME PVP - Vol. 178, 1989, pp. 44-50.
2. Vinson, J. R. and Sierakowski, R. L., "The Behavior of Structures Composed of Composite Materials", Dordrecht, The Netherlands, Martinus Nijhoff Publishers.

# **THERMAL BUCKLING AND SUPERSONIC FLUTTER OF LAMINATED THIN PLATES**

D.G. Liaw  
Sverdrup Technology Inc.  
Lewis Research Center Group  
Brook Park, OH 44142

## **ABSTRACT**

Thin plates are a popular and useful form of structural components with significant applications in aerospace vehicles which are subjected to thermal loads due to aerodynamic and/or solar radiation heating. Due to boundary constraints, compressive stresses are induced and may cause buckling. In addition to buckling, supersonic flutter is another significant failure mode considered in the structural design of aerospace vehicles.

It appears that in most past studies, the phenomena of thermal buckling [1,2] and supersonic flutter [3,4] were investigated separately. However, it is important and desirable to consider the interactive effects of aforementioned both failure characteristics in the analysis, design, and safety assessment of practical aerospace structures simultaneously.

In this study, the plate is assumed to be thin so that the classical lamination theory is applicable. The aerodynamic pressure due to supersonic potential flow is described by the two-dimensional quasi-steady supersonic theory. The formulation includes the linear stiffness, initial stress, mass, and aerodynamic matrices. For more practical applications, the temperature is assumed to be various both over the surface and through the thickness.

A series of examples were studied to evaluate the validity and to demonstrate the practical applicability of the present finite element formulation and solution procedure. Two examples with selected results are presented here.

The first example is a supersonic flutter analysis of laminated plates. The rectangular plates studied were assumed as simply supported with a length  $a=100$  inches. The laminate construction was assumed as  $[\theta/-\theta/-\theta/\theta]$  with thickness of each lamina equal to 0.25 inches. The material of each lamina was assumed as boron/epoxy with the following properties:  $E_L = 10$  msi,  $E_T = 1.0$  msi,  $G_{LT} = 0.33$  msi,  $\nu_{LT} = 0.3$  and  $\rho = 0.145 \times 10^{-3}$  lb-sec<sup>2</sup>/in<sup>4</sup>.

The effects of aspect ratio ( $a/b$ ) and fiber orientation ( $\theta$ ) on the critical aerodynamic pressure were investigated in this example. A 4x4 finite element mesh was used to model the whole plate. Figure 1 shows the results for critical aerodynamic pressure of the plates with various aspect ratios and fiber orientations. The critical aerodynamic pressure for the case of  $a/b=2$  was obtained previous by Sawyer [4] using the Galerkin method. His results are plotted for comparison. Excellent agreement is seen.

The second example is a supersonic flutter analysis of laminated plates with thermal effects. The rectangular plates studied were assumed as simply supported with a length  $a=100$  inches and a width  $b=50$  inches. The laminate construction and material properties of

each lamina were assumed the same as those in the previous example.

The effects of type of temperature distribution and fiber orientation on the critical temperature difference and critical aerodynamic pressure were investigated in this example. Two types of temperature distribution were considered.

Figure 2 shows the results for the critical aerodynamic pressure of the plate with constant temperature distribution in both transverse and horizontal directions. It is noted that the results shown in Fig. 2 are also applicable for the plate with linear temperature distribution through thickness. However, the critical temperature differences ( $T_{cr}$ ) for both cases are different.

The present numerical results show that the aspect ratio and fiber orientation of the plate, as well as the type of temperature distribution have obvious effect on the critical temperature difference and critical aerodynamic pressure of laminated plates.

Moreover, the present element formulation and solution procedure provide a useful tool for studying the supersonic flutter behavior of practical laminated plate structures subjected to thermal loads with complex temperature distributions.

#### REFERENCES

1. Whitney, J.M. and Ashton, J.E., "Effect of Environment on the Elastic Response of Layered Composite Plate," *AIAA Journal*, Vol. 7, 1971, pp. 1708-1713.
2. Chen, L.W. and Chen, L.Y., "Thermal Buckling Analysis of Laminated Cylindrical Plates by the Finite Element Method," *Computers and Structures*, Vol. 34, 1990, pp. 71-78.
3. Rossettos, J.N. and Tong, P., "Finite-Element Analysis of Vibration and Flutter of Cantilever Anisotropic Plates," *Journal of Applied Mechanics*, Vol. 41, 1974, pp. 1075-1080.
4. Sawyer, J.W., "Flutter and Buckling of General Laminated Plates," *Journal of Aircraft*, Vol. 14, 1977, pp. 387-393.

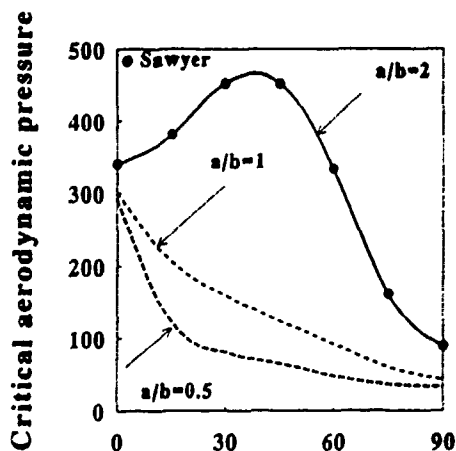


Figure 1

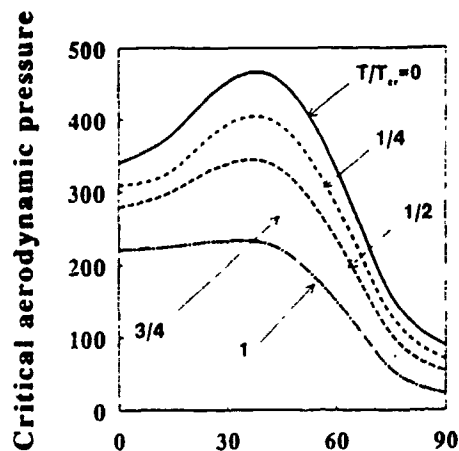


Figure 2

# NON-LINEAR RESPONSE OF A CLAMPED COMPOSITE PLATE OF VARIABLE THICKNESS

Z. Lu, S. Venkatasubramanian, C. L. D. Huang, and H. S. Walker  
Department of Mechanical Engineering  
Durland Hall  
Kansas State University  
Manhattan, KS 66506

The non-linear response of a cylindrically orthotropic composite plate with variable thickness is studied. The plate has a concentric rigid mass. The equations of motion and the associated boundary conditions are derived by using Hamilton's principle. The non-linear boundary value problem is converted into a corresponding eigenvalue problem by using a Kantorovich averaging method. Numerical solutions are obtained by introducing and solving the related initial value problem.

The transverse oscillations of a variable thickness cylindrically orthotropic composite plate with a concentric rigid mass are found in many engineering applications of which modelling of printed circuit boards is one. Since vibrations may be disastrous, reliable predictions of their nature is of great importance. The amplitude of vibrations may be of sufficient magnitude that it can result in malfunction of delicate components. When the amplitude of vibration is of the same order of magnitude as the thickness of the plate, the membrane effects of the middle plane must be included. The consideration of the membrane effect results in a set of two basic non-linear coupled partial differential equations. Due to the complexity of the governing equations, the only present means of solution is by numerical approximate methods.

Assuming harmonic vibrations the time variable is eliminated by using Kantorovich method. Then, by using a Newton iteration technique and the concept of analytic continuation, the solutions of the fundamental responses of the non-linear vibration of the clamped composite circular plate of variable thickness with a concentric rigid mass are obtained.

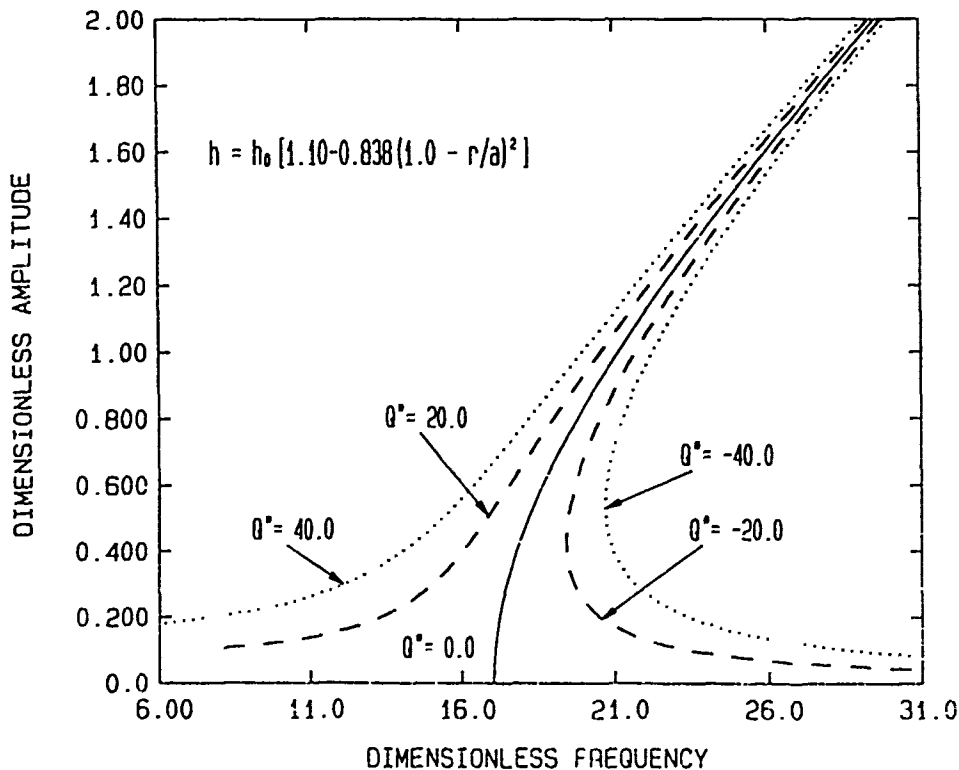
For the purpose of a numerical study, a variable thickness plate with thickness profile

$$h = h_0[C_1 + C_2(1 - \xi)^2]$$

is considered. In the above equation  $h_0$  represents the thickness of a plate having constant thickness,  $C_1$  and  $C_2$  are thickness parameters, and  $\xi$  is the dimensionless length coordinate. It is assumed that the volume of a variable thickness plate is the same as that of a constant thickness plate of thickness  $h_0$ . Based on this assumption, the parameter  $C_2$  can be expressed as a function of the outer thickness  $C_1$  and the ratio of the radius of the concentric rigid mass and the outer radius of the plate. Numerical solutions are obtained for various values of outer thickness, radius ratio, and ratio of elastic constants (circumferential to radial). All computations are carried out on an Apollo Domain workstation. The results for one case are shown in the figure in which  $Q^*$  represents the dimensionless load,  $r$  the radius of a point on the plate, and  $a$  the outer radius of the plate.

### Conclusion

The characteristics exhibited by the responses of the clamped composite circular plate of variable thickness with a concentric rigid mass are similar to that of a hard spring Duffing's system. It is hoped that the information provided in the figure will be of valuable importance to the designer.





## NONDIMENSIONAL ANALYSIS OF AXISYMMETRIC CIRCULAR PLATES

C. V. Girija Vallabhan, Professor of Civil Engineering;  
Y. C. Das, Visiting Professor of Civil Engineering; and  
Manjunatha Ramasamudra, Research Assistant,  
Dept. of Civil Engineering, Texas Tech University, Lubbock, Texas

When a thin plate deflects laterally into a nondevelopable surface with a deflection equal to and larger than its thickness, the linear theory of bending of plates due to Kirchhoff is not applicable for its analysis, and may lead to erroneous results. The reason, of course, is that membrane stresses are developed in the plate in addition to bending stresses. To account for these additional membrane stresses, a nonlinear plate theory was developed in 1910 by von Karman and his theory has been proven by many researchers to be valid experimentally for the nonlinear analysis of thin plates. Since the governing equations are nonlinear, a numerical iterative procedure has to be employed to solve them. The von Karman equations contain the Airy stress function to represent the membrane stresses, but here the equations are derived using displacements as variables. The finite difference method with iteration is employed to solve the above governing differential equations. Maximum values of nondimensional lateral deflections, in-plane displacements, and stresses are determined as functions of nondimensional uniformly distributed pressure. As the pressure increases the location of the maximum stress moves from the center towards the support, a phenomenon, that according to the authors has not been published by other researchers.

Earlier investigators such as Nadai in 1925, Way in 1934, Federhofer and Egger in 1946 have made substantial contributions to this topic. With the advent of electronic computers, modern researchers used more sophisticated techniques such as finite difference and finite element methods. Using the Airy stress function, Vallabhan and Das (1990) solved the same problem with various boundary conditions using the finite difference method with a special iterative technique. A summary of all previous work is given by Ramasamudra (1991) in his master's thesis on "Nonlinear Analysis of Axisymmetric Laminated Circular Plates".

The governing differential equations are derived using variational calculus and minimum potential energy theorem employing the von Karman assumptions, with simply supported boundary conditions and zero in-plane edge restraints at the support. The finite difference method is employed to solve the above equations, using a special iterative technique as

used by Vallabhan (1987) to analyze nonlinear rectangular glass plates.

Two specific contributions are made in this analysis. First is the determination of the absolute maximum stress in the plate, which is the combination of the membrane stress and the tensile bending stress on the unloaded side of the plate. A very important characteristic observed here is that the maximum stress occurs at the center of the plate for low levels of lateral pressures, but as the lateral load increases, the maximum tensile stress occurs in a region between 0.6 and 0.85 times the radius of the plate. While analyzing circular laminated glass plates, Ramasamudra (1991) has encountered similar conditions, which can become the major determining characteristic for the evolution of the ultimate strength of glass plates in a similar setup. Secondly, the two governing differential equations are nondimensionalized, and solved to determine the relationship between the nondimensional parameters such as applied nondimensional pressure,  $Q_n = \frac{q}{E}(\frac{a}{h})^4$ , maximum nondimensional lateral deflection,  $W_n = \frac{w}{h}$  at  $r=0$ , maximum nondimensional in-plane deflection,  $U_n = \frac{u}{h}$  at  $r=a$ , maximum nondimensional stress,  $\sigma_n^{max} = \frac{\sigma^{max}}{E}(\frac{a}{h})^2$ , nondimensional stress at center,  $\sigma_n^c = \frac{\sigma^c}{E}(\frac{a}{h})^2$  at  $r=0$ , where  $u$ ,  $w$ ,  $a$ ,  $h$ ,  $E$  are the in-plane displacement, lateral deflection, radius, thickness and the Young's modulus of elasticity of the plate. Nondimensional curves are obtained connecting the above parameters. To facilitate further, a cubic regression analysis is performed to obtain  $W_n$ ,  $U_n$ ,  $\sigma_n^{max}$ , and  $\sigma_n^c$  as a function of  $Q_n$ , the coefficients of which are presented in Table below.

Nondimensional parameter	$=\alpha_1 + \alpha_2 Q_n + \alpha_3 Q_n^2 + \alpha_4 Q_n^3$			
	$\alpha_1$	$\alpha_2$	$\alpha_3$	$\alpha_4$
$W_n$	1.65	$2.16 \times 10^{-1}$	$-2.64 \times 10^{-3}$	$1.28 \times 10^{-5}$
$U_n$	$8.41 \times 10^{-4}$	$-2.35 \times 10^{-3}$	$1.05 \times 10^{-5}$	$-4.2 \times 10^{-8}$
$\sigma_n^{max}$	$6.57 \times 10^3$	$1.03 \times 10^3$	-9.79	$4.64 \times 10^{-2}$
$\sigma_n^c$	1.95	0.15	$-5.23 \times 10^{-4}$	$8.19 \times 10^{-7}$

The authors wish to acknowledge the support from the National Science foundation, Grant # CES-8803416 for research on glass units which made this research possible.

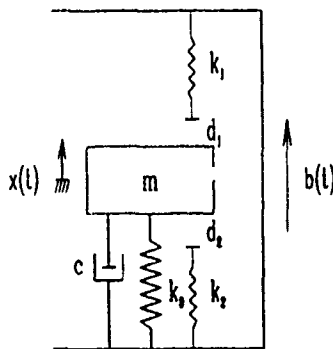
## REFERENCES

1. Ramasamudra, M., "Mathematical Model for Nonlinear Analysis of Laminated Glass by Finite Difference Method," Master's Thesis, submitted to Dept. of Civil Engrg., Texas Tech Univ., Lubbock, Texas, 1991.
2. Vallabhan, C. V. G., "Iterative Analysis of Nonlinear Glass Plates," Journal of Structural Engineering, ASCE, 109(2) : pp. 2416-2426, 1987.
3. Vallabhan, C. V. G., and Das, Y. C., "Nonlinear Stress Analysis of Circular Plates," Advances in Structural Testing, Analysis and Design, ICSTAD Proceedings, Vol. II, pp. 931-937, July 1990, Bangalore, India.

# ESTIMATION OF CLEARANCES USING RANDOM VIBROIMPACT RESPONSE

S. Q. Lin and C. N. Bapat  
Department of Mechanical Engineering  
The City College of the City University of New York  
New York, New York, 10031 U. S. A.

Clearances exist in many mechanical and industrial structures and produce many detrimental effects. However they could also be used for a beneficial purpose as an important monitoring parameter to reach an accurate assessment of the system's health. A novel clearance estimation approach called Spectral Analysis Approach is presented in this paper for systems under random excitation.



A model of an impact oscillator.

An impact oscillator model shown in the figure is used as an example to develop the clearance estimation approach. This approach could also be applied to other systems with clearances. Let  $y(t) = x(t) - b(t)$  be the relative displacement between the mass and the base. The differential equation of motion of mass  $m$  can be written as  $m\ddot{y}(t) + c\dot{y}(t) + k_0y(t) = -m\ddot{b}(t) - u[y(t)]$ ,

where

$$u[y(t)] = \begin{cases} k_2(y(t) + d_2) & -\infty < y(t) \leq -d_2, \\ 0 & -d_2 < y(t) < d_1, \\ k_1(y(t) - d_1) & d_1 \leq y(t) < \infty. \end{cases} \quad (2)$$

The nonlinear relation between the response  $y(t)$  and the impact force  $u(t)$  can be expressed as a series of Chebyshev-Hermite polynomials  $H_n$ . The first two terms  $W_0$  and  $W_1$  relate to unknown clearances,  $d_1$  and  $d_2$ , by

$$W_0 = \frac{\sigma_y}{\sqrt{2\pi}} \left[ k_1 \exp\left(-\frac{(d_1 - m_y)^2}{2\sigma_y^2}\right) - k_2 \exp\left(-\frac{(d_2 + m_y)^2}{2\sigma_y^2}\right) \right] + \frac{1}{2} \left[ k_2(m_y + d_1) \operatorname{erfc}\left(\frac{d_2 + m_y}{\sqrt{2}\sigma_y}\right) + k_1(m_y - d_1) \operatorname{erfc}\left(\frac{d_1 - m_y}{\sqrt{2}\sigma_y}\right) \right], \quad (3)$$

$$W_1 = \frac{\sigma_y}{2} \left[ k_2 \operatorname{erfc}\left(\frac{d_2 + m_y}{\sqrt{2}\sigma_y}\right) + k_1 \operatorname{erfc}\left(\frac{d_1 - m_y}{\sqrt{2}\sigma_y}\right) \right]. \quad (4)$$

The erfc in the above equations is the complementary error function.  $W_0$  and  $W_1$  can be obtained experimentally as

$$W_0 = m_u, \text{ and } W_1 = \sigma_y \frac{\int_{\omega_1}^{\omega_2} S_{yu}(\omega) d\omega}{\int_{\omega_1}^{\omega_2} S_y(\omega) d\omega}, \quad (5,6)$$

where  $m_u$  is the mean value of the impact force  $u(t)$ ,  $s_y(\omega)$  is the power spectral density function of  $y(t)$ ,  $s_{yu}(\omega)$  is the cross spectral density function of  $y(t)$  and  $u(t)$ , and  $\omega_1 < \omega < \omega_2$  is within the frequency band of  $y(t)$  and  $u(t)$ . The values of  $m_y$ ,  $\sigma_y$  and  $S_y(\omega)$  can be estimated from the base excitation  $b(t)$  and response  $y(t)$ . The  $m_u$  and the  $S_{yu}(\omega)$  can be obtained as

$$m_u = \lim_{T \rightarrow \infty} \frac{1}{T} U(0, T) \quad \text{and} \quad S_{yu}(\omega) = \lim_{T \rightarrow \infty} \frac{1}{T} E \{ Y^*(\omega, T) U(\omega, T) \}, \quad (7,8)$$

where

$$U(\omega, T) = m \omega^2 B(\omega, T) - \frac{Y(\omega, T)}{H(\omega)}, \quad H(\omega) = \frac{1}{(k_0 - m\omega^2 + ic\omega)}. \quad (9,10)$$

The  $B(\omega, T)$ ,  $Y(\omega, T)$  and  $U(\omega, T)$  in above equations are the finite Fourier transforms of  $b(t)$ ,  $y(t)$  and  $u(t)$ ,  $0 \leq t \leq T$ , respectively.

Based on above equations, clearances could be estimated using the spectral analysis approach as follows. Estimate the statistical properties  $m_y$ ,  $\sigma_y$ ,  $S_y(\omega)$ ,  $m_u$  and  $S_{yu}(\omega)$  from the experimentally obtained  $b(t)$  and  $y(t)$ . The  $W_0$  and  $W_1$  can be obtained using the experimentally obtained values in equations (5) and (6), respectively. Substituting the values of  $W_0$  and  $W_1$  into the left hand sides of equations (3) and (4) respectively, generates two coupled nonlinear equations in two unknowns  $d_1$  and  $d_2$  and could be solved using numerical iteration.

The approach were tested using computer simulated experiments and mechanical experiments. Some estimates using data from mechanical experiments with  $m=0.1061$  kg,  $k_0=1746$  N/m and  $c=0.7127$  Ns/m are shown in the table below. The comparison of actual clearances to their estimates indicates a good agreement.

$k_1$ (N/m)	$k_2$ (N/m)	Actual Clearances		Estimated Clearances	
		$d_1$ (mm)	$d_2$ (mm)	$d_1$ (mm)	$d_2$ (mm)
11600±100	11600±100	1.22±0.05	1.19±0.05	1.18	1.08
11600±100	11600±100	0.99±0.05	1.40±0.05	1.20	1.48
1750±50	1750±50	0.79±0.05	0.79±0.05	0.77	0.82
1750±50	1750±50	0.81±0.05	1.52±0.05	0.76	1.13
1750±50	11600±100	0.81±0.05	1.45±0.05	0.45	1.58

# **TRANSIENT RMS RESPONSE OF DYNAMICAL SYSTEMS TO MULTI-SUPPORT, MULTI-COMPONENT RANDOM EXCITATION**

*by*

Mohammad A. Zahraee  
Purdue University Calumet  
Hammond, IN 46322-2094

## **ABSTRACT**

The dynamic analysis of structural subsystems like piping systems in nuclear facilities, lifeline facilities, and control equipment supported on heavier primary systems subject to random, blast, earthquake, or turbulent air is of wide engineering interest.

The exact analytical solutions for the stochastic response of a general multiple degrees of freedom system, supported at multiple points, to non-stationary, colored, vector valued, multi-component excitation are obtained by using a state space time domain random vibration formulation. The primary system could be supporting tuned secondary and tertiary subsystems at multiple support points.

The non-whiteness of excitation is achieved by passing a white noise through a new class of filter. Besides other attractive advantages it has over the previous ones, this filter is capable of producing any arbitrary power spectral density function with as many peaks as desired. The non-stationarity of excitation is achieved via a modulating piecewise linear function which practically encompasses all other modulating functions used by previous researchers, and is generated to match the desired excitation. Here, one can directly prescribe the time history of RMS values and cross correlation coefficients of any desired excitation.

Closed form analytical solutions are obtained for transition and covariance matrices. Availability of all cross terms of time-dependent variances, makes it possible to prescribe all correlation coefficients of excitations, directly. This, in turn, facilitates the analysis of a multiple support excitation which plays an important role in the analysis of long bridges and light equipment supported on heavier structures.

The modal equations of the system are used in their general form and therefore, all three approaches, namely absolute displacement, pseudo static displacement, and relative displacement approach can be handled by the present formulation. It will also

be shown that a multiple component excitation can be modeled and solved with no addition to this formulation.

The capabilities of formulation are demonstrated through examples for correlated and uncorrelated excitations, multiple support excitation, two dimensional ground motion, and cascaded secondary systems supported at multiple points on a primary structure.

# Random Vibration of Point-Driven Beams

Raymond J. Nagem

Department of Aerospace and Mechanical Engineering  
Boston University

Random vibration of continuous structures has many applications in applied mechanics, and is an important problem in structural dynamics. Consider, for example, a locally one-dimensional beam structure with local spatial coordinate  $x$ , excited by a point force  $f$  at spatial location  $x_0$ . If the point force is a stationary random process with mean-square spectral density  $S_f(\omega)$  and the structure is modeled as a linear time-invariant system, then the mean-square value of a general beam response variable  $y(x)$  is given by

$$E[y^2(x)] = \int_{-\infty}^{\infty} |H_{fy}(x, \omega; x_0)|^2 S_f(\omega) d\omega \quad (1)$$

where  $H_{fy}(x, \omega; x_0)$  is the transfer function between the excitation  $f$  at location  $x_0$  and the response  $y$  at location  $x$ . The response variable  $y$  can be a displacement, velocity, rotation, bending moment, bending stress or any other quantity for which a transfer function  $H_{fy}$  can be defined.

For a very general class of beam structures, the generalized transfer matrix method recently developed by the author is a convenient way to compute the transfer function  $H_{fy}$  in eqn. (1). The generalized transfer matrix method is numerically accurate over a wide of frequency  $\omega$  and can be applied to arbitrary three-dimensional networks of one-dimensional elements or members. The transfer matrix method has the advantage of being based directly on the differential equations which comprise the beam model, and the advantage that force, moment, displacement and rotation variables are all explicitly included in the formulation. Also, an explicit modal decomposition is not required, so that the method can be applied to structural models for which conventional normal modes do not exist or are difficult to find.

In this paper, the spatial distribution of mean square bending moment (and therefore of bending stress) is computed for a variety of beam structures which are subjected to a random point force. Both single span and double span structures are considered. The Timoshenko beam model is used, with

viscous, structural and viscoelastic damping. Local intensifications and reductions in the mean square response are observed, and the effects of different damping models and different boundary conditions on these local intensifications are demonstrated. The results show that local reductions and intensifications in the mean square response of point driven beam structures are strongly affected by the type of beam damping mechanism. The generalized transfer matrix method is shown to give good numerical results for all the various beam and damping models. The results for the two-span beams also suggest that unexpected intensifications and reductions may exist in *unforced* sections of multi-span structures. This phenomenon is currently being studied, with the same techniques described here, in frame and ring structures.



# CHAOTIC MOTION OF AN ARBITRARILY SHAPED SATELLITE IN AN ELLIPTIC ORBIT

Ardéshir Guran  
Department of Mechanical Engineering  
University of Toronto, M5S-1A4, Canada

The understanding of the nonlinear behaviour of an orbiting satellite in a central force field is one of the most interesting areas of mechanics today [1,2,3]. In particular it is of practical importance to maintain an artificial satellite on a fixed orientation relative to the earth [4,5].

The present paper sets out to investigate the attitude motion of an arbitrarily shaped satellite in its orbital plane. To that end we consider the motion of a satellite with the principal inertia moments  $A$ ,  $B$ , and  $C$  in an elliptic orbit with the eccentricity  $\epsilon$ . The equation of motion reads

$$(1 + \epsilon \cos \theta) \frac{d^2 \psi}{d\theta^2} - 2\epsilon \sin \theta \left( \frac{d\psi}{d\theta} + 1 \right) + \frac{3}{2} \kappa \sin 2\psi = 0 \quad (1)$$

where  $\theta$ ,  $\psi$  are the position and libration angles (see Figure 1), and  $\kappa = \frac{B-A}{C}$  is the inertia-moment ratio of the satellite.

For satellites on circular orbit ( $\epsilon = 0$ ), a closed form solution can be obtained in terms of Jacobi elliptic functions [5]. However, the planar motion in an elliptic orbit is nonintegrable and recourse to numerical techniques is unavoidable. In fact the nonintegrability of equation (1) can be verified by calculation of its Melnikov function, viz.

$$M(\theta_0) = 2\epsilon\pi\omega^2 \left( 3\text{Sech}\frac{\omega\pi}{2} + 4\text{Csch}\frac{\omega\pi}{2} \right) \sin \omega\theta_0 \quad (2)$$

where  $M(\theta_0)$  oscillates in sign as one changes  $\theta_0$  for a given eccentricity.

In what follows, equation (1) was numerically integrated using a fourth-order Runge-Kutta integrator. The Poincaré section was obtained by looking at the satellite stroboscopically with orbital period  $2\pi$ . A total of 100 points have been calculated for each of 14 different initial conditions in the  $\frac{d\psi}{d\theta}$ ,  $\psi$  plane. The two different types of motion, regular and chaotic, are readily distinguished on Poincaré maps.

The Poincaré maps shown in Figure 2 illustrate the two types of motion mentioned

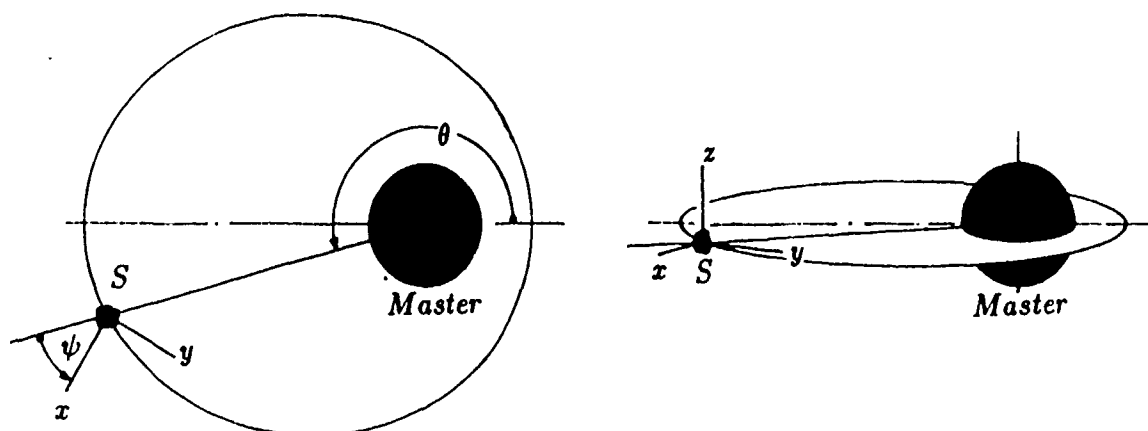


Figure 1 Configuration of the satellite in an Elliptical orbit.

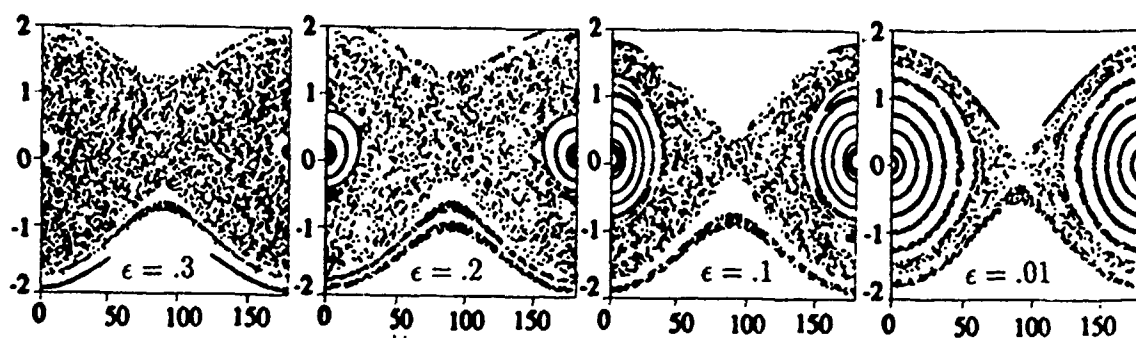


Figure 2 Poincaré sections  $\frac{d\psi}{d\theta}$  versus  $\psi$  for a satellite with small inertia-moment-ratio,  $\kappa = 1.0$ , eccentricity as indicated.

above. The attitude denoted by  $\psi$  is equivalent to that of  $\psi + \pi$ . Consequently,  $\psi$  is restricted to an interval between 0 and  $\pi$ . For small  $\epsilon$  the motion is regular, as one increases  $\epsilon$  to relatively large value, the whole poincaré map is covered by chaotic trajectories except a few islands. The onset of global chaos is  $\epsilon = .14$ , if  $\kappa = 1.0$ .

## References

1. Wisdom, J., Pearle, S.J., and Mignard, F., "The Chaotic Rotation of Hyperion", *Icarus*, Vol. 58, pp. 137-152, 1984.
2. Guran, A., "On the Stability of a Spinning Satellite in a Central Force Field", *Bifurcation and chaos: Analysis, Algorithms, Applications*, Editors: R. Sydel, T. Kupper, H. Troger, and F. Schneider, Birkhauser, Boston, 1990.
3. Guran, A., Tong, X., "Instabilities in the Restricted Three Body Problem : An Old Problem with a New Twist", *Mechanics Research Communications*, 1991(in press).
4. Zlatoustov, V.A., Okhotsimsky, D.E., Sarychev, V.A., and Torzhevsky, A.P., "Investigation of Satellite Oscillation in the Plane of an Elliptic Orbit", *Proc. Eleventh International Congress of Applied Mechanics*, Munich, pp.436-439, 1964.
5. Modi, V.J., Brereton, R.C., "Periodic Solutions Associated with the Gravity-Gradient-Oriented Systems", *AIAA Journal*, Vol.7, pp.1465-1468, 1969

# STOCHASTIC DYNAMIC ANALYSIS OF NONLINEAR VISCOELASTIC PLATES

T-P. Chang

Associate Professor, Department of Applied Mathematics  
National Chung-Hsing University, Taichung, Taiwan, R.O.C.

## ABSTRACT

Stochastic equivalent linearization is used to develop a finite element formulation for the dynamic response analysis of nonlinear viscoelastic plates subjected to random excitation. The nonlinear viscoelastic properties of plates are characterized in terms of the constitutive equation which linearly involves the hysteretic tensors and in terms of the auxiliary equation which nonlinearly involves the strain, hysteretic tensors and their time derivatives. The nonlinear auxiliary equation is linearized by stochastic equivalent linearization so that the original nonlinear problem can be converted into a system of finite element equation of motion which is readily solved. The proposed method generates the covariance and variance functions of the nodal displacement and velocity and some other quantities such as element stress resultants and shear forces. These statistical functions play an important role in estimating the structural reliability of nonlinear viscoelastic plates.

## Introduction and Results

Most plate and shell structures are subjected to excitations which are random in nature. Examples range from aircraft and missile structure subjected to acoustic and aerodynamic loads to civil engineering structures acted upon by earthquake and wind loads.

In this paper, a nonlinear model first proposed by Bouc [1] and generalized by Wen [5] adopted and extended to simulate the nonlinear viscoelastic plate. Stochastic equivalent linearization technique [4,5,6] has been used to determine the dynamic response of a nonlinear viscoelastic plate under random excitation [2] which is non-stationary [3,7]. The advantage of using such a linearization is that, upon linearization, the complex modal analysis [8,9] can be performed to evaluate the stochastic dynamic responses of the structure.

A nonlinear plate with finite element mesh (see Fig.1) subjected to out-plane horizontal earthquake is analyzed using the proposed method. The standard deviations of maximum stress resultant and shear force are represented on Fig.2 and Fig.3 respectively. These statistical responses, which were checked by Monte Carlo simulation, play an important role in estimating structural reliability.

## References

- [1] Bouc, R. (1967). "Forced vibration of mechanical systems with hysteresis." *Proc. of the 4th Conference on Nonlinear Oscillation*, Prague, Czechoslovakia.
- [2] Kanai, K. (1967). "Semi-empirical formula for the seismic characteristics of the ground." *Bulletin of the Earthquake Research Institute*, Univ. of Tokyo, Japan, 35, June, 308-325.
- [3] Shinozuka, M., and Sato, Y. (1967). "Simulation of nonstationary random processes." *J. Engrg. Mech.*, ASCE, 93(EM1), 11-40.
- [4] Atalik, T. S., and Utku, S. (1976). "Stochastic linearization of multidegree of freedom nonlinear systems." *Earthquake Eng. Struct. Dyn.*, 4, 411-420.
- [5] Baber, T. T., and Wen, Y. K. (1979). "Stochastic equivalent linearization for hysteretic, degrading, multistory structures." *Technical Report*, Dept. of Civ. Engrg., Univ. of Illinois, Urbana, Ill., Dec.
- [6] Spanos, P. D. (1981). "Stochastic Linearization in Structural Dynamics." *Appl. Mech. Rev.*, 34, 1-8.
- [7] Shinozuka, M. (1983). "Random processes in engineering mechanics." *Proc. of the EMD Specialty Conference*, Purdue Univ., Lafayette, Ind., May 23-25, 18-46.
- [8] T-P. Chang, T. Mochio and E. Samaras (1986) "Seismic Response Analysis of Nonlinear Structures", *J. of Prob. Engrg. Mech.*, Vol. 1, No. 3, 157-166.
- [9] Simulescu, I., T. Mochio, and M. Shinozuka (1989) "Equivalent Linearization Method in Nonlinear FEM." *J. Engrg. Mech.*, ASCE, Vol. 115, No. 3, 475-492.

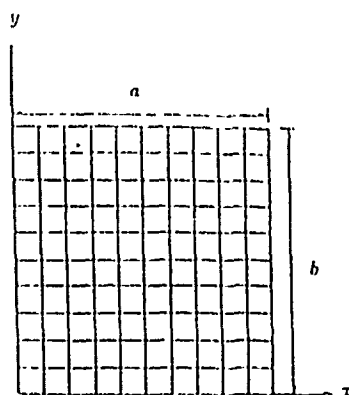


Fig.1 Finit Element Mesh of  
Nonlinear Plate

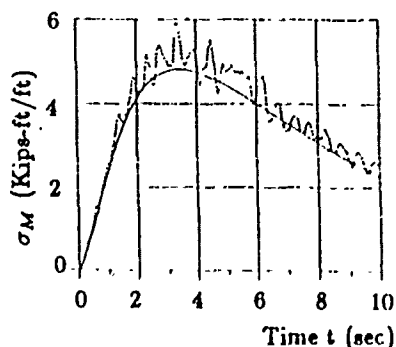


Fig.2 Standard Deviation of  
Max. Stress Resultant

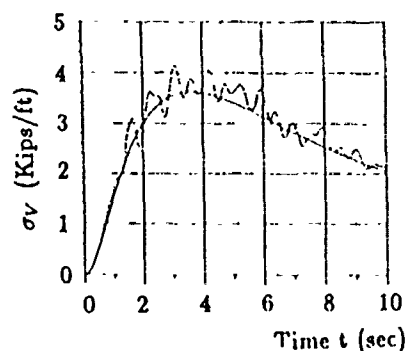


Fig.3 Standard Deviation of  
Max. Shear Force

# MODAL INTERACTIONS IN THE NONLINEAR RESPONSE OF ELASTIC CABLES CONTAINING A TWO-TO-ONE INTERNAL RESONANCE

Christopher L. Lee  
Graduate Student Research Assistant

Noel C. Perkins  
Assistant Professor

Department of Mechanical Engineering and Applied Mechanics  
University of Michigan  
Ann Arbor, MI 48109-2125

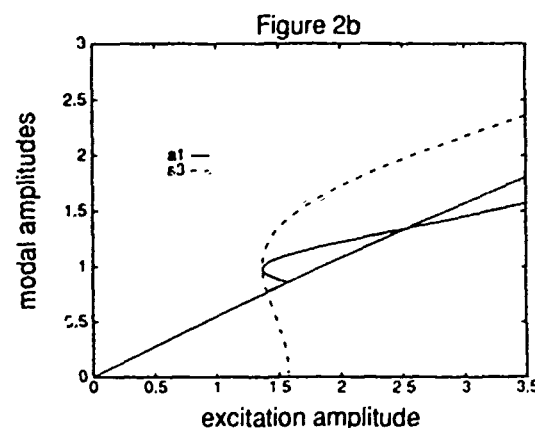
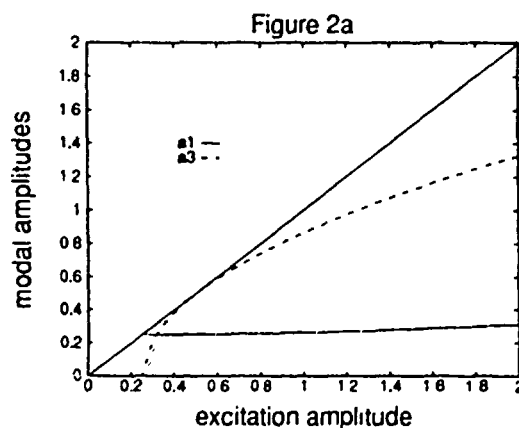
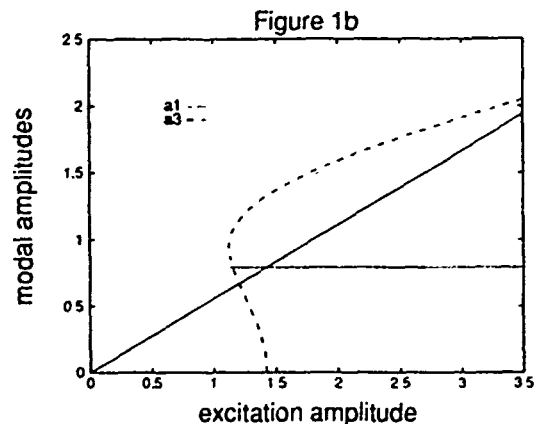
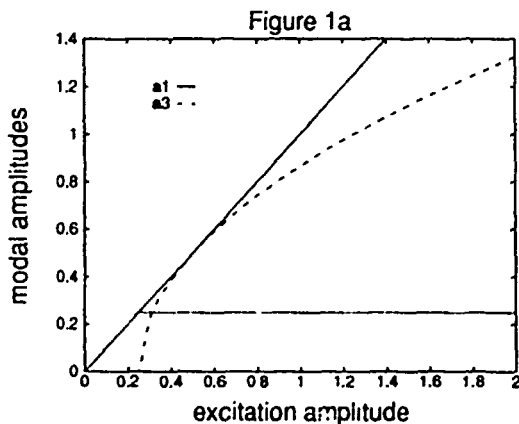
Cables are flexible, lightweight structural elements frequently used in structural and marine engineering applications. In such applications, cables are readily excited and tend to undergo large amplitude oscillations which cannot be described using linear theory. The purpose of this study is to examine an important class of nonlinear cable oscillations which have been observed in recent experiments.

A two degree of freedom model of an elastic cable with a small sag to span ratio is derived using a two mode approximation. A symmetric, in-plane mode with natural frequency  $\omega_1$  represents motion in the plane of the cable equilibrium and an out-of-plane mode with natural frequency  $\omega_{3m} \approx \frac{1}{2}\omega_1$  represents motion normal to the plane. An external, in-plane harmonic excitation of frequency  $\Omega$  is applied normal to the cable. The equations of motion contain two types of nonlinear terms: quadratic terms arising from equilibrium cable curvature and cubic terms arising from nonlinear cable stretching. The quadratic terms, alone, lead to the *saturation* of the in-plane response under near resonant excitation,  $\Omega = \omega_1 + \epsilon\sigma_1$ . The saturation phenomenon has been extensively examined in the context of other dynamical systems [1].

The equations governing the modulation of the amplitudes and phases of the two cable modes are found to second ( $\epsilon^2$ ) nonlinear order using a second-order version of the method of multiple scales [2]. The first-order equations describe the effect of the quadratic terms and lead to saturation solutions. The second-order equations capture the effect of the cubic terms and lead to higher-order corrections to the saturation solutions. To the authors' knowledge, these are the first corrections obtained for a dynamical system which exhibits saturation.

Figures 1 and 2 show the dependence of the steady-state, in-plane ( $a_1$ ) and out-of-

plane ( $a_{3m}$ ) modal amplitudes on the excitation amplitude ( $f$ ). Figures 1a and 1b represent the first-order solutions with constant excitation frequency ( $\epsilon\sigma_1$ ) for  $\sigma_1 = 0$  and  $\sigma_1 = 6$ , respectively. In both cases, the amplitude of the directly excited mode ( $a_1$ ) saturates beyond some critical value of  $f$ . For the same cases, second-order solutions are shown in Figure 2 for  $\epsilon = 0.025$ . The second-order solutions demonstrate that, in general, the cubic nonlinearities disrupt the saturation phenomenon to a degree dependent on their magnitude ( $\epsilon$ ) and the external detuning ( $\sigma_1$ ). For the case where  $\sigma_1 = 0$ , the corrections indicate that  $a_1$  slowly increases with  $f$ . This increase is more rapid for the case where  $\sigma_1 = 6$ . Furthermore, for this case, the corrections split the degenerate solutions for  $a_1$ .



- [1] Nayfeh, A. H. and Balachandran, B., 1989, "Modal Interactions in Dynamical and Structural Systems," *Appl. Mech. Rev.*, vol. 42, no. 11, part 2, pp. S175-S201.
- [2] Rahman, Z. and Burton, T. D., 1989, "On the Higher Order Methods of Multiple Scales in Non-Linear Oscillations - Periodic Steady State Response," *J. Sound and Vib.*, vol. 133, no. 3, pp. 369-379.

# MONITORING VIBRATION FOR ADAPTIVE MACHINING

N. TARABISHY, A. JAFFAL, B. BAHR

MECHANICAL ENGINEERING DEPARTMENT  
COMPUTER INTEGRATED MANUFACTURING LABORATORY  
THE WICHITA STATE UNIVERSITY  
WICHITA, Ks. 67208

## ABSTRACT

This paper summarizes the results of an investigation on the control of cutting process in a CNC machine tool. The vibrations of the workpiece were used as an indicator for the quality of the process and the cutting condition.

## INTRODUCTION

To cope with the increasingly tougher competition in manufacturing, and to boost productivity; smart control of the cutting process is essential for producing quality parts. To achieve this goal continuous assessment of the machining process condition has to be done, and based on that, the appropriate action needs to be carried out instantaneously. Several approaches for monitoring the process are employed, however, in this study, the amplitude of vibration was used as a "safety valve" to control the machining process.

## METHODOLOGY

An accelerometer was mounted on the aluminum workpiece and experiments were conducted with a high speed steel end mill insert (PUTNAM 51330, LEAD 2.721, 0.5 inch Diameter). Milling operation was performed on a FIDAL CNC 88 machining center at 20 in/min nominal feed rate, 50/1000" depth of cut, with the spindle spinning at 3500 RPM. The critical level of the vibration was found by trial and error, and was set as a fixed threshold. The signal was sampled and read through an A/D converter by the microcomputer, then, its level was compared with the threshold limits. If the signals are within the limits no action takes place, however, if the signals are out of bound the appropriate commands will be issued to change the feed-rate of the CNC machine.

The results of cutting an aluminum piece with one millimeter step change on material thickness is shown in Figure 1. As it can be seen the vibration of the tool is bounded within the acceptable limits while cutting the normal thickness, but as the tool encounters the thicker part the vibration has increased significantly. This type of abnormalities as well as others that may occur in the machining processes could cause the breakage of the tool as well as damage of the workpiece. In order to overcome these types of problems in a manufacturing process, a controller was developed to monitor the cutting condition. The result of using the developed feedback controller is shown in Fig 2. This figure shows how the controller has changed the feed-rate, so that the vibration of the workpiece has decreased when encountering the step change in the material. The spike in the Figure 2, is due to the step change of the thickness of the material which triggers the controller to take appropriate action.

## Conclusion

The application of a monitoring device for machine tool has proven to be very effective in preventing the damage to the tool or workpiece. Therefore, quality parts can be produced faster with less operator involvement. It is possible that an operator can monitor several machine tools, which could be translated to greater savings. The work done here is in initial state and further work remains to be done in order to make an intelligent monitoring and control system for the machine tool using new methods like neural networks.

## References

1. A. Okafor Chukwujekwu, Marcus Michael, Tipirneti Ramesh  
"Multiple Sensor Integration Via Neural Networks For Estimating Surface Roughness And Bore Tolerance In Circular End Milling."  
1990 Transactions of NAMRI/SME.
2. S. Vajpayee and A. Sampath, "Development of a microcomputer-based AE system for tool condition monitoring". Computers Ind. Engng., School of Engineering Technology, University of Southern Mississippi, Hattiesburg, Miss. and School of Engineering, Oakland University, Mich., vol. 18, No. 2, pp. 211-223, 1990.

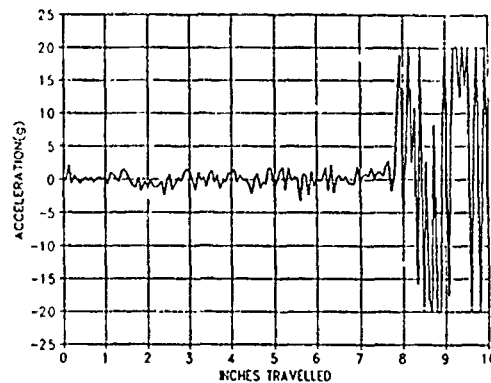


Figure 1 The vibration at the workpiece without the controller.

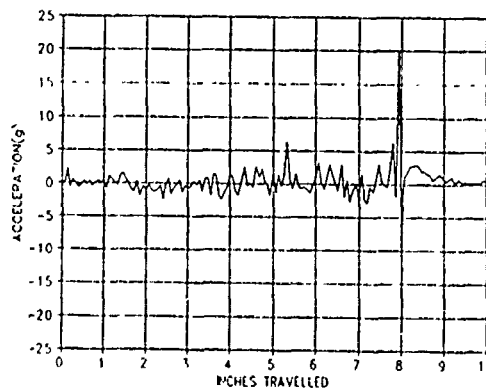


Figure 2 The vibration at the workpiece with the controller.



## NONLINEAR FREE VIBRATIONS OF SUSPENSION BRIDGES

Yuriy A. Rossikhin and Marina V. Shitikova

Department of Theoretical and Structural Mechanics,  
Voronezh Civil Engineering Institute, Voronezh 394006,  
U.S.S.R.

The paper is devoted to analysis of nonlinear free vibrations of suspension bridges in the cases of one-to-one and two-to-one internal resonances by using the method of multiple scales via a perturbation technique.

A.M. Abdel-Ghaffar and L.I. Rubin<sup>1</sup> investigated influence of an internal amplitudes' absolute level on nonlinear free vibrations of suspension bridges in the case of a one-to-one internal resonance (an absolute level of initial amplitudes is defined by a magnitude of the whole mechanical energy imparted to the system at the moment of motion onset). In the present analysis, dependence of vibrational processes on an initial amplitudes' relative level is traced (this level doesn't depend on the original system's energy but it is defined as a ratio of two interacting modes initial amplitudes). In accordance with a value of that level there exist three types of energy-exchange mechanism between the system's vertical and torsional modes: a two-sided, one-sided energy exchange or an energy interchange doesn't occur. A two-sided energy exchange is in agreement with a periodic energy exchange from one subsystem to another, with that an amplitude is a periodic function of time and a phase difference may be periodic or aperiodic function. A one-sided energy interchange conforms to a complete or partial energy transfer from one subsystem to another, with that amplitudes and phase difference velocities are constants. Theorems allowing to detect on the basis of initial values of amplitudes and phases the corresponding type of the energy exchange are stated and proved.

Analysis of the nonlinear free vibrations of the Golden Gate Bridge in San Francisco shows that during interaction of some modes, as a relative level of initial amplitudes changes continuously, all three types of the energy exchange may be realized. Suspension bridge's vibrational motions can be modelled by perfect incompressible phase fluid flow in an infinitely long channel which width is equal to unit.

<sup>1</sup>A.M. Abdel-Ghaffar and L.I. Rubin, Nonlinear Free Vibrations of suspension Bridges: Theory and Application. J. Eng. Mech., ASCE 109, 313-345 (1983).

Figures 1 and 2 show the stream-lines for the Golden Gate Bridge in the cases when  $\omega_3^s \approx \Omega_1^s$  and  $\omega_6^s \approx 2\Omega_1^s$ , respectively ( $\omega_3^s$  and  $\omega_6^s$  are the linear natural frequencies of the 3d and 6th symmetric vertical modes, respectively,  $\Omega_1^s$  is the linear natural frequency of the 1st symmetric torsional mode). By digits near curves levels of the stream function are indicated, by arrows on the stream-lines the direction of phase fluid flow is shown. The coordinate axes are the phase difference  $\gamma$  and the value  $\xi$  determining the relative level of initial amplitudes. The lines corresponding to the values 0.487 (Fig.1) and 0.0 and -0.5 (Fig.2) are the boundaries of the closed and non-closed stream-lines areas and conform to the one-sided energy interchange: from the torsional vibrations to the vertical (the lines with 0.487 on Fig.1 and -0.5 on Fig.2) and from the vertical to the torsional ones (the line with 0.0 on Fig.2). In the both given cases the internal stationary regimes are stable as they are surrounded by the closed stream-lines. The closed and unclosed stream-lines are in accordance with the two-sided energy exchange. The upper channel boundaries in Figs.1 and 2 have strong instability because small initial changes of amplitudes and phases grow without bound as the time goes on. The lower boundary regime in Fig.1 has weak instability because small initial changes of amplitudes and phases lead to the following: the amplitudes' increments are remained small but the phase difference grows beyond all bounds as the time goes on.

Therefore, the hydrodynamic analogy (phase fluid flow) allows to analyze qualitatively the nonlinear free vibrations of suspension bridges: to determine the types of vibrating processes (energy exchange), to investigate stability of each vibrational regime, to define the character of amplitudes' and phase differences' dependences from initial conditions and so on.

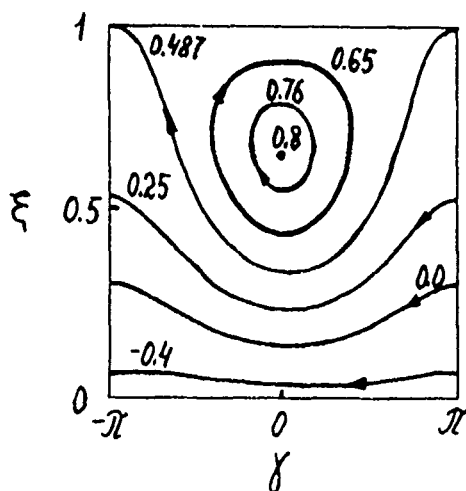


Fig.1

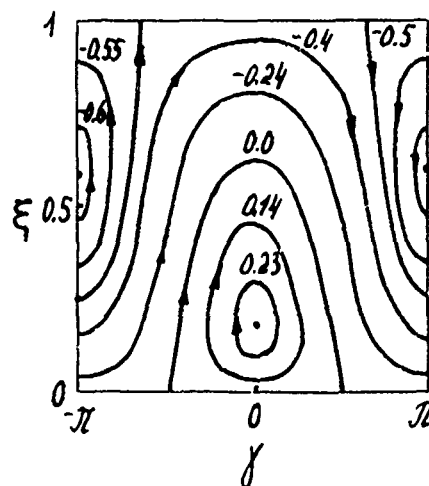


Fig.2

# The First Passage Time for Randomly Parametric Excited Structures with Initial Imperfections

Xiaofeng Shen\*

Ph.D

Dept. Mechanical Engineering, Jiaotong University  
Shanghai, P.R. China

Huiqiao Zhang

Professor

## 1. INTRODUCTION

The first passage time is analysed for randomly parametric excited structures with initial imperfections. The equation governing the reliability function is derived, and the numerical and simulational results for the moments of the first passage time are given.

## 2. DEFINITIONS

The reliability function  $R(t)$  is defined as follow:

$$R(t) = 1 - P(t)$$

$P(t)$  in the above equation gives that the probability of the response,  $x(t)$ , of structure exits from the safe domain at least once within time  $t$  given.

The moments  $M_n$  of the first-passage time are given as

$$M_n = E(T^n) = \int_0^\infty t^n p(t) dt$$

## 3. FORMULATIONS

For the simply-supported beam with initial displacements under randomly parametric load, the equation of motion is given [1]

$$\frac{d^2 X}{dt^2} + 2\xi\omega_0 \frac{dX}{dt} + \omega_0^2 [1 - \mu p_1(t)] X = \omega_0^2 f_0$$

where  $X$  is the factor of displacement,  $f_0$ , random number with normal distribution, is the factor of initial displacements, the the damping factor  $\xi \ll 1$  and  $P(t)$  is the randomly wide-band load with the power spectrum function  $s(w)$  and  $\xi\omega_0 \ll$  the bandwidth of excitation.

By using stochastic average method and FPK equation, the reability function  $R(t)$ , which is the proability for structure response amplitude less than  $A$  under initial condition  $\bar{A}$ , is given by equation

$$\frac{\partial R}{\partial t} = \left[ \left( -\xi\omega_0 + \frac{3}{8}\alpha \right) A_0 + \frac{f_0^2 \beta}{2A_0} \right] \frac{\partial R}{\partial A_0} + \frac{1}{2} \frac{\partial^2 R}{\partial A_0^2} \left( \frac{A_0^2 \alpha}{4} + f_0^2 \beta \right)$$

---

at present Inst. f. Massivbau, TH Darmstadt, Germany

with initial conditions:

$$R(0 | A_0) = 1 \quad 0 \leq A_0 \leq \bar{A}$$

$$R(t | \bar{A}) = 0 \quad t \geq 0$$

and boundary condition:

$$R(\infty | A_0) = 0$$

The equations for moments of first passage time can further be derived:

$$\left[ \xi \omega A + \frac{3}{8} \alpha A_0 + \frac{f_0^2 \beta}{2 A_0} \right] \frac{dM_{n+1}}{dA_0} + \frac{1}{2} \left( \frac{A_0^2 \alpha}{4} + f_0^2 \beta \right) \frac{d^2 M_{n+1}}{dA_0^2} = -(n+1) M_n(t)$$

with conditions:

$$M_n(t) = 0$$

$$if A_0 = \bar{A}$$

$$\frac{dM_n(t)}{dA_0} = 0$$

$$if A_0 = 0$$

In table 1, the numerical and simulated results for the mean and variance of first passage time are given. The results by simulating method are in agreement with the results by numerical method.

Parameter	Theoretical Result		Simulation Result	
$\alpha = 0.00625 \quad f_0 = 0.5 \quad \bar{A} = 0.2$	Mean	Variance	Mean	Variance
$\xi = 0.00625 \beta = 0.00625 \omega_0 = 1.0$	13.26	263.30	13.2	277.80
$\xi = 0.001 \beta = 0.00625 \omega_0 = 1.0$	12.80	243.90	12.9	274.87
$\xi = 0.00625 \beta = 0.00625 \omega_0 = 1.5$	5.73	50.30	5.9	52.15
$\xi = 0.00625 \beta = 0.014 \omega_0 = 1.0$	6.20	57.80		

#### 4. CONCLUSIONS

From Table 1. the follow conclusions are obtained.

(1) The mean and variance of the first-passage time are directly proportionat to the damping of structure, but they are inverse proportionat to the natural frequency of structure.

(2) Due to the existence of initial displacement imperfections, the first passage time is affected by the value of power spectrum density function respond at the natural frequency of structure.

#### REFFENCES:

- [1] V.V. Bolotin, The Dynamic Stability of Elastic System.
- [2] J.B. Robert, Stochastic Averaging: An Approximate Method of Solving Random Vibration Problems, Int. J. Nonli. Mech., Vol.21, No.2, 1986

# Experimental Investigation of Specific Energy Absorption of Fiberglass/Vinylester Tubes Under Various Crushing Modes

Yongbin Yuan, Gary L. Viegelaan, Ronald K. Wlosinski\*

ME-EM Department, College of Engineering

Michigan Technological University, Houghton, MI 49931

\* Scientific Laboratory, Ford Motor Company, Dearborn, MI 48121-2053

Crushing behavior of composite materials has been an interest topic of many crashworthiness researchers. Although much research work has been done on the axial crushing of many types of composite materials<sup>(1-3)</sup>, little is known so far about their behaviors under external inversion, internal inversion and lateral compression.

This study is intended to investigate the crushing behavior of  $[(90/0/2R_c)/(2R_c/0/90)/R_{c.75}]$  Fiberglass/Vinylester circular tubes. Tubes with a thickness of 2.35mm and an inner diameter of 33.0 or 50.8 mm are tested in the following four distinct crushing modes: 1. Axial compression between two steel platens; 2. External inversion between two shaped dies; 3. Internal inversion between two shaped dies; 4. Lateral compression between two steel platens. Under axial compression, a triangular wedge forms of the debris in the middle of the wall after the initiation stage of crushing. The wedge splits the outer frond into about 9 strips and bends over the inner frond inward. When compressed against shaped external or internal inverting dies, the tube is inverted externally or internally. Four bending hinges appear when the tube is subjected to lateral compression.

It has long been known that thin-walled metallic tubes can be internally inverted and result in high specific energy. However, if the die radius is carefully selected, metallic tubes often show folding collapse rather than internal inversion. In comparison, the composite tubes tested in this study demonstrated successful internal inversion over a fairly large range of die radius, as is shown in Table 1.

For the material tested, the following findings are obtained:

1. The specific energy absorption depends strongly on the crushing modes.

In general, the specific energy absorption decreases in the order of axial compression, internal inversion, external inversion and lateral compression. However, internal inversion may result in a higher specific energy than axial compression, when the die radius is close to the tube thickness.

2. Die radius has a very significant influence on the specific energy for both internal and external inversion mode.

When the die radius is reduced to 2.54 mm from 12.7 mm, the specific energy of internally

inverted 50.8mm diameter tubes increased by 100%.

3. Regardless of the crushing modes, tubes with smaller diameter exhibit higher specific energy absorption in most of the cases.

4. The axial compression is basically a combination of internal inversion and external inversion, with the debris wedge functioning as a die.

This study shows that the high energy absorption capability of internal inversion mode should deserve more attention of crashworthiness designers. The self-containment of the fiber debris of internal inversion mode of crushing will result in less environmental damage which is of particular interest for automobile industry.

#### References:

1. Thornton, P. H. 1979. "Energy Absorption in Composite Structures", J. Composite Materials, Vol.13, October, pp247-263
2. Farley, G. L. 1983. "Energy Absorption of Composite Materials", Journal of Composite Materials, Vol. 17, May, pp267-279
3. Mamalis, A. G., D. E. Manolakos and G. L. Viegelaahn. 1990. "Crashworthy Behavior of Thin-Walled Tubes of Fiberglass Composite Materials Subjected to Axial Loading", Journal of Composite Materials, Vol. 24, January, pp72-91

**Table 1. Experimental Results**

Inner Diameter (mm)	Number of Specimens Tested	Die Radius (mm)	Crushing Mode	Average Specific Energy (kJ/kg)
33.0	4	2.54	External	43.58
33.0	4	6.35	External	27.08
33.0	4	2.54	Internal	52.64
33.0	6	6.35	Internal	51.39
33.0	3	None	Normal	56.52
33.0	3	None	Lateral	2.10
50.8	3	2.54	External	39.29
50.8	3	6.35	External	20.03
50.8	6	2.54	Internal	69.87
50.8	3	6.35	Internal	41.82
50.8	3	12.7	Internal	35.43
50.8	4	None	Normal	60.15
50.8	7	None	Lateral	1.12

# The Effect of Cone Angle on Energy Absorption as a Design Criterion

F. W. Hannapel, G. L. Viegelaahn, Y.B. Yuan  
ME-EM Department, College of Engineering  
Michigan Technological University  
Houghton, Michigan 49931

Energy Absorption during impact has become an important design criterion over the past several years. Much work has been done in the area of metals and plastics<sup>(1) (2) (3)</sup>, but little information is available for composites. Now with the recent trends to design based on strength to weight ratio, the use of composite materials has found its way into just about every field. Many designs make use of circular shapes or tubes as load carrying members. Experimental results indicate that a straight tube tends to produce the maximum crushing energy absorption, but tends to fail in a global manner if end conditions are not exactly correct. By introducing a slight angle to the tube, thus causing it to be a cone, the crushing energy can be controlled as a function of angle as shown in Figure 1. As the angle of the cone is increased another limit is encountered as the cone will tend to split along the axis. Present research indicates that for cone angles over twenty degrees a critical crush distance is reached at which point the cone suddenly splits axially resulting in no load or energy absorbing capability. Cones of different angles and thickness were crushed to the point of axial splitting with the results shown in Figure 2, from which the following relation is generated when using conical shapes for energy absorption design.

$$\text{Critical Mean Diameter} = 5.56 * \text{Thickness} + 4.5$$

Work at this point has been confined to composite members made of chopped random fiberglass mat in a thickness range of up to one half inch. Future work must be expanded to include different types of fiberglass mat and combinations of mat lay-up.

## References:

1. Mamalis, A. G., Johnson, W. and Viegelaahn, G. L., 1984, "Crumpling of Steel Thin Walled Tubes and Frustra Under Axial Compression at Elevated Strain-Rates", International Journal of Mechanics Science, Vol. 26, pp. 537-547.
2. Mamalis, A. G., Viegelaahn, G. L., and Johnson, W., 1986, "The Inextensible Collapse of Thin-walled Cylinders of PVC Under Axial Loading", International Journal of Impact Engineering, Vol. 4, No. 1, pp. 41-56.
3. Mamalis, A. G., Manolakos, D. E., Viegelaahn, G. L., and Johnson, W., 1988, "The Modelling of Progressive Inextensible Plastic Collapse of Thin-Walled Shells", International Journal of Mechanical Science, Vol. 30, No. 3/4, pp. 249-261.

# COMPARISON OF 4 LAYER RANDOM MAT FIBERGLASS CONES.

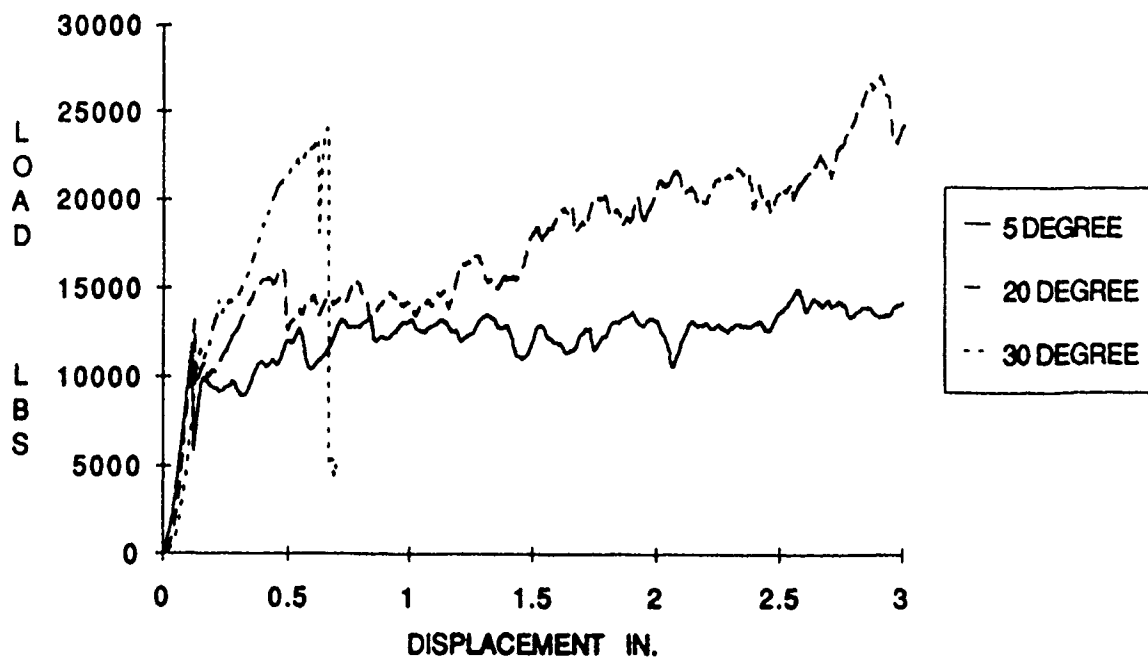


FIGURE 1

# GLOBAL SPLITTING OF, RANDOM FIBERGLASS MAT, CONES.

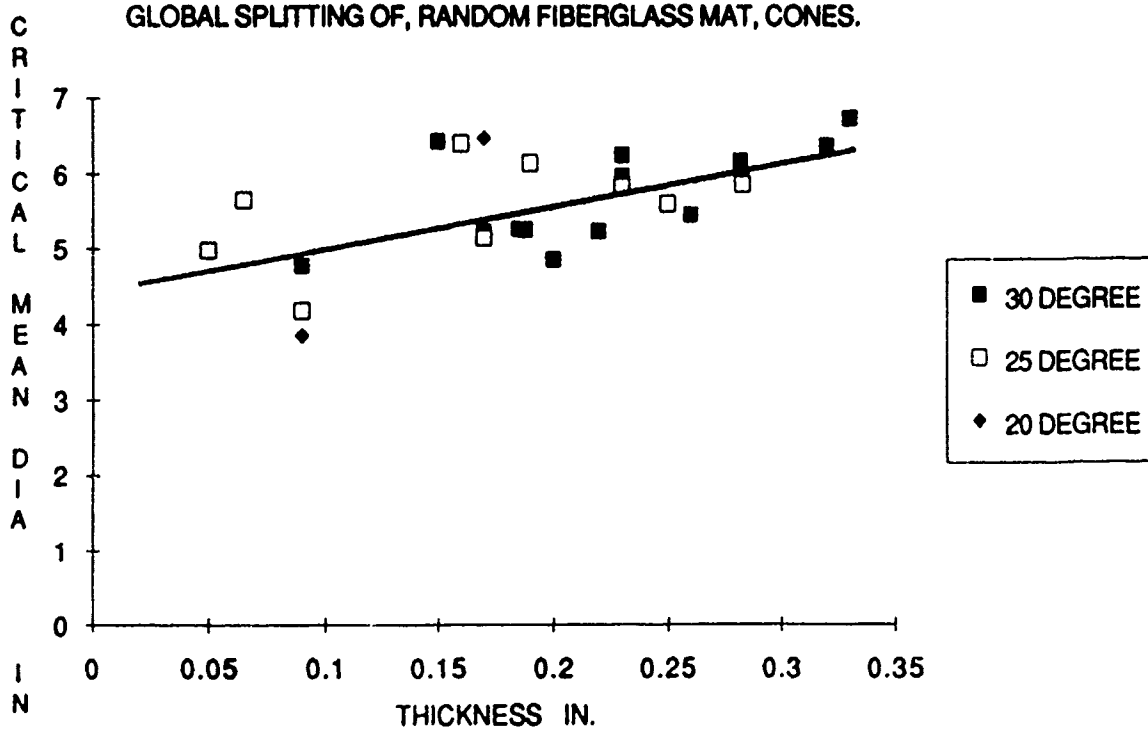


FIGURE 2



## **Crushing Characteristics of Composite Sections Subject to High Speed Axial Loading**

Y. B. Yuan, G. L. Viegeln, A. G. Mamalis\*

ME-EM Department, Michigan Technological University  
Houghton, Michigan 49931, USA

\*National Technical University of Athens, Athens Greece

A specially manufactured high loading rate device is used in dynamic crushing of circular tubes and conical shells made of fiberglass and polyester resin in a speed range of 18 - 24 m/s. The results are compared with corresponding static crushing results to investigate the effects of specimen geometry and crush speed on the specific energy absorption of the composite material.

From the results of this study, it is found that for specimens showing stable crushing, greater thickness tends to reduce the specific energy absorption; square tubes have less specific energy absorption than circular tubes, and greater semi-apical angle results in lower specific energy. Crushing speed has greater effect on the specific energy absorption of thick tubes than thin tubes. Specific energy of thin-walled circular conical specimens was reduced by some 35% at a crushing speed of about 21 m/s. The experimental results are presented in Tables 1 and 2.

Microscopic observation reveals that there is always a wedge formed of debris in the crushing zone of statically crushed tubular specimens. The wedge forces the fronds inward and outward, and delamination occurs in severely curved zone, as is shown in Figure 1(a). As crushing progresses, the fronds fracture into small solid debris due to bending and splitting. The static crushing mechanisms are identified as: 1. Bending of the inward and outward fronds; 2. Friction between the steel platen and the fronds; 3. Friction between the fronds and the wedge; 4. Delamination caused by the wedge and bending; 5. Hoop breakage of the outward frond; 6. Hoop compression of the inward frond. In dynamically crushed specimens, however, the high crush speed prevents the wedge from being well formed. The wedge is negligibly small, thus the total friction energy is conceivably smaller. In dynamic crushing no discrete fracture was observed. Resin is separated from the fiber mats in the debris. Observation of the dynamic crushing zone suggests that in dynamic crushing the high pressure and high loading rate caused compressional failure of resin in the crushing zone and the failed plies were further bent over and forced out.

For square tubes, four splitting cracks appear at the corners. In comparison, the outward frond of circular tubes is usually split into nine strips. The smaller crack number is considered responsible for the reduction in specific energy for square tubes.

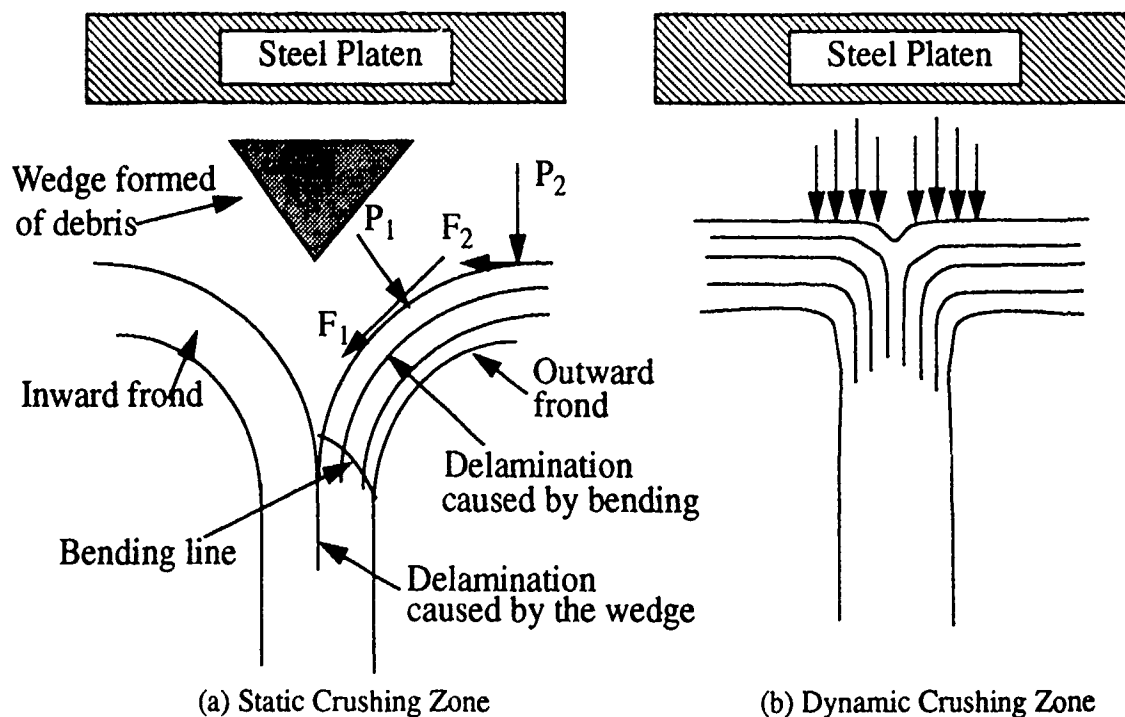


**Figure 1. Depiction of Static and Dynamic Crushing Zones**

**Table 1. Experimental Results for Square and Circular Tubes**

Specimen Shape	Inner Dimension (mm)	Thickness (mm)	Crush Speed (m/s)	Average Specific Energy (J/g)
Square	42.2x42.2	4.45	$2.1 \times 10^{-4}$	47.67
Square	42.2x42.2	4.60	21.34	48.51
Square	42.2x42.2	7.11	$2.1 \times 10^{-4}$	46.95
Square	42.2x42.2	7.37	25.30	41.45
Circular	43.18	4.06	$2.1 \times 10^{-4}$	58.77
Circular	43.18	3.81	19.2	54.23
Circular	43.18	7.00	$2.1 \times 10^{-4}$	57.78
Circular	43.18	7.62	21.34	51.53

**Table 2. Experimental Results for Conical Shells**

Semi-Apical Angle	Top Inner Diameter (mm)	Thickness (mm)	Crush Speed (m/s)	Average Specific Energy (J/g)
5°	31.24	3.60	$2.1 \times 10^{-4}$	54.91
5°	31.75	3.66	19.8	44.05
10°	26.92	3.60	$2.1 \times 10^{-4}$	52.75
10°	33.50	3.38	19.2	45.76
15°	31.75	3.32	$2.1 \times 10^{-4}$	56.42
15°	36.83	3.60	24.38	36.42
20°	27.94	3.50	$2.1 \times 10^{-4}$	48.49
20°	31.75	3.81	19.20	30.90

# Crashworthy Characteristics of Thin-Walled Tubes in Bending

G. L. Viegelaahn, D. J. Johnson\*, R. K. Wlosinski\*, A. G. Mamalis\*\*

ME-EM Department, College of Engineering

Michigan Technological University, Houghton, MI 49931

\* Scientific Laboratory, Ford Motor Company, Dearborn, MI 48121-2053

\*\*National Technical University of Athens, Athens Greece

Energy absorption in crashworthy design has been limited mainly to the area of axial collapse because of ease in obtaining data. The area of bending collapse presents many difficulties to obtain data quickly, accurately, and without long setup time. This issue has been addressed at Michigan Technological University by designing a machine to give the direct moment-rotational collapse data for tubes of different shapes. Previous setups by McIvor<sup>(1)</sup> and Kecman<sup>(2)</sup> gave reasonable results but were difficult to setup and were very time consuming. These testing setups also exhibited serious limitations when trying to determine deep collapse characteristics. Experiments were run on the new machine, which was based on the cantilever beam principle, using steel tubes and compared to the work of Kecman<sup>(2)</sup> as shown in Figure 1. The results were in good agreement with at maximum a 5% error which could be attributed to the clamping conditions used in the machine. Work on steel circular and square tubes was conducted by Johnson<sup>(3)</sup> and is being extended into composite tubular sections. A typical moment-rotation collapse history of a square tube made of random fiberglass mat - polyester resin of various thickness is shown in Figure 2. Work is just beginning in this area and there is much to discover in the area of bending collapse for composite materials.

## References:

1. McIvor, I. K., Anderson, W. J. and Bijak-Zochowski, M., "An Experimental Study of the Large Deformation of Plastic Hinges", *Int. J. Struct.*, 13, 53, 1977.
2. Kecman, D., "Bending Collapse of Rectangular Section Tubes in Relation to the Bus Rollover Problem", Ph.D. Thesis, Cranfield Institute of Technology School of Automotive Studies, 1979.
3. Johnson, D. J., "Crashworthy Characteristics of Thin Wall Cylindrical Steel Tubes in Bending", M.S. Thesis, Michigan Technological University, 1990.

# COMPARISON OF POSTBUCKLING REGIONS FOR SQUARE STEEL TUBES IN BENDING

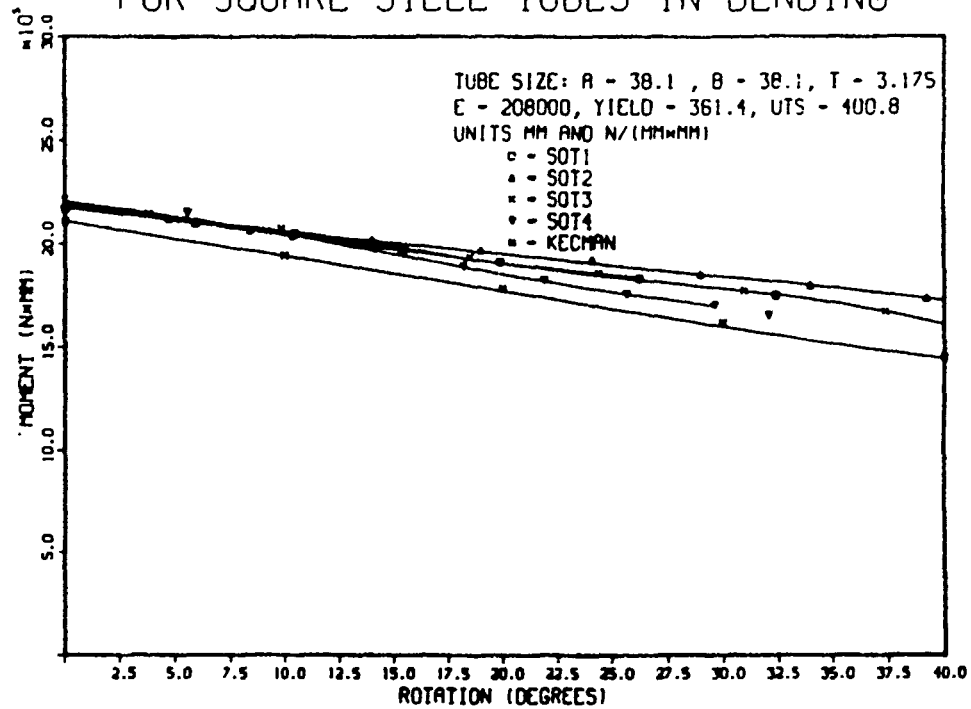


Figure 1. Comparison of Postbuckling Moment

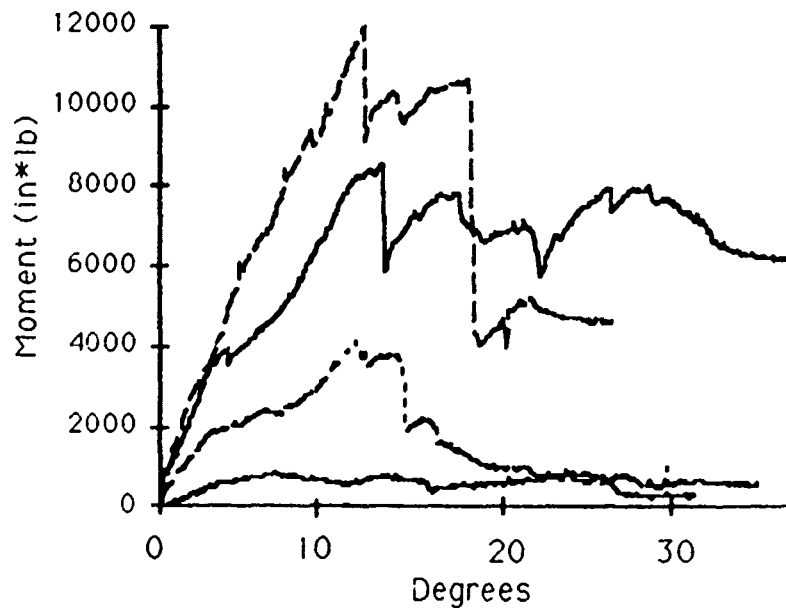


Figure 2. Moment-Rotation History

# A Numerical Study of the Stability of Shearing in an Elastohydrodynamic Contact

R. Malek-Madani<sup>1</sup> A. S. Douglas<sup>2</sup> and K.T. Ramesh<sup>2</sup>

<sup>1</sup>Department of Mathematics  
U.S. Naval Academy, Annapolis, MD 21402

<sup>2</sup>Department of Mechanical Engineering  
The Johns Hopkins University, Baltimore, MD 21218

A detailed knowledge of the constitutive response of elastohydrodynamic lubricants is critical to the effective design of several tribological components. Typical lubricants sustain a shearing stress which is dependent on the rate of shearing, the temperature and the pressure. In an elastohydrodynamic (EHD) contact, pressures may reach as high as 3 GPa with average shear rates on the order of  $10^6$  per second. These conditions are extremely difficult to simulate in controlled experiments which enable the constitutive response of the lubricants to be determined. However, recent work by Ramesh & Clifton (1987) has been able to replicate the EHD pressure and shear-rate conditions.

One difficulty encountered in characterizing these contacts is that the shear-rate may not be uniform. This means that the data obtained from experiments can only be interpreted in an averaged sense and that locally severe thermal and strain gradients may exist in an actual EHD contact.

In order to evaluate the likelihood of strongly nonuniform or even localized strain rates, a numerical study of an idealized EHD system is performed. The lubricant is assumed to have a linear dependence on strain rate and an exponential dependence on temperature and pressure for relatively low pressures and strain rates. For higher pressures and strain rates, the stress is assumed to be linear in the pressure and temperature, while varying logarithmically with the strain rate. The pressure is prescribed as a quasi-Hertzian distribution and the elastic compliance of the confining surfaces is ignored.

It is found that the initial velocity profile is very similar to the distribution characteristic of Couette-Poiseuille flow in a Newtonian fluid. However, under certain conditions, the viscous work causes the temperature to rise locally (when it cannot be conducted away fast enough) which causes the flow profile to become unstable, leading to highly inhomogeneous velocity profiles.

## Reference

Ramesh, K.T. & Clifton, R.J. "A pressure-shear plate impact experiment for studying the rheology of lubricants at high pressures and high shearing rates," *Journal of Tribology*, 109, pp. 215-223 (1987).

# Characterization of Severe Localization in Dynamic Viscoplasticity

By

T. G. Shawki, R.A. Sherif<sup>(1)</sup> and H.P. Cherukuri<sup>(2)</sup>

Department of Theoretical and Applied Mechanics  
University of Illinois at Urbana-Champaign  
Urbana, Illinois 61801

## Abstract

The evolution of narrow regions of intense plastic flow during the dynamic deformation of rate-sensitive materials is an outstanding problem in mechanics. A unified framework for the analysis of the pre-localization regime was recently presented by Shawki (1991a,b). In the former work, the onset of flow localization was tied to the increased importance of inertial effects. An energy criterion was developed for the characterization of localization initiation. On the other hand, the aforementioned criterion did not provide the critical strain associated with *severe localization*. The current work examines the extension of the energy criterion towards the determination of the critical strain for the onset of the so-called "stage III" of the localization evolution history. A regular expansion of the solution is assumed for small values of the deformation number (introduced by Shawki (1991c)); i.e. for deformations in which inertial stresses are smaller than viscous stresses. This expansion illustrates the role of inertia as regards the localization evolution *history*. Furthermore, the onset of severe localization is tied to the attainment of an inflection point in the total kinetic energy of the system. Closed form expressions for the critical strain are derived for a general class of thermal viscoplastic materials. Estimates of critical strain based on this proposed criterion are compared to late-time numerical results of the fully nonlinear and coupled system of governing equations. The excellent agreement suggests the validity of the proposed criterion.

(1,2) Ph.D. graduate students.

# ADIABATIC SHEAR BANDING IN BODIES CONTAINING THREE-DIMENSIONAL VOIDS/INCLUSIONS/CRACKS

by

J.S. Jubran\* and H.M. Zbib\*\*

\*Department of Civil Engineering

\*\*Department of Mechanical and Materials Engineering  
Washington State University, Pullman, WA 99164-2920

## ABSTRACT

Adiabatic shear bands are usually observed in materials subjected to very high strain rates. Heat generation and trapping, leading to strain softening in the stress-strain graph, is believed to be the main cause of shear banding. Imperfections within the material matrix usually serve as sites for the initiation of these bands, from which they propagate across the body with very high speeds. These imperfections include, among others, voids, cracks, grain boundaries, and inclusions. In this study we investigate the effect of shear band formation on void growth, crack opening displacement and the interaction between various imperfections.

The problem is treated numerically where a block containing either ellipsoidal voids/inclusions, planar cracks, or an array of cracks or crack-voids is analyzed. The material considered for the analysis is of a von Mises type whose flow stress exhibits strain hardening, strain rate hardening and thermal softening. High strain rates in the order of 5000/sec are considered. In order to produce sharp strain gradients, eight-node brick elements with one integration point are used. It is shown that shear bands emanates at the tips of these imperfections and propagate outwards at high speeds. It is illustrated that rapid void growth and fast crack opening displacement can, indeed, be related to the formation of shear bands, suggesting that shear banding is a main mechanism for coalescence of voids and crack propagations in ductile materials. Comparison with experimental results and analytical models found in the literature will also be given.

## MODEL OF PLASTIC FLOW INVOLVING MICRO-SHEAR BANDING

Ryszard B. Pecherski

Institute of Fundamental Technological Research, Polish Academy of Sciences, Warsaw

The so called "micro-shear banding" is related with the concept of plastic deformations produced by two competing mechanisms, *viz* slip and micro-shear. They are observed on the surface of the specimen as slip lines, slip bands, coarse slip bands and micro-shear bands, respectively. Certain kind of micro-to-macro transition approach based on the elements of the theory of discrete nonlinear dynamical systems is proposed to formulate the phenomenological model of plasticity with an account of discrete and heterogeneous character of the active micro-shear bands developing in the course of plastic flow. The micro-shear bands produce the non-coaxiality between the principal directions of the stress tensor and those of the plastic rate of deformation tensor. The noncoaxiality induces plastic spin and leads to the similar relations that appear in the vertex - type plasticity models. The formalism developed by H. Zbib, Scripta. Metall., 23, 789-794, 1989, is applied by that.

Additional evolution equation is proposed to determine the fraction of the rate of plastic deformations produced by the active micro-shear bands. The simple form of this equation comes out from the study of the experimental observations of slip and micro-shear bands. Certain microscopic models of micro-shear bands development formulated with use of the nonlinear differential equations of Lotka-Volterra type are referred from the literature. They provide heuristic guidelines to assume that the evolution equation mentioned can be governed by the one-dimensional, quadratic, iterated map represented by the logistic equation. The equations of elastic - plastic material with Huber - Mises yield condition and vertex - type effect of micro-shear bands are presented and the implications for the analysis of material instabilities are discussed.



## 22nd MIDWESTERN MECHANICS CONFERENCE

October 6-9, 1991  
University of Missouri-Rolla

Name: ..... Alan Needleman ..... Viggo Tvergaard .....  
Affiliation: Brown University ..... Technical University of Denmark  
Division of Engineering ..... Department of Solid Mechanics  
Address: ... Providence, R.I. 02912 ..... 2800 Lyngby .....  
U.S.A. ..... Denmark  
Office Telephone: ..... E-mail: .....

### Title & Abstract

#### ANALYSES OF PLASTIC FLOW LOCALIZATION IN METALS

Alan Needleman and Viggo Tvergaard

#### Abstract

The prediction of the localization of deformation into shear bands is known to be very sensitive to the constitutive description. The classical isotropic hardening elastic-plastic solid with a smooth yield surface and normality is very resistant to localization, but deviations from these idealizations have a strong effect. Thus, a material that forms a sharp vertex on the yield surface, as predicted by crystal plasticity, shows flow localization at quite realistic levels of strain, and even the formation of a rounded vertex on the yield surface has an important influence. Also softening induced by material damage or by the heating due to plastic dissipation have significant influence in promoting the onset of flow localization. In a practical situation one effect, such as thermal softening under high deformation rates, may be the dominant cause of localization, but often the interaction of different effects appears to be the more realistic explanation of observed flow localization. Some relevant constitutive models will be reviewed and the effect of the different material models on localization predictions will be illustrated. Important information on localization behavior in uniformly strained solids is obtained by a simple model analysis, but often failure by flow localization occurs in nonuniformly strained regions, where numerical solution procedures are necessary to obtain theoretical predictions. Computational methods for such cases will be discussed. The numerical results to be presented will cover time independent elastic-plastic material models as well as the effect of material strain-rate sensitivity on flow localization.

# EXPERIMENTAL STUDY ON THE FREQUENCY RESPONSE OF FLEXIBLE MECHANISMS

F. W. Liou  
Assistant Professor

K. C. Peng  
Graduate Research Assistant  
Department of Mechanical and Aerospace Engineering  
and Engineering Mechanics  
University of Missouri - Rolla

## ABSTRACT

Due to the complexity of the dynamic analysis of high-speed mechanisms, to design a high-speed mechanism, a lot of factors need to be considered. Recently, experimental studies of flexible mechanisms have been reviewed by Peng and Liou[1]. There are still several problems pending to be solved in the area of kineto-elasto-dynamics(KED). For instance, the modeling of damping in a mechanism, the quasi-static response that exists at higher speeds[2], and the natural frequencies which appeared to be variable in static testing but rather stable in dynamic condition[3-5]. This paper presents an experimental analysis of frequency response of flexible mechanisms to provide a new understanding of the system behavior. Doubtlessly, the natural frequency is a crucial factor in designing a mechanism. The operating speed must not be too close to the system's critical speed region. When operating within this region, the vibration amplitude of the system will be much higher than that running at the neighborhood speeds.

Liao et al.[2] have conducted an experimental study of four-bar linkages to document the different classes of flextural mid-span elastodynamic responses of the links. It was found that the coupler and follower links which different in geometric shape showed different resonant frequencies and at various crank speed these responses could be a combination of three response regimes. These regimes are quasi-static, dynamic, and resonance. It is very interesting to see that in their results, the quasi-static response appears in the high speed ranges. This finding may lead to a breakthrough in the design process of KED systems if the development of the analytical tool can be developed. This paper is to present the result of some experimental analyses in the frequency domain to help understand the phenomenon.

This paper presents some experimental results of the frequency analysis of flexible mechanisms. The objective is to help understand the general trend of vibration characteristics of the flexible mechanisms, and to clarify some

debatable phenomena in the KED area from the frequency domain view point. Both single link and assembled linkage analyses have been conducted to compare the single link natural frequency with the system natural frequency. Some of the experimental results are quite different from the predictions of the current analytical models.

This paper presents the frequency aspect of the dynamic response of flexible mechanisms. The conclusion can be summarized as follows:

- 1) In the steady state condition, the dynamic response of each link behaves like an individual beam so the resonant frequency of each link can be different and is very close to the corresponding link's natural frequency. However, in the static case, the system natural frequencies of a mechanism are varied with respect to different position.
- 2) The super-harmonic frequencies ( $1 \cdot \omega_{cs}$ ,  $2 \cdot \omega_{cs}$ , ..  $n \cdot \omega_{cs}$ ), which are induced by the inertia force nonlinearity, are integer multiples of the input speed  $\omega_{cs}$ . Whenever a harmonic frequency falls into a link's resonance region, a dynamic amplification will occur, and if the harmonic frequency equals to the natural frequency, a resonance will occur.
- 3) The system natural frequencies of a flexible mechanism can be estimated based on the individual link's natural frequency. For example, a coupler link may be estimated to be at resonance when the input speed or one of its harmonics is close to its link's natural frequency.
- 4) If the input speed is carefully chosen so that all of its harmonic frequencies can avoid falling into the resonance region of any link, then a quasi-static response will occur. There will be a good chance for a designer to synthesize a flexible four-bar mechanism to operate at higher input speed and reduce the vibration problem.

Since the above observations are quite different from the result of the current analytical models, it is very challenging to develop more analytical tools to simulate the above phenomena.

## REFERENCES

1. Peng, K. C. and F. W. Liou, "A Survey of the Experimental Studies on Flexible Mechanisms" Proceedings of the 1990 ASME Mechanisms Conference, DE-VOL-28, pp.37-44.
2. Liao, D. X., Sung, C. K., Thompson, B. S. and Soong, K., 1986. "A Note on the Quasi-Static Responses, Dynamic Responses and the Super-Harmonic Responses of Flexible Linkages: Some Experimental Results" ASME paper No. 86-DET-146.
3. Alexander, R. M. and Lawrence, K. L., 1973. "An Experimental Investigation of the Dynamic Response of an Elastic Mechanism" Design Engineering Technical Conference, Cincinnati, Ohio, Sept. 1973, ASME paper No. 73-DET-27.
4. Sanders, J. R. and Tesar, D., 1978. "The Analytical and Experimental Evaluation of Vibratory Oscillations in Realistically Proportioned Mechanisms" Transactions of the ASME, 762 / Vol. 100, October 1978.
5. Turcic, D. A., Midha, A. and Bosnik, J. R., 1983. "Dynamic analysis of elastic mechanism systems, part-II: application and experimental results" ASME paper No. 83-WA/DSC-38.

# DESIGN OF A MINE TUNNEL DRILL FRAME USING FIVE POSITION KINEMATIC SYNTHESIS

Wenguang G. Wang  
Reda M. Batra  
Kenneth H. Means

Department of Mechanical and Aerospace Engineering  
West Virginia University  
Morgantown, WV 26506

## ABSTRACT

A planar linkage for a given 5-position performance is synthesized using the complex number method. The linkage is designed through solving a group of closed loop nonlinear equations and is used as a drill frame which can be employed to develop mine tunnels. This linkage synthesis procedure is demonstrated in this paper.

## INTRODUCTION

The graphical solutions for five position synthesis can be obtained by the intersection of 2 four position solutions. This graphical construction is simple but is too time consuming to repeat until a suitable solution is obtained. Several mathematical techniques for analytical modeling linkages have been accomplished for planar synthesis objectives. They are the algebraic method [1,2] the complex number method [2-5], and the displacement matrix method [6,7]. The complex number technique is versatile and the numerical design example by using a modified complex number method is presented in this paper. The aim is to design a 4-bar linkage for 5 position synthesis which is used in coal mine tunnel developing (Fig.1). A drill bit can be installed on the coupler to make holes in the tunnel wall. The cement aggregate slurry is pumped into the holes for strength in the tunnel. And also a broom can be fixed at the coupler to clean the coal dust at the tunnel wall.

With these purposes, the design criteria are established as follows. 1) The two pivot points are fixed in the central line of the coal tub which is driven by the mine locomotive. 2) The outer point of the coupler is designed against or very close to the tunnel wall. 3) The tunnel surface is a combination of several curvature arcs. But the left side is symmetric to the right side. Therefore the coupler is against or close to the left side wall when the tub goes into the tunnel, and finishes the same task for the right side when the tub comes out from the tunnel. 4) The dimensions of the mechanism must fit the tunnel cross-section.

## SYNTHESIS AND ANALYSIS

The mechanism is synthesized by means of complex number equations. The complex number is an ideal tool for modeling linkage members as parts of planar chains. Figure 2 shows the line diagram of the mechanism with required nomenclature. There are two independent dyads (left, right) in the four-bar linkage. Each dyad connects a ground pivot (a central point, which is fixed on the coal tub) to the path point on the coupler (the circle point). The equations describing the displacements of the left-hand side and the right side of the linkage may be written as

$$\vec{Z}_2(e^{i\phi_j}-1) + \vec{Z}_3(e^{i\psi_j}-1) = \vec{\delta}_j \quad (j=2,3,4,5) \quad (1)$$

$$\vec{Z}_4(e^{i\psi_j}-1) + \vec{Z}_5(e^{i\phi_j}-1) = -\vec{\delta}_j \quad (j=2,3,4,5) \quad (2)$$

Substituting the position vector by cosine, sine terms and the operator  $j$  and separate the real and image parts, from equation (1), (2), we can get the 4 scalar equations. For  $j=2$  to 5, we get  $4 \times 4 = 16$  equations. There is a loop equation which contains the link  $Z_2, Z_3, Z_5, Z_4, Z_1$ .

$$\vec{Z}_1 + \vec{Z}_4 + \vec{Z}_5 - \vec{Z}_2 - \vec{Z}_3 = \vec{0} \quad (3)$$

This vector equation also can be separated into 2 scalar equations.

For 5 position synthesis, eighteen nonlinear equations must be solved and the Newton-Raphson method with the JACOBI matrix is incorporated in the solution procedures. The results are shown in Fig.3.

It is very important to guess the initial values as close the results as possible. The solutions will diverge if the initial values were too far away from the actual ones. A three position graphical synthesis solutions may give good initial guesses for the 5 positions solutions. In this study, the initial values were obtained from position point 1, 3, 5, then guess the values for the other two position points.

## CONCLUSION

A model for 5 position synthesis have been constructed in this project. A 4-bar linkage fixed at coal tub is designed for mine tunnel. The model allows the freedom to choose the prescribed positions, therefore, it indicates its great flexibility in synthesis.

## REFERENCES

1. F. Freudenstein, Approximate Synthesis of Four-bar Linkages, Trans. ASME, 77, 853-861 (1955).
2. R. S. Hartenberg and J. Denavit, Kinematic Synthesis of linkages, McGraw-Hill, New York (1964).
3. G. N. Sandor, R. E. Kaufman, A. G. Erdman et al., Kinematic Synthesis of Reared linkage, J. Mech.5, 59-87, 1970.
4. A. G. Erdman, Three and Four Precision Point Kinematic Synthesis of Planar Linkages, Mach. Theory 16, 227-245, (1981).
5. A. Midha, D. A. Tracic and J. R. Bosnik, Creativity in the Classroom A Collection of Case Studies in mechanism Synthesis, Mach. Theory 19, 25-44 (1984).
6. C. H. Suh and C. W. Radcliffe, Synthesis of Plane Linkages with Use of the Displacement Matrix, J. Eng. Ind., 206-214, (1967).
7. C. H. Suh and C. W. Radcliffe, Kinematics and Mechanisms Design, Wiley, New York (1978).

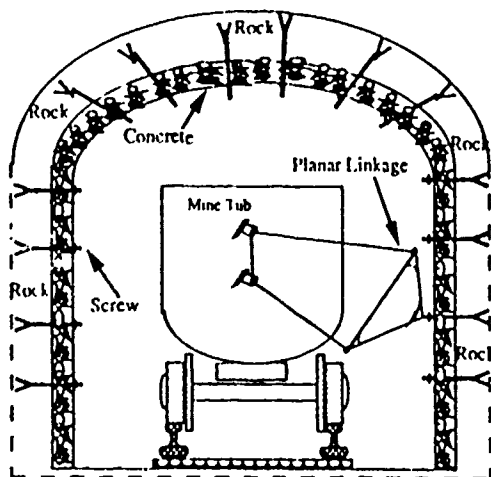


Fig. 1 Mine tunnel and the proposed drill frame

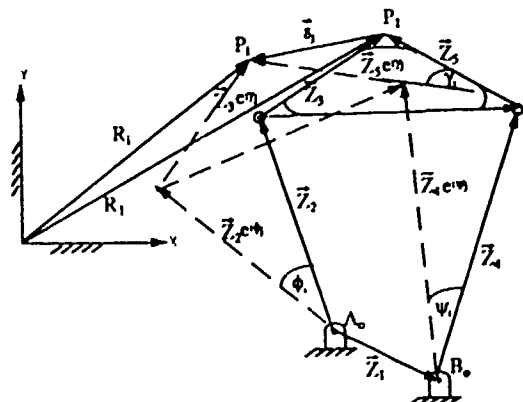


Fig. 2 Line diagram of the mechanism

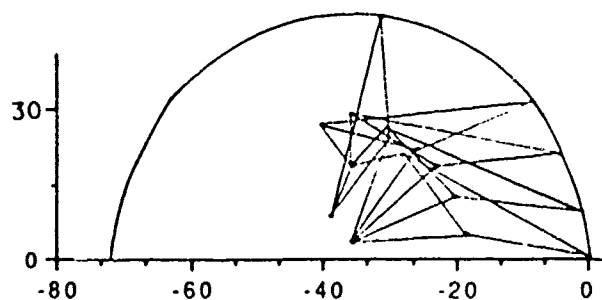


Fig. 3 Results of the five position synthesis

## **CRASH RESPONSES OF A DISCRETE-PARAMETER MODEL OF THE HUMAN HEAD-NECK**

**Hamid Lankarani, Assistant Professor; Rajiv Menon, Graduate Research Assistant  
Mechanical Engineering Department, National Institute for Aviation Research  
The Wichita State University, Wichita, KS 67208**

### **Abstract**

Head-neck injuries have become quite common to a crash victim especially due to the high speeds of traffic and it is a widely accepted notion that as many as 60-70% of automotive fatalities [1] are due to severe head injuries. Head-neck injuries may also occur in falls or due to use of excessive force. In this paper a multibody model of the head-neck of a 10 percentile male has been developed. This model is a collection of two-dimensional bodies, interconnected by an array of kinematic joints, and consists of the head and the seven vertebrae attached to the upper torso. This model was subjected to a series of half-sinusoidal frontal crash forces. The aim was to observe the effects of different crash loads on this model.

### **Introduction**

There has been a great interest in the mechanisms that cause injuries to the head-neck. This has simulated the development of many different methods, to study the effects of crashes under varying conditions. Measurements were made on inanimate models [2,3], cadavers [4], and animals [5]. Many different, two and three dimensional models have also been developed [6-9]. Computer models and methods avoid the necessity of experiments involving cadavers, laboratory animals and anthropomorphic dummies, hence cost efficient, less time consuming and less controversial. They yield substantial and more detailed results quickly, and are capable of simulating many different crash scenarios which may not be feasible or more still possible in a laboratory program. This paper presents a description of a two-dimensional multibody model which was subjected to a series of crash forces. The results show the response of the head-neck model to the different variations in the crash forces.

### **Dynamic Modeling**

Dynamic modeling involves selecting a kinematic model; defining the initial conditions, forces, and the inertia properties of components of the system; and forming and solving the equations of the mechanism, kinematic constraints that act between pairs of bodies, and time-dependent kinematic drivers. Body-fixed frames must be attached to each body with their origin at the center of mass of the body. As shown in Figure 1, ten bodies were taken into account, the head, the seven vertebrae, the upper torso and ground. The joints between the vertebrae are revolute joints and the effects of muscles, intervertebral discs, cartilage, and ligaments, cerebrospinal fluids, and other tissues are depicted by nonlinear rotational spring dampers. Between the upper torso and ground a translational joint was considered.

### **Crash Simulations**

Once the model of the head-neck is complete, a variety of input forcing conditions may be applied to this model, and its behavior under each specific conditions be studied. A half-sinusoidal force,  $F = F_m \sin(2\pi t/\tau)$ , was used for depicting the crash force. Parameter  $F_m$  is the amplitude of the acceleration force, and  $\tau$  is the period (time duration).

Results were obtained and studied for two cases. Case 1 : The amplitude was varied; Case 2 : The period was varied. A simple post processing graphics program was also developed to draw the configuration of the system at different time intervals. The response of the model to varying conditions was generated by a dynamic analysis program developed at the Wichita State University. The output of the program gave the coordinates, velocities, accelerations, rotational spring damper data, and the reaction forces of each element/body, at different time intervals. Among many different results of the simulations, only a sample is presented here. From Figure 2 of the magnitude of the joint reaction force at the skull C1 (occipital-atlantal), it can be seen that the peak values of the neck joint forces get higher as the amplitude is increased. Figure 3 shows variations of the duration of the force. It can be seen that as the periods increase, the force, although at higher amplitude, acts more evenly. Figure 4 shows a graphical representation of the system to a crash force of  $F_{cr} = 4g$ ,  $\tau = 200ms$ .

An accurate dynamic model of the human head and neck was constructed in this study. The model can be subjected to various inputs simulating a variety of crash configurations of a vehicle occupant. The results of this study help in separating the effects of different crash force parameters, and investigating the mechanisms that cause head/neck injuries.

## References

- [1] Huston, R.L., Huston, R.C., Harlow, N.W., "A Comprehensive Three-dimensional Head-Neck Model for Impact and High Acceleration Studies," *Aviation, Space, and Environment in Medicine*, Vol.49, pp.205-210, 1978.
- [2] Landkof, B., Goldsmith, W., and Tackman, J.L., "Impact on a head-neck structure" *J. Biomechanics*, Vol.9, pp.141-151, 1976.
- [3] Mertz, H.J. and Patrick, L.M., "Strength and response of the human neck", *Proc.15th Stapp Car Crash Conf.*, pp.207-255, SAE Paper No.710955, 1971.
- [4] Prasad, P. and King, A.I., "An experimentally validated dynamic model of the spine" *J. appl. Mech.*, Trans. A.S.M.E., Vol.96, pp.546-550, 1974.
- [5] Hodgson, V., "In impact Injury and Crash Protection", (Edited by Gurdjian, E.S. et al.), pp.275-307, Thomas, Springfield, 1970
- [6] Deng, Y.C., and Goldsmith, W., "Response of a Human Head/Neck/Upper-Torso Replica to Dynamic Loading II. Analytical/Numerical Model," *J. Biomechanics*, Vol.2, pp.487-497, 1987.
- [7] Reber, J.G., and Goldsmith, W., "Analysis of Large Head-Neck Motions," *J. Biomechanics*, Vol.12, pp.211-222.
- [8] Khalil, T., and Hubbard, R., "Parametric Study of Head Response by Finite Element Modeling," *J. Biomechanics*, Vol.10, pp.119-132.
- [9] Lankarani, H.M., Ma, D., and Ermer, G., "Biodynamic Simulations of an Aircraft Pilot/Passenger in Various Crash environments," NIAR Report No.90-6, National Institute for Aviation Research, The Wichita State University, April 1990.

Figure 1



Figure 3

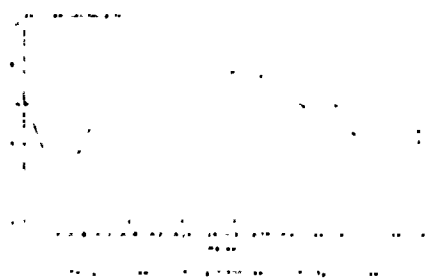


Figure 2

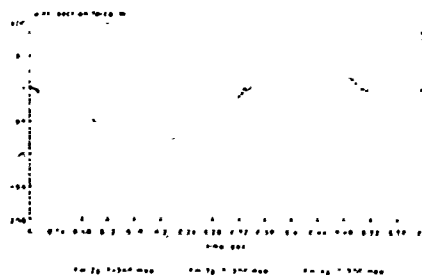


Figure 4



A SIMPLIFIED MODEL CAPABLE OF PREDICTING THE KINETIC  
RESPONSE OF A SEATED LIVE HUMAN SUBJECT TO +GZ IMPACT

Norman S. Phillips, University of Dayton  
300 College Park Dr., Dayton Ohio, 45469-0243

Human force response to an acceleration has been observed and measured for many years to provide design criteria for the development of safer designs of aircraft, automobiles, tractors and lifeboats, to name a few examples. Future designs of aircraft escape systems for single crewmembers may be lightweight seats with controlled thrusters, movable fins, and an onboard computer. The seat becomes a miniature aircraft with some of the problems associated with the parent aircraft. This is particularly true when the mass of the subject becomes a significant portion of the weight of the system, and the inertial response of the aircrewman to the ejection acceleration generates large forces and moments.

Over the years, as measurement capabilities have improved, more test programs have been conducted with increased numbers of data channels. For a seated subject it is possible to instrument the restraint straps, the seat belts, and negative "g" strap if applicable, the head rest, the upper seat back, the lower seat back, arm supports, the seat pan, the leg rests, and the foot rests. This information is supplemented by kinematic data such as the accelerations of all structural components, and by high speed photography. Hence, the kinetic and kinematic response of the human to acceleration environments, and the total force response can be computed.

As part of a program conducted at Wright Patterson Air Force Base, forty channels of data were collected for +Gz tests with humans and manikins. One particular test has been examined in detail. The test selected was one with an 8G peak deceleration, of 150 milliseconds duration, with a triangular waveform. The subject was 163 pounds, supported by an X-band harness, with legs dangling beneath the structural seat.

The mass and center of gravity data were available for all components of the test equipment as were all locations of the accelerometers and force cells. This, in addition to the strap angles available from high speed photography, permitted the calculation of the force and moment resultants acting upon the seat. A data processing program generated the three dimensional force and moment contribution of every measured force, as well as

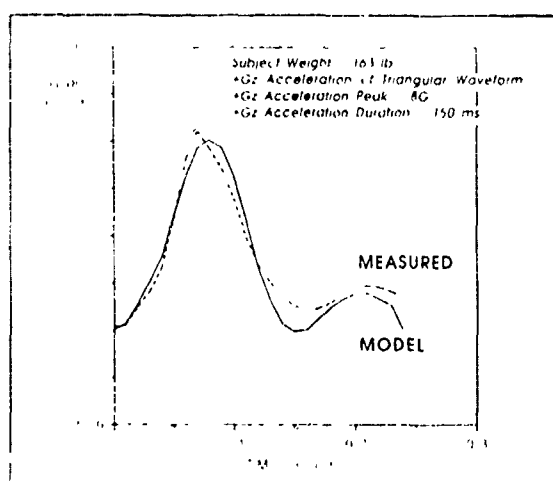


the resultants, as functions of time.

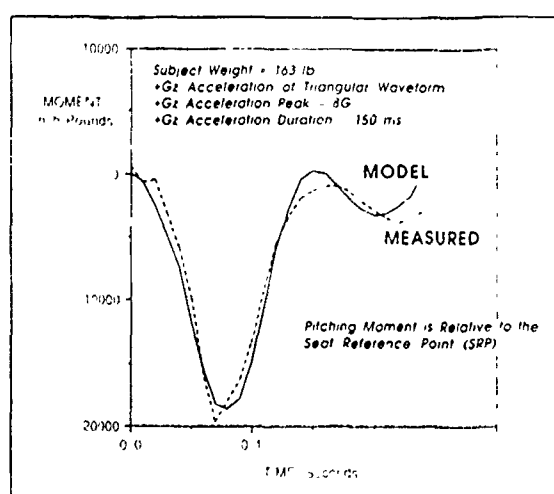
A simple linear elements-nonlinear configuration, model of the seated human was evolved and programmed to replicate the measured force response of the seated live human. The model consists of one mass suspended in space by a vertical element, and two elements going diagonally from the mass to locations outboard and behind the mass. This configuration provides a model that visually represents the seated human supported by "shoulder harness straps" going from the mass rearward and upward to shoulder harness attachment points.

Many combinations of parameter values were attempted to match the measured resultant force and moment responses in the plane of symmetry, as would be required for an assumed coplanar escape sequence. By using the known weight of the subject as that of the suspended mass, and by locating the mass at the center of gravity of the seated subject, based upon the location of the fiftieth percentile subject, and by locating the strap attachment points at ten inches either side of the centerline and at shoulder height, the computed resultants were compared with those measured as shown in the figures.

The comparisons shown have peak values that are within ten per cent of those measured for the greatest difference, and are within one percent of the maximum if an rms value is calculated for the differences between computed and measured for every millisecond. The model results shown are for a model having an undamped natural frequency of 9.14 Hz and a damping ratio of 0.48. This compares favorably with the historical "10 Hz" model, and implies that the original models predictive capability can be extended, if it is now located properly with attachments, to replicate both the force and the moment response as functions of time.



Vertical Force Response



Pitching Moment Response

## DYNAMIC AND SENSITIVITY ANALYSIS OF MECHANICAL SYSTEMS

Q. Cao, J.T. Twu and P. Krishnaswami  
Mechanical Engineering Department  
Kansas State University  
Manhattan, Kansas 66506

With the recent advances of computer hardware, simulation and sensitivity analysis of multibody dynamic mechanical systems have become computationally viable. A good formulation for constrained dynamic analysis as well as first and second order design sensitivity analysis for such systems is an essential need. This paper presents a formulation in a general form so that it can be applied to a large class of mechanical systems.

In modeling mechanical multibody systems, the equations of motion and kinematic constraint equations have to be derived. The constrained Lagrangian equations are suitable for such a system. They form a combined set of second order Differential equations and nonlinear Algebraic constraint Equations (DAE). Since many mechanical systems are stiff, a stiff integrator for the dynamic analysis has to be used. Gear's algorithm [1] is stiffly stable and has demonstrated reliability in solving DAE's. The dynamic analysis equations are derived from the constrained Lagrangian equation, kinematic constraint equations, and Gear's equations. The first and second order sensitivities are derived from direct differentiation of the equations of motion and the kinematic constraint equations [2].

The governing equations for the dynamic analysis are the following:

Constrained Lagrangian equation:  $f = M\ddot{q} + G_q^T \lambda - Q = 0$

Kinematic constraint equations:  $G(q, t) = 0$

Gear's equation: 
$$\dot{q}_{n+1} = \frac{1}{hb_0} \left( -q_{n+1} + \sum_{j=1}^k a_j q_{n-j+1} \right)$$

Here,  $q$  is the vector of system generalized coordinates,  $M$  is the system mass matrix,  $Q$  is the vector of generalized forces and  $h$  is the integration stepsize. The constants  $b_0$  and  $a_j$  are the Gear's constants, while  $k$  is the order of the integration. The subscripts in Gear's equation indicate time steps. The set of equations given above is solved iteratively at each time step to obtain the dynamic response of the system.

The first order sensitivity analysis is done by direct differentiation of the constrained Lagrangian equations, constraint equations and Gear's equations with respect to the vector of design variables. Also the accelerations are written in terms of velocities and their histories. The first order sensitivity equation takes the form:

$$\begin{pmatrix} f_q & f_u - f_{\dot{u}} \frac{1}{hb_0} & -G_q^T \\ \frac{1}{hb_0} I & I & Q \\ G_q & Q & Q \end{pmatrix} \begin{pmatrix} (q_b)_{n+1} \\ (u_b)_{n+1} \\ (\lambda_b)_{n+1} \end{pmatrix} = \begin{pmatrix} -f_b - f_{\dot{u}} \frac{1}{hb_0} \sum a(u_b)_{n-j+1} \\ \frac{1}{hb_0} \sum a(q_b)_{n-j+1} \\ -G_b \end{pmatrix}$$

The second order sensitivity can be obtained in the same way by differentiating the equations for first order sensitivity. Both first and second order sensitivity equations have the same Jacobian matrix. The second order sensitivity equation takes the form:

$$\begin{pmatrix} f_q & f_u - f_{\dot{u}} \frac{1}{hb_0} & -G_q^T \\ \frac{1}{hb_0} I & I & Q \\ G_q & Q & Q \end{pmatrix} \begin{pmatrix} (q_{bp_k})_{n+1} \\ (u_{bp_k})_{n+1} \\ (\lambda_{bp_k})_{n+1} \end{pmatrix} = \begin{pmatrix} A \\ -\frac{1}{hb_0} \sum a(q_{bp_k})_{n-j+1} \\ -[G_q \tilde{q}_b]_q q_{b_k} - [G_q \tilde{q}_b]_{b_k} - [G_q \tilde{q}_b]_{b_k} - G_{bp_k} \end{pmatrix}$$

where

$$A = -[(f_q \tilde{q}_b)_q + (f_q \tilde{u}_b)_u + f_{b_k q}] q_{b_j} - [(f_u \tilde{q}_b)_q + (f_u \tilde{u}_b)_u + f_{b_k u}] u_{b_j} - f_{b_k \dot{u}} \dot{u}_{b_j} - f_{\dot{u}} \frac{1}{hb_0} \sum a(u_{bp_k})_{n-j+1} \\ - [(f_{\lambda} \tilde{q}_b)_q + f_{b_k \lambda}] \lambda_{b_j} - (f_q \tilde{q}_b)_{b_j} - (f_u \tilde{u}_b)_{b_j} - (f_{\dot{u}} \tilde{u}_b)_{b_j} - (f_{\lambda} \tilde{\lambda}_b)_{b_j} - f_{bp_k}$$

With the use of a symbolic computing language such as REDUCE, the problem dependent subroutines for dynamic and sensitivity analysis can be automatically generated and derivatives can be calculated analytically by the computer. This makes the human effort in the process much less. Because of the inherent parallelism of the formulation, parallel algorithms for the whole system of dynamic and sensitivity analysis can be implemented effectively. Examples solved using this formulation indicate that it is very accurate and is reasonably efficient.

#### References:

- [1] Gear, C.W., (1971). "Simultaneous Numerical Solution of Differential Algebraic Equation", IEEE Transactions on Circuit Theory, CT-18(1), 88-95.
- [2] Krishnaswami, P and Ramaswamy, S. "Second Order Design Sensitivity analysis of Constrained Dynamics Systems", (submitted to the ASME journal of Mechanisms, Transmissions and Automation in Design)

# Fourth-order parametric splines for turbine design

Theodosios Korakianitis<sup>†</sup> and George I. Pantazopoulos<sup>‡</sup>

Department of Mechanical Engineering,  
Washington University,  
Campus box 1185,  
One Brookings Drive,  
St. Louis, MO 63130

**Introduction:** In past work (Korakianitis, 1987, 1989) we showed that continuous-slope-of-curvature is a requirement for the design of turbine blades with smooth surface Mach number and pressure distributions, which in turn are essential for high-efficiency cascades. Since curvature is a function of the first and second derivatives, continuous slope of curvature means third derivative continuity. Most parametric splines have only first- and second-derivative continuity. In the following we outline the development of fourth-order parametric splines which have been used for turbine design (Korakianitis and Pantazopoulos, 1991). These curves may have additional applications, such as automobile-surface generation for aesthetically-smooth reflections.

**Cascade geometry:** The inputs in turbine design are the inlet and exit flow angles, the tangential spacing of the blades, and the throat diameter, which is the minimum area available to the flow passage between the trailing edge and the blade immediately below the trailing edge. An additional important geometric feature is the stagger or setting angle of the cascade. This is the angle between the line joining the leading edge with the trailing edge and the horizontal ( $x$ ) direction. The area should be smooth, and in high Mach number subsonic passages the area should be continuously decreasing.

**Method:** The suction and pressure surfaces of the tur-

bine blades are specified by a series of parametric splines in  $s$  of the form:

$$\begin{aligned} X_j(s) &= a_{j0}^x + a_{j1}^x s + a_{j2}^x s^2 + a_{j3}^x s^3 + a_{j4}^x s^4 \\ Y_j(s) &= a_{j0}^y + a_{j1}^y s + a_{j2}^y s^2 + a_{j3}^y s^3 + a_{j4}^y s^4 \end{aligned} \quad (1)$$

where  $0 \leq s \leq 1$  in each of the  $(n-1)$  segments  $j$ , and  $a$  are the spline coefficients for  $X(s)$  and  $Y(s)$ . In the following we show the derivations applicable to  $X(s)$ ; the derivation for  $Y(s)$  is exactly analogous. Requiring point ( $x_i$ ), first derivative ( $fx_i$ ) continuity at  $s = 0, 1$  and second derivative ( $sx_i$ ) continuity at  $s = 0$  gives:

$$\begin{aligned} a_{j0}^x &= x_i \\ a_{j1}^x &= fx_i \\ a_{j2}^x &= sx_i/2 \\ a_{j3}^x &= 4(x_{i+1} - x_i) - fx_{i+1} - 3fx_i - sx_i \\ a_{j4}^x &= 3(x_i - x_{i+1}) + fx_{i+1} + 2fx_i + sx_i/2 \end{aligned} \quad (2)$$

Requiring second and third derivative continuity at  $s = 1$  gives:

$$\begin{aligned} 6fx_{i-1} + sx_{i-1} + 6fx_i - sx_i &= \\ 12(x_i - x_{i-1}) & \\ 5fx_{i-1} + sx_{i-1} + 6fx_i - sx_i + fx_{i+1} &= \\ 4(x_{i+1} + x_i - 2x_{i-1}) & \end{aligned} \quad (3)$$

Equations (3) are manipulated into the matrix form shown at the top of page 2 and solved for the derivatives. Then equations (2) give the spline coefficients,

<sup>†</sup> Assistant Professor

<sup>‡</sup> Graduate Research Assistant

$$\begin{bmatrix}
1 & 0 & 0 & 0 & 0 & 0 & 0 & 0 & . & . & . & . & . \\
0 & 1 & 0 & 0 & 0 & 0 & 0 & 0 & . & . & . & . & . \\
5 & 1 & 6 & 1 & 1 & 0 & 0 & 0 & . & . & . & . & . \\
6 & 1 & 6 & -1 & 0 & 0 & 0 & 0 & . & . & . & . & . \\
0 & 0 & 5 & 1 & 6 & 1 & 1 & 0 & . & . & . & . & . \\
0 & 0 & 6 & 1 & 6 & -1 & 0 & 0 & . & . & . & . & . \\
. & . & . & . & . & . & . & . & . & . & . & . & . \\
. & . & . & . & . & . & . & . & . & . & . & . & . \\
. & . & . & . & . & . & . & . & . & . & . & . & . \\
. & . & . & . & . & 0 & 0 & 5 & 1 & 6 & 1 & 1 & 0 \\
. & . & . & . & . & 0 & 0 & 6 & 1 & 6 & -1 & 0 & 0 \\
. & . & . & . & . & 0 & 0 & 0 & 0 & 0 & 0 & 1 & 0 \\
. & . & . & . & . & 0 & 0 & 0 & 0 & 6 & 1 & 6 & -1
\end{bmatrix}
\begin{bmatrix}
fx_1 \\
sx_1 \\
fx_2 \\
sx_2 \\
fx_3 \\
sx_3 \\
. \\
. \\
. \\
. \\
fx_{n-1} \\
sx_{n-1} \\
fx_n \\
sx_n
\end{bmatrix}
=
\begin{bmatrix}
BC_{1x,1} \\
BC_{1x,2} \\
4(x_3 + x_2 - 2x_1) \\
12(x_2 - x_1) \\
4(x_4 + x_3 - 2x_2) \\
12(x_3 - x_2) \\
. \\
. \\
. \\
. \\
4(x_n + x_{n-1} - 2x_{n-2}) \\
12(x_{n-1} - x_{n-2}) \\
BC_{rx,1} \\
12(x_n - x_{n-1})
\end{bmatrix}$$

which in turn are used in equations (1) to evaluate the  $(x, y)$  locations of the splines.

The left and right boundary conditions  $BC_{1x,1}$ ,  $BC_{1x,2}$  and  $BC_{rx,1}$  are evaluated from the slopes of the surfaces near the leading and the trailing edge, and curvature near the leading edge.

The leading edge geometry is designed by specifying thickness distributions added perpendicularly to parabolic construction lines that pass through the leading edge. The parameters for the thickness distributions are such as to result in continuous first, second and third derivatives where the parametric splines meet the thickness distributions.

A computer program has been implemented on a personal computer, which uses as inputs the ranges of  $(x, y)$  values of the spline knots, and the ranges of values for the boundary conditions. Search and optimization routines for desirable types of curvature distributions, and for continuously decreasing area along the blade passage have been implemented.

Using the above we have designed cascades such as the sample shown in figure 1.

**Acknowledgements:** The financial assistance of the Department of Mechanical Engineering for portions of this work is gratefully acknowledged.

#### References:

- T. Korakianitis (1987). "A design method for the prediction of unsteady forces on subsonic, axial gas-turbine blades", Doctoral thesis (Sc.D.) in Mechanical Engineering, Massachusetts Institute of Technology, Cambridge, MA, USA.
- T. Korakianitis (1989). "Design of airfoils and cascades of airfoils," *AIAA Journal*, Vol. 27, No. 4, April 1989, pp. 455-461.
- T. Korakianitis and G. Pantazopoulos (1991). "Continuous-slope-of-curvature parametric splines with appli-

cation to turbine-blade design", Washington University, WU-ICE report no. 91-1, March.

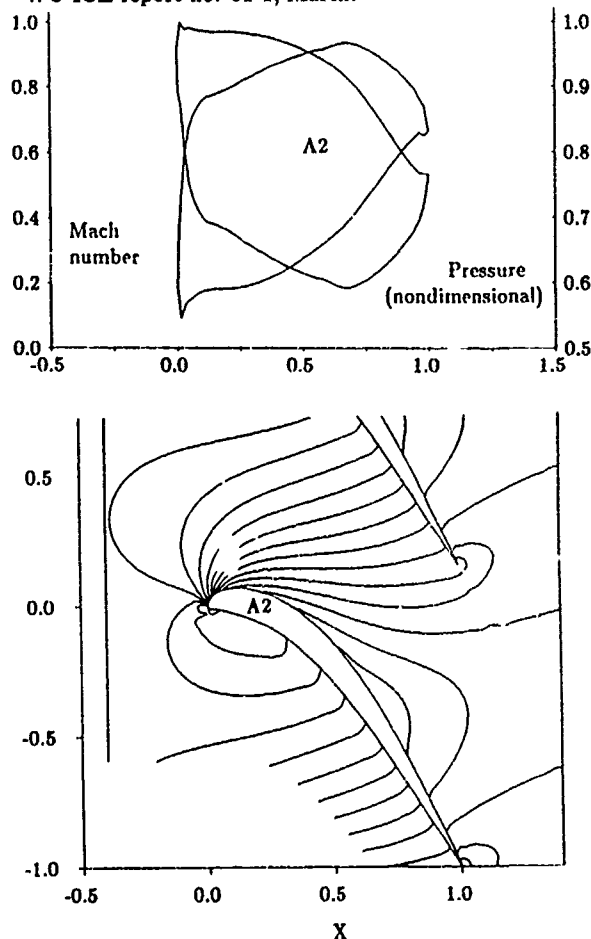


Figure 1: Surface Mach number surface distribution and contours of increment 0.05 for the sample cascade. Inlet flow angle  $0^\circ$ ; outlet flow angle  $-60^\circ$ ; tangential loading coefficient  $C_L = 1.0$ .

# SOME INVERSE SOLUTIONS OF STEADY PLANE FLOWS OF A NON-NEWTONIAN FLUID

A. M. SIDDIQUI  
Department of Mathematics  
The Pennsylvania State University  
York Campus, York, PA 17403

In general, exact solutions in non-Newtonian fluid flows are rare. This is because of the inherent non linearity which occurs in the governing equations of motion of such fluids. As a result no general analytical solution of these equations is possible. However, some flow situations of interest are such that a number of the terms in these equations are either identically zero [1] or may be neglected, so that the resulting equations reduces to a form that can be readily solved.

In recent papers, Kaloni et al [2, 3] gave solutions to the equations of motions of a second grade fluid by employing inverse methods. In the present note we neglect the inertial effects and study the inverse solutions of these equations by assuming the certain forms of the vorticity and the Laplacian of the vorticity.

If  $\psi(x,y)$  represents the streamfunction so that the components of velocity are

$$u = -\frac{\partial \psi}{\partial y}, \quad v = -\frac{\partial \psi}{\partial x} \quad (1)$$

then the equation of motion of a second grade fluid may be wirtten as [2]

$$-\rho \left[ \frac{\partial(\psi, \nabla^2 \psi)}{\partial(x,y)} \right] + \alpha_1 \left[ \frac{\partial(\psi, \nabla^4 \psi)}{\partial(x,y)} \right] = \mu \nabla^4 \psi \quad (2)$$

In the case of plane creeping flow, the equation (1) reduces to

$$\alpha_1 \left[ \frac{\partial(\psi, \nabla^4 \psi)}{\partial(x,y)} \right] = \mu \nabla^4 \psi \quad (3)$$

Now we seek the motion for which

$$\nabla^2 \psi = f(x) \quad (4)$$

On substituting this relation into equation (3), we find the following expression for the streamfunction:

$$\psi = \frac{-\mu}{\alpha_1} y(Ax + B) + C \left[ \frac{(Ax + B)}{(A+1)(2A+1)(3A+1)4A+1} \right] + \frac{A_0}{6} x^3 + \frac{B_0}{2} x^2 + C_0 x + D_0 \quad (5)$$

Here  $A, B, C, A_0, B_0, C_0, D_0$  are all constants. Next we consider the creeping flow for which

$$\nabla^4 \psi = g(x) \quad (6)$$

On substituting (6) into (3), we find that the streamfunction, in this case, takes the following form:

$$\psi = \frac{-\mu}{\alpha_1} [A_1 x^3 + B_1 x^2 + C_1 x + D_1] y + \iiint g(x) (dx)^4 \quad (7)$$

where

$$g(x) = K_1 \exp \left[ \frac{\log(x-x_1)}{3A_1 x_1^2 + 2B_1 x_1 + C_1} + \frac{\log(x-x_2)}{3A_1 x_2^2 + 2B_1 x_2 + C_1} + \frac{\log(x-x_3)}{3A_1 x_3^2 + 2B_1 x_3 + C_1} \right], \quad (8)$$

where

$x_1, x_2, x_3$  being roots of

$$A_1 x^3 + B_1 x^2 + C_1 x + D_1 = 0.$$

In a similar fashion, on assuming  $\nabla^2 \bar{\psi} = f(r)$  and  $\nabla^4 \bar{\psi} = g(r)$  we have obtained streamfunctions in plane polar coordinates.

#### REFERENCES

- [1] K. R. Rajagopal and A. S. Gupta, "On a class of exact solutions to the equations of motion of a second grade fluid," Int. J. Engng. Sci. 19, 1009-1014 (1981).
- [2] P. N. Kaloni and K. Huschilt, "Semi-inverse solutions of a non-Newtonian fluid." Int. J. Non-linear Mech. 19, 373-381 (1984).
- [3] A. M. Siddiqui and P.N. Kaloni, "Certain inverse solutions of a non-Newtonian fluid." Int. J. Non-linear Mech. 21 (459-473) (1986).

## SUSPENSION OF PARTICLES IN POWER-LAW FLUIDS

Ali J. Chamkha  
Department of Mechanical Engineering  
Tennessee Technological University  
Cookeville, Tennessee 38505

Equations for two-phase flow past a surface of a power law fluid/particle suspension with negligible particulate volume fraction are developed. Closed-form solutions are obtained for particulate suspension in pseudo-plastic and dilatant fluids past an infinite porous flat plate for low particle loading. Numerical computations of the exact solutions are performed and some of the results are presented graphically to illustrate interesting features of this type of flow. The fluid phase is assumed to be incompressible and exhibits uniform suction and the particle phase is assumed to be incompressible and pressureless. The solutions obtained generalize the solutions of Kapur [1] to two-phase flows and the solutions of Chamkha and Peddieson to non-Newtonian power-law fluids.

Some typical results are shown in Figures 1 through 6 below. In these figures  $F$  is the fluid-phase tangential velocity,  $F_p$  is the particle-phase tangential velocity,  $\eta$  is a dimensionless normal coordinate,  $r_v$  is the suction parameter,  $n$  is a behavior coefficient [which determines whether the fluid is Newtonian ( $n=1$ ) or non-Newtonian ( $n \neq 1$ )], and  $\alpha$  is the inverse-Stokes number.

Figures 1 through 4 show  $F$  and  $F_p$  for various values of  $n$ , respectively. It can be seen from these figures that increases in  $n$  tend to reduce the nonuniformities to an increasingly small region close to the wall. Figures 5 and 6 show the influence of  $\alpha$  on  $F_p$  for both pseudo-plastic ( $n < 1$ ) and dilatant ( $n > 1$ ) fluids, respectively.

### REFERENCES

- [1] Kapur, J.N., Journal of the Physical Society of Japan 18, 578 (1963).
- [2] Chamkha, A.J., and Peddieson, J., Developments in Theoretical and Applied Mechanics 14, 215 (1988).



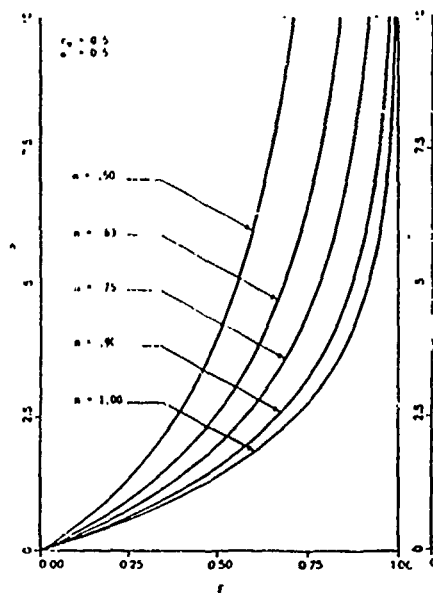


Figure 1. Fluid-Phase Tangential Velocity

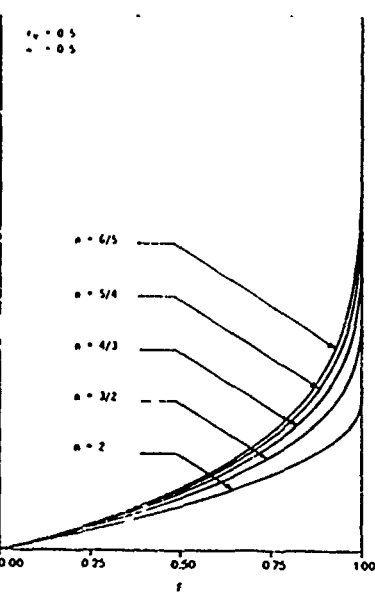


Figure 2. Fluid-Phase Tangential Velocity

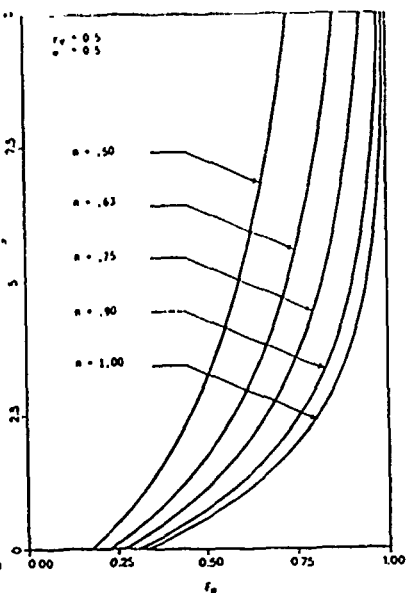


Figure 3. Particle-Phase Tangential Velocity

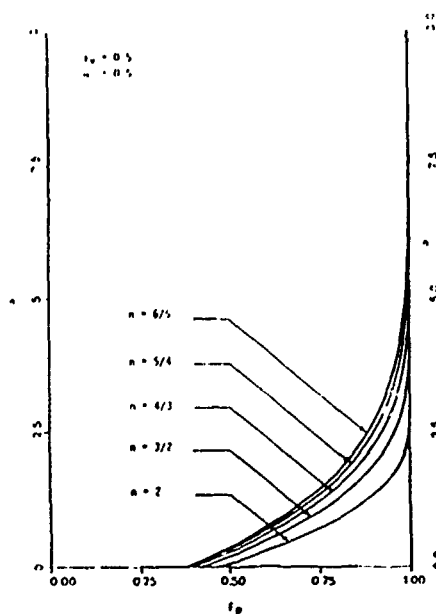


Figure 4. Particle-Phase Tangential Velocity

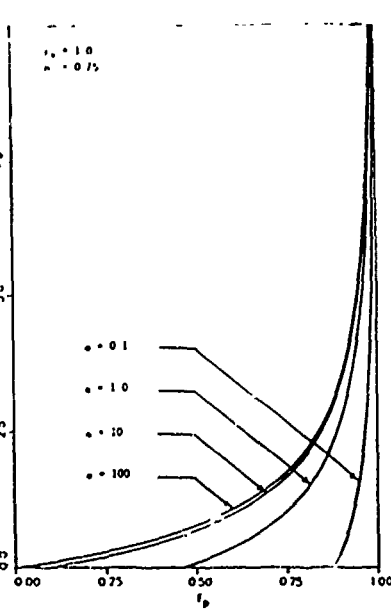


Figure 5. Particle-Phase Tangential Velocity

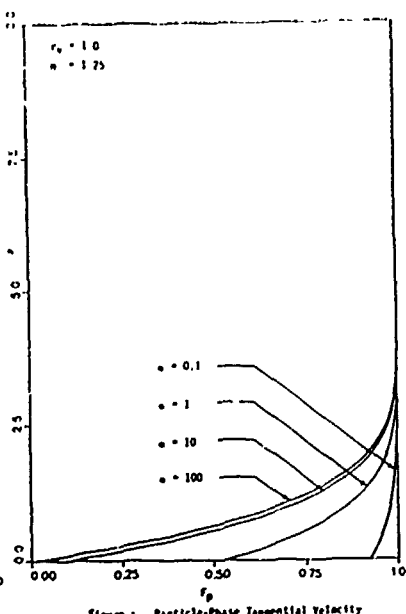


Figure 6. Particle-Phase Tangential Velocity

# UNSTEADY HYDROMAGNETIC FLOW OF A PARTICULATE SUSPENSION

Ali J. Chamkha  
Department of Mechanical Engineering  
Tennessee Technological University  
Cookeville, Tennessee 38505

This work is concerned with the unsteady laminar hydromagnetic flow of a particulate suspension over an infinite porous flat plate. The fluid phase is assumed to be incompressible and electrically conducting and the particle phase is assumed to be incompressible and electrically nonconducting. In addition, the magnetic field is assumed to be uniform, and the magnetic Reynolds number is assumed to be small so that the induced magnetic field can be neglected. Since no external electric field is applied, and the effect of polarization of ionized fluid is negligible, it is assumed that the electric field is negligible.

Let the plate occupy the half of the  $x, z$  plane corresponding to  $x > 0$  with the  $y$  axis being normal to the plate. Let  $\rho$ ,  $u$ ,  $v$ , and  $\nu$  denote the fluid-phase density, tangential velocity, normal velocity, and kinematic viscosity, respectively. Let  $\rho_p$ ,  $u_p$ , and  $v_p$  denote the particle-phase density, tangential velocity, and normal velocity, respectively. Let the free-stream velocity be denoted by  $V_\infty$ , the uniform suction velocity by  $v_0$ , the suspension momentum transfer coefficient by  $N$ , the electrical conductivity by  $\sigma$ , and the magnetic induction by  $B_0$ . Substituting the variables

$$t = \nu\tau/V_\infty^2, \quad y = \nu\eta/V_\infty \quad (1)$$

$$u = V_\infty F(\tau, \eta), \quad u_p = V_\infty F_p(\tau, \eta)$$

into the original dusty-gas equations (see, Marble [1]) modified to include a magnetic body force leads to

$$\partial_\tau F - \partial_\eta^2 F - r \partial_\eta F + \kappa \alpha (F - F_p) + M^2 (F - 1) = 0 \quad (2)$$

$$\partial_\tau F_p - r \partial_\eta F_p + \alpha (F_p - F) = 0 \quad (3)$$

where  $r = v_0/V_\infty$ ,  $M = \sqrt{\sigma/(\rho\nu)} B_0 \nu/V_\infty$ ,  $\kappa = \rho_p \omega/\rho$ , and  $\alpha = N\nu/V_\infty$ .

Equations (2) and (3) were solved by a standard implicit finite-difference method (see, Blottner[2]). The initial and boundary conditions employed were

$$F(0, \eta) = 1.0, F_p(0, \eta) = 1.0, F(\tau, 0) = 0$$

$$\lim_{\eta \rightarrow \infty} F(\tau, \eta) = 1.0, \lim_{\eta \rightarrow \infty} F_p(\tau, \eta) = 1.0 \quad (4)$$

For the subsequent presentation of numerical results it is convenient to define the displacement thickness coefficients of the fluid and particulate phases as

$$\Delta = \int_0^{\infty} (1 - F(\tau, \eta)) d\eta, \Delta_p = \int_0^{\infty} (1 - F_p(\tau, \eta)) d\eta, \quad (5)$$

respectively and the skin-friction coefficient of the fluid phase as

$$C = \partial_{\eta} F(\tau, 0) \quad (6)$$

Figures 1 through 3 present  $\Delta$ ,  $\Delta_p$ , and  $C$  versus  $\tau$ , respectively. It can be seen from these figures that increases in the Hartmann number  $M$  cause decreases in the values of  $\Delta$  and  $\Delta_p$  and increases in the values of  $C$ . The dotted lines in these figures correspond to the steady-state values. It should be mentioned that all the steady values are consistent with those reported by Chamkha [3].

#### REFERENCES

- [1] Marble, F.E., Annual Reviews of Fluid Mechanics 2, 397 (1970).
- [2] Blottner, F.G., AIAA Journal 8, 193 (1970).
- [3] Chamkha, A.J., Accepted for publication in AIAA Journal.

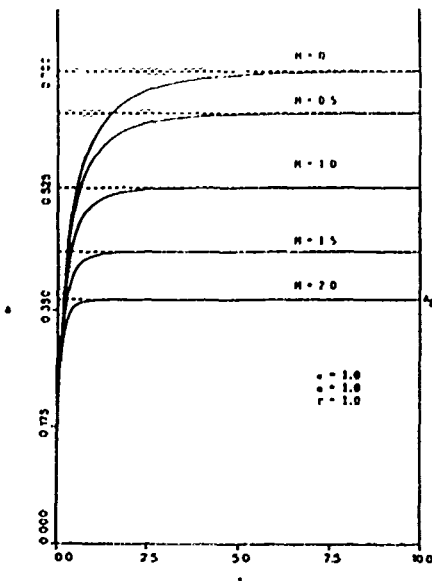


Figure 1. Fluid-Phase Displacement Thickness Versus Time

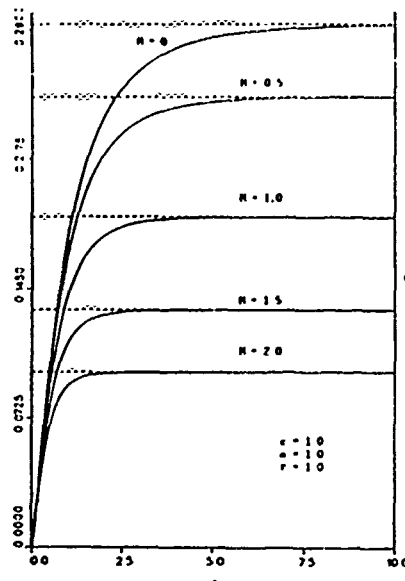


Figure 2. Particle-Phase Displacement Thickness Versus Time

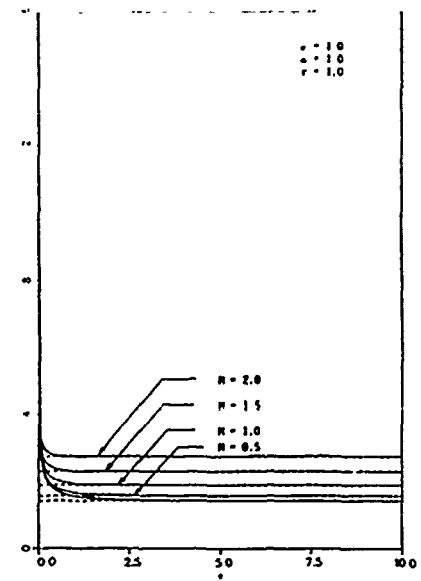


Figure 3. Fluid-Phase Skin Friction Coefficient Versus Time

# HYDRODYNAMIC STABILITY OF THE MELT DURING DIRECTIONAL SOLIDIFICATION OF A BINARY ALLOY

Daniel N. Riahi  
Department of Theoretical and Applied Mechanics  
216 Talbot Laboratory  
University of Illinois  
104 S. Wright Street  
Urbana, IL 61801

Recently Riahi (1988, henceforth referred to as RI) investigated the problem of small amplitude solutal convection in the melt during solidification of a binary alloy in the limit of small segregation coefficient  $k$  and large Peclet number  $z_\infty$ . Systems with  $k < 0.01$  have great practical interest since they become nearly pure substance upon solidification. The work reported in RI was based on a weakly nonlinear analysis of the type developed by Busse and Riahi (1980) and was valid only for sufficiently small amplitude  $\epsilon$  ( $\epsilon \ll 1$ ) of convection. From the previous work (Hurle et al., 1983), it is known that the horizontal wave number  $\alpha$  vanishes when  $k$  tends to zero and  $z_\infty$  tends to infinity. It was found appropriate here to introduce a perturbation parameter  $\gamma = k^{1/2}$ , and the solutions were determined by a perturbation technique expanding the dependent variables and the solute Rayleigh number  $R$  in terms of series in powers of  $\gamma$ . However since  $\alpha$  is small for small  $k$ , the nonlinearities in the governing equations are small, provided that  $\epsilon \ll k^{-1/2}$ . Hence, expansion of the dependent variables and  $R$  in terms of single series in powers of  $\gamma$  only will lead to solutions which are valid in the range above for  $\epsilon$ . With the analysis similar to that given in recent work (Hadjji et al., 1990) an evolution equation is derived here which described the temporal and spatial behavior of the horizontal structure of the convective flow.

We consider the problem of solutal convection in a layer of a binary alloy melt from which a semi infinite slab of crystal is being grown (Hurle et al., 1983). A coordinate system is considered which is moving with the solidification front at the vertical variable  $z = 0$ . We assume that  $k \ll 1$ ,  $z_\infty \gg 1$  and the crystal growth is promoted vertically downward (in the positive  $z$ -direction) so that the solidification process generates destabilizing density gradient. As in the works by Hurle et al. (1983) and in RI, solute gradient dominates over that of temperature so that we neglect the thermal contribution to the density gradient. The system of the non-dimensional forms of the boundary conditions and the two governing equations for poloidal component  $v$  of velocity vector (RI) and for the deviation  $c$  of solute concentration from basic static concentration contain the non-dimensional parameters  $z_\infty, R, k$  and the Schmidt number  $S$ .

Since  $\alpha \ll 1$  for  $k \ll 1$  near the onset of instability, the characteristic horizontal dimension of the convective flow is much greater than the thickness of the layer. Hence, we scale the horizontal gradient by  $\gamma$ . Further analysis shows that the scaling for  $R$  and expansion for  $v$  and  $c$  are  $R = R_0 + \gamma R_1$ ,  $v = v_0 + \gamma v_1 + \gamma^2 v_2$ ,  $c = c_0 + \gamma c_1 + \gamma^2 c_2$ , and that time  $t$  scales as  $t = \tau \gamma^2$ . The  $O(1)$  system for equations and boundary conditions yields solutions of the form  $v_0 = H_0(z)A(x, y, \tau)$ ,  $c_0 = G_0(z)A(x, y, \tau)$ . Here  $A$  is the amplitude function. The order  $\gamma$  system yields solutions  $v_1$  and  $c_1$ , and the corresponding solvability condition yields  $R_0 = 2$  in the limits of  $z_- \rightarrow \infty$  and  $S \rightarrow \infty$ . Vertical averaging of the order  $\gamma^2$  equation for  $c_2$  yields an evolution equation for  $A$ . To keep the presentation relatively simple we present here the results of a two-dimensional  $(x, z)$  analysis only, though extension to three dimension is straightforward. The differential equation for  $A$ , in the limit of  $z_- \gg 1$ , has a relatively simple approximated form and is nonlinear and fourth order in  $x$ .

The growth rate  $\sigma$  of modes with small amplitude is determined by considering the linear part of the equation for  $A$  which admits solutions of the form of  $\exp(\sigma\tau + i\alpha x)$ , where  $\sigma$  and  $\alpha$  satisfy a linear dispersion relation. Using this relation we find that instability sets in for  $R_1 > R_{1c}$  and  $\alpha = \alpha_c$ , where  $R_{1c}$  increases with  $z_-$  and  $\alpha_c$  decreases with increasing  $z_-$ .

In order to study the nonlinear effects on the stability of the solution, we investigate the regime slightly deviated from the critical one by considering the expansions in a small positive parameter  $\delta$ , where  $\delta$  measures the deviation from the critical state. Using these expansions in the equation for  $A$ , we obtain equations in orders  $\delta$  and  $\delta^2$  which are then solved analytically and the results are used in the equation in order  $\delta^3$ . The resonant term in the  $\delta^2$  equation for  $A$  is already removed using the corresponding solvability condition so that there is no secular term in the order  $\delta$  solution for  $A$ . Solvability condition for order  $\delta^3$  equation yields a Landau type equation for  $A$  with positive Landau constant. This equation has a steady solution for large time which is stable with respect to infinitesimal disturbances.

The fully nonlinear differential equation for  $A$  is also solved numerically in the limit of large  $z_-$  and for two dimensional  $(x, z)$  case. We consider simulation in the interval  $(-l, l)$  and impose horizontal periodic boundary conditions with smoothness conditions up to third derivatives. We chose  $l = 10\pi/\alpha_c$  so that interval  $(-l, l)$  contains about 10 characteristic length scales. An explicit scheme is used, where all space and time derivatives are approximated by forward difference formulas. We adopt  $\Delta x = .25$  and  $\Delta\tau = 10^{-7}$  so that a stability criterion derived based on the linear part of the equation for  $A$  is satisfied, and initial condition of the form  $A = .25 \sin(\alpha_c x/10)$  is used (Young and Davis, 1986). An integration forward in time is then performed until a steady behavior is reached. The steady solution is periodic in  $x$  whose period increases with  $z_-$ .

#### References

- Busse, F. H. and Riahi, N., *J. Fluid Mech.* **96**, 243-256 (1980).
- Hadji, L., Schell, M. and Riahi, D. N., *Phys. Rev. A* **41**, 863-873 (1990).
- Hurle, D.T.J., Jakeman, E. and Wheeler, A. A., *Phys. Fluids* **26**, 624-626 (1983).
- Riahi, D. N., *Phys. Fluids* **31**, 27-32 (1988).
- Young, G. W. and Davis, S. H., *Phys. Rev. B* **34**, 3388-3396 (1986).

## STABILITY OF A DEFORMED SOLIDIFYING INTERFACE IN A FLUID FLOW SYSTEM

Bijoy S. Mazumder  
Illinois State Water Survey  
Office of Hydraulics and River Mechanics  
2204 Griffith Drive  
Champaign, IL 61820

Daniel N. Riahi  
Department of Theoretical and Applied Mechanics  
216 Talbot Laboratory, University of Illinois  
Urbana-Champaign, IL 61801

The problems of the hydrodynamic stability of the melt during the solidification of a binary alloy in the linear and weakly nonlinear regimes and under the assumption of planar solidification front were investigated by Hurle et al. (1983) and Riahi (1988) respectively, in the limits of small segregation coefficient  $k$  and large Péclet number  $z_\alpha$ . Systems with  $k < 0.01$  have great practical interest since they become nearly pure substance upon solidification. The assumption of large  $z_\alpha$  is also reasonable in practice since it implies that the depth of the melt layer is large in comparison to the effective depth (ratio of solute diffusivity to crystal growth rate  $v_0$ ). However, the assumptions of planar solidifying interface made in above studies are not in accord with the experimental observations (Morris and Winegard, 1969; Jackson, 1971). The present work extends the studies of Hurle et al. (1983) and Riahi (1988) to the case of a deformed solidifying interface.

We consider the problem of solutal convection in a layer of a binary alloy melt from which a semi-infinite slab of crystal is being grown. In a frame of reference moving at the velocity  $v_0$ , the system of the non-dimensional forms of the boundary conditions and the governing equations contain the non-dimensional parameters  $z_\alpha$ ,  $k$ , the solute Rayleigh number  $R$ , the Schmidt number  $S$ , the morphological parameter  $M$  and the surface free energy parameter  $E$ . We obtain the solutions for flow velocity, solute concentration and deformed interface using a perturbation technique similar to that of Riahi (1988) and assuming that the amplitude  $\epsilon$  of convection is small. We seek solutions for dependent variables, deformed interface  $\eta$  and  $R$  in terms of a double series in powers of  $\gamma \equiv k^{1/2}$  and  $\epsilon$ . Our analysis shows that  $M\eta$  equals solute concentration at interface to the leading order terms. The critical horizontal wave

number  $\alpha_c$  is in the form  $d_c \gamma^{1/2}$ , where  $d_c$  depends on  $z_\alpha$ ,  $M$  and  $E$ . Systems of orders  $\epsilon$ ,  $\epsilon\gamma$ , and  $\epsilon\gamma^2$  were needed to obtain the linear results. Critical solute Rayleigh number  $R_c$  depends weakly on  $M$ ,  $z_\alpha$ ,  $E$  and  $k$ .  $R_c$  decreases with increasing  $S$ ,  $E$ ,  $k$ ,  $z_\alpha$  and  $1/M$ . Our present approach is applicable if  $M = 0$  ( $\gamma^2 E^{-2}$ ) or  $0 < M - 1 = o(\gamma)$ . Such later range for  $M$  leads to a particularly reasonable situation at small  $E$  when silicon or germanium with trace contaminants are processed (Young and Davis, 1986).  $d_c$  increases with  $M$ ,  $z_\alpha$ , and  $1/E$ . Systems of orders  $\epsilon^2$  and  $\epsilon^3$  were needed to obtain the nonlinear results. Various cellular solutions for corresponding to two-dimensional, rectangular, square and hexagonal structures are determined. Stability analysis of all the steady spatially periodic solutions indicates that cellular structures of the solidifying interface in the form of hexagons are generally preferred.

## REFERENCES

- Hurle, D.T.J., Jakeman, E. and Wheeler, A. A., Phys. Fluids 26, 624-626 (1983).  
 Jackson, K.A., In Solidification, edited by T. J. Hughel and G. F. Bolling, American Soc. for Metals (1971).  
 Morris, L.R. and Winegard, W.C., J. Inst. Met. 97, 220-222 (1969).  
 Riahi, D. N., Phys. Fluids 31, 27-32(1988).  
 Young, G. W. and Davis, S. H., Phys. Rev.B 34, 3388-3396 (1986).

# EFFECTS OF FLUID ON THE VIBRATION OF DEGRADING STRUCTURE

X.Z. Yu  
Division of vibration research  
Northern Jiaotong University  
Beijing, P.R. of China

J.H. Ding  
Dept of Civil Engr  
Hebei Agriculture Univ.  
Baoding, P.R. of China

D., Wang  
Dept of Civil Engr.  
University of Arizona  
Tucson, U. S. A.

## INTRODUCTION

The fault diagnoses of structure belong to the problem of physical and mechanical parameter identification from physical field and to inverse problem of integral or differential equation or solution problem of inverse problem from mathematical field. Generally, it is a part of ill-posed problem.

As the inverse problem of differential equation, that is, separating the Kernel of an integral equation, which contains unknown stiffness-variable  $k(z)$  produced by fault. This kind of equation may be ill-posed mathematics, which cannot searches out approximate solution with classical calculation. In order to satisfy the stability of solution, except the known restraint condition, the prior restraint condition is added.

To solved the 1st kind Fredholm's integral equation, the technique of least square is adopted. It makes the problem of calculus of variations equal to integral equation (1), so that to avoid directly solving integral equation, approximate solution of problem of calculus of variation is discussed. Moreover, the experimental study is made to basic model, in which some damage is given. The results indicated that the method of this paper may be used to practice.

## GOVERNING EQUATION AND ITS SOLUTION

The paper considered dynamic coupled system as shown in Fig.1, in which the water is regarded as ideal incompressible fluid.

Under the such condition, the fluctuating velocity-potential function satisfies the three-dimensional Laplace equation:

$$\nabla^2 \phi = \frac{\partial^2 \phi}{\partial x^2} + \frac{1}{x} \frac{\partial \phi}{\partial x} + \frac{1}{x^2} \frac{\partial^2 \phi}{\partial \theta^2} + \frac{\partial^2 \phi}{\partial z^2} = 0 \quad (1)$$

When neglecting the effects of surface waves, the boundary conditions of the fluid are Eq. (2):

$$\left. \frac{\partial \phi}{\partial z} \right|_{z=0} = 0, \quad \phi_{x=a} = 0, \quad \phi_x = 0, \quad \left. \frac{\partial \phi}{\partial r} \right|_{r=a} = \frac{\partial Y(z, t)}{\partial t} \cos \theta \quad (2)$$

and

$$Y(z, t) = y(z, t) + \delta(t)$$

where  $y$  is the relative displacement of structure,  $\delta(t)$  is input displacement of ground.

Under the mentioned above conditions, the additional mass of the fluid along the height of the cylinder is:

$$M(z) = \frac{4\rho a}{Yz} \sum_{s=1}^{\infty} \frac{K_1 \frac{(2s-1)\pi a}{2h}}{(2s-1) K_1 \frac{(2s-1)\pi a}{2h}} \cos \frac{(2s-1)\pi a}{2h} \int_0^h Y(z) \cos \frac{(2s-1)\pi a}{2h} dz \quad (3)$$

The bending vibration equation of cylinder-water coupled system and its restraint conditions are:

$$EI \frac{\partial^4 y(z, t)}{\partial z^4} + (m_1 + m(z)) \frac{\partial^2 y(z, t)}{\partial t^2} = -(m_1 + m(z)) \delta(t) \quad (4)$$

$$y_{x=0} = 0, \quad \left. \frac{\partial y}{\partial z} \right|_{z=0} = 0, \quad \left. \frac{\partial^2 y}{\partial z^2} \right|_{z=h} = 0, \quad \left. \frac{\partial^3 y}{\partial z^3} \right|_{z=h} = 0 \quad (5)$$

$$y(z, t)|_{t=0} = 0, \quad \left. \frac{\partial y(z, t)}{\partial t} \right|_{t=0} = 0 \quad (6)$$

where  $m_1$ ,  $EI(z)$  are the mass per unit length and flexural rigidity of the structure;  $m(z)$  is additional mass of fluid;  $\delta(t)$  is the given ground acceleration of the motion.



Because the cracks exist in structure, then

$$\begin{aligned} K(z) &= EI(z) = K_0 + k(z) \\ m_1(z) &= \text{const} \\ y(z, t) &= u_0(z, t) + v(z, t) \end{aligned} \quad (7)$$

where  $K_0$  and  $u_0(z, t)$  are stiffness and displacement of original structure;  $k(z)$  and  $v(z, t)$  are damage induced increment of the stiffness and displacement.

Substituted (7) into (4), (5), (6) and separated increment  $k(z)$  from differential equations. Two sets of system of equations were obtained. First one is the vibrating differential equation without damage, and belongs to positive problem.

The second system of equations is inverse problem. Through Fourier transform and complicated mathematical manipulation of equations, we obtain 1st kind Fredholm's equation as following:

$$\int_0^H k(z) \left( \frac{d^2 U_0(z, \omega)}{dz^2} \right) dz = -D(\omega) \int_0^H (m_1 + m(z)) U(z, \omega) dz + D(\omega) \int_0^H (m_1 + m(z)) U_0(z, \omega) dz \quad (8)$$

where

$$\begin{aligned} D(\omega) &= F[\delta(t)], & U_0(z, \omega) &= F[u_0(z, t)] \\ U(z, \omega) &= F[y(z, t)], & V(z, \omega) &= F[v(z, t)] \end{aligned}$$

Eq. (8) contains unknown function  $k(z)$ . To solve Fredholm's eq. (8), the method of Ritz-least square [1] was adopted. The precision and stability of solution are enhanced through choosing proper coordinate function.

#### THE NUMERICAL VALUE SIMULATION

First, assuming the exact form of the stiffness,  $U(z, \omega)$  (response spectrum of damage structure) is determined with identification of eq.(8); and then making use of the known additional condition  $U(z, \omega)$ , the stiffness is solved by inverse problem; and compared with assumed stiffness, that is the unknown coefficient  $A = (a_1, a_2, \dots, a_n)$  is searched; finally the variable function  $k(z)$  is obtained, i.e.  $k(z) = \sum a_i u_i(z)$ , where  $u_i(z)$  is the coordinate function satisfied Ritz conditions.

#### CONCLUSIONS

According to the results of analysis and experiment, we can obtain the conclusions as follows:

- 1) The inverse problem method of integral or differential equation may identify the small change of system, which is caused by fault.
- 2) For degrading structure, the frequency of system decreases with the increase of crack's number. When the numbers of crack are two, for cylinder the relative rate of 1st order frequency is 20%, if cracks are four, then becomes 32.2%.
- 3) When the structure has cracks, the modal change is not regular and the difference value takes place sudden changes nearby the cracks (fig. 2).
- 4) The effect of water on the frequency, the relatively variable quantity  $\Delta f$  of frequency increases with depth of water. When  $h=0.924H$ , without cracks structure, the  $\Delta f$  of 1st order frequency is 22.6%, but with two cracks on the structure, then becomes 26.96%, etc. (fig. 3). Therefore, the damage is greater when a reservoir is full than empty.

#### REFERENCE

- [1] Wang Deming, Liu Jiaqi, Huang Wenhui: A method for Inverse Problems of Partial Differential Equation being Applied to Fault Diagnosis of A Structure. Journal of vibration and Shock, No. 3, (1986)
- [2] Yu Xizhe, Ding Jihui: Fluid-Cantilever Structure- Elastic Foundation Interaction, Inter. Symposium on Earthquakes and Dams. Vol. 1, May, (1987), Beijing

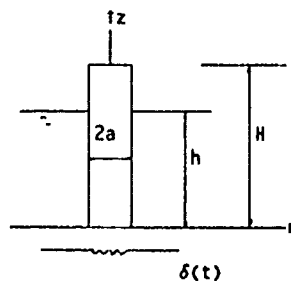


Fig.1 Model of System

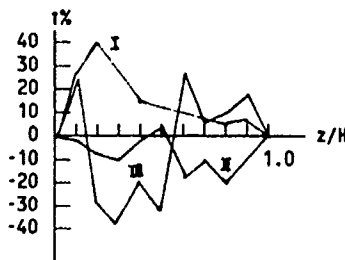


Fig.2 Relatively variable of model, when exist two crack

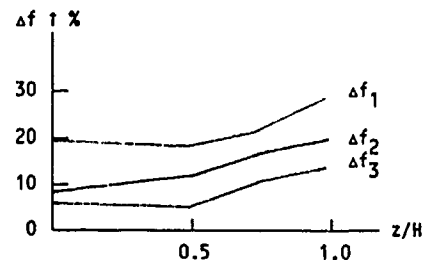


Fig.3 Relationship of  $\Delta f$  with  $z/H$ , when exist two cracks

# EFFECT OF SOME EXTERNAL FORCE FIELDS ON THE ORIENTATION OF A SLENDER ROD IN SIMPLE SHEAR FLOW

T.R.Ramamohan C.Chandra Shekara Bhat,  
S.K.Vijayalekshmi, and K.Rajalekshmy Ammal  
Regional Research Laboratory(CSIR),  
Trivandrum-695 019, INDIA.

The general theory of the effect of external force fields on axisymmetric bodies in homogeneous shear flows has been developed by Brenner(1974). Since his interest was for developing constitutive equations, he did not perform detailed calculations on the above problem. In this paper we present detailed calculations of the above problem. We focus our attention on the effects of two types of force field namely, a constant force field and a sinusoidally varying force field. These force fields could be induced on the slender rod either by imposing electric or magnetic fields or by unequally weighting the fibre and placing it in a uniform gravitational field. The results of this work may be of value in the technologically important problem of tailoring the properties of composites to specific requirements. The analysis is based on slender body theory, Batchelor(1970) as modified by Berry and Russel(1987) The basic equation used is

$$\dot{\mathbf{q}} = (3/2) \int_{-1}^1 \mathbf{s} (\mathbf{u}_0 - (\mathbf{u}_0 \cdot \mathbf{y}) \mathbf{y}) d\mathbf{s} + \mathbf{q} \times \mathbf{k} \times \mathbf{q}$$

In this equation  $\mathbf{q}$  is a unit vector directed along the length of the rod,  $\mathbf{s}$  is dimensionless length along the length of the rod,  $\mathbf{u}_0$  is the undisturbed flow field and  $\mathbf{k}$  is given by

$$\mathbf{k} = \int_{-1}^1 \mathbf{s} f(\mathbf{s}) d\mathbf{s}$$

Here  $f(\mathbf{s})$  is the force per unit length acting on the rod. In the case of a constant force field, it was found that the rod usually oriented itself in the direction of force field whenever the components of the force were in the plane of constant velocity. When the force field vector had a large component perpendicular to the direction of shear, equilibrium orientations were obtained. However the component in the direction of shear had to be fairly large for the rod to orient itself in the direction of the force field. In the case of a sinusoidal torque, periodic oscillations between two extreme values of orientation were obtained. The typical variation of the azimuthal angle  $\phi$  and the polar angle  $\theta$  are shown in Fig.(1) and Fig.(2).

The result for the constant force field can be understood from Jeffery's (1922) analysis of the above problem for force free rods. In the case of a sinusoidal force field, the rod appears to oscillate very rapidly between two equilibrium orientations. These results can also be understood in relation to Jeffery's (1922) analysis.

Fig. 1

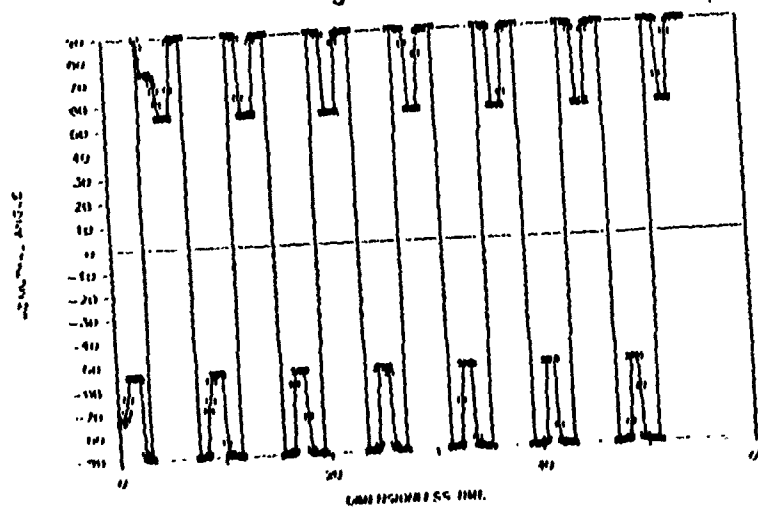
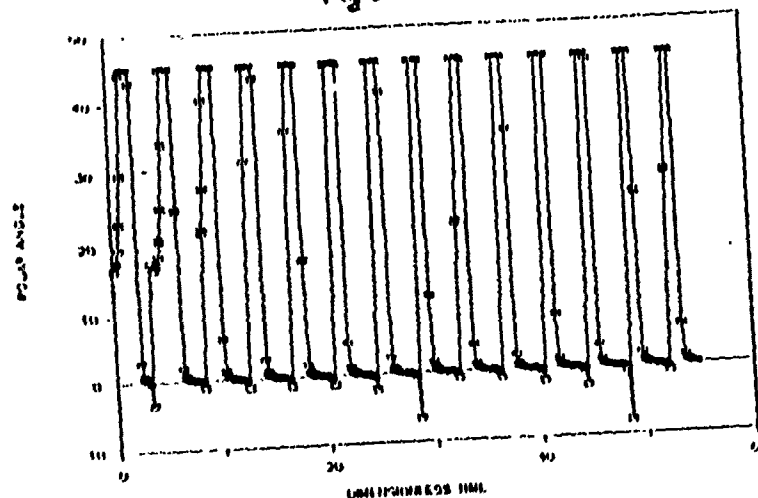


Fig. 2.



#### References:

- Batchelor, G.K., J. Fluid Mech., 44(3), 419(1970),  
 Berry, D.H., and Russel, W.B., J. Fluid Mech. 180  
 475(1987),  
 Brenner, H., Int. J. Multiphase Flow, 1 195(1974)  
 Jeffery, G.B., Proc. Roy. Soc., London(A) 102,  
 161(1922).

## FLOW-FORCE COMPENSATION IN A HYDRAULIC PISTON VALVE

by Dr. Jan Ługowski

Mailing address: ul. Kotuli 5/38, 35-111 Rzeszów, Poland

Almost forty years ago researchers from the Massachusetts Institute of Technology, Cambridge, Mass., explained the compensation of the axial flow force on a profiled piston /1/. They shaped the piston like a turbine bucket to obtain the negative, or compensating, flow force, according to the often cited equation:

$$F = \rho Qu(\cos \theta_1 - \cos \theta_2) \quad (1)$$

The theory is based on the assumption that the velocity of jet at vena contracta,  $u$ , diverts from angle  $\theta_1$  to  $\theta_2$  and remains constant along the piston profile.

There exists a simple and reliable way to verify this theory, namely by recording the static-pressure distribution on the piston. Disregarding friction forces, it is the static pressure that produces the flow force on the piston.

Figure 1 shows the recorded static pressure,  $p$ , on the piston of diameter 28 mm (1.1 in.). Eight measuring slots, each 0.05 mm (0.002 in.) high and 8 mm (0.3 in.) wide, were distributed spirally on the piston bevel. They covered the distance of 1.8 mm (0.07 in.) downstream the piston control edge. Each of the measuring slots was connected to a manometer. The dynamic pressure,  $p_d$ , was recorded 3 mm (0.12 in.) downstream the piston control edge. The valve outflow pressure,  $p_o$ , was equal to the atmospheric pressure.

The recordings of both static and dynamic pressures show that the velocity of jet sharply decreases downstream the vena contracta. Any diversion of a slow jet cannot result in the compensating flow force given in eqn. (1). The diversion should produce a positive static pressure acting on the piston downstream the vena contracta. Such a pressure does exist on the piston bevel, but upstream the vena contracta. It produces the opening flow force,  $F_o$ , given in Figure 1. The negative-pressure area downstream the vena contracta produces the closing flow force  $F_c$ . Both flow forces were computed from the recorded static-pressure distribution on the piston.

The static-pressure distribution shown in Figure 1 for inlet pressure  $p_i = 337$  kPa (48.9 psi), valve opening  $x = 0.23$  mm (0.009 in.) and rate of flow  $Q = 10$  L/min (10.17 in<sup>3</sup>/sec) was also similar at different parameters /2/.

It is the high static pressure acting on the piston bevel upstream the vena contracta that produces the opening flow force  $F_o$ . This force can be greater than, or overcompensate, the closing flow force  $F_c$ .

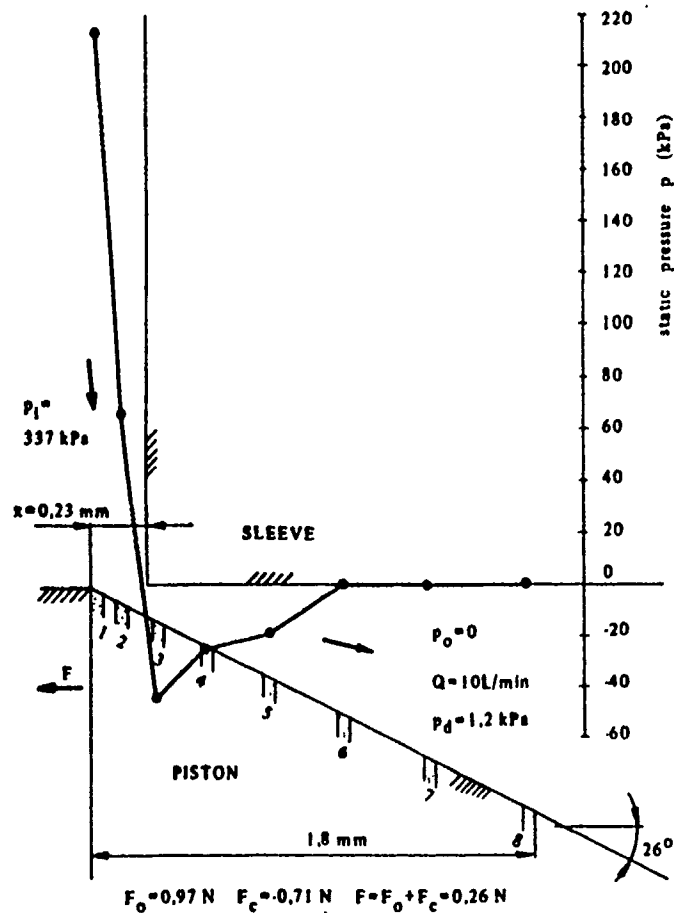


Fig. 1 Recorded static-pressure distribution on the piston

And, since the compensating flow force originates more upstream, there is no need to shape the piston like a turbine bucket.

#### References:

- /1/ S.-Y. Lee, J.F. Blackburn: "Contributions to Hydraulic Control - 1 - Steady-State Axial Forces on Control-Valve Pistons", Transactions of the ASME, Vol. 74, August 1952, pp. 1005-1011.
- /2/ J. Ługowski: "Flow-Force Compensation in a Hydraulic Piston Valve", manuscript sent in January 1991 for publication in the Transactions of the ASME, Journal of Fluids Engineering (Log Number 3111-FTD).

## On Local Stress Field

Dr. Albert B. Ku, Professor of Engineering Mechanics  
College of Engineering and Science  
University of Detroit Mercy  
4001 W McNichols Road  
Detroit, Michigan 48221

In reference [1], a local stress correction procedure which utilized a displacement field  $\{du\}$  was presented. This continuous displacement field  $\{du\}$  was required to vanish at all the nodal degrees of freedom of the finite element. Since for a linear problem, it is always possible to express

$$\{du\} = p\{q\} \quad (1)$$

where  $p$  is a parameter related to the distributed loading. The near stress field correction was found in [1] to be

$$\{d\sigma\} = p[E]\{\mathcal{L}\}\{q\} \quad (2)$$

where  $\{\mathcal{L}\}$  is a differential operator which relates stresses to displacements. Since the stress correction satisfies the local equilibrium, the corrected total stress field satisfies Saint venant's principle on near stress field distribution. Consider a finite element of  $n$  degrees of freedom. Let the local displacement field  $\{q_p\}$  of the element be obtained by satisfying the local equilibrium. The displacement field  $\{q\}$  of Eq.(1) may then, be obtained as follows:

$$\{q\} = \{q_p\} + \sum \alpha_i N_i \quad (3)$$

where  $N_i$  is the shape function of degree of freedom  $i$  of the finite element. By requiring  $\{q\}$  to vanish at all the degrees of freedom of the finite element, the coefficients  $\alpha_i$ ,  $i=1,2,\dots,n$  are determined. Equation (2) may now, be used to calculate the local stress correction. For structures consisted of truss and beam elements, the above procedure yields exact stress correction as expected. The accuracy of stress correction for other elements depends on the shape functions used in the general formulation. As an example, consider a triangular membrane element under the distributed loading  $p \vec{e}_x$  in the plane of the membrane. It can be shown that Eq.(3) is given by

$$\{q\} = \frac{p}{2E} (q_1 - q_2)$$

$$\{q_1\} = \begin{Bmatrix} x^2 \\ -2\sqrt{3}xy \end{Bmatrix}$$

$$\{q_2\} = \begin{Bmatrix} x_1^2 & x_2^2 & x_3^2 \\ -2\sqrt{3}x_1y_1 & -2\sqrt{3}x_2y_2 & -2\sqrt{3}x_3y_3 \end{Bmatrix} \begin{Bmatrix} N_1 \\ N_2 \\ N_3 \end{Bmatrix}$$

Using Eq.(2), the stress correction due to the distributed loading becomes

$$\{\Delta \sigma\} = \frac{P}{2E(1-\nu^2)} \begin{bmatrix} 1 & \nu & 0 \\ \nu & 1 & 0 \\ 0 & 0 & \frac{(1-\nu)}{2} \end{bmatrix} \begin{Bmatrix} f_1 \\ f_2 \\ f_3 \end{Bmatrix}$$

where the f components are given by

$$\begin{aligned} f_1 &= 2x - \sum x_1^2 N_{1,x} \\ f_2 &= -2(x - \sum x_1 y_1 N_{1,y}) \\ f_3 &= -2\nu y + \sum x_1(x_1 N_{1,y} - 2\nu y_1 N_{1,x}) \end{aligned}$$

Should a more complex loading  $p_x(x,y) \vec{e}_x + p_y(x,y) \vec{e}_y$  be applied, then, the stress correction given by

$$\{\Delta \sigma\} = \begin{Bmatrix} S_1 \\ S_2 \\ S_3 \end{Bmatrix}$$

are the solutions of the following differential equations:

$$\nabla^4 S_1 = -\frac{\partial}{\partial x} \left( \frac{\partial^2}{\partial x^2} + \frac{2-\nu}{1-\nu} \frac{\partial^2}{\partial y^2} \right) P_x + \frac{\partial}{\partial y} \left( \frac{\partial^2}{\partial x^2} + \frac{2-\nu}{1-\nu} \frac{\partial^2}{\partial y^2} \right) P_y$$

$$\nabla^4 S_2 = \frac{\partial}{\partial x} \left( \frac{2-\nu}{1-\nu} \frac{\partial^2}{\partial x^2} + \frac{\partial^2}{\partial y^2} \right) P_x - \frac{\partial}{\partial y} \left( \frac{2-\nu}{1-\nu} \frac{\partial^2}{\partial x^2} + \frac{\partial^2}{\partial y^2} \right) P_y$$

$$\nabla^2 S_3 = - \left( \frac{\partial P_x}{\partial y} + \frac{\partial P_y}{\partial x} \right) - \frac{\partial^2}{\partial x \partial y} (S_1 + S_2)$$

The above procedure is applicable generally to two as well as three dimensional problems. It is to be noted that the construction of  $\{q_p\}$  presents no problem, since no associated stress boundary conditions are required. While the required conditions at the nodal degrees of freedom are easily satisfied because of the special form of Eq.(3).

#### References:

1. Albert B. Ku, On Nodal Point Loading, Proc. of the 21st Midwestern Mechanics Conference, edited by Ligon etc, (1989)
2. Albert B. Ku, Finite Element Structural Analysis, Lecture Notes to be published.

# OPTIMAL LINEAR MULTISTEP, ASYMPTOTICALLY ANNIHILATING ALGORITHMS FOR STRUCTURAL DYNAMICS

G. M. Hulbert and J. Chung

Department of Mechanical Engineering and Applied Mechanics  
The University of Michigan  
321 W. E. Lay Automotive Laboratory  
Ann Arbor, Michigan 48109-2121

When solving the equations of structural dynamics using direct time integration methods, algorithmic damping is useful to control spurious high-frequency oscillations. Ideally, an algorithm should possess asymptotic annihilation of the high-frequency response, i.e., spurious oscillations are eliminated after one time step. In a recent paper<sup>1</sup>, the first author proved that Houbolt's algorithm is the only three-step linear multistep (LMS) algorithm that achieves asymptotic annihilation. However, its asymptotic annihilation is achieved at the expense of introducing too much dissipation in the important low frequency regime; to obtain the same accuracy as other commonly used time integration algorithms, Houbolt's method requires using a smaller time step.

Four-step and five-step LMS algorithms are presented that attain asymptotic annihilation. These algorithms are optimal in the sense that their low frequency dissipation is minimized. In addition, they are unconditionally stable and second-order accurate for linear problems. One disadvantage of algorithms cast only in LMS form is that additional equations are needed to start such algorithms. The new asymptotic annihilation algorithms are cast in one-step, multivalued form and thus need no special starting conditions. Numerical results are presented that highlight the spectral behavior and the low frequency dissipation and dispersion of the new methods.

---

<sup>1</sup> "Limitations on linear multistep methods for structural dynamics," *Earthquake Engineering and Structural Dynamics*, **20**, pp. 191-196 (1991).



# Strain Rate Effects in the Dynamic Analysis of Steel Frames

Norbert Gebbeken, Teaching and Research Associate  
Heinrich Rothert, Head of Institute

*Institut für Statik (Inst. of Structural Analysis), Universität Hannover, Appelstr. 9A, D-3000 Hannover 1*

## 1 Introduction

The economical (as far as the effort of discretization, CPU time and evaluation of the results are concerned) and dynamical inelastic calculation of entire steel-frames is only feasible on the basis of the yield hinge theory, which is applied here and of which a detailed description concerning static forces is given for example in [3]. Based on the methods of computational mechanics, this paper deals mainly with a proper method of physical modeling for the dynamic inelastic analysis of steel frame structures taking into account strain rate effects. The rod theory applied here is an extended geometrical non-linear theory of the second order ([1]). On principle arbitrary rod theories can take as a basis for the procedure which will be described as follows.

## 2 Rate dependent inelastic FE-modeling

Manjoine [4] carried out uniaxial tension tests at unalloyed and untreated steel. The strain rates varied from  $\dot{\epsilon} = 10^{-6} \text{ s}^{-1}$  to  $\dot{\epsilon} = 10^3 \text{ s}^{-1}$ . The Young's modulus  $E$  was found to be independent of the strain rates. The yield stress and failure stress rise monotonously with increasing strain rates. For economical and safety reasons it makes sense to take into account the rate dependency of the material behaviour. Cowper and Symonds [2] developed a formula for the relation between the dynamic yield stress  $\gamma\sigma$ , the quasi-static yield stress  $\gamma_s\sigma$  and the strain rate  $\dot{\epsilon}$ .

Here the yield condition according to Huber, v. Mises and Hencky is applied in which the strain rate is an additional parameter. For the yield hinge theory the interaction relations in the space of internal forces have to be determined. With the help of Cowpers and Symonds' material law the rate dependent interaction relations can be derived as explained in [1]. Applying rate dependent interaction relations the strain rate  $\dot{\epsilon}$  and the curvature rate  $\dot{\kappa}$  in the examined cross section have to be computed. However, the exact analysis in plasticized cross sections is not possible by using a yield hinge model because the reference length equals zero. Thus it is indispensable to find a proper solution for this problem. Therefore the plastic strains are calculated with the lengths of the plastic zones which were found by "mesh adaptation". The influence of the length of the plastic zones on the strain rates can be shown by comparative calculations. The relevant results differ only up to 8 %.

A realistic representation of plasticized cross sections on the basis of the yield hinge theory is of essential importance for the correct description of the plastic load-carrying behaviour. Yield hinge models are not only used for the computation of plastic deformations and the energy dissipation in the yield hinges, but also to establish criteria that indicate the situation when a yield hinge is unloaded making that cross section once again elastic. For the yield hinge model it is assumed that all hypotheses of the theory of plasticity which are valid for the stress-strain-space are also applicable for the internal force-deformation-space. Thus, a theoretically consistent formulation is obtained. The plastic deformations of plasticized cross sections are determined using Drucker's postulate of material stability and an associated flow rule ([1]). The equation of motion is solved applying the Newmark procedure.

### 3 Numerical results

With the above described method various rod structures have been examined which were exposed to earthquake and impact loads. The comparative calculations in this paper are based on the saddle roof frame (all members IPE360, St37) illustrated in Fig. 1 which is subjected to a fork-lift impact as shown in Fig. 1. The material law is linear elastic-visco plastic and linear elastic-rigid plastic.

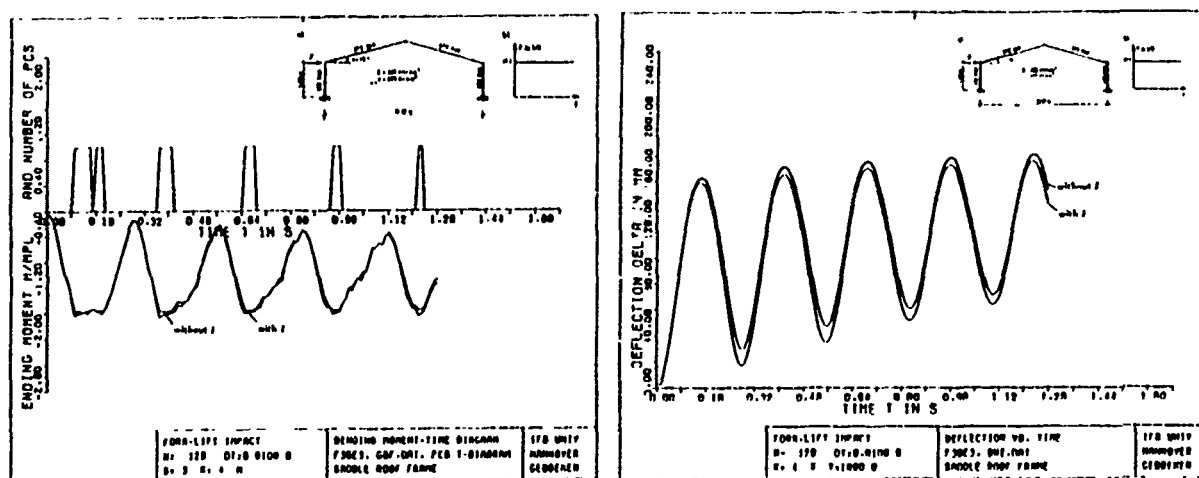


Fig. 1 Bending moment vs. time and displacement vs. time diagram with respect to the horizontal displacement of the left frame edge

On the basis of a first FE-model a mesh adaptation has been carried out until the lengths of the plastic zones were found. The time increment  $\Delta t$  was taken as 1 ms. The bending moment vs. time diagram is given in Fig. 1a. It provides also some information about the number of plasticized cross sections (pcs) and their time dependent distribution. The location of the plastic hinges turned out to be in the top of the columns. Fig. 1b shows the displacement vs. time diagrams with respect to the horizontal displacement of the left frame edge. The static limit load was 118.7kN.

### 4 Conclusions

Every realistic simulation of the reality by means of models in the range of computational mechanics requires assumptions and hypotheses which have to be checked. When using the very clearly-structured yield hinge theory, the physical modeling of plasticized cross sections presents the most important problem, especially if strain rate dependent material laws are to be taken into account. Therefore a mixed plastic zone -, plastic hinge theory with respect to the cross sections has to be applied.

### 5 References

- [1] Brandt, V.; Gebbeken, N.; Rothert, H.: Dynamic inelastic analysis of plane steel structures taking into account the effect of rate dependent behaviour. European Conference on Structural Dynamics (EURODYN '90), in Eds W.-B. Krätzig et al. Structural Dynamics, Rotterdam, Brookfield: A.A. Balkema (1991) 1023-1029
- [2] Cowper, G.R.; Symonds, P.S.: Strain hardening and strain rate effects in the impact loading of cantilever beams. Tech. rep. 28, Brown Univ., Prov., 1957
- [3] Gebbeken, N.: Eine Fließgelenktheorie höherer Ordnung für räumliche Stabtragwerke. Stahlbau 57, H.12 (1988) 365-372
- [4] Manjoine, M.J.: Influence of rate of strain and temperature on yield stress of mild steel. Journal of Applied Mechanics 11 (1944) A211-A218

## THE DEFORMATION OF O-RINGS COMPRESSED BETWEEN FLAT RIGID PLATES\*

J. A. Weese, Dept. of Eng. Tech., Texas A & M University, College Station, TX 77843  
W. E. Warren, Org. 1813, Sandia National Laboratories, Albuquerque, NM 87185

Toroidal shaped o-rings are used extensively as environmental or pressure seals to prevent leakage of gas and moisture. O-rings are generally molded from relatively soft incompressible elastomeric materials and in application are compressed between relatively rigid flat plates. Effective sealing depends upon the contact pressure between o-ring and plate, and some interesting and significant effects of compression ratio, roughness, and surface flaws on this contact pressure have been determined through two-dimensional plane strain analysis. There are, however, three-dimensional effects related to sealing of o-rings which are not revealed through a two-dimensional analysis. For example, transverse compression of the o-ring changes its toroidal radius. Material incompressibility then induces a change in cross-sectional radius which may relax contact pressure and threaten the integrity of the seal.

In this work we provide a theoretical analysis of the three-dimensional effects of symmetrically compressing an o-ring between flat rigid plates. We assume the o-ring to be an incompressible elastic material and the problem is formulated within the framework of classical linear elasticity theory. We make use of our previous analysis in which we obtain asymptotic approximations for the general axisymmetric solutions to the field equations of elasticity in terms of Boussinesq-Papkovich potentials defined in the orthogonal toroidal coordinate system. These asymptotic approximations provide solutions to the stress and displacement boundary value problems on the solid torus for a range of geometries typical of o-ring applications where  $(a/R) \ll 1$  (see Fig. 1b).

The o-ring problem under consideration here represents a mixed boundary value problem in which the displacements due to the rigid flat plates are prescribed on a portion of the toroidal surface while the remaining portion of the surface is stress free. To formulate this problem, we first make use of the asymptotic potentials to obtain the singular solution to the problem of a circular line force on the o-ring surface of magnitude  $p$  per unit length in the  $z$ -direction and of magnitude  $q$  per unit length in the  $r$ -direction as shown in Fig.1. These singular solutions then provide the kernels for

\* Partial support from the US Dept. of Energy under contract #DE-AC04-76DP00789

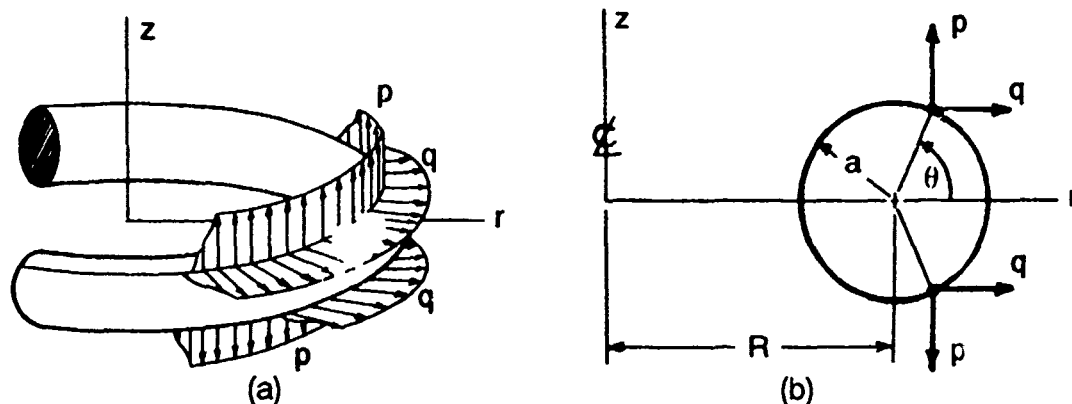


Figure 1. Torus with circular line load at angle  $\theta$  : (a) schematic, and (b) in section.

a distribution of tractions over the portion of the o-ring surface which is in contact with the rigid compressing plates. Integration of these kernels over the region of plate contact provides expressions for the boundary displacements as a function of the traction distribution functions  $p(\theta)$  and  $q(\theta)$ . This formulation insures that the o-ring surface not in contact with the compressing plates is stress free. Invoking the displacement boundary conditions in the region of plate contact leads to singular integral equations of Hilbert type to evaluate the distribution functions  $p(\theta)$  and  $q(\theta)$ .

The distribution functions have been evaluated for two limiting compression boundary conditions, the first representing no slip between o-ring surface and plate, the second representing no friction. The o-ring surface deformations for these two cases are shown in Fig. 2 for a 4% compression and the difference between the two

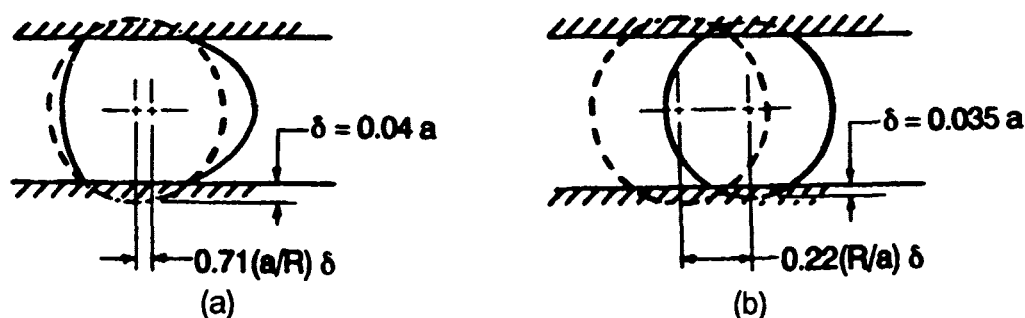


Figure 2. O-ring deformation at 4% compression for (a) no slip, and (b) no friction. Solid line is deformed and dashed line undeformed position.

is significant. Compression of the o-ring enlarges the toroidal radius  $R$  and for the case of no slip, this change in  $R$  is small of order  $(a/R)$ . For the case of no friction, the change in  $R$  is large of order  $(R/a)$ . For ease of installation, o-rings are typically lubricated during assembly and this lubrication provides an essentially frictionless contact. In this situation, the large increase in  $R$  reduces the cross-sectional radius  $a$  and the compression is reduced from an initial 4% to an effective 3.5% as shown. The resulting reduction in contact pressure may pose a threat to the integrity of the seal.

# USE OF REACTION FORCES TO DETERMINE THE IMPACT LOADING FUNCTION ON AIRCRAFT GAS TURBINE CONTAINMENT RINGS

Tim Dewhurst, Mechanical Engineering Department  
University of Maine, Orono, Maine 04469

The purpose of this study is to use the finite element method to determine the time dependent loading function exerted on the containment ring during a multiple blade shed in aircraft gas turbine engines. The ability to determine this loading function and thus to model the containment ring performance is a key step in analyzing various designs without resorting to cost-prohibitive experimentation.

Noncontained fragments from commercial aircraft gas turbine rotor failures occur at a rate of 0.7 failures per million engine hours according to the Naval Air Propulsion Center [1987]. While only 45% of these failures are due to escaped turbine blades, most engineering effort is invested in containing failed blades instead of burst disks or seals. Turbine blades fail at a rate of 10 times that of disks and can be contained with simple devices. Disk failures, which occur much more seldomly, are very difficult to contain without incurring excess weight penalties. The engineering effort there is expended on preventing, as opposed to containing, burst disks.

Containment rings typically surround the rotor just above the blades and are designed to prevent perforation by absorbing the kinetic energy of the blade fragments in the strain energy of the ring. This requires extensive plastic deformation of the ring. Unfortunately, observation of many failed rings indicates that little, if any, plastic deformation occurs resulting in minimal energy absorption.

In this study, experimental results from a failed containment ring are used as input data to the ANSYS finite element program. The finite element mesh used, shown in Figure 1, consists of 216 8-noded isoparametric shell elements. The data input to the program consists of a series of time dependent displacements imposed on the ring. The experimental results show the ring bulges. In time this bulge grows in amplitude and also travels around the ring in the same direction as the rotor, at a rate of approximately 1/3 of the rotor speed. The time dependent peak amplitude and position is imposed upon the ring and a transient dynamic solution procedure is followed.

The governing equation for the transient dynamic solution is

$$M \ddot{\underline{u}} + C \dot{\underline{u}} + K \underline{u} = \underline{F} \quad (1)$$

Initially a linear solution procedure has been followed where static material properties and a lumped mass matrix have been used with a 2% damping ratio.

The solution to Equation (1) is carried out where the displacement vector  $\underline{u}$  is specified at various nodal points above the rotational plane of the blades. At the positions where the displacements are applied, the reaction forces are determined. The time dependent magnitude and position of these reaction forces is indicative of the loading function exerted by the failed blades on the containment ring.

While it is inappropriate to use static material properties to model such a high strain rate event, and even though a linear solution with no plasticity is used, the initial phase of this work is to establish the solution procedure. Once the loading function for these conditions is obtained and the validity of this approach is established, then increased complexity will be introduced into the problem by including rate dependent material properties and an elastic-plastic constitutive law.

Typical results of the reaction forces as a function of time are plotted in Figure 2. A comparison of the kinetic energy of the blades at failure and the impulse (reaction force x time) on the ring indicate that the obtained reaction forces are somewhat high.

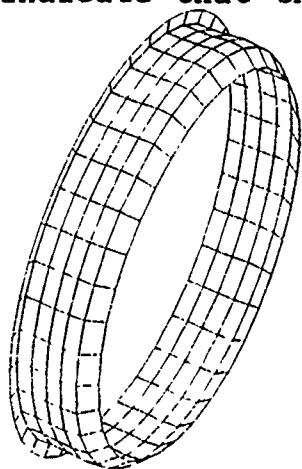


Figure 1. Finite Element Mesh  
8-noded Isoparametric Elements

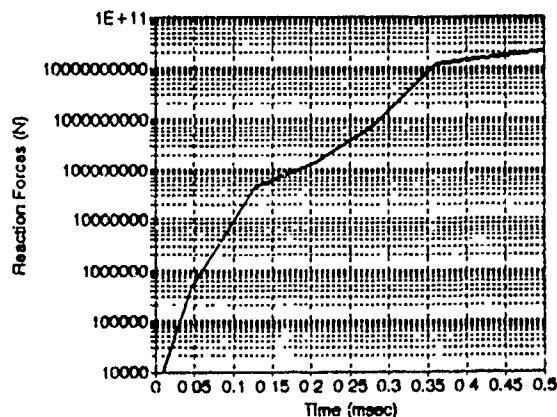


Figure 2. The Reaction Forces  
Due To Imposed Displacements

"Ansys - Engineering Analysis System," Swanson Analysis, Inc.  
Houston, PA, May 1989.

Napc, "Statistics on Aircraft Gas Turbine Engine Power Failures  
That Occurred in U.S. Commercial Aviation During 1981," DOT/FAA/  
CT-86/42, March 1987.

# SINGLE CUSP, DOUBLE CUSP, AND BUTTERFLY CATASTROPHES IN A COMPRESSIBLE ELASTIC ROD

A. Guran

Department of Mechanical Engineering, University of Toronto,  
Toronto, Ontario, M5S 1A4 Canada

The problem of elastic stability of a compressible rod has been treated in [1], [2], and [3]. In [1] using a three-hinged two degree of freedom structure (see Figure 1), Poston and Stewart classify the singularity of the equilibrium surface for this system as a butterfly catastrophe. In [2] the global stability analysis of the same model is studied. In [3] the effects of imperfections on the same model is studied, and the finite element analysis of the compressible, continuous elastic beam is treated.

In the present paper a refined version of the aforementioned model is presented. Rather than assuming that the torsional stiffness of the spring at mid-span of the structure to be a constant (as in [1,2,3]), we assume that it depends on the previous state of the compressed rod. The singularity of the equilibrium paths of the system will be classified according to pre-buckling state of the rod. To that end the potential energy of the system is expressed as follows

$$V = K_A x^2 + 2\phi^2 K_\phi(x_A) + 2P(l-x)\cos\phi. \quad (1)$$

The equilibrium states of the rod correspond to the stationary values of the potential energy, hence

$$\begin{aligned} K_A x - P \cos \phi &= 0 \\ 2\phi K_\phi(x_A) - P(l-x)\sin \phi &= 0 \end{aligned} \quad (2)$$

Denoting the Hessian Matrix by  $H$ , for critical state in addition to (2) one should have

$$\det H = \begin{vmatrix} K_A & P \sin \phi \\ P \sin \phi & 2K_\phi(x_A) - P(l-x_A)\cos \phi \end{vmatrix} = 0$$

The condition of singularity at  $\phi = 0$ ,  $x_A = \frac{P}{K_A}$  (trivial state) becomes

$$K_\phi(x_A) = \frac{K_A}{2} x_A (l - x_A) \quad (3)$$

Eliminating  $x$  from Equations (2), the equilibrium paths are determined by a single equation, viz.

$$g(\phi, p, \frac{x_A}{l}) = \frac{x_A}{l} (1 - \frac{x_A}{l}) - p(1 - p \cos \phi) \sin \phi \quad (4)$$

where  $p = \frac{P}{K_A l}$ . The 6-jet of  $g(\phi, p, \frac{x_A}{l})$  can be expressed as

$$j^6 g = (-\frac{x_A^2}{l^2} + \frac{x_A}{l} + p^2 - p)\phi - \frac{4p^2 - p}{6} \phi^3 + \frac{16p^2 - p}{120} \phi^5 \quad (5)$$

Examining the coefficient of  $\phi$ , in (5) bifurcation occurs only if

$$p^2 - p - \frac{x_A^2}{l^2} + \frac{x_A}{l} = 0 \quad (6)$$

Thus for  $\frac{x_A}{l} < \frac{1}{2}$  there are two distinct bifurcations, but for  $\frac{x_A}{l} > \frac{1}{2}$  none.

An examination of the coefficient of  $\phi^3$  reveals that for  $\frac{x_A}{l} = \frac{1}{4}$ , the coefficients of  $\phi$  and  $\phi^3$  in 6-jet of  $g$  vanish simultaneously, and we catch a butterfly. The following table summarizes the results of the stability analysis presented in this paper

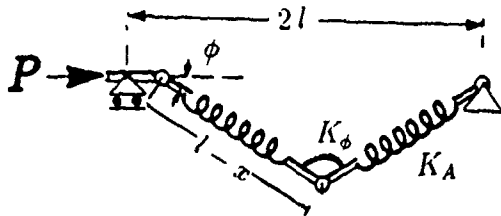


Figure 1 The model

Interval	Type of singularity
$\frac{x_A}{l} \in (0, \frac{1}{4})$	Cusp catastrophe
$\frac{x_A}{l} = \frac{1}{4}$	Butterfly catastrophe
$\frac{x_A}{l} \in (\frac{1}{4}, \frac{1}{2})$	Dual cusp catastrophe
$\frac{x_A}{l} = \frac{1}{2}$	Trifurcation
$\frac{x_A}{l} \in (\frac{1}{2}, 1]$	None

## References

1. T. Poston, I.N. Stewart, *Catastrophe Theory and its Applications*, Pitman, London, 1978.
2. Z. Gáspár, G. Domokos, "Global Description of a Simple Mechanical Model". *Pro Stab. Steel Struct.*, Editor: M. Iványi, Vol. 1, pp. 69-76, Budapest, 1990.
3. A. Guran, A. Shirazi-Adl, "Some Remarks Concerning the Post-buckling Behaviour of a Compressible Column", *Impact and Buckling of Structures*, Editors: D. Hui, and I. Elishakoff, Vol. AD-20, pp.93-100, 1990.



# An Improved Mixed Approach of Finite Element Method for Three-Dimensional Elastic Contact Problems with Friction

Ou Hengan, Li Runfang, Gong Jiansia

No. 1 Dept. of Mechanical Engineering, Chongqing University,  
Chongqing, P.R. of China, 630044

## 1. Introduction

Finite element method of contact problems can be classified into four categories: stiffness method[1], flexibility method[2], mathematical programming method[3] and gap element method[4]. Since the iterations are condensed to the contact region by the flexibility method, it is of high efficiency. However, much time is wasted when establishing the flexibility matrix of the contact region. This paper presents an improved mixed approach of finite element method for three dimensional elastic contact problems with friction and an example is also presented. In this procedure, the flexibility matrix of contact region is calculated by means of a modified Cholesky elimination algorithm. In the process of solving contact problems, as the elimination of stiffness matrix and the calculation of flexibility matrix of contact region can be conducted simultaneously, the computational efficiency of this approach is much higher than that of general flexibility method.

## 11. Algorithm

In this approach, the displacement compatibility condition, force equilibrium condition and Coulomb's law of friction on the normal and tangential directions are satisfied along the contact surface. As the boundary conditions on contact surface can be formulated into coefficient matrices, the matrix equation of two contact bodies is as follow:

$$\begin{bmatrix} K_x & K_{xc} & 0 & 0 \\ K_{xc}^T & K_x^c & D_1 & 0 \\ 0 & K_{xc} & K_x^c & 0 \\ 0 & 0 & K_{xc}^T & K_x^c \end{bmatrix} \begin{bmatrix} u_x \\ u_x^c \\ u_x^c \\ u_x^c \end{bmatrix} = \begin{bmatrix} P_x \\ P_x^c \\ P_x^c \\ P_x^c \end{bmatrix} \quad (2-1)$$

where  $K$ ,  $u$ ,  $P$ ,  $R_x$  denote stiffness matrices, displacement vectors, loading vectors and contact force vectors respectively, the subscripts 1, 11 denote the number of contact body respectively, the subscript c denotes the contact region,  $C_1$ ,  $C_2$  denote the coefficient matrices including the displacement compatibility condition on the contact surface,  $D_1$ ,  $D_2$ ,  $D_3$  denote the coefficient matrices including the force equilibrium condition and Coulomb's law of friction on the contact surface,  $\delta_0$  is the initial gap between the contact node pairs.

A modified Cholesky decomposition-elimination algorithm is adopted. The process of decomposition-elimination will continue until the stiffness sub-matrices relative to contact region of two bodies become unit matrices I. The revised stiffness sub-matrices  $K_x^c$ ,  $K_{xc}^c$ ,  $K_{xc}^c$ ,  $K_x^c$ , coefficient matrices  $D_1^c$ ,  $D_2^c$  and the revised loading vectors  $P_x^c$ ,  $P_x^c$ ,  $P_x^c$ ,  $P_x^c$  can be calculated simultaneously. As the coefficient matrices  $C_1$ ,  $C_2$  are diagonal matrices and the values of the diagonal element are only one or zero, the flexibility matrix equation of the contact region can be written as:

$$(F)(R_x) = -(Sp) + \{\delta_0\} \quad (2-2)$$

where  $F$  denotes the flexibility matrix of contact region,  $Sp$  is the relative displacement vector between the contact node pairs caused by loading vectors

$$(F) = (D_1) - (C_1) (D_1^c) - (C_2) (D_2^c) \quad (2-3a)$$

$$(Sp) = (C_1) (P_x^c) - (C_2) (P_x^c) \quad (2-3b)$$

Once the flexibility matrix equation (2-2) is obtained, the iterations is condensed to the contact region. After the forces and displacements of contact nodes have been solved, we can obtain the numerical solution of contact problems by back-substituting the matrix equation (2-2) with the results of contact surface.

### III. Example

The Example is the contact problem of semi-infinite elastic surface and an elastic hexahedron body. Figure 1 shows the finite element mesh. Figure 2 shows the deformation of the finite element mesh on the symmetric section. Figure 3 and 4 show the contours of stress tensor ( $\sigma_3$ ) on the symmetric sections, which represent the pressure distribution along the contact surface. Several other examples of contact problems were calculated as well.

With the approach presented, we have applied it to the numerical solutions of contact stress analysis for spur gears and helical gears. The researches are now concentrated on the solutions of dynamic contact problems.

### IV. References

- [1] Satoshi Ohte, Finite Element Analysis of Elastic Contact Problems, Bulletin of JSME, Vol. 16, No. 95 (1973), 797-804
- [2] T. O. Sachdeva, C. V. Ramakrishnan, A Finite Element Solution for The Two-Dimensional Elastic Contact Problems With Friction, Int. J. Num. Meth. in Engng., Vol. 17 (1981), 1251-1271
- [3] T. F. Conry, A. A. Seirey Mathematical Programming Method For Design of Elastic Body in Contact Problems, J. Appl. Meth. Vol. 6 (1971)
- [4] J. T. Stadler, R. O. Weiss, Analysis of Contact Through Finite Element Gaps, Computers & Structures, Vol. 19, 867-873

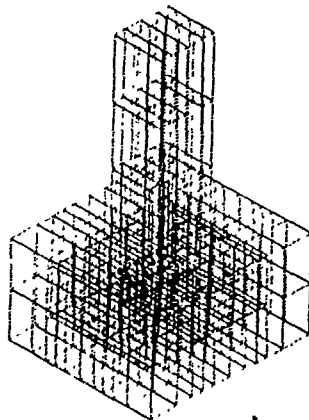


Fig 1  $E_1 = E_2 = 2.1 \times 10^4 \text{ N/mm}^2$   
 $\mu = 0.15$

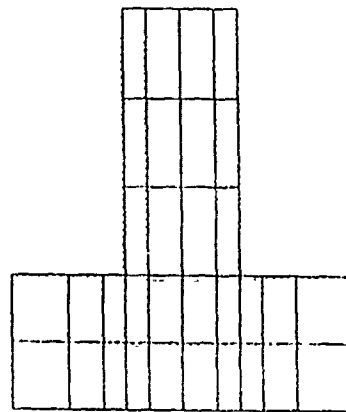


Fig 2 Section 3

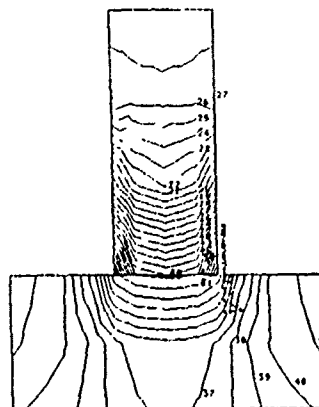


Fig 3 Section 1

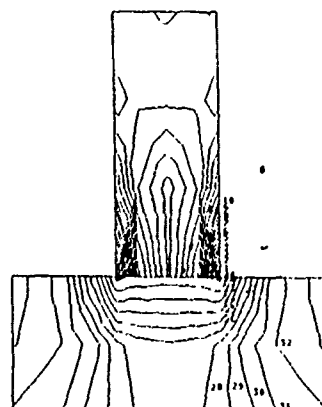


Fig 4 Section 3

# EFFECTS OF UP WEIGHTING AND DOWN UNWEIGHTING IN SKIING ON SKIS

Toshiyuki SAKATA

Department of Mechanical Engineering  
Chubu University

1200 Matsumoto-cho, Kasugai, Aichi, 487 Japan

## 1. Introduction

Various studies have been reported on dynamics of skiing, motion of skiers, and skiing goods. By developping these studies, it is considered that one will be able to simulate the dynamics of the system consisting of skier, skiing goods and snow. To discuss the dynamics of skiing, it is very important but difficult to know the deformation of skis and the resulting force acting on skis through snow while skiing. However, one can find few studies discussing them. The purpose of the study is to estimate them experimentally and numerically.

## 2. Numerical approach

Let us consider the bending deformation of the ski, which is shown in Fig.1. The shoes center of the ski is taken as the origin. When the external force  $Q$  acts on the shoes center, the ski does the vertical displacement,  $W_0$ , and rotation,  $\theta_0$ , as shown by the dotted line, and deforms  $w$ , as shown by the solid line. The differential equations of the ski are given by

$$L[w^{(r)}] + \gamma^{(r)} (\partial^2 w^{(r)} / \partial t^2) = -f^{(r)} + \gamma^{(r)} g \quad (1)$$

$$r=1, 2$$

where,  $L[ ]$  is the differential operator for the bending deformation of a nonhomogeneous beam, that is skis,  $\gamma^{(r)}(x)$  is the mass per unit length,  $w^{(r)}(x, t)$  is the deflection. The function  $f^{(r)}(x, t)$  is the force acting on the ski through the snow, and given by

$$f^{(r)}(x, t) = k^{(r)}(x) [W_0 - x\theta_0 + w^{(r)}(x, t)] \quad (2)$$

The coefficients  $k^{(r)}(x, t)$  are determined by the contact mechanism between ski and snow, the camber height, and the surface condition of slope, and the spring constant of snow. The boundary conditions are given by

$$w^{(r)}(0, t) = 0, \quad dw^{(r)}(0, t)/dx = 0 \quad (3)$$

$$m^{(r)}(l_r, t) = v^{(r)}(l_r, t) = 0 \quad (4)$$

where,  $m^{(r)}(x, t)$  and  $v^{(r)}(x, t)$  are the bending moment and shearing

force, respectively. The equilibrium equations are given by

$$\int_{l_1}^0 [\gamma^{(1)} g - f^{(1)} - \gamma^{(1)} (\partial^2 w^{(1)} / \partial t^2)] dx + \int_0^{l_2} [\gamma^{(2)} g - f^{(2)} - \gamma^{(2)} (\partial^2 w^{(2)} / \partial t^2)] dx = Q \quad (5)$$

$$\int_{l_1}^0 [\gamma^{(1)} g - f^{(1)} - \gamma^{(1)} (\partial^2 w^{(1)} / \partial t^2)] x dx + \int_0^{l_2} [\gamma^{(2)} g - f^{(2)} - \gamma^{(2)} (\partial^2 w^{(2)} / \partial t^2)] x dx = 0 \quad (6)$$

Equations (1) to (6) are solved by using an iteration method.

### 3. Mechanical properties and force

The mass per unit length and the flexural rigidity vary along the longitudinal direction. The mass per unit length was estimated numerically. The flexural rigidity was measured by using a simple apparatus. The forces  $Q$  caused by up weighting and down unweighting were measured by using force plate and image analysis. Examples of the force are shown in Fig. 2. The property of the snow was approximated by various elastic and plastic springs. The effect of the camber height also discussed.

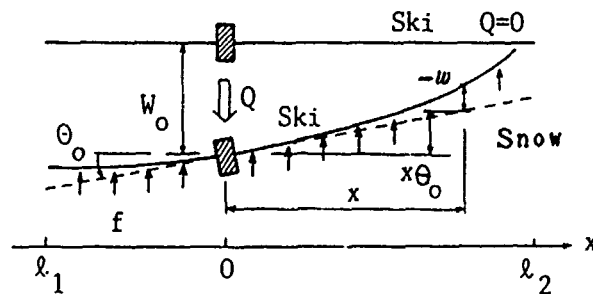


Fig. 1 Deformation of the ski

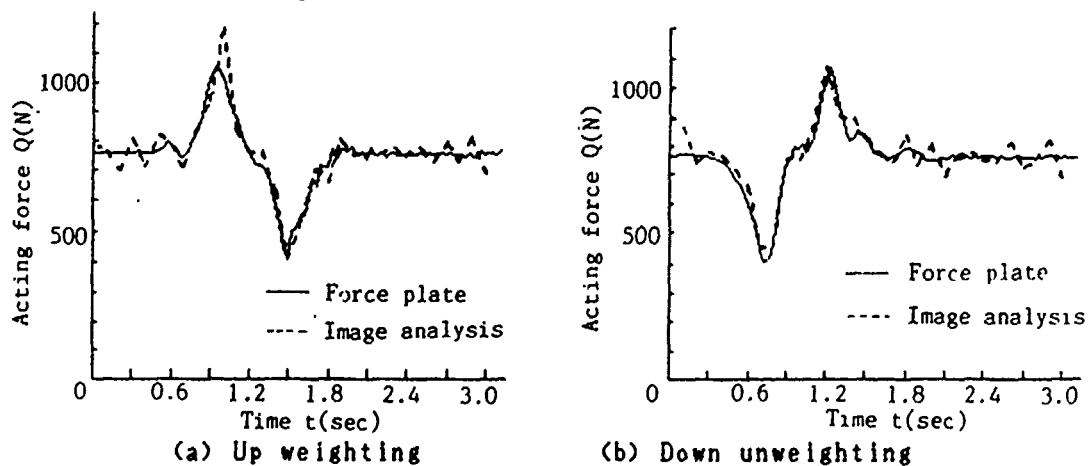


Fig. 2 Examples of the force caused by skier's action.

## AXIAL RESPONSE OF MULTILAYERED STRANDS WITH COMPLIANT LAYERS<sup>1</sup>

Raymond A. LeClair

Lincoln Laboratory, Massachusetts Institute of Technology  
244 Wood Street, Lexington, Massachusetts 02173-9108

Wire rope investigators have usually neglected the effect of contact deformation in analyzing the response of metallic strands. However, strands incorporating non-metallic components may experience significant effects due to this deformation. This paper extends a linear theory for wire rope to include contact deformation effects on axial strand response. The linear theory considers an individual helical wire to undergo small changes in helix angle and helix radius, due to wire Poisson's contraction, under given axial strand strains. Corresponding changes in the helix centerline components of curvature and twist determine bending moment components and torque resultants on the wire cross section. Equilibrium of the wire determines the remaining stress resultants and external loads. This theory is extended by allowing the change in helix radius to depend on the contact force between wire layers through their contact compliance. Hertz contact theory determines the contact compliance for wire layers experiencing point contact and results from contact mechanics determine the contact compliance for the second layer which experiences line contact with the center wire. Analysis is presented for simple as well as multilayered strands and a numerical procedure is introduced for the solution of the resulting simultaneous nonlinear equations.

Numerical results are presented for typical three and ten layer metallic strands. Neglecting contact deformations results in predicting greater wire

---

<sup>1</sup>This work was sponsored by the Department of the Air Force.

tension and equilibrium contact force by 3% for the three layer strand and as much as 11% for the ten layer strand. Though not negligible, the effects are small. Numerical results are also presented for a typical three layer instrumentation cable having a compliant layer between signal carrying wires. The presence of the compliant layer reduces the tension and equilibrium contact force by at least an order of magnitude over the case in which the deformation is neglected or the compliant layer is absent. The introduction of compliant layers, therefore, is an effective means of reducing the load in the signal carrying wires of instrumentation cables.

# WAVE PROPAGATION IN FINITE RING-STIFFENED CYLINDRICAL SHELLS

M. S. Bennett

General Dynamics/Electric Boat Division  
Eastern Point Road, Groton, CT 06340

## INTRODUCTION

Numerous studies have been conducted that investigate free wave propagation in stiffened cylindrical shells. Generally, free wave propagation calculations assume that the cylinder is infinite and free from boundary conditions (1,2). The effects of boundary conditions on the free wave propagation characteristics of the structure are generally not discussed. Other investigations have been performed in which boundary effects have been included. Typically, the objective of these investigations is the prediction of natural frequencies and mode shapes (3,4). To date, little has been reported on the existence, or preservation, of infinite cylinder free wave propagation characteristics in cylinders of finite length. This investigation attempts to address this subject.

## TECHNICAL APPROACH

The primary concern of this investigation is the axial propagation of vibrational energy along a circumferentially stiffened cylindrical shell (Fig. 1). Transmission characteristics are predicted using both a free wave approach (infinite cylinder assumption) and a forced wave approach (using straight forward application of the finite element method and a finite cylinder model). Results from each analysis are compared for axisymmetric (circumferential wave number,  $n=0$ ) and non-axisymmetric ( $n=2$ ) vibrations.

## INFINITE CYLINDER ANALYSIS

Two techniques were utilized to predict the free wave propagation characteristics of an infinite undamped circumferentially stiffened cylinder. The first approach developed by Accorsi and Bennett (5) is applicable to cylindrical shells periodic in both the axial and circumferential directions. This methodology is finite element based and only a single periodic unit (panel) must be modeled (Fig. 2a). In this methodology, propagation constants are calculated directly by solution of a linear eigenvalue problem. Stop and pass bands associated with periodic structures are then determined from the propagation constants by inspection. The second

approach utilized an axisymmetric finite element model to predict the propagation constants. This analysis utilized the formulation presented by Signorelli and von Flotow (6). While their formulation was developed for application to beams and beam truss structures, it is equally applicable to axisymmetric finite element models (7). In this analysis, as before, only a single periodic unit must be modeled (Fig. 2b).

## FINITE CYLINDER ANALYSIS

A finite axisymmetric model of the cylinder depicted in Fig. 1 was developed (3841 DOF). A radial ring load ( $n=0$  or  $n=2$ ) excited the left end of the cylinder and the radial response (displacement) at the right end was calculated. In this analysis, unlike the free wave propagation analysis described above, damping, in the form of a structural loss factor, was included. Analyses were performed for both a lightly damped ( $\eta=0.005$ ) and a moderately damped ( $\eta=0.05$ ) structure.

## RESULTS AND CONCLUSIONS

The results from each analysis described above are shown in Figs. 3 and 4 for  $n=0$  and  $n=2$  respectively. Stop and pass bands predicted by the infinite cylinder (free wave) analysis are shown in the upper portion of each figure. Stop bands or attenuation zones are indicated by solid black fill, while unfilled or white regions indicate pass bands or propagation zones. The results from the finite cylinder (forced wave) analysis are shown in the lower portion of each figure.

Figures 3 and 4 strikingly demonstrate that most free wave propagation characteristics are well preserved even in finite short aspect ( $l/d=1.25$ ) cylinders. Results from the two free wave propagation analyses agree quite well, and agreement with the finite cylinder analysis is excellent when similar element types are utilized. Subtle differences in the two infinite cylinder analyses are attributed to the different finite elements utilized (4 noded quadrilateral plate/shell vs. 3 noded axisymmetric shell). The discrete stop band at  $\Omega \approx 3.4$  predicted by both free

wave propagation analyses, for both circumferential wave numbers, does not appear in the finite cylinder analysis. The reason for this is still being investigated.

### ACKNOWLEDGEMENT

Funding for the work reported herein was provided by General Dynamics/Electric Boat Division's IR&D Program

### REFERENCES

1. Hodges, C., Power, J., Woodhouse, J., "The Low Frequency Vibration of a Ribbed Cylinder, Part 1: Theory." *J. Sound Vib.* (1985), 101(2), 219-235.
2. Mead, D., Bardell, N., "Free Vibration of a Thin Cylindrical Shell with Periodic Circumferential Stiffeners." *J. Sound Vib.* (1986), 115(3), 499-520.
3. Leissa, A., "Vibration of Shells" *NASA Report NASA-SP-283*, Ohio State University, 1973.
4. Wilke, J., Soedel, W., "The Receptance Method Applied to Ring-Stiffened Cylindrical Shells: Analysis of Modal Characteristics." *J. Sound Vib.* (1976), 44(4), 563-576.
5. Accorsi, M., Bennett, M., "A Finite Element Based Method for the Analysis of Free Wave Propagation in Stiffened Cylinders" *J. Sound Vib.* (1991), 147(3), In press.
6. Signorelli, J., von Flotow, A., "Wave Propagation, Power Flow and Resonance in a Truss Beam." *J. Sound Vib.* (1988), 126(1), 127-144.
7. Private discussions with Dr. Michael Accorsi, University of Connecticut, Storrs, Connecticut.

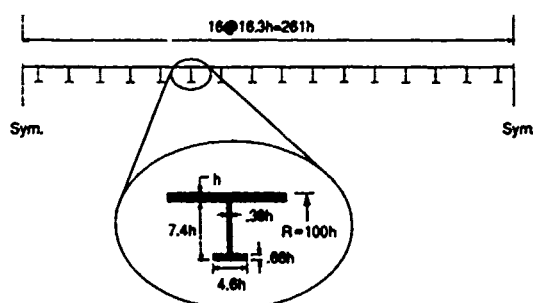


Figure 1 Dimensions of Ring Stiffened Cylindrical Shell

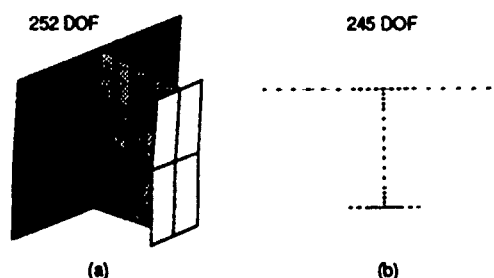


Figure 2 Periodic Finite Element Models for Wave Propagation Analysis, (a) Doubly Periodic Model, (b) Axisymmetric Model

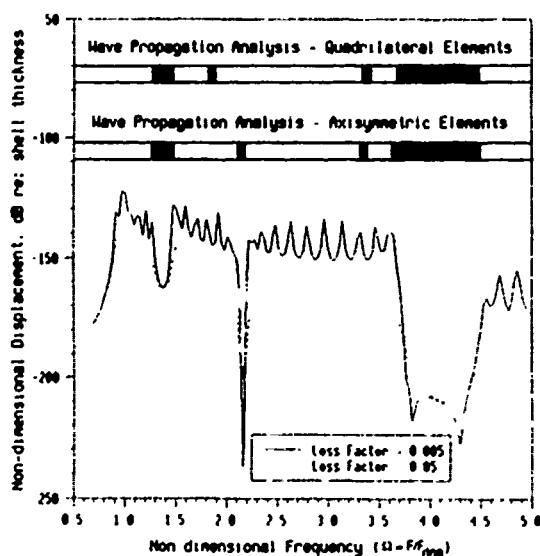


Figure 3 Transmissibility Investigation,  $n=0$

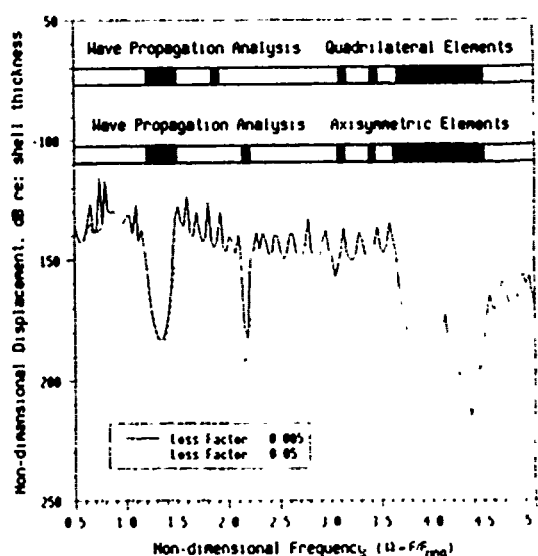


Figure 4 Transmissibility Investigation,  $n=2$



# VIBRATIONS OF ROTATING CIRCULAR CYLINDRICAL SHELLS WITH VARYING THICKNESS

K. SUZUKI, K. HAYASHI\*, T. KOSAWADA AND G. SHIKANAI  
Faculty of Engineering, Yamagata University, 4-3-16 Jyonan, Yonezawa 992, Japan  
\* Nippon Kokan, Co., Ltd., 1-1-2 Marunouchi, Chiyoda Ward, Tokyo 100, Japan

## 1. INTRODUCTION

An exact method using power series expansions is developed for solving free vibrations of rotating thin circular cylindrical shells with varying thickness. Equation of motion, which takes account of initial tensions due to rotation and variation of shell thickness, are solved exactly by utilizing power series expansions.

## 2. ANALYSIS

Let us consider the free vibrations of a thin circular cylindrical shell with varying thickness which rotates at the angular velocity of  $\Omega$ . The geometry of the shell and coordinate system are shown in Fig.1. The thickness of the shell is  $h = h_0 H(x)$ , where  $h_0$  is the thickness at  $x=0$ . The displacements of the shell, which vibrates infinitesimally under the initial tensions due to steady rotation, are put as:

$$\bar{u} = u^* + \tilde{u}, \quad \bar{v} = \tilde{v}, \quad \bar{w} = w^* + \tilde{w} \quad (1)$$

where, \* denotes the steady rotating state and  $\tilde{\phantom{x}}$  does the vibrating one. Substituting Eq.(1) into Lagrangian function of the vibration, equations of motion of the vibrating state are obtained as follows:

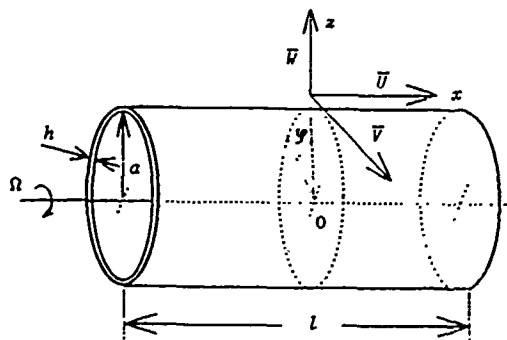


Figure 1 Geometry and coordinates

$$\left. \begin{aligned} -\lambda H \frac{\partial^2 \bar{u}}{\partial t^2} + \frac{\partial}{\partial \xi} (N_\xi) + \frac{1}{2} (1-\nu) \frac{\partial}{\partial \varphi} (N_{\varphi \xi}) + N_\varphi^* \frac{\partial^2 \bar{u}}{\partial \varphi^2} + N_\xi^* \frac{\partial^2 \bar{u}}{\partial \xi^2} &= 0 \\ \lambda H \left( \Omega^2 \bar{v} - \frac{\partial^2 \bar{v}}{\partial t^2} - 2\Omega \frac{\partial \bar{w}}{\partial t} \right) + \frac{\partial}{\partial \varphi} (N_\varphi - M_\varphi) + \frac{1}{2} (1-\nu) \frac{\partial}{\partial \xi} (N_{\xi \varphi} + 2M_{\xi \varphi}) \\ + N_\xi^* \frac{\partial^2 \bar{v}}{\partial \xi^2} + N_\varphi^* \left( \frac{\partial^2 \bar{v}}{\partial \varphi^2} + 2 \frac{\partial \bar{w}}{\partial \varphi} - \bar{v} \right) &= 0 \\ \lambda H \left( \Omega^2 \bar{w} + 2\Omega \frac{\partial \bar{v}}{\partial t} - \frac{\partial^2 \bar{w}}{\partial t^2} \right) + \frac{\partial^2}{\partial \xi^2} (M_\xi) - \frac{\partial^2}{\partial \varphi^2} (M_\varphi) + \frac{1}{2} (1-\nu) \frac{\partial^2}{\partial \xi \partial \varphi} (2M_{\xi \varphi} + M_{\varphi \xi}) \\ - N_\varphi + N_\xi^* \frac{\partial^2 \bar{w}}{\partial \xi^2} + \left( \frac{\partial^2 \bar{w}}{\partial \varphi^2} - 2 \frac{\partial \bar{v}}{\partial \varphi} - \bar{w} \right) &= 0 \end{aligned} \right\} \quad (2)$$

where  $\bar{U}=\tilde{u}/\alpha$  ,  $\bar{V}=\tilde{v}/\alpha$  ,  $\bar{W}=\tilde{w}/\alpha$   $\xi=x/\alpha$  ,  $\lambda=\rho\alpha^2(1-\nu^2)/E$  (3)

and where  $t$ ,  $\nu$ ,  $E$  and  $\rho$  are the time, Poisson's ratio, Young's modulus and density.  $N_\xi^*$  and  $N_\phi^*$  are the initial tensions due to steady rotation and other  $N$  and  $M$  are resultant forces and moments which are typically used in shell theory. Considering the separation of variables, the vibration displacements are put as

$$\bar{U}=U(\xi)\cos(n\phi+pt), \quad \bar{V}=V(\xi)\sin(n\phi+pt), \quad \bar{W}=W(\xi)\cos(n\phi+pt) \quad (4)$$

where  $n$  and  $p$  are the circumferential wave number and the circular frequency. The shell cross section is symmetric about  $x=0$  plane and that the vibrations are divided into symmetric and antisymmetric vibrations. The solutions of the symmetric vibrations take form as

$$U=\sum_{m=0}^{\infty} P_m \xi^{2m+1}, \quad V=\sum_{m=0}^{\infty} Q_m \xi^{2m}, \quad W=\sum_{m=0}^{\infty} R_m \xi^{2m} \quad (5)$$

where  $P_m, Q_m$  and  $R_m$  are coefficients which are successively determined in terms of  $P_0, Q_0, R_0$  and  $R_1$ .

### 3. NUMERICAL RESULTS AND DISCUSSION

In the numerical calculations, Poisson's ratio is taken as 0.3 and solutions  $U, V$  and  $W$  of Eq.(5) are calculated by retaining 60 terms of the coefficients  $P_m, Q_m$  and  $R_m$ . Considering the boundary conditions, one obtains frequency equations in the form of fourth order determinant. In this report, the variation of shell thickness is assumed as parabolic along its  $x$ -axis by taking  $H=1+\epsilon\xi^2$ . The nondimensional number of revolutions, natural frequencies, shell thickness and length are defined as follows;

$$\left. \begin{aligned} \alpha_0^4/\beta &= (1-\nu^2)\rho\alpha^2\Omega^2/E, \\ \alpha^4/\beta &= (1-\nu^2)\rho\alpha^2p^2/E, \\ \beta &= 12\alpha^2/h_0^3, \quad \mu=1/(2\alpha) \end{aligned} \right\} \quad (6)$$

Figure 2 shows the typical frequency curves of both ends clamped rotating circular cylindrical shell. It is observed that the effects of variations of shell thickness upon natural frequencies are quite considerable.

The method of solution developed here is a general one applicable to various rotating shell with varying thickness.

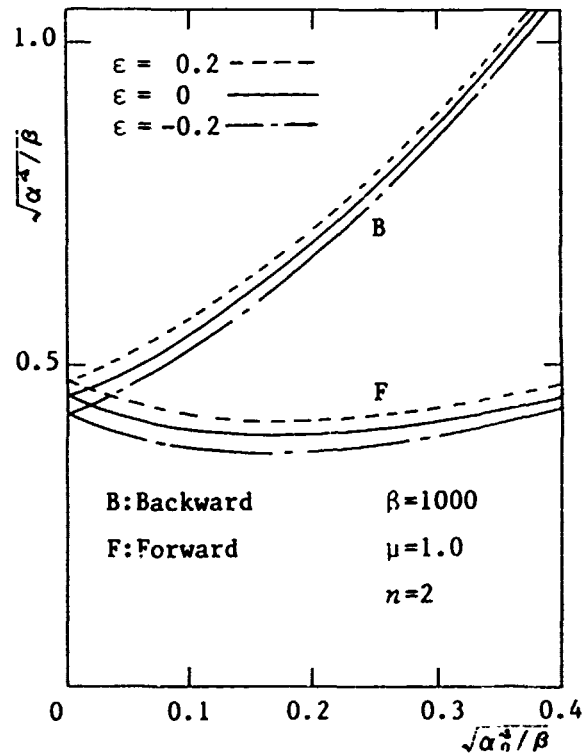


Figure 2 Frequency curves (Both ends clamped, symmetric vibration)

### REFERENCES

1. K.Suzuki, R.Takahashi and T.Kosawada, 1991 JSME International Jour.34-309C (in press) Analysis of vibrations of rotating thin circular cylindrical shells.
2. K.Suzuki, H.Arakawa and T.Kosawada, 1991 Trans.JSME 57-536C(in press) Analysis of vibrations of rotating thick circular cylindrical shells(in Japanese).

# THE INFLUENCE OF AXIAL-TORSIONAL COUPLING ON THE NATURAL FREQUENCIES OF AN AERIAL CABLE

S. H. Venkatasubramanian and W. N. White  
Department of Mechanical Engineering  
Durland Hall  
Kansas State University  
Manhattan, Kansas 66506

The equations of motion for the small oscillations about the static equilibrium position of a single stranded, sagged elastic cable are derived by using Hamilton's principle and linearized about the static equilibrium configuration. The cable is fixed at both ends at the same elevation. Motion in three Cartesian directions together with torsional motion is considered. The influence of axial-torsional coupling due to stranded geometry on the natural frequencies is studied analytically and an expression is presented for the coupled natural frequency in torsion. In order to verify the analytical results, a finite element analysis of the linearized coupled differential equations is carried out. The results of each analysis are compared and show close agreement. The results of the zero coupling case also closely agree with previous work.

Assuming normal mode of oscillations, the equations of motion are analytically solved for the case where the spatial variation of forces along the axial direction is negligible. The coupled natural frequency, in Hertz, of torsional oscillation is found to be

$$f_{\theta} = \frac{n}{2(2\ell)} \left[ \frac{(GJ - B^2/AE)}{I} \right]^{1/2}$$

where  $n = 1, 2, 3, \dots, \ell$  is the semi free length of the cable,  $GJ$  is the torsional rigidity,  $B$  is the coupling parameter,  $AE$  is the axial stiffness, and  $I$  is the mass moment of inertia per unit length of the cable. The expressions for frequencies for vertical oscillations are identical to those given by Shea(1955). In order to check the validity of the assumption that the spatial variation of forces along the axial direction is negligible, a finite element analysis of the coupled differential equations is carried out. A Galerkin weighted residual approach is used with linear interpolation polynomials.

To check the finite element formulation, an example given by McConnell and

Chang(1986) is solved using the finite element program. Also, calculations for vertical natural frequency for symmetrical modes are performed using the transcendental equation given by Shea(1955). The torsional natural frequencies are calculated using the approximate formula presented earlier and using the finite element program. The results for one case are shown in the figure. Calculations are performed for various values of sag-to-span ratios (both above and below critical sag)with the same level of agreement as shown in the figure.

### Conclusions

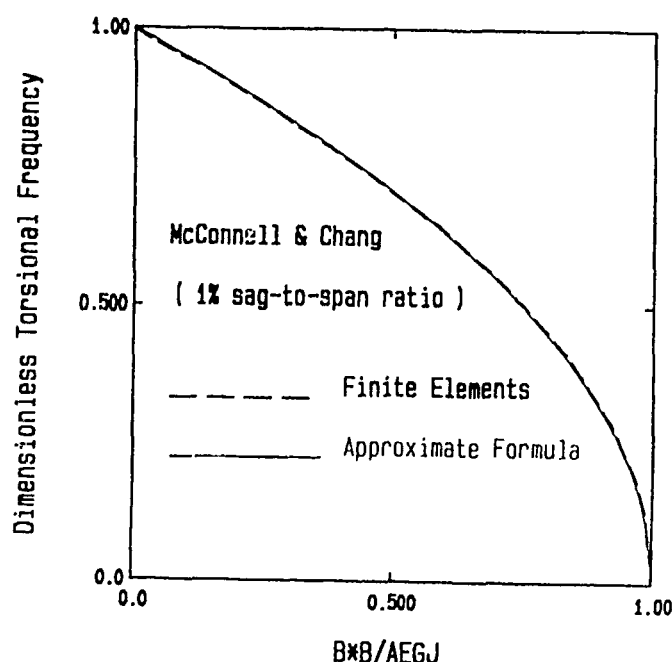
From this study, several conclusions can be made. These are:

1. Axial-torsional coupling does not influence the frequency of vertical oscillation whereas it reduces the frequency of torsional oscillation.
2. The approximate formula presented for calculating torsional frequencies may be used for design purposes.
3. Sag-to-span ratio does not have an appreciable effect on torsional frequencies for the range tested.
4. The assumption of quasi-static stretching(i.e., tension is almost constant throughout the length of the cable but varies with time) is valid.

### References

McConnell, K. G., and Chang, C. N., 1986, "A Study of the Axial-Torsional Coupling Effect on a Sagged Transmission Line," J. Expt. Mechanics, December, pp 324-329.

Shea, J. F., 1955, "A Study of Wind Forces on Suspended Cables and Related Structures," Ph.D. Thesis, University of Michigan, Ann Arbor, Michigan.



# FREE VIBRATION OF SHELLS OF REVOLUTION

Xianxin Cai

Department 7, Nanhua Powerplant Research Institute  
P O Box 215, Zhuzhou, Hunan 412002, P.R.China

## ABSTRACT

A shell of revolution is an important structural component in all industrial applications, especially those relating to aerospace, nuclear, and petrochemical engineering. Analysis of the vibration of the shells is of great importance. In this paper an efficient method is presented for the free vibration of shells of revolution. This method is based on the theory of conical shells from which the first-order differential equations of the shells of revolution are derived. The equations are then solved by the discrete-variable method. The presented method is able to deal with a shell of revolution with acute-angled meridian. For branched structures, a sub-structure method is proposed so that this sort of structures can be analysed, and by using this method the accumulative error can also be reduced. The present method is simple, easy to perform and has a good accuracy.

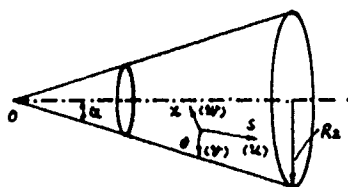


Fig. 1

Fig. 1 shows a truncated conical shell. The coordinates  $(s, \theta, z)$  and displacement directions  $(u, v, w)$  are taken as shown in the figure. The thickness of the shell is assumed to be variable along its meridian and constant along its circumference. For the mode of harmonic term  $m$  (the circumferential wave number), displacements can be expressed as

$$\begin{aligned} u(s, \theta, t) &= U(s) \cos m\theta \sin \omega t \\ v(s, \theta, t) &= V(s) \sin m\theta \sin \omega t \\ w(s, \theta, t) &= W(s) \cos m\theta \sin \omega t \end{aligned} \quad (1)$$

where  $\omega$  is the frequency in rad / s.

From the theory of conical shells and (1), a set of the first-order differential equations about the eight state parameters  $\{Y\} = [UVW\Psi N_s S_{\theta} P_s]^T$  can be obtained:

$$(d/ds)\{Y\} = [H]\{Y\} \quad (2)$$

A shell of revolution with smoothly curved meridian can be modeled by a series of truncated conical shells. At the joint, by using the continuity and equilibrium conditions, the following relation can be obtained:

$$\{Y(s_i + 0)\} = [\lambda]^{(i)} \{Y(s_i - 0)\} \quad (3)$$

where  $s_i + 0$  and  $s_i - 0$  mean right side and left side of the joint  $i$  (see Fig. 2) respectively.



Fig. 2

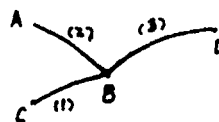


Fig. 3

By differentiating (3) with respect to  $s$ , and then substituting (2) into it, we have the first-order differential equations of a shell of revolution:

$$(d/ds)\{Y\} = [F]\{Y\} \quad (4)$$

The discrete-variable method is used to solve (4). For a shell of revolution with acute-angled meridian, the relation between the two sides of the angle has the same form as (3). For a branched structure, a sub-structure method is proposed. As shown in Fig. 3, for instance, the relations of the parameters among the three sub-structures are established by using continuity and equilibrium conditions at the joint B.

Three examples, a casing, a lightweight gear, and a semispherical shell, are presented and the results are compared with those of experiment and those reported by other investigators utilizing various analytical and numerical techniques. The examples show that the accuracy of the present method is satisfactory.

Vibrations of a non homogeneous rectangular membrane:  
exact solution and the optimized Kantorovich method

by V.H.Cortinez and P.A.A.Laura

Department of Engineering

Universidad Nacional del Sur

and

Institute of Applied Mechanics

(CONICET - SENID - ACCE)

8000 - Bahía Blanca

A R G E N T I N A

Abstract

The title problem is solved according to classical, linear theory. It is assumed that a rectangular subdomain possesses density  $\rho_1$  while the remaining, also rectangular, portion is characterized by  $\rho_2$ . An exact solution is obtained and the lower eigenvalues are determined for several combinations of the mechanical and geometric parameters.

An approximate solution, using the recently developed optimized Kantorovich method, is also determined and it is shown that the calculated eigenvalues are in excellent agreement with the exact ones. It is concluded that a similar, approximate procedure will be advantageous when dealing with more complex structural elements.

# BENDING OF VISCOELASTIC BEAMS ON VISCOELASTIC UNILATERAL FOUNDATIONS

Mieczysław S. Kuczma

Technical University of Poznań, 60-965 Poznań, Poland

## 1. Introduction

We deal with bending of viscoelastic beams on Winkler-type viscoelastic foundations as a quasi-static unilateral frictionless contact problem. This is a continuation of [1,2].

The flexural behavior of the beam is modeled by the Bernoulli-Euler beam theory, whilst the constitutive laws both for the beam and the foundation is assumed in the form:

$$a_0 \sigma + a_1 \dot{\sigma} + a_2 \ddot{\sigma} = b_0 \epsilon + b_1 \dot{\epsilon} + b_2 \ddot{\epsilon} . \quad (1)$$

In (1)  $\sigma$  and  $\epsilon$  stand for stress and strain, respectively,  $a, b$  are coefficients,  $(\dot{\phantom{x}})$  indicates partial time differentiation.

## 2. A discretized model of the viscoelastic body

A discretized model for the viscoelastic body governed by (1) has been proposed in [3] where the discontinues piecewise linear or quadratic time approximation of stress is applied, which eventually results in recurrent formulae ( $\tau = 1, 2, \dots$ ):

$$\epsilon_\tau = \gamma_\tau \sigma_\tau + \Lambda_\tau \epsilon_{\tau-1} , \quad \dot{\epsilon}_\tau = \dot{\gamma}_\tau \sigma_\tau + \dot{\Lambda}_\tau \tilde{\epsilon}_{\tau-1} , \quad (2)$$

The index  $\tau$  in (2) and henceforth is related to the instant  $t_\tau$ ,  $\Lambda_\tau, \dot{\Lambda}_\tau$  and  $\dot{\gamma}_\tau, \gamma_\tau$  denote  $(1 \times 6)$  matrices and coefficients, respectively,  $\tilde{\epsilon}_{\tau-1}$  determines the state of the body at  $t_{\tau-1}$ :

$$\tilde{\epsilon}_{\tau-1} = \text{col}(\epsilon_{\tau-1}, \dot{\epsilon}_{\tau-1}, \sigma'_{\tau-1}, \dot{\sigma}'_{\tau-1}, \sigma_{\tau-1}, \dot{\sigma}_{\tau-1}) . \quad (3)$$

The mark  $(\dot{\phantom{x}})$  indicates the right limit on the time axis, e.g.  $\sigma'_\tau = \sigma_\tau + \Delta \sigma_\tau$ ; at an instant  $t_\tau$  the following formulae hold:

$$\Delta \epsilon_\tau = \gamma_0 \Delta \sigma_\tau , \quad \Delta \dot{\epsilon}_\tau = \gamma_0 \Delta \dot{\sigma}_\tau + \dot{\gamma}_0 \Delta \sigma_\tau , \quad (5)$$

where  $\Delta$  is the symbol of a finite increment,  $\tau = 0, 1, 2, \dots$ .

## 3. Viscoelastic foundation

Let  $v_\tau$  be deflection and  $q_\tau$  pressure of the foundation, then the discretized constitutive law for the foundation reads

$$v_\tau = \gamma_\tau q_\tau + \Lambda_\tau s^f_{\tau-1} , \quad \dot{v}_\tau = \dot{\gamma}_\tau q_\tau + \dot{\Lambda}_\tau s^f_{\tau-1} , \quad (6)$$

with  $s^f_{\tau-1} = \text{col}(v_{\tau-1}, \dot{v}_{\tau-1}, q'_{\tau-1}, \dot{q}'_{\tau-1}, q_{\tau-1}, \dot{q}_{\tau-1})$ .



#### 4. Viscoelastic beams

Multiplying (2a) by  $z$ , integrating over cross-section and using classical relations for the beam, we finally arrive at

$$L_{\tau} w_{\tau} = r_{\tau} + \frac{d^2}{dx^2} \left[ \frac{I}{\gamma_{\tau}^b} \left( A_{1\tau} \frac{d^2}{dx^2} w_{\tau-1} + A_{2\tau} \frac{d^2}{dx^2} \dot{w}_{\tau-1} \right) \right] + \frac{1}{\gamma_{\tau}^b} \left( A_{3\tau} r'_{\tau-1} + A_{4\tau} \dot{r}'_{\tau-1} + A_{5\tau} r_{\tau-1} + A_{6\tau} \dot{r}_{\tau-1} \right)$$

or in brief, 
$$L_{\tau} w_{\tau} = p_{\tau} - q_{\tau} + A_{\tau}^b s_{\tau-1}^b, \quad (7)$$

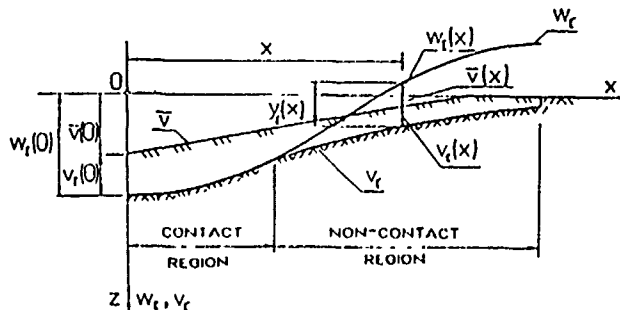
with:  $w_{\tau}, p_{\tau}$ —deflection and active load of the beam,  $r_{\tau} = p_{\tau} - q_{\tau}$

$$L_{\tau}(\cdot) \equiv \frac{d^2}{dx^2} \left( \frac{I}{\gamma_{\tau}^b} \frac{d^2(\cdot)}{dx^2} \right), \quad I \text{— moment of inertia,}$$

$$A_{i\tau} \text{— elements of } A_{\tau}.$$

#### 5. Formulation of the contact problem

Let  $\bar{v} = \bar{v}(x)$  be an initial gap, then a temporary gap, cf Fig.,  $y_{\tau} = v_{\tau} - w_{\tau} + \bar{v}$ .



With these notations this contact problem is governed at  $t_{\tau}$  by the system - (P1):

$$L_{\tau} w_{\tau} = p_{\tau} - q_{\tau} + A_{\tau}^b s_{\tau-1}^b$$

$$w_{\tau} + y_{\tau} = \gamma_{\tau}^f q_{\tau} + A_{\tau}^f s_{\tau-1}^f + \bar{v}$$

$$q_{\tau} \geq 0, \quad y_{\tau} \geq 0, \quad q_{\tau} y_{\tau} = 0.$$

In addition, due to the inherent nonlinear character of the problem and the time integration method used we have to solve at some instants  $t_{\tau}$ , two additional problems [1,2].

Finally, after a variational formulation of the problem in the form of a variational inequality and its discretization by FEM, we solve it as LCP; results of numerical experiments will be presented at the Conference.

The analogous problem for a plate is being investigated.

#### Acknowledgements

I wish to thank Professor R. Świtka for helpful discussions on the subject and the Polish Ministry of National Education (MEN) for financial support under the research project 11-479/91.

#### References

1. Kuczma M.S., Świtka R., *Comp. & Struct.*, 125-136, **34**, 1990
2. Kuczma M.S., *The unilateral contact problem of beams and plates on viscoelastic foundations*, Ph.D. Thesis, Poznań 1990
3. Świtka R., Husiar B., *Mech. Teor. Stos.*, 209-233, **22**, 1984

# EQUILIBRIUM ANALYSIS OF AUTOMOTIVE SERPENTINE BELT DRIVE SYSTEMS UNDER STEADY OPERATING CONDITIONS

R.S. Beikmann

Noise and Vibration Laboratory, General Motors Corp., Milford, MI.

N.C. Perkins and A.G. Ulsoy

Mech. Eng. and Applied Mechanics, University of Michigan, Ann Arbor, MI

Despite certain engineering advantages over V-belts, automotive serpentine belt drive systems may exhibit noise and vibration problems, as well as difficulties in driving accessories without slippage. Analyzing these problems requires determining the operating span tensions and geometry. Two methods developed in this study calculate the operating equilibrium span tensions and tensioner arm position, given the reference state (zero speed, zero accessory loads) geometry and tension.

The first method determines the operating state which would produce the reference state, if loads and engine speed effects were removed. A nonlinear function of the tensioner arm deflection is derived which accounts for the change in belt length and tension induced by drive torques, centrifugal tension, and tensioner deflection. The function approaches zero as the solution converges to the actual operating condition. Newton-Raphson iteration is used to numerically determine the operating tensioner arm deflection. The numerical solutions converge rapidly to the exact equilibrium state, but provide little insight of how design variables affect the quality of the belt/tensioner system.

The second method, which generalizes work by Mote on band saw systems<sup>1</sup>, is a closed-form linear approximation to the equilibrium problem. The linear approximation leads to a key design parameter,  $\eta$ , which indicates 1) the ability of the system to maintain tractive tension under high operating speeds, and 2) the static stability of the belt/tensioner system. The support constant,  $\eta$ , may be expressed as (see Fig. 1 for nomenclature)

$$\eta = k_b / (k_b + k_s + k_g)$$

where  $k_b = (EA/L)(\cos\psi_1 + \cos\psi_2)^2$ ,  $k_s = k_r/r_1^2$ ,  $k_g = P_r(\zeta_1 + \zeta_2)$ ,  $\zeta_i = d(\cos\psi_i)/dx_s$ ,  $E$  is the average Young's Modulus of the belt,  $A$  is the belt cross-sectional area,  $L$  is the overall belt length,  $x_s$  is the support motion, and  $P_r$  is the reference tension. The quantities  $k_b$ ,  $k_s$ , and  $k_g$  are the translational stiffnesses in the direction of  $x_s$  deriving from belt stiffness, the tensioner spring and span geometry changes, respectively. Given  $\eta$ , one may express the operating tension ( $P_o$ ) and the tractive tension ( $P_t$ ) as

$$P_o = P_r + \eta mc^2$$

---

<sup>1</sup>Mote, C.D., Jr., "Some Dynamic Characteristics of Band Saws", Forest Products Journal, January 1965, pp. 37-41

and

$$P_t = P_r - \kappa mc^2$$

where  $m$  is the belt mass/length,  $c$  is the axial belt speed, and  $\kappa = 1 - \eta$ . While any values of  $\eta$  may be achieved,  $\eta$  typically varies between 0 and 1. For constant tractive ability and belt vibration characteristics with respect to speed, it is desirable that  $\eta \approx 1$ . In a typical system,  $\eta$  asymptotically approaches unity as  $k_s$  and  $k_g$  approach zero. Alternatively,  $\eta$  may exceed unity if  $k_g$  becomes sufficiently negative. In extreme cases ( $k_g < 0$ ),  $\eta$  may pass through a singularity and become negative. Negative values of  $\eta$  indicate a static instability and occur under conditions of high tension, short tensioner arm radius, or a sub-optimum tensioner position.

Fig. 2 shows how  $\eta$  may vary with design geometry in a typical system. In this example, the reference position of the tensioner arm ( $\gamma_1$ ) was varied, for three values of tensioner stiffness,  $k_s$ . For the analyzed system (Fig. 1),  $\eta=0$  when  $\gamma_1 = \pm 90^\circ$ , indicating "locked-center" behavior. When  $\gamma_1$  is in the neighborhood of 0 or 180 degrees,  $\eta$  approaches its maximum. As  $k_s$  becomes smaller, the maximum  $\eta$  approaches unity, and the curve broadens. Thus, lower tensioner stiffness leads to 1) near optimal values of  $\eta$ , and 2) lower sensitivity of  $\eta$  to tensioner position.

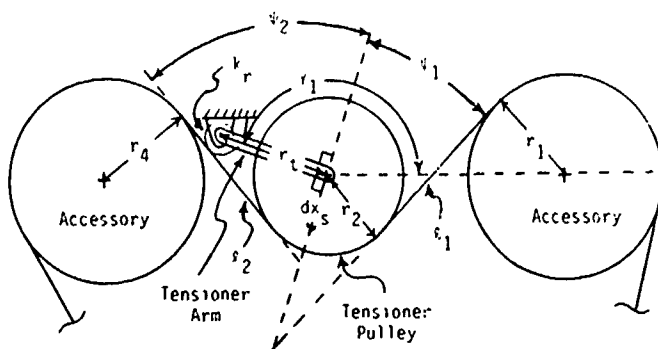


Fig. 1. Typical Belt/Tensioner Layout

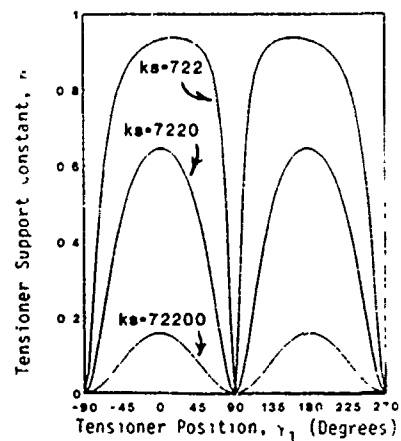


Fig. 2. Variation of  $\eta$  With Tensioner Position and Tensioner Stiffness

## FLAT BELT 217 NEWTON-METER CONTINUOUSLY VARIABLE TRANSMISSION

Theodore C. Kraver, President  
Kumm Industries Inc.  
225 West Orchid Lane  
Phoenix, AZ 85021

Flat belt CVT's for the 1.0 and 3.0 liter sized automobile have been designed, fabricated, and laboratory/vehicle tested. Vehicle testing in a Ford Fiesta and a Mercury Sable included low speed acceleration and high speed road tests. The 6:1 nominal speed ratio designs were launched with a programed clutch. Success of these prototypes was based on extensive development of the pulley and belt components.

Variable radius pulleys were of the proprietary Kumm design. They included pairs of spiral grooved disks that support 20 belt drive elements. Pulleys are actuated to the required ratio and belt tension by rotary hydraulic or spring actuators and centrifugal force of the belt drive elements.

Belts were Kevlar corded with urethane or Neoprene bodies and fabric backed. Several vendors provided the development belts. Belt testing focused on efficiency, strength, torque-tension capacity, and durability.

Segmented pulley-belt tests displayed the expected 98 to 99 percent efficiency from input speeds of 2700 to 4800, and up to 6000 rpm output at the higher power levels. Efficiency correlated closely with slip. Urethane belts exhibited higher torque capacity and slightly higher efficiencies.

Designs were limited to a maximum of 20% of the breaking strength of the new belt. This provided adequate torque capacity of 85 newton-meters on a 70 mm diameter by 25 mm wide pulley and 250 newton-meters on a 100 mm diameter by 50 mm wide pulley. The controller provided the optimum belt tension to produce minimum temperature. It centered the belt between the low tension slip and high tension loss limits. If breakaway slip occurred at low tension, the belt temperature rise rate was well within the controller's time response to prevent belt damage.

Bench tests explored the BDE-belt pressure, slip velocity, and friction coefficient relationship at the BDE-belt surface. Torque capacity vs pulley speed was tested on the dynamometer. BDE-belt pressure and slip velocity both increased the effective friction coefficient. Pulley speed decreased the effective friction coefficient.

Accelerated 300 hour durability tests of programmed high speeds and torques simulated a 3000 hour automotive cycle. After an initial weight loss of 2%, the belts stabilized and performed well over the life of the test.

Segmented pulleys produced additional noise. Tests demonstrated that this noise was a log function of the radial belt strike velocity.

Encased flat belt - pulley systems require dry air cooling. Rig testing determined the air flows required to maintain the internal transmission air temperature at 32 degrees C. Tests from 32 to 80 degrees C demonstrated that belt slip was not a strong function of the internal air temperature. Hot day conditions will not present a significant problem. Maximum air flow was 75 cfm at full power for the 217 newton-meter transmission.

Results of these tests supported the development of a range of flat belt power drives. The 25 kw, 2.3:1 speed ratio range continuously variable front end accessory drive (CVAD) has licensed for cars and light trucks. It has undergone extensive development. A 2:1 speed ratio range supercharger drive operates by the centrifugal force of the belt drive elements.

Department of Energy has supported the design and testing of a 100 meter per second 2:1 speed ratio range 75,000 rpm turbine to diesel crankshaft drive. This fuel saving drive targets long haul truck engines.

Several novel tensioner designs provided actuation of the CVAD. This allowed a narrow, reactive, variable diameter, flat belt pulley mounted on the crankcase. A compact FEAD tensioner with variable viscous damping evolved from this design program.

Analysis/simulation programs are being developed to model the CVAD and CVT's. These programs address the steady state, transient and harmonic states of these flat belt systems.

This testing and development of Kevlar corded flat belt power drives has advanced the understanding of their capabilities. Many decades ago, Vee-belts replaced most flat belt drives. The tide is starting to turn. Timing belts and the polyvee belts are close cousins of the flat belt. It is time to reconsider the simplicity and efficiency of flat belt systems for a wide range of applications.

## AUTOMATIC TENSIONERS FOR AUTOMOTIVE CAMSHAFT DRIVE SYSTEMS

Vincenzo Macchiarulo, Director, Automotive Division  
and  
Melvin D. Gayer, Chief Engineer, Automotive Systems  
Engineering, Pirelli Transmissions, Via  
Erasmus, 28, Chieti Scalo, Italy, 66013

Automatic tensioners for camshaft drives on automotive engines are fast becoming an important factor in the design of new drive systems. The use of automatic tensioners has been well accepted in the field of automotive accessory drives and has enabled enormous improvements in belt system durability. This, along with numerous other advantages, has created the desire to attain identical improvements and advantages in the camshaft drive system.

Where proper system design rules are followed concerning sufficient teeth in mesh, belt and pulley width, minimum pulley diameters, use of pulley flanges, proper pulley surface finish and hardness, system alignment, etc., it can be said that essentially all premature camshaft drive belt failures are tension related. These failures can consist of:

1. Unacceptable noise due to incorrect meshing of belt and sprocket (pulley) teeth from either insufficient or excess tension;
2. Premature failure due to damage of the belt tensile member and/or fabric abrasion in the land area during periods of extremely high tension;
3. Tooth shear resulting from moderately low tension;
4. Tooth jump resulting from extremely low tension.

In a majority of today's overhead cam engines the procedure for tensioning the drive belt involves the use of some type of spring loaded mechanism to provide a known force to the tensioning idler pulley. This pulley is then locked in place. From this point in time, the tension on the belt continually changes throughout the life of the belt. Not only is the belt subjected to tension levels due to engine temperature changes, but there exists a wide range of installation tensions on most production engines. To prevent exposing the belt to this full range of tensions which can result in high bearing loads, unacceptable noise,

premature belt destruction, less than acceptable mean belt life, and total overall insufficient system durability, automatic tensioners are being validated.

Known advantages for automatically tensioned systems:

1. Normalization of the distribution curve of installation tensions;
2. Enables installation tension at desired operating tension;
3. Some designs enable a lower level of operating tension;
4. Enables tension to be controlled at a noise free level;
5. Automatically compensates for thermal expansion;
6. Maintains proper tension throughout the life of the belt;
7. Improves drive serviceability;
8. Enables 160,000 Km belt system durability.

Known disadvantages:

1. Results in an initial overall system cost;
2. Results in an overall system weight increase;
3. Usually required additional space for packaging.

Two basic types of automatic tensioners for camshaft drives are in existence today. These are:

1. Mechanical tensioners utilizing torsional springs to supply force with little or no controllable damping;
2. Hydraulic tensioners which utilize compression springs to supply force with controllable levels of essentially one-way damping.

These two types of automatic tensioners are extremely different in their design and overall function. Test data exists on both gasoline and diesel engines comparing the results. This data, along with design features of each type, will be presented which will show the advantages of each design and basis for selection of the type to be used on a specific engine.

## TRANSIENT VIBRATIONS OF A CONVEYOR BELT

Dr. Pedro Saavedra G.  
Facultad de Ingeniería  
Casilla 53-C  
Concepción-CHILE

M. SC. Osvaldo Amigo R.  
Depto. Ingeniería Mecánica  
Casilla 5-C  
Concepción-CHILE

### ABSTRACT

Conventional analytic methods of evaluating the conveyor's starting and stopping actions treat the system as a rigid-body, without elastic content. The transient force is then computed by superimposing the acceleration or deceleration force of masses to the steady - state force. Treatment of this method is given in belt engineering standards: CEMA (1979), GOODYEAR (1975), DIN (1982).

These standards consider high operating factor of safety (f.o.s.) which are considered to be necessary to overcome transient stresses in the belt during starting and stopping. A reduction in the f.o.s. can be achieved calculating the true stress generated in the transient operations of the belt.

This paper presents a close look at two methods presently used for calculating belt transient stress: 1) Stress calculation from the resolution of wave equation 2) Stress calculation from belt velocity measurement. In the first method the motion equations are presented using a modelation used by Harrison (1). These equations are resolved by the finite difference, finite elements



and analitical methods. In the second method the velocity of the conveyor belt during the starting and stopping period is measured. The transient stress in the belt are calculated using the experimentally derived value of in-plane belt acceleration.

The previous methods are illustrated with the dynamic analysis of a long conveyor belt existing at a Chilean industry. The peak stresses in the belt conveyor are determined during starting, stopping and aborted stopping. The peak loads occur at highest tension location of the system, and these peak belt tensions occur for the fully loaded belt.

We concluded that the calculation of transient stress in conveyor belts permits a reduction of the high operating factor of safety used by the engineering standards and a reduction the high cost of the most belt conveyor installations.

#### REFERENCES.

- 1 Harrison A. Criteria for minimising transient stress in conveyor belts. International Material Handling Conference. South-Africa. May 1983.

## TORSIONAL VIBRATIONS OF POWER TRANSMISSION BELTS

Serge ABRATE, Ph.D.  
Department of Mechanical and Aerospace Engineering  
and Engineering Mechanics  
University of Missouri-Rolla  
Rolla, MO 65401

The vibration of power transmission belts and belt drives and more generally the vibration of axially has been studied extensively [1,2]. Most publications concentrate of transverse vibration of the belt which is modeled as a moving string or a moving beam. Another type of studies considers torsional motion of the pulleys; the entire drive being viewed as a set rotational inertias coupled by springs accounting for the axial elasticity of the belt. Fawcett [3] pointed out that this type of vibration is often improperly called torsional belt vibration.

In this investigation, torsion of the belt itself is considered. In this type of motion, the belt cross-section rotates about its longitudinal axis. While some investigators mention their existence, torsional belt vibrations have largely been ignored. Here, a model for analyzing vibrations and dynamic stability is presented. A simple inexpensive test is proposed for determining the torsional rigidity and results are given for typical automotive belts.

First the equation of motion for a stationary belt subjected to initial tension is derived from first principles. The torsional rigidity is shown to consist of a term depending of cross-sectional shape and material properties and another term which increases with initial tension. Simple expressions are obtained to determine the influence of the governing parameters on the torsional rigidity, with two parameters to be determined experimentally for a given specimen. The equation of motion for the moving string is similar to that of the moving string model for transverse vibration. Therefore, torsional belt vibrations can be analyzed using the analytical or numerical methods developed for moving string problems once the torsional rigidity of the belt is known.

A simple apparatus was designed and built to determine the torsional rigidity of the belt. The basic principle behind this test is to observe the variation in the fundamental natural frequency of a belt segment as its length  $L$  and the initial tension  $T$  increase. In order to lower the frequencies to be measured, a rectangular aluminum bar is attached at midspan, normal to the axis of the belt. The inertia of the belt itself can be neglected when compared to the inertia of the bar. The oscillations of the bar are sensed by a photocell and plotted using a strip chart recorder. Free vibrations of the system are recorded as the system is released from an initial position. The natural frequencies of the system are directly obtained from the charts and repeating the test for different combination of span length and initial tension, the two unknown parameters in the constitutive equations are obtained.

While originally designed to simply measure the torsional rigidity, these tests also indicated that a significant amount of damping is also present during torsional vibrations. This is evidenced by the strong exponential amplitude decay recorded during free vibration tests. The envelope of the free vibration decay curve was corrected to account for the strong non-linear characteristic of the sensor. Then a least square curve fit procedure was used to determine the appropriate damping coefficients. Results are presented for poly-V belts currently in use in automotive drives.

Analyses of torsional vibrations under periodic excitation including damping effects are presented. Dynamic stability considering periodic tension variations are also considered.

#### ACKNOWLEDGEMENTS:

Partial support from the Goodyear Tire and Rubber Co. is gratefully acknowledged.

#### REFERENCES

- 1- S. Abrate, "Vibration of a Moving Belt," Proc. of the First Int. Applied Mechanical System Design Conf., Nashville, TN, June 12-14, 1989
- 2- S. Abrate, "Vibrations of Belts and Belts Drives," submitted for publication
- 3- Fawcett J.W., "Chain and Belt Drives - A Review," The Shock and Vibration Digest, Vol 13, No 5, pp 5-12, 1981

**INVESTIGATING THE FEASIBILITY OF USING TLC TO MEASURE THE EFFECT  
OF VIBRATION ON TEMPERATURE AND HEAT TRANSFER RATE FROM A  
HORIZONTAL CYLINDER**

**SAID DINI  
Associate Professor  
Mechanical Engineering Department  
Western New England College  
Springfield, MA 01119**

This work is aimed at developing a technique for measuring surface temperature and heat transfer rate for a vibrating specimen. The vibrational heat transfer coefficient if predicted accurately could benefit many commercial and industrial applications. For example detailed knowledge of temperature distribution and accurate flux patterns can often be of critical importance in evaluating the performance of electronic engine controls mounted on the nacelle of jet engines.

Thermochromic liquid crystals (TLC), as their name implies, react to changes in temperature by changing color. The materials show color change by selectively reflecting incident white light. Most mixtures turn from colorless to red at low temperature, and pass through other colors of visible spectrum before turning colorless again at higher temperature. The color changes are reversible, and on cooling the color change sequence is reversed.

The liquid crystal was used to paint two aluminum cylinders of one inch diameter. The surfaces were thoroughly cleaned using chloroform to remove all dirt, grease and finger prints. A water based paint was used to coat the surface of the cylinders black. The TLC coating was sprayed through a compressed gas sprayer to a wet-film thickness of about 10 microns. The coating was built up to about 40-microns by spraying a number of coats, and drying between each. Drying took about 35 minutes.

Six thermocouples were connected to each cylinder, three on one side (top, center, and the bottom) and the other three on the opposite side of the cylinder. The cylinder was mounted to a shaker table (Figure 1). The shaker table is part of a TRIG-TK shaker table system. The system consisted of a compressor, vibration monitor, sweep generator, power supply, and a shaker table. An extension arm was designed to connect the cylinder to the shaker system away from the table and out into the open air to allow free flow of air around the cylinder. An accelerometer was bolted to the extension arm next to the cylinder to measure the frequency and the g force in each run.

An insulated high temperature water container was used to provide water at about 113°F to the cylinder. Hot water was circulated using a water pump. A powerstat controlled the speed of the pump (Figure 2). A flow restriction valve was installed at the inlet of the container to adjust the mass flow rate. When the system achieved steady state condition the pump was turned on and each of the six thermocouple readings were recorded. Once the digital readout indicated that the surface temperatures were close to that of the liquid crystal lower temperature limit, a video camera and a 35 mm camera were used to capture the changes in the color of the liquid crystal.

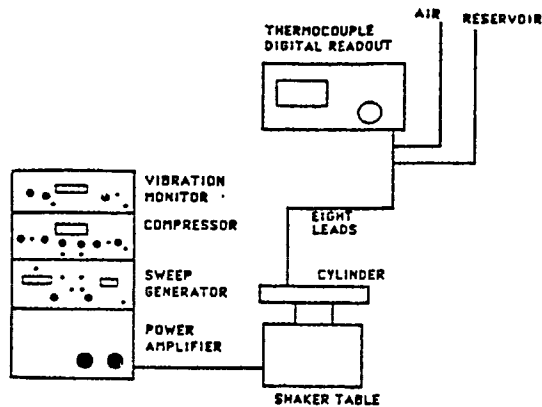


**Figure 1** Schematic diagram of the vibration test system.

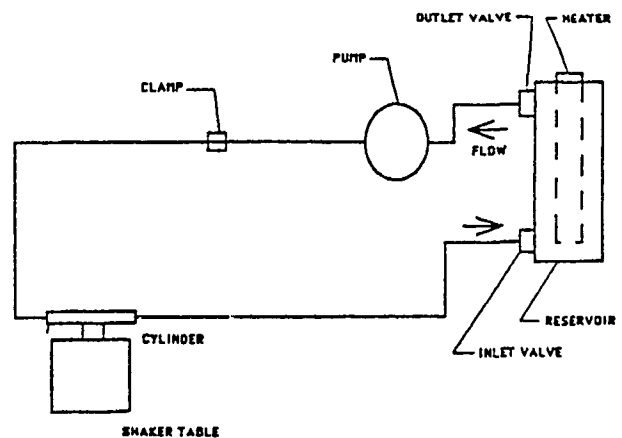


**Figure 2** Schematic diagram of the hot water loop.

Visual inspection and analysis of the data indicated that maximum heat transfer rate occurs at the bottom followed by the sides and the top of the cylinder regardless of vibration. The results compare favorably with published experimental data. It appears that with some improvement on the experimental set up this technique could be useful in the determination of the surface temperature for vibrating and non-vibrating specimens.

# A nonlinear damping model for plunger mechanisms

George I. Pantazopoulos<sup>†</sup> and Theodosios Korakianitis<sup>‡</sup>

Department of Mechanical Engineering,  
Washington University,  
Campus box 1185,  
One Brookings Drive,  
St. Louis, MO 63130

**Introduction:** A plunger mechanism consists basically of two parts (see fig. 1): a tappet body which is the external part of the mechanism; and a moving plunger inside the tappet. An analytical model for the damping coefficient of a plunger mechanism is presented. Geometric complexity of the mechanism introduces non linear effects on the damping forces. Such mechanisms are used in automotive valve trains as hydraulic lifters. The complexity of the dynamic behavior of such mechanisms, and the importance of an analytical model for these investigations, has been proven by experimental investigations [1].

**Analytic model:** The basic operation of the mechanism consists of two phases: compression; and expansion. During compression oil is forced through the gap between the plunger and the tappet; and during expansion oil flows through the check valve ball to refill the high pressure chamber. The damping forces acting on the plunger (the moving part of the mechanism) are due to the oil flow through the gap between the plunger and the tappet. Considering the configuration shown in figure 2, the actual length of the oil passage is neither the actual length of the plunger nor the actual length of the tappet. The whole length of the passage is divided into two parts.

## (a) Part 1:

This is of length  $L_1$ , where  $L_1(\Delta X) = L_p$  when  $0 \leq \Delta X \leq \Delta/2$ , and  $L_1(\Delta X) = (L_p + \Delta/2) - \Delta X$  when  $\Delta/2 < \Delta X \leq \Delta$ . In the above  $\Delta X = X_{plunger} - X_{tappet}$ . In this part there is always a thin film of lubricant between the plunger and the tappet. Since the length of the passage is much larger than its height, the damping forces acting on the plunger can be found considering Couette flow. The velocity profile is given by:

$$u(y) = U_{p,t} \frac{y}{h} \quad (1)$$

where  $U_{p,t}$  is the plunger-tappet relative velocity. The only damping force acting on the plunger is the viscous force given by:

$$F_v(\Delta X) = 2\pi R_p \mu L_1(\Delta X) \left. \frac{du}{dy} \right|_{y=h} = C_v(\Delta X) U_{p,t} \quad (2)$$

where  $C_v(\Delta X) = 2\pi \mu R_p L_1(\Delta X)/h$  is the equivalent damping coefficient.

## (b) Part 2:

This is of length  $L_2$ , where  $L_2(\Delta X) = L_t$  when  $0 \leq \Delta X \leq \Delta/2$ , and  $L_2(\Delta X) = (L_t + \Delta/2) - \Delta X$  when  $\Delta/2 < \Delta X \leq \Delta$ .

To find the forces acting on the plunger due to oil flow through this part of the gap we need to consider the two phases of the plunger operation: During compression we

<sup>†</sup> Graduate Research Assistant

<sup>‡</sup> Assistant Professor

use Couette flow to find the velocity profile given by:

$$u(y) = U_{p,t} \frac{y}{h} + \frac{1}{2\mu} \left[ \frac{dp}{dx} \right] y(y-h) \quad (3)$$

Applying continuity we find that:

$$\frac{dp}{dz} = - \frac{6\mu U_{p,t} (R_p + h)}{h^3} \quad (4)$$

Therefore the force due to viscous drag on the plunger surface is

$$F_v(\Delta X) = 2\pi R_p \mu L_2(\Delta X) \left| \frac{du}{dy} \right|_{y=h} = C_v(\Delta X) U_{p,t} \quad (5)$$

where  $C_v(\Delta X) = 2\pi\mu R_p L_2(\Delta X)(3R_p + 4h)/h^2$  is the equivalent damping coefficient.

The force due to pressure difference is

$$F_p(\Delta X) = \pi R_p^2 L_2(\Delta X) \left| \frac{du}{dy} \right|_{y=h} = C_p(\Delta X) U_{p,t} \quad (6)$$

where  $C_p(\Delta X) = 6\pi\mu R_p^2 L_2(\Delta X)(R_p + h)/h^3$  is the equivalent damping coefficient.

During expansion there is only a thin film of oil, therefore the solution is the same as for part 1, and equations (2) and (3) can be applied for the determination of the equivalent damping coefficient.

**Numerical solution:** All the above results have been implemented in a computer model to give the dynamic behavior of a plunger mechanism when the tappet is actuated by a cam on its base. The model resembles the actual mechanism used in valve trains. Because of the nonlinear damping coefficient and the large differences between the values of the damping factors at the compression and the expansion phases, a numerical scheme was used to integrate the dynamic equations of motion and to give the results shown in fig. 4.

**Acknowledgements:** This work was performed under sponsorship by the Department of Mechanical Engineering and C-K Engineering, Inc.

#### Reference and Bibliography:

- (1) P. Kreuter and G. Maas (1987). "Influence of Hydraulic Valve Lash Adjusters on the Dynamic Behavior of Valve Trains", SAE paper 870086, Feb.
- (2) F. M. White (1974). "Viscous Fluid Flow", McGraw-Hill.

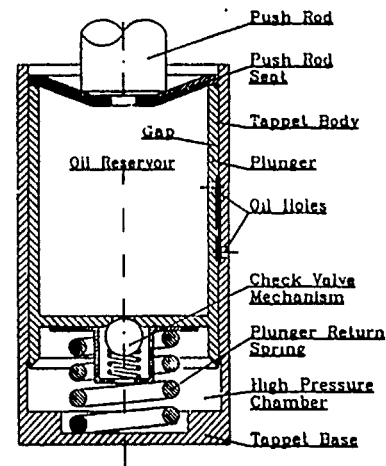


Figure 1: Typical plunger mechanism

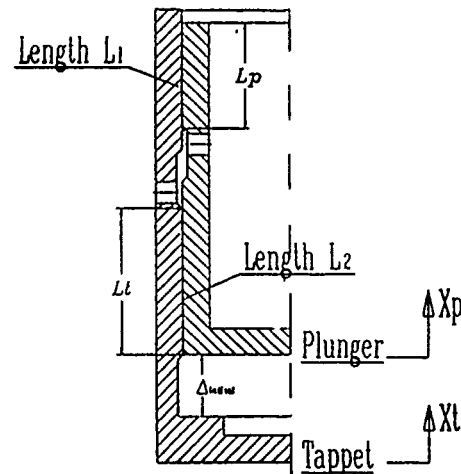


Figure 2: Typical oil-passage configuration

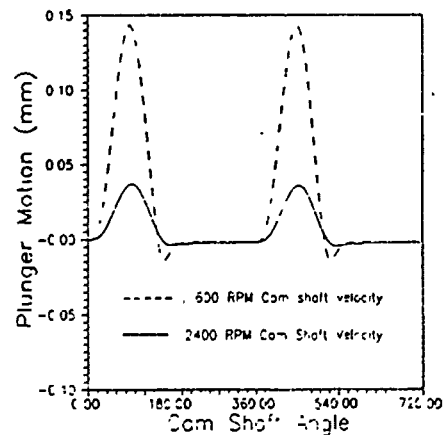


Figure 3: An example of the dynamic response of the plunger with nonlinear damping coefficients

# NONAXISYMMETRIC HEAT TRANSFER MEASUREMENT ON A ROTATING DISK USING LIQUID CRYSTALS AND COMPUTER VISION

Y.W. Kim and D.E. Metzger, Mechanical and Aerospace Engineering Department  
Arizona State University, Tempe, Arizona 85287-6106

**Introduction** The acquisition of local heat transfer information on rotating disks historically has been slow because of the expense and complexity involved in making heat transfer measurements on rotating surfaces. Conventionally, such measurements involve mounting sensors and heaters on the disk surface, and transmitting information from and to the rotating apparatus through slip rings. Even then, the heat transfer information acquired is usually in the form of averages over all or part of the disk. In the measurements of the present study, very localized convection rates are measured using thermochromic liquid crystal (TLC) surface coatings together with a thermal transient procedure. Encapsulated TLCs are sprayed directly onto the disk surface and their response is processed during the transient with an automated computer vision system. Local heat transfer rates are calculated from the transient response of the test surface, as determined by color display from the thin coating. Recently very localized heat transfer results have been obtained for axisymmetric situations[1]. The present work extends the technique to non-axisymmetric situations so that variation in local heat transfer rates around disk surface features such as bolt heads can be determined in both the radial and circumferential directions.

**Experimental Apparatus and Procedures** The apparatus used in the present study consists of a plane clear acrylic plastic test disk of 0.635 cm thickness and radius,  $r_0$ , of 10.160 cm. The disk is cantilevered from a twin bearing shaft, and a plane shroud is positioned 1.016 cm axially from the disk. Laboratory air is supplied through an electric heater through the shroud to the disk center for flow radially outward between disk and shroud.

In the technique used, detailed local convection coefficients over the test region of interest are deduced from measurements of transient surface temperature response to the supplied heated fluid. The classical short-time response for one-dimensional conduction is:

$$(t_s - t_i)/(t_r - t_i) = 1 - \exp(h^2 \alpha \theta / k^2) \cdot \operatorname{erfc}(h \sqrt{\alpha \theta} / k).$$

With properties,  $\alpha$ , of the disk known, the local convection coefficient,  $h$ , is inversely obtained from this equation through measurements of transient surface temperature,  $t_s$ , response and fluid temperature,  $t_r$ . In testing, application of a sharp step change in the fluid temperature is unnecessary. The reference temperature can be measured as function of time,  $\theta$ , with the above equation used as a fundamental solution to superpose the effect of a series of step changes in  $t_r(\theta)$  using superposition [2].

For the acrylic plastic test surface material used, the depth of heating into the disk over the time duration needed to complete the test is less than the disk thickness. In addition, departure from one-dimensionality because of finite lateral conduction in the disk is not expected to have a significant effect on the local surface temperature response for the surface heat transfer gradients anticipated [3].

In the technique used, the transient surface temperature information is provided by application of TLC coating material and a PC-based image processing system employing a frame grabber. The encapsulated coating is applied to the surface with an airbrush. The coating displays colors in response to temperature with red, green, and blue display values of 38.4°C, 39.8°C, and 43.5°C for the TCL used. The process is reversible and calibration remains unchanged for a large number of cycles under laboratory conditions.



A typical experimental run begins with heating of the supply air to a desired steady temperature while the test section is maintained at room temperature. A three-way ball diverter valve is used to route the heated air away from the test section until the air temperature reaches a preselected value indicated by a monitoring sensor in the diversion line. The heated air is then suddenly routed to the test section, and local color information from the TLC coating is captured by a color video camera and digitized pixel-by-pixel. The frame grabber compares to a pre-set threshold corresponding to the calibrated color intensity. For axisymmetric situations, the coated surface is continuously illuminated, and all circumferential locations contribute to the color display at any radius. The outcome of the image digitization process is a pixel time-temperature matrix covering the entire test region monitored by the video camera. This information, together with the transient reference temperature data, is sufficient for high resolution determination of local  $h$  values using the given equation and superposition. Uncertainties in  $h$  are estimated to be  $\pm 10$  percent. Further details of the procedures are given in the references.

For the non-axisymmetric measurements of the present work, a technique was developed that uses stroboscopic illumination of the rotating test surface to capture variations in the liquid crystal display in both the radial and circumferential directions. Special attention was required for problems associated with synchronization of the video camera and strobe. These problems were overcome by adding a sorting algorithm into the frame grabber assembler program, so that only illuminated frames are processed.

**Results** Eight evenly-spaced balsa-wood 1.27 cm diameter cylinders, 0.64 cm high, were glued to the test disk at a radius,  $r$ , of 3.81 cm to simulate the protrusion of boltheads from the disk surface. For the results shown in the figure, the disk was rotated at  $\omega$  and air was supplied at rate,  $Q$ , to produce the flow Reynolds number,  $Q/2\pi r\nu$ , and rotational Reynolds number,  $\omega r_0^2/\nu$ , shown. Figure 1 shows, as Nusselt number,  $Nu$ , (non-dimensional  $h$ ) variation with radius along radial lines on either side of the protrusions, that heat transfer is significantly changed (symbols) from the measured values on a smooth disk (dashed line) only in the immediate vicinity of the protrusions.

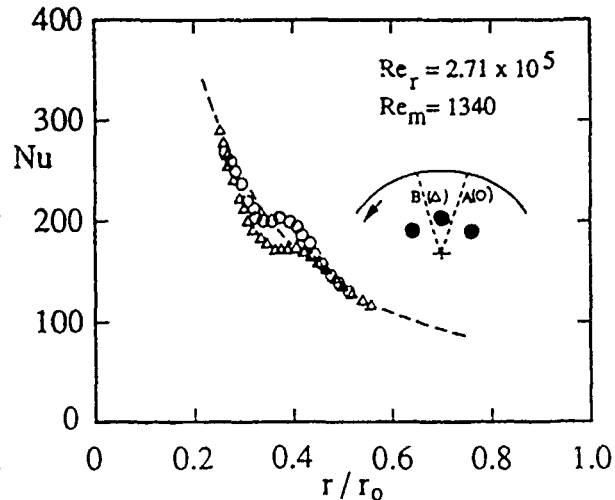


Figure 1  
Radial Variations in Nusselt Number

#### References

1. Metzger, D.E. and Kim, Y.W., "Experimental Modeling of Jet-Ring Turbine Disk Cooling," AIAA Paper 91-0343, Jan., 1991.
2. Larson, D.E., and Metzger, D.E., "Use of Fusion Point Surface Coatings for Local Convection Heat Transfer Measurements in Rectangular Channel Flows with 90-Deg Turns," Journal of Heat Transfer, Trans. ASME, 108, 48-54, 1986.
3. Vedula, R.P., Bickford, W. and Metzger, D.E., "Effects of Lateral and Anisotropic Conduction on Determination of Local Convection Heat Transfer Characteristics with Transient Tests and Surface Coatings," Collected Papers in Heat Transfer, ASME HTD-14, 21-27, 1988.

## Comparison of Solutions due to FEM, BEM and FDM in Heat Conduction Problems Using a Micro Computer

Katsuhiko Hojo, Hiroshi Masuda and Futoshi Shirai

Department of Mechanical Engineering  
Osaka Institute of Technology  
Omiya, Asahi-ku, Osaka, 535, Japan

As the technology of electronics progresses rapidly, the necessity and importance of numerical analysis have been increasing day by day. Numerical analysis methods as FEM, BEM and FDM are considered to be effective for both research workers and designers. For example, if designs in hot rolling, hot forging or casting are performed through the repeated examinations, a great deal of expense and labor would be required. So, simulations using a computer have been used very often lately because of the economy. And, the data obtained in the simulations have also been used for designs. But, the numerical analysis using a micro computer have the problems that CPU time and memory capacity are not enough in the case of complicated-shaped models. But, a micro computer is often used for various purposes because of the convenience and economy.

The goal of this study is to analyze numerically heat conduction problems using a micro computer and to compare the solutions due to FEM, BEM and FDM. With respect to both steady-state and unsteady-state heat conduction problems, the solutions due to the numerical methods are compared with a strict solution due to an analytical analysis in this study. The two-dimensional analysis model used in this study is a square plate model with four isothermal sides. The three-dimensional analysis model used in this study is a cube with six isothermal surfaces. With respect to the number of partition for numerical

computations, the time required for computations, the error due to computation and the propagation of the error, the solutions are examined in detail.

We will explain the characteristics of FEM, BEM and FDM for each of the analysis methods, and the application to the model.

# Multiaxial Fatigue Life Prediction of an SAE Axle Shaft

by

C.-C. Chu

Research Staff  
Rm. S-2046  
Scientific Research Lab  
Ford Motor Company  
Dearborn, MI 48121-2053

## Abstract

A multiaxial hardening model generalized from Mroz's yield surface field concept is used to obtain the stress states from rosette strain measurements at the notch root of an SAE axle shaft subjected to combined bending-torsion spectrum loading. With both the stress and strain histories completely determined, fatigue life prediction is made by using several fatigue damage parameters that have been proposed in the literature. They include simple stress amplitude, simple strain amplitude, the above with mean stress correction such as Smith-Watson-Topper parameter, shear strain amplitude with normal strain and/or stress correction such as Brown and Miller's, and plastic work. For each criterion different planes on which normal and shear dominance varies are examined. By comparing the life predictions with the observed ones, and by comparing the observed failure mechanisms with that implied by the individual criterion, the potential as well as the limitation of our current methodology for multiaxial fatigue analysis is addressed.

# ANALYSIS OF LINEAR AND NONLINEAR MOTION UNDER PIECEWISE CONSTANT FORCES

L. Dai Graduate student M.C. Singh Professor  
Department of Mechanical Engineering  
University of Calgary  
Calgary, Alberta, Canada

## INTRODUCTION

Since 1980's, the equations with arguments of form  $[t]$ , the greatest integer function of time  $t$ , especially the first-order differential equations in the form of

$$x'(t) = ax(t) + a_0 x([t]) + a_1 x([t] \pm 1), \quad (1)$$

have been studied for the solutions, existence and uniqueness of the solutions[1,2], as well as its oscillatory behaviour[3].

For the second-order differential equations, which are extremely important in dynamic problems such as oscillations under the piecewise constant forces, there is still a lack of systematic analysis of the problems and properties of the solutions. In Eq.(1), the variable  $x([t])$  varies piecewisely with the integral argument  $[t]$  which has two restrictions, 1)  $x([t])$  is constant in between the integers; 2)  $[t]$  is finite with a unit constant time segment no matter how small the unit of  $t$  is chosen.

The present paper studies the motion of the dynamic systems subjected to a displacement related piecewise constant force  $F(x([t]))$  and analyzes the oscillatory or asymptotic properties of the motion with assistance of the matrix theory. According to an argument  $[Nt]/N$  introduced by the authors, the phenomena of dynamics involving the force  $F(x([t]))$  that have arbitrary value of segment (instead of a unit) can be analyzed, and the discontinuous force  $F(x([t]))$  can now be related to the continuous force in the form of  $F(x(t))$ . Therefore, the present technique can be considered as a novel theoretical and numerical approach in solving the initial value problems of dynamics.

## EQUATION OF MOTION AND ITS SOLUTION

Consider a spring-mass system subjected to a force  $F = Ax([t])$ , such that

$$m\ddot{x}(t) + c\dot{x}(t) + kx(t) = Ax([t]) \quad (2)$$

with initial conditions of  $x(0)=c_0$  and  $\dot{x}(0)=d_0$ , mass  $m$ , damping coefficient  $c$ , parameter  $A$ , spring constant  $k$  and the unknown function  $x(t)$ . According to a recursive procedure and considering the conditions of continuity for  $x(t)$  and  $\dot{x}(t)$  at  $t=[t]$ , the complete solution of Eq.(2) on  $t \in [0, \infty)$  can be expressed as

$$x(t) = e^{-\theta t} \left[ \left(1 - \frac{A}{k}\right) [\cos(\xi t - \xi[t]) + \frac{\theta}{\xi} \sin(\xi t - \xi[t])] + \frac{A}{k} e^{-\theta(t-[t])} \frac{1}{\xi} \sin(\xi t - \xi[t]) \right] D_1, \quad (3)$$

in which  $k/m > c^2/4m^2$ ,  $\theta = c/2m$ ,  $\xi = (k/m - c^2/4m^2)^{1/2}$ , and

$$D_1 = \Gamma^{(1)} \begin{bmatrix} c_0 \\ d_0 \end{bmatrix} = \begin{bmatrix} (1-A/k)[\cos\xi + (\theta\sin\xi)/\xi] + (Ae^\theta)/k & \sin\xi/\xi \\ -(1-A/k)[(\theta^2/\xi + \xi)\sin\xi] & \cos\xi - (\theta\sin\xi)/\xi \end{bmatrix} \begin{bmatrix} c_0 \\ d_0 \end{bmatrix}.$$

Since the exponential matrix can be indicated as  $\Gamma^{(1)} = P D^{(1)} P^{-1}$  where  $P$  is a set of linearly independent eigenvectors for all the corresponding eigenvalues of  $\Gamma$ ,  $D$  is a diagonal matrix of the eigenvalues, we may easily analyze the oscillatory properties of the motion. Graphical and numerical results for the solution show entirely

different characteristics from the vibration under continuous forces  $F=F(x(t))$ .

#### LIMITING CASES OF THE SOLUTION

It can be proved that  $([Nt]/N)$  is equal to  $t$  as  $N \rightarrow \infty$ , where  $N$  is a real positive coefficient. Taking the new argument  $[Nt]/N$  to replace the  $[t]$  in Eq.(2), a unit time interval is divided into  $N$  segments on  $N \in [1, \infty)$ . We now may take a limiting case as  $N \rightarrow \infty$  for the motion under the forces  $F(x([t]))$ , therefore, the gap between the motion with the finite piecewise constant forces  $F(x([t]))$  and the one under continuous forces  $F(x(t))$  such as spring forces can now be filled up. For sake of clarity, consider a simple case

$$\ddot{x}(t) + \beta x\left(\frac{[Nt]}{N}\right) = 0. \quad (4)$$

With the same initial conditions as Eq.(2) and  $\beta = -A/m$ , the corresponding solution can be written as

$$x(t) = \begin{bmatrix} 1 - \frac{\beta}{2}\left(t - \frac{[Nt]}{N}\right)^2 & t - \frac{[Nt]}{N} \end{bmatrix} \begin{bmatrix} 1 - \beta/2N^2 & 1/N \\ -\beta/N & 1 \end{bmatrix}^{[Nt]} \begin{bmatrix} c_0 \\ d_0 \end{bmatrix}. \quad (5)$$

Using the eigenvectors and eigenvalues similar as in Eq.(3), a limiting case as  $N \rightarrow \infty$  is taken with result as

$$x(t) = \begin{bmatrix} \cos(\sqrt{\beta}t) & \beta^{-1/2}\sin(\sqrt{\beta}t) \\ 0 & 0 \end{bmatrix} \begin{bmatrix} c_0 \\ d_0 \end{bmatrix} \quad (6)$$

which is identical to the classical solution as  $\beta x = \beta x(t)$  in Eq.(4). The time segment will be expanded by  $1/N$  of time unit if  $N$  is on  $0 < N < 1$ . A limiting case as  $[Nt] \rightarrow 0$ , ( $N < 1/t$ ), can also be taken with the expected result identical to the corresponding classical solution.

#### NUMERICAL SIMULATION OF NONLINEAR VIBRATION

The method employing the parametric piecewise constant argument  $[Nt]/N$  can be used in solving the vibration problems governed by equation of motion

$$\ddot{x}(t) + a_1 \dot{x}(t) + a_2 x(t) = f(t), \quad (7)$$

where  $a_1$  and  $a_2$  may not be constants. In solving those linear or quasi-linear problems, one (or a few) of the terms can be chosen to be replaced by a proper form of a discontinuous function of the argument  $[Nt]/N$ , therefore, the method discussed in section two can be used for obtaining the solutions. Theoretically, the exact solution for the vibration equation can be obtained when taking a limiting case as  $N \rightarrow \infty$ . For nonlinear vibration problems such as the vibration of a system with a hardening spring expressed by equation of motion[4]:

$$\ddot{x}(t) + \omega^2 x(t) = \beta x^3(t) \quad (8)$$

can be analogically solved by the present technique. Replacing the nonlinear term  $\beta x^3(t)$  by  $\beta x^3([Nt]/N)$ , via a procedure discussed previously, its solution can be gained. Due to the properties of the integer argument  $[Nt]$ , it is convenient in using the present technique in a computer program. The numerical solution calculated ( $N=40$ ) shows very good convergency and matches well with the known numerical results[4]. As  $N \rightarrow \infty$ , theoretically, the corresponding solution will be the exact solution for the nonlinear equation (8).

#### REFERENCES

1. Cooke, Kenneth L. and Wiener, Joseph, "Retarded Differential Equations with Piecewise Constant Delays," *Journal of Mathematical Analysis and Applications*, Vol.99, pp 265-297, 1984.
2. Cooke, Kenneth L. and Wiener, Joseph, "An Equation Alternately of Retarded and Advanced Type," *Proceedings of the American Mathematical Society*, Vol.99, pp 726-732, 1987.
3. Aftabizadeh, A.R. and Wiener, Joseph, "Oscillatory Properties of First Order Linear Functional Differential Equations," *Applicable Analysis*, Vol.20, pp 165-187, 1985.
4. Timoshenko, Young, D.H. and Weaver, Jr., W., "Vibration Problems in Engineering," John Wiley & Sons, Inc., New York, 1974.

## Entropy Analysis of Thermal Systems

S.A. Fartaj, C.L. Huang and D.L. Fenton  
Department of Mechanical Engineering  
Durland Hall  
Kansas State University  
Manhattan, Kansas 66506

This study investigates the applicability of the the Second Law of Thermodynamics using an entropy balance to analyze and design thermal systems. The development of thermodynamics incorporates a parameter called "effectiveness" that characterizes how well a device or component uses its input energy. The entropy balance technique determines thermodynamic effectiveness of components and the complete system by quantitative assessment of the irreversibilities associated with the processes involved. Thus, adjustments to the components can be made in order to decrease the irreversibility of those units. Ultimately, an optimum thermal system is identified where "life-cycle-cost" is minimized. The central focus of this project was to develop such a procedure based on the physical laws required to describe a system's behavior, namely, the first and second thermodynamic law analysis by the entropy balance technique.

The entropy balance procedure is capable of determining the performance of a thermal system, and identifying the irreversibilities concerned with each process in the system. As a demonstration, the case of the single stage absorption heat transformer cycle is shown in the following figure and investigated. The following resultant expressions for heat input ( $Q_{in}$ ), Coefficient of Performance (COP), and effectiveness (EFEC) have been derived from the First and Second Law of Thermodynamics, and the results are:

$$Q_{in} = Q_a \frac{t_m(t_h - t_l)}{t_h(t_m - t_l)} + \frac{t_l t_m}{(t_m - t_l)} \Sigma \delta S_i \quad (1)$$

$$COP = \frac{Q_a}{Q_{in}} = \frac{t_h(t_m - t_l)}{t_m(t_h - t_l)} - \frac{t_h t_l}{Q_{in}(t_h - t_l)} \Sigma \delta S_i \quad (2)$$

$$EFEC = \frac{COP}{COP_{rev}} = 1 - \frac{t_m t_l}{Q_{in}(t_m - t_l)} \Sigma \delta S_i \quad (3)$$

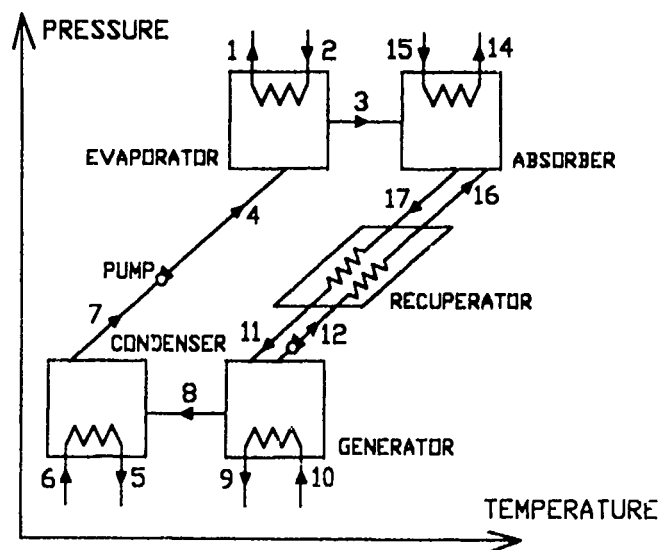
Where  $t_l$  and  $t_h$  are the low and high temperature corresponding to that of the heat source, and  $t_m$  is the intermediate temperature corresponding to the heat sink. The  $\delta S_i$  is the irreversible entropy increase in  $i$ -th component.

Results obtained from this analysis are compared with those obtained by traditional techniques of energy and exergy analysis which have been followed widely. Furthermore, these results are compared with experimental data taken from measurements on lithium bromide-water absorption cycles, developed and tested at Oak Ridge National Laboratory.

The conclusion drawn is that the entropy analysis yields the same information as are conveyed by analyses of the energy and exergy techniques. Furthermore, the advantage of the entropy analysis is that it shows the influence of irreversibilities of individual component on the coefficient of performance, in particular, to the process properties. Also, in contrast to exergy balances, the entropy balances yield design indexes by which the effectiveness of a process can be determined based on the temperature of process rather than on undefined environmental temperature ( $T_0$ ).

Therefore, the entropy balance technique is capable of presenting the overall distribution of the heat input by displaying the additional heat supplied to overcome each components irreversibility free of any undefined parameter. Furthermore, this analysis reveals the effect each component has in deteriorating the COP and effectiveness of the system unambiguously.

In order to do analysis on a given thermal system the entropy balance only requires the entropy data of working fluids, as compare to exergy balance which requires the enthalpy data also. Unfortunately, the entropy data of various fluids are not readily available. However, once entropy data is established for other working fluids the same technique will be effective in analyzing those systems. The experience gained from this study will improve the performance of thermal systems and generate cost-effective alternatives to currently employed systems.





# Experimental and Analytical Study of Tens on Field in Web of Plate Girder under Shear

Fan Zuyao  
Shanghai Jiao Tong University  
Shanghai, China

Shen Jiazhen  
Shanghai Maritime University  
Shanghai, China

## 1. Introduction

The thin walled plate girders and box girders are most widely used in steel structures. The stability of the thin web under shear, especially in the high web, has also received more and more attention. When the shear stress in web exceeds the critical value, the phenomenon of tension field was observed in experiments. This is a problem of the postbuckling behavior. In this paper, recent researches on postbuckling in web of plate girder and box girder under shear are reviewed and some important results of theoretical and experimental study on the tension field of web are presented.

## 2. The collapse mode and calculating formula of tension field

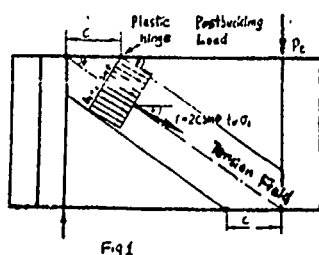
The web under uniform shear stress from the beginning to collapse has three states: critical state, postbuckling state and ultimate state. According to the above three states, the ultimate load  $P_u$  can be divided into critical load  $P_{cr}$  and postbuckling load  $P_t$ .  $P_{cr}$  is carried by the simply supported web panel and  $P_t$  is carried by the tension band.

Using the condition of equilibrium, the calculating formula of the ultimate load is obtained as follows (Fig. 1)

$$P_u = P_{cr} + P_t = \tau_{cr} t_w h_w + 2c t_w \sigma_t \sin \theta \sin \phi$$

where,

- $\tau_{cr}$  the critical shear stress;
- $h_w, t_w$  the web depth and the web thickness respectively;
- $c$  the distance from the plastic hinge in flange to the vertical stiffeners;
- $\sigma_t$  the tension field stress in web given by Von-Mises Criterion;
- $\theta$  the angle of inclination of resultant of tension field stresses;
- $\phi$  the angle of inclination of diagonal of a web panel.



## 3. The characteristics of tension field

From The above calculating formula of ultimate load and the analyses of experiment results, the developing process of tension field depends upon following main parameters which are described as follows:

### (1) The effective width of tension field

Many experiments have shown that the stress of tension field within the zone of the plastic hinge in flange can reach the yield stress. According to the characteristics of the stress distribution of tension field and the experimental data, the concept of effective width of tension field is presented, effective width  $b_e = 2c \sin \phi$ , it is an important parameter of the capacity of tension field. In which  $c = 5 \sqrt{I \alpha \lambda \frac{\sigma_{r,f}}{\sigma_{r,w}}}$  where

$I$  the moment of inertia of the flange;

$\alpha$  the aspect ratio of web panel  $\alpha = a/h_w$

the ratio of web thickness  $\lambda = h_w/t_w$

$\sigma_{r,f}$ ,  $\sigma_{r,w}$  the yield stress of the flange and the web, respectively.

### (2) The angle of inclination of the stress resultant of tension field

It is founded that the direction major stress of every point within the tension field varies with increasing of the load. Finally, in the case of the web panel:  $\alpha \geq 1$  closed to  $\theta = \phi$  and  $\alpha < 1$  closed to  $\theta = 45^\circ$  the experimental data compare well with the theoretical results.

### (3) The distribution and development of tension field

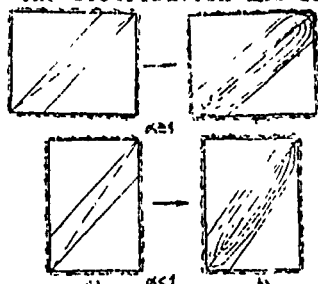


Fig 2

According to the experimental results, the distribution of  $\alpha \geq 1$  panel is different from that  $\alpha \leq 1$ . The distribution of the primary buckling is shown in Fig2a. With the increase of the load and the change of the waveform, the tension field extends gradually. When the load increases close to the load of collapse, the tension field is distributed on both sides of the diagonal (Fig.2b)

### 4. The comparison between the calculated values and the experiment results

To verify theoretical analyses, the postbuckling experiments of rectangular webs under shear have been made. We have calculated and tested ten specimens in Shanghai Jiao Tong University. The theoretical results are basically coincident with the experimental data (Fig. 3).

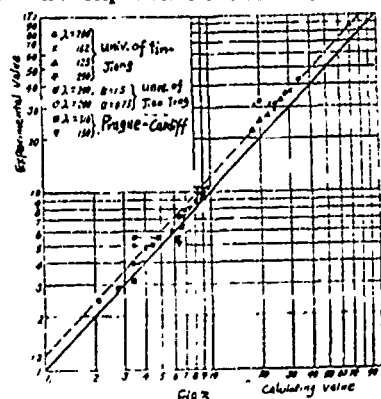


Fig 3

### 5. Conclusion

This paper has presented a collapse mode and a practical formula for calculating the ultimate load of web of plate girder under shear which is also suitable for various  $\lambda$  and  $\alpha$  of webs.

Based on the analyses of experimental results, the formula of effective width  $b$  of tension field and the position of plastic hinge  $C$  in flange are given. The angle of inclination  $\theta$  of stress resultant of tension field is comparison well with the experimental results.

### References

1. 'Design of Webs of Plate and Box Girders'. ECCS, 1978.
2. C.G. Salmon and J.E. Johnson, 'Steel Structure Design and Behavior', 1972.
3. K.C. Rockey and M. Skaland, 'the Ultimate Load Behavior of Plate Girders Loaded In Shear', The structural Engineer, Jan. 1972.

# The Dynamic Characteristics of Bridge Structure of Overhead Travelling Crane Using Transfer-Matrix Method

Fan Zujiao

Huang Zhitao

Shanghai Jiao Tong University, Shanghai, China

## 1. Introduction

The overhead travelling crane is a widely used hoisting equipment. With the development of industry, the higher requirements are demanded on its lifting weight, span of bridge structure, working speed and working property. Therefore it is necessary to study dynamic characteristics of bridge structure which are not only the most basic parameter but also one of the criterion for criticizing dynamic characteristic. In this paper, the natural frequencies and the modes of bridge structure of overhead travelling crane are calculated by using Transfer-Matrix Method. The influence of the stiffness of endbeam and of lifting wire on the natural frequencies are also considered. In order to check the accuracy of calculation, the experiments in many overhead travelling cranes have been tested. The results of calculation are good agreements with experiments. Base on the calculated and experimental analyses, various simplified formulas which are commonly used for dynamic calculations of natural frequency of bridge structure of overhead travelling crane in case of loading and unloading is suggested.

## 2. The Calculation of Dynamic Characteristics of Bridge Structure Using Transfer-Matrix Method

The bridge structure of the overhead travelling crane is a system with many degrees of freedom. To simplify calculation, the Transfer-Matrix Method is applied to analyze the natural frequencies and models of bridge structure. The Transfer-Matrix Method disparts the whole complex system to sub-systems which possess simple elastic characteristics and dynamic characteristics, then determines its natural frequencies according to the boundary conditions. This method is simple and suitable for computer calculating and its concept is clear. Using Transfer-Matrix Method, the 10 ton series of overhead travelling cranes are calculated in this paper. The results obtained from calculating are well coincident with experimental data.

## 3. The influence of Stiffness of endbeam and lifting wire on frequency

In simplified calculation, the influence of the stiffness of endbeam is neglected and the mainbeam of bridge structure is supposed simply supported. The results of calculation shows that the influence is small, so the simplification is permissive. But the influence of the stiffness of lifting wire on frequency must consider because the length of the wire changes in the lifting loads, hence its stiffness

changes correspondently. The increase of the stiffness will rise the frequency, its influence will be greater in large spans than in small spans.

#### 4. Discussion on Various Simplified Formulas

Satisfactory accuracy of bridge structure's dynamic characteristics can be obtained by using Transfer-Matrix Method. We shall compare the results by Transfer-Matrix Method and by other simplified formulas:

(1)  $f = \frac{1}{2\pi} \sqrt{\frac{K}{M}}$ , where  $K$  is stiffness of bridge structure,  $M$  is concentrated mass of beam. The beam supposed simply supported and the weight of lifting trolleys and stiffness of wire are neglected. This formula is suitable to the case of unloading.

(2)  $f = \frac{1}{2\pi} \sqrt{\frac{K}{M+M_0}}$ , the  $M$  of load is considered and the stiffness of lifting wire is supposed to be infinitely large. The results obtained by this formula will be higher.

(3)  $f = \frac{1}{2\pi} \sqrt{\frac{KK_1}{M_0(K+K_1)}}$ , the mass  $M$  of load and stiffness  $K$  of lifting wire are considered. The system is simplified to a spring-mass system with singular degree of freedom, its stiffness consists of the stiffness  $K$  and  $K_1$  in series, the mass of load is regarded as its mass. The frequency of this system is regarded as the frequency of the bridge structure.

(4)  $f = \frac{1}{2\pi} \sqrt{\frac{g}{(\lambda_0 + \gamma_0)(1 + \xi/(1 + \eta)^2)}}$ , where  $\xi = \frac{M}{M_0}$ ,  $\gamma = \frac{\lambda_0}{\gamma_0}$ ,  $\lambda_0$  is the static deformation of pulley block of lifting wire,  $\gamma$  is the static deflection of bridge structure in the middle point of span. The bridge structure and lifting wire are regarded as a spring in series and the two degrees of freedom is simplified to a singular degree of freedom. It considers not only the mass of bridge structure but also the load. The value in calculation is almost identical to that in experiments.

#### 5. Conclusion

(1) Transfer-Matrix Method is a simple and convenient method which is suitable to accurately calculate natural frequencies and normal method of bridge structure of overhead travelling crane.

(2) The influence of the stiffness of endbeam on natural frequencies is small, so the main beam can be simplified as a simply supported beam. The influence of the stiffness of lifting wire is bigger. We can not neglect it especially in small spans.

(3) The advanced simplified formulas  $f = \frac{1}{2\pi} \sqrt{\frac{K}{M}}$  is suitable to the case of unloading and  $f = \frac{1}{2\pi} \sqrt{\frac{g}{(\lambda_0 + \gamma_0)(1 + \xi/(1 + \eta)^2)}}$  suitable to the case of loading.

#### Reference

- [1] D.J. Haller 'Matrix Computer Method of Vibration Analyses', 1973.
- [2] W.T. Thomson 'Theor. of Vibration with Applications', 1980.
- [3] S.T. Zhu 'Calculation of Dynamic Stiffness of Overhead Travelling Crane's Hoisting and Conveying Machinery', 1980, 5.

# A NONLOCAL DAMAGE MODEL WITH AN ALE CODE FOR GROUND SHOCK AND CRATERING

Z. CHEN<sup>1</sup> and H.L. SCHREYER<sup>2</sup>

<sup>1</sup> Research Engineer, New Mexico Engineering Research Institute

<sup>2</sup> Professor, Department of Mechanical Engineering  
University of New Mexico  
Albuquerque, NM 87131

## SUMMARY

Several computer programs are now available for simulating cratering and ground shock phenomena due to explosive and nuclear events. The post-peak part of the constitutive models employed in these programs, however, has not been appropriately developed because of experimental, theoretical and computational obstacles associated with failure simulation so that an unrealistic energy dissipation is often predicted in numerical solutions. As an attempt to remedy this unpleasant feature in existing codes, AFTON 4.2, a typical set of Arbitrary-Lagrangian-Eulerian (ALE) finite difference codes for ground shock and cratering [Rudeen, 1988], is modified, and a nonlocal model based on continuum damage mechanics is proposed in this work to replace the original directional cracking model used in AFTON 4.2. One-dimensional examples are given to show that both computational efficiency and realistic failure patterns can be obtained for the post-peak structural responses. Extensions to two- and three-dimensional problems can be made.

From a micromechanical point of view, physical failures of engineering structures arise from two distinct modes of micro-structural changes: one is plastic flow and the other is the damaging or degradation of material properties. Plastic flow is the consequence of a dislocation process along preferred slip planes, as reflected through permanent deformation. Because the number of bonds between material particles is hardly altered during the slip process, the material stiffness remains insensitive to this mode of microstructural motion, and the change of strength is mainly characterized by strain hardening phenomena. On the other hand, the nucleation, growth and coalescence of microcracks and microvoids result in debonding between material particles, as reflected through the decrease or damage of material stiffness and strength. These two modes often interact and play different roles in ductile and brittle materials, and a structure is said to fail when macrocracks occur inside the localization zone of large deformation and propagate through it. For geological materials such as concrete, rock and soil which are of particular interest in ground shock and cratering problems, a constitutive model involving plastic strain hardening and damage softening can catch the essential feature of constitutive behaviors [Chen and Schreyer, 1990]. Recently, much research effort has been conducted to resolve theoretical arguments associated with softening accompanied by localization, to make clear the physical nature behind the evolution of localization zone, and to model the softening of material properties and localized failure modes. Although each approach proposed for softening problems has an appealing feature, this investigation will generalize previous work on theoretical and computational aspects of nonlocal strain-gradient plasticity models [Chen and Schreyer, 1987 and 1990; Schreyer and Chen, 1986], and develop a nonlocal strain-gradient damage model for which analytical solutions for one-dimensional damage softening with

localization can be obtained. As a result, a semi-analytical solution procedure can be constructed for softening problems of higher dimensions.

According to experimental observations that for quasi-brittle structures tensile cracks usually occur perpendicular to the maximum principal direction [Chen et al., 1990], a simple nonlocal damage model is defined in the principal space as follows:

$$f_i^d := \sigma_i - \sigma_i^L \left[ 1 - c_i^l (\varepsilon_i^d + N) \right]$$

$$\sigma_i = E^e (1 - I_i) \varepsilon_i$$

$$\varepsilon_i^d = \varepsilon_i - \varepsilon_i^e = \varepsilon_i - \frac{\sigma_i}{E^e}$$

where  $f_i^d$ ,  $\sigma_i$ ,  $\varepsilon_i$ ,  $\varepsilon_i^d$  and  $\varepsilon_i^e$  are the damage surface, stress, total strain, damage strain and elastic strain in the principal directions with positive principal values, respectively. The letter  $N$  denotes a nonlocal function of damage strain-gradient and the others are material constants. With the use of the procedure similar to that for nonlocal strain-gradient plasticity models [Schreyer, 1990], one-dimensional analytical field solutions can be obtained for damage softening with localization that are representative of the post-peak response of quasi-brittle structures. Since the analytical one-dimensional solutions are still valid in the principal space of stress in higher dimensions and the stress field is taken to be constant in each cell or element, the damage softening with localization along each direction can be captured by an analytical solution. Although the principal space of stress varies with the position, an approximation of localized deformation can be obtained within a cell or element which softens based on the nonlocal softening criterion. The contour enclosing the softened cells represents the localization zone. As the analytical solution between the total strain and stress fields is available, no elastic predictor and damage corrector are needed for strain-driven programs such as AFTON 4.2.

The proposed numerical approach for ground shock and cratering is robust and should also be of value for other codes of failure simulation, with the result that a realistic energy dissipation can be predicted in numerical solutions.

## REFERENCES

- Chen, Z., and Schreyer, H.L., 1987, "Simulation of Soil-Concrete Interfaces with Nonlocal Constitutive Models," Journal of Engineering Mechanics, Vol. 113(11), pp. 1665-1677.
- Chen, Z., and Schreyer, H.L., 1990, "A Numerical Solution Scheme for Softening Problems Involving Total Strain Control," Computers and Structures, Vol. 37(6), pp. 1043-1050.
- Chen, Z., and Schreyer, H.L., 1990, Formulation and Computational Aspects of Plasticity and Damage Models for Geological Materials with Emphasis on Concrete, SAND90-7102, Sandia National Laboratories, Albuquerque, New Mexico.
- Chen, Z., Rutland, G.A., Schreyer, H.L., and Wang, M.L., 1990, Experimental, Theoretical and Computational Investigations of Failure of Quasi-Brittle Structures, WL-TR-90-XX, Phillips Laboratory, Air Force Systems Command, KAFB, Albuquerque, New Mexico.
- Rudeen, D.K., 1988, AFTON 4.2, A Set of Arbitrary-Lagrangian-Eulerian Finite Difference Codes for Ground Shock and Cratering: A User's Guide, NMERI-WA11-17, New Mexico Engineering Research Institute, University of New Mexico, Albuquerque, New Mexico.
- Schreyer, H.L., and Chen, Z., 1986, "One Dimensional Softening with Localization," Journal of Applied Mechanics, Vol. 53, pp. 791-797.
- Schreyer, H.L., 1990, "Analytical Solutions for Nonlinear Strain-Gradient Softening and Localization," Journal of Applied Mechanics, Vol. 57, pp. 522-528.

# Long Discontinuous Fibers Toughening The Composites by Full or Partial Bridging of Cracks

Chao-Hsun Chen and Pao-Hwa Cheng  
Institute of Applied Mechanics  
National Taiwan University, Taipei Taiwan R.O.C.

## ABSTRACT

A complete solution is given for a fully or partially bridged straight crack in orthotropic elastic materials which may correspond to unidirectionally fiber-reinforced thermoplastic or thermosetting laminate. These orthotropic bodies which have three mutually perpendicular planes of material symmetry and the properties at any point are different in three mutually perpendicular directions. The unidirectional lamina has three mutually perpendicular planes of symmetry and is, therefore, orthotropic. The overall elastic moduli of these orthotropic composites are estimated by Mori-Tanaka's (1973) method. Followed Ting's (1988) by using new sum rules for Stroh formalism the governing equation of fiber-bridging cracks is formulated explicitly in real form as following. The straight crack is in terms of the superposition of dislocation density distribution and the bridging-force are linearly dependent on the crack-opening-displacement (Nemat-Nasser and Hori, 1987). The stiffness of the bridging materials may have an arbitrary variation along the crack, representing partially failed fibers or ligaments. The crack may have any orientation with respect to the axis of the material symmetry. The solution is explicit in terms of Chebychev polynomials and compared with complex-boundary element method. The mechanism of crack kinking is studied for an oblique partially or fully bridged, or unbridged crack in a macroscopically orthotropic elastic solid. The crack is assumed to grow in the matrix material (containing unbroken strong fibers) under local driving forces which are calculated on the basis of the overall anisotropic material response. The results of various fracture criteria are studied.

## REFERENCES

- Mori, T. and Tanaka, K. (1973) " Average Stress in Matrix and Average Elastic Energy of Materials with Mistfitting Inclusions," *ACTA Metal.* 21, pp.571-574.
- T.C.T. Ting (1988) " Line Forces and Dislocations in Anisotropic Elastic Composite Wedges and Spaces," *Phys. Stat. sol. (b)* 145, pp. 81-90, 1988.
- Siavouche Nemat-Nasser and Munco Hori (1987), " Toughening by Partial or Full Bridging of Cracks in Ceramics and Fiber Reinforced Composites," *Mechanics of Materials* 6, 1987, pp. 245-269.

## NONCLASSICAL PLASTICITY: CONTEXT AND CURRENT DEVELOPMENTS

Jinghong Fan

Department of Aerospace Engineering & Engineering Mechanics  
University of Cincinnati, Cincinnati, Ohio 45221-0070

The essential premises of the classical mathematical theory of plasticity (CP) are the assumptions of the a priori existence of a yield surface and of time-independent plasticity. To the extent that these two assumptions are mostly an idealization, one should be in a good position to develop alternative theories to CP. The contributions by Valanis, Bonder-Pardom, Hart, Krempl, this author and his co-workers, to name a few, take this direction. To investigate the relations and common problems of those different theories, this author recently proposed the classification of Nonclassical Plasticity (NCP). By definition, NCP encompassed all those theories which do not use the above two assumptions a priori. Since NCP is a more realistic theory, one of its predominate characteristics is that it will be more physically based or micromechanically based. In this paper, models for creep-plasticity interaction and nonproportional cyclic loading, given by this author and his co-workers Peng, Qing et al. (1991), are introduced to show this aspect. The common problems of NCP, such as its numerical implementation as well as general properties of NCP are also mentioned to distinguish them from those of CP.

### Creep-Plasticity Interaction

Creep-plasticity interaction is a technically very important and theoretically unsolved problem. If we take classical point of view, plasticity and creep are completely different since the former is time-independent and the later time-dependent. As reported by Krempl (1979), Yamada and Li (1973), et al., experimental results show some metals exhibit rate-sensitivity, creep, and relaxation at room temperature. To find the underlying mechanisms for creep-plasticity interaction, the experimental measurement of evolution of dislocation density given by Orlova (1973) and the measurement of internal stresses in power-law creep given by Takeuchi, et al. (1976) have been carefully examined. While both creep and plasticity are considered to be a thermally activated process in this model, a glide-plus-climb micromechanism of dislocation is proposed for the modeling of creep-plasticity interaction. Internal resistance (back stress) is therefore divided into two interactive parts: resistance for dislocation glide within the grains or subgrains and resistance for dislocation climb within grain boundaries or subgrain boundaries. They are mainly responsible for transient behavior and long time behavior.



respectively. Furthermore, the dislocation climb is considered to interactive with the dislocation glide by releasing the concentrated internal stress of pile-up dislocation, caused by the dislocation gliding accumulatively into grain or subgrain boundaries. A unified model for creep-plasticity interaction is then developed. A comparison between the model prediction and experimental results for 2 1/4Cr-1Mo Steel at 600° are quite encouraging. In fact, almost all the 10 models used in the report given by the Japanese High Temperature Committee (1986) predicted a wrong tendency for the softening effect after the loading sequence of prior plasticity-creep-plasticity; however, this NCP model shows satisfactory agreement qualitatively and quantitatively.

#### Nonproportional Cyclic Loading

In nonproportional cyclic loading, there are no explicit yield points even for mild steel, and its modeling has been found to be notoriously difficult using classical plasticity theory. Based on the microscopic experimental results given by Plumtree (1987) and Hoong (1988), the hardening behavior of materials due to the effect of strain amplitude of nonproportional cyclic loading is related to the changes of characteristic dimensions of substructures, such as dislocation cell for wavy slip material and ladder or vein substructures for planar slip material. The loading direction effects are separated into the instantaneous hardening caused mainly by the intersection of dislocations and a hereditary hardening associated with nonproportional loading. The multiplicatively separated form of the hardening function,  $f=f_1f_2f_3$ , is then proposed and explained on a physical foundation, in which  $f_1$ ,  $f_2$  and  $f_3$  are hardening functions, responsible for the above mentioned three mechanisms respectively. By this way, different hardening mechanisms through  $f_i$  are embedded into a thermomechanical constitutive framework which is based on the introduction of a generalized frictional force in terms of the hardening functions and irreversible entropy production. The comparison for stress responses of 304 and 316 stainless steels subjected to biaxial nonproportional loadings at room temperature between the calculated results and experimental data given by Chaboche, Tanaka, and Ohno showed excellent agreement.

#### Numerical Algorithm for NCP

The unavoidable common difficulty for NCP theories is how they can treat the initial extremely small inelastic strain with its stress-plastic strain slope being infinite at the origin. This author and Valanis circumvented this difficulty by introducing three internal variables with one internal variable describing particularly the initial inelastic strain. The corresponding kernel function to that internal variable is expressed by a highly decaying exponential function which takes the unit-impulse function  $\delta(z)$  as its limit. A differential constitutive equation and its FEM code have then been developed and implemented, and now further improved.

#### Extremal Properties for NCP

The NCP extremal properties and shakedown theorems show great advantages in the structure design than those of CP.

# THE CRACK CLOSURE METHOD USING BOUNDARY ELEMENTS

S.A. Hacker      T.N. Farris  
School of Aeronautics and Astronautics  
Purdue University  
West Lafayette, IN 47907

The boundary element method is a general purpose tool for calculating stresses and displacements in elasticity problems. However, accurate evaluation of singular quantities, such as the stress near a crack tip, requires a large number of elements or special crack tip elements. In this paper, the crack closure method is shown to accurately and efficiently calculate stress intensity factors using boundary element data.

Using equilibrium, compatibility, and linear elastic constitutive behavior, as well as Kelvin's point force solution, the boundary integral equation representing the exact elastic solution can be formulated. The exact formulation of the integral equation is approximated by using piecewise constant elements to approximate the integration; this creates constant boundary conditions along each element. A fortran program [1] was written and verified based on this method using the constant element assumption.

Irwin [2] observed that if the extension of a crack tip is the small amount  $\delta a$ , the work required in the closing of the crack to its original length is equivalent to the strain energy released in the closure; hence, the crack closure integral can be implemented in the calculation of the strain energy release rate,  $\mathcal{G}$ . Using a two dimensional polar coordinate system originating at the extended crack tip, this assertion in equation form is  $\mathcal{G} = \mathcal{G}_I + \mathcal{G}_{II}$ :

$$\mathcal{G}_I = \lim_{\delta a \rightarrow 0} \frac{1}{2\delta a} \int_0^{\delta a} \sigma_{22}(\delta a - r, 0) \bar{u}_2(r, \pi) dr, \quad \mathcal{G}_{II} = \lim_{\delta a \rightarrow 0} \frac{1}{2\delta a} \int_0^{\delta a} \sigma_{12}(\delta a - r, 0) \bar{u}_1(r, \pi) dr$$

where  $\sigma_{11}$  and  $\sigma_{12}$  are the stresses near the crack tip and  $\bar{u}_1$  and  $\bar{u}_2$  are the relative sliding and opening, respectively, between points on the crack faces.

While many previous applications of BEM and FEM in crack problems require that the numerical analysis be done twice, the second analysis incorporating a slight increase in crack length, an approximation made for element displacement eliminates the need for a second computer run (greatly saving computer time) and facilitates the implementation of the crack closure method. The use of the displacement of the element just before the crack tip as an

approximation for the displacement of the element ahead of the crack tip that would occur in a future increment of growth, affords these benefits. A similar approach was applied by Jih and Sun [3] using the finite element method.

The finite width correction factor, as defined and computed by Isida [4], is determined using the crack closure method, as well as through the use of the near tip solutions for displacement and stress. As indicated in Figure 1, the use of the near tip stress and displacement equations in obtaining the SIF is not efficient, however, the same numerical results can be used in the crack closure method to obtain a better correlation with Isida's solution. This indicates that energy based methods of SIF extractions can be more reliable and that elaborate schemes are not always necessary for investigating crack problems. Examples from steady-state thermoelasticity and interface crack problems will be presented.

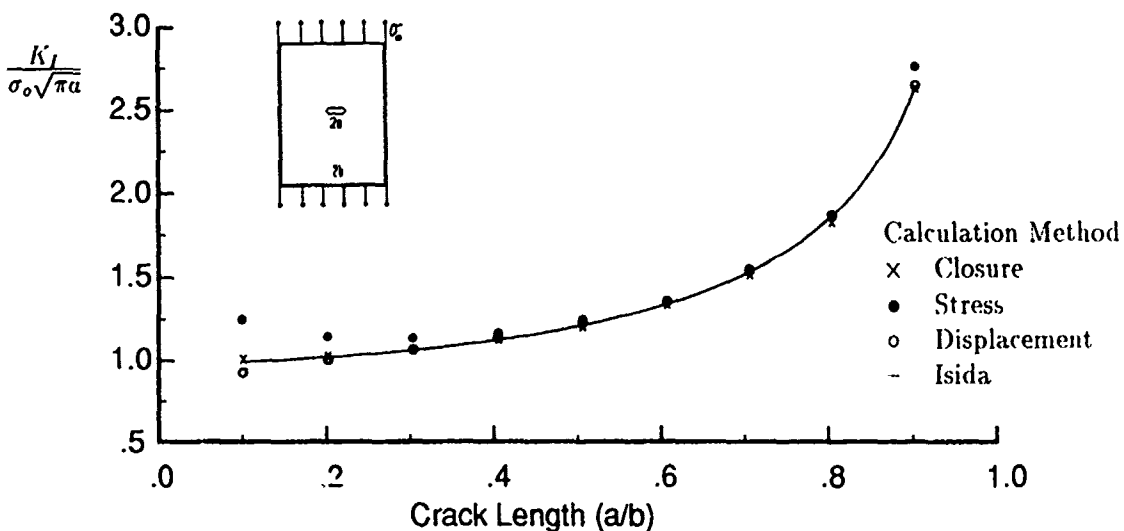


Figure 1: Finite width SIF correction factor based on the three methods investigated for a centrally cracked plate

## References

- [1] Scott A. Hucker. A boundary element approach to thermoelastic crack problems. Master's thesis, Purdue University, December 1990.
- [2] George R. Irwin. Fracture. *Handbuch der Physik*, 6:551-590, 1958.
- [3] C. J. Jih and C. T. Sun. Evaluation of a finite element based crack-closure method for calculating static and dynamic strain energy release rates. *Engineering Fracture Mechanics*, 37(2):313-322, 1990.
- [4] M. Isida. Analysis of stress intensity factors for the tension of a centrally cracked strip with stiffened edges. *Engineering Fracture Mechanics*, 5:647-665, 1973.

---

**Rafaat Hussein, Ph.D., P.E.**  
P.O. Box 387, Syracuse, NY 13210

---

**ON THE APPLICATIONS OF  
MICROSCOPIC MODELING OF FAILURE PROCESS IN  
HETEROGENEOUS MATERIALS USING THE IMAGE ANALYSIS  
TECHNIQUE**

Rafaat Hussein  
Associate Professor  
Syracuse, NY 13210

Using a new micro-testing system in conjunction with image analysis and an image correlation technique, the microscopic strains under axial compression and tension loadings and bending were analyzed and results are available. The aim has been to investigate failure processes, modeling of damages at the microscopic level of heterogeneous materials, microcrack-macrocrack interaction, and damage induced.

Small size specimens consisting of size 1 x 1 x 4 mm; 2.5 x 0.15 x 15 mm; 1 x 1 x 16 mm were prepared and tested in micro-testing device. A micro-testing device, a light microscope, a black and white video camera, a microcomputer with an image digitizer, scanning and transmission electron microscopes were the main experimental tools.

Strains in the longitudinal and transverse surfaces of the specimens; strain fields at the microscopic level were obtained using the micro-testing system with the image correlation technique.

Isostrain maps were constructed and correlated with the anatomical structure of the specimens. The isostrain maps reveal that failure could be detected before the proportional limit was reached. In addition, the failure location was found to be determined by the location and arrangement of any local effects.

It is believed that the results obtained provide enough knowledge about mechanical behavior at the microscopic level. It is also believed that microscopic deformation and failure mechanics, where deformation at the microscopic level may not be assumed to be homogeneous, have been investigated.

This paper discusses the applicability of this technique. It addresses also the analytical foundation for this approach. This paper is of particular interest to professionals from many areas such as bioengineering, mechatronics, optics in mechanics.

## STRESS CONCENTRATION AROUND HOLE AS A SIMPLE TOOL FOR RESIDUAL STRESSES MEASUREMENT

M.M. El-Sayed; Assoc. Prof. in Mechanical Design Dept., Faculty of Engineering and Technology, Mataria, Cairo, P.O. Box 11718 Mataria, Egypt.

### Abstract :-

One of the most widely used methods for determining residual stresses is blind hole drilling method . In which the radial relieved strains produced by hole drilling are measured with special strain gage rosette. In the present work the tangential relieved strain and hence the stress concentration will be considered instead of the radial relieved strain . The tangential relieved strain due to drilling small hole is higher than radial relieved strain around the hole boundry , therefore it is found that the measuring accuracy was increased by 16 times than the blind hole method accuracy .

Experimental verification was carried out in the case of uniaxial loading on standard flat plate and round bars . The flat specimens were made of annealed steel , and aluminum , while the round specimens were made of only annealed steel .

After residual stress measurements , the stress concentration created in the tested specimen is reduced with 30 % by repeating the loading and unloading of the specimen 25 times (shaking the load ) .

### Conclusion :-

Residual stresses measurement using stress concentration caused(created) by drilling small holes is a powerful tool . The technique of this new method has been described in details , where the tangential relieved strain ( $\epsilon_t$ ) was measured by strain gage . The application of this method for standard flat plates made of steel and aluminum as well as for round bars made of steel has been verified experimentally in the case of uniaxial loading . The mathematical approach for the determination of the principal residual stresses and their direction for the case of biaxial loading has been presented using three independent tangential relieved strain measurements .

It is to be noted that the accuracy of this method is about 16 times higher than the accuracy of the blind hole drilling method , because of the maximum relieved strain by later method is 0.25 the residual strain but by the present technique it is about 4.3 the residual strain. Therefore this method should be very useful and powerful when the value of the residual stresses are small in sophisticated mechanical members .

The effect of hole depth on the relieved tangential strain has been

investigated in round bars . The stress concentration created into the specimen due to drilling holes was reduced to about 40 % by loading and unloading repetition ( shaking the load ) .Additional investigation may be furnished later to obtain more details about residual stresses relaxation and redistribution of stresses using method of shaking load .

#### future work :-

It is planned to investigate the next points

1. Effect of shaking the load on the tangential relieved strains and stress concentration
2. Effect of hole diameter and its location with respect to the measuring point .
3. The application of this method in the case of biaxial loading .

#### Referecncas :-

1. S.S Bierley and A ." Owens Blind hole drilling technique for residual stress measurment , application in ndt" NDT InterNational , February 1980 . Strain , january 1974 .
2. E . M. Beaney and E .Procter " A critical evalution of the center hole technique for the measurment of residual stresses " strain , julg 1976
3. Alan Owens " Calibration of the centre hole technique of residual stress Measurment " Analytical services , stress Engineering services LTD 1982 .
4. M . O. Hendy , M. M Elsayd , El soaly " A simple Method for determination of residual stresses using double - hole drilling technique " ASAT conference 14 - 16 May 1991 , Cairo .
5. M .M El Sayed , S . A . khalil , N . M. Ashour . " Residual stress measurment for a finite plate under tension using two double edge cracks method " ASAT conference 14 - 16 May 1991 , Cairo .
6. M .M El Sayed " New method for measuring residual stresses using stress concentration phenomena near crack tip Midwestern Mechanics Conference" October 1991 U.S.A.
7. R .E. Peterson "Stress concentration factors" New york , 1973, U.S.A.
8. R .L. Johnson and M .M leven "stress - concentration factors at intrsecting and closely approaching orthogonal coplaner holes "Experimental Mechanics , 1977 .

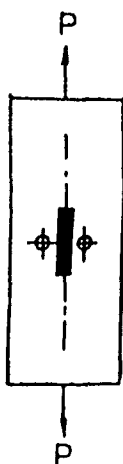


Fig.8 Drilling double holes in the flat specimen .

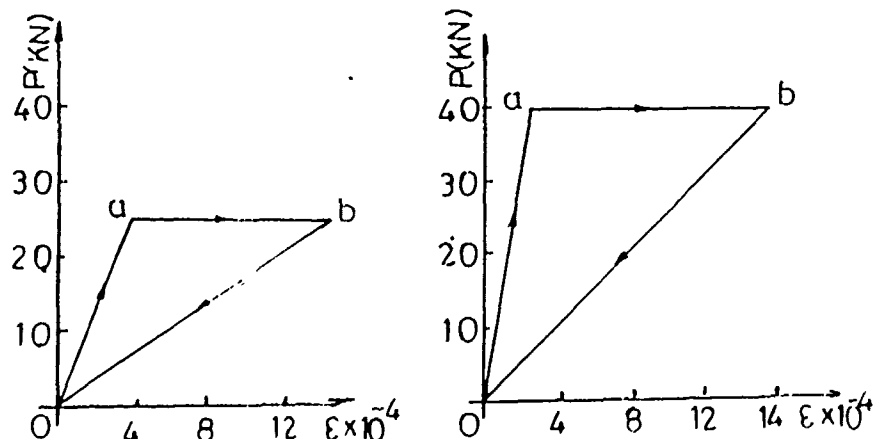


Fig.9 The loading cycle ( p - ε )for a - aluminum flat sp  
b - annealed flat steel sp .

## New Method for Measuring Residual Stresses Using Stress Concentration Phenomena Near Crack Tip

M.M. El-Sayed, Assoc. Professor Mechanical Design Department, Faculty of Engineering and Technology, Mataria, Cairo, P.O. Box 11718, Mataria, Egypt

### Abstract

Many methods for residual stress measurements were used as blind hole drilling method, X-Ray, ect. [1,2,]. In this paper, a new technique has been proposed in order to measure this residual stress in a direct way. In this technique, a certain limited crack is made in the specimen edge in order to create stress concentration, which can be measured by using resistance strain gauges. This stress concentration is a function in the residual stress in addition to applied stress.

If drilling or cutting has happened in the specimen using the known methods such as blind hole drilling method, or cutting methods, the stress distribution will change and cause some relaxation in the strain. This relaxation is measured and then the residual stresses can be calculated [3,4,5,]. But in the new technique which has been adapted in the present work, the stress concentration will happen instead of relaxation, i.e., the magnitude of the strain will be increased.

### Elastic Stresses Near Crack Tip:

In the present paper theoretical stresses near crack tip ( $r = mm$ ) has been calculated for each crack depth by using results given in [8] for the determination of stress intensity factor  $K$ . The theoretical stress concentration was calculated and plotted in fig. 3, where it shows the difference between theoretical and experimental results. The effect of strain gauge width have been considered in the calculation of stress near crack tip.

### Experimental Investigation:

Three sets of flat standard specimens were used in the present experimental work (5 steel specimens, 3 laminated brass, 2 aluminum). Four strain gauges are mounted on each specimen as shown in Fig.(2). The specimen is loaded gradually to 20 KN (fig.5) while the strain gauge readings were recorded at every incremental load, so that line (oa) can be plotted. At constant load of (20 KN) one edge crack was made by hand saw, (Fig.4.) The crack was made with limited depth ( $2a$ ) and then increased gradually from  $2a=4$  to 16 mm. This crack creates high stresses at the measuring points where the strain gauges are mounted. Then points ( $b_1, b_2, \dots, b_n$ ) can be plotted and so line (ab). The specimen was unloaded gradually and strain gauge readings were recorded. So that line (bc) can be drawn. This test procedure was repeated ten times with different loading values (where  $P=10-50$  KN) on ten standard specimens. Then the loading cycle ( $p-e$ ) was drawn for each specimen. Figs.(5,6,) show two loading cycles ( $p-e$ ) for two steel specimens when the loading force was (20, 30 KN) respectively. It can be seen that the strain increases due to making single edge crack and equal to  $(\epsilon_b - \epsilon_a)$  and the residual strain equals to  $(\epsilon_c)$ . Comparing these values from Figs. 3 and 4, we can see that the value of the residual strain is almost the same  $(\epsilon_c)$  and independent on the loading value. A deviation of analytical and experimental results is around 17%.

A proposed simple method for determination of residual stresses in uniaxially stressed plates has been introduced, using two (or one) edge cracks and measure the stress concentration near the crack tip.

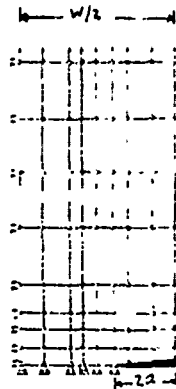


Fig. 3 The new quarter finite element network.

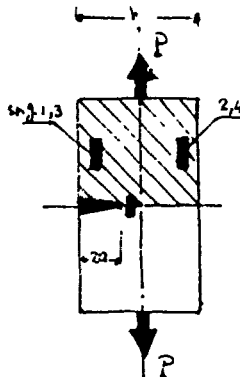


Fig. 4 The tested specimen

Fig. 5 The loading cycle (P-C) for steel specimen No. 1

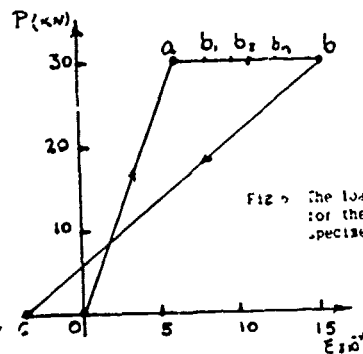
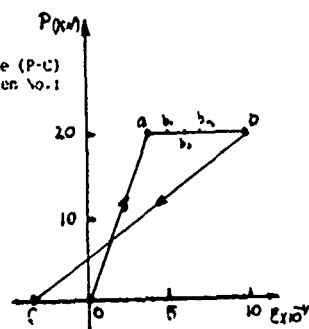


Fig. 6 The loading cycle for the steel specimen No. 2

#### References:

1. Beane, E.M. and E. Procter "A critical evaluation of the center hole technique for the measurement of residual stresses" Strain (London) Vol. 10, January, 1974.
2. S.S. Birley and A. Owens "Blind hole drilling technique for residual stress measurement-application in NDT" NDT International, February, 1980.
3. Jia-Yong Wang "Measurement of residual stress by hole drilling method on the direction of maximum residual stress" Experimental mechanics, March, 1988.
4. M.O. Hendy, M.M. El-Sayed and E. El-Soally "A simple method for determination of residual stresses using double-hole drilling technique" Fourth ASAT conference, Cairo, Egypt, 1991.
5. M.M. El-Sayed, S.A. Khalil and N.M. Ashour "Residual stresses measurement for a finite plate under tension using two double edge crack method" Fourth ASAT conference, Cairo, Egypt, 1991.
6. Pin Tong, T.H.H. Pian and S.J. Lasry "A hybrid element approach to crack problems in plane elasticity" International Journal for Numerical methods in Engineering, Vol. 7, 297-308, 1973.
7. Hinton, E. and Owen, D.R.J. "Finite element programming" Academic press, London 1977.
8. J.R. Dixon, J.S. Stranniger "Determination of Energy release rates and stress intensity factors by finite element method" Journal of Strain Analysis Vol. 7 No. 2, 1972



# Practical Limitations on Updating Finite Element Models Using Mathematical Optimization Techniques

Mark S. Ewing, Senior Research Engineer  
Wright Laboratory, Wright-Patterson Air Force Base  
(WL/FIBRA, WPAFB, OH 45433-6553)

Updating finite element models is of great importance in structural development programs in which a structure is expected to be modified, or supported in alternative ways, later in its service life. Updating techniques include those which directly alter elements of the mass and stiffness matrices (see, for instance, Baruch [1] and Berman [2,3]). An alternative is to alter the physical parameters upon which the mass and stiffness matrices are based (see Ojalvo [4]). Most techniques incorporate optimization principles in the form of "least squares" minimization of some error norm. However, another possibility is to use mathematical optimization techniques instead [5].

Consider a structural model with physical parameters,  $r_i$ , as well as analytically determined mode shapes, or eigenvectors,  $\phi_j$  (with individual elements,  $\phi_j^k$ ), and natural frequencies,  $\omega_j$ . (For notational convenience,  $\lambda = \omega^2$ .) The actual structure has physical parameters,  $\bar{r}_i$ , mode shapes,  $\bar{\phi}_j$ , (with individual elements,  $\bar{\phi}_j^k$ ), and natural frequencies,  $\bar{\omega}_j$ . To identify the structure in terms of the model's physical parameters, the following optimization problem may be solved.

Minimize either:

$$\sum_{j=1}^J \|\phi_j - \bar{\phi}_j\|^2 \quad (1)$$

or:

$$\sum_{j=1}^J \left( \frac{\lambda_j}{\bar{\lambda}_j} - 1 \right)^2 \quad (2)$$

subject to the constraints:

$$\left| \frac{\lambda_j}{\bar{\lambda}_j} - 1 \right| < a_j \quad \text{for } j = 1, 2, \dots, J' \quad (3)$$

$$\|\phi_j - \bar{\phi}_j\|^2 < b_j \quad \text{for } j = 1, 2, \dots, J'' \quad (4)$$

where:  $J$  is the number of modes used for the identification task (some inappropriate modes can be neglected); both  $a_j$  and  $b_j$  are "small" numbers chosen to quantify how close to target is "close enough";  $J'$  is the number of modes which are to have particularly accurate frequency matching;  $J''$  is the number of modes which are to have particularly accurate mode shape matching.

The optimization problem posed above has been used to solve a number of popular "textbook" problems as well as problems encountered involving "real" test data. The so-called "textbook"

problems, often called "computer experiments", start with a finite element model for which modal frequencies and modeshapes are known. Next, the model is perturbed, and new modal frequencies and modeshapes are calculated. The update problem, then is to update the model to arrive at the original model. This is not always easy, as a result of many obstacles, which have been described in an earlier study [5]. One key observation of the earlier study was that the extent of these problems is lessened when the number of physical parameters being updated remains relatively small with respect to the number of degrees of freedom.

When "real" data is used, the most pathological of all model updating problems often surfaces: if the model is inadequate to begin with, no amount of updating will make it a good model. This seems obvious, but the real significance of this fact is that model updating can, in some cases, alert the analyst to this truth when there is no other reason to doubt the model.

There are, fortunately, many cases where the model is "good enough" and other, less troublesome issues become paramount. For instance, if a model has a number of physical parameters which are not known with great accuracy - or which have been inadvertently entered into the model with a numerical error - the mathematical optimization algorithm may call for the design to change a great deal in a single iteration. This large "design change" can introduce large errors into the linearization schemes incorporated in such algorithms. As a result, one must selectively invoke tight change (or, "move") limits on the updated variables.

As part of an engineering support effort for an on-going tactical missile development program, the need arose to be able to update the model of the missile with its launcher on a number of different aircraft, *without* any detailed knowledge of the missile-to-launcher-to-aircraft interface, and in very short order. However, modal parameters associated with the missile in these various situations *were* available. As a result, the decision was made to attempt to update a crude model of the launcher-to-aircraft interface, thereby bypassing detailed analyses of many launch configurations. A detailed accounting of the use of updating technique, using mathematical optimization will be presented.

#### REFERENCES

1. Baruch, M. and Bar Itzhack, I. Y., "Optimal Weighted Orthogonalization of Measured Modes", AIAA Journal, vol. 16, April 1978, pp 346-351.
2. Berman, A. and Flannelly, W. G., "Theory of Incomplete Models of Dynamic Structures", AIAA Journal, vol. 9, Aug 1971, pp 1481-1487.
3. Berman, A., "System Identification of Structural Dynamic Models - Theoretical and Practical Bounds", Proceedings, AIAA 25th Structures, Structural Dynamics and Materials Conference, Palm Springs, CA, 14-16 May, 1984. (AIAA paper 84-0929)
4. Ojalvo, I. U., Ting, T., and Pilon, D., "Practical Suggestions for Modifying Math Models to Correlate with Actual Model Test Results". Proceedings, 7th International Modal Analysis Conference, Las Vegas, NV, Jan 1989, pp 347-354
5. Ewing, M. S. and Venkayya, V. B., "Structural Identification Using Mathematical Optimization Techniques", Proceedings, AIAA 32nd Structures, Structural Dynamics and Materials Conference, Baltimore, MD, April 1991, pp 840-845. (AIAA paper 91-1135)

# RESPONSE OF A ROTATING CLAMPED-PINNED BEAM SUBJECT TO AN ACCELERATING FORCE

Alan Argento

Department of Mechanical Engineering  
The University of Michigan- Dearborn  
Dearborn, Michigan 48128

Richard A. Scott

Department of Mechanical Engineering and Applied Mechanics  
The University of Michigan  
Ann Arbor, Michigan 48109

The problem of a force passing over a rotating beam has recently been studied in [1]-[3]. As described in [1], an application of this problem is in machining, in which the tool (regarded as rigid) and workpiece are represented by the force and beam, respectively. In [1]-[3], particular attention was given to the gyroscopically induced displacement component, transverse to the beam and the force; this component can become significant in high speed machining operations. In [1], a pinned Timoshenko beam subjected to a constant speed force was treated; in [2], the boundary conditions were generalized to clamped-pinned, but a Rayleigh beam model was used. The effect of an accelerating force was studied in [3], for a pinned Timoshenko beam. It was found that the beam displacements under the load can be significantly reduced by use of an accelerating load; the transverse, gyroscopically induced, displacement component was found to be particularly effected.

In the present work, a clamped-pinned rotating Timoshenko beam subject to an accelerating force is studied. The boundary conditions correspond to supports in typical machining equipment. The motion is described by four partial differential equations for the two displacement components and the two shear angles. The force is taken to be uniformly distributed, and to accelerate up to some steady speed,  $V_0$ , according to the relation

$$V = V_0 (1 - e^{-\alpha t}) \quad (1)$$

where  $\alpha$  is a parameter controlling the rapidity with which the steady speed is attained.

In [3] (pinned supports), it was possible to determine the solution to the equations of motion by means of finite Fourier transforms in space, and Laplace transforms in time. Finite Fourier transforms, however, will not satisfy clamped-pinned boundary conditions, so here a different solution approach is given. As in [2], the mode shapes of a non-rotating Euler-Bernoulli beam are used as comparison functions in a Galerkin formulation. This results in an infinite system of coupled differential equations in time, which are then truncated. In this formulation, the use of Laplace transforms as in [3] leads to very complicated convolution integrals, so direct numerical integration of the time dependent differential equations is employed.

Results are given for a variety of physical parameters. Comparison is made between the beam's response to a load traveling with constant speed,  $V_0$ , and an accelerating load having speed described by (1). The effect of the load's acceleration on the response of a clamped-pinned beam is compared with its effect on a pinned-pinned beam.

## References

- [1] R. Katz, C.W. Lee, A.G. Ulsoy, and R.A. Scott 1988 *Journal of Sound and Vibration* **122**, 131-148. The dynamic response of a rotating shaft subject to a moving load.
- [2] C.W. Lee, R. Katz, A.G. Ulsoy, and R.A. Scott 1988 *Journal of Sound and Vibration* **122**, 119-130. Modal Analysis of a distributed parameter rotating shaft.
- [3] A. Argento and R. A. Scott *Journal of Sound and Vibration* submitted for publication. Dynamic response of a rotating beam subjected to an accelerating distributed surface force.

# A SINGULAR PERTURBATION PROBLEM IN THE LATERAL STABILITY OF A THREE-WHEELED VEHICLE

Nellore S. Venkataraman  
Department of Mechanical Engineering  
University of Puerto Rico, Mayaguez Campus  
P.O. Box 5000  
Mayaguez, Puerto Rico 00708

Three-wheeled vehicles have been widely used all over the world as passenger, cargo and recreational vehicles. The dynamics and lateral stability of these vehicles, that is, the behavior of a straight running vehicle moving with a constant forward velocity when subject to a lateral disturbance has been studied by many authors [1,2,3]. It is a common practice to assume a "bicycle model" where the rear wheels are lumped together to reduce book-keeping terms. In all these analyses a two degree of freedom model, where the mass and moment of inertia of the front wheel are neglected is considered. The lateral velocity of the vehicle center of mass and the vehicle lateral angular velocity are taken as the two degrees of freedom of the vehicle.

In this paper we consider a full three degree of freedom model for the three-wheel vehicle lateral dynamics where the mass and moment of inertia of the front wheel are not neglected. In addition to the above two degrees of freedom, the vehicle steer rate is taken as the third degree of freedom. It is shown that this is a singular perturbation problem. The main characteristic of a singular perturbation problem is that in the governing differential equation, a small parameter multiplies the highest order derivative. Singular perturbation problems are of common occurrence in fluid mechanics, for example high Reynolds number viscous flows [4]. The methods of regular perturbation cannot be applied to singular perturbation problems. For example the inviscid flow results can never be recovered from viscous flow problems just by equating the coefficient of viscosity equal to zero [5]. A similar situation arises here where the results for the two degree of freedom model cannot be recovered from the three degree of freedom model just by equating the front wheel inertia equal to zero because of the singular perturbation nature of the problem.

The dynamical equations of motion have been derived using

Kane's method [6]. The equations were linearized and the stability analysis was made using Routh's stability criterion. The critical velocity, that is the velocity at which the vehicle becomes unstable was obtained as a function of vehicle geometric and dynamic parameters as well the tire properties. In this velocity expression if we set the front wheel inertia equal to zero we do not recover the two degree of freedom model results.

Even though it turns out that the two degree of freedom model results are more conservative, the analyses here raises the question about the correctness of using the two degree of freedom model for the study of lateral dynamics because of the singular perturbation nature of the full three degree of freedom model.

On the other hand, the analysis of vehicle behavior for a constant radius steady turn for two and three degree of freedom model is similar and the two degree of freedom model results are recoverable from the three degree of freedom model results. This is as it should be, in this case the three degree of freedom model is not a singular perturbation problem,

**ACKNOWLEDGEMENT:** This research has been supported by the National Science Foundation under Puerto Rico ESPCoR Project, Component No. IX.

#### REFERENCES

1. Ellis, J.R., "Vehicle Dynamics", Business Books, London, 1969
2. Wong, J.Y., "Theory of Ground Vehicles", John Wiley & Sons, New York, 1978
3. Huston, J.C., Graves, B.J. and Johnson, D.B., "Three Wheeled Vehicle Dynamics", SAE Transactions, Vol. 91, Paper No. 820139 (SP-509)
4. White, F.M., "Viscous Fluid Flow", McGraw-Hill, Inc. New York, 1991
5. Van Dyke, M., "Perturbation Methods in Fluid Mechanics" Academic Press, New York 1975
6. Kane, T.R. and Levinson, D.A., "Dynamics", McGraw Hill Book Company, New York, 1985

# TANGENTIAL IMPACT IN RIGID BODY DYNAMICS

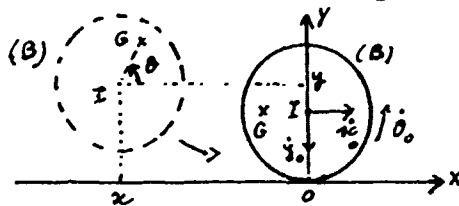
René SOUCHET, Laboratoire de Mécanique Théorique  
40, avenue du Recteur Pineau, 86022 POITIERS CEDEX, France

## 1. INTRODUCTION

The collision of two rigid bodies B and B' occurs when the normal component  $n.v_A$  of "the velocity of approach" is different from zero. Then the bodies suffer impulses that generate some velocity discontinuities [1]. However, even though the collision occurs with  $n.v_A = 0$ , impulses and velocity discontinuities can appear when the friction coefficient is large enough. We propose to study this so-called "tangential impact" on an example, by taking the limiting process " $n.v_A$  tends to zero" and using appropriate restitution and friction laws [3].

## 2. IMPACT PROBLEM

Fig. 1 gives an abstract of the studied example, considered in [2] : an eccentric falling disk B striking an horizontal plane B'.



(B) : center I and radius a  
(x,y,0) : coordinates of I  
O : point of impact  
m : mass of (B)  
G : mass center,  $IG = \ell$   
 $mk^2$  : central moment of inertia

Fig. 1 : Initial conditions :  $x_0 = 0$ ,  $y_0 = a$ ,  $\theta_0 = \pi$ ,  $\dot{x}_0 > 0$ ,  $\dot{y}_0 < 0$ ,  $\dot{\theta}_0 > 0$ .

The slip velocity  $u = \dot{x} + a \dot{\theta}$  takes the initial value  $u_0 = \dot{x}_0 + a \dot{\theta}_0 > 0$ . We choose :  $m = 1$ ,  $\ell = 1$ ,  $a = 2\ell$ ,  $k = \ell$ .

The balance equations of impact are

$$\dot{x}_1 - \dot{x}_0 = T, \quad \dot{y}_1 - \dot{y}_0 - \dot{\theta}_1 + \dot{\theta}_0 = N, \quad \dot{\theta}_1 - \dot{\theta}_0 = N + 2T$$

where (T, N) is the contact impulse and the index (1) denotes the final velocities. We must complete by friction and restitution laws. In order to do that, we consider the two phases of impact, first the compression and second the restitution, with the respective partial impulses ( $T_0$ ,  $N_0$ ) and ( $T_1$ ,  $N_1$ ) [3] :

Restitution laws (e : restitution coefficient)

$$(H_1) \quad N_1 = e N_0, \quad y_1 = -e y_0, \quad 0 \leq e \leq 1$$

Friction law (f : friction coefficient)

$$(H_2) \quad \begin{cases} T_0 = -f N_0 \quad (\text{since } u_0 > 0) \\ T_1 < f N_1, \quad u_1 = 0 \quad \text{or} \quad |T_1| = f N_1, \quad u_1 \cdot T_1 < 0. \end{cases}$$

(H<sub>3</sub>)  $|T| < f N$ ,  $u_1 = 0$ , if (H<sub>2</sub>) collapses.

Note that (H<sub>3</sub>) is used only for the large values of  $f$ , since no slipping is assumed during the first phase, though  $u_0 > 0$ .

### 3. RESOLVING WITH $\dot{y}_0 < 0$

Fig. 2 shows the discussion of the problem according to  $f$  and  $u_0$ .

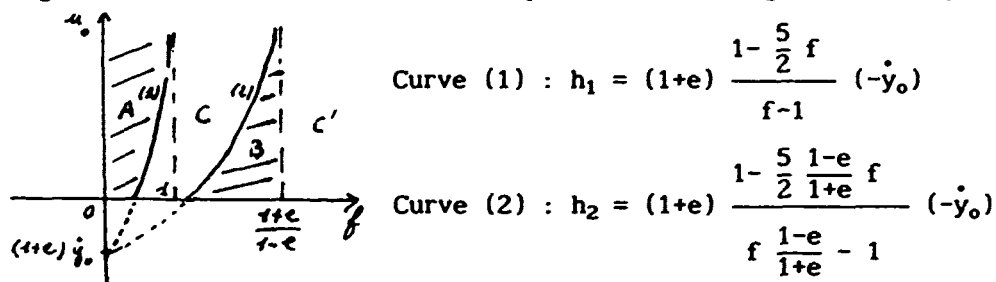


Fig. 2 : Regions : A,  $u_1 > 0$  ; B,  $u_1 < 0$  ; C, and C',  $u_1 = 0$ .

Note that the slip velocity can reverse its sign and that the slip velocity falls to zero from the very start of impact, though  $u_0 > 0$ , for  $f > \frac{1+e}{1-e}$  (H<sub>3</sub> hypothesis).

### 4. LIMITING PROCESS $\{\dot{y}_0 \rightarrow 0\}$

Due to the lack of place, it is not possible to write the different values obtained in cases  $u_1 > 0$ ,  $u_1 < 0$  and  $u_1 = 0$ . Here we give an abstract of the discussion where we use the limiting process  $\{\dot{y}_0 \rightarrow 0\}$  in the relevant formula.

Case  $u_1 > 0$  :  $\dot{x}_1 = \dot{x}_0$ ,  $\dot{y}_1 = 0$ ,  $\dot{\theta}_1 = \dot{\theta}_0$ ,  $T = N = 0$  if  $f < 1$

Case  $u_1 < 0$  : impossibility since  $u_1 = u_0$ , and  $u_0 > 0$ .

Case  $u_1 = 0$  : 
$$\begin{cases} \dot{x}_1 = \frac{2}{3} (\dot{x}_0 - \dot{\theta}_0), \dot{y}_1 = 0, \dot{\theta}_1 = -\frac{1}{3} (\dot{x}_0 - \dot{\theta}_0) \text{ if } f > 1 \\ T = -\frac{1}{3} u_0, N = \frac{1}{3} u_0 \end{cases}$$

So, if  $f < 1$ , no discontinuities of velocities and no impulses appear. If  $f > 1$ , the disk suffers discontinuities and impulses : we have a tangential impact due to the important values of  $f$ . It is known [2] that the study of motions with continuous velocities gives an impossibility for  $f > 1$ . The discussion of motions is then complete and we have obtained a unique and available solution for all values of  $f$ .

In conclusion the restitution and friction laws, written in part 2, are available not only for usual problems of impact ( $n.v_A < 0$ ), but also for tangential impacts ( $n.v_A = 0$ ) by using the very simple limiting process  $\{n.v_A \rightarrow 0\}$ .

### 5. REFERENCES

- [1] T.R. KANE and D.A. LEVINSON, "Dynamics : Theory and Applications", Mc Graw-Hill, New-York, 1985.
- [2] M. ROY, "Mécanique - I. Corps rigides", Dunod, Paris, 1965.
- [3] R. SOUCHET, "Restitution and friction laws in rigid body collisions", proposed to J. of Appl. Mech.



# THE CORRECTED NEWTON'S GREAT FOUR LAWS OF MORE EFFECTIVENESS THAN EINSTEIN'S RELATIVITY

Lü Jiahong  
(Gannan Teachers' College, 77 Hongqi Road,  
Ganzhou 341000, Jiangxi, P. R. China.)

## Abstract

The Corrected Newton's Great Four Laws are introduced. The main principles and effects of Einstein's relativity are given by these Corrected Laws. The problems of difficult to relativity, such as superlight speed motion, have also been explained.

In 1987 the author of this paper had made the corrections for Newton's Great three Laws without using relativity but equivalent to it.<sup>(1)</sup> In the Corrected Newton's First Law the inertia of light had been included. In the Corrected Newton's Second and Third Laws a new formula of the effect between motion and force had been given as follows:

$$\vec{F}_r = \frac{\vec{V} \times (\vec{F} \times \vec{V})}{c^2} \quad (1)$$

thus we have

$$\frac{d}{dt}(\vec{p}) = \vec{F} + \frac{\vec{V} \times (\vec{F} \times \vec{V})}{c^2} \quad (2)$$

where

$$\vec{p} = \vec{p}_0 \exp\left(\frac{\int \vec{F} \cdot \vec{V} dt}{\vec{p}_0 c^2}\right) = \frac{\vec{p}_0}{\sqrt{1-v^2/c^2}} \quad (3)$$

The Corrected Newton's Universal Gravitation Law had been obtained by the author of this paper in 1984, which could be given only if  $\vec{F}$  representing Newtonian gravitation force by putting it into Eq.(2):

$$\vec{F}_G = - \frac{G M_1 m_2}{r^3} \vec{r} + \frac{\vec{V} \times (\vec{r} \times \vec{V})}{c^2} \exp\left(-\frac{G M_2}{c^2 r}\right) \quad (4)$$

Using Eq.(4) the four effects of general relativity had been obtained only by simple non-Riemannian geometry calculations.<sup>(2)</sup>

Experiences have proved that not only the problems of usual motion of sublight speed (such as one-dimensional relativistic vibration)<sup>(3)</sup> could be studied, but also the problems of difficult to relativity (such as the motion of superlight speed) could be explained by the Corrected Newton's Great Four Laws. Let the two sides of Eq.(2) multiplied by  $V$ , the author of this paper had obtained the fundamental equations of high speed motion<sup>(4)</sup>:

$$V^2 + \frac{dV^2}{d(\ln m^2)} = c^2 \quad (5)$$

when  $v < c$

$$m_+ = \frac{m_0}{\sqrt{1-v^2/c^2}}, \quad E_+^2 = p_+^2 c^2 + m_0^2 c^4 \quad (6)$$

when  $v > c$

$$m_- = \frac{m_0}{\sqrt{v^2/c^2 - 1}}, \quad E_-^2 = p_-^2 c^2 - m_0^2 c^4 \quad (7)$$

It is clear that Eq.(1)-(7) are more effectiveness than Einstein's relativity.

#### Reference

- [1] Lü Jiahong: Revising Newton's Three Laws of Motion, Inquiring Into The Physical Significance of Relativity, STUDIES IN DIALECTICS OF NATURE, Vol.3, No.6, 1987, Peking, P.R.China.
- [2] Lü Jiahong: A Possible Correction Made for Newton's Law of Gravitation, JOURNAL OF CHINA UNIVERSITY OF SCIENCE AND TECHNOLOGY, Vol.14, No.1, March, 1984, Hefei, Anhui, P.R.China.
- [3] Lü Jiahong & Zhou Lingyun: About One-dimensional Relativistic Vibrators, MATHEMATICA ACTA SCIENTIA, 7(1987), 3, 259-263, Wuhan P.R.China.
- [4] Lü Jiahong: Through Superlight Speed and 3°K Background to Consider the Unity of Newton and Einstein's Theories of Space-time, JOURNAL OF GANNAN TEACHERS' COLLEGE (Natural Sciences) No.2 1989, Ganzhou Jiangxi P.R.China.

## SENSORY FEEDBACK FOR SEAM TRACKING ROBOT

Behnam Bahr, Assistant Professor  
Mechanical Engineering Department  
The Wichita State University  
Wichita KS 67208

### ABSTRACT

The Purpose of this paper is to illustrate the design of a simple optical sensor for seam tracking. The proposed solution is based on the illumination of the trajectory with a light beam, imaging the reflected beam on a linear array, and the determining of the location and orientation of the seam from the image using a microprocessor.

### INTRODUCTION

One of the present applications of the robot is for continuous motions along a specified spatial path. There are many reasons why one requires such characteristics from a robot, e.g., in welding processes, painting, and sealant applications. Assuming that the nominal path can be taught easily and accurately to the robot, there remain many problems with manufacturing errors. Due to manufacturing inaccuracies and stacked-up tolerances, the path that the robot has to follow will vary from one part to the next.

Therefore, the objective of this paper is to illustrate a microprocessor based, opto-electronic sensor for an input or a feedback device which can guide a robot along any path. The need for automation of this process is best explained by the following statement from the Ford Motor Company [1]. "In an effort to improve quality of the product, reduce labor and material costs, and improve the working environment, sealant application should become a prime target for robotic automation."

The seam path is usually a three-dimensional spatial curve, so that teaching the robot by leading it along the path cannot be utilized because of the requirement for high accuracy. Therefore, the manipulator has to be taught point-by-point in small increments, which is very tedious. Most industrial robots use a fixed data base program for their operations. Any minor change in their task or environment requires reprogramming the robot. Thus, there have been many studies involved with making more intelligent robots by the incorporation of sensory control system such as force/torque, sonar, and vision feedback systems [2]. All the above sensors are very expensive and usually are

too slow for real-time application, especially for sealant application where high speed of motion is required.

The intensity and image of the reflected light will be influenced by the presence of the seam, and results in a signal pattern that is typically of the form shown in Figure-1. The location of the peak in the image can now be related to the Y-coordinate of the seam. The work-piece distance, Z is obtained by measuring the distance of the side lobes from the beginning of the first pixel (picture element). The seam orientation in a plane perpendicular to the seam i.e. about the x-axes is proportional to the difference in magnitude of the light intensity on the two sides of the peak.

#### CONCLUSION

The sensory feedback sensor was developed for high speed and high accuracy seam tracking robot. The developed sensor is much faster than the vision system which operates at 60 frames/sec. Further work is required to improve the signal analysis of this sensor.

#### REFERENCES:

- 1- V. Milenkovic & B. Hung, "Kinematics of major robot linkage", 13th ISIR/Robots 7, v.2, Chapter 16, pp. 31-47
- 2- Sweet, M. L., "Sensor-Based Control Systems for Arc Welding Robots", Robotics & Computer Integrated Manufacturing, vol. 2 pp. 125-153, 1985.
- 3- B. Bahr "Application of Computer Vision and Adaptive Control for an Industrial Robot", Ph.D. Thesis University of Wisconsin-Madison 1988.

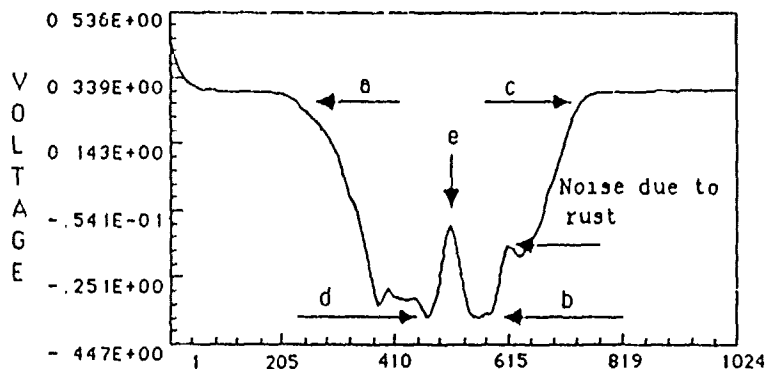


Figure 1 The typical video signal.

# EQUILIBRIUM PROFILE OF A TWO-DIMENSIONAL PENDANT DROP ON A CONVEX SURFACE

John C. Petrykowski  
Mechanical and Aerospace Engineering Department  
University of Dayton, Dayton, OH 45469-0210

Determining the size and shape of pendant drops is of importance in a number of processing operations including dip and spray coating and physical vapor deposition. This paper considers the case of a two-dimensional pendant drop centered about a convex solid surface where the contact point is located on the vertical sides of the surface (see figure 1a). A solution is presented for the equilibrium profile of the liquid-vapor interface in terms of elliptic integrals which depend parametrically on the Bond number, Laplace number and contact conditions.

The starting point of the analysis is the dimensionless Young-Laplace equation

$$y_{\pm}''(x_{\pm}) = \mp [y_{\pm}'(x_{\pm}) + (La/Bo)] Bo \{1 + [y_{\pm}'(x_{\pm})]^2\}^{3/2} \quad (1)$$

which describes the mechanical equilibrium requirements at a liquid-vapor interface where  $y_{\pm}(x_{\pm})$  represents the dimensionless coordinates along the upper (+) and lower (-) branches of the interface. The parameters  $La = (P_1 - P_{\infty}) x_0^*/\sigma$  and  $Bo = \rho g x_0^{*2}/\sigma$  are the Laplace number and Bond number which measure, respectively, the relative importance of capillary pressure and gravitational forces to surface tension forces. Here,  $P_1$ ,  $\rho$  and  $\sigma$  are capillary pressure, density and surface tension;  $P_{\infty}$  and  $g$  are ambient pressure and gravity, and;  $2x_0^*$  is the width of the solid. Boundary conditions are

$$y_-'(1) = \cot \theta, \quad y_-(1) = y_1 \quad \text{and} \quad y_+'(\bar{x}) = 0, \quad y_+(0) = y_m \quad (2a,b,c,d)$$

where  $\theta$  and  $y_1$  are the contact angle and dimensionless contact point and  $x$  and  $y_m$  are dimensionless interface coordinates at vertical and horizontal tangency, respectively.

The solutions obtained by twice integrating equation (1) along both branches are

$$x_- = 1 + \{ [F(\phi, K) - F(\phi_1, K)] \bar{y}^2/\hat{y}_m \} - [E(\phi, K) - E(\phi_1, K)] \hat{y}_m \\ + ([\hat{y} \sin \phi \cos \phi - \hat{y}_1 \sin \phi_1 \cos \phi_1] \hat{y}_m K^2/\hat{y}_s) \quad , \phi_1 \leq \phi \leq \bar{\phi} \quad (3)$$

and

$$x_+ = \bar{x} + [E(\psi, K) - E(\bar{\psi}, K)] \hat{y}_m - \{ [F(\psi, K) - F(\bar{\psi}, K)] \bar{y}^2/\hat{y}_m \}, \quad 0 < \psi < \bar{\psi} \quad (4)$$

In equations (3,4),  $F(\phi, K)$  and  $E(\psi, K)$  are elliptic integrals<sup>1</sup> of the first and second kind where the arguments  $\phi$  and  $\psi$ , the modulus  $K$  and the quantities  $\hat{y}_1$ ,  $\bar{y}$ ,  $\hat{y}_m$  and  $\hat{y}_s$  are given by

$$\phi(\hat{y}) = \sin^{-1} \{ [Bo(\hat{y}^2 - \hat{y}_s^2)]^{1/2} \hat{y}_m/2\hat{y} \}, \quad \phi_1 = \phi(\hat{y}_1), \quad \bar{\phi} = \phi(\bar{y}) \quad (5a,b,c)$$

$$\psi(\hat{y}) = \sin^{-1} \{ [Bo(\hat{y}_m^2 - \hat{y}^2)]^{1/2}/2 \}, \quad \psi_1 = \psi(\hat{y}_1), \quad \bar{\psi} = \psi(\bar{y}) \quad (6a,b,c)$$

$$K = [(\hat{y}_m^2 - \hat{y}_s^2)/\hat{y}_m^2]^{1/2} \quad (7)$$

$$\hat{y}_1 = y_1 + (La/Bo), \bar{y} = [\hat{y}_1^2 + (2/Bo) \sin \phi]^{1/2} \quad (8a,b)$$

$$\hat{y}_m = [\hat{y}_1^2 + 2(1+\sin\phi)Bo^{-1}]^{1/2}, \hat{y}_s = [\hat{y}_1^2 - 2(1-\sin\phi)Bo^{-1}]^{1/2} \quad (8c,d)$$

The Laplace number in equation (8a) is specified by first imposing the requirement that the interface be continuous at the junction of the branches. This requirement imposes on equations (3,4) a compatibility condition which is expressed as

$$[(K^2 - 2) F(\psi_1, K) + 2 E(\psi_1, K)] / Bo^{1/2} = K \quad (9)$$

The Laplace number is then found by combining equations (7.8a,c,d) to get

$$La = -y_1 Bo + \{ [-2(1 + \sin \phi) + 4/K^2] Bo \}^{1/2} \quad (10)$$

where the K value is an iterative solution to equation (9).

Drop profiles are presented in figure 10 for contact conditions  $y_1 = -0.1$  and  $\Theta = 45^\circ$ . The Bond number ranges from  $10^{-2}$  for the lightest drop to  $6 \times 10^{-2}$  for the heaviest drop. As the Bond number decreases, the surface tension force dominates and the interface approaches the familiar circular arc associated with a small pendant bubble. For larger Bond numbers, the Laplace number is seen to decrease which means that the shape of the interface is more greatly influenced by the weight of the drop than by the contact conditions. Finally, these results may apply to the corresponding axisymmetric case as well since the Bond numbers considered here are within the range for which Hartland and Hartley<sup>2</sup> found close agreement between two-dimensional and axisymmetric drops on horizontal surfaces.

This work was performed with support from the U.S. Department of Energy.

#### REFERENCES

1. P.F. Byrd and M.D. Friedman, Handbook of Elliptic Integrals for Engineers and Scientists (Springer, Berlin, 1971), 2nd ed.
2. S. Hartland and R.W. Hartley, Axisymmetric Fluid-liquid Interfaces (Elsevier, 1976).

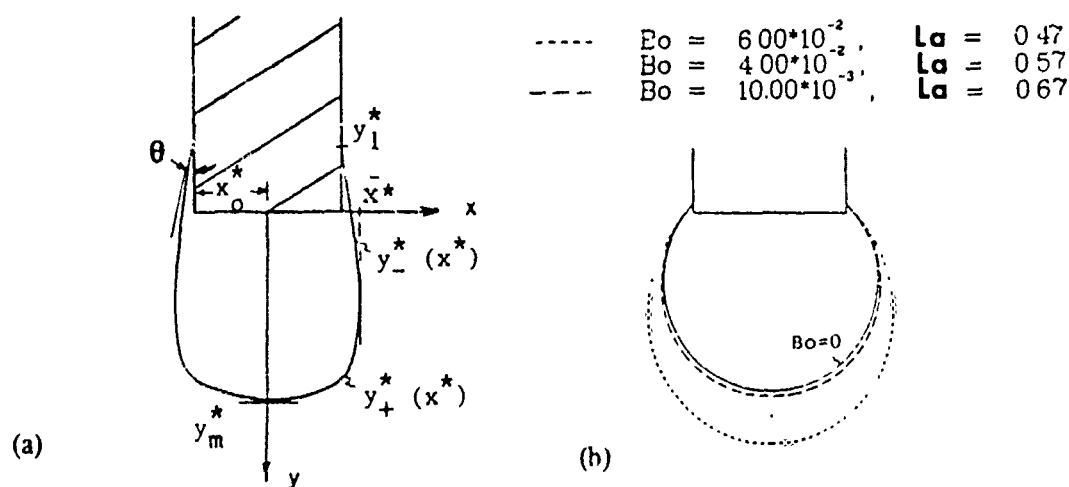


Figure 1: (a) Coordinates of a pendant drop (b) Pendant drop profiles for selected Bond and Laplace numbers for contact conditions  $y_1 = -0.1$ ,  $\Theta = 45^\circ$ .

# ENERGY DISSIPATION AND DAMPING IN BOLT JOINED STRUCTURES

Meshulam Groper and Jefferey Dowd  
Department of Mechanical Engineering  
Western Michigan University  
Kalamazoo, MI 49008

## ABSTRACT

A global damping ratio for a simple metallic structure composed of beams and columns connected with bolted joints is determined. This is done by employing a criterion of equivalence developed by Jacobsen [1] and by evaluating the dissipated energies in the structure's different elements.

## INTRODUCTION

The friction forces which occur in structures whose joined parts slide during dynamic loading are associated with energy dissipation. In such structures the joined parts are connected with high strength bolts tightened to the proof load such that large clamping pressure are developed at the contact surfaces of the joints.

According to ref. [2] the friction force and the amount of microslip are estimated by

$$F(x) = m \int_A \mu(x) \rho(x) dA \quad (1)$$

where  $m$  is the number of contact surfaces,  $\mu(x)$  and  $\rho(x)$  are the coefficient of friction and pressure distributions, and

$$\Delta(x) = \frac{2F(x)}{3hE} \quad (2)$$

where  $h$  is the thickness of the joined elements and  $E$  is the modulus of elasticity of the material comprising the joint's parts.

According to the same source [2], the corresponding work done by  $F(x)$  is,

$$\Delta W = \frac{3nm^2\mu^2(x)}{3\pi} \times \frac{N^2}{hE} \quad (3)$$

where  $n$  is the number of bolts,  $m$  the number of contact surfaces which slide, and  $N$  is the preload of the bolt.

## ENERGY DISSIPATION IN BOLT JOINED STRUCTURES

The evaluation of the global damping ratio could be done by employing a method suggested by Ragget [3] and further developed by Groper [4] whose principal lines are presented in continuation.

The dissipation of energy of the structure is the scalar addition of energies dissipated by all its elements.

$$\Delta W = \sum \Delta W_i \quad (4)$$

If  $\xi_i$  is the equivalent viscous damping ratio of element  $i$ , then Jacobsen's criterion of equivalence could be written as

$$\Delta W_i \approx 4\pi \xi_i W_i \quad (5)$$

where  $W_i$  is the energy of deformation of element  $i$ , while the sign  $\approx$  indicates some limitations of the above criterion when applied to highly non-viscous vibrational systems [5].

Eqs. (4) and (5) lead to

$$\Delta W = \sum \Delta W_i = 4\pi \sum \xi_i W_i = 4\pi \xi E \quad (6)$$

from which,

$$\xi = \frac{1}{4\pi} \cdot \frac{\sum \Delta W_i}{\sum W_i} \quad (7)$$

where  $\xi$ ,  $\Delta W$ , and  $W$  are related to the structure as a whole while  $\xi_i$ ,  $\Delta W_i$ , and  $W_i$  are related to the structural element  $i$ .

Using the above method a global damping ratio for a simple structure - beams and columns connected with bolted joints was determined. The result was compared with the damping ratio of the structure obtained in a steady - state - response.

## REFERENCES

- [1] Jacobsen, L.S., (1960) "Damping in Composite Structure," Proc. 4th WCEE, Tokyo, Japan, 2.
- [2] Groper, M., (1985, a), "Microslip and Macroslip in Bolted Joints," Experimental Mechanics, Vol. 25, No. 2.
- [3] Ragget, D.J., (1975), "Estimating Damping of Real Structures," Journal of Structural Div., ASCE, Vol. 101.
- [4] Groper, M., (1979), Energy Absorption in Structural Elements of Precast Buildings During Static and Dynamic Loading, Technion, Israel Institute of Technology.
- [5] Jennings, P.C., "Equivalent Viscous Damping for Yielding Structures," J. Eng. Mech. Div., ASCE, 94 (EMT, A.M.).



## A COMPUTER SIMULATION FOR COACHING POLE VAULTING

Philip G. Kirmser, Professor Emeritus  
Electrical and Computer Engineering Department  
Durland Hall, Kansas State University  
Manhattan, Kansas 66506

A computer program for the two dimensional simulation of pole vaulting using an elastica for the pole and a simple, variable moment of inertia mass with variable extension to a pinned end [1] has been modified for use with a pole of arbitrary stiffness distribution and to include arbitrary couples used by a vaulter for control of attitude during a jump.

The optimal performance, as measured by the height of the jump attained, is a functional of a number of parameters (such as the vaulter's weight and height, the stiffness distribution in the pole, input velocities, and length of the pole used) and time dependent functions of body configuration, arm extension, and applied couples.

No clear analytic, or even numerical methods for the direct optimization of pole vaulting seem to exist.

The optimization problem is partially solved here by using a repeated shooting method in which simulations are "coached" by means of varying parameters and input functions in successive runs to achieve greater heights until an acceptable greatest lower bound for the maximum obtainable height has been found.

Examples of simulations of a good jump are shown in Fig. 1, and a bad jump in Fig. 2, both for a pole of variable stiffness as given in Fig. 3, using a model as shown in Fig. 4.

Repeated simulations show that the performance of a vaulter is extremely sensitive to small changes in initial conditions, stiffness parameters, weight, and the timing of actions taken during a jump. They suggest that anything which can be done to increase consistency can help to improve performance.

For example, vaulters should always jump at the same weight, using weighted belts to achieve this if necessary. Poles should always be used at the same temperature because minor changes in elasticity caused by temperature changes affect the timing of actions taken in unexpected ways.

The simulations suggest, too, that a pole used must be matched to the vaulter carefully. The 15 foot pole used here is a better choice for a 150 lb vaulter than for a 160 lb vaulter. They appear to show that the application of couples by the vaulter are helpful in attitude control, but don't do much to increase the greatest lower bound attainable.

The variable extension of arms in the hand hold shortly after take-off and the effects of push-off at the proper time are more important than the use of couples in increasing the maximum height attained.

The simulations suggest, too, that the world record jump of 20' 1/4" set by Bubka [2], [3] is likely to be bettered, sooner or later, by a foot or so.

Ht, ft measured from bottom of pole pit

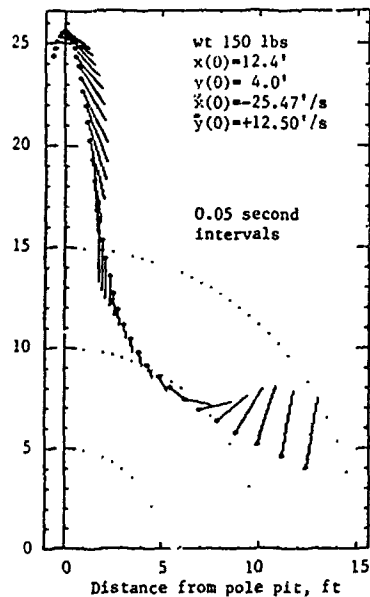


Fig. 1 A Good Jump

Ht, ft measured from bottom of pole pit

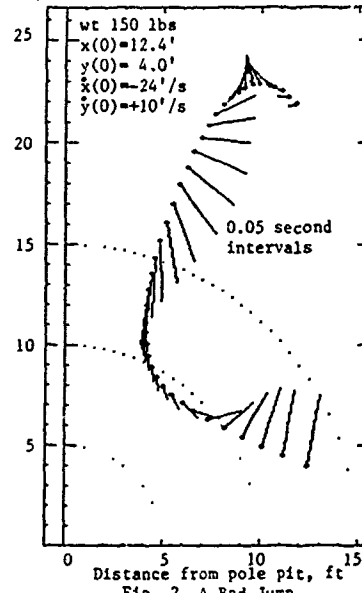


Fig. 2 A Bad Jump

Stiffness, lb ft<sup>2</sup>

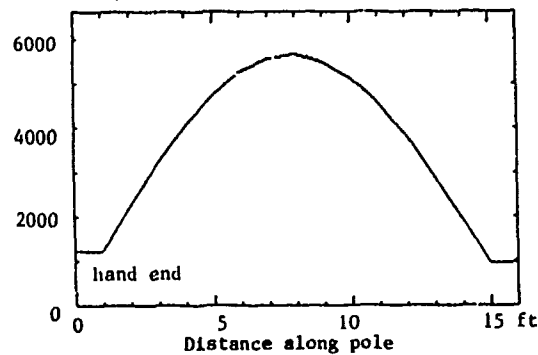


Fig. 3 Stiffness Distribution

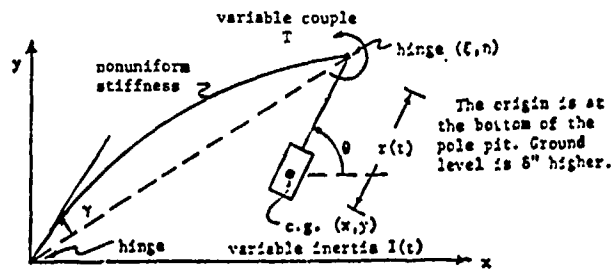


Fig. 4 The Model Used

## References

- [1] Walker, H.S., and P.G. Kirmser, Computer Modeling of Pole Vaulting, Mechanics and Sport, American Society of Mechanical Engineers, United Engineering Center, New York, 1973. pp. 131-141.
- [2] Bubka, S., Over the Bar, Legkaya Atletika 12:16-17, 1983 (translated by V.Mansvetov, Soviet Sports Review 20(3):127-130, 1985)
- [3] Bubka Clears 20 Feet in Pole Vault, Manhattan Mercury, March 17, 1991, page B8. (c) New York Times.

# A MODEL FOR THE SINTERING OF CONSTRAINED POLYCRYSTALLINE THIN FILMS

Douglas R. Carroll  
Basic Engineering Department  
University of Missouri-Rolla  
Rolla, Missouri 65401

Mohamed N. Rahaman  
Ceramic Engineering Department  
University of Missouri-Rolla  
Rolla, Missouri 65401

## INTRODUCTION

The sintering of thin ceramic films is of both theoretical and practical interest. Thin films are used for magnetic recording devices, wear resistant coatings, high temperature coatings, optical films and in many areas of electronics. Two models have been developed recently for the sintering of constrained films. A common feature of these models is that the film is assumed to be a continuum. Scherer and Garino<sup>1</sup> used a cubic cylinder model which was an extension of previous work by Scherer. The cubic array of cylinders is used to establish the kinetics for the model, but for the kinematics, the material was assumed to be a viscous continuum. Bordia and Raj<sup>2</sup> modeled the thin film as a linear viscoelastic solid with spherical isolated pores. Neither model accurately represents the sintering of thin polycrystalline films.

Two important reasons may be put forward to explain why continuum models are inadequate to represent the sintering of polycrystalline films. First, the kinematics associated with continuum mechanics is not at all similar to the kinematics of a sintering process governed primarily by diffusion processes which are directionally specific. Second, continuum models neglect the grain boundaries and grain growth phenomena, which is equivalent to putting the grain boundary energy equal to zero. This is a serious limitation since the grain boundary energy in ceramic materials can be comparable to the surface energy. In this paper, a model in which the kinematics more closely resemble those of a directionally-specific diffusion process is developed. The effect of the grain boundary energy is also considered. Continuum mechanics is not used in developing the model. An approach based on the more fundamental ideas of conservation of mass and minimization of the total free energy is used.

## KINEMATICS

The model assumes that the material is made up of spherical particles stacked in a simple cubic array as shown in Figure 1, and that densification occurs at constant temperature. As the material densifies, necks form between the spheres and the centers of the spheres get closer together. If the material is unconstrained, the spheres will get closer together in all three directions. However, if the film is deposited on a rigid substrate in the x-z plane, then the

spheres can get closer only in the y direction. This geometric constraint is the difference between constrained sintering and unconstrained sintering. Since sintering is done without any pressure applied, conservation of mass requires that the volume of material in the necks be equal to the volume of material removed from between the spheres. The shape of the necks will be such that the total free energy (surface and grain boundary energy) will be minimized. These requirements completely define the kinematics of the model.

## KINETICS

The driving force for densification is the reduction in the free energy. As the material densifies, surface energy is eliminated, but grain boundary energy is created. Densification will proceed only if there is a net reduction in the free energy. For this model, it is assumed that the densification occurs only through grain boundary diffusion. With this assumption, the kinetics can be derived from the basic principles of atomic flux and chemical potential.

## RESULTS

The model shows that a thin film may not completely densify. Densification stops because a local minimum is reached in the free energy, i.e. further densification would increase the free energy. It shows that densification of a thin film is strongly dependant on the ratio of grain boundary to surface energy, and weakly dependant on grain growth. Figure 2 shows the model fit to the experimental data for ZnO by Garino and Bowen<sup>3</sup>. The ZnO was sintered at 778°C, and the initial relative density was 55% which compares favorably with 52.4% used in this model. The top curve on the figure shows the volumetric shrinkage of an unconstrained film, and the bottom curve shows the linear shrinkage of an unconstrained film. The middle curve shows the volumetric shrinkage of a constrained film. A ratio of grain boundary to surface energy of 1.5 was used in the curve fits.

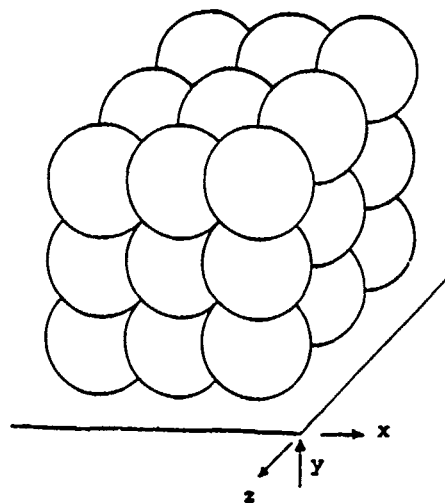


Figure 1. Model Geometry.

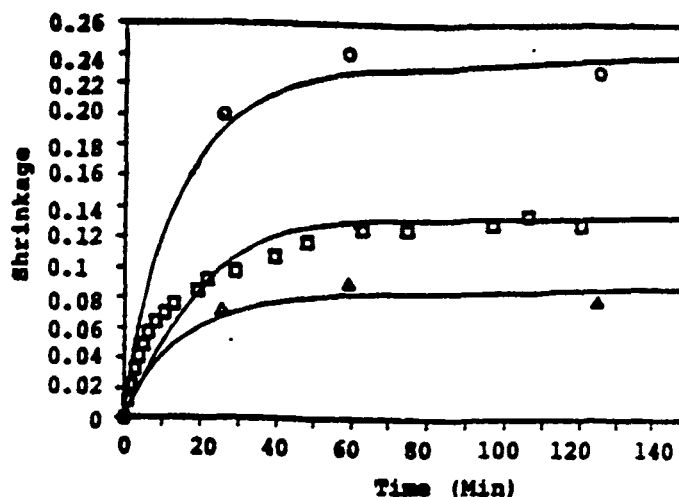


Figure 2. Comparison of Model and ZnO Data.  
( O Vol. Shrinkage - Unconstrained Film,  
□ Vol. Shrinkage - Constrained Film,  
▲ Linear Shrinkage - Unconstrained Film)

## REFERENCES

1. G. W. Scherer and T. Garino, J. Am. Ceram. Soc., 68 [4] 216-20 (1985).
2. R. K. Bordia and R. Raj, J. Am. Ceram. Soc., 68 [6] 287-92 (1985).
3. T. Garino and H. K. Bowen, J. Am. Ceram. Soc., 73 [2] 251-57 (1990).

# **Crack Detection in Aircraft Structures by Pulse Probing**

N. Tarabishy, R. Menon, B. Bahr, H. Lankarani, J. Talia

Mechanical Engineering Department  
National Institute for Aviation Research  
The Wichita State University  
Wichita, Ks. 67208

## **Abstract**

This paper describes the results of testing a simple structure for the presence of cracks using the analysis of its frequency spectrum. The defect is identified by the changes in the vibration pattern of the structure. The change can be characterized by a shift of the waveform frequency or power at which maximum amplitude is occurred.

## **Introduction**

Frequency analysis method is a nondestructive evaluation technique which utilizes the changes in the frequency spectrum of a structure for detection of flaws within the structure. A hammer with a force transducer is used to excite the structure at specific points. Dropping of a ball is an alternative way to produce uniform pulses. The analysis of the waveform (frequency spectrography) can be used to detect the presence of defects.

## **Methodology**

Several samples of Aluminum 7075 T6 QQ-A-250/12, of thickness 0.075 inches, were made to the size of 8 x 11 inches. By randomly picking a plate, the response map of the plate was determined in the following manner. Several points were marked on the plate, as in Figure 1. The impact points were 2, 3, 4, and 5 inches from the sensor, and the sensor was 1 inch from the center of the plate. The impact was done on the plate in several angles with center line forming a half circle with the sensor at its center. Impact at 0, 10, 20, ... 90° was performed, and the maximum response frequency was recorded by an HP frequency spectrum analyzer. After performing the above procedure for every one of the positions from the sensor, the sensor was shifted to 2 inches from the center of the plate and the same process of impact at different positions and recordings were repeated.

After getting reference maps for the uncracked plate, a very small crack was introduced by drilling a hole of diameter 0.0135 inch, and the tests were repeated as with the uncracked plate. This hole was enlarged to 0.021 and then 0.031 inches. The tests were carried on for the plate with each crack.

In order to compare the results, a graph of the power shift was plotted at a specific angle, as shown in Figure 2. It can be observed that at a distance of 2 inches, there is a difference in the frequency at which maximum amplitude occurred. This indicates the presence of a crack. The difference in the frequency response of the cracked and uncracked plates can be observed until the distance between the transducer and the impact position reaches 4 inches, after which the crack is not detected by the transducer.

### References

- [1] Kurta, M., and Okamura, H., "Bending and Vibration of a Simply Supported but Partially Clamped Rectangular Plate", Proc. 8th Jap. Natl. Congr. Appl. Mech., 1958, pp.397-403.
- [2] Reed, R., Jr., "Comparison of Methods in Calculating Frequencies of Corner-Supported Rectangular Plates. NASA TN D-3030, 1965.
- [3] Barton, M. V., "Vibration of Rectangular and Skew Cantilever Plates", Appl. Mech. Div., The American Soc. Of Mech. Eng., March 1950, paper No.50-A-12.
- [4] Warburton, G., "The Vibration of Rectangular Plates", proc. Inst. Mech. Eng., ser. A, vol. 168, no.12, 1954, pp.371-384.

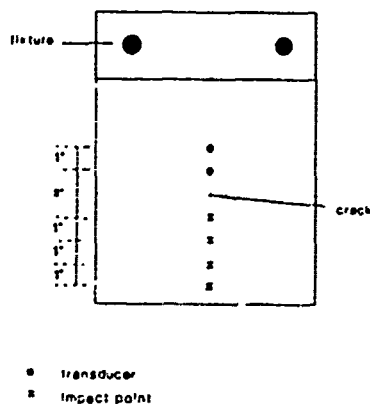


Fig 1 Plate setup

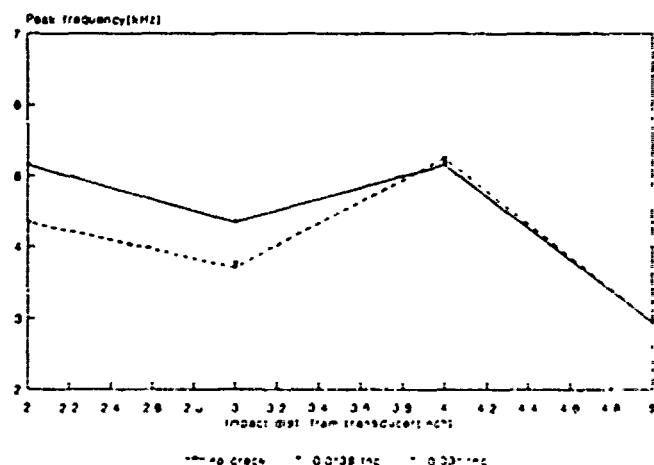


Fig 2 Peak frequency shift due to a crack (Transducer 1" from center)

This project was sponsored by Federal Aviation Administration, Atlantic City, NJ.

# UNDERGROUND CAVERN DESIGN FOR COMPRESSED AIR ENERGY STORAGE

M. REZA SALAMI

Assistant Prof., Department of Civil Engineering, North Carolina A. & T. State University, Greensboro, NC 27411

## ABSTRACT

This paper contains the results of stability assessment of CAES caverns to be excavated in the McIntosh salt dome. The study consists of two major parts: the stability assessment of the whole dome under the operation of Compressed Air Energy Storage (CAES) caverns and the operation of existing caverns, and the determination of safe boundary distance for CAES caverns using a single cavern. In this paper the whole dome was analyzed [1-2].

## INTRODUCTION

For many years, Compressed Air Energy Storage (CAES) has been the subject of research among electric utility companies, in order to determine the feasibility of storing off-peak excess electricity in the form of compressed air. Conceptually, the compressed air would be stored in underground geological formations which have pressure integrity and are stable under CAES operating pressure and temperature ranges. This compressed air would later be converted back into electricity to meet peak hour demand by running the turbines. It has been realized for many years that underground salt domes are very suitable for this purpose, since the first CAES cavern, excavated in a salt dome in Huntorf, West Germany, has been operating successfully since 1977 [1-2].

## ANALYSIS

Due to the uncertainty and unavailability of the full data required for analysis, numerical finite element analysis of solution mining and cavern storage networks has been difficult. The data needed for computer simulation include the geology of the area, the geometry of the cavern network, the properties of the materials involved, in situ stress level, and cavern operating conditions. The existing data in these categories should be carefully evaluated to obtain the necessary information related to the particular analysis. The following subsections describe the data which were used to analyze of the McIntosh salt dome cavern field.

## MATERIAL PROPERTIES AND IN-SITU STRESS

The results of the finite element analysis depend greatly on the material property parameters which are used to characterize the ground material. The reliable methods of obtaining such parameters are (1) laboratory testing on cores obtained from the particular sites; and (2) in situ measurements. In situ stress is the primary cause of cavern deformation and perhaps the most important variable in the analysis of deep geological structures.

## CAVERN PRESSURE

All the caverns in the McIntosh dome, except the CASE caverns, were assumed to be filled with brine, which has a density of  $1.2 \text{ g/cm}^3$ . In all our analysis, a pressure of 875 psi was used for CAES caverns.

## METHOD OF STUDY

The method of study involves construction of finite element models (FEM) of the McIntosh salt dome, representing the actual excavation geometries of existing brine wells and the geometries of the proposed CAES caverns [1-2].

### Site-Specific Meshes

In order to simulate the 3-dimensional nature of the deformation, two 2-dimensional plane strain meshes of the whole dome, as shown in Figs 1 and 2, were constructed [1-2]:

1. A horizontal section through the entire salt dome, including all brine wells and CAES caverns.
2. A vertical section passing through the maximum possible number of brine wells and CAES caverns.

## RESULTS OF VERTICAL AND HORIZONTAL PLAIN STRAIN ANALYSIS

Results obtained for the vertical and horizontal sections using plane strain analysis are shown in Figs 1-3.

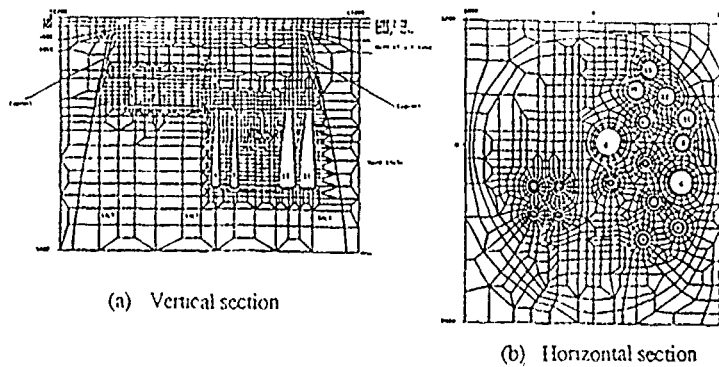


FIG. 1. Close-up of finite element network of 15-cavern system illustrating the cavern geometry and the geological formations for the vertical and horizontal sections.

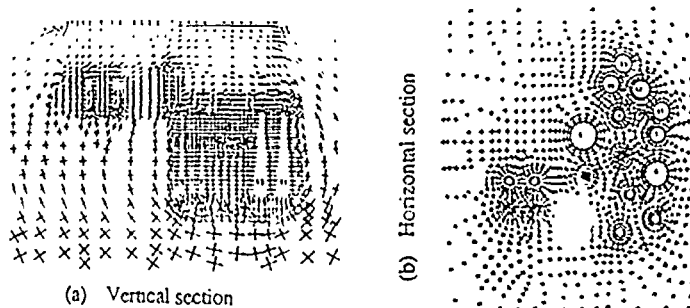


FIG. 2. The principal stress distribution patterns around caverns for vertical and horizontal sections (scales: 1" = 15,000 psi for vertical section and 1" = 20,000 psi for horizontal section at the depth of 2,400 ft).

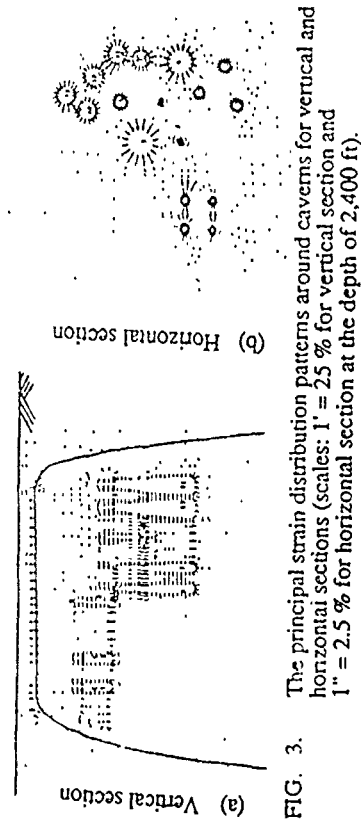


FIG. 3. The principal strain distribution patterns around caverns for vertical and horizontal sections (scales: 1" = 2.5 % for vertical section and 1" = 2.5 % for horizontal section at the depth of 2,400 ft).

## CONCLUSIONS

The following conclusions are drawn from this study:

1. **Stability of Cavern Field**  
Finite element analysis shows a stable condition around the cavern field.
2. **Stability of CAES Caverns**  
The whole dome analysis shows that the site selected for the study is stable, where the sensitivity analysis strengthens this conclusion.
3. **Stress Distributions**  
A large plastic region is developing at the bottom of the solution caverns, but not around the CAES caverns.
4. **Material Property Parameters**  
Correct estimation of the material property parameters plays a major role in this analysis. It is worth while to mention here that the above analysis is important for the future use in analyzing and designing all the compressed under-ground storage used for storing oil, chemical or air.

## REFERENCES

1. M. Reza Salami, Serata Geomechanics Inc., "Preliminary Computer Analysis on Long-Term Stability of McIntosh Salt Dome in Relation to Compressed Air Energy Storage (CAES) Cavern Development," Preliminary report for EPRI, Presented at Solution Mining Research Institute Spring Meeting, Tulsa, Oklahoma, (1987).
2. Electric Power Research Inst., "General Electric Company, Conceptual Design for a Pilot/Demonstration Compressed Air Storage Facility Employing a Solution-Mined Salt Cavern," section 7, (1977).



# Analytic investigation of pressure and damping forces acting on check valve mechanisms

Theodosios Korakianitis<sup>†</sup> and George I. Pantazopoulos<sup>‡</sup>

Department of Mechanical Engineering,  
Washington University,  
Campus box 1185,  
One Brookings Drive,  
St. Louis, MO 63130

**Introduction:** Check-valve mechanisms are used to regulate a fluid flow based on pressure differences as illustrated in figure 1. The pressure and damping forces acting on the components of a check valve mechanism are investigated. Three different geometric configurations for the components of the check valve are studied. The results found could be easily used in a computer model to investigate the dynamic response of check valve mechanisms used in realistic applications.

**Assumptions:** Assuming that the velocity of the check valve sphere is much faster than that of the fluid stream, the problem is considered as quasi steady (steady for small intervals of time). For cases where the Reynolds Number (evaluated with characteristic length the height of the gap) is small, the problem of determining the viscous and pressure forces on the check valve sphere can be solved using lubrication theory. Assuming that the (lubrication) characteristic number  $Rey$   $(h_0/R_b)^2$  is much less than 1, all the assumptions of lubrication theory are valid, and the momentum equations become:

$$\begin{aligned} 0 &= \frac{\partial p}{\partial x} + \mu \frac{\partial^2 u}{\partial z^2} \\ 0 &= \frac{\partial p}{\partial z} \end{aligned} \quad (1)$$

<sup>†</sup> Assistant Professor

<sup>‡</sup> Graduate Research Assistant

**Analytic solutions:** The determination of the pressure and damping forces acting on the check valve sphere when it is open, requires the solution of the flow problem through the passage formed by the check valve sphere and the wall as shown in figure 2. Three different wall geometries have been considered: convex; concave; and plane wall. For small passage length with respect to the radius of the sphere the solutions can be written as functions of the equivalent radius  $R_{eq}$ , a function of the sphere radius  $R_b$  and the wall radius  $R_w$ , where:  
for concave wall  $R_{eq} = R_w R_b / (R_w + R_b)$ ;  
for convex wall  $R_{eq} = R_w R_b / (R_w - R_b)$ ; and  
for plane wall  $R_{eq} = R_b$ .

The velocity of the sphere  $U_b$  is analyzed into its components  $U_x$  and  $U_z$  as shown in figure 2. Since the governing equations are linear, the problem is solved by adding three solutions: (a) the squeeze of the oil film (when the sphere approaches the wall perpendicularly with velocity  $U_z$ ); (b) the shear of the oil film (when the sphere moves parallel to the wall with velocity  $U_x$ ); and (c) the flow of oil through the passage due to pressure differences between the two reservoirs (keeping the sphere fixed). The velocity distribution in each case is given by:

$$u(x, z) = U^* \frac{z}{h(x)} + \frac{1}{2\mu} \frac{dp}{dx} z [z - h(x)] \quad (2)$$

where  $U^* = U_x$  for shear (case b), and  $U^* = 0$  otherwise.

The height of the passage is given by:

$$h(x) = h_0 + \frac{x^2}{2R_{eq}} \quad (3)$$

The pressure gradient is found by integrating the continuity equation (4) from 0 to  $h(x)$  in each case

$$\frac{\partial u}{\partial x} + \frac{\partial w}{\partial z} = 0 \quad (4)$$

The pressure gradients for each of the three cases are integrated using asymptotic approximations (from 0 to  $\infty$ ) to provide the final solutions for the pressure distributions.

**Conclusions:** The pressure forces are distinguished in two categories: (a) damping forces of the form  $F_{dx} = C_{dx}U_x$  and  $F_{dz} = C_{dz}U_z$ ; and (b) static pressure forces  $F_p$ , where:

$$C_{dx} = \frac{6\pi\mu R_b}{h_0} [I_1(L_2) - I_1(L_1)] \quad (5)$$

$$C_{dz} = \frac{6\pi\mu R_{eq} R_b}{h_0} [I_2(L_2) - I_2(L_1)] \quad (6)$$

$$F_p = \frac{-3\pi\mu R_p^2 (U_p - U_t)}{2h_0^2} [I_3(L_2) - I_3(L_1)] \quad (7)$$

In the above expressions  $L_1$  and  $L_2$  are the lengths of the converging and diverging passages in the flow direction, and the auxiliary functions are given by:

$$I_1(L) = \frac{L^3(1 + L\Phi(L)/R_{eq})}{L(2h_0 + 3h_L) + 3h_L^2\Phi(L)}$$

$$I_2(L) = \frac{L}{h_L^2}(h_L - 2h_0) + \Phi(L)$$

$$I_3(L) = L \left[ \frac{L}{h_L} + 3\Phi(L) \right] \quad (8)$$

$$\Phi(x) = \sqrt{\frac{2R_{eq}}{h_0}} \arctan \left[ \frac{x}{\sqrt{(2R_{eq}h_0)}} \right]$$

$$h_L = h(x = L)$$

The above expressions can be used for dynamic investigations involving check-valve mechanisms.

**Acknowledgements:** This work was performed under sponsorship by the Department of Mechanical Engineering and C-K Engineering, Inc.

#### Bibliography:

A. Cameron and C. M. McEttles (1981). "Basic lubrication theory". 3rd edition, Ellis Horwood Ltd.  
F. M. White (1974). "Viscous fluid flow", McGraw Hill.

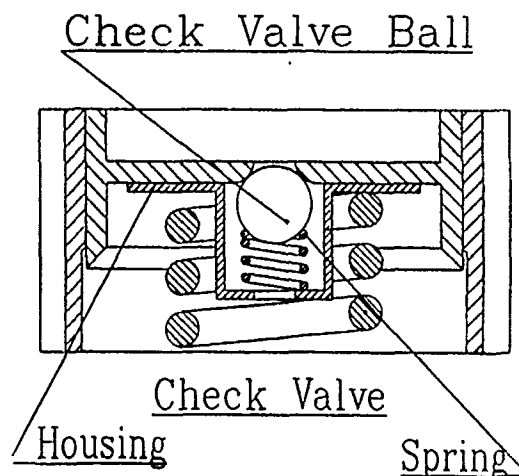


Figure 1: Typical check-valve mechanism

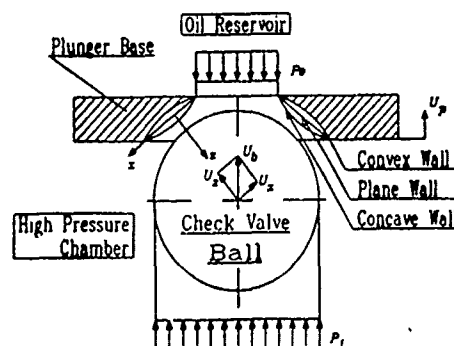


Figure 2: Problem configuration

## NONLINEAR ANALYSES OF LONG REINFORCED CONCRETE FOLDED PLATE STRUCTURES

Yousef N. Ahmad, Department of Civil  
Engineering, Sana University, Yemen

Pattabhi Sitaram, Department of Civil  
Engineering, Kansas State University,  
Manhattan, KS

Stuart E. Swartz, Department of Civil  
Engineering, Kansas State University,  
Manhattan, KS

### ABSTRACT

The service level response of long, reinforced concrete folded plate structures is analyzed using the finite difference (FD) and layered, finite element (FE) methods in order to study the performance of the steel reinforcing and its influence on cracking and deflection behavior. This is considered as important as studying the collapse behavior and is certainly a preliminary step in such a study. In the FD method, the cracks are constrained to occur in the longitudinal and/or transverse directions, and also only the bending stiffness corresponding to the crack point is modified. Such restrictions are relaxed in the FE method. The analytical results are compared with available experimental results from well-executed, model studies.

### INTRODUCTION

In the analysis of reinforced concrete folded plate structures it is important to consider the effects of reinforcement on the cracking and the load-deflection response. Cracking reduces the overall flexural rigidity of the slab, causing an increase in deflection. And rigidity of a cracked section, depends greatly on the percentage of reinforcing steel. Extensive cracking may damage serviceability of the structure. The FD method, which is simple and advantageous for a rectangular domain was chosen for a preliminary analysis (1).

In contrast to the FD approach, a more general analysis by a layered finite element procedure is being developed to study the service level response and ultimate behavior of folded plate structures. Almost all the nonlinearities exhibited by reinforced concrete under short-term monotonic loading are considered in this method.

## RESULTS AND DISCUSSION

For the finite different method an incremental - iterative procedure (step-by-step analysis) was used (1). The solution stopped when the maximum compressive strain in the concrete was reached. The analytical solutions are compared here with one test specimen (2), Figure 1. One half of one of the plates of the v type structure is shown. The following conclusions may be seen.

(1) The analytical results of cracking agreed reasonably well with experimental results. The crack patterns predicted by the analytical solution were in reasonable agreement with the experimental results (Fig. 1). The cracking load predicted by the analytical solution was 33 psf, and that obtained experimentally was 40 psf.

(2) Figure 2 shows load vs. deflection curves at different locations. The analytical results agreed qualitatively and quantitatively with the experimental results and the analytical results are on the conservative side.

(3) It is seen that the elastic solution without considering cracking is grossly in error after cracking commences.

## REFERENCES

1. Ahmad, Yousef N., "Analytical Study of a Long-Span Reinforced Concrete Folded Plate", PhD Thesis, Kansas State University, 1990.
2. Sutton, C.D., "An Experimental and Analytical Study of a Reinforced Concrete Folded Plate Structure", PhD Thesis, Purdue University, August 1971.

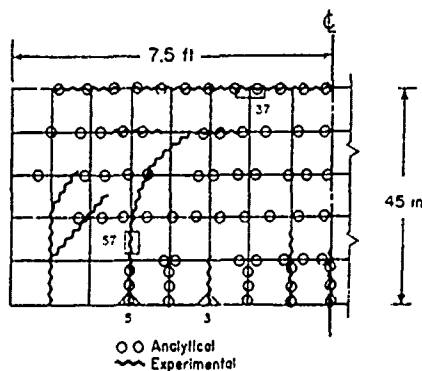


FIGURE 1. CRACK PATTERNS AND GAGE LOCATIONS, MODEL 2, REF. [2]

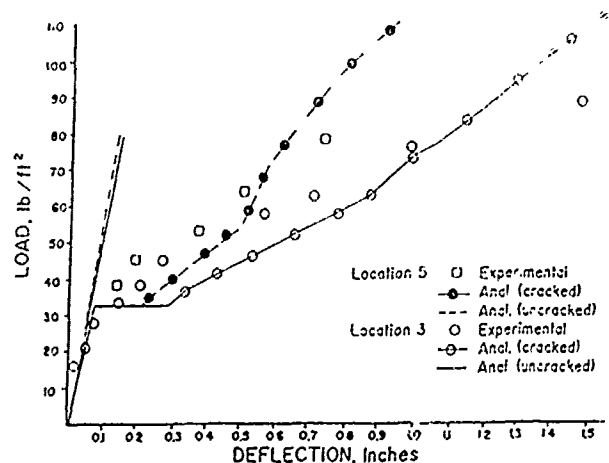


FIGURE 2. DEFLECTIONS, MODEL 2, REF. [2]

# VIBRATION FREQUENCIES OF A TAPERED PILE PARTIALLY EMBEDDED IN AN ELASTIC FOUNDATION

W. Lionel Craver Jr., Professor  
and Fernando Mendez, Graduate Student  
Mechanical and Industrial Engineering Department  
The University of Texas at El Paso  
El Paso, Texas USA 79968

## Introduction

This paper is a study of the free transverse vibrational frequencies of a tapered pile partially embedded in an elastic foundation and subjected to an axial load. This is an extension of the work performed by Valsangkar and Pradhanang [1] to include tapered piles. The tapered pile is assumed to be Bernoulli-Euler beam and the foundation in which the pile is embedded is assumed a Winkler type foundation. The equations of motion were derived, the natural frequencies were solved by applying a finite difference method, and parameter studies were performed.

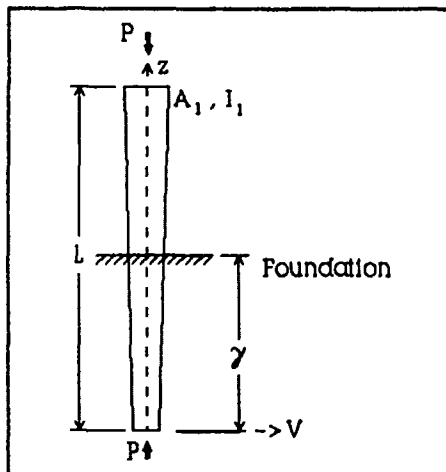


Figure 1. Tapered Pile in Elastic Foundation.

## Analysis

The differential equations governing small amplitude, transverse vibrations, of the pile shown in Figure 1, are

$$\frac{d}{dx^2} \left[ EI(x) \frac{d^2 V}{dx^2} \right] + P \frac{d^2 V}{dx^2} + k(x) V - \omega^2 \rho A(x) V = 0 \quad (1)$$

$$\frac{d}{dx} \left[ EI(x) \frac{d^2 V}{dx^2} \right] + P \frac{d^2 V}{dx^2} - \omega^2 \rho A(x) V = 0 \quad (2)$$

Equation (1) governs motion of the portion of the pile which is contained within the elastic foundation, while equation (2) governs the motion of the unembedded portion of the pile.

where : V is the transverse deflection

A is the cross-sectional area

I is the area moment of inertia

$\rho$  is the material density

$\omega$  is the natural frequency

k is the foundation elastic parameter

P is the axial load

The pile is assumed to have equal tapers in both directions, the cross-section can therefore be either circular or rectangular. Defining  $I(x)$ ,  $A(x)$ , and  $k(x)$  the differential equations become:

$$\frac{d^4 V}{dz^4} + \left[ \frac{8(\alpha-1)}{(1+(\alpha-1)z)} \right] \frac{d^3 V}{dz^3} + \left[ \frac{12(\alpha-1)}{(1+(\alpha-1)z)^2} + \frac{P^*}{(1+(\alpha-1)z)^4} \right] \frac{d^2 V}{dz^2} + \frac{k^* V}{(1+(\alpha-1)z)^3} = \frac{q^4 V}{(1+(\alpha-1)z)^2} \quad (3)$$

$$\frac{d^4 V}{dz^4} + \left[ \frac{8(\alpha-1)}{(1+(\alpha-1)z)} \right] \frac{d^3 V}{dz^3} + \left[ \frac{12(\alpha-1)}{(1+(\alpha-1)z)^2} + \frac{P^*}{(1+(\alpha-1)z)^4} \right] \frac{d^2 V}{dz^2} = \frac{q^4 V}{(1+(\alpha-1)z)^2} \quad (4)$$

where:  $z = x/L$

$\alpha = \text{taper ratio}$

$A_1 = \text{cross-sectional area at the top}$

$I_1 = \text{area moment of inertia at the top}$

$$q^4 = \frac{\omega^2 \rho A_1 L^4}{EI_1} ; k^* = \frac{k_0 L^4}{EI_1} ; P^* = \frac{PL^2}{EI_1}$$

### Solution and Results

The lack of a closed form solution for equation (3) necessitated the use of a central difference finite difference method for solution. In this research the parameters were varied as follows;  $\alpha$  1.0 to 1.5,  $k^*$  1.0 to 10,000,  $P^*$  had values of 0.25 and 1.0, and  $\gamma$  (the fraction of length embedded) 0.0 to 1.0. Results, which are the first three eigenfrequencies,  $q^2$  will be presented in tabular and graphical form.

Reference: [1] Valsangkar, A. J. and Pradhanang, R. B., "Free Vibration of Partially Supported Piles," ASCE Journal of Engineering Mechanics, Vol.113, No.8, Aug.1987, pp 1244-1247.

This material is based on work supported by NASA grant NAG9-382 from NASA Johnson Space Center.

# BUCKLING OF NONPRISMATIC COLUMNS MADE OF TWO MATERIALS

R. A. Hilsbos & R. Yair  
Department of Mechanical Engineering  
Western Michigan University  
Kalamazoo, MI 49008

## INTRODUCTION

For the nonprismatic columns shown in Figure 1 A-B the critical load, originally obtained by Dinnik [1], are given by the following equations:

$$\tan\left(\sqrt{\frac{P_{cr}}{EI_1}} l_1\right) \tan\left(\sqrt{\frac{P_{cr}}{EI_2}} l_2\right) = \sqrt{\frac{l_2}{l_1}} \quad (\text{for column 1A}) \quad (1)$$

$$\tan\left(\sqrt{\frac{P_{cr}}{EI_1}} \frac{l-a}{2}\right) \tan\left(\sqrt{\frac{P_{cr}}{EI_2}} \frac{a}{2}\right) = \sqrt{\frac{l_2}{l_1}} \quad (\text{for column 1B}) \quad (2)$$

In the same paper [1], Dinnik shows that equations (1) and (2) can be represented by the formulae:

$$P_{cr} = \frac{m_1 EI_2}{l^2} \quad (1')$$

$$P_{cr} = \frac{m_2 EI_2}{l^2} \quad (2')$$

where  $m_1$  and  $m_2$  are numerical factors dependent on the ratios  $l_1/l_2$  and  $l_1/l_1$  for column 1A and  $a/l$  and  $l_1/l_2$  for column 1B. Dinnik also calculated the numerical factors for different geometric configurations.

The critical load for nonprismatic columns constructed of two different materials as shown in Figure 2 A-B-C-D, can be determined by using the equations developed by Groper and Kenig [2] for obtaining the critical load of Dinnik's inelastic columns. By substituting  $E_1$  for  $E_{i1}$  and  $E_2$  for  $E_{i2}$  in the solutions presented in reference [2], the following equations are obtained:

$$\tan\left(\sqrt{\frac{P_{cr}}{E_1 I_1}} l_1\right) \tan\left(\sqrt{\frac{P_{cr}}{E_2 I_2}} l_2\right) = \sqrt{\frac{E_2 I_2}{E_1 I_1}} \quad (\text{for column 2-A}) \quad (3)$$

$$\tan\left(\sqrt{\frac{P_{cr}}{E_1 I_1}} \frac{l-a}{2}\right) \tan\left(\sqrt{\frac{P_{cr}}{E_2 I_2}} \frac{a}{2}\right) = \sqrt{\frac{E_2 I_2}{E_1 I_1}} \quad (\text{for column 2-B}) \quad (4)$$

$$\tan\left(\sqrt{\frac{P_{cr}}{E_1 I_1}} l_1\right) \tan\left(\sqrt{\frac{P_{cr}}{E_1 I_1}} l_2\right) = \sqrt{\frac{E_1 I_1}{E_1 I_1}} \quad (\text{for column 2-C}) \quad (5)$$

$$\tan\left(\sqrt{\frac{P_{cr}}{E_1 I_1}} \frac{l-a}{2}\right) \tan\left(\sqrt{\frac{P_{cr}}{E_1 I_1}} \frac{a}{2}\right) = \sqrt{\frac{E_1 I_1}{E_1 I_1}} \quad (\text{for column 2-D}) \quad (6)$$

$E_e$  represents the equivalent modulus of elasticity of the composite cross-section of columns 2C and 2D. The values of  $E_e$  and  $I_e$ , calculated from conditions of equilibrium, are:

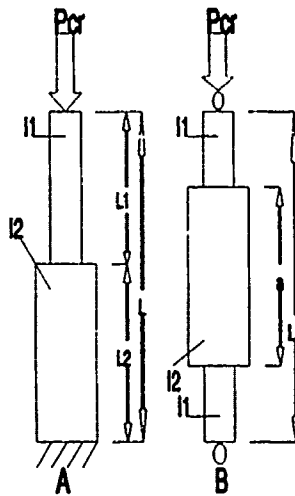


Fig. 1 - Dinnik's Columns

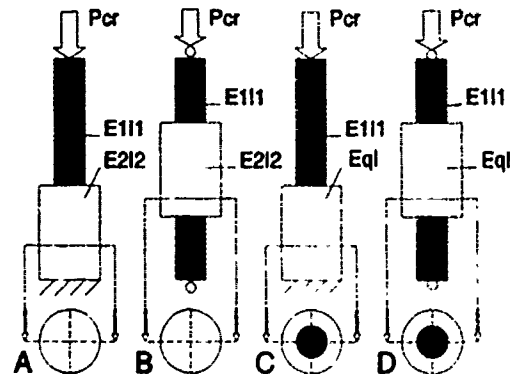


Fig. 2 - Two-Material Columns

$$E_g = \frac{E_1 I_1 + E_2 I_2}{I_1 + I_2} \quad (7); \quad I = I_1 + I_2 \quad (8)$$

#### DETERMINING CRITICAL LOAD FOR COLUMNS MADE OF TWO MATERIALS

The procedure used by Dinnik to obtain solutions (1') and (2') can be extended to equations (3) through (6) as follows: Consider, for example, equation (4) for the buckling load of the nonprismatic column made of two different materials (2B). The solution is in the form:

$$P_{cr} = \frac{BE_2 I_2}{l^2} \quad (4')$$

where B is a numerical factor depending on the ratios  $\alpha = a/l$  and  $\beta = E_1 I_1 / E_2 I_2$ . Substituting equation (4') into equation (4) yields:

$$\tan \left( \sqrt{\frac{B}{E_2 I_2}} 0.5(1-\alpha) \right) \tan \left( \frac{\sqrt{B} \alpha}{2} \right) = \sqrt{\frac{E_2 I_2}{E_1 I_1}} \quad (9)$$

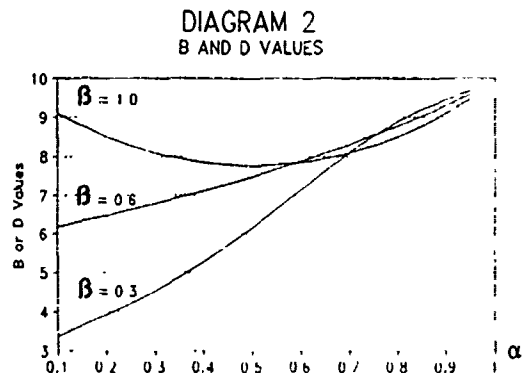
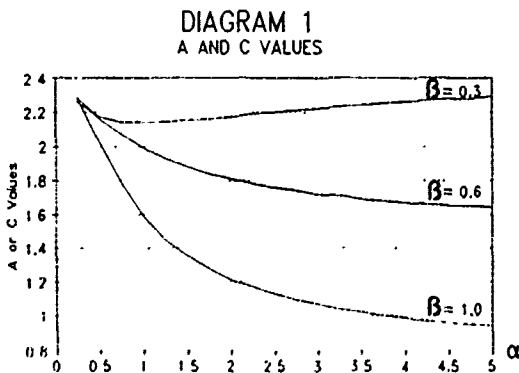
Similarly, equations (3), (5) and (6) can be written as:

$$P_{cr} = \frac{AE_2 I_2}{l^2} \quad (3')$$

$$P_{cr} = \frac{CE_2 I_2}{l^2} \quad (5')$$

$$P_{cr} = \frac{DE_2 I_2}{l^2} \quad (6')$$

The values of the coefficients A, B, C and D were calculated for different geometrical configurations and moduli of elasticity. They are presented in Diagrams 1 and 2.



#### References

- [1] Timoshenko, S.P., and Gere, J.M., *Theory of Elastic Stability*, 2nd. Ed., pp. 113-115, McGraw-Hill Book Company, 1961.
- [2] Groper, M., and Kenig, M.J., "Inelastic Buckling of Nonprismatic Columns", *Journal of Engineering Mechanics*, pp. 1233-1239, Vol. 113, No. 8, Aug. 1987.



# BUCKLING OF MULTIPLY LOADED NONPRISMATIC COLUMNS COMPOSED OF TWO MATERIALS

Q. SUN & Y. Lu  
Department of Mechanical Engineering  
Western Michigan University  
Kalamazoo, MI 49008

## INTRODUCTION

For the columns composed of two materials and loaded as shown in Figures 1 A-B, the critical load can be determined by using the equations developed by Groper and Kenig [1].

$$\tan\left(\sqrt{\frac{P_1}{E_1 I_1}} l_1\right) \tan\left(\sqrt{\frac{P_1+P_2}{E_2 I_2}} l_2\right) = \sqrt{\frac{P_1+P_2}{P_1} \frac{E_2 I_2}{E_1 I_1}} \quad (1)$$

$$\tan\left(\sqrt{\frac{P_1}{E_1 I_1}} \frac{l-a}{2}\right) \tan\left(\sqrt{\frac{P_1+P_2}{E_2 I_2}} \frac{a}{2}\right) = \sqrt{\frac{P_1+P_2}{P_1} \frac{E_2 I_2}{E_1 I_1}} \quad (2)$$

Where  $E_1$  and  $E_2$  are the two moduli of elasticity of the composed columns.

An approximate method to find the critical load is described in continuation.

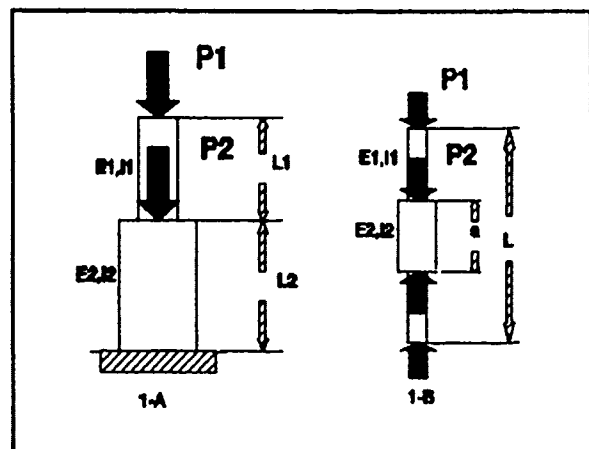
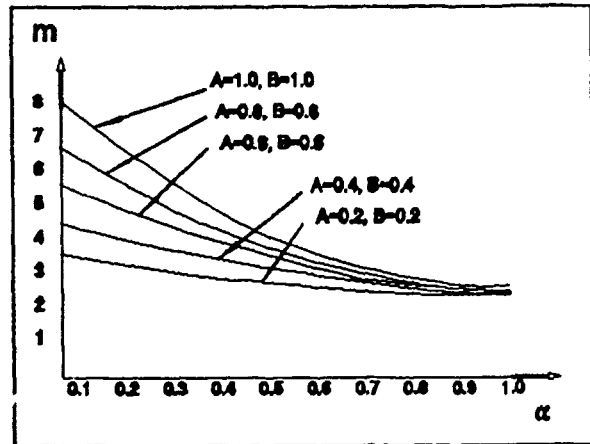


Figure 1 Columns



### THE APPROXIMATE METHOD

Assume

$$P_1 = \alpha (P_1 + P_2) \quad P_{cr} = P_1 + P_2 = m \frac{E_2 I_2}{l^2} \quad (3)$$

where  $m = m(A, B)$

$$A = \frac{E_1 I_1}{E_2 I_2}, \quad B_1 = \frac{l_1}{l_2}, \quad B_2 = \frac{a}{l}$$

The Eq. (1) and Eq. (2) then become

$$\tan\left(\sqrt{\frac{\alpha m}{A}} \frac{B_1}{1+B_1}\right) \tan\left(\sqrt{m} \frac{1}{1+B_1}\right) = \frac{1}{\sqrt{\alpha A}} \quad (1')$$

$$\tan\left(\sqrt{\frac{\alpha m}{A}} \frac{1-B_2}{2}\right) \tan\left(\sqrt{m} \frac{B_2}{2}\right) = \frac{1}{\sqrt{\alpha A}} \quad (2')$$

By using Newton-Raphson algorithm we can express  $P_{cr}$  in terms of  $\alpha$ ,  $A$  and  $B_1$  or  $B_2$  for column A or B.

# STEADY STATE DYNAMIC RESPONSE OF LIGHTWEIGHT EQUIPMENT IN STRUCTURES ON A FRICTION TYPE SUPPORT SUBJECTED TO GROUND MOTION

Alan G. Hemried  
Associate Professor  
and  
Kai-Ming Lei  
Graduate Student  
Department of Civil Engineering  
Oregon State University  
Corvallis, OR 97331

The concept of vibration isolation is not new. Recently this idea has been used to isolate civil engineering structures from severe ground motions and has been given the term base isolation. Effective base isolators remove the fundamental period of the structure from the period of strong ground shaking, in addition to providing energy dissipation. Significant attention has been focused on rubber-type base isolators; which include high damping rubber, laminated rubber (layers of steel and rubber bonded together), as well as laminated rubber with a central lead core. A relatively new isolation device, the resilient-friction base isolator (R-FBI) has been proposed. The isolator is composed of layers of teflon coated steel and a central rubber core. Energy dissipation is achieved through friction between the steel plates while the rubber core provides the restoring force. The system has been shown to be effective in isolating structures. The research to be presented examines whether the R-FBI will be equally effective in protecting sensitive lightweight equipment (such as computers or medical equipment) from ground motion.

The shear type three-degree-of-freedom equipment-structure-base system subjected to harmonic ground motion shown in the figure below is examined.

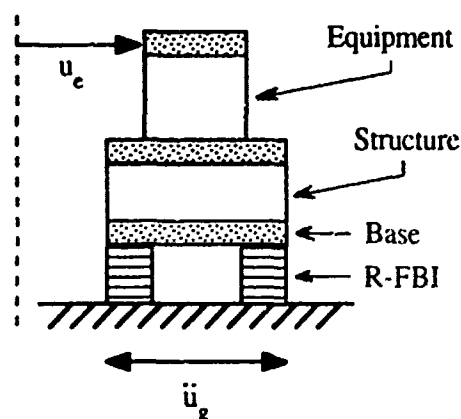


Figure One. Model of Equipment-Structure-Base on R-FBI Subjected to Ground Motion

It is assumed that the mass of the equipment is small in comparison to that of the structure and/or base. The motion of the system can be divided into two phases, whether the base is sliding or not. In each phase the response of the system is linear. The solution in each phase can therefore be determined exactly. The approach used is standard Laplace transform theory. The initiation and termination of sliding is determined numerically. This "semi-analytical" method for determining the equipment response is highly accurate and computationally efficient.

Depicted in Fig. 2 is the influence of friction coefficient on equipment response. The effects of other important system parameters on equipment response will be presented at the conference.

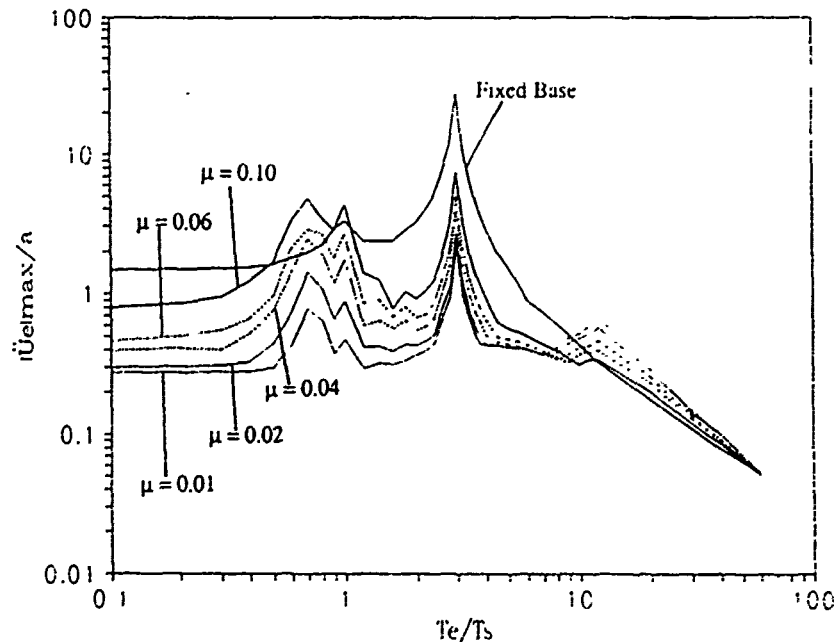


Figure Two. Effect of Friction Coefficient on Equipment Response versus Period Ratio

In the above figure  $T_e$  and  $T_s$  ( $=0.3$  secs) are the natural periods of the equipment and structure,

while  $\mu$  is the friction coefficient. Other relevant properties of the system are damping ratios

$\zeta_e = 0.02$ ,  $\zeta_s = 0.02$ ,  $\zeta_b = 0.08$ ; masses  $m_e = 0.01$  kg,  $m_b = 1.0$  kg,  $m_s = 1.0$  kg; ground motion

$\ddot{u}_g = a \sin(2\pi t/T_g)$ ,  $a = 0.5$  g; and natural periods  $T_g = 0.9$  s,  $T_b = 4.0$  s. The subscripts  $e$ ,  $s$ , and  $b$  indicate equipment, structure and base respectively. One notices that the largest amplification occurs when the equipment natural period is tuned to the period of the ground motion.

Amplification also occurs when the equipment and structure period are the same (conventional tuning). In most instances the R-FBI reduces the response of the equipment, and the smaller the friction coefficient the greater the reduction. There are several exceptions, however. At  $T_e/T_s =$

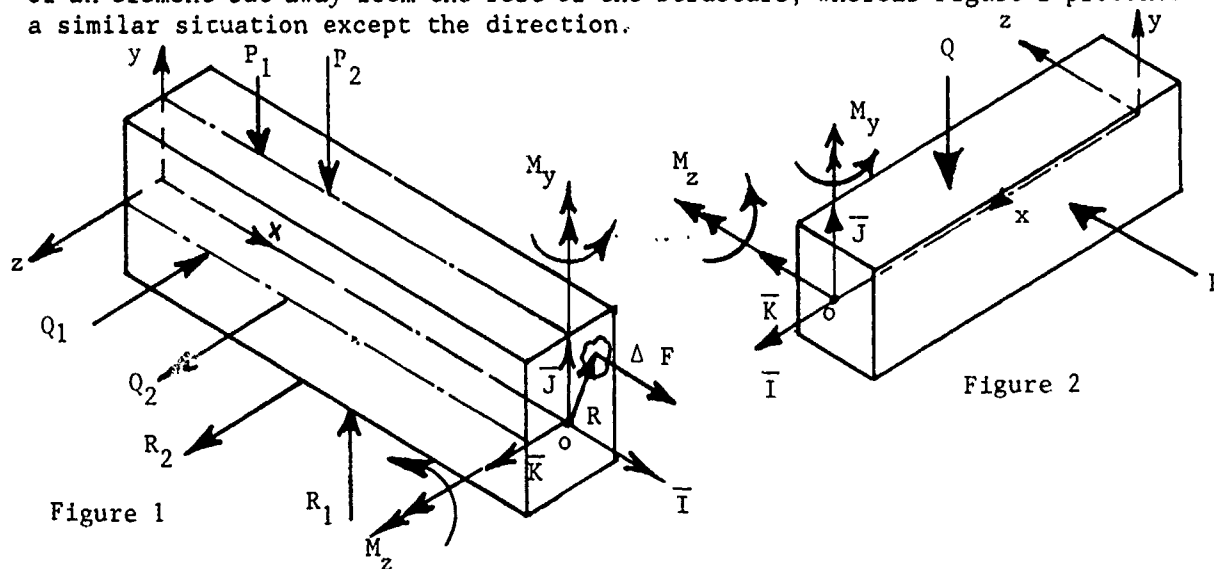
1.0 and  $\mu = 0.1$ , the isolated response exceeds the fixed base response. For this friction coefficient and system period, significant energy is imparted into the structure due to the stick-slip friction action. This energy is then transmitted in turn to the equipment. Quantitatively this effect can be observed by examining the Fourier transform of the response of the structure on the R-FBI system. This effect also explains the amplifications that exist in equipment response for friction coefficients  $\mu = 0.04$ ,  $\mu = 0.06$ , and  $\mu = 0.1$  for  $T_e/T_s = 0.6$ . There are amplifications in the high period region  $T_e/T_s \geq 12.0$ . At  $T_e/T_s = 13.3$  the equipment is tuned to the natural period of the isolator which yields a resonance effect. Interaction between the equipment and the base-isolator contributes to the amplifications in response in this region.

GENERAL FLEXURE EQUATION  
 "A More Comprehensive Approach"  
 Robert B. Salajekeh, Associate Professor  
 GMI Engineering & Management Institute  
 Flint, Michigan

The use of the general one-dimensional bending equation relating the fiber stress to bending moment and some geometrical properties of the element is not clear enough for the students as far as sign conventions are concerned. This sign convention which varies from one textbook to another relies to a great extent on common sense as how the element is stressed as the top is compared to the bottom. Of course, this common sense fails where the loading and geometric configuration are complex, leaving many students confused and usually arriving at wrong answers. The situation is by far more serious where the element has no axis of symmetry and bending occurs in two different planes.

The main objective of this article is to come up with a set of criteria which is common sense proof and can be applied to any element systematically in a straightforward manner. The approach employs vector mechanics and general flexure theory to arrive at the desired results.

Consider Figures 1 and 2 as illustrated below. Figure 1 presents the left part of an element cut away from the rest of the structure, whereas Figure 2 presents a similar situation except the direction.



In both Figures 1 and 2 a Right Hand System is employed for the analysis, where  $M_y$  and  $M_z$  are the necessary bending moments assumed to be both positive along y and z to keep the body in equilibrium momentwise, the rest of the internal forces are not shown as we are dealing with bending stresses only.

At any arbitrary section of Figure 1, obviously, a small force  $\Delta F = (\sigma_x \Delta A) \bar{I}$ , will have the following moment  $\Delta M_o$ .

$$\Delta M_o = R \times \Delta F = R \times (\sigma_x \Delta A) \bar{I} \quad (1)$$

Now, assuming plane section, will remain plane as in the case of simple bending, we can write  $\sigma_x = \alpha y + \beta z$ , (2) Where  $\alpha$  and  $\beta$  being constant. Substitution of Equation 2 into (1) will result in . . .

$$\Delta M_o = \Delta M_y \bar{J} + \Delta M_z \bar{K} = (y \bar{J} + z \bar{K}) \times (\sigma_x \Delta A) \bar{I} \quad (3)$$

from Equation 3, obviously we have

$$\begin{aligned} \sigma_x y \Delta A &= - \Delta M_z \\ \sigma_x z \Delta A &= \Delta M_y \end{aligned} \quad (4)$$

or

$$\begin{aligned} \int \sigma_x y dA &= - M_z \\ \int \sigma_x z dA &= M_y \end{aligned} \quad (5)$$

Replacing  $\sigma_x$  from Equation 2 into Equations 5 and simplifying the results will lead to:

$$\begin{aligned} \alpha I_z + \beta I_{yz} &= -M_z \\ \alpha I_{yz} + \beta I_y &= M_y \end{aligned} \quad (6)$$

Where,  $I_y$ ,  $I_z$  and  $I_{yz}$  are area moment of inertia and product of inertia respectively, solving for  $\alpha$  &  $\beta$  in Equation (6) will result in

$$\alpha = - \frac{M_z I_y + M_y I_{yz}}{I_y I_z - I_{yz}^2}, \quad \beta = \frac{M_z I_{yz} + M_y I_z}{I_y I_z - I_{yz}^2}$$

Replacing these values for  $\alpha$  &  $\beta$  into Equation 2 will yield

$$\sigma_x = - \left( \frac{M_z I_y + M_y I_{yz}}{I_y I_z - I_{yz}^2} \right) y + \left( \frac{M_z I_{yz} + M_y I_z}{I_y I_z - I_{yz}^2} \right) z \quad (7)$$

In term of the moment of applied forces, Equation 7 will become

$$\boxed{\sigma_x = - \left( \frac{M_z I_y + M_y I_{yz}}{I_y I_z - I_{yz}^2} \right) y + \left( \frac{M_z I_{yz} + M_y I_z}{I_y I_z - I_{yz}^2} \right) z} \quad (8)$$

Now find  $M_y$  and  $M_z$  for all applied forces, moments and reactions with respect to point O, vectorally. If they are along the positive y and z, replace their magnitude into Equation 8 to find  $\sigma_x$ , and change signs otherwise.

# FURTHER STUDY ON HERTZ'S CONTACT PROBLEM\*

Tian-quan Yun

Department of Mechanics, South China University of Technology  
Guangzhou, 510641, The People's Republic of China

Two new ideas are presented in this paper: 1, according to the characteristic of the integral equation of the Hertz's contact problem, the corresponding homogeneous integral equation has numerous solutions, i.e., the solution of the Hertz's contact problem is not unique, 2, the classical form of the integral equation of Hertz's contact problem is not exact, since it neglects the horizontal component of displacement. An exact integral equation of this smooth contact problem is given.

The corresponding homogeneous integral equation of Hertz's contact problem [1] is

$$\iint_{\Omega} q(s, \psi) ds d\psi = 0 \quad (1)$$

Where the integral domain  $\Omega$  is a fixed circle in the base plane under given load  $P$ .  $q$  is the unknown intensity of pressure.  $s, \psi$  are polar coordinates (Fig. 1). Now, we can always construct an integral equation

$$\int_a^b \int_c^d q_1(s, \psi) ds d\psi = 0 \quad (2)$$

with constants  $a, b, c, d$ , such that  $\Omega$  is included in  $(b-a) \times (d-c)$  and

$$q_1 = q_1(s, \psi) = q = q(s, \psi) \quad \text{for } (s, \psi) \in \Omega$$

$$q_1 = 0, \quad \text{otherwise.}$$

Then, (1) is equivalent to (2). However, (2) is a special case of Fredholm integral equation of the first kind

$$\int_a^b \int_c^d K(t, \phi; s, \psi) q_1(s, \psi) ds d\psi = F(t, \phi) \quad (3)$$

with  $K(t, \phi; s, \psi) \equiv 1$ ,  $F(t, \phi) \equiv 0$ . Obviously, (2) has numerous solutions. For example, we take

$$\int_c^d q_1 ds = 0 \quad \text{or} \quad \int q_n ds = 0 \quad (4)$$

There are numerous  $q_n$  can satisfy (4), e.g.,

$$q_n(s, \psi) = A(\psi) \cdot \sin \{ \pi(s - r \cos \psi) / [R \{ 1 - (r/R)^2 \sin^2 \psi \}^{1/2}] \}, \quad \psi \neq \pi/2.$$

$$q_n(s, \psi) = \begin{cases} h, & |s| < [R^2 - r^2]^{1/2}/2 \\ -h, & |s| > [R^2 - r^2]^{1/2}/2 \end{cases} \quad \psi = \pi/2. \quad (\text{see Fig. 2})$$

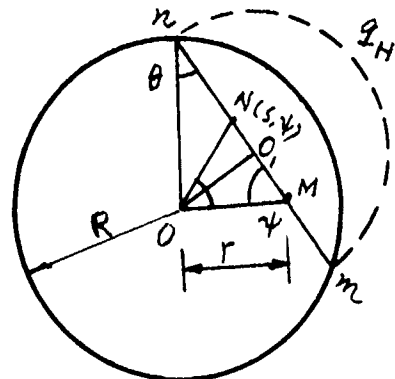


Fig. 1

Where  $\Lambda(\psi)$  is so chosen that  $q_n(0, \psi) = h$  (constant). Since the general solution  $q = q_H + q_n$ , where  $q_H = (q_0/R) [R^2 - r^2]^{1/2}$  is the Hertz's solution of the equation

$$\iint q \, ds d\psi = (\alpha - \beta r^2)/(k_1 + k_2) \quad (5)$$

where  $q_0, \alpha, \beta, k_1, k_2$  are constants. Therefore the general solution  $q$  of (5) is not unique.

Fig. 3 shows that points  $M_1, M_2$  with radii  $r_1, r_2$  coincide in  $M$  with radius  $r$  in the contact base circle  $R$  under load  $P$ . When horizontal displacements of  $M_1$  and  $M_2$  are taken into account, we have, from the geometric condition,

$$+ \delta \left( \iint q \cos \psi \, ds d\psi \right)^2 = \alpha - \beta r^2 \quad (6)$$

where  $\alpha, \beta, k_1, k_2$  are the same as above,

$$\gamma = \left[ \frac{(1-2\nu_1)(1+\nu_1)}{E_1 R_1} + \frac{(1-2\nu_2)}{(1+\nu_2)/(E_2 R_2)} \right] / (2\pi)$$

$$\delta = \left[ \frac{(1-2\nu_1)(1+\nu_1)}{(2\pi E_1)} \right]^2 / (2R_1) + \left[ \frac{(1-2\nu_2)(1+\nu_2)}{(2\pi E_2)} \right]^2 / (2R_2)$$

where  $R_1, E_1, \nu_1$  and  $R_2, E_2, \nu_2$  are radii, Young's modulus, Poisson's ratio of spherical body 1 and 2 respectively.

(6) is an exact non-linear, with small parameters, integral equation for smoothy contact problem of spherical bodies. Similar equation can be obtained for general bodies in smoothy contact.

#### Reference

1. Timoshenko, S.P., and Goodier, J.N., Theory of Elasticity, McGraw-Hill, New York, 3rd Edition, (1970), p.411.

\* The Project is supported by National Natural Science Foundation of China

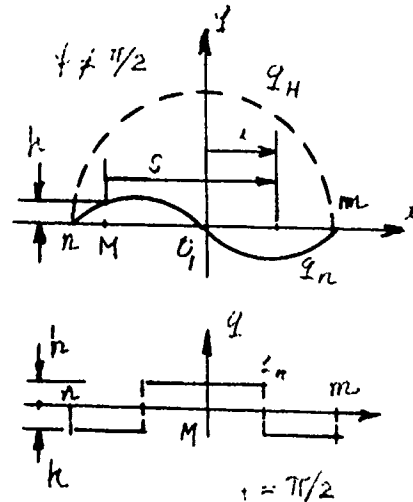


Fig. 2

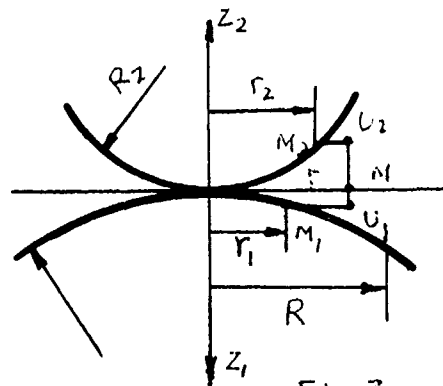


Fig. 3



# Investigation of Frictional Contact Interaction of Moving Elastic Bodies

Dr. Alexander Spector, All-Union Bearing Institute,  
115470, Moscow, USSR, Prospect Andropova, 19, apt.35

In this report non-stationary three-dimensional problems of local frictional contact between the moving elastic body and elastic foundation are considered. A formulation taking into account initial conditions, inertial properties of the body, external forces and moments, slip and adhesion sub-areas and also different components of local slip is proposed.

Main stages of the development of the considered range of problems were works of K.Johnson, J.Kalker (stationary, non-stationary rolling), R.Mindlin, H.Deresiewicz (quasi-stationary problems of shear and torsion), G.Duvant, J.-L. Lions, J.Oden, P.Panagiotopoulos (dynamics of elastic bodies with friction), J.Moreau (dynamics of rigid bodies with friction).

Boundary conditions of the considered problems take the form

$$w^+ - w^- + f = F \geq 0, \quad p \geq 0, \quad F \cdot p = 0$$

$$|\bar{\tau}| \leq \rho p, \quad \bar{\tau} \bar{s} - \rho p |\bar{s}| = 0$$

where  $w^\pm$  - normal elastic displacement of the body and foundation,  $f$  - function defining their surfaces,  $-p, \bar{\tau}(\tau_{xz}, \tau_{yz})$  - normal and tangential contact stresses,  $\bar{s}(s_x, s_y)$  - local slip velocity taking the form

$$\bar{s} = \bar{v} - \bar{V}^* \text{grad } B(p, \bar{\tau}) - B(\dot{p}, \bar{\tau})$$

where  $\bar{v}, \bar{V}^*$  are determined by kinematics of the moving body as a rigid one,  $B(\cdot)$  - integral operator with the kernel of Boussinesq-Cherutti. All functions owing to contact locality depend on two coordinates  $x, y$  and also on time  $t$ .

Equations of body motion are

$$M\dot{\bar{V}} = \bar{F}_{ex} + \int \bar{\sigma}(-p, \bar{\tau}) dx dy$$

$$\dot{\bar{K}} = \bar{M}_{ex} + \int [\bar{\tau} \times \bar{\sigma}] dx dy$$

where  $\bar{F}_{ex}, \bar{M}_{ex}$  - external forces and moments applied to the body,  $M, \bar{K}, \bar{V}$  - body mass, body central moment of momentum and body center mass velocity,  $\bar{r}$  - radius-vector to the considered point of the contact area.

Methods of solution of the formulated problem were developed. They consist of time-differential approximation, transition to variational problem sequence (in general non-smooth) concerning boundary stress, piecewise-linear (piecewise-constant) space approximation and numerical solution of obtained problems of mathematical programming.

Different regimes of body motion and body contact interaction with the foundation were investigated qualitatively (mathematically) and numerically.

Problems of evolution of contact fields with given kinematics of the moving body (given forces and moments) when inertial properties of the body could be neglected

were considered. Stabilization of all solutions to the solution of the stationary problem was proved, properties of different force and energetic characteristics as a function of time were determined.

Solutions of problems of transition from the initial state of rest (Fig.1) to the stationary regime (rolling with spin) and also from one stationary regime to another were obtained.

Essentially dynamic (in the sense of body inertia) problems were considered. Oscillating regimes of body motion and frictional force evolution both in case of external forces absence (Fig.2) and of their presence were defined; Characteristic time periods of interaction were described. Limit behaviour of solutions was investigated.

#### References

- Spector A., PMM, 50, N°1 (1987) 76-83  
 Spector A., Sov.Journ. of Friction and wear, 11, N°1 (1990) 49-56  
 Spector A., Proc. of Japan Intern. Tribology Conf. Nagoya, 1990, 1243-1246.

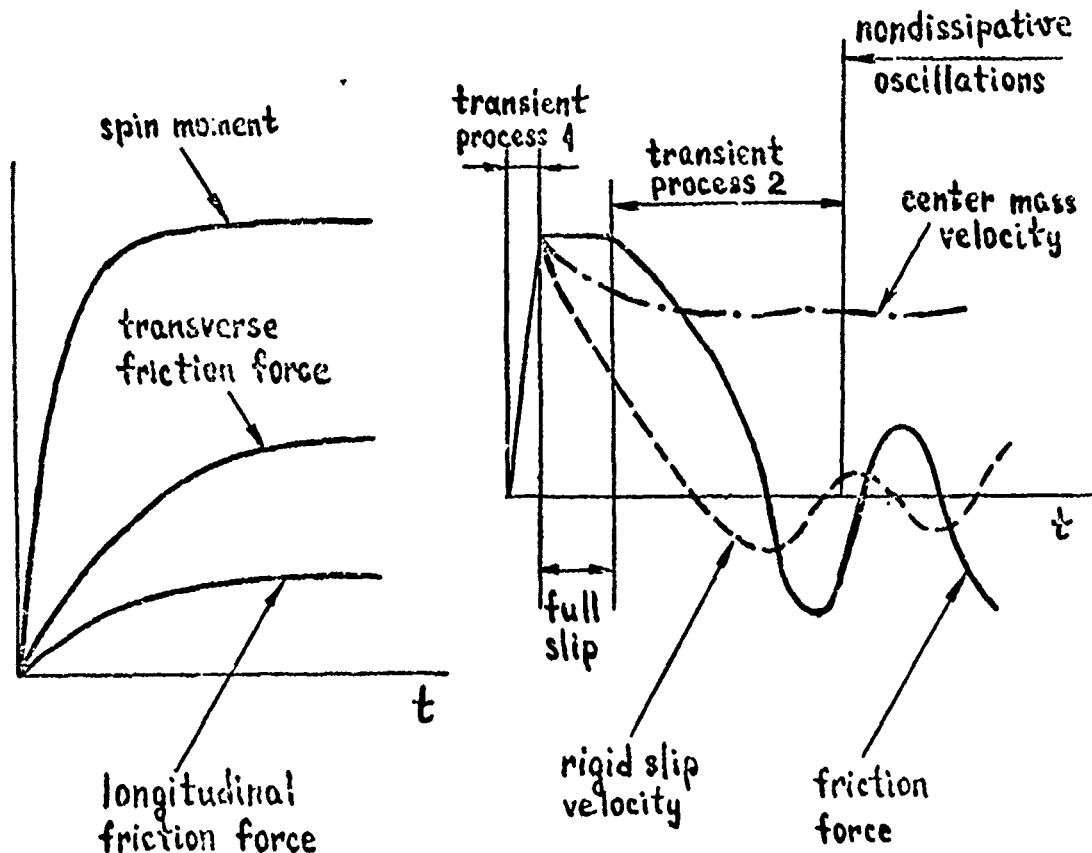


Fig.1  
 A transient regime: from the rest to stationary rolling with spin

Fig.2  
 A oscillating regime in dynamic problems

To the Problem of Elastic Equilibrium of Cylindrical  
Bodies with Noncircular Contour and its Applications.

D.Ya.Byalik

Chair of Highest Mathematics, NISKT, K. Marks 26, Novosibirsk,  
630087, USSR.

Nonaxisymmetrical problems of classical elasticity for cylindrical region with circular boundary come across in important applications/1-3/. When the directrix is uncircular spatial problems are even more interesting. The solvability and the approaches to approximate solution for such problems were considered in/5,4/, where the methods of complex function theory have been used effectively enough. The estimation of contact stresses in rail's head with transversal displacement of wheel's bandage is adduced in this report with the aim in view to show the possible applications of results mentioned above/6/.

Literature

1. Бялик Д.Я. Некоторые пространственные неосесимметричные задачи теории упругости для полого цилиндра. Автореф. диссертации, Новосибирск, СОАН СССР, 1969.
2. Byalik D.Ya. Proc. of the II Congr. of the Intern. Soc. for Rock. Mech., Beograd, 1970, p. 645-646
3. Бялик Д.Я., Томас Ч. - Основания, фундаменты и механика грунтов, 1969, №5, стр. 29-30

4.Вялик Д.Н., дифференц.уравн., Т.ХХІІ, №8, Минск, 1986,  
с.1393-1399

5.Gyalic D.Ya. Proc.of the Fifth Nation. Congr. on Theoret  
and Appl. Mech., v.2, Sofia, 1985, p.21-25.

6.Вялик Д.Н. к оценке контактных напряжений в головке рельса  
при смещении бандажа. Проблемы прочности материалов и  
сооружений на транспорте. Тез.докл. Всесоюзной конфе-  
ренции. Ленинград, 1990.

### 3-D VIBRATIONS OF CANTILEVERED SKEWED QUADRILATERAL PLATES

O.G. McGee and G.T. Giaimo, Department of Civil Engineering  
The Ohio State University, Columbus, Ohio 43210, U.S.A.

Accurate free vibration data for cantilevered skewed quadrilateral plates is essential to the force response of rudimentary aerodynamic lifting and stabilizing surfaces. An extensive data base is available which addresses the free vibration of cantilevered rectangular plates, however a sparse amount of data exists for cantilevered skewed (parallelogram) ones [1]. Very few theoretical results exist in the literature for the free vibration of trapezoidal plates [2-8], although a good experimental data base [9,10] has endured since the 1950s.

The present work is the first 3-D analysis of the title problem. No kinematic constraints (as in 2-D plates) are imposed, except the essential ones at the clamped end. Using 3-D energy equations and mathematically complete displacement polynomials, the expression for the Lagrangian is numerically integrated and minimized according to the Ritz method to determine accurate upper-bounds on the true free vibration frequencies and mode shapes. Nondimensional frequencies for rectangular, parallelogram, and trapezoidal plates are presented in Table 1. The present 3-D results are compared with those of other investigators using experimental methods [9] and various 2-D analyses, such as Raleigh-Ritz [2-4], finite elements [5], series solution techniques [6,7], and variational procedures [8]. It can be observed here that the present 3-D analysis not only delineates the ranges of accuracy of the 2-D analyses, it also predicts additional modes that are not identified by the 2-D analytical and experimental methods.

#### REFERENCES

1. A.W. Leissa, Vibration of Plates, U.S. Government Printing Office, 353 pp. (1969).
2. J.V. Nagaraja, "Effect of tip removal upon the frequency of natural vibration of triangular plates", J. Sci. Ind. Res. (India) **20 B** (5), 193-197 (1961).
3. D. Young, "Vibration of rectangular plates by Ritz method", J. Appl. Mech. **17**, Trans. ASME **72**, 448-453 (1950).
4. M.V. Barton, "Vibration of rectangular and skew cantilever plates", J. Appl. Mech. **18**, Trans. ASME **73**, 129-134 (1951).
5. J.H. Argyris, "Continua and discontinua", Matrix Meth. of Struc. Mech. (Proc. Conf. held at WPAFB, OH), AFFDL-TR-66-80 (1966).
6. R.W. Claasen, "Vibration of skew cantilever plates", AIAA J. **1** (5), 1222 (1965).
7. R.W. Claasen and C.J. Thorone, "Vibrations of rectangular

cantilever plates", *J. Aero. Sci.* **29**, 1300-1305 (1962).

8. R.S. Srinivasan and B.J.C. Babu, "Free vibration of cantilever quadrilateral plates", *J. Acoust. Soc. Am.* **73** (3), 851-855 (1983).

9. A.E. Heiba, "Vibration characteristics of a cantilever plate with swept back leading edge", Report No. 82, Cranfield College of Aeronautics (1964).

10. P.N. Gustafson, W.F. Stokey, and C.F. Zorowski, "The effect of tip removal on natural vibration of uniform cantilever triangular plates", *J. Aero. Sci.* **21**, 621-623 (1954).

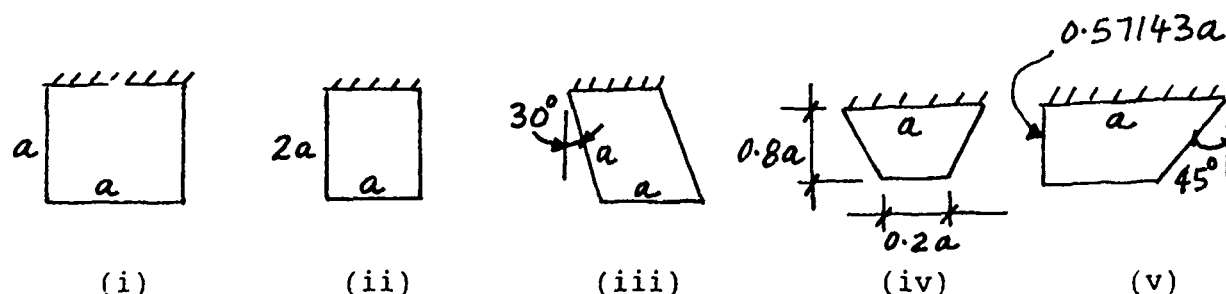


Figure 1. Cantilevered Skewed Quadrilateral Plate Configurations

Table 1. Comparison of theoretical frequency parameters  $[\Omega a^2(\rho/D)^{1/2}]$  for cantilevered skewed quadrilateral plates

Plate	Theory	Mode Number					
		1	2	3	4	5	6
(i)	3-D <sup>a</sup>	3.490	8.428	21.150	26.993	30.389	53.092
	[8]	3.479	8.561	21.277	27.167	31.043	54.290
	[3]	3.494	8.547	21.440	27.460	31.170	----
	[7]	3.47	8.55	21.29	27.20	31.10	54.30
(ii)	3-D <sup>b</sup>	3.464	14.704	21.532	47.800	57.860	92.940
	[8]	3.444	14.816	21.360	48.160	59.392	91.988
	[7]	3.444	14.840	21.480	48.400	60.120	92.800
(iii)	3-D <sup>c</sup>	3.954	9.322	25.058	25.688	40.494	49.864
	[8]	3.935	9.562	25.364	26.054	41.707	50.827
	[6]	3.947	9.653	25.467	26.133	42.400	51.600
	[4]	3.961	10.190	----	----	----	----
	[5]	3.797	9.497	25.394	26.501	41.990	----
(iv)	3-D <sup>d</sup>	5.090	18.351	23.581	47.655	54.389	61.447
	[8]	5.192	13.486	24.418	45.693	56.833	64.922
	[2]	5.418	15.357	----	----	----	----
(v)	3-D <sup>e</sup>	4.013	9.876	20.365	24.657	34.263	39.799
	[8]	4.058	8.336	21.202	24.886	35.200	41.928
	[9]	3.837	9.864	19.649	26.034	35.044	42.097

+432 polynomial terms was used in the 3-D Ritz analysis, which also predicts additional frequencies falling near modes 4 and 5 of plates (i)-(v). They are: <sup>a</sup>43.739, <sup>b</sup>61.908, <sup>c</sup>44.933, <sup>d</sup>52.763, <sup>e</sup>34.311.

## FREE VIBRATIONS OF SKEW ORTHOTROPIC PLATE STRUCTURES

Nabil F. Grace, Ph.D., P.E.  
Associate Professor of Civil Engineering  
Lawrence Technological University  
21000 West Ten Mile Road  
Southfield, Michigan 48075

Reinforced and prestressed concrete waffle (orthotropic) slabs have been used extensively in airport terminals, parking garages, as floors in semiconductor manufacturing facilities and highway bridges. These slabs can be well represented by an orthotropic plate.

In this paper, the free vibration response of rectangular and skew orthotropic plates are investigated theoretically and experimentally. A solution for the free vibration response is derived based on the classical orthotropic plate theory. The theoretical results are verified and substantiated by experimental results obtained from tests on two prestressed concrete waffle slab models. The tests were aimed at obtaining the natural frequencies, damping ratios, and variations in the prestressing force due to repeated loading.

The two models were rectangular and skew in plan and represented 1/8-scale concrete waffle slab floor. The cross-sectional geometries of the two models were identical, as shown in Figure 1, with transverse ribs being orthogonal to the longitudinal ribs.

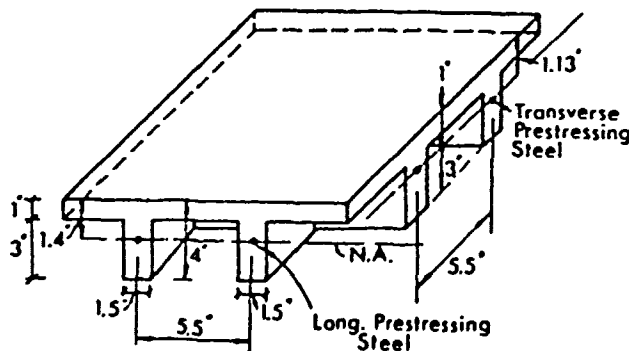






Figure 1. Cross-Section Geometries of Waffle (Orthotropic) Slab Models




Each model was instrumented by seven piezoelectric accelerometer  $\pm 25$  g, three were installed along the transverse centerline of each model, three accelerometers along the quarter span, and one in the center of the opposite quadrant of the model.

Figure 2 (a,b) shows the comparison of results for the rectangular and skew waffle slab models. The theoretical results were derived on the basis of: (1) Beam theory; (2) SAP IV finite element program; and (3) present analysis using the classical orthotropic plate theory.

MODE SHAPE NUMBER	MODE SHAPE	BEAM THEORY	PRESENT CLASSICAL APPROACH	SAP IV FINITE ELEMENT	EXPERIMENT
1		14.3 (7.5) <sup>a</sup>	14.4 (7.5)	14.1 (7.3)	8.0
2		--	22.3 (14.5)	24.9 (19.3)	16.0
3		57.3 (30.0)	57.3 (29.3)	56.4 (29.3)	29.5
4		--	69.9 (40.1)	69.6 (46.1)	--

<sup>a</sup>For cracked section

Figure 2(a)

MODE SHAPE NUMBER	MODE SHAPE	BEAM THEORY	PRESENT CLASSICAL APPROACH	FINITE ELEMENT		EXPERIMENT
				SAP IV	STRUDL-DYNAL	
1		14.3 <sup>a</sup> 28.6 <sup>b</sup>	24.4	23.3	24.8	23.8
2		--	25.3	24.9	26.1	25.8
3		57.3 114.5	53.8	52.7	41.7	--

(a) Based on span along traffic, (b) Based on normal span.

Figure 2(b)

Figure 2. Comparison of Theoretical and Experimental Natural Frequencies (Hz) of Rectangular and Skew Slab Model with Mode Shapes

Based on the theoretical and experimental results, the following conclusions can be made:

1. Considerable enhancement in the natural frequencies can be realized due to increased stiffness in the waffle slabs versus solid slabs.
2. Prestressing of concrete waffle slabs enhances their frequencies; thus resonance can be avoided when the slabs are subjected to a low-frequency excited source of vibration.



## DESIGN OF LAMINATED PLATES SUBJECTED TO FREQUENCY CONSTRAINTS

Serge Abrate  
Department of Mechanical and Aerospace Engineering  
and Engineering Mechanics  
University of Missouri-Rolla  
Rolla, MO 65401

By carefully selecting the number of plies in the laminate and the fiber orientation in each ply, composite materials can be tailored for each individual application. While methods of analysis of composite structures received considerable attention, the optimal design problem has seen only limited progress. A recent review of the optimal design of laminated plates and shells is available [1] and shows that publications in this area are generally concerned with maximizing the strength, the fundamental natural frequency or the lowest buckling load or minimizing the static deflections of the structure. Some investigations are concerned with multi-criterion optimization. The results available to date are usually of limited interest to designers since they are generally consist of a few numerical examples to illustrate the validity of the procedure proposed to determine the optimal design. Approximate solutions for plates with simple planforms and a variety of boundary conditions are needed for preliminary design.

In the present investigation, the design of right triangular plates with constraints on the minimum natural frequency for transverse vibration are considered. Only plates with symmetric lamination are studied but previous studies have shown that symmetric layups yield higher natural frequencies. A general procedure is presented to determine the the natural frequencies of right triangular plates for any combination of boundary conditions along the edges based on simple polynomial displacement approximation functions and the Rayleigh-Ritz method. Increasing the number of terms in the displacement approximation functions, natural frequencies can be calculated with any degree of accuracy. Free vibration of isotropic right triangular plates were studied by Kim and Dickinson [2] for isotropic plates and the optimal design of rectangular compo-

site plates was studied in Ref. 3. The bending rigidities of the plate are expressed in terms of the laminate thickness  $h$ , four lamination parameters which depend strictly on the fiber orientation in each ply, and five stiffness invariants which are simply related to the engineering constants for the material system used.

For a given material system and boundary conditions, the optimum combination of the four lamination parameters can be determined numerically. As the number of plies increases, the influence of the bending-twisting coupling terms become negligible and therefore only two lamination parameters need to be considered. In addition, for material systems presently available, Fukunaga [4] showed that the five stiffness invariants can be simply approximated in terms of the modulus in the fiber direction and the problem becomes independent of the material system used. In addition, if only one term is used in the displacement approximation then a formal numerical optimization procedure is not necessary and simple results can be obtained analytically. In this paper, the validity of the simplifications just discussed will be examined for right triangular plates. Exact expressions will be obtained for the first natural frequency using a one term approximation for all combinations of boundary conditions. All differentiations and integrations to be performed in the variational approximation are performed using a symbolic manipulation software package. Results obtained using the simple models are compared with exact results.

#### REFERENCES

- 1- S. Abrate, "Optimal design of Plates and Shells," submitted for publication
- 2- Kim C.S., Dickinson S.M., "The Free Flexural Vibration of Right Triangular isotropic and Orthotropic Plates," J. Sound and Vibration, Vol 141, No 2, pp 291-311, 1990
- 3- Abrate S., "Optimal Design of Laminated plates," Presented at the Eighth Int. Conf. on Mathematical and Computer Modeling, University of Maryland, College Park, Maryland, April 1-4, 1991
- 4- Fukunaga H., "Netting Theory and its application to Optimum Design of Laminated Composite Plates and Shells," Proc. 29th AIAA Structures, Structural Dynamics and Material Conf., Williamsburg, VA, April 18-20, 1988, pp 983-991

### 3-D VIBRATIONS OF PARALLELOGRAM PLATES OF VARIABLE THICKNESS

O.G. McGee and G.T. Giaimo, Department of Civil Engineering  
The Ohio State University, Columbus, Ohio 43210, U.S.A.

To solve problems related to forced vibration response and panel flutter of practical aerodynamic lifting or stabilizing surfaces, an accurate data base for the natural vibration of cantilevered rectangular and parallelogram plates of variable thickness would be indeed useful. Documented in the published literature are a number of exact solutions for the subject plates under static loading, however no exact solutions exists for the corresponding vibrational problems [1,2]. Some good approximate analyses for the title problem have been proposed using finite elements [3,4], shallow shell theory [5], and combined transfer matrix and finite element methods [6]. Moreover, a good experimental data base [3,7] has endured since the 1960s.

The present work is the first 3-D continuum analysis of the title problem. No kinematic constraints (as in 2-D plates) are imposed, except the essential ones at the clamped end. Using 3-D energy equations and mathematically complete displacement polynomials, the expression for the Lagrangian is numerically integrated and minimized according to the Ritz method to determine accurate upper-bounds on the true free vibration frequencies and mode shapes. Shown in Tables 1-3 are nondimensional frequencies for rectangular ( $\beta=0^\circ$ ) and parallelogram ( $\beta=30^\circ$ ) plates with variable thickness ( $h$ ) in the spanwise (a) and chordwise (b) directions ( $\mu=0.3$ ,  $r=h_{\max}/h_{\min}$ ). The present 3-D results, which are compared with those of other investigators [3-7], show that the 3-D analysis is accurate and useful for delineating the applicability of other theories. It can also be observed in Table 3 that the present 3-D analysis predicts additional modes that are not identified by the 2-D analytical and experimental methods.

#### REFERENCES

1. Leissa, A.W., "Plate vibration research: 1976-1980, complicating effects", Shock Vib. Dig. **13** (10) 19-36 (1981).
2. Leissa, A.W., "Recent studies in plate vibrations: 1981-1985, part II, complicating effects", Shock Vib. Dig. **19** (3) 10-24 (1987).
3. Dawe, D.J., "Vibration of rectangular plates of variable thickness", J. Mech. Eng. Sci., **8** 42-51 (1966).
4. Liu, W.H. and Chang, I.B., "Some studies on the free vibration of cantilever plates with uniform and non-uniform thickness", J. Sound and Vib. **130** (2) 337-341 (1989).
5. Lee, J.K., Leissa, A.W., and Wang, A.J., "Vibrations of blades with variable thickness and curvature by shell theory", ASME Trans.-J. Eng. Gas Turbine and Power, **106** 11-16 (1984).

6. Liu, W.H. and Chang, I.B., "Vibrations of non-uniform skewed cantilever plates by the method of finite element transfer matrix", J. Sound and Vib. **136** (1) 157-163 (1990).

7. Plunkett, R., "Natural frequencies of uniform and non-uniform rectangular cantilever plates", J. Mech. Eng. Sci. **5** (2) 146-156 (1963).

Table 1 Nondimensional frequencies  $[\Omega a^2(\rho h_{\max}/D_{\max})^{1/2}]$  for a flat plate with spanwise taper ( $a/b=1$ ,  $r=3.86$ ,  $h_{\max}/a=0.0576$ ,  $\beta=0^\circ$ )

Mode no.	3-D Ritz (432 dof)		2-D Ritz [5] Shell Theory	FEM [3] (90 dof)	Test [7]
	Var. h	Const. h			
1	4.102	3.427	4.137	4.083	4.069
2	6.904	8.390	6.992*	6.985*	7.127*
3	14.857	21.049	15.11	14.89	15.19
4	16.466	26.839	16.70	16.52	16.39
5	19.414	30.159	19.75*	19.35*	19.55*
6	30.726	37.969	31.34*	30.70	30.98*
7	31.301	52.479	32.09	30.51*	31.54
8	38.581	60.346	39.22	38.97	37.67
9	42.546	63.120	43.39*	42.30	41.64*
10	50.662	69.196	51.09	51.65	51.30

\*antisymmetric modes as identified in [3,5].

Table 2 Nondimensional frequencies  $[\Omega a^2(\rho h_{\max}/D_{\max})^{1/2}]$  for a flat plate with chordwise taper ( $a/b=2$ ,  $r=3.26$ ,  $h_{\max}/a=0.0352$ ,  $\beta=0^\circ$ )

Mode no.	3-D Ritz (384 dof)		2-D Ritz [5] Shell Theory		FEM [3] (90 dof)	Test [7]
	Var. h	Const. h <sup>+</sup>	Var. h	Const. h		
1	3.880	3.461	3.867	3.444	3.864	3.881
2	16.21 <sup>+</sup>	14.562	16.46	14.81*	16.47	16.53
3	23.65	21.446	23.65	21.45	23.78	23.72
4	48.00 <sup>+</sup>	41.094	48.23	48.21	48.19	48.85
5	60.50	47.250	60.25	57.51	61.42	61.00
6	60.52	61.213	60.63	60.21	---	---
7	89.80 <sup>+</sup>	91.644	90.11	92.60*	89.73	90.83
8	95.30 <sup>+</sup>	91.862	95.19	93.26	94.05	95.76
9	104.76 <sup>+</sup>	120.445	109.4	123.9	106.9	105.4
10	123.40	127.558	125.1	130.6	121.7	124.6

\*antisymmetric modes as identified in [5]. <sup>+</sup>3-D Ritz (432 dof).

Table 3 Nondimensional frequencies  $[\Omega a^2(\rho h_{\text{avg}}/D_{\text{avg}})^{1/2}]$  for a parallelogram plate with chordwise taper ( $a/b=1$ ,  $h_{\max}/a=0.05$ ,  $\beta=30^\circ$ )

r	Mode 1	Mode 2	Mode 3	Mode 4	Mode 5	Mode 6	Mode 7	Mode 8
1.0	3.951	9.199	24.806	25.548	40.115	44.428*	49.587	70.364
	3.915 <sup>+</sup>	9.310 <sup>+</sup>	25.107 <sup>+</sup>	25.872 <sup>+</sup>	41.178 <sup>+</sup>	---	50.830 <sup>+</sup>	73.291 <sup>+</sup>
0.8	4.070	9.280	24.731	26.586	39.530	43.878*	49.712	69.314
	4.040 <sup>+</sup>	9.412 <sup>+</sup>	25.040 <sup>+</sup>	26.931 <sup>+</sup>	40.491 <sup>+</sup>	---	51.128 <sup>+</sup>	71.430 <sup>+</sup>
0.4	4.554	9.841	23.981	30.110	36.988	41.965*	49.047	62.740
	4.507 <sup>+</sup>	10.051 <sup>+</sup>	24.392 <sup>+</sup>	30.515 <sup>+</sup>	38.016 <sup>+</sup>	---	50.688 <sup>+</sup>	63.999 <sup>+</sup>

\*additional 3-D modes. <sup>+</sup>finite element results (80 dof) [4,6].

# FREE VIBRATION ANALYSIS OF TWO-LAYERED SHELL OF REVOLUTION

T. KOSAWADA, K. SUZUKI AND H. SATOH\*

Faculty of Engineering, Yamagata University, 4-3-16 Jyonan, Yonezawa 992, Japan

\* Pioneer, Co., Ltd., 1-4-1 Meguro, Meguro Ward, Tokyo 153, Japan

## 1. INTRODUCTION

An exact solution procedure is developed for determining the free vibration frequencies and mode shapes of shell of revolution having two bonded elastic layers and circular meridional curvature.

## 2. ANALYSIS

The Cartesian coordinates are assumed as (X,Y). A shell of revolution, the middle surface of which is developed by rotating a circular arc lying on the X-Y plane with respect to Y axis, is considered. Middle surface of the overall shell and its coordinate system ( $\theta, \phi, z$ ) are shown in Figure 1. To derive the governing equations of two layered shell of revolution, the following assumptions are made: (1) each layers are elastic and isotropic and suffer no transverse shear deformation; (2) no slip occurs at the interface of the layers. The dimensions and the displacements relations of the shell cross sections are shown in Figure 2, where  $R_1$  and  $R_2$  are the principal radii of curvature of the meridian and the pararell circle of the overall shell, respectively. According to the assumptions, displacements of the middle surface of layer 1 and layer 2 are given as follows;

$$\begin{aligned} \bar{u}_1 &= \frac{R_{11}}{R_{11}+d_0} \bar{u} - \frac{d_0}{R_{11}+d_0} \frac{\partial \bar{w}}{\partial \theta} & \bar{u}_2 &= \frac{R_{21}}{R_{21}-H+d_0} \bar{u} + \frac{H-d_0}{R_{21}-H+d_0} \frac{\partial \bar{w}}{\partial \theta} \\ \bar{v}_1 &= \frac{R_{11}\phi_1}{R_{11}+d_0\phi_1} \bar{v} - \frac{d_0\phi_1}{R_{11}+d_0\phi_1} \frac{\partial \bar{w}}{\partial \phi} \\ \bar{v}_2 &= \frac{R_{21}}{R_{21}-(H-d_0)\phi_2} \bar{v} - \frac{(H-d_0)\phi_2}{R_{21}-(H-d_0)\phi_2} \frac{\partial \bar{w}}{\partial \phi} \\ \bar{w}_1 &= \bar{w}_2 = \bar{w} \end{aligned} \quad (1)$$

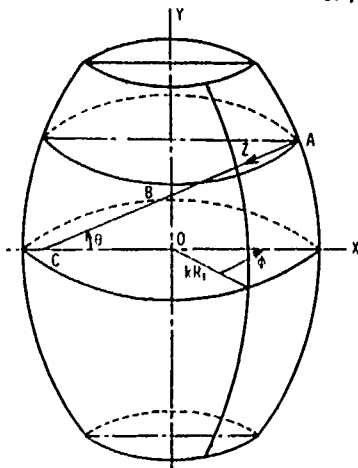


Figure 1 Middle surface and coordinate system

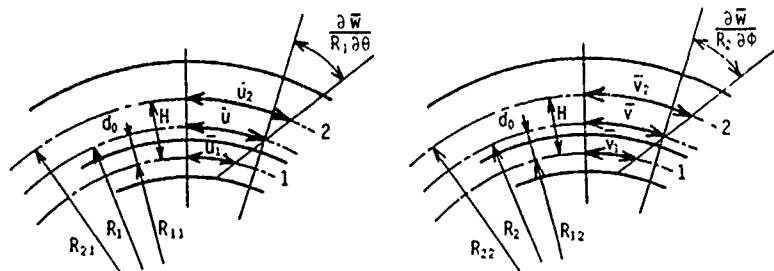


Figure 2 Cross sections and displacements

where,  $\bar{u}$ ,  $\bar{v}$  and  $\bar{w}$  are the displacements of middle surface of the overall shell and  $\phi_1$  and  $\phi_2$  are functions related to curvatures of each layers. Considering the relations between the displacements of Eq.(1), one can obtain a set of governing equations of motion by utilizing Hamilton's principle to the lagrangian function of the vibration. Although those equations of motion are very complicated higher order partial differential equations having many variable coefficients, exact solutions are obtained by expanding these variable coefficients into infinite power series of  $\theta$ . Let us consider the separation of variables as  $u(\theta, \phi) = u(\theta) \cos n\phi$ ,  $v(\theta, \phi) = v(\theta) \sin n\phi$ ,  $w(\theta, \phi) = w(\theta) \cos n\phi$ , where  $n$  is the circumferential wave number. The solutions of symmetric vibrations with respect to  $\theta = 0$  plane, for example, take form as

$$u = \sum_{m=0}^{\infty} P_m^* \theta^{2m+1}, \quad v = \sum_{m=0}^{\infty} Q_m^* \theta^{2m}, \quad w = \sum_{m=0}^{\infty} R_m^* \theta^{2m} \quad (2)$$

where  $P_m^*$ ,  $Q_m^*$  and  $R_m^*$  are coefficients which are successively determined in terms of  $P_0^*$ ,  $Q_0^*$ ,  $R_0^*$  and  $R_1^*$ .

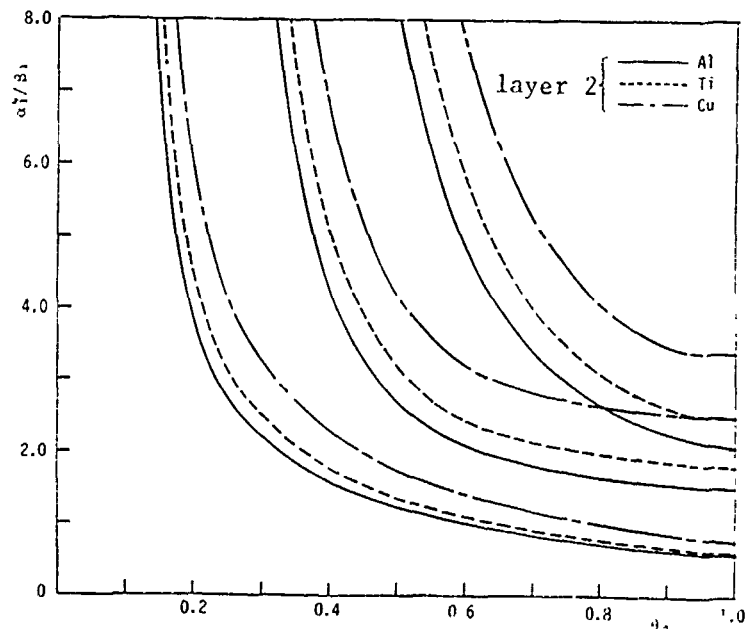
### 3. NUMERICAL RESULTS AND DISCUSSION

The nondimensional frequency parameter  $\alpha_1^4/\beta_1$  and thickness parameter  $\beta$  are defined by

$$\alpha_1^4/\beta_1 = (1-\nu_1^2)\rho_1 R_1^2 p^2/E_1, \quad \beta = 12R_1^2/h^2, \quad (h: \text{total shell thickness}) \quad (3)$$

Equation (2) were calculated by retaining 120 terms for each of the coefficients. Considering the boundary conditions, one obtains frequency equations in the form of fourth order determinant. The roots of these finite (and relatively small) order frequency determinants are exact values of frequency parameter.

Figure 3 shows the typical frequency curves of two layered shell of revolution calculated here. It is observed that the material properties of the layer 2 have considerable effects upon the natural frequencies.



(Symmetric vibration,  $\beta = 10800 (R_1/h=30)$ ,  $n=2$ ,  $k_1=0.8$ ,  $h_2/h_1=1.0$ , layer 1: steel)

Figure 3 Frequency curves of both ends clamped shell

### REFERENCES

1. T. Kosawada, K. Suzuki and S. Takahashi 1983 Bull. Japan Soc. Mech. Engineers 26-222, pp. 2165-2171. Asymmetric vibrations of thin shells of revolution
2. K. Suzuki, T. Kosawada and S. Katoh 1989 ASME PVP Conference, Hawaii Vol. 178, pp. 33-38. Free vibrations of inhomogeneous thick shells of revolution having meridionally varying curvature.

EXPERIMENTAL AND THEORETICAL CYCLIC FREQUENCIES  
OF CANTILEVERED PARALLELOGRAM PLATES

O.G. McGee, Department of Civil Engineering  
The Ohio State University, Columbus, Ohio 43210, U.S.A.  
R.M. French, Air Force Wright Aeronautical Laboratories  
Aeronautical Systems Division, Wright-Patterson AFB, Ohio, U.S.A.

In this work theoretical and experimental results for the natural vibrations of cantilevered skewed (or parallelogram) thin plates are summarized and compared. Cyclic frequencies are determined for parallelogram plates (Figure 1) having side ratios ( $a/b$ ) ranging from 1.35 to 2.80, skew angle ( $\beta$ ) ranging from  $0^\circ$  to  $60^\circ$ , and each having thickness ( $h$ ) of 0.040 inches. The plate specimens were carefully fabricated in the laboratory from aluminum and mild steel sheets. Both analytical and experimental skew plate cyclic frequencies are determined to reveal interesting analogies between the various 2-D and 3-D analytical models, and any parallelism that may exist with the experimental data obtained for the title problem.

Experimental cyclic frequency measurements are captured by using a relatively new technique called Electronic Speckle Pattern Interferometry (ESPI) [1,2]. With ESPI (often described as video holography), skew plate resonant data is electronically measured analogous to conventional real time-averaged holography. The ESPI system used in this study was the Conspectum Retra 1000 with a 1603/16 lens. The mounting holes in the skew plate specimen were drilled slightly oversized to permit exact alignment in the clamping fixture. The fixture was fabricated from 2.54 cm steel stock and was securely bolted to a massive table. The skew plates were excited using a Wavetek model 650 variable phase digital synthesizer, a McGohan MS1004 power amplifier, and a University ID60CB Horn Driver. The modal response of the skew plates was recorded on a Panasonic NV 8950 VCR and photographic samplings [2] of the holographic images were taken with a Polaroid Freeze Frame unit using Kodak 2415 35mm film.

Theoretical data was derived from several independent computer analyses, including 2-D and 3-D finite element and variational Ritz idealizations [3-5]. Shown in Table 1 and 2 are a sample of the cyclic frequencies obtained in the present study. Aluminum plate results for Skew Plate I ( $a=5.72"$ ,  $b=2.04"$ ,  $\beta=15^\circ$ ) and Skew Plate II ( $a=5.54"$ ,  $b=2.28"$ ,  $\beta=30^\circ$ ) are listed in Tables 1 and 2, respectively. For each plate the elastic modulus was  $10.3 \times 10^6$  psi, the mass density was  $0.0002442 \text{ lb-sec}^2/\text{in}^4$ , and Poisson's ratio was 0.333. In Tables 1 and 2 the analytical results are in good agreement with the experimental ones, although they are somewhat higher in the range of 1-5%. Effects of minor support compliance on the test data was studied, however the resulting data showed no significant variations.

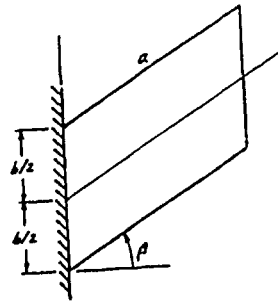


Figure 1. Cantilevered Skewed Plate

Table 1. Cyclic frequencies (Hz.) for Skew Plate I

Theory	Mode 1	Mode 2	Mode 3	Mode 4	Mode 5
Exper.	40.30	225.90	265.20	664.40	795.50
A	41.62	229.10	270.57	675.18	806.63
B	42.44	236.40	277.48	695.13	832.08
C	42.40	235.91	277.04	694.05	830.23
D	42.72	236.97	278.79	697.48	834.26
E	42.39	236.31	277.32	694.97	831.65
F	42.95	237.93	280.54	701.99	846.30
G	42.20	234.28	275.62	690.73	825.57
H	42.19	234.21	275.49	689.89	824.53

Table 2. Cyclic frequencies (Hz.) for Skew Plate II

Theory	Mode 1	Mode 2	Mode 3	Mode 4	Mode 5
Exper.	45.30	224.90	314.20	647.80	938.40
A	46.71	228.12	320.95	659.26	956.03
B	47.72	235.64	329.52	680.88	985.11
C	47.66	235.06	329.23	679.58	984.01
D	48.02	236.03	331.23	682.54	988.83
E	47.64	235.19	328.94	680.37	982.94
F	48.36	237.68	337.48	684.48	1008.31
G	47.44	233.32	327.06	675.86	977.63
H	47.42	233.22	326.75	675.19	975.48

<sup>+</sup>Exper. = experimental data using ESPI; A=ASTROS (using 120 NASTRAN QUAD4 finite elements and 480 dof); B=2-D Ritz Kirchhoff/Love thin plate (36 dof); C=2-D Ritz-Reissner/Mindlin thick plate (108 dof); D=2-D Ritz Higher-Order Shear Deformable Plate (HOSDP) (144 dof); E=2-D Ritz thin plate with stress singularity functions (38 dof); F=3-D Ritz elasticity-based (432 dof); G=2-D FEM 3dof Mindlin shear deformable plate elements (867 dof); H=2-D FEM 9dof HOSDP (2601 dof).

#### REFERENCES

1. Lokberg, O.J., "The present and future importance of ESPI", SPIE Proc., Vol. 746, pp. 86 (1987).
2. Maddux, G.E. and French, R.M., "Modal characteristics of swept plate flutter models", Soc. for Exper. Mech., Proc. 7th Int'l. Modal Analysis Conf., Las Vegas, Nevada, 30 Jan. - 2 Feb. (1989).
3. Hanna, N.F., "Thick plate theories with applications to vibration", Ph.D. Dissertation, The Ohio State University (1990).
4. McGee, O.G. and Butalia, T.S., "Natural vibrations of shear deformable cantilevered skewed thick plates", submitted for publ.
5. McGee, O.G., Leissa, A.W., and Huang, C.S., "Vibrations of cantilevered skewed plates with corner stress singularities", submitted for publ.



# NATURAL VIBRATIONS OF CANTILEVERED SKEWED PARALLELOGRAM TRAPEZOIDAL AND TRIANGULAR PLATES WITH CORNER STRESS SINGULARITIES

O.G. McGee, Department of Civil Engineering  
A.W. Leissa and C.S. Huang, Department of Engineering Mechanics  
The Ohio State University, Columbus, Ohio 43210, U.S.A.

The few theoretical analyses for the natural vibration of skewed, cantilevered parallelogram, trapezoidal, and triangular plates which exist are approximate. Of particular importance to the natural vibration of such plates is that the bending moments and stresses at the reentrant clamped corner (point O, see Figure 1) are unbounded when the obtuse plate angle ( $\theta$ ) at the reentrant corner exceeds  $90^\circ$ . Moreover, the strength of the singularity increases with the angle (according to elasticity theory). Inasmuch as the accuracy of the existing vibration results for the subject using classical thin-plate theory is at least suspect if one ignores the unbounded stresses at the reentrant corner, recent work [1,2] has addressed a lingering question: "Does inclusion of the complicating stress singularities have a profound effect on the nature of the coupled-mode sensitivities of natural vibration of highly skewed parallelogram, trapezoidal, and triangular plates?"

The transverse displacement ( $w$ ) of these skewed plates in natural vibration is assumed sinusoidal in time:  $w(x,y,t)=W(x,y)\sin(\Omega t)$ , where  $\Omega$  is a natural frequency. Further, admissible displacements are taken as  $W=W_p+W_c$ , where  $W_p$  is a sum of mathematically complete polynomials:  $W_p(x,y)=A_{mn} x^m y^n$  ( $m=2,\dots,M; n=0,\dots,N$ ), and  $W_c$  is a sum of corner functions:  $W_c(x,y)=B_k W_k(x,y)+C_l W_l^*(x,y)$  ( $k=1,\dots,K; l=1,\dots,L$ ), where  $W_k$  and  $W_l^*$  are the real and imaginary parts of the complex eigenfunctions [3] satisfying the clamped and free boundary conditions along the radial lines ( $\theta=0$ ) and  $(\pi/2+\beta)$  (see Figure 1). Substituting the above assumed displacements into the appropriate energy functionals [1,2] and minimizing according to the Ritz method, accurate upper bounds on the free vibration frequencies are obtained.

The efficacy of admissible corner functions used in conjunction with mathematically complete polynomials has been demonstrated in an exhaustive amount of Ritz convergence tables apropos to cantilevered skew (or parallelogram) plates [1], and to skewed plates having trapezoidal and triangular shapes, which are derived from three parallelogram plate configurations [2]. Representative samples of this data base are given in Table 1, which lists fundamental frequency parameters for highly skewed, short aspect ratio ( $a/b=0.5$ ,  $\beta=75^\circ$ ) parallelogram ( $c/b=1$ ), trapezoidal ( $c/b=0.5$ ), and triangular ( $c/b=0$ ) plates ( $\mu=0.3$ ). Clearly, poor convergence is exhibited when only the simple polynomials ( $W_p$ ) are used, and that augmenting the Ritz trial space with corner functions ( $W_c$ ) improves the convergence

of solution considerably. Using polynomials alone should, in principle, yield results that converge properly to accurate upper bounds on the exact values. However, a considerable number of terms are needed, and roundoff errors (ill conditioning) often destroys the accuracy of solution before adequate convergence is achieved.

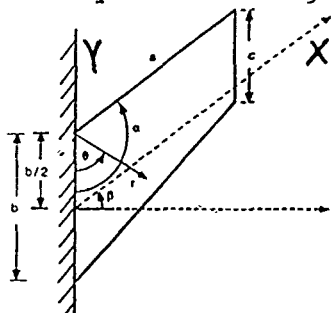


Figure 1. Cantilevered Skewed Trapezoidal Plate

Table 1. Convergence of fundamental frequency parameters  $[\Omega a^2 \cos^2 \beta (\rho/D)^{1/2}]$  for a cantilevered skewed plate ( $a/b=0.5$ ,  $\beta=75^\circ$ )

c/b	Corner Functions	Number of Polynomial Terms ( $W_p$ )				
		9	25	36	49	64
	( $W_C$ )					
1	0	1.3980	0.7848	0.6400	0.5566	0.5046
	2	0.4255	0.4179	0.4120	0.4084	0.4071
	10	0.4100	0.4076	0.4065	0.4060	----
	20	0.4060	0.4059	0.4058	0.4056	----
	*	(0.4104) <sub>10</sub>	(0.4071) <sub>15</sub>	(0.4061) <sub>20</sub>	(0.4056) <sub>30</sub>	(0.4055) <sub>40</sub>
0.5	0	1.3368	0.9661	0.7485	0.6159	0.5380
	2	0.4199	0.4158	0.4130	0.4079	0.4056
	10	0.4082	0.4067	0.4056	0.4049	----
	20	0.4048	0.4048	0.4047	----	----
	*	(0.4085) <sub>10</sub>	(0.4055) <sub>15</sub>	(0.4048) <sub>20</sub>	(0.4046) <sub>30</sub>	----
0	0	1.6466	1.0959	0.8346	0.6732	0.5788
	2	0.4496	0.4413	0.4346	0.4282	0.4251
	10	0.4304	0.4277	0.4251	0.4238	----
	20	0.4238	0.4237	0.4237	0.4233	----
	*	(0.4313) <sub>10</sub>	(0.4262) <sub>15</sub>	(0.4238) <sub>20</sub>	(0.4226) <sub>30</sub>	----

\* $W_C \sim N$  corner functions and no polynomials used in ( )<sub>N</sub> values.  
(----) indicates no results due to ill-conditioning.

#### REFERENCES

1. McGee, O.G., Leissa, A.W., and Huang, C.S., "Vibrations of cantilevered skewed plates with corner stress singularities", submitted for publication.
2. McGee, O.G., Leissa, A.W., and Huang, C.S., "Vibrations of cantilevered skewed trapezoidal and triangular plates with corner stress singularities", submitted for publication.
3. Williams, M.L., "Surface stress singularities resulting from various boundary conditions in angular corners of plates under bending", Proc. U.S. Nat. Cong. of Appl. Mech., 325-329, (1951).

# PERTURBED BOUNDARY ELEMENT METHOD AND ITS SOLUTION TO THE STABILITY OF PLATES

Chen Guang-Xia

Dept. of Material Science and Engineering, Central South Uni.  
of Technology, Changsha, Hunan 410083, P.R.China

With many advantages, the Boundary Element Method is useful for the solution of problems governed by the differential equations. But it often fails in solving the nonlinear problems. In this paper the above method is combined with the perturbational method to form the new Perturbed Boundary Element Method which possesses the special advantages of both. It can solve some complicated problems more quickly and more effectively than others. By means of Perturbed Boundary Element Method, we firstly solve the problem of stability of plates.

Firstly the basical equation of the plate subjected to the vertical and horizontal load is changed into a non-dimensional form. It is assumed that  $q$  is the vertical load,  $N_x, N_{xy}, N_y$  are the horizontal loads,  $h$  is the thickness of plate, and  $a$  is planar geometric size of plate. So, the non-dimensional form of basical equation is:

$$\nabla^4 W = q + (h/a)[N_x \cdot W''_{xx} + 2N_{xy} \cdot W''_{xy} + N_y \cdot W''_{yy}] \quad (1)$$

It is always dependent on non-dimensional parameter when the perturbed method is adopted. Given  $N_m$  is the maximum among  $N_x, N_y, N_{xy}$ . Given  $Q_m$  is the maximum of  $q$ . That is:

$$N_m = \max(N_x, N_{xy}, N_y) \quad (2)$$

$$Q_m = \max(q) \quad (3)$$

$$P = N_m / Q_m \quad (4)$$

If  $p$  is small enough, that is to say if  $N_m$  is much smaller than  $Q_m$ , the horizontal load can be neglected. Therefore, the equation (1) is changed into:

$$\nabla^4 W = q$$

It means that the stable problem of plate is changed into a generally curved one of plate. Based on this mathematical idea, the article suggests that  $P$  is the perturbational parameter.

By the perturbational parameter  $P$ , every function in the equation (1) is expressed as the power series form of  $P$ :

$$W = W_0(x, y) \cdot P + W_1(x, y) \cdot P^2 + \dots + W_m(x, y) \cdot P^m \quad (5)$$

$$Q = Q_0(x, y) \cdot P + Q_1(x, y) \cdot P^2 + \dots + Q_m(x, y) \cdot P^m \quad (6)$$

$$N_x = N_{x0}(x, y) \cdot P + N_{x1}(x, y) \cdot P^2 + \dots + N_{xm}(x, y) \cdot P^m \quad (7)$$

$$N_y = N_{y0}(x, y) \cdot P + N_{y1}(x, y) \cdot P^2 + \dots + N_{ym}(x, y) \cdot P^m \quad (8)$$

$$N_{xy} = N_{xy0}(x, y) \cdot P + N_{xy1}(x, y) \cdot P^2 + \dots + N_{xym}(x, y) \cdot P^m \quad (9)$$

The eqns (5)-(9) are used in the basical equation (1). Here, the sign  $L_i$  is introduced,

which means:

$$L_1 = (h/a) \cdot (N_{x1} \frac{d^2}{dx^2} + N_{xy1} \frac{d^2}{dx dy} + N_{y1} \frac{d^2}{dy^2})$$

So, the eqn (1) becomes:

$$\begin{aligned} & \nabla^4 W \cdot P + \nabla^4 W \cdot P^2 + \dots + \nabla^4 W_m \cdot P^m \\ & = A_1 \cdot P + A_2 \cdot P^2 + \dots + A_m P^m \\ & - (L_1 \cdot P + L_2 \cdot P^2 + \dots + L_m P^m) (W_1 P + W_2 \cdot P^2 + \dots + W_m P^m) \end{aligned} \quad (11)$$

Depending on the equation (11), a series of linear equations are obtained:

$$\nabla^4 W = Q_i$$

$$\nabla^4 W = Q_i(x,y) \quad i = 1, 2, 3, \dots$$

Here,  $Q_i = A_i$ , and  $Q_i(x,y) = A_i - (h/A_j) \cdot [L_j W_{j-1} + \dots + L_j W_s]$ , and  $s = (j - 1)$ . Therefore, the basical nonlinear equation is turned into a series of linear differential equations by means of perturbational principle.

Secondly, by imitating the basical equation of the curved problem of plates, the perturbational Boundary Element Integral equations of stable problem of plate are produced in the article. And then solving every equation, the solutions are iteratively added perturbationally. On the other hand, the idea of imitating load is successfully adopted, and the analytics is employed to cope with the field integral of some problems frequently appeared in engineering in order to obtain higher accuracy and bring more conveniences. At last, the numerical solution is obtained.

It is resulted in that the accuracy of solution has something to do with the shape of plate, the ratio of the vertical and horizontal load, and the perturbational times. The results are compared with those of other methods and show that the method has advantages of clearly physical idea, convenience of calculation and higher accuracy. It is the first time to solve the stable problem by means of Perturbed Boundary Element Method. The paper puts forward a new idea and method to solve the stable problem, and makes a successful trial on nonlinear problems. The idea and method can also be used in some other loading, geometric, and material non-linear problems. We can greatly extend the applied fields of Perturbational Method and overcome the limitation of Boundary Element Method in the nonlinear aspect.

Example: Rectangular plates are subjected to the even vertical load "q" and horizontal load "Px". The width is b and the length is a. The solution is shown below:

a / b	0.5	1.0	1.4	2.0	3.0
Pcr(energy meth.)	4.460	1.460	0.970	0.710	0.570
Pcr (FEM)	4.4400	1.4300	1.0100	0.7700	0.6500
Pcr' (PRKM)	4.4500	1.4690	1.0080	0.7350	0.5950
Pcr''	4.4590	1.4640	1.0020	0.7250	0.5850

\*Pcr' is the solution by twice perturbation. Pcr'' is the one by three times.

# Index of Authors

	Session #		Session #
AbdulNour, Bashar S.	TMI-4	Bhat, C. Chandra Shekara	WMII-4
Abrate, Serge	TMII-6,WMII-7,WA-6	Bhattachar, V.	TAI-6
Adachi, T.	WMI-2	Bhattacharyya, A.	MM-1
Adrian, R. J.	TAI-4	Birman, Victor	WMI-6
Afolabi, D.	MAII-6	Bissonnette, Laurent C.	MAII-4
Agarwal, R. K.	MM-4	Bless, S. J.	MM-2
Ahmad, Yousef, N.	WA-5	Blume, Janet A.	TMI-3
Ahmed, S.	TAII-6	Brar, N. S.	MM-2
Aifantis, E. C.	TAI-2	Brock, L. M.	TMII-4
Al-Gothani, Ali	MM-6	Brown, S.B.	MAI-5
Alabi, B.	MAII-6	Buchanan, George R.	MAI-6
Alghothani, Ali M.	TAI-1	Butson, Gary J.	MAII-6
Amigo R., Osvaldo	WMII-7	Byalik, D. Ya.	WA-5
Ammal, K. Rajalekshmy	WMII-4	Byerlee, J.	TMII-2
Anderson, Charles E., Jr.	MM-2	Byun, K. Y.	TAII-1
Anigbo, Felix	TAII-1,MAI-5	Caglayan, N	TAI-7
Antman, Stuart S.	MM-3	Cai, Xianxin	WMII-6
Argento, Alan	TAI-7,WA-3	Caipen, T. L.	MAII-6
Arruda, Jose Roberto F.	MAII-6	Cao, Q.	WMII-3
Arya, V. K.	TMI-2	Capriz, Gianfranco	TAI-3
Azarkhin, Alexander	TAI-5	Carlson, Donald E.	TMII-3
Azzi, Bechara M.	MM-2	Carroll, Douglas R.	TMII-1,WA-4
Bahei-El-Din, Yehia A.	MM-1	Celik, Ismail	TAI-4
Bahr, Behnam	TAII-2,WMI-7,WA-3	Chamkha, Ali J.	WMII-4
	WA-4	Chandrashekhara, K.	MAII-1
Balla, Mihaly	MAII-3	Chang, T.P.	WMI-7
Bangera, Kiran M.	MAII-1	Chao, Jey-Chung	TAII-1
Bapat, C. N.	MAII-6,WMI-7	Chaturvedi, Shive K.	MAI-1
Baptiste, D.	TAII-1	Chen, Caho-Hsun	WA-2
Bardet, J. P.	TMII-2	Chen, E. P.	TAI-6
Barez, Fred	TMII-6	Chen, G. X.	WA-6
Barton, Oscar	MAI-1	Chen, Yi-Chao	MM-3
Basavaraju, C.	MAI-6	Chen, Y. J.	TAII-6
Bata, Reda M.	WMII-3	Chen, Zhen	TMII-2,WA-2
Batra, Gautam	TMI-3	Cheng, Pao-Hwa	WA-2
Batra, Romesh C.	TAI-2	Chern, C. Y.	MAI-6
Bayoumi, A. E.	TAI-2	Cherukuri, H. P.	WMII-2
Beatty, Millard F.	TAI-3	Chou, Chuen-Shii	TAII-5
Beaudoin, Armand	TMII-5	Chow, C. L.	MAII-5
Becker, R.	TMII-5	Chu, Chin-Chan	WA-1
Beikmann, R. S.	WMII-7	Chung, J.	WMII-5
Benharbit, A.	TAII-4	Cofer, W. F.	TMII-2
Bennett, Mark S.	WMII-6	Cohen, H.	MM-3
Benson, David J.	MM-4	Coleman, Bernard D.	MAII-2
Bert, Charles W.	TAI-1	Collicott, Steven H.	TAII-6
Besterfield, Glen H.	TMI-1	Cortinez, V. H.	WMII-6
Bezerra, L.M.	MAII-4	Cox, Donald L.	MAII-4
Bhalla, K.	MAII-1	Craver, W. Lionel, Jr.	WA-5

	Session #		Session #
Cummings, Don	MAII-4	Ghosh, Somnath	TAI-1
Dai, L.	WA-1	Giaimo, G. T.	WA-6
Das, Y. C.	TMII-6,WMI-6	Gilat, Amos	MM-5
Dave, Vivek	MAI-5	Gillis, Peter P.	MAI-2
Dawson, Paul	TMII-5	Giovine, P.	TAI-3
DeGiorgi, V. G.	MAI-2, TMII-4	Glinka, G.	TMII-4
Del Piero, Gianpietro	TMII-3	Glockner, P. G.	TMII-4
Demir, I.	MAII-5	Goddard, J. D.	TMI-5
Dewhurst, Tim	WMII-5	Gollahalli, S. R.	MM-4
Dharani, L. R.	TMI-1, TMII-1	Gong, J.	WMII-5
Dickinson, S. M.	MAI-7	Gopal, P.	MAII-1
Dillon, Oscar W., Jr.	TMI-2	Gopalaratnam, Vellore S.	TMII-1,
Ding, J. H.	WMII-4		TAII-3
Dini, Said	WA-1	Gorman, D. J.	TMII-6
Dolinska, Malgorzata	TAII-2	Govindarajan, R.	TAII-1
Douglas, Andrew S.	WMII-2	Grace, Nabil F.	WA-6
Dowd, Jefferey	WA-4	Grahramani, A.	TAII-5
Drew, Donald A.	WMI-3	Groper, Meshulam	WA-4
Du, Q.	TAII-6	Grove, D. J.	MAI-2
Dubey, R. N.	TMII-4	Grzymkowski, R.	TAII-2
Dutta, Piyush K.	MAI-1	Gu, Qun	MAII-3
Dutton, Rollic	TMII-1	Gudhe, R.	TMI-5
Dvorak, George J.	MM-1	Guran, Ardesbir	WMI-7, WMII-5
El Naschie, M. S.	WMI-4	Gurtin, Morton E.	MAI-3
El-Sayed, M. M.	TAII-3, WA-2	Guttalu, Ramesh S.	TMI-6
Epstein, Marcelo	TMI-3	Hadji, Layachi	WMI-4
Ewing, Mark S.	WA-3	Hamoush, S. A.	TAII-3, WMI-1
Fan, Jinghong	WA-2	Hannapel, F. W.	WMII-1
Fan, Zuyao	WA-1	Hao, Jaimey J. M.	MM-4
Farris, T. N.	WA-2	Haque, K. A.	MAII-4
Fartaj, S. A.	WA-1	Harmon, D. M.	TMI-1
Fenton, D. L.	WA-1	Hayashi, K.	WMII-6
Flower, Elanc C.	TMII-5	Hayes, Mike	TMII-3
Follansbee, Paul S.	MAI-2	Hernried, Alan G.	WA-5
Foroudastan, Saeed	MM-6	Herrmann, J. M.	MAII-5
Fosdick, Roger	TAI-3	Hickox, C. E.	TMI-5
Foss, John	TAI-4	Hiemstra, D. L.	WMI-1
Foster, J. C., Jr.	MAI-2	Hill, James L.	TAII-2
Francois, D.	TAII-1	Hilsbos, R. A.	WA-5
Frantziskonis, G.	WMI-2	Hirth, J. P.	MAII-5, WMI-2
French, R. M.	WA-6	Ho, Wei	MAI-1
Fujii, S.	TAII-2	Hojo, Katsuhiko	TAII-2, WA-1
Gadiraju, Manohar	TMI-4	Hong, W.	TMII-1
Gandhi, Mukesh V.	TAII-4	Hosokawa, Kenji	WMI-6
Gartling, David K.	TMI-5	House, J. W.	MAI-2
Gayer, Melvin D.	WMII-7	Howell, Rodney	TAII-2
Gebbeken, Norbert	WMII-5	Hsui, Albert T.	WMI-4
Georgiou, I. T.	MAII-1	Hu, G. K.	TAII-1
Ghamat-Rezaei, Amir	MAI-7	Huang, C. L. D.	MAI-6, WMI-6, WA-1
Ghia, K. N.	TAI-4	Huang, C. S.	TMII-6, WA-6
Ghia, U.	TAI-4	Huang, Zhitao	WA-1
Ghorbanpoor, Al	MAII-5	Hucker, Scott A.	WA-2

	Session #		Session #
Hui, David	MAI-1	Lazcano, Juan	TAII-2
Hulbert, Gregory M.	WMII-5	LeClair, Raymond A.	WMII-6
Huntley, Hugh E.	MAII-3	Lee, Christopher L.	WMI-7
Husen, Bisma	TAII-6	Lec, J. K.	TAI-5
Hussein, Rafaaf	WA-2	Lee, Y. K.	TAI-5
Ibekwe, S. I.	TAII-1,MAI-5	Lei, Kai-Ming	WA-5
Ichinose, Kensuke	MM-5,MAI-5	Leissa, Arthur W.	MAI-7,TMII-6, WA-6
	MAII-1,WMI-1		
Ihekweazu, Stanley N.	MAII-1	Li, Hua	TAII-1
Ikegami, Koza	MAI-5	Li, R.	WMII-5
Isaac, K. M.	TAII-6	Li, Xu	MAII-3
Jaffal, A.	WMI-7	Li, Yaoming	TAII-4
Jain, R. K.	TAI-7	Liaw, Leslie D. G.	WMI-6
Jeng, De-Yin	TMI-1	Libai, Avinoam	TAI-1
Jenkins, J. T.	TMI-5	Lin, Chang-Sheng	MAII-4,TAII-4
Jennings, D. J.	MAII-1	Lin, S. Q.	WMI-7
Joh, Dukung	TAII-1	Lindberg, William R.	TAI-4
Johnson, Arthur R.	MAII-3	Liou, Frank W.	WMII-3
Johnson, D. J.	WMII-1	Liu, De-Shin (Scott)	MAI-6
Johnson, Millard W.	MAI-4	Liu, I-Shih	WMI-3
Jones, Norman	MM-2	Liu, Kuo-Hsiao	MAI-6
Jones, S. E.	MAI-2,MAII-6	Liu, Yijun	MAII-4
Jubran, J. S.	WMII-2	Lockner, D.	TMII-2
Kalavar, S. R.	MAI-6	Lü, Jiahong	WA-3
Kamath, R.	WMI-3	Lu, T. J.	MAII-5
Kaneda, Teruo	MAII-1,WMI-1	Lu, Wei-Yang	MAII-3
Kasiviswanathan, S. R.	TAII-4	Lu, Yuan	WA-5
Kattan, P. I.	WMI-2	Lu, Z.	WMI-6
Kaw, Autar K.	TMI-1	Lugowski, J.	TAII-5,WMII-4
Kaykayoglu, C. Ruhi	TAII-5	Luk, Vincent K.	MM-2
Khan, A. S.	MAI-5	Macchiarulo, Vincenzo	WMII-7
Khan, Arshad Y.	WMI-6	Malek-Madani, Reza	MAII-2,WMII-2
Kim, Kyung-Suk	WMI-1	Malkus, David S.	MAI-4
Kim, Y. W.	WA-1	Mamalis, A. G.	WMII-1
Kingsbury, Herbert B.	MAII-1	Man, Chi-Sing	MAII-3
Kirby, G. C. III	MAI-2	Mansutti, D.	TAII-4,WMI-3
Kirmser, Philip G.	WA-4	Massoudi, Mehrdad C.	TMI-5
Korakianitis, Theodosios	WMII-3, WA-1,WA-4	Masuda, Hiroshi	TAII-2,WA-1
	WMII-5,WA-6	Matic, P.	MAI-2,TMII-4
Kosawada, Tadashi	WMII-5,WA-6	Maugin, Gerard A.	TMI-3
Kraver, Theodore C.	WMII-7	Mazumder, Bijoy S.	WMII-4
Krempf, Erhard	MM-1	McGee, Oliver G.	TMII-6,WA-6
Krishnamurthy, A. V.	TAII-1	Means, Kenneth H.	WMII-3
Krishnaswami, Prakash	TAII-2, WMII-3	Mendez, Fernando	WA-5
	WMII-3	Menon, Rajiv	WMII-3,WA-4
Ku, Albert B.	WMII-5	Metzger, Darryl E.	WA-1
Kuczma, Mieczyslaw S.	WMII-6	Minami, Kazutaka	TAI-6
Kuo, Hsin-Chuan	TMI-4	Ming, Zhou	MAI-6
Kwak, Moon K.	MAII-6	Misra, Anil	MAII-5,TAII-5
Lance, Richard H.	MAII-1	Mohamadian, H. P.	TMI-4
Lankarani, Hamid	WMII-3,WA-4	Moore, Robert E.	TMII-1
Laura, P. A. A.	TMI-6,WMII-6	Motavalli, Sacid	TAII-2

	Session #		Session #
Mukherjee, Subrata	TMII-5	Raftenberg, M.N.	MM-5
Müller, Ingo	MAI-3	Raghuram, P. V.	TAII-1
Munukutla, Sastry S.	TMI-4	Rahaman, Mohamed N.	TMI-1,WA-4
Nagem, Raymond J.	WMI-7	Rajagopal, K. R.	TMI-5,TAI-3
Narain, A.	WMI-3	Rajapakse, Yapa D. S.	MM-1
Nath, Y.	TAI-7	Rajendran, A. M.	MAI-2
Nazmeev, Y. G.	TAII-4	Ramamohan, T. R.	WMII-4
Needleman, A.	WMII-2	Raman, G.V.	WMI-5
Negahban, Mehرداد	TMI-6	Ramasamudra, Manjunatha	WMI-6
Neilsen, Mike K.	TMII-2,TMI-2	Ramesh, K. T.	WMII-2
Newman, Daniel C.	MAII-2	Raouf, Raouf A.	MM-6
Nie, Guo-Hua	TAI-7	Reddy, J. N.	TAI-1
Nigam, N. C.	MAI-7	Reed, X. B., Jr.	TMI-4,WMI-4
Niitsu, Yasushi	MM-5,MAI-5	Reiss, Robert	MAI-1
Nikkel, D. J., Jr.	TMII-5	Renardy, Michael	MAI-4
Offutt, P. W.	TAI-4	Renardy, Yuriko	MAI-4
Ohno, Tomonori	TAI-6	Reynolds, David	TMI-3
Oka, F.	WMI-2	Riahi, Daniel N.	WMI-4,WMII-4
Okuno, Akihiro	MAII-1	Richmond, O.	TAI-5
Onoda, T.	TAII-2	Rizzo, Frank J.	MAII-4
Ostoj-Starzewski, M.	WMI-2	Robbins, D. H.	TAI-1
Ou, H.	WMII-5	Rosakis, Ares J.	MAI-1
Ozkol, I.	TAII-5	Rossikhin, Yuriy A.	WMI-7
Ozturk, Abdullah	TMII-1	Rothert, H.	WMII-5
Padovan, Joe	MAII-4	Roy, S.	TAI-5
Paglietti, Andrea	MAI-3	Saavedra G., Pedro	WMII-7
Palazotto, Anthony N.	MM-6	Sabzevari, A.	TAII-5
Pan, Jwo	TMII-4	Saigal, S.	MAII-4
Pantazopoulos, George I.	WMII-3, WA-1,WA-4	Sakata, Toshiyuki	WMI-6,WMII-6
Passerello, C. E.	WMI-5	Salajekeh, Robert B.	WA-5
Passman, Stephen L.	WMI-3	Salami, M. Reza	TAII-3,WMI-1, WA-4
Patterson, Gary K.	TMI-4	Sallah, N. M.	MAI-6
Paul, H.S.	WMI-5	Sam, D. D.	TMII-5
Peach, M. O.	WMI-5	Saniei, Nader	TAII-6
Pecherski, R. B.	WMII-2	Satoh, H.	WA-6
Peddieson, John, Jr.	MM-6,TMI-4	Savory, E.	TAII-6
Pendleton, R. L.	TAII-1,MAI-5	Saxena, A.	MAII-5
Peng, K. C.	WMII-3	Sayani, Seshumohan	TAII-2
Perkins, Noel C.	WMI-7,WMII-7	Shurlati, Roberta	MAII-3
Petrykowski, John C.	WA-4	Schafbuch, P. J.	MAII-4
Phillips, Norman S.	WMII-3	Scheidler, Mike	TMI-2
Pidaparti, Ramana M. V.	WMI-1	Schneider, Steven P.	TAII-6
Pitman, E. Bruce	TAII-5	Scott, Richard A.	WA-3
Podio-Guidugli, Paolo	MM-3	Schreyer, Howard L.	TMI-2,TMII-2,WA-2
Podzimek, Josef	TAII-6	Selvarathinam, Alex	TMI-1
Prouhet, J.	TMII-2	Senator, M.	MAII-6
Pu, Liu	MM-6,MAII-5	Shaffer, F. D.	TAI-4
Qatu, Mohamad S.	MM-6	Shan, Duan Wen	MAII-6
Qing, J.	MAII-5	Shawki, T. G.	MAII-2,WMII-2
Raafat, G.	MAII-1,TAII-1	Shen, Jiazhen	WA-1
Raboin, P. J.	TMII-5	Shen, Wei Qin	MM-2



	Session #		Session #
Shen, Xiaofeng	TAII-3,WMI-7	Tzavaras, Athanasios	MAII-2
Sherif, R. A.	WMII-2	Ulsoy, A. G.	WMII-7
Sheu, Tony W. H.	MM-4,TMI-4	Vachagina, E. K.	TAII-4
Shikanai, G.	WMII-6	Vallabhan, C. V. Girija	TMII-6,
Shirai, Futoshi	TAII-2,WA-1		WMI-6
Shitikova, Marina V.	WMI-7	Venkataraman, Nellore S.	WMI-6,
Shu, M.	MM-4		WA-3
Siddiqui, A. M.	TAII-4,WMII-4	Venkaasubramanian, S.	WMI-6,
Simitses, George J.	WMI-6		WMII-6
Singh, M. C.	MAII-3,TMII-4,WA-1	Viegelahn, Gary L.	WMI-5,WMII-1
Sitaram, Patabhi	WA-5	Vilmann, C. R.	WMI-5
Smelser, Ron	TMII-5	Vijayakumar, K.	TAII-1
Soboyejo, W. O.	TMII-1	Vijayalekshmi, S. K.	WMII-4
Soedel, W.	TAII-2	Voyiadjis, George Z.	WMI-2
Sosa, Horacio A.	MAI-6	Wagoner, R. H.	TAI-5
Sottos, Nancy R.	WMI-1	Walker, H. S.	WMI-6
Souchet, Rene	WA-3	Walter, John W., Jr.	TAI-2
Spears, Andre Trevor	WMI-4	Walton, J. R.	MAII-5
Spector, Alexander	WA-5	Wang, D.	WMII-4
Stouffer, Donald C.	TAI-6	Wang, P. T.	MM-5
Straughan, W. Thomas	TMII-6	Wang, Wenguang G.	WMII-3
Strouboulis, T.	MAII-4	Wark, C. E.	TAI-4
Stutts, D. S.	TAII-2	Warren, William E.	WMI-1,WMII-5
Sukere, A. A.	MAII-5	Wauer, Jorg	TMI-4
Sun, C. T.	MAII-1	Weerasooriya, Tusit	MAI-5
Sun, Q.	WA-5	Weese, John A.	WMII-5
Suzuki, Goro	MAII-1,WMI-1	Weng, George J.	MM-1
Suzuki, Katsuyoshi	WMII-6,WA-6	White, W. N.	WMII-6
Swartz, Stuart E.	WA-5	Wilson, L. L.	MAI-2
Szabo, Barna A.	TMI-6	Wineman, Alan	MAII-3
Szeri, Andras Z.	MAI-4	Wlosinski, Ronald K.	WMII-1
Szyszkowski, W.	TMII-4	Wu, Enboa	TAII-1
Tabaddor, Farhad	MAII-4	Wu, Han C.	MM-5
Tabarrok, B.	MAII-6	Wu, Julian J.	MAI-7
Tahouri, B.	TAII-6	Wung, T. S.	MAI-4
Takeda, Takenobu	MM-5	Xiong, Yuexi	MAII-6
Talia, J.	WA-4	Xu, Z. Y.	MM-5
Tang, Wenliang	MAII-3	Yair, R.	WA-5
Tarabishy, N.	WMI-7,WA-4	Yang, Ming-Fa	WMI-1
Tekinalp, O.	TAI-7,TAII-1	Yao, Sheng	TMII-6
Thompson, Erik	TMII-5	Yap, S.	WMI-5
Tippur, Harceesh V.	MAI-1	Yardimci, Nesrin	TAI-7
Topakoglu, H. C.	TMI-4	Yashima, A.	WMI-2
Toy, N.	TAII-6	Yavuz, A.K.	TAII-1
Tran, D. V. D.	MAII-3	Ye, Einshan	TAII-3
Triantafyllidis, Nicolas	TMI-3	Yen, Ching-Shih	TAII-1
Truskinovsky, L.	MAI-3	Yen, S. C.	MAII-1
Tsai, Lung	TMII-5	Yih, Huang	TMII-6
Tseng, F. G.	MAI-4	Yoon, Kee Bong	MAII-5
Tsujikawa, Y.	TAII-2	Yu, M.	TAII-4
Tvergaard, V.	WMII-2	Yu, X. Z.	TAII-6,WMII-4
Twu, J. T.	WMII-3	Yuan, Dongping	TAII-1

	Session #
Yuan, J.	MAI-7
Yuan, Yongbin	WMII-1
Yuceoglu, U.	TAI-7,TAII-1
Yun, T. Q.	TAII-3,WA-5
Zahraee, Mohammad A.	WMI-7
Zbib, Hussein M.	MAII-5,TAI-2, WMII-2
Zebib, Abdelfattah	WMI-4
Zhang, H.	WMI-7
Zhang, Jiping	MAII-5
Zhang, Shucheng	TAII-6
Zheng, Weiguo	TMI-4
Zufiria, Pedro J.	TMI-6